NASA/CP-1999-209704/VOL1/PT1

1999 NASA High-Speed Research Program Aerodynamic Performance Workshop

Volume I—Configuration Aerodynamics

Edited by
David E. Hahne
Langley Research Center, Hampton, Virginia

December 1999

The NASA STI Program Office . . . in Profile

Since its founding, NASA has been dedicated to the advancement of aeronautics and space science. The NASA Scientific and Technical Information (STI) Program Office plays a key part in helping NASA maintain this important role.

The NASA STI Program Office is operated by Langley Research Center, the lead center for NASA's scientific and technical information. The NASA STI Program Office provides access to the NASA STI Database, the largest collection of aeronautical and space science STI in the world. The Program Office is also NASA's institutional mechanism for disseminating the results of its research and development activities. These results are published by NASA in the NASA STI Report Series, which includes the following report types:

- TECHNICAL PUBLICATION. Reports of completed research or a major significant phase of research that present the results of NASA programs and include extensive data or theoretical analysis. Includes compilations of significant scientific and technical data and information deemed to be of continuing reference value. NASA counterpart of peer-reviewed formal professional papers, but having less stringent limitations on manuscript length and extent of graphic presentations.

- TECHNICAL MEMORANDUM. Scientific and technical findings that are preliminary or of specialized interest, e.g., quick release reports, working papers, and bibliographies that contain minimal annotation. Does not contain extensive analysis.

- CONTRACTOR REPORT. Scientific and technical findings by NASA-sponsored contractors and grantees.

- CONFERENCE PUBLICATION. Collected papers from scientific and technical conferences, symposia, seminars, or other meetings sponsored or co-sponsored by NASA.

- SPECIAL PUBLICATION. Scientific, technical, or historical information from NASA programs, projects, and missions, often concerned with subjects having substantial public interest.

- TECHNICAL TRANSLATION. English-language translations of foreign scientific and technical material pertinent to NASA's mission.

Specialized services that complement the STI Program Office's diverse offerings include creating custom thesauri, building customized databases, organizing and publishing research results . . . even providing videos.

For more information about the NASA STI Program Office, see the following:

- Access the NASA STI Program Home Page at ***http://www.sti.nasa.gov***

- Email your question via the Internet to help@sti.nasa.gov

- Fax your question to the NASA STI Help Desk at (301) 621-0134

- Telephone the NASA STI Help Desk at (301) 621-0390

- Write to:
  NASA STI Help Desk
  NASA Center for AeroSpace Information
  7121 Standard Drive
  Hanover, MD 21076-1320

NASA/CP-1999-209704/VOL1/PT1

1999 NASA High-Speed Research Program Aerodynamic Performance Workshop

Volume I—Configuration Aerodynamics

Edited by
David E. Hahne
Langley Research Center, Hampton, Virginia

Proceedings of a workshop sponsored by the National Aeronautics and Space Administration, Washington D.C., and held in Anaheim, California February 8–12, 1999

National Aeronautics and
Space Administration

Langley Research Center
Hampton, Virginia 23681-2199

December 1999

Available from:

NASA Center for AeroSpace Information (CASI)
7121 Standard Drive
Hanover, MD 21076-1320
(301) 621-0390

National Technical Information Service (NTIS)
5285 Port Royal Road
Springfield, VA 22161-2171
(703) 605-6000

PREFACE

The High-Speed Research Program sponsored the NASA High-Speed Research Program Aerodynamic Performance Review on February 8-12, 1999 in Anaheim, California. The review was designed to bring together NASA and industry High-Speed Civil Transport (HSCT) Aerodynamic Performance technology development participants in areas of: Configuration Aerodynamics (transonic and supersonic cruise drag prediction and minimization) and High-Lift. The review objectives were to: (1) report the progress and status of HSCT aerodynamic performance technology development; (2) disseminate this technology within the appropriate technical communities; and (3) promote synergy among the scientist and engineers working HSCT aerodynamics. The HSR AP Technical Review was held simultaneously with the annual review of the following airframe technology areas: Materials and Structures, Environmental Impact, Flight Deck, and Technology Integration. Thus, a fourth objective of the Review was to promote synergy between the Aerodynamic Performance technology area and the other technology areas within the airframe element of the HSR Program.

The work performed in the Configuration Aerodynamics (CA) element of the High-Speed Research Program during 1998 was presented in the following sessions:

Propulsion Integration
Analysis Methods
Design Optimization
Testing

The work performed in the High Lift (HL) element of the High-Speed Research Program during 1998 was presented in the following sessions:

High-Lift Configuration Development
Tools and Methods Development

The proceedings for the Aerodynamic Performance Annual Review are published in three volumes:

Volume I, Parts 1 and 2	Configuration Aerodynamics
Volume II, Parts 1 and 2	High Lift

AP Review Chairperson: David Hahne
NASA Langley Research Center

CONTENTS

*Part 2 is presented under separate cover.

Testing Session

Isolated Nozzle Analysis Using OVERFLOW

Tin-Chee Wong (AS&M)
Karen A. Deere (LaRC)
S. Paul Pao (LaRC)

Aerodynamic Performance Workshop
HSR Annual Airframe Review
Anaheim, CA
February 8 - 11, 1999

LaRC conducted a code validation study for the OVERFLOW code to ascertain its accuracy for boattail drag prediction. The OVERFLOW results compared favorably with the LaRC 16-ft TWT data, and prior CFD solutions from PAB3D and CFL3D.

The ultimate goal is to investigate the installation drag of the nacelle boattails with powered nozzles at transonic Mach numbers. The OVERFLOW solver was chosen because of its ability to accept volume overlapping structured grid for very complex airframe configurations. Structured grid components for representing the transonic nozzle boattail can be added to the BCAG grid for a TCA airframe with 2D bifurcated inlet and flow through nacelle without alteration.. The focus of this research was to determine the suitability of the OVERFLOW solver for accomplishing this ultimate goal.

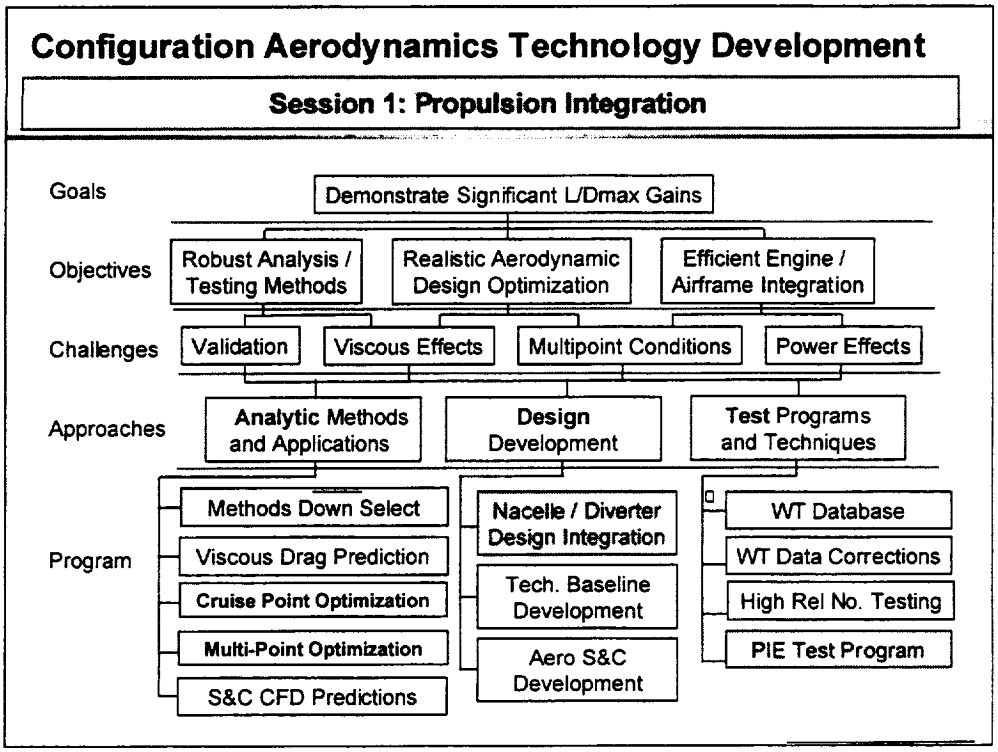

This study was performed under **High Speed Research II** - Configuration Aerodynamics

WBS 4.3.1.3.2: Propulsion Induced Effects

Milestone 4.3: Initial Propulsion Induced Effects

Coordination Responsibility: NASA Ames Research Center

Outline

- N1-S1 Rectangular Nozzle Boattail Geometry
- Review of Aerodynamic Features and Comparisons to Prior PAB3D Solutions
- Comparison of OVERFLOW Solutions to Experiment and Other CFD Solutions at M = 0.9, 1.11, 1.20
- Boattail Drag Prediction Assessment
- Work Plan for FY99

This presentation will first introduce the transonic nozzle boattail wind-tunnel model geometry, followed by an examination of aerodynamic features based on the current OVERFLOW solutions and the solutions obtained previously using PAB3D, comparisons of Cp on the flap surface between the OVERFLOW solutions, wind tunnel data, and solutions from other CFD codes, an assessment of boattail drag count prediction, and a work plan for FY99.

Isolated Nozzle Geometry (Transonic)

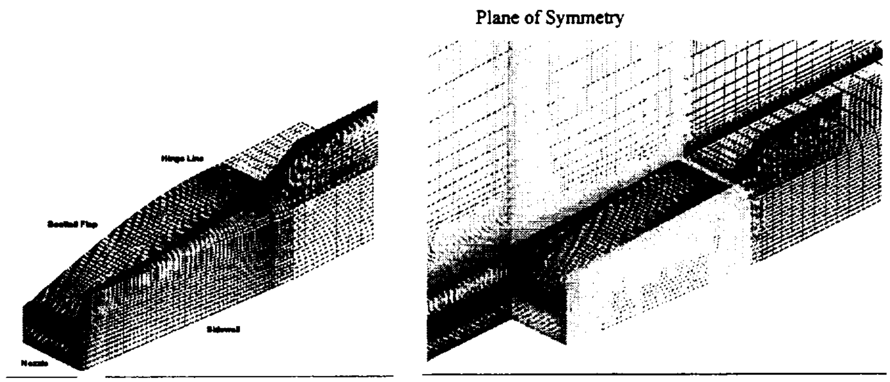

The N1 flap has a circular are profile between its hinge line and the flap trailing edge at the nozzle exit. The nominal nozzle flap angle setting is 8 degrees in reference to the nozzle horizontal plane of symmetry. Surface slope at the trailing edge is actually 16 degrees. The S1 sidewall has a taper angle of 4 degrees. The top of the side wall is rounded by a quarter circle according to the local thickness. The computational mesh represents a quarter of the nozzle configuration with two planes of symmetry. The upstream portion of this isolated nacelle model, not show in this figure, is a pointed forebody with super-elliptic cross sections. The total model length is 64 inches. The computational mesh used here for OVERFLOW analysis, other than volume overlap between blocks, is identical to the multiblock grid used for PAB3D (LaRC) and CFL3D (Boeing-LB) computations. The nozzle internal convergent-divergent flow path and the supersonic jet exhaust flow following the nozzle exit are included in the computational domain.

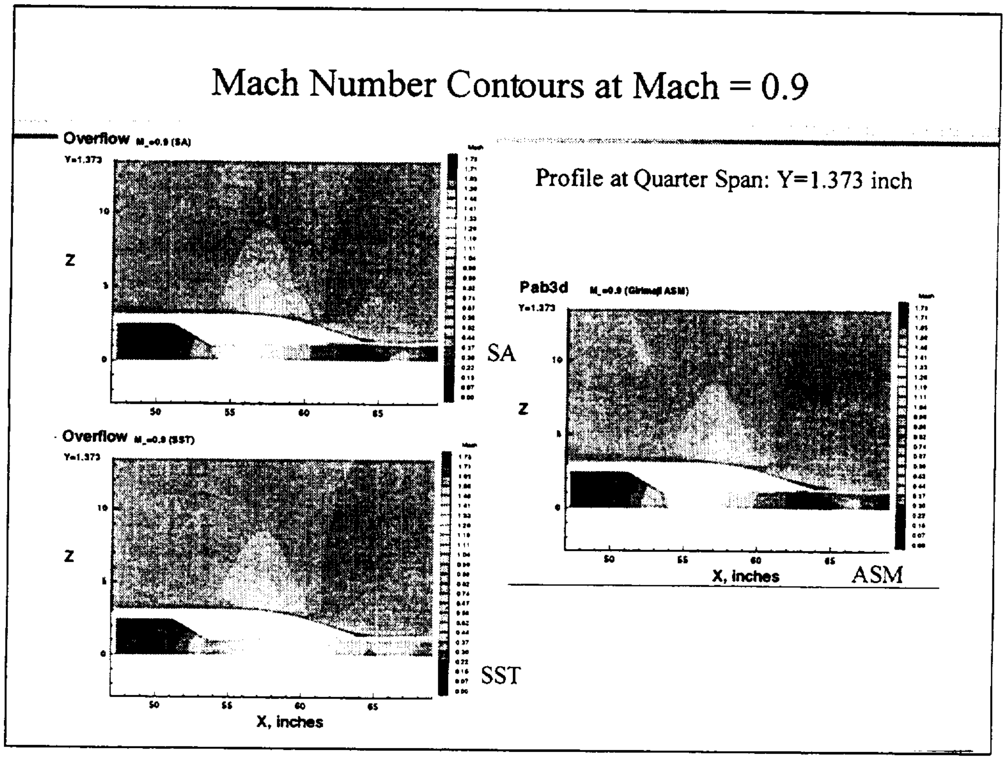

Two versions of the OVERFLOW solutions are shown on the left hand side: one based on the SA turbulence model and another based on the Menter's SST model. A corresponding PAB3D solution is shown on the right hand side which is computed using a two equation k-e turbulence model and the Girimaji algebraic Reynolds stresses. A local transonic expansion-compression pressure pattern can be seen in all three solutions. A small region of flow separation can be seen near the flap trailing edge. The nozzle internal flow path and the exhaust flow are also shown in this figure. The nozzle pressure ratio (NPR) is 5.0 for all three cases: M=0.9, 1.11, and 1.20. Important flow features to be demonstrated in the next three sets of flow quality figures are: flow expansion and recompression over the nozzle flap, shock boundary layer interaction, flow separation, and the formation of vortices as a result of cross flow over the top of the side wall.

Normalized Pressure Contours on Nozzle Flap

OVERFLOW:
SA Turbulence Model

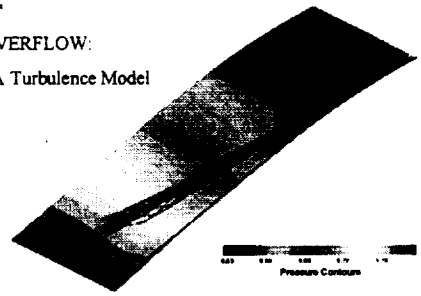

OVERFLOW:
SST Turbulence Model

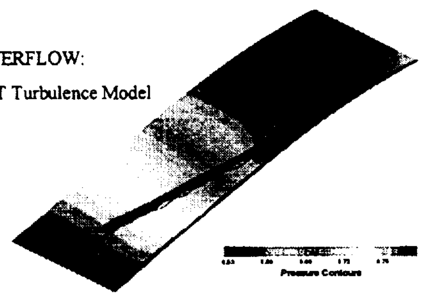

PAB3D: ASM Turbulence Model

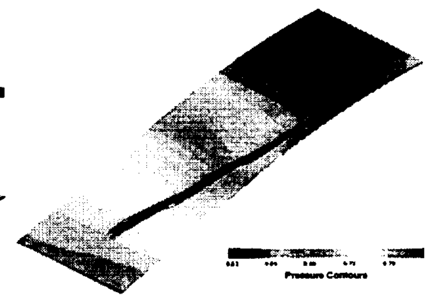

An isometric view of the normalized contour over the nozzle flap is shown in this figure. The pressure pattern near the hinge line is three dimensional in nature. As the flow proceed down the flap, the confinement of the side wall causes the pressure distribution to show typical two dimensional features. A particle trace, in red color, shows the position and width of the induced vortex over the side wall.

Mach Number Contours at M = 0.9

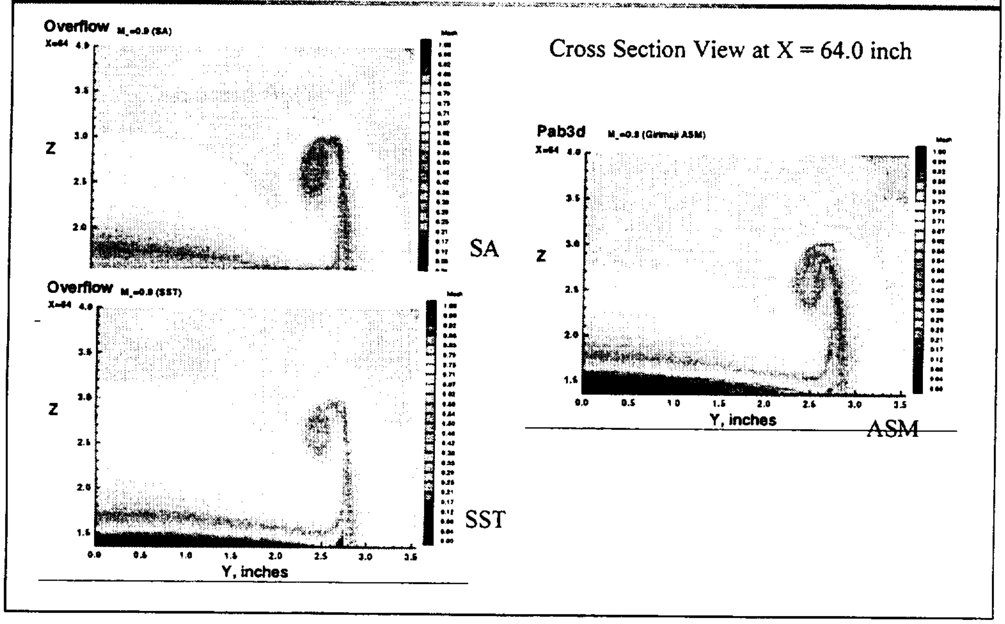

Mach number contours for a cross section at the trailing edge of the flap are show for the same solutions at M=0.9. The flow outside of the side wall is pulled over the top of the side wall toward the low pressure region above the nozzle flap. A strong vortex is formed inboard of the side wall. The induced change in pressure distribution on the flap surface should reflect a drag component equal to the momentum loss carried away by the detached vortex element. The difference in thickness of flow separation at the trailing edge of the flap can be seen in this figure.

Mach Number Contours at M = 1.11

Profile at Quarter Span: Y = 1.373

SA Turbulence Model

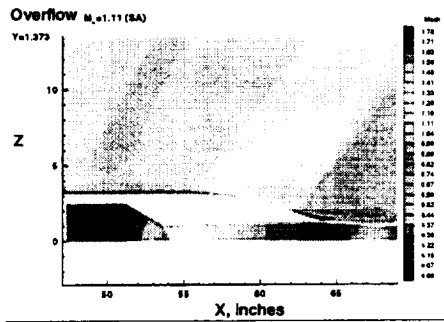

OVERFLOW

ASM Turbulence Model

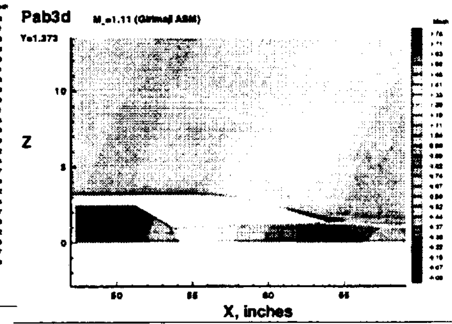

PAB3D

The OVERFLOW solutions for M=1.11 was computed by using the SA-turbulence model alone. The flow expansion over the flap starts at the hinge line, and continues much farther downstream over the flap. The expansion was eventually terminated by a shock. Shock boundary layer interaction has crated a flow separation which extend from the root of the shock down to the flap trailing edge. Since the NPR for the internal flow remains the same as the M=0.9 case, the internal and exhaust flow characteristics remains the same as before.

Normalized Pressure Contours on Nozzle Flap

Mach Number = 1.11

OVERFLOW: SA Turbulence Model

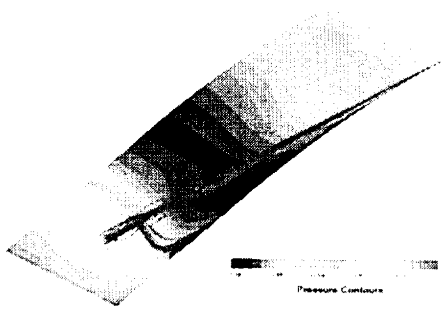

PAB3D: ASM Turbulence Model

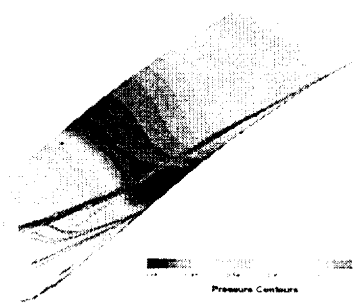

The normalized pressure contours for the OVERFLOW and the PAB3D solutions show significant differences in pressure distribution of the flow surface where most of the drag force is produced. While the low pressure area of the OVERFLOW solution covers a much larger area, the pressurization near the trailing edge is also much stronger. The particle traces for the two solutions are also quite different. The vortex as shown by the OVERFLOW solution is more diffused in appearance. Furthermore, clear entrainment paths from a significant length of the side wall directly to the vortex core region. The PAB3D solution, on the other hand, does not show such a pattern.

Mach Number Contours at M = 1.11

Cross Section View at X = 64.0 inch

SA Turbulence Model

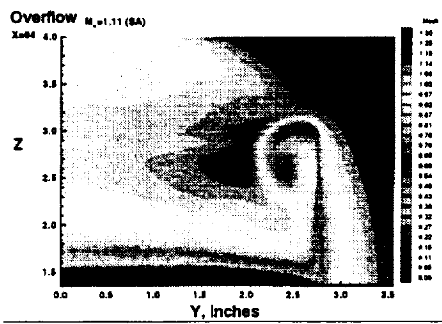

OVERFLOW

ASM Turbulence Model

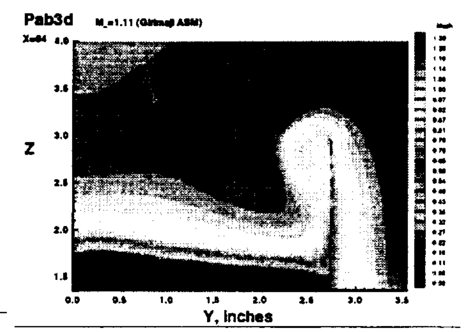

PAB3D

The vortex strength as shown by the OVERFLOW solution appears to be much more diffused than the corresponding vortex structure in the PAB3D solution. Flow separation over the flap surface for the OVERFLOW solution appears to be much thinner than its counterpart in the PAB3D solution. However, these qualitative flow features do not tell much about the change in drag count.

Velocity Vector Distribution at M = 1.11

Cross Section View at X = 64.0 inch

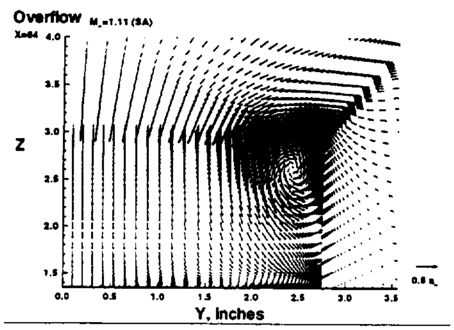

OVERFLOW: SA Turbulence Model

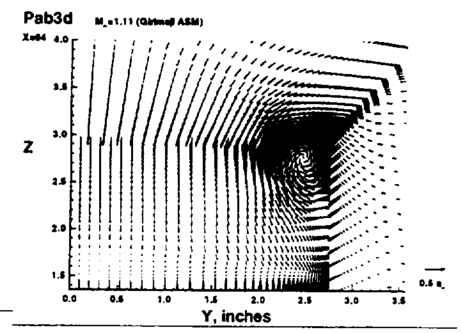

PAB3D: ASM Turbulence Model

In order to provide a better understanding of the quantitative nature of the vortices depicted in the OVERFLOW and the PAB3D solutions, velocity vector plots are shown in this figure. Velocity vectors of the same magnitude are located farther away from the vortex core in the OVERFLOW solution versus the PAB3D solution. Again, the significance of these patterns in terms of drag forces is not obvious with a quantitative analysis of various aerodynamic quantities such as mass flux over the side wall, momentum flux, and total circulation around the vortex.

Mach Number Contours at M = 1.2

Profile at Quarter Span: Y = 1.373

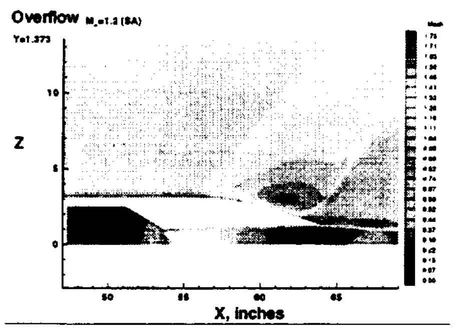

OVERFLOW: SA Turbulence Model

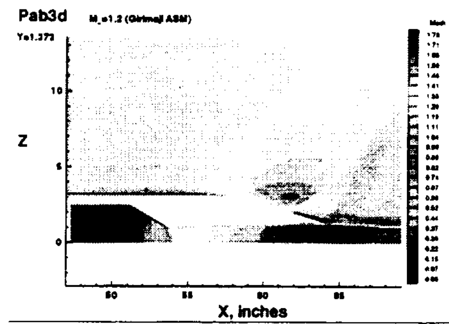

PAB3D: ASM Turbulence Model

The OVERFLOW and the PAB3D solution are very similar in this comparison. There are differences in shock position as well as the size and thickness of flow separation near the trailing edge of the nozzle flap. The shock is definitely stronger than the M=1.11 case, and the shock position is further downstraam on the flap surface. Again, the internal and the exhaust flow regions remain similar to the M=0.9 and 1.11 cases since the NPR remains the same as before: NPR = 5.0.

Normalized Pressure Contours on Nozzle Flap

Mach Number = 1.20

OVERFLOW: SA Turbulence Model

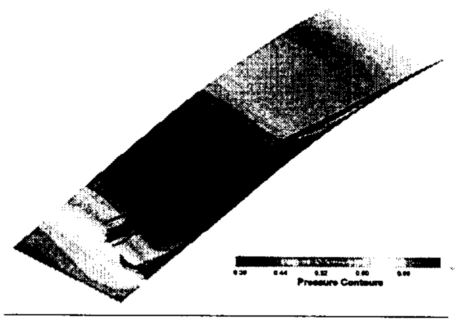

PAB3D: ASM Turbulence Model

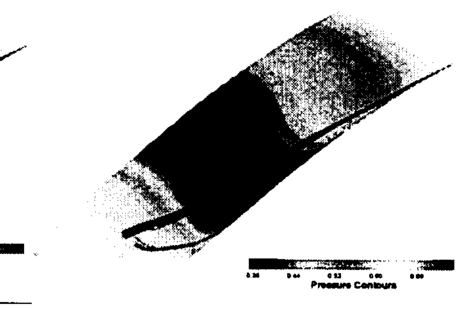

Other than the strong influences of the vortex, the flow expansion and compression patterns on the flap surface is decidedly two dimensional in appearance. As was in the M=1.11 case, the OVERFLOW solution, in comparison to the PAB3D solution as shown on the right hand side, has larger regions of low pressure as well as stronger recompression hear the trailing edge. In essence, these two effects cancels each other as far as overall drag forces are concern.

Mach Number Contours at M = 1.20

Cross Section View at X = 64.0 inch

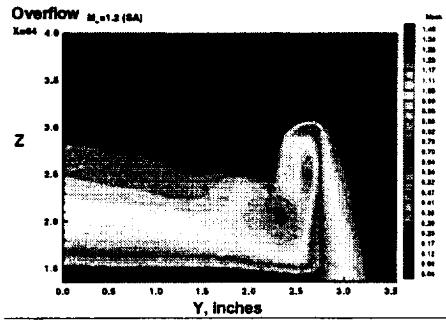

OVERFLOW: SA Turbulence Model

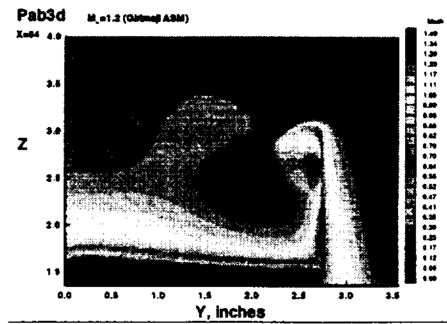

PAB3D: ASM Turbulence Model

Similar to the M=1.11 case, the PAB3D vortex is much stronger than the vortex in the OVERFLOW solution. The influence of the vortex on the flow field above the flap and near the side wall is evident in this figure.

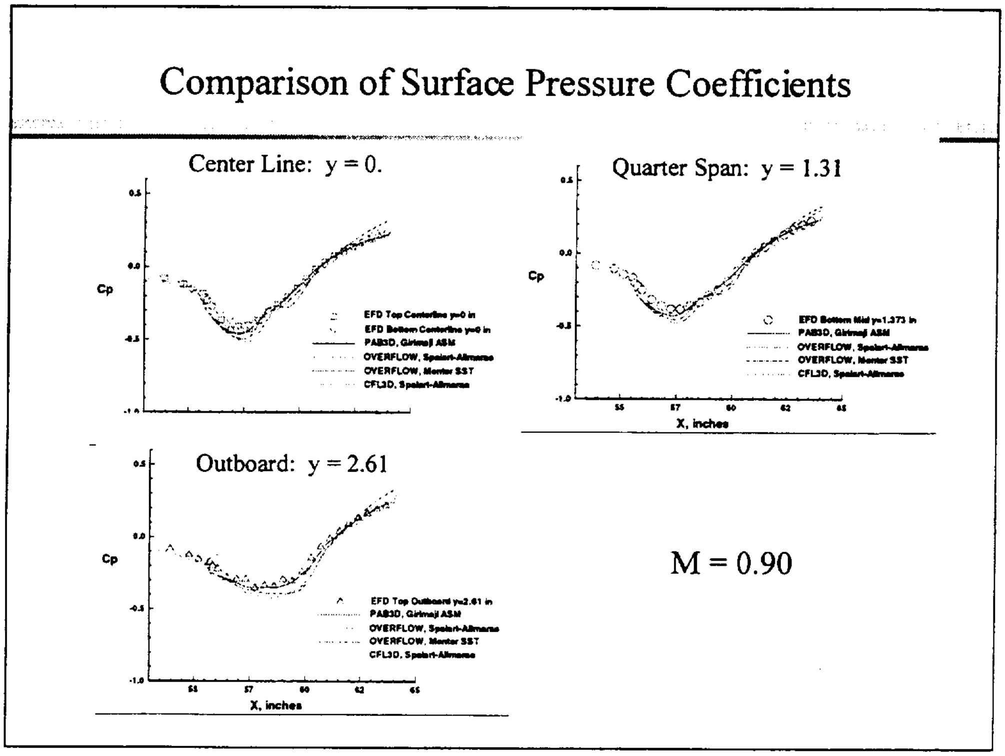

Wind tunnel measurement data and CFD results from OVERFLOW, PAB3D, and CFL3D are shown in this figure. The CFL3D solutions were obtained by Boeing Phantom Works at Long Beach. At M=0.9, the flow initiated supercritical expansion near the hinge line, and continued over the initial portion of the flap surface. Pressure recovery started at approximately at model station 57. Two OVERFLOW solutions, using the SA and the SST turbulence models are shown in this figure.

Good agreement is shown comparing to wind tunnel data and pressure coefficients computed by other codes. The OVERFLOW solutions show a stronger and more extended flow expansion over a significant portion of the nozzle flap. The pressure recovery of the OVERFLOW solution achieved a higher pressure at the trailing edge of the flap in comparison to the data and the PAB3D and CFL3D solutions.

Comparison of Surface Pressure Coefficients

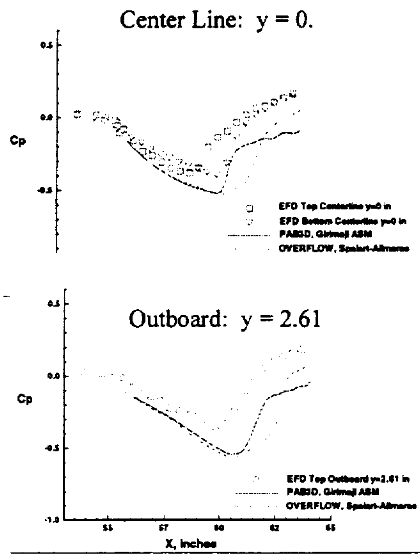

M = 1.11

The nozzle boattail measurements conducted in the LaRC 16-FT transonic wind tunnel had produced an accurate database for boattail drag. However, the overall model length of 64 inches was long than most other propulsion component models tested in this tunnel. At M=1.11, shock reflected from the tunnel wall had pressurized the base of the nozzle boattail. As a result, the measured pressure coefficient was raised to much higher values, with the strongest influence near the trailing edge of the nozzle flap. The correct value for pressure coefficient at this mach number is much better represented by the PAB3D solution.

Hence, only the CFD solutions between OVERFLOW and PAB3D can be compared. Flow expansion between the hinge line and model station 61 as predicted by the two solutions are nearly identical. Flow expansion in the PAB3D solution is terminated by a shock shortly downstream of station 61. The OVERFLOW solution shows further expansion before a shock is set up farther downstream. As was in the M=0.9 case, the recovery pressure at the flap trailing edge is higher for the OVERFLOW solution.

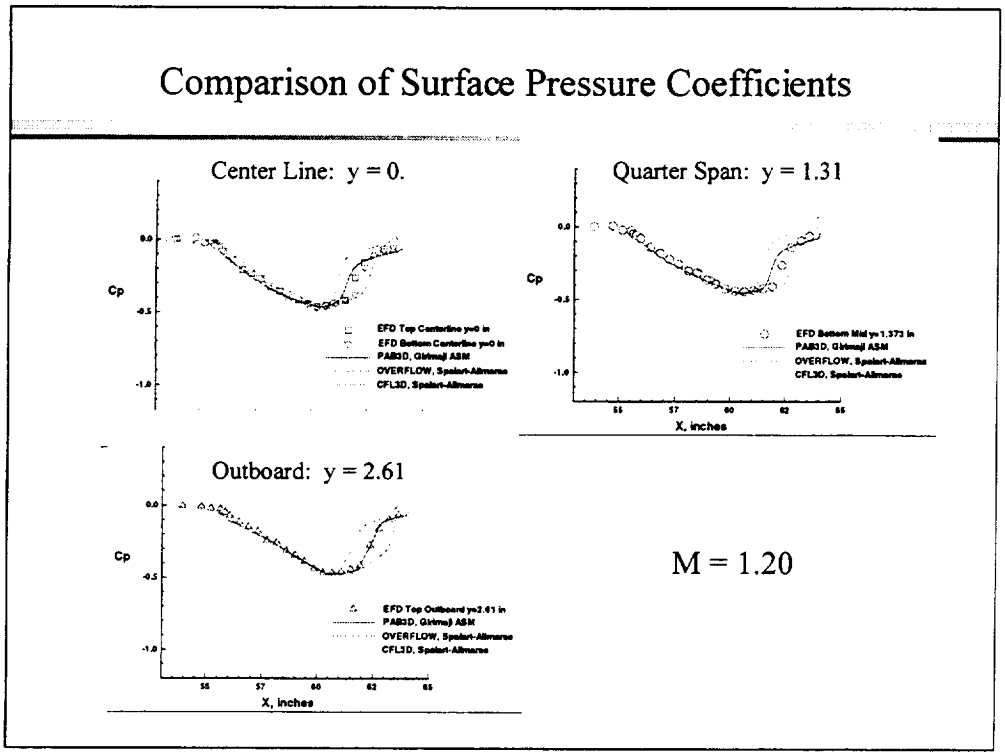

Wind tunnel measurement data and CFD results from OVERFLOW, PAB3D, and CFL3D are again shown in this figure. The CFL3D solutions were obtained by Boeing Phantom Works at Long Beach. At M=1.2, the pressure coefficients throughout the expansion phase up to model station 61. Although both OVERFLOW and CFL3D solutions were computed by using the SA turbulence model, the shock positions are downstream and upstream of the data for the two solutions, respectively. Both OVERFLOW and CFL3D solutions show recovery pressures which are higher than the measured data near the flap trailing edge. From previous studies of nozzle boattail pressure recovery using the PAB3D code, turbulence models have a strong effect on pressure recovery characteristics in the transonic speed range.

Integrated Boattail Drag Summary

	Cdp			Cd		
	Experiment	PAB3D	OVERFLOW	Experiment	PAB3D	OVERFLOW
M=0.9						
Sidewall	0.000065	0.000057	0.000502 SA		0.000137	0.000507
			0.000503 SST			0.000508
Flap	0.000109	0.000117	0.001207 SA		0.000187	0.001210
			0.001211 SST			0.001214
Nozzle	0.000174	0.000174	0.001710 SA	0.000324	0.000324	0.001717
			0.001715 SST			0.001721
M=1.11						
Sidewall	0.000062	0.000184	0.000295 SA		0.000257	0.000299
Flap	0.000289	0.000820	0.000589 SA		0.000864	0.000593
Nozzle	0.000351	0.001004	0.000884 SA	0.000501	0.001121	0.000892
M=1.20						
Sidewall	0.000168	0.000151	0.000253 SA		0.000211	0.000258
Flap	0.000843	0.000830	0.000473 SA		0.000882	0.000467
Nozzle	0.001011	0.000981	0.000726 SA	0.001161	0.001093	0.000734

These numbers shows a complex picture for boattail drag predictions in the transonic range. According the IMS method proposed by Hoyt Wallace (BPW), the presence of side walls would significantly modify the Mach number trends of nozzle boattail drag through the transonic range. The drag rise begins at approximately M=0.9. Drag rises rapidly beyond M=0.95, and continue to rise through M=1.1. For nozzle boattails without side walls, the drag coefficient begins to decline rapidly beyond M=1.10. However, the drag coefficient would maintain its peak value through M=1.2 before declining to much lower values.

The nozzle boattail measurements conducted in the LaRC 16-FT transonic wind tunnel had produced an accurate database for boattail drag. However, the overall model length of 64 inches was long than most other propulsion component models tested in this tunnel. At M=1.11, shock reflected from the tunnel wall had pressurized the base of the nozzle boattail. As a result, the measured drag coefficient was less than half of what would be expected by using the IMS method. The correct value for drag coefficient at this mach number is much better represented by the PAB3D solution.

Drag count computed using FOMOCO and the OVERFLOW solution at M=0.9 is 17.2, much higher than anticipated from either the experiment or the PAB3D solution. Drag counts at M=1.11 and 1.20 are 8.92 and 7.34, respectively, somewhat lower than the measured values for this configuration. The source of the differences are being investigated. The most likely sources of variation are the difference between upwind and central difference schemes and differences in turbulence models used in these computations. However, it remains possible that procedural errors could have been made in the force integration process.

Most of the drag forces resulted from flow expansion over the deflected nozzle flap. The side wall drag contribution is small for this geometry because the taper is 4 degrees. The full scale nozzle design would require a taper of at least 8 degree for closure of a much thicker side wall. Hence, the differences in side wall drag count between a wind t[illegible]l model and the full scale design should be noted.

Overall Remarks

- OVERFLOW VALIDATION
  - » Flow feature predictions are similar to prior PAB3D solutions
  - » Cp distribution compared favorably with LaRC 16-FT wind tunnel data and PAB3D solutions
  - » Shock position and magnitude of pressure recovery are different between CFD solutions and measured data (CFL3D solution was obtained by BWP-LB)
  - » Variation of drag count predictions is noted in this study; numerical scheme, turbulence model, or simply procedural error in force integration may be responsible
- Aerodynamics
  - » Understanding of aerodynamic features can lead to nozzle boattail design improvements and drag reduction
  - » CFD drag prediction is a useful tool for expanding nozzle boattail drag data base beyond range of wind tunnel measurements

No notes for this slide.

Future Plans

- HSR - FY99
  - » Add transonic nacelle grid components to TCA chimera grid constructed by BCAG (Chaney)
  - » Compute installed nozzle boattail drag components using OVERFLOW with SA turbulence model
  - » Powered effect will be included in the analysis
- Computational Methods Development
  - » Add chimera grid capability to PAB3D
  - » Compute same cases and compare all available results

The installed nacelle boattail study using OVERFLOW and a modified TCA chimera grid for Mach numbers 0.9, 1.10 and 1.20 will be completed within FY99. However, support for further studies of the installation effect, such as change in geometry or drag optimization will not be available. The proposal to extend PAB3D for chimera capability is based on its excellent ability to predict propulsion component performance for both internal flow and configuration aerodynamics. Support for such work could come from the base program or other sources.

PIE Nacelle Flow Analysis and TCA Inlet Flow Quality Assessment

C. F. Shieh, Alan Arslan, P. Sundaram, Suk Kim
The Boeing Company, Phantom Works - Long Beach
and
Mark J. Won
NASA Ames Research Center

High Speed Research Airframe Review
Anaheim, California
February 8-11, 1999

AMES
Research Center

BOEING

Outline

This presentation includes three topics: (1) Analysis of Isolated Boattail Drag, (2) Computation of TCA-installed nacelle effects on aerodynamic performance, and (3) Assessment of TCA inlet flow quality.

Outline

- Analysis of isolated PIE boattail drag at $M_\infty = 0.9$ and 1.1
- Computation of TCA-installed PIE nacelle effects at $M_\infty = 2.4$
- Assessment of TCA inlet flow quality at $M_\infty = 2.4$

Objective

The primary objective of this study is to analyze the effects of PIE (Propulsion Induced Effect) nacelle on TCA aerodynamic performance using Computational Fluid Dynamics techniques. This presentation includes three topics as mentioned earlier. The objectives for these topics are:

(1) For the isolated boattail study, the objective is to evaluate the boattail drag at critical transonic condition and to support Milestone 4-3. (2) For the TCA-installed case, the objective is to assess the PIE nacelle effects on aerodynamic performance at supersonic cruise condition and to support Milestone 4-14. (3) For the inlet flow quality study, the objectives are to obtain wind-tunnel test data, to evaluate the CFD computational capability for predicting the inlet flow Mach number and flow angle distributions, and to support Milestone 3-7. The wind-tunnel test was carried out by the NASA Ames Research Center and the CFD validation was performed by the Boeing Company, Phantom Works-Long Beach.

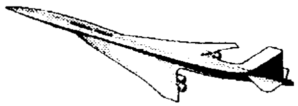

Objective

- Use CFD techniques to evaluate isolated PIE boattail drag at $M_\infty = 0.9$ and 1.1
  - WBS 4.3.1.3, Milestone 4-3
- Assess TCA-installed PIE nacelle effects on aerodynamic performance at $M_\infty = 2.4$
  - WBS 4.3.1.3, Milestone 4-14
- Evaluate inlet flow quality for TCA configuration at $M_\infty = 2.4$
  - WBS 4.3.1.3, Milestone 3-7

AMES
Research Center

BOEING

Approach

The CFL3D flow solver was used for this CFD study. For the isolated PIE nacelle boattail drag and TCA-installed nacelle calculations, the Spalart-Allmaras turbulence model was applied. The boattail study was carried out at transonic Mach numbers, $M_\infty = 0.9$ and 1.1. The results were compared with those of other HSCT nacelle configurations such as Ref. H Axi- and 2D-nacelles. For the TCA installed case, drag polar at supersonic cruise condition, $M_\infty = 2.4$, was calculated and compared with those of other HSCT configurations. The inlet flow quality was computed using Baldwin-Lomax turbulence model and the results were compared with the wind-tunnel data from the Test 1701 (3/1-3/13/98).

Approach

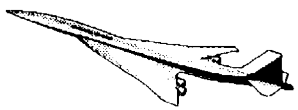

- Isolated PIE Nacelle
  - Compute boattail drag and compare the results to other isolated HSCT nacelles
- TCA-installed PIE Nacelle
  - Compute drag and compare the result to other nacelles installed on TCA
- Inlet Flow Quality Assessment
  - Compare CFD results to wind-tunnel test data
    - M, α, and β distributions

Isolated PIE Nacelle

The primary components of PIE nacelle are illustrated. It includes a 2-D inlet and inlet ramp, 2-D nozzle with aspect ratio 1.5, and nozzle flaps which is longer than the side-walls.

Isolated PIE Nacelle

- 2-D Inlet and Ramp, 2-D Nozzle (aspect ratio 1.5)
- Operational and Aero Reference Nozzles
- Mach 0.9 and 1.1 Nozzle Configurations
- Nozzle Flaps Longer than Side-walls
  - More complicated in CFD grid generation than Ref H 2-D

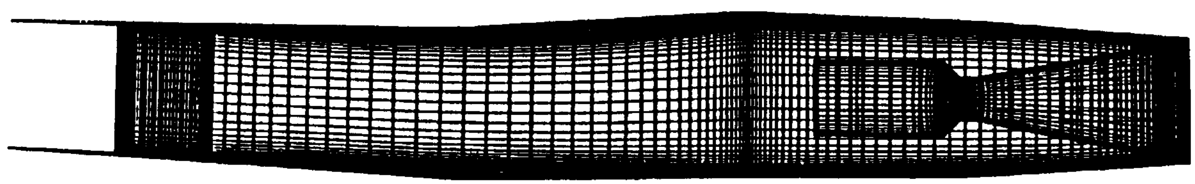

Isolated PIE nacelle Flow Analysis

CFL3D with the Spalart-Allmaras turbulence model was used for analysis. The boattail calculations were made at subsonic cruise (M_∞= 0.9, nozzle flap 13.0 degrees) and transonic climb (M_∞= 1.1, nozzle flap 12.6 degrees) conditions. The performance evaluation condition was set at $Re_c = 40 \times 10^6$, which is consistent with previous boattail drag analysis in HSR program. The reference case for boattail drag calculations is called the aero reference case, whose geometry is the same as the supersonic cruise nacelle configuration with the nozzle flap angle of 4 degrees. The aero reference nozzle was designed to match the Nozzle Pressure Ratio (NPR) requirements at transonic conditions.

Isolated PIE Nacelle Flow Analysis

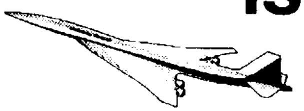

- CFL3D, Spalart-Allmaras Turbulence Model
- 2-D Nozzle with Aspect Ratio 1.5
- Transonic Flow Regime
  - Subsonic cruise: $M_\infty = 0.9$, nozzle flap angle of 13.0°
  - Transonic climb: $M_\infty = 1.1$, nozzle flap angle of 12.6°
- Performance Evaluation Point: $Re_c = 40 \times 10^6$
- Aero Reference Nozzle
  - Supersonic cruise configuration, nozzle flap 4°
  - Re-designed by Hoyt Wallace to satisfy NPR requirement at transonic conditions

BOEING

Isolated PIE-2D Nacelle

Flow patterns and pressure distributions at $M_\infty = 1.1$ are shown for the supersonic (the reference case) and the transonic boattail configurations. The boattail drag at transonic speed is defined as the difference in drag between the transonic and the supersonic (the reference case) boattail configurations at transonic flow condition. As shown in the figure, the flow expansion over the nozzle flap hinge line for the transonic boattail configuration causes a local low pressure region and, therefore, a higher pressure drag comparing with the supersonic boattail configuration.

Isolated PIE–2D Nacelle

C_p and Streamlines on Surface, $M_\infty = 1.1$, $Re_c = 40 \times 10^6$

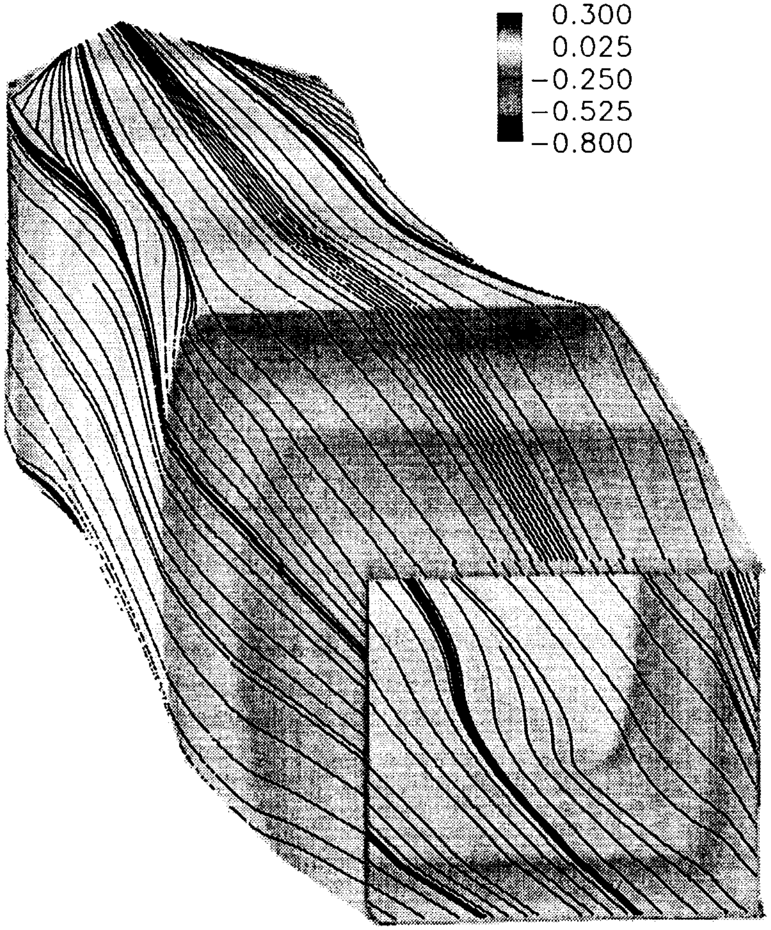

Supersonic Boattail

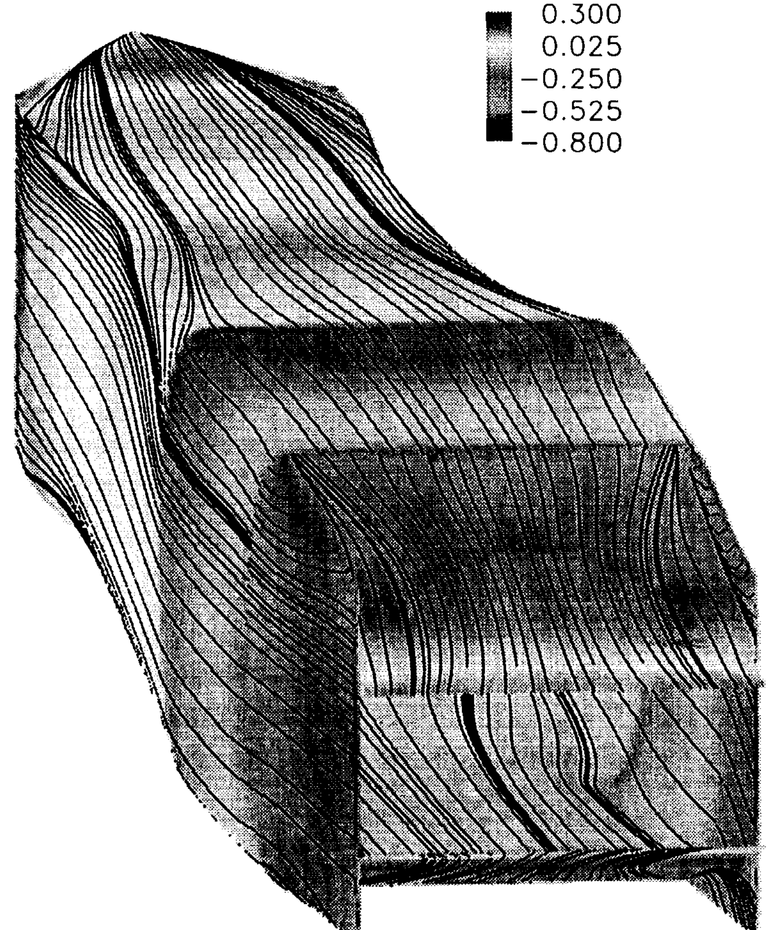

Transonic Boattail

BOEING

Isolated Nacelle Boattail Drag

The PIE 2-D nacelle boattail drag is compared with previous results of Ref. H 2-D and Ref. H Axi configurations. In general, the boattail drag at $M_\infty = 1.1$ is approximately 4 to 5 cts. higher than the $M_\infty = 0.9$ case. For $M_\infty = 1.1$, The TCA PIE 2-D boattail drag is 0.77 cts. higher than the Ref. H 2-D nacelle configuration. The isolated 2-D nacelle boattail drag is approximately 1 ct. higher than the Axi case.

Isolated Nacelle Boattail Drag

High Speed Configuration Aerodynamics

CFL3D N-S, (S-A), $\alpha = 0^\circ$, $Re_c = 40 \times 10^6$

			Transonic Nacelle	Supersonic Nacelle	Boattail Drag
M_∞=1.1	TCA PIE 2-D (AR=1.5)	C_{Dp}	9.87	3.06	6.81
		C_{Dv}	3.37	2.49	0.88
		C_D	13.24 cts.	5.55 cts.	7.69 cts.
	Ref. H 2-D (AR=1.2)	C_{Dp}	8.42	1.58	6.84
		C_{Dv}	2.10	2.02	0.08
		C_D	10.52 cts.	3.60 cts.	6.92 cts.
	Ref. H Axi	C_{Dp}	7.57	1.57	6.00
		C_{Dv}	2.16	2.57	- 0.41
		C_D	9.73 cts.	4.14 cts.	5.59 cts.
M_∞=0.9	Ref. H 2-D (AR=1.2)	C_{Dp}	2.27	0.40	1.87
		C_{Dv}	2.07	2.08	- 0.01
		C_D	4.34 cts.	2.48 cts.	1.86 cts.
	Ref. H Axi	C_{Dp}	1.07	0.21	0.86
		C_{Dv}	2.83	2.50	0.33
		C_D	3.90 cts.	2.71 cts.	1.19 cts.

	C_D (M_∞ = 1.1)
TCA PIE 2-D	7.69
Ref. H 2-D	6.92
ΔC_D	0.77 cts.

	C_D (M_∞ = 1.1)	C_D (M_∞ = 0.9)	ΔC_D
Ref. H 2-D	6.92	1.86	5.06
Ref. H Axi	5.59	1.19	4.40 cts.
$C_{D\,2D} - C_{D\,Axi}$	1.33 cts.	0.67 cts.	-------

BOEING

Isolated Boattail Drag

The isolated boattail drag at $M_\infty = 1.1$ for the PIE-2D, Ref H 2-D, and Ref H Axi configurations are summarized here. Also shown are the results from the IMS (Integrated Mean Slope) method. In general, the boattail pressure drag is about 6.8 cts., and it is nearly the same between the PIE 2-D and the Ref. H 2-D configurations.

Isolated Boattail Drag

High Speed Aerodynamics, Long Beach

CFL3D N-S (S-A) and IMS Results, $M_\infty = 1.1$, $Re_c = 40 \times 10^6$

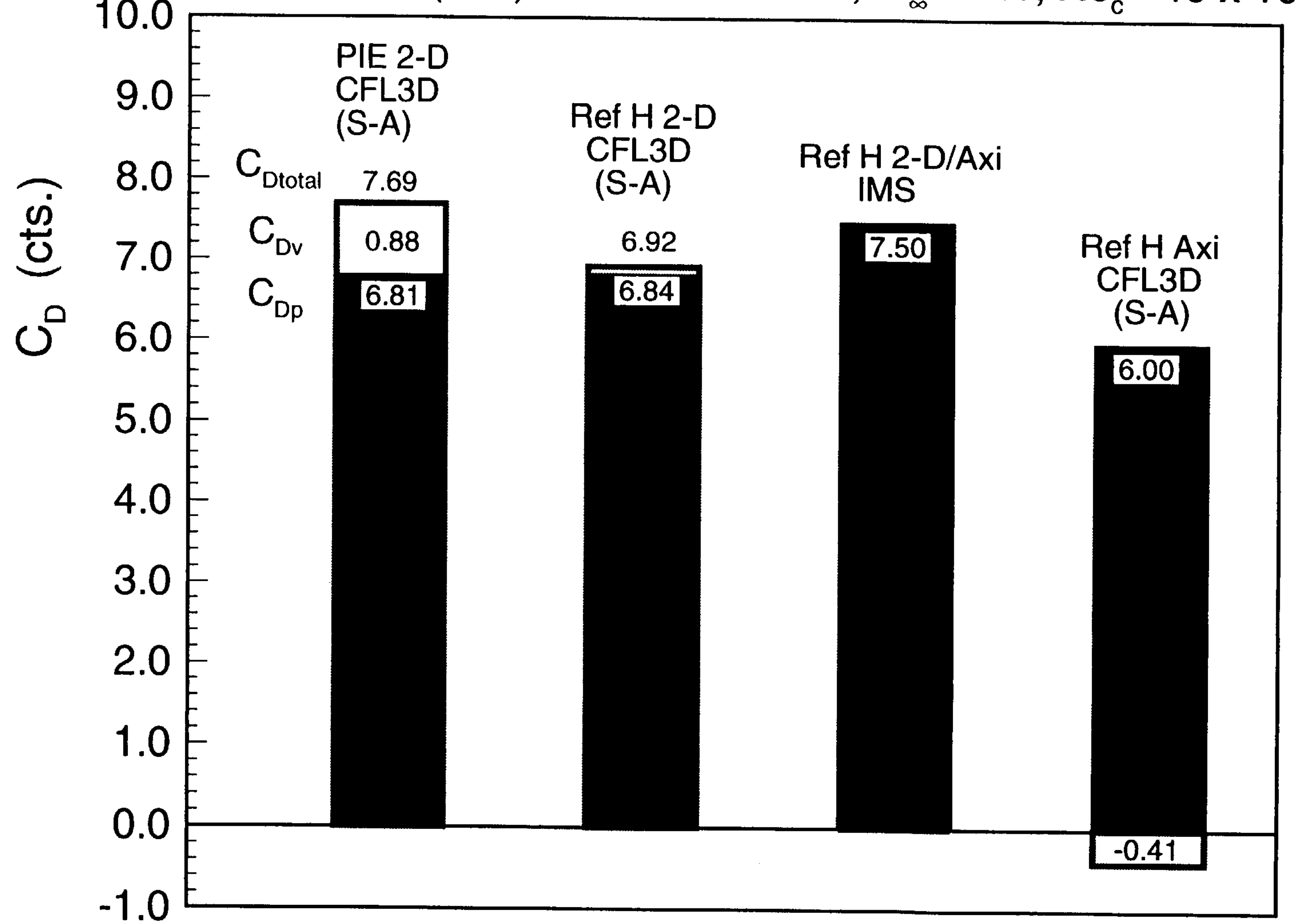

TCA-Installed PIE Nacelle Analysis

To evaluate the installed PIE nacelle effects on TCA aerodynamic performance, the installation drag of the PIE nacelles at cruise condition is analyzed and compared with the baseline nacelles. The analysis is based on the CFL3D Navier-Stokes solutions with the Spalart-Allmaras turbulence model at $M_\infty = 2.4$, $Re_c = 6.36 \times 10^6$ for the flow-through nacelle configuration.

TCA-Installed PIE Nacelle Analysis

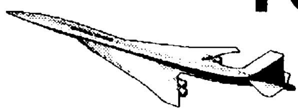

High Speed Configuration Aerodynamics

- CFL3D, Spalart-Allmaras Turbulence Model
- Supersonic Cruise at Wind-Tunnel Conditions
  - $M_\infty = 2.4$, $Re_c = 6.36 \times 10^6$
  - Flow-through nacelles
  - Nozzle aspect ratio of 1.2 and 1.5

BOEING

Lower Surface Pressure Contours for the TCA W/B/N/D Configuration

The wing lower surface pressure contours in the vicinity of the nacelles for the TCA W/B/N/D configurations with axi and 2-D inlet nacelles are compared. Two shock systems are shown for the wing lower surface pressure contours for 2-D inlets. They are: (1) the nacelle shocks and (2) the diverter leading-edge shocks. It appears that the 2-D inlet has weaker diverter leading-edge shocks than the axi inlets. This is expected as the flow in the diverter leading-edge region has been observed to be slower than the axi-inlet case. An interesting feature is observed for the 2-D inlets with the flow expansion regions extended upstream forming two "horn" shapes near each diverter. This effect is perhaps due to the diverter channel flow that expands over the nacelle rectangular edges in front of the diverters.

Lower Surface Pressure Contours

CFL3Dhp N-S, Spalart-Allmaras, M_∞=2.4, C_L = 0.1, Re_c = 6.36 x10^6
TCA W/B/N/D Configuration

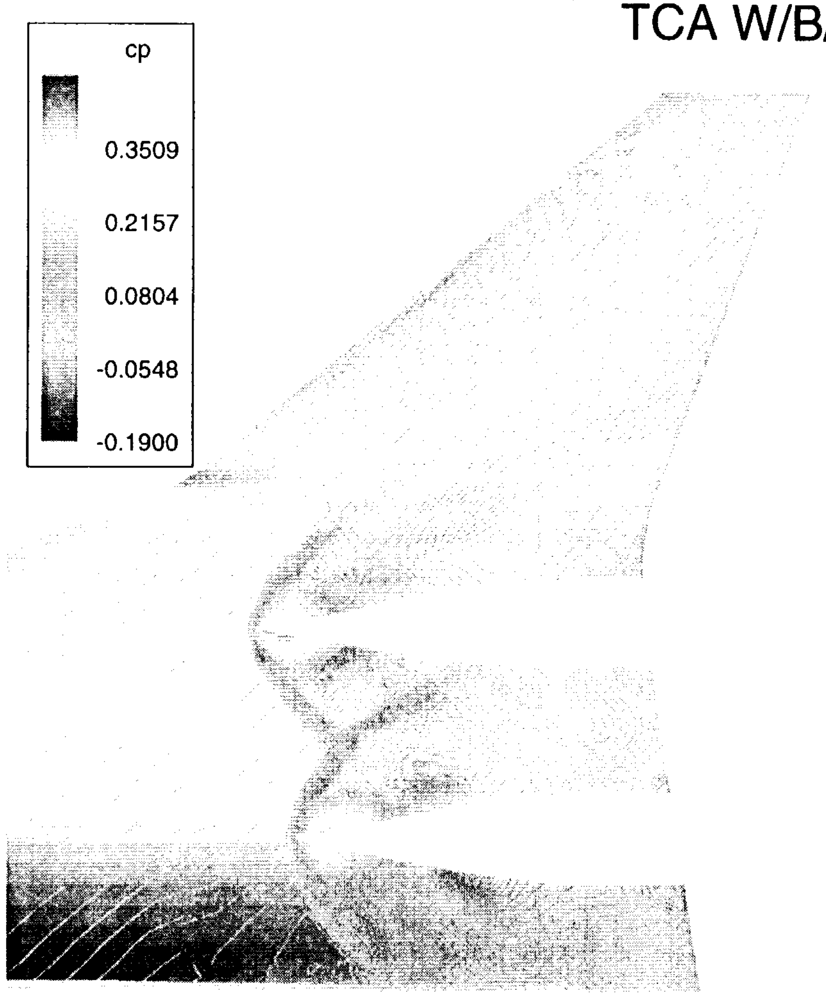

Axi Inlet/2-D Nozzle, AR= 1.2

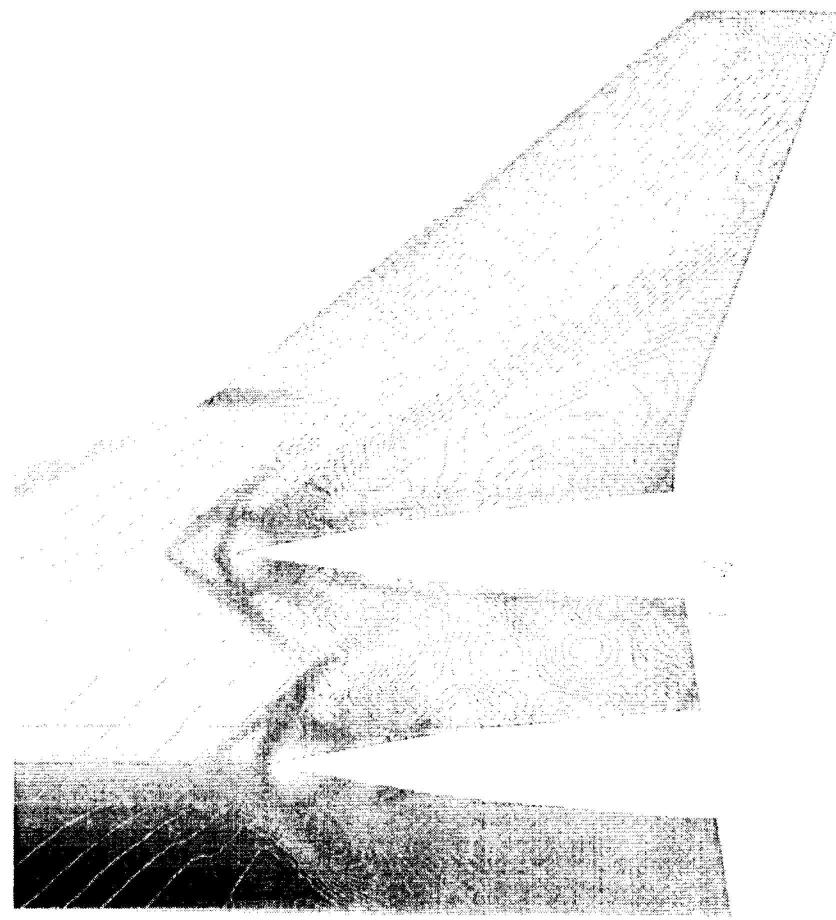

2-D Inlet/2-D Nozzle, AR= 1.5

PIE Nacelle Analysis on TCA at Cruise

The computed total pressure drag and total drag for various TCA nacelle configurations are shown. The results of PIE 2-D nacelles (nozzle aspect ratio 1.5) are compared with the axi and 2-D inlets with 2-D nozzle (aspect ratio 1.2) cases.

The total drag predictions show that the PIE 2-D nacelles have about 1.7 counts more drag than the axi and 2-D inlet nacelle configurations with nozzle aspect ratio 1.2. The pressure drag predictions show that the PIE nacelles have similar performance as the reference axi inlet/2-D nozzle case, and the reference 2-D inlet/2-D nozzle (nozzle aspect ratio 1.2) nacelles have about 0.5 counts less pressure drag than the PIE nacelles.

PIE Nacelle Analysis on TCA at Supersonic Cruise

High Speed Configuration Aerodynamics

CFL3D N-S, S-A , $M_\infty = 2.4$, $Re_c = 6.36 \times 10^6$

Pressure Drag for Three TCA Installed Nacelles

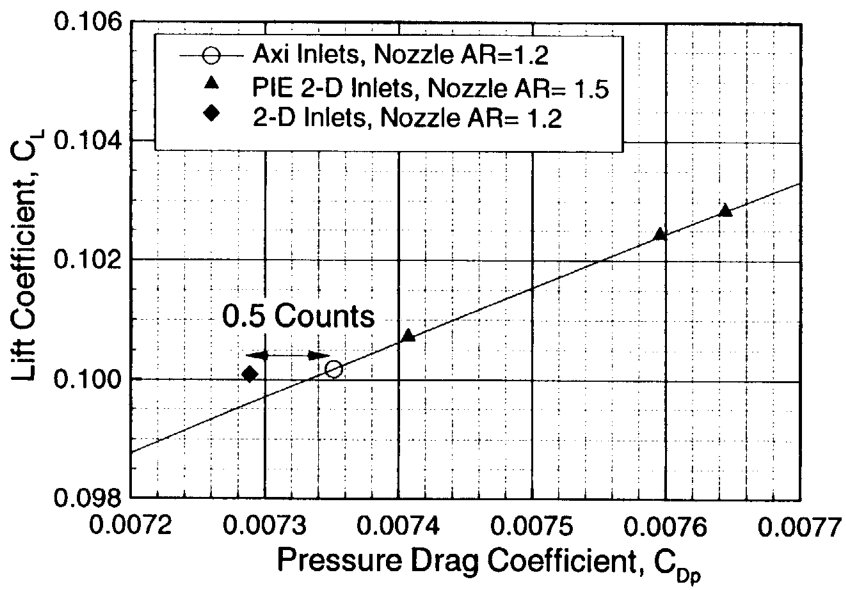

Total Drag for Three TCA Installed Nacelles

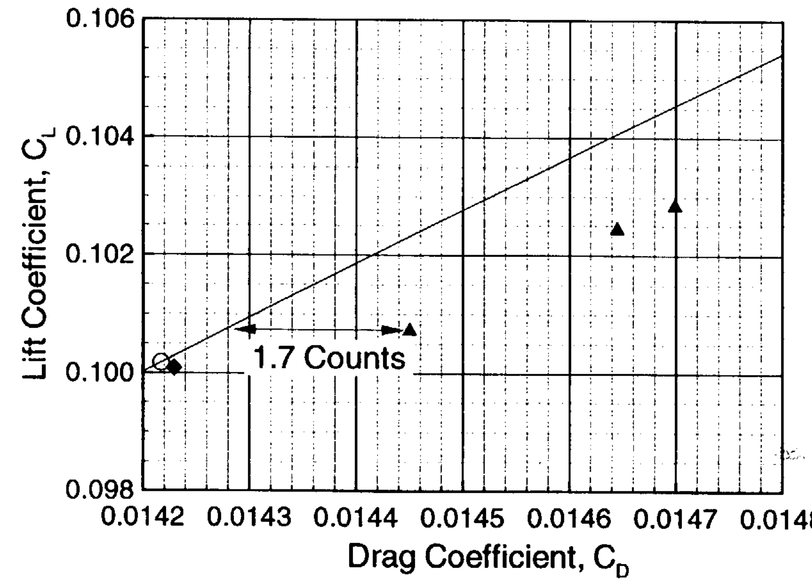

BOEING

TCA Inlet Flow Quality Assessment

The TCA inlet flow quality assessment studies included a wind-tunnel test study and a CFD analysis. The wind-tunnel test study was carried out for the baseline TCA, i.e. the TCA configuration with Axi inlets/2-D nozzles (nozzle aspect ratio 1.2). Details of the test procedure and test results were presented at the 3rd HSR Config Aero Testing Workshop, AMES Research Center, August, 1998. Highlights of the test data related to the CFD validations are given in this paper.

For the CFD validation, Navier-stokes solutions were obtained using CFL3D with Baldwin-Lomax turbulence model. Effects of angle-of-attack and side-slip were studied. The solutions were compared with the wind-tunnel test data. The results were used to assess the inlet flow qualities. The requirements for Mach number and flow-angle variations across the inlet face are less than or equal $\pm0.01$and $\pm0.25°$, respectively.

TCA Inlet Flow Quality Assessment

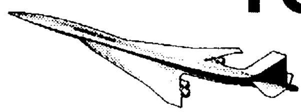

High Speed Configuration Aerodynamics

- Obtain Wind-tunnel Test Data on Baseline TCA
  - 1.675%-scale model, $M_\infty = 2.4$, $Re_c = 6.36 \times 10^6$
  - 5-hole cone probe rake for flow survey
  - 3rd HSR Config Aero Testing Workshop, August 1998
- Validate CFL3D Navier-Stokes Results
- Assess Inlet Flow Quality
  - $|\Delta M| \leq 0.01$
  - $|\Delta \alpha| \leq 0.25°$
  - $|\Delta \beta| \leq 0.25°$

AMES
Research Center

Rake Offset Arrangement

The rake offset arrangements used in the wind-tunnel test are shown. The test data released for CFD validation were based on the 2x4 rake arrangement.

Rack Offset Arrangement

High Speed Configuration Aerodynamics

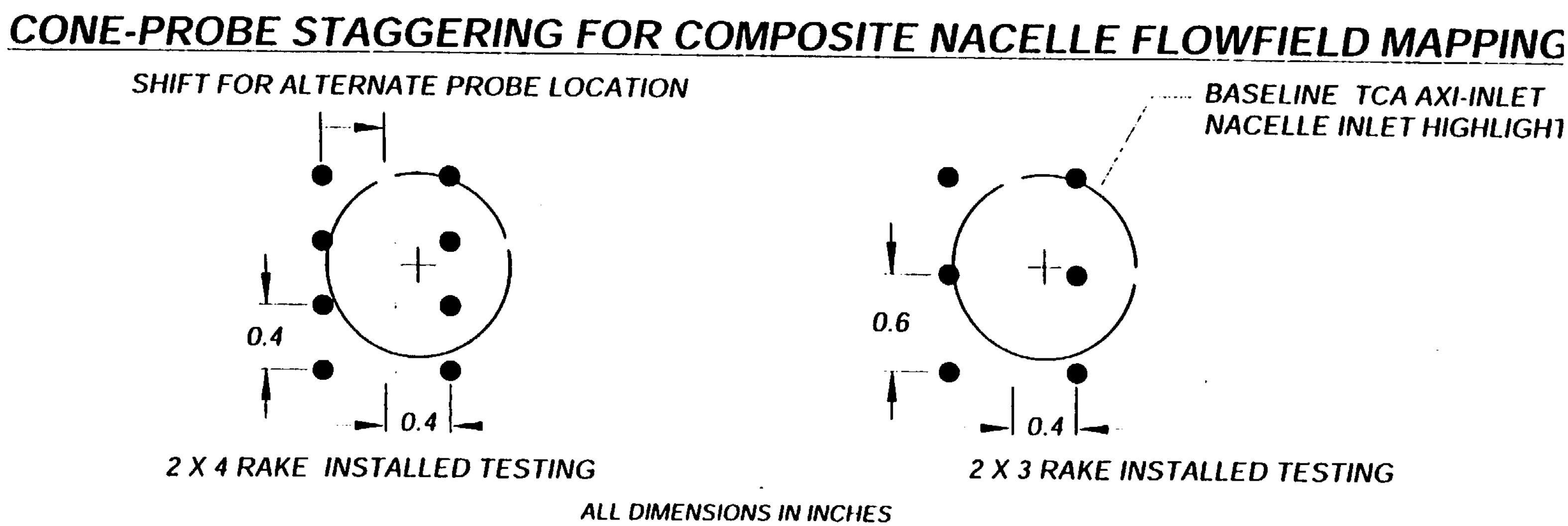

AMES
Research Center

BOEING

Instrumentation Array for Inlet Flowfield Study

The instrumentation array for TCA inlet flow quality study is shown. Also shown is the wing location relative to the array. The z-coordinates are shown in inches in full-scale. The fuselage nose (x,y,z)-coordinate is (0,0,226.8).

Instrumentation Array for Inlet Flowfield Study

High Speed Configuration Aerodynamics

TCA W/B, UPWT Wind-tunnel Test #1701

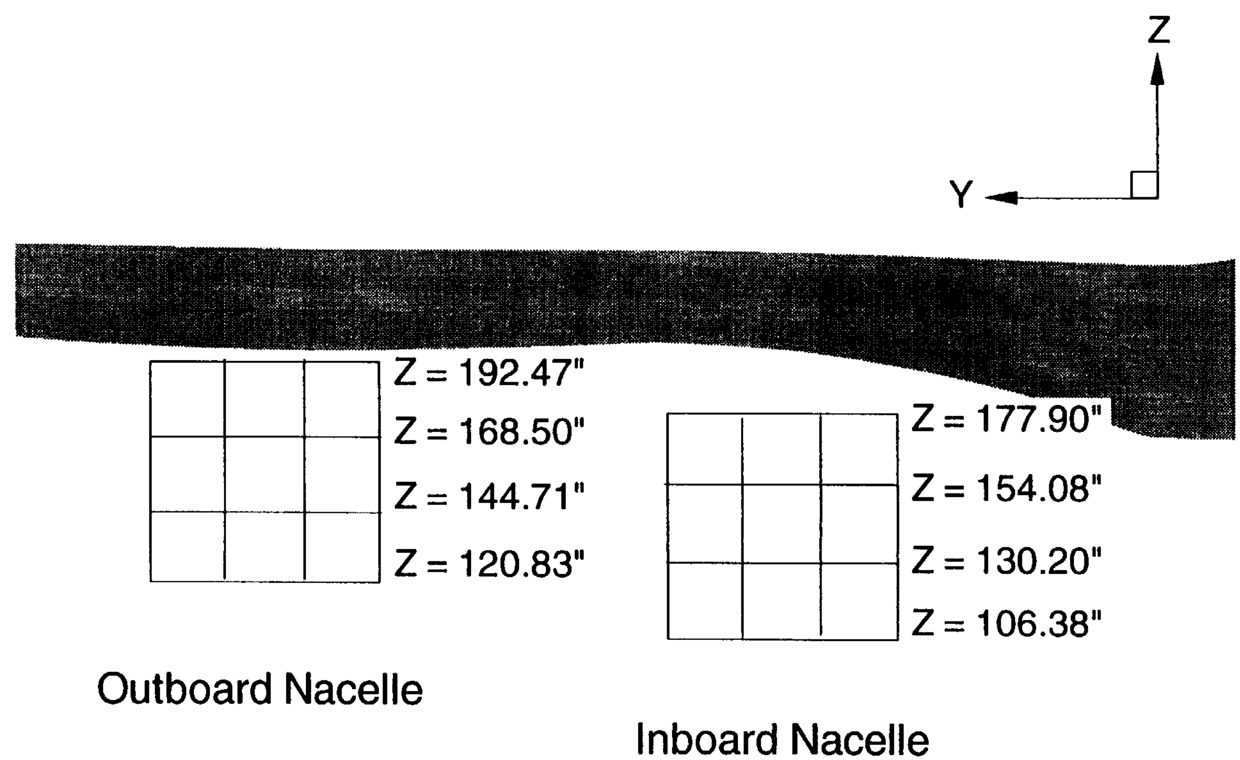

Inlet Flowfield Data Measurement Accuracy

The wind-tunnel data measurement accuracy for Mach number and flow angles are evaluated through wind-tunnel data calibration. The total accuracy for measurements are ±0.035 and ±0.2° for Mach number and flow angle measurements, respectively.

Inlet Flowfield Data Measurement Accuracy

- Total accuracy of measurement includes:
  - w.t. condition and force balance calibrations
  - Instrumentation precision
  - Data representation (curve fitting)
- Data are calibrated for
  - M: 2.15 to 2.40
  - α: 0° to 10°
  - β : ± 4°
- Total accuracy for measurements are:
  - M : ± 0.035
  - α , β : ± 0.2°

TCA Nacelle Inlet Mach Number Variation, M_∞=2.4, α=4°, β=0°

The computed inlet Mach number distributions and the wind-tunnel test data are shown for α=4°, β=0°. In general, the CFD solutions agree with the wind-tunnel data except the station z=106.38" of the inboard inlet, The maximum difference in Mach number between CFD and the wind-tunnel test data is 0.11 at that station. At the outboard inlet, high data fluctuation is observed in testing results.

TCA Nacelle Inlet Mach Number Variation

High Speed Configuration Aerodynamics

CFL3D B-L, W/B, $M_\infty = 2.4$, $\alpha = 4^\circ$, $\beta = 0^\circ$, $Re_c = 6.36 \times 10^6$
Wind-tunnel data from UPWT Test 1701

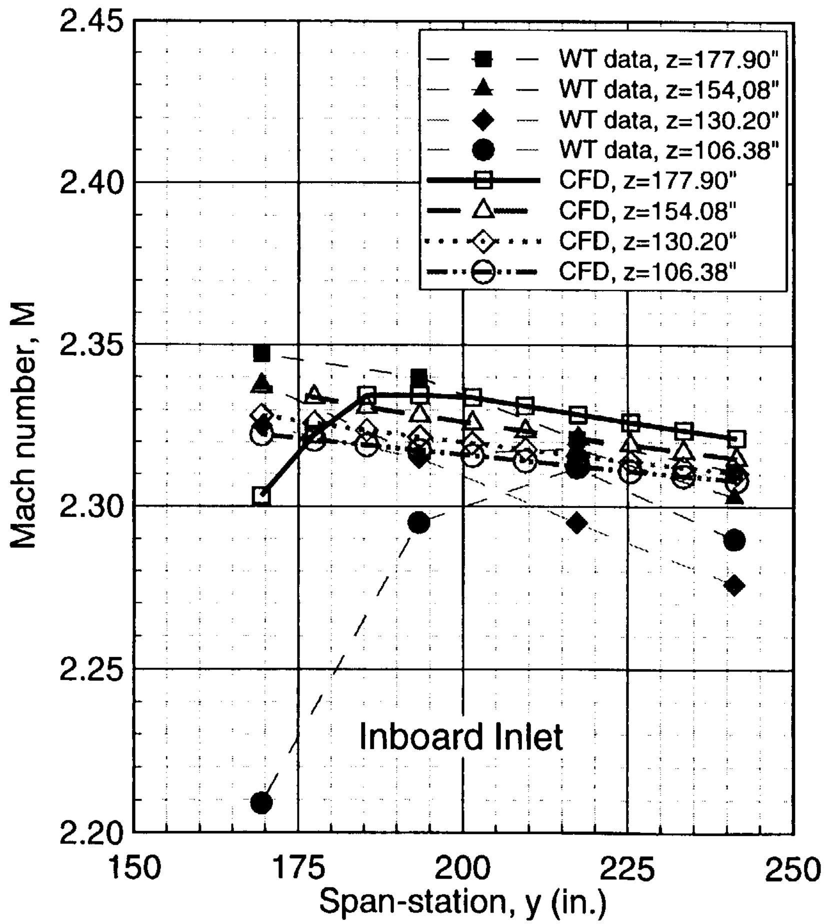

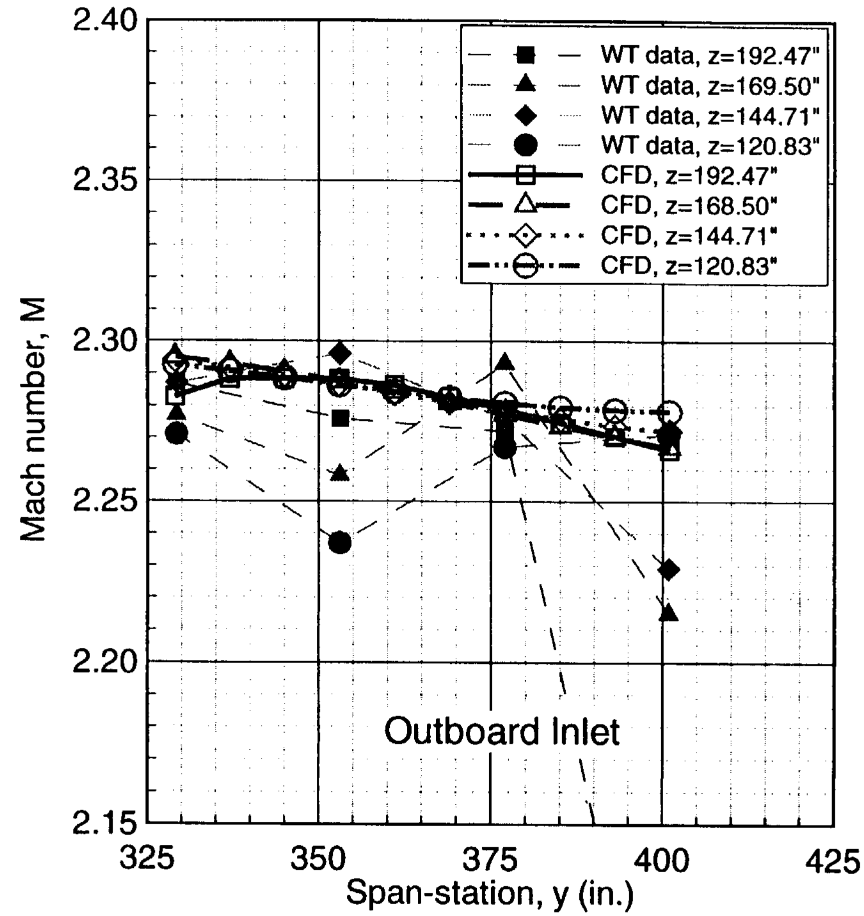

BOEING

TCA Nacelle Inlet Upflow Variation, M_∞=2.4, α=4° , β=0°

The computed inlet upflow distributions and the wind-tunnel test data are shown for α=4°, β=0°. In general, the CFD solutions agree with the wind-tunnel data at both the inboard and outboard inlets with the wind-tunnel test results showing some data fluctuations.

TCA Nacelle Inlet Upflow Variation

High Speed Configuration Aerodynamics

CFL3D B-L, W/B, $M_\infty = 2.4$, $\alpha = 4^\circ$, $\beta = 0^\circ$, $Re_c = 6.36 \times 10^6$
Wind-tunnel data from UPWT Test 1701

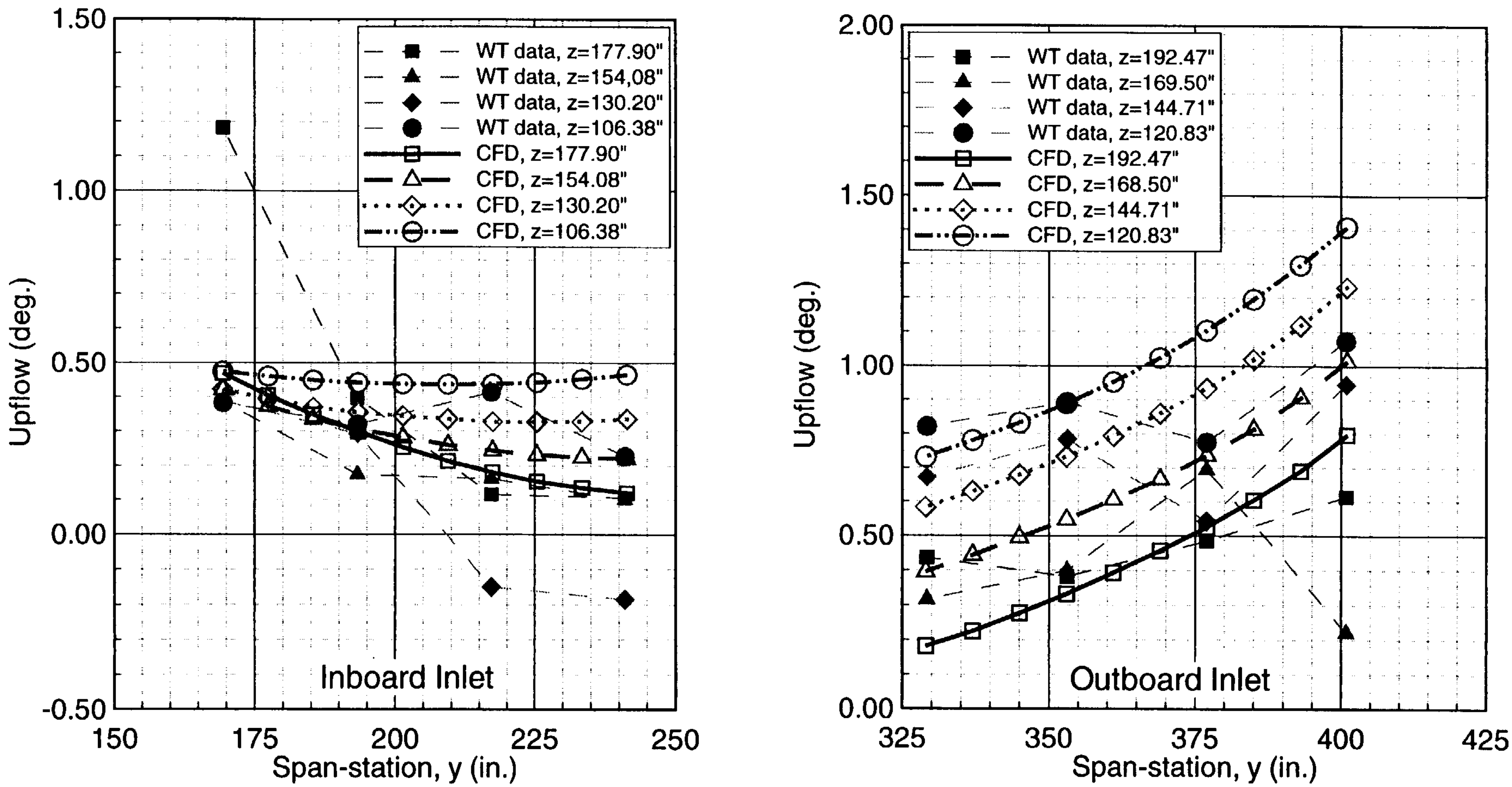

BOEING

TCA Nacelle Inlet Crossflow Variation, M_∞=2.4, α=4°, β=0°

The computed inlet crossflow distributions and the wind-tunnel test data are shown for α=4°, β=0°. The CFD solutions indicate that the crossflow angle variations are less than 0.3° and 0.9° at the inboard and outboard inlet, respectively.

TCA Nacelle Inlet Crossflow Variation

High Speed Configuration Aerodynamics

CFL3D B-L, W/B, $M_\infty = 2.4$, $\alpha = 4^\circ$, $\beta = 0^\circ$, $Re_c = 6.36 \times 10^6$
Wind-tunnel data from UPWT Test 1701

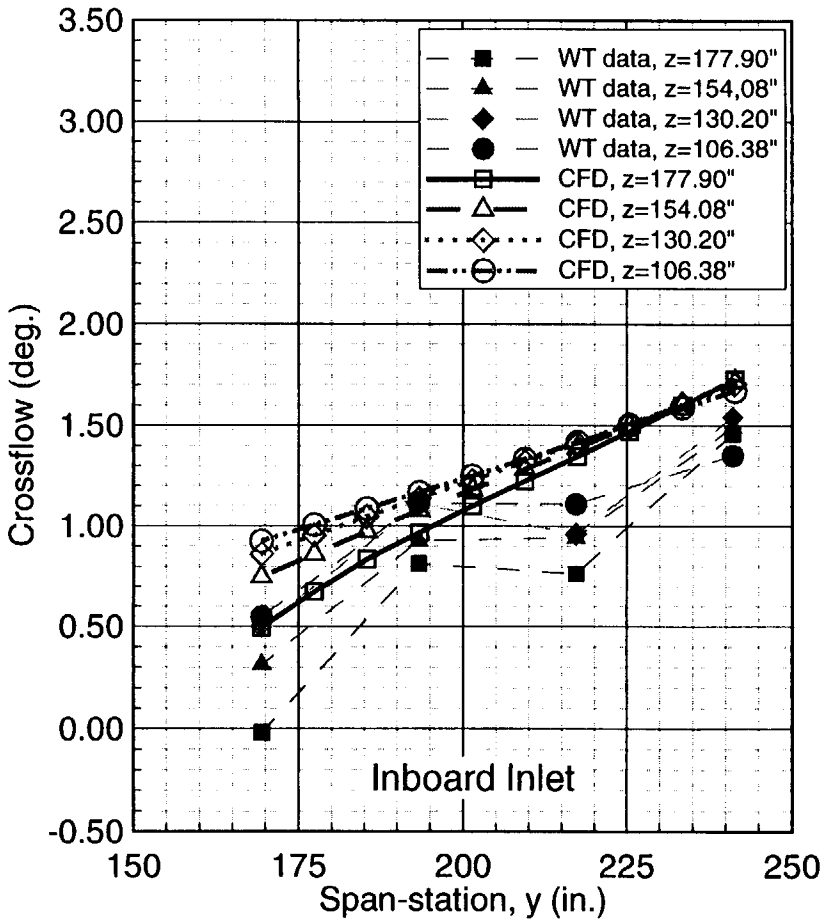

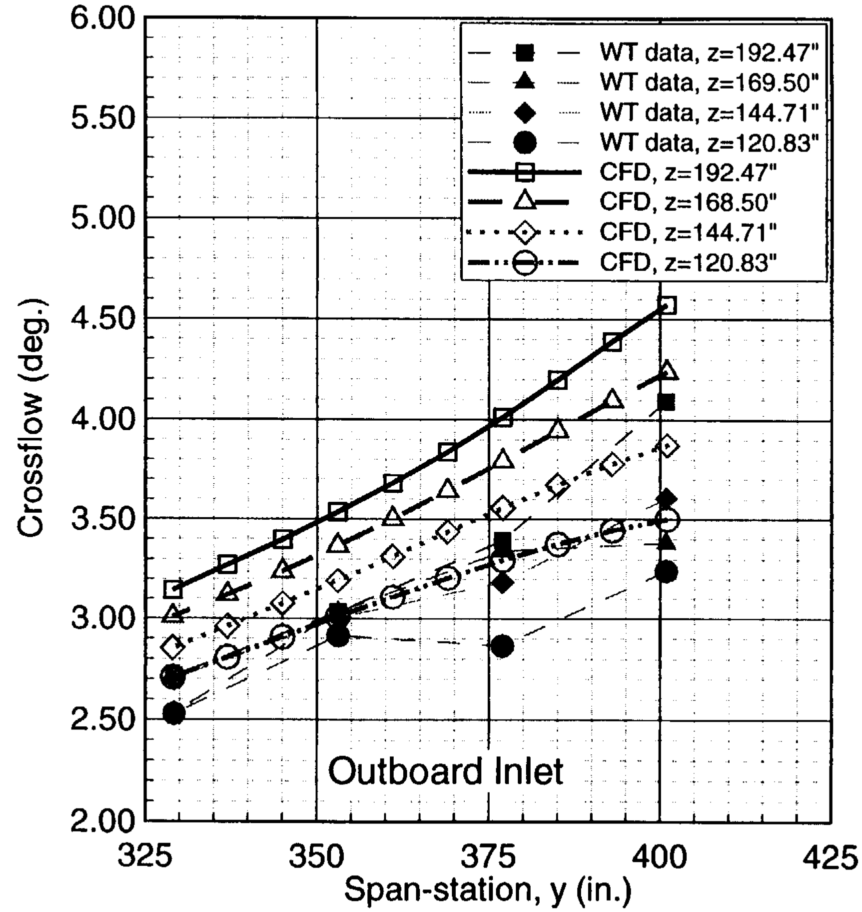

BOEING

TCA Nacelle Inlet Mach Number Variation, M_∞=2.4, α=4° , β=4°

A comparison between the computed inlet Mach number distributions and the wind-tunnel test data is shown for α=4°, β=4°. The data represent the windward inlets results. Similar to the α=4°, β=0° case, large data fluctuation in the wind-tunnel test results is seen at the outboard inlet. The CFD results indicate that the Mach number variations are less than 0.04 at the inboard inlet.

TCA Nacelle Inlet Mach Number Variation

High Speed Configuration Aerodynamics

CFL3D B-L, W/B, $M_\infty = 2.4$, $\alpha = 4^\circ$, $\beta = 4^\circ$, $Re_c = 6.36 \times 10^6$
Wind-tunnel data from UPWT Test 1701

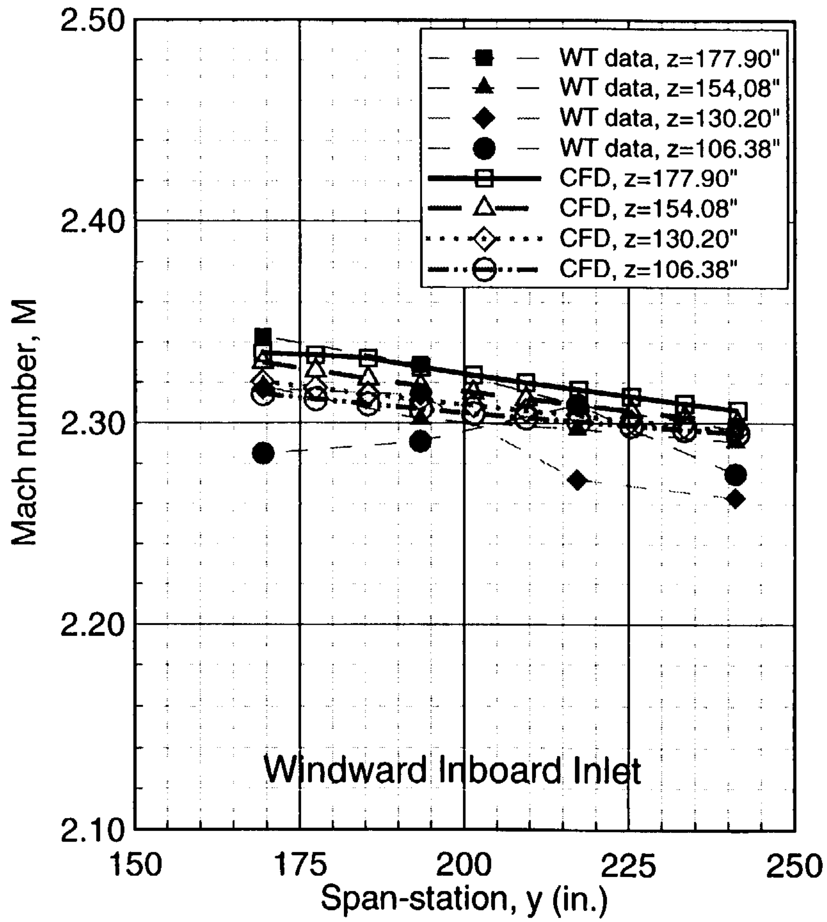

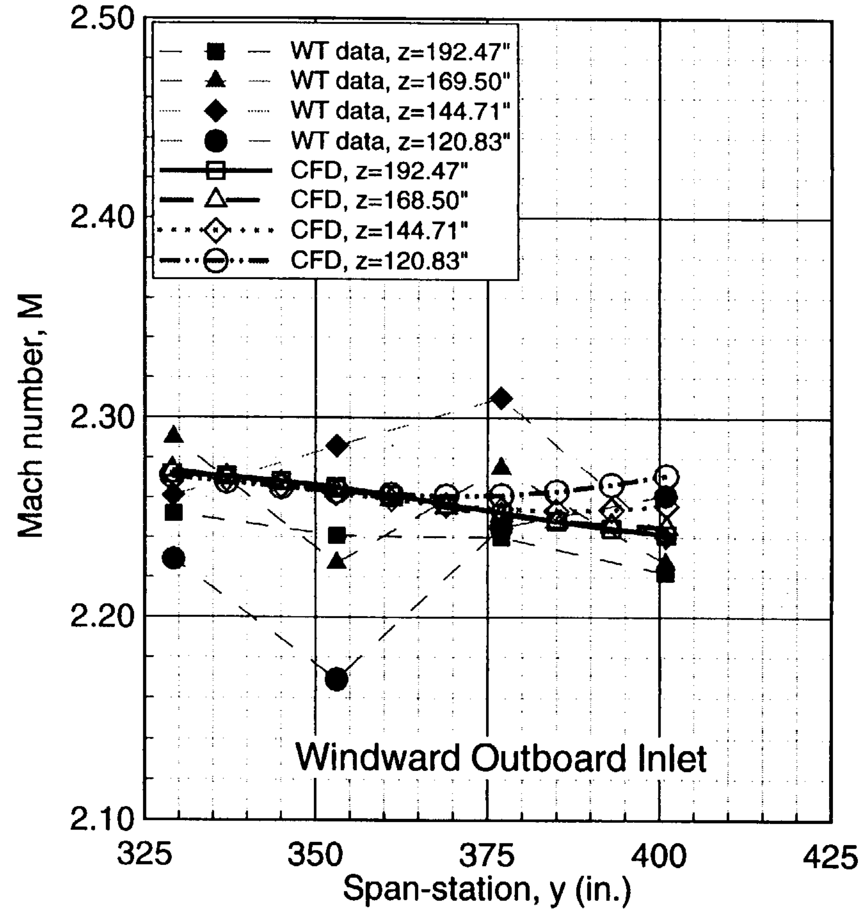

TCA Nacelle Inlet Upflow Variation, M_{∞}=2.4, α=4°, β=4°

The computed inlet upflow distributions are compared with the wind-tunnel test data are shown for α=4°, β=4°. The data represent the windward inlets results. At both of the inboard and outboard inlets, high data fluctuations in wind-tunnel test results are observed.

TCA Nacelle Inlet Upflow Variation

High Speed Configuration Aerodynamics

CFL3D B-L, W/B, $M_\infty = 2.4$, $\alpha = 4^\circ$, $\beta = 4^\circ$, $Re_c = 6.36 \times 10^6$
Wind-tunnel data from UPWT Test 1701

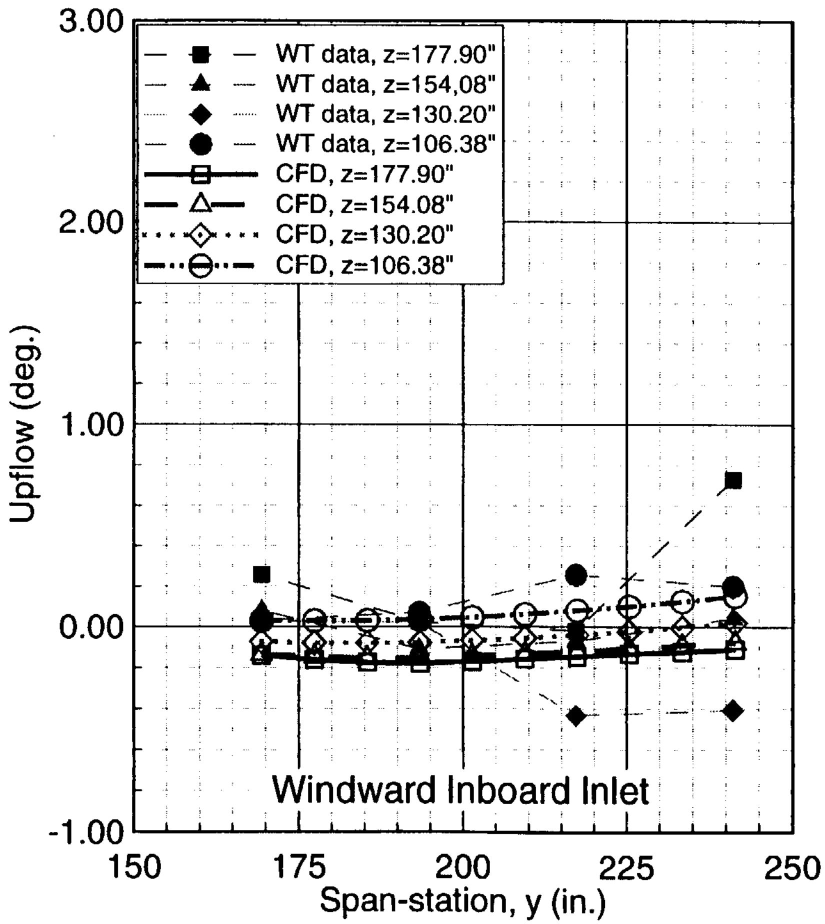

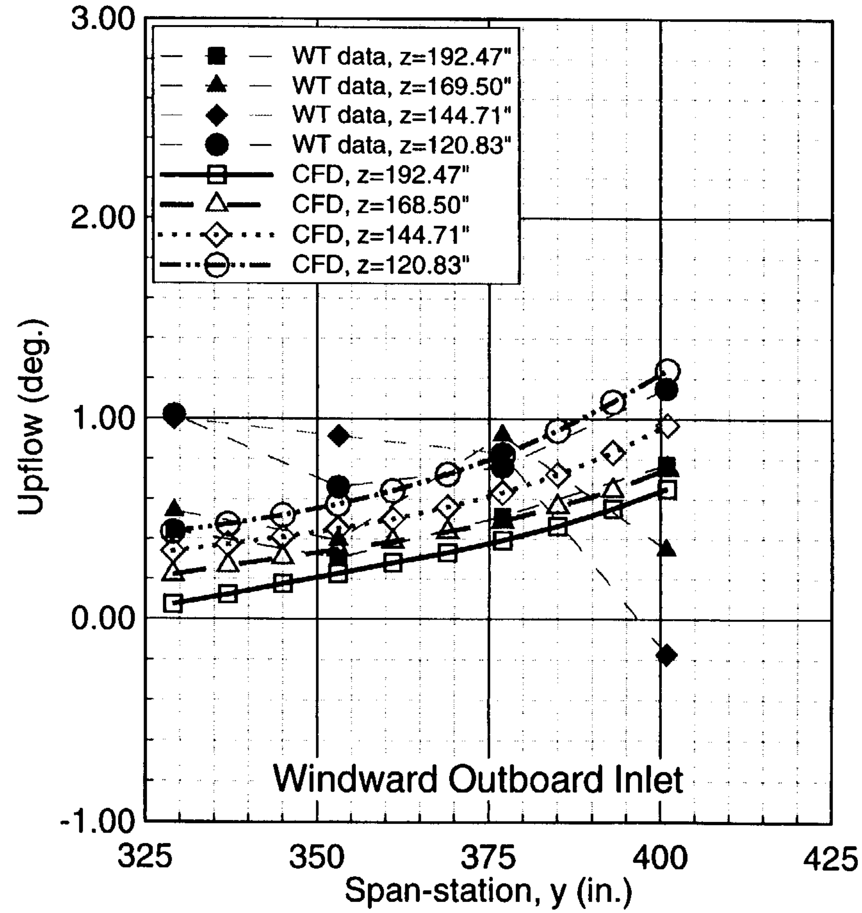

BOEING

TCA Nacelle Inlet Crossflow Variation, $M_\infty=2.4$, $\alpha=4°$, $\beta=4°$

The computed inlet crossflow distributions are compared with the wind-tunnel test data are shown for $\alpha=4°$, $\beta=4°$. The data represent the windward inlet results. The CFD results indicate that the crossflow variations are less than 0.4° and 0.6° at the inboard and outboard inlet, respectively.

TCA Nacelle Inlet Crossflow Variation

High Speed Configuration Aerodynamics

CFL3D B-L, W/B, $M_{\infty} = 2.4$, $\alpha = 4^{o}$, $\beta = 4^{o}$, $Re_{c} = 6.36 \times 10^{6}$
Wind-tunnel data from UPWT Test 1701

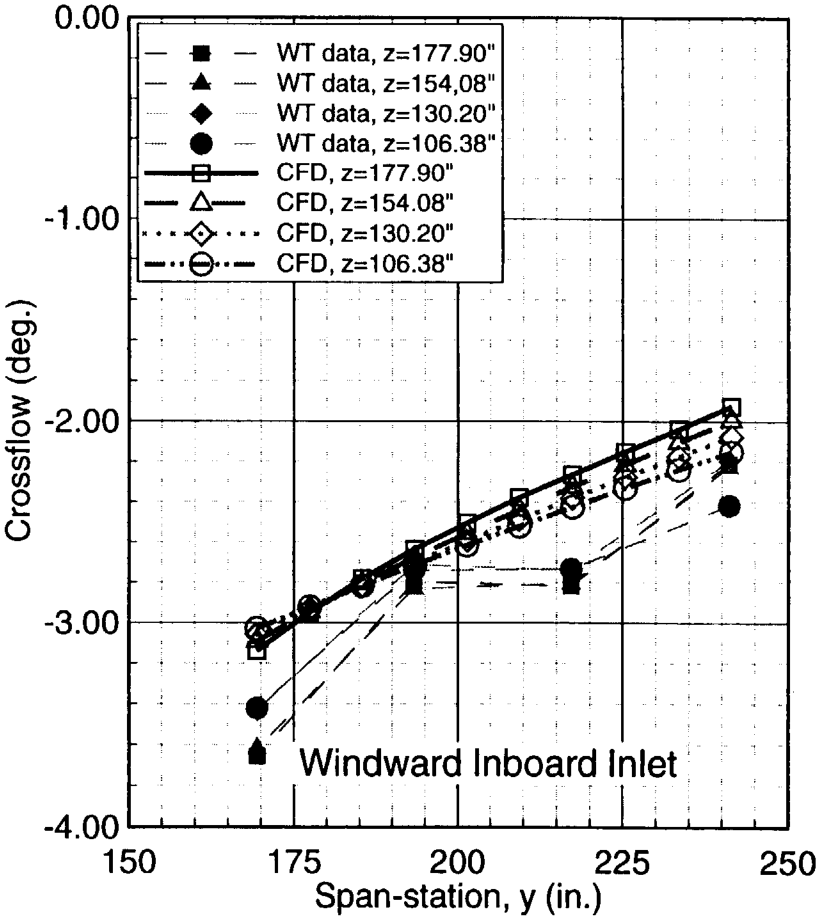

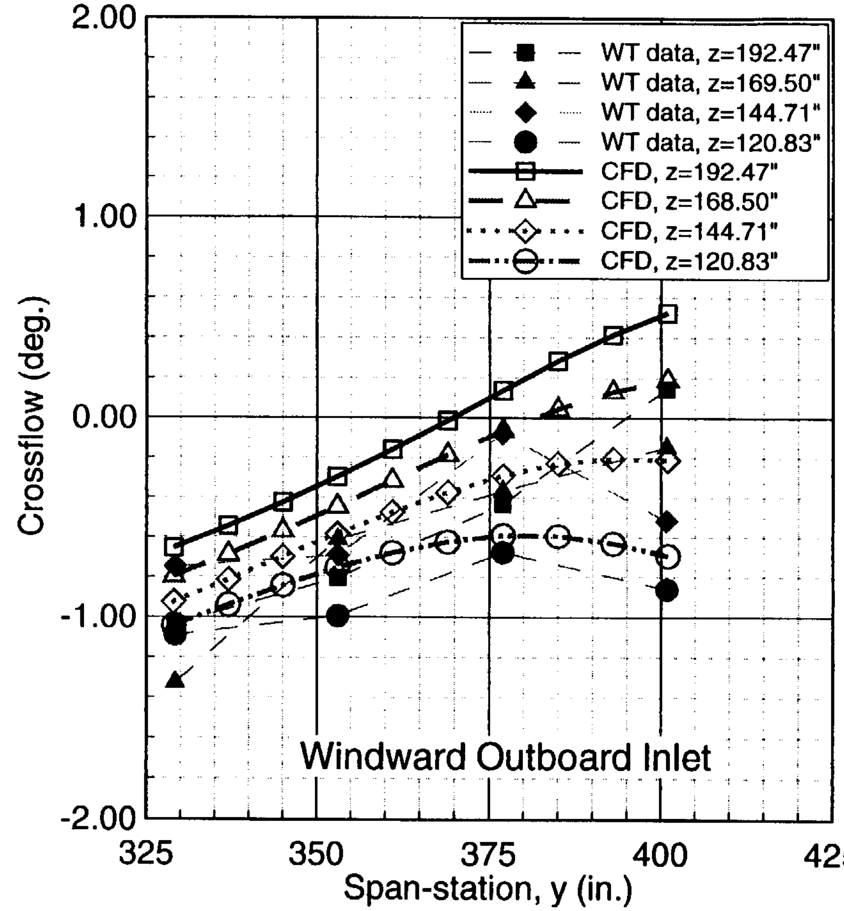

BOEING

Conclusions

The isolated PIE nacelle boattail drag calculations indicate that the PIE 2-D boattail drag is 0.77 cts. higher than the Ref. H 2-D boattail at $M_\infty = 1.1$. Primary source of the higher drag is due to the higher skin friction for the larger PIE 2-D nacelle.

The study of TCA-installed PIE nacelle effects on aerodynamic performance was carried out at supersonic cruise condition, $M_\infty = 2.4$. The study indicates that the TCA configuration with PIE nacelles has 1.7 cts. of drag higher than the TCA with baseline (Axi inlets / 2-D nozzles) nacelles. Similar to the isolated nacelle case, the difference in drag is due to the difference in skin friction.

The TCA inlet flow quality analysis was made to investigate Mach number and flow angle variation distributions at nacelle inlets. Both of the wind-tunnel test data and the CFD results indicate that the present baseline TCA configuration doesn't meet the inlet performance requirements. For the wind-tunnel test data, high data fluctuation was observed, particularly for the data for the outboard inlet.

Conclusions

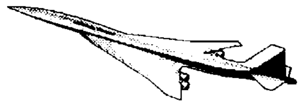

- Isolated PIE 2-D Nacelle, $M_\infty = 1.1$, $Re_c = 40 \times 10^6$
  - Boattail drag is 0.77 cts. higher than the Ref. H 2-D
  - Skin friction is 0.8 cts. higher
- TCA-installed PIE 2-D, $M_\infty = 2.4$, $Re_c = 6.36 \times 10^6$
  - Total drag is 1.7 cts. higher than the baseline configuration (Axi inlet / 2-D nozzle)
  - Skin friction is 1.7 cts. higher
- Inlet flow quality assessment, $M_\infty = 2.4$, $Re_c = 6.36 \times 10^6$
  - TCA baseline do not meet the inlet flow quality requirements
  - High data fluctuations showed in the test data, particularly for the outboard inlet

AMES
Research Center

BOEING

Nacelle / Diverter Design and Airframe Integration

4.3.1.3

Team

BCAG: Steve Chaney
Robyn Wittenberg

Northrop–Grumman:
Mike Malone
Steven Speer
Arsenio Dimanlig

Configuration Aerodynamics Technology Development

This report documents the propulsion/airframe integration (PAI) and propulsion induced effects (PIE) analyses performed by Boeing Commercial Airplane (BCA) in Seattle, and subcontractor Northrop–Grumman Corporation (NGC) in Los Angeles.

Configuration Aerodynamics Technology Development

Program Selects Best Analysis / Design Optimization Methods

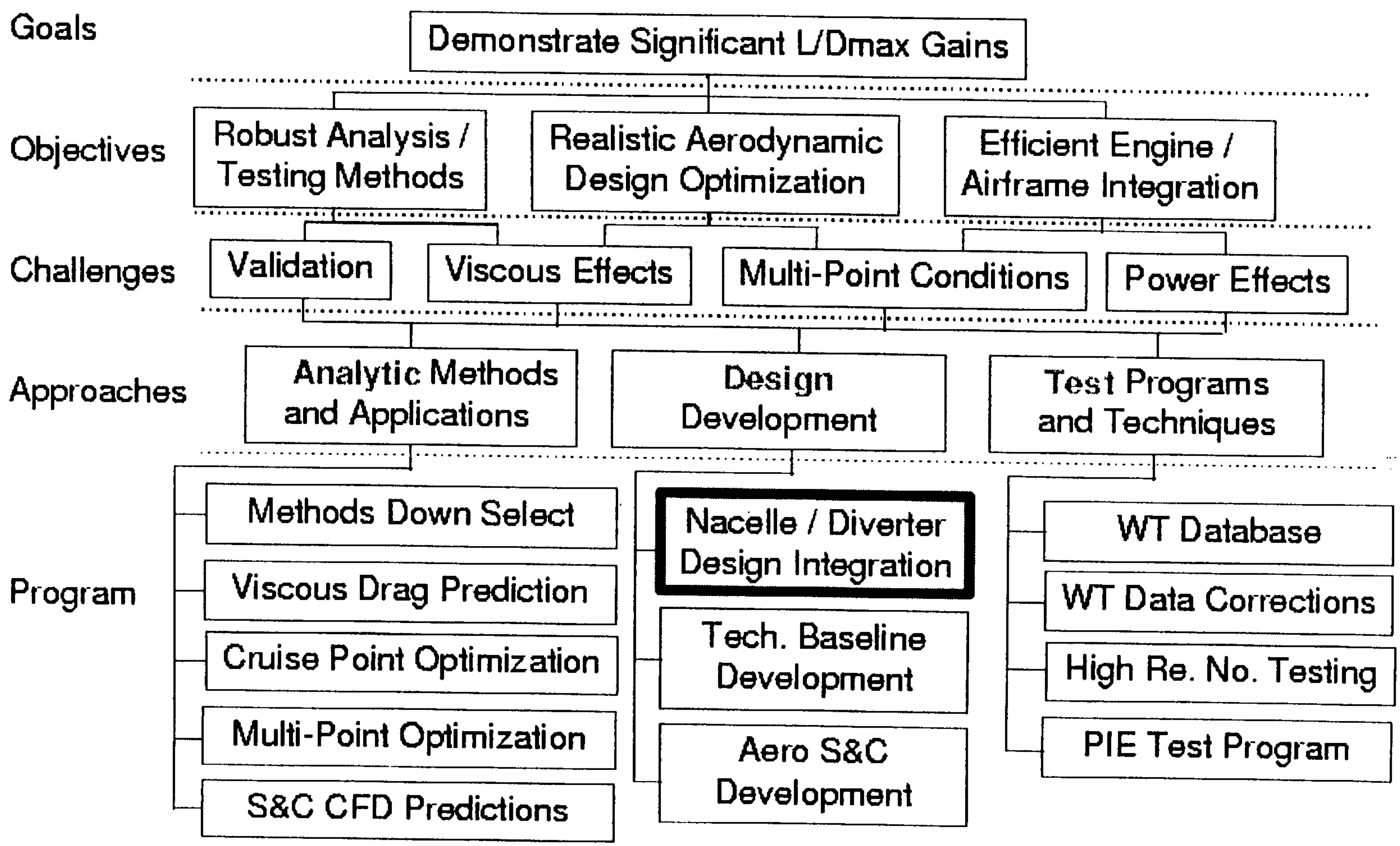

Outline

After the objective and approach are discussed the report is broken down into two main sections. The supercruise studies focussed on various configuration issues regarding installation of the bifurcated inlet, and analysis of bleed door and flow effects on external aerodynamics. The transonic cruise and climb studies were focussed on spillage and bypass effects.

Outline

- Objective
- Approach
  - Tasks
  - Tools
- Supersonic Cruise Studies
  - Conclusions
- Transonic Cruise & Climb Studies
  - Conclusions
- Plans

Objective 1994–1999

The primary objective for propulsion/airframe integration (PAI) work stated in the planning and control document (PCD) is to develop technology required to support the development of the High Speed Civil Transport (HSCT). The technology development includes:

1) Developing computational and empirical based tools for the aerodynamic design & analysis of complex geometry configurations. This development consists primarily of adapting current state-of-the-art computational fluid dynamics (CFD) codes to the HSCT PAI configurations and conditions. This is followed by validation with wind tunnel or flight aerodynamic data.

2) Identifying the key design variables for HSCT PAI installations with the tools described above. Exercising these variables in parametric or direct design optimization studies in order to develop design guidelines for efficient nacelle installations.

Objective 1994–1999

The challenge:

"Provide experimentally validated propulsion / airframe integration technologies and associated design methods and tools for the design of economically viable HSCT configurations."

The objectives:

- Develop, adapt, apply, validate, evaluate computational and empirical based aerodynamic design/analysis tools
- Identify key design variables and develop design guidelines for efficient nacelle installations

Approach

The HSR PAI work performed by BCA and subcontractors has been primarily focussed on inlet integration under the wing (with the exception of the NGC nozzle boattail study). The original wing/body platform upon which these studies was based was the Reference H which had an axisymmetric inlet as the baseline configuration (also an axisymmetric nozzle). A bifurcated inlet was also designed and integrated on the Ref. H. This configuration was both tested and analyzed with CFD. In 1994 and 1995 one of the main tasks was resolving the discrepancies between the test and CFD results. At the end of 1995 a study was performed to determine the feasibility of integrating the 2D nozzles preferred by propulsion/noise. The results indicated that this configuration would not penalize the aerodynamic performance and as a result 2D nozzles were incorporated on the next HSCT baseline (TCA).

In 1995 Northrop–Grumman Corporation (NGC) was subcontracted to analyze the transonic performance of 2D nozzles with CFD. Lockheed (LMAS) was subcontracted to analyze the NASA ARC 9x7 spillage test data and begin CFD analysis of the Reference H configuration with spilling axisymmetric and bifurcated inlet nacelles.

Approach

- BCAG and subcontractors (NGC & LMAS) primary PAI focus was inlet external aero design and integration with diverter onto wing

Reference H based studies

1994
- Initiate OVERFLOW validation (2.7%–scale data ARC 9x7)
- Axisymmetric to Bifurcated inlet comparison

1995 Supersonic cruise
- OVERFLOW prediction accuracy
- Complete analysis of axi and bifurcated inlet on Ref H
- Assess impact of 2d nozzles and larger nacelles (673 vs 540 pps)
- Inlet flow field assessment

Transonic
- Analytical study of transonic nozzle boattail drag (NGC)
- ARC spillage test analysis and assess CFD spillage modeling (LMAS)

Approach (cont.)

The Technology Concept Airplane (TCA) incorporated 2D nozzles but retained the axisymmetric inlets. A complete CFD and wind tunnel assessment of this configuration was completed in 1996. In addition, the lessons learned from the Ref H bifurcated installation were applied in designing a bifurcated inlet installation on the TCA. CFD analysis of this configuration proved that the bifurcated could be installed for the same drag as the axisymmetric. Comparison of the axisymmetric and bifurcated inlets on the TCA was extended to transonic conditions in 1997. BCA analyzed both inlet configurations with transonic compression surfaces (ramps or centerbody) to simulate proper spillage conditions; these analyses were performed at wind tunnel Reynolds Number. The axisymmetric and bifurcated inlet installations were found to have equivalent aerodynamic performance at transonic conditions. Flight Reynolds Number transonic analyses were performed on the axisymmetric configuration by NGC (the bifurcated analysis started in 1998 is still in progress). NGC also performed an analysis of the inlet boundary layer bleed flow effect on the external aerodynamic characteristics of the axisymmetric inlet configuration at Mach 2.4. The effect of the bleed doors and exhaust flow was negligible.

Approach (cont.)

Technology Concept Airplane (TCA) based studies

1996 Supersonic cruise

- OVERFLOW analysis of alternate diverter position Ref H bifurcated
- OVERFLOW analysis of TCA at wind tunnel and flight conditions
- Inlet flow field assessment
- Design, integrate, analyze bifurcated inlet on TCA
- Nacelle orientation study (NGC)
- Diverter design: aft fairing, width, channel flow (NGC)

1997 Transonic Cruise & Climb

- Validate OVERFLOW W/B/N/D at Mach 0.9 / 1.2 with LaRC 16ft data
- W/B/N/D/<u>centerbody</u> analysis with flight spillage rates:
  - Wind tunnel Reynolds Number
  - Full scale flight Reynolds Number (NGC)
- Analysis of spilling <u>bifurcated</u> inlet with ramp (M=0.9 & 1.2)

Supersonic Cruise

- Bleed flow external aero analysis on TCA axi inlet baseline (NGC)

Approach (cont.)

The bifurcated installation on the TCA has continued to be examined in some detail. This investigation was fueled somewhat by the results of a BCA IR&D test that did NOT confirm the equal drag of the bifurcated and axisymmetric installations (BS644: bifurcated about 2 counts higher drag). NGC has examined bleed flow effects on the bifurcated inlet at supercruise and spillage/bypass effects on the bifurcated at transonic cruise & climb conditions.

Approach (cont.)

1998 Supersonic Cruise
- Complete bifurcated to axisymmetric inlet comparison
- Enhance bifurcated inlet installation design
- Boeing IR&D wind tunnel test data /CFD resolution
- CFD assessment of bleed effects on external aero of bifurcated (NGC)
- Continue assessment of alternate nacelle concepts

Transonic Cruise & Climb
- CFD assessment of bifurcated inlet spillage/bypass effects (NGC)

Tools

OVERFLOW has continued to be used extensively in BCA HSCT high-speed aerodynamics. It has proven to be a robust and accurate flow solver across the Mach and Reynolds Number range of interest. NGC used their in-house code GCNSfv which is very similar to OVERFLOW. Cross checks completed in previous years have shown that the codes produce equivalent results. All of the CFD results presented in this report have been run with the Spalart-Allmaras turbulence model.

GCNSfv is based on the ARC3D thin-layer Navier-Stokes algorithm created at NASA Ames . The solution method is an implicit, node-based finite-volume scheme. Complex geometries are analyzed by using multi-block structured grids. The boundary conditions between blocks can be specified as patched class 1 through 4, where class 1 is point-to-point matching, class 2 is incremental point-to-point matching, class 3 is arbitrary face matching, and class 4 is arbitrary sub-face matching. A Chimera overlapping grid block option is also available. To speed convergence, grid sequencing and multigrid schemes can be used. GCNSfv provides four turbulence models to the user: Menter's k-w SST 2-equation, a k-w algebraic Reynolds stress model, the Spalart-Allmaras model, and the Baldwin-Barth model. GCNSfv offers a wide variety of boundary conditions including propulsion specific conditions such as characteristic inflow (mass flow ratio and corrected mass flow, inlet bleed) and outflow (nozzle pressure ratio, nozzle temperature ratio, transpiration) conditions. The code runs at approximately 12 ms/iteration/grid-point on the Cray C-90 and parallelization allows the code to utilize six of the available sixteen processors allowing effective use of the multi-task batch queue.

Tools

BCAG	*common features*	NGC
OVERFLOW		GCNSfv
Finite–Difference	Implicit, ARC3D	Finite–Volume
	Grid Sequencing	
	Multi–Gridding	
	Multi–Block	
	Chimera Interface	Patched Interface
	S–A Turb Model	Menter k–ω SST

Supersonic Cruise Studies

The bifurcated installation on the TCA was compared to the axisymmetric configuration at flight Reynolds Number using OVERFLOW results. The conclusions were the same as for wind tunnel Reynolds Number: the drag was equivalent. The other bifurcated analyses performed in 1998 at BCA involved configuration perturbations of the baseline configuration. The inlet bleed study was performed by NGC.

Supersonic Cruise Studies

- Axisymmetric vs Bifurcated Inlet, Reynolds Number Study
- Bifurcated Inlet Shoulder Radius Study
- Bifurcated Inlet As–Tested Configuration Study
- Bifurcated Inlet Bevel Angle Study
- Nozzle Width Study
- Inlet Bleed External Aerodynamics Study

Axisymmetric vs Bifurcated Inlet, Reynolds Number Study

TCA W/B/N/D OVERFLOW Analysis: Drag Polar
Mach 2.4, Re_{MAC} = 194.2 & 6.4 million (Flight & WT)

The drag polar for the bifurcated nacelle is virtually identical to the axisymmetric results over a range of angle of attack values at both wind tunnel and flight conditions.

Axisymmetric vs Bifurcated Inlet, Reynolds Number Study

TCA W/B/N/D OVERFLOW Analysis: Drag Polar
Mach 2.4, Re_{MAC} = 194.2 & 6.4 million (Flight & WT)

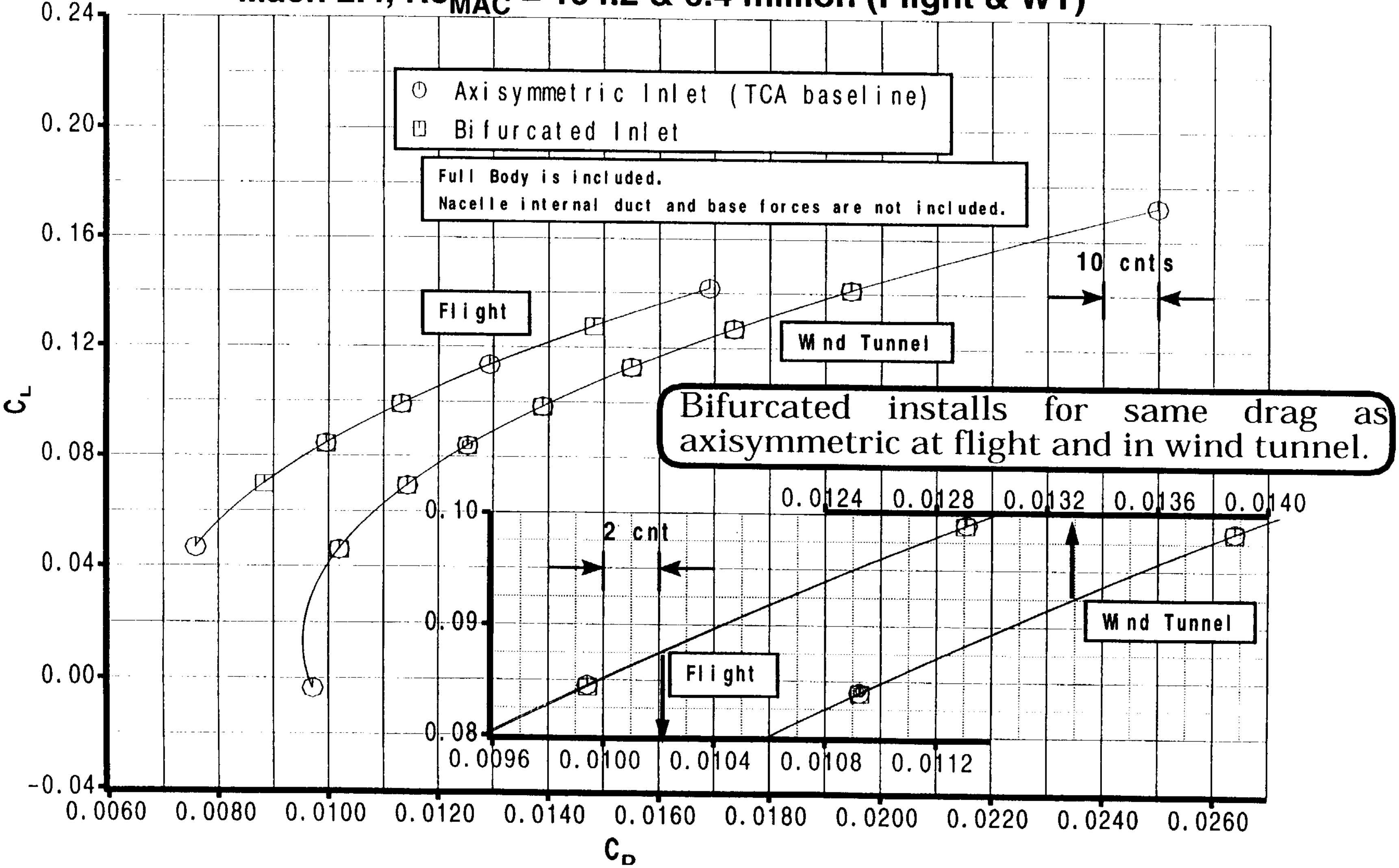

Axisymmetric vs Bifurcated Inlet, Reynolds Number Study

TCA W/B/N/D OVERFLOW Analysis: Pressure Drag Polar
Mach 2.4, Re_{MAC} = 194.2 & 6.4 million (Flight & WT)

Breakdown of the drag result into pressure and friction components confirms the constant (over a range of angle of attack values) and equal but opposite friction and pressure drag differences for the bifurcated and axisymmetric.

Axisymmetric vs Bifurcated Inlet, Reynolds Number Study

TCA W/B/N/D OVERFLOW Analysis: Pressure Drag Polar
Mach 2.4, Re_{MAC} = 194.2 & 6.4 million (Flight & WT)

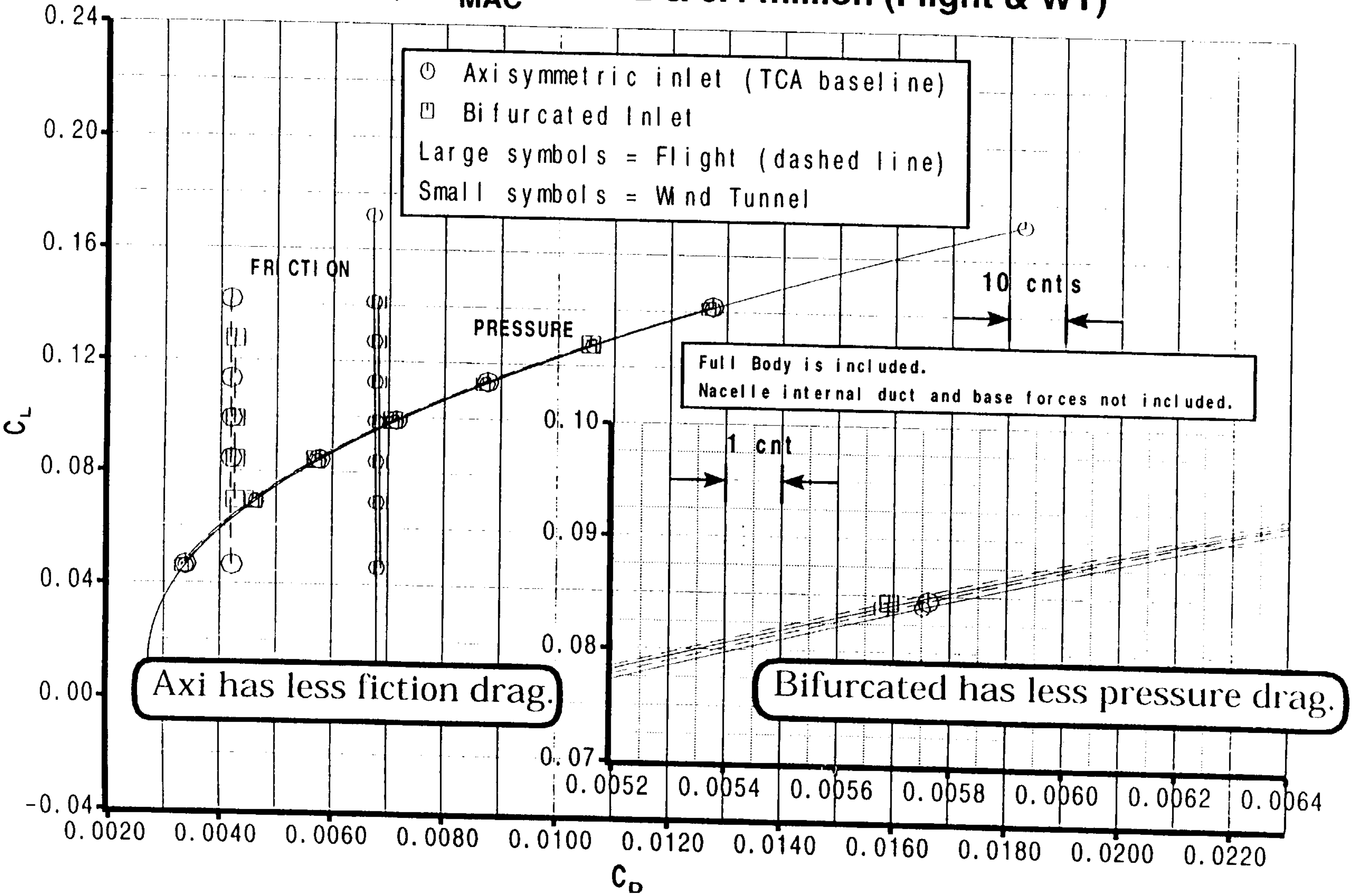

Axisymmetric vs Bifurcated Inlet, Reynolds Number Study

TCA W/B/N/D OVERFLOW Analysis: PAI Force Increments
Mach 2.4, Re_{MAC} = 194.2 & 6.4 million (Flight & WT)

The nacelle force increments are shown for flight conditions. This plot confirms the results shown in the previous pressure drag polar. The bifurcated nacelle actually had a slightly smaller pressure drag then the axisymmetric but this was made up by the higher friction drag of the longer bifurcated nacelle.

Axisymmetric vs Bifurcated Inlet, Reynolds Number Study

TCA W/B/N/D OVERFLOW Analysis: PAI Force Increments
Mach 2.4, Re_{MAC} = 194.2 & 6.4 million (Flight & WT)

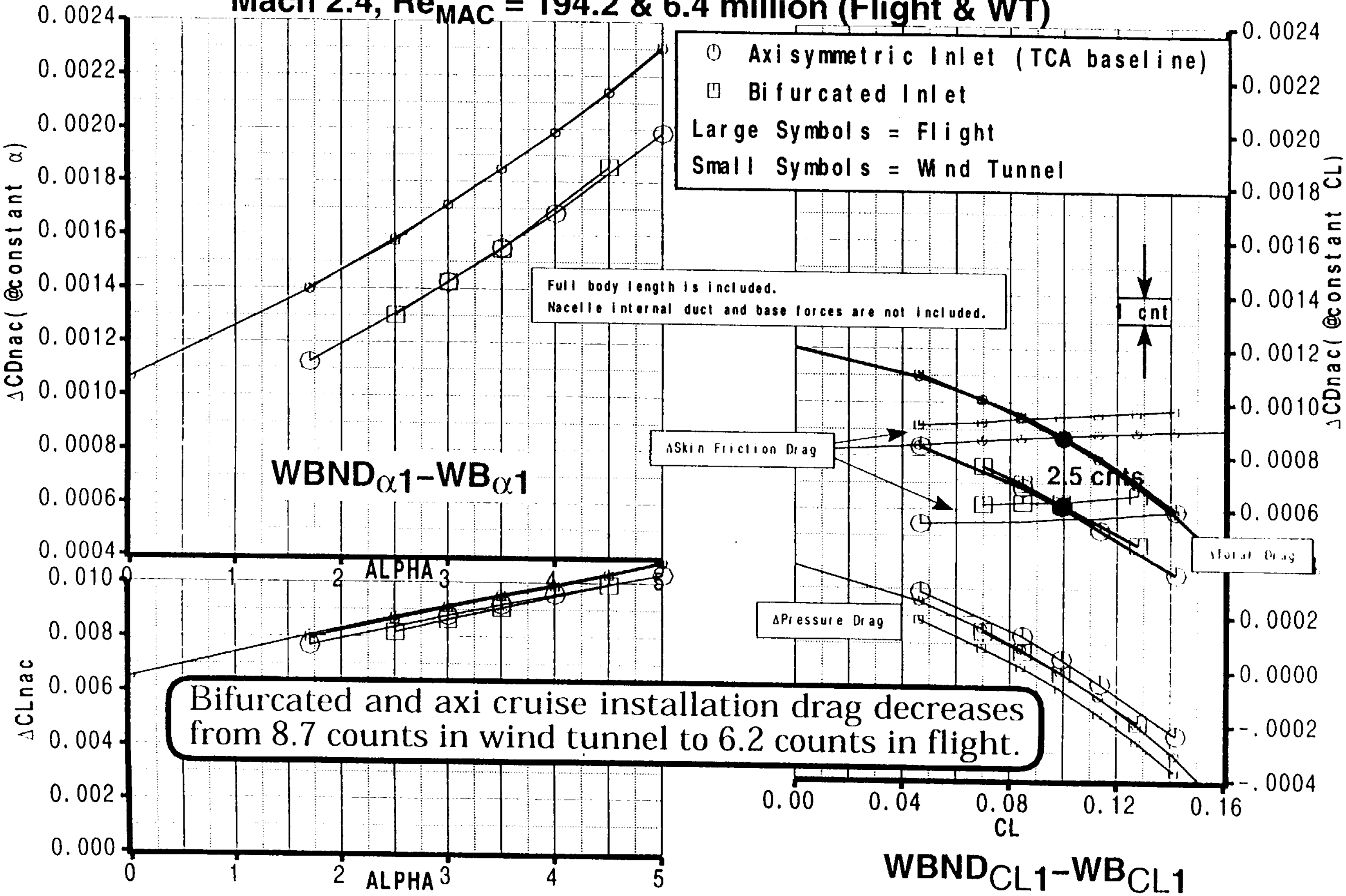

Axisymmetric vs Bifurcated Inlet, Reynolds Number Study

TCA W/B/N/D OVERFLOW Analysis: Nacelle/Diverter Pressure drag
Mach 2.4, Re_{MAC} = 194.2 & 6.4 million (Flight & WT)
Bifurcated

This figure shows a comparison of the wind tunnel and flight, nacelle and diverter pressure drag results from the OVERFLOW solutions. The difference in diverter drag between flight and wind tunnel for the inboard installation (attached diverter shocks in both cases) was identical to the drag difference for the outboard installation (one attached, one detached). In addition, these results were very similar to axisymmetric nacelle/diverter pressure drag differences shown in the next Figure. The choked diverter channel for the wind tunnel case appeared not to have corrupted the force results that led to the conclusion that the bifurcated and axisymmetric inlet nacelle drag values were equal.

Axisymmetric vs Bifurcated Inlet, Reynolds Number Study

TCA W/B/N/D OVERFLOW Analysis: Nacelle/Diverter Pressure drag

Mach 2.4, Re_{MAC} = 194.2 & 6.4 million (Flight & WT)

Integrated pressure force on nacelle and diverter surfaces.

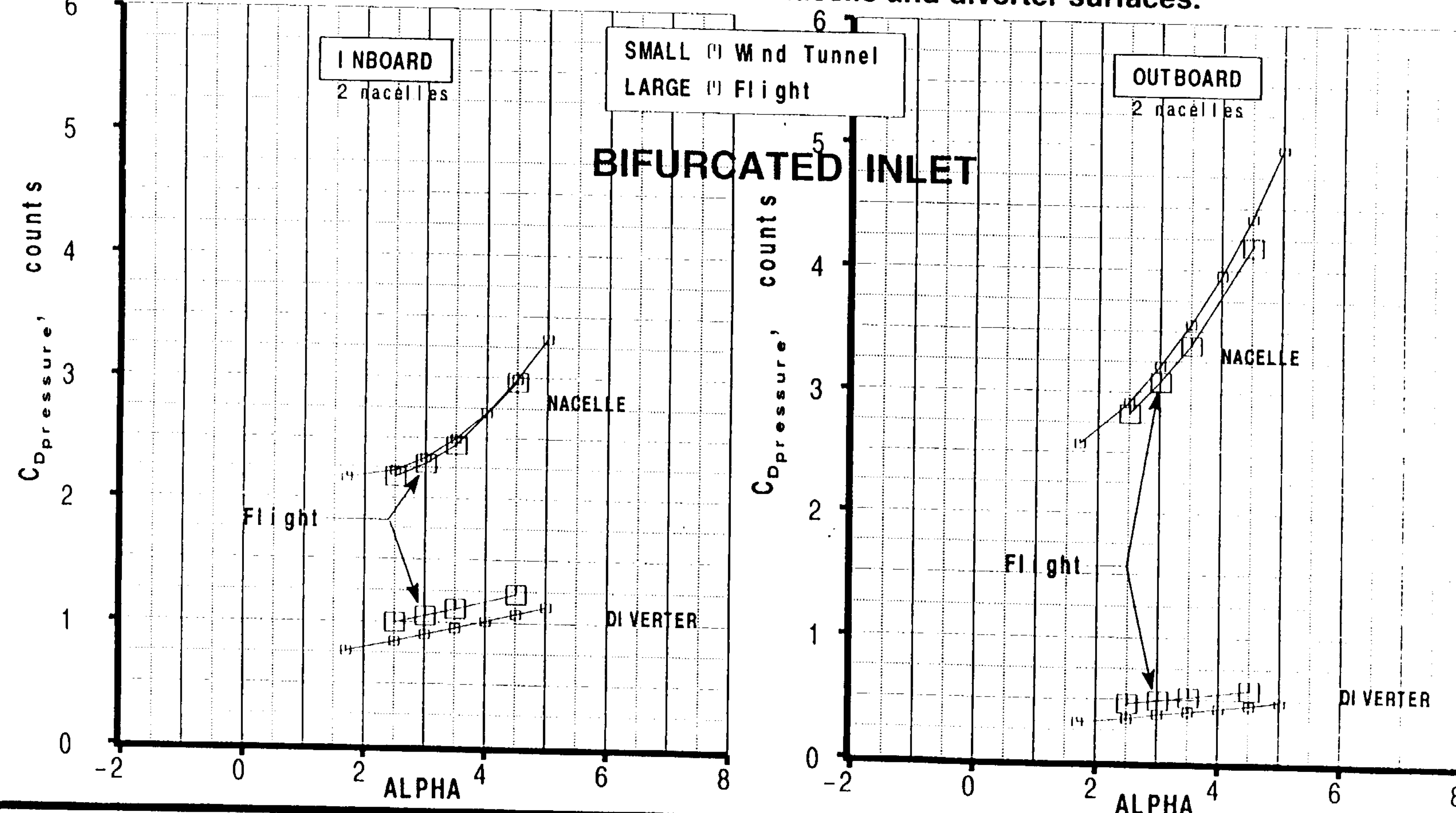

Outboard diverter drag increase (wind tunnel to flight) for bifurcated is nearly identical to axi despite flow change from choked channel to attached diverter shock.

Axisymmetric vs Bifurcated Inlet, Reynolds Number Study

TCA W/B/N/D OVERFLOW Analysis: Nacelle/Diverter Pressure drag
Mach 2.4, Re_{MAC} = 194.2 & 6.4 million (Flight & WT)
Axisymmetric

See text for previous figure.

Axisymmetric vs Bifurcated Inlet, Reynolds Number Study

TCA W/B/N/D OVERFLOW Analysis: Nacelle/Diverter Pressure drag
Mach 2.4, Re_{MAC} = 194.2 & 6.4 million (Flight & WT)

Integrated pressure force on nacelle and diverter surfaces.

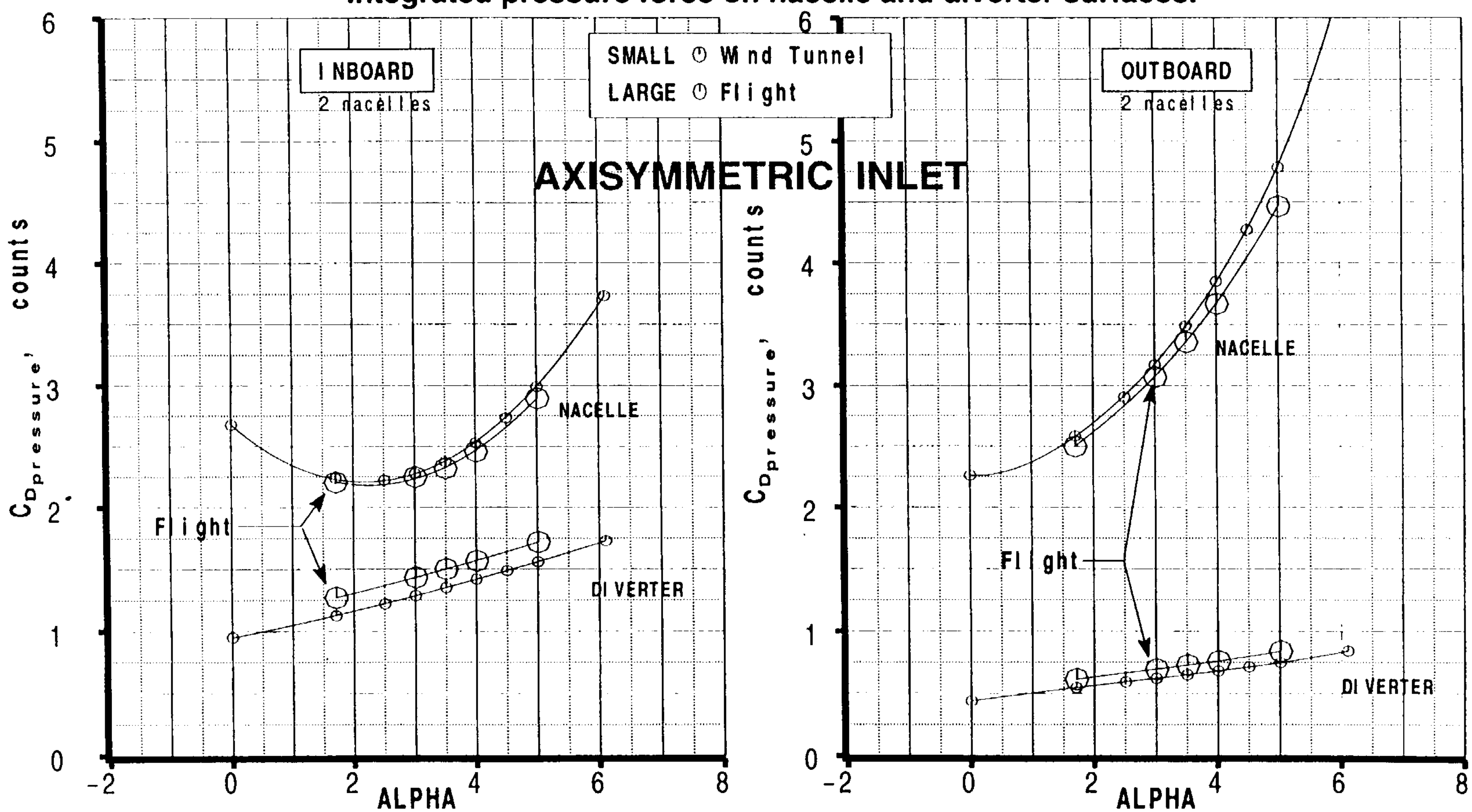

Nacelle surface pressure drag smaller in flight; diverter drag is larger.

Axisymmetric vs Bifurcated Inlet, Reynolds Number Study

TCA W/B/N/D OVERFLOW Analysis: Wing Lower Surface Pressure
Mach 2.4, α = 3 deg, Re_{MAC} = 194.2 & 6.4 million (Flight & WT)

This figure shows the wing lower surface pressure contours compared to the wind tunnel condition results. The effect of the thinner boundary layer at flight was very evident in the diverter region. The diverter shocks had a larger aft sweep angle (the average Mach Number in the diverter channel is higher) and the outboard diverter channel appeared to have an attached diverter shock instead the normal shock produced by a choked channel in the wind tunnel case.

Axisymmetric vs Bifurcated Inlet, Reynolds Number Study

TCA W/B/N/D OVERFLOW Analysis: Wing Lower Surface Pressure
Mach 2.4, α = 3 deg, Re_{MAC} = 194.2 & 6.4 million (Flight & WT)

BIFURCATED INLET

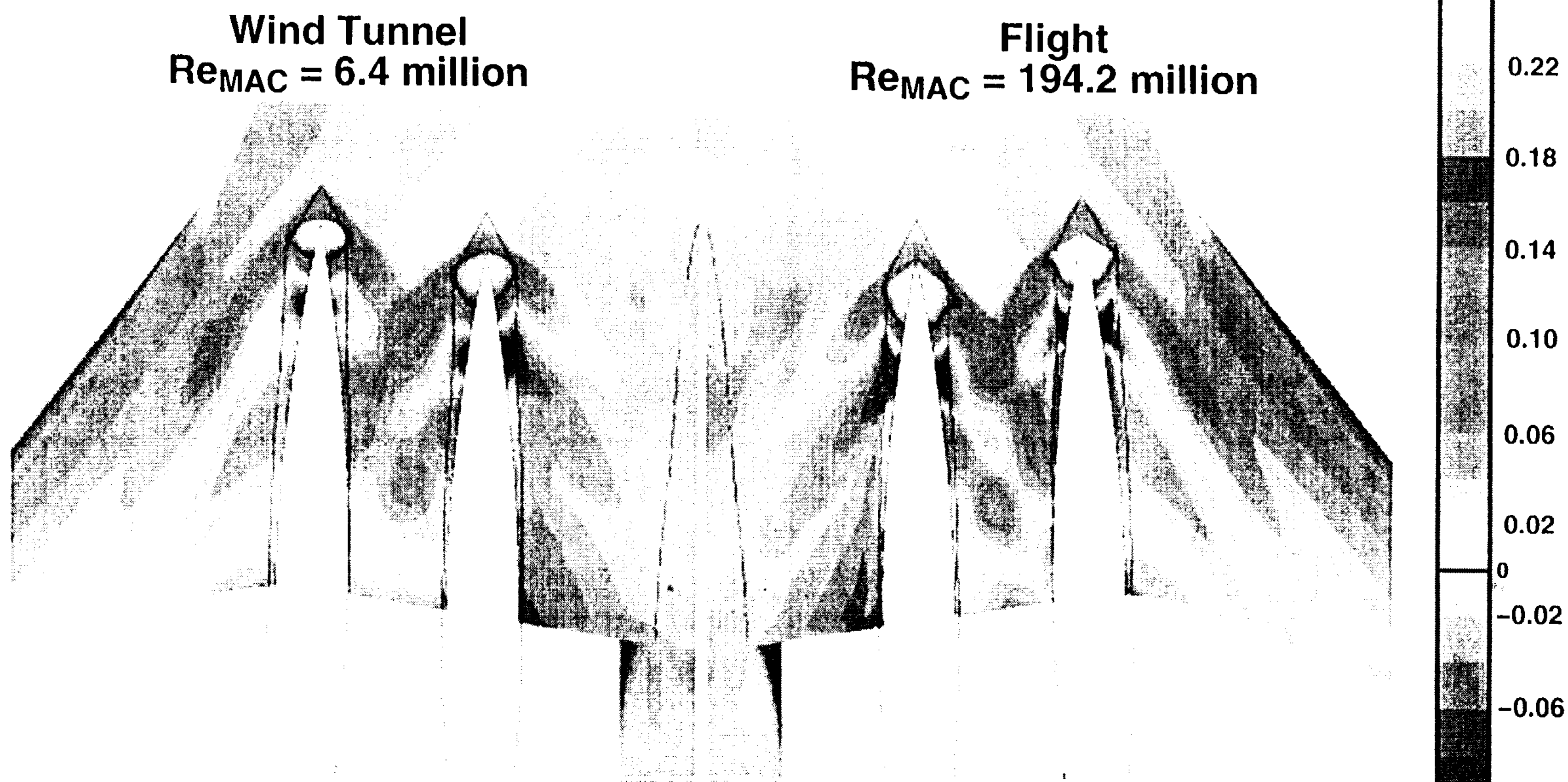

High pressure region at diverter LE and low pressure region at shoulder are both larger in flight condition solution.

Axisymmetric vs Bifurcated Inlet, Reynolds Number Study

TCA W/B/N/D OVERFLOW Analysis: Inboard Nacelle Surface Pressure
Mach 2.4, α = 3 deg, Re_{MAC} = 194.2 & 6.4 million (Flight & WT)

This figure confirmed the shock angle change on the inboard nacelle installation; in fact, the shock angle was swept aft of the inlet lip confirming the design location of the diverter leading edge for flight conditions to keep the shock out of the inlet flow field.

Axisymmetric vs Bifurcated Inlet, Reynolds Number Study

TCA W/B/N/D OVERFLOW Analysis: Inboard Nacelle Surface Pressure
Mach 2.4, $\alpha = 3$ deg, $Re_{MAC} = 194.2$ & 6.4 million (Flight & WT)

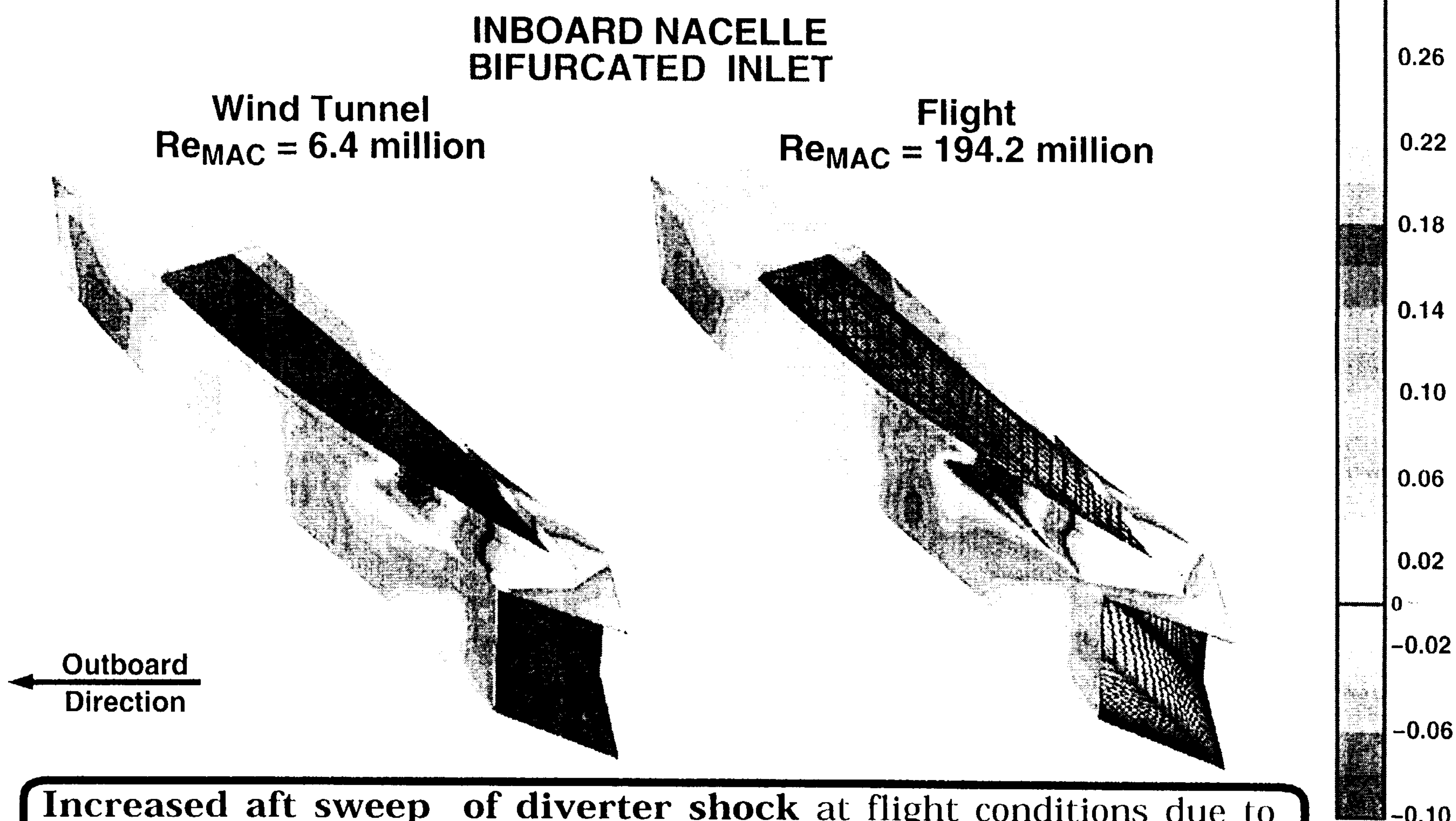

Increased aft sweep of diverter shock at flight conditions due to thinner wing boundary layer.

Axisymmetric vs Bifurcated Inlet, Reynolds Number Study

TCA W/B/N/D OVERFLOW Analysis: Outboard Nacelle Surface Pressure
Mach 2.4, α = 3 deg, Re_{MAC} = 194.2 & 6.4 million (Flight & WT)

This figure shows nacelle surface pressure contours for the outboard nacelle installation. In contrast to the wind tunnel detached diverter shock, the diverter shock for the flight case was clearly attached and also appears to just clear the inlet lip.

Axisymmetric vs Bifurcated Inlet, Reynolds Number Study

TCA W/B/N/D OVERFLOW Analysis: Outboard Nacelle Surface Pressure
Mach 2.4, $\alpha = 3$ deg, $Re_{MAC} = 194.2$ & 6.4 million (Flight & WT)

OUTBOARD NACELLE BIFURCATED INLET

Wind Tunnel
$Re_{MAC} = 6.4$ million

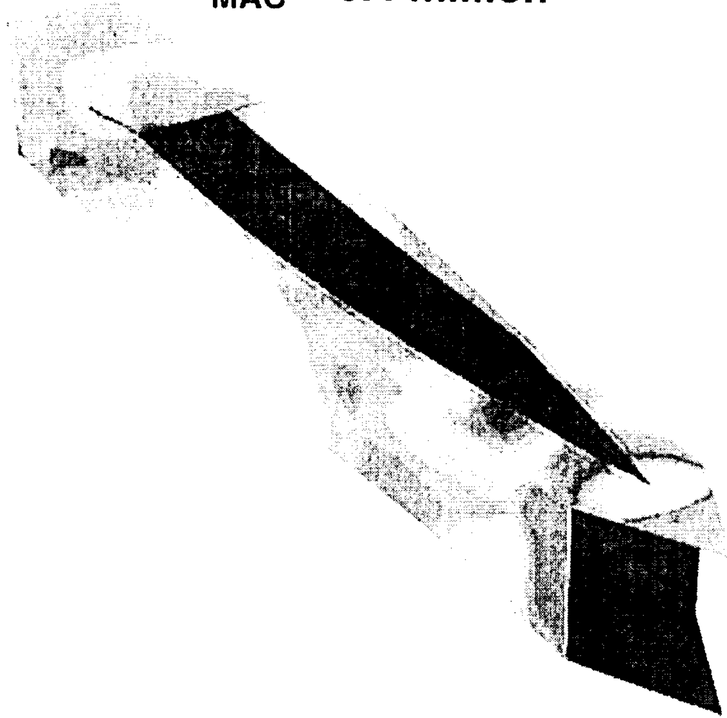

Flight
$Re_{MAC} = 194.2$ million

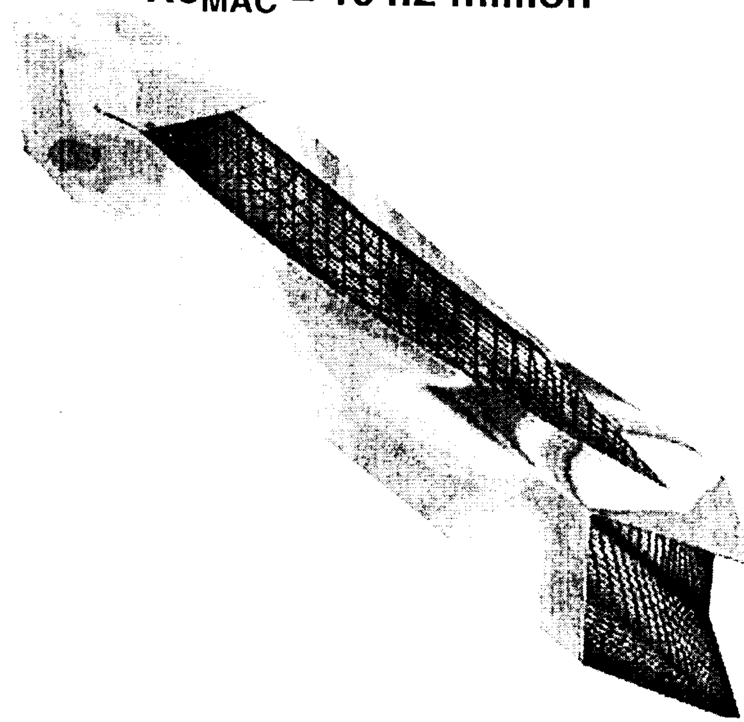

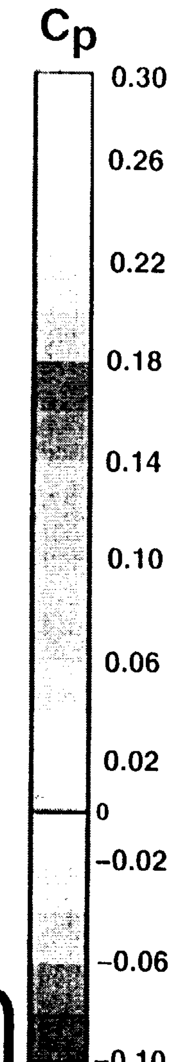

Attached outboard diverter shock at flight conditions due to thinner wing boundary layer; shock not ingested by inlet confirms bifurcated diverter placement.

Bifurcated Inlet Shoulder Radius Study

TCA W/B/N/D OVERFLOW Analysis: Surface Lofts

In order to understand the effect of the large shoulder radius applied to the baseline bifurcated a modified geometry was constructed with most of this effect removed. This design has the square cross section of the inlet lip carried all the way back to the maximum area and was called the 'flat-sided' configuration.

The installation on the airplane was difficult. The large increase in corner radius aft of the inlet on the baseline allows for the diverter to get out to the sides of the nacelle with out undo channel pinching. But the straight line connectors from inlet to maximum area of the modified nacelle penetrate into the lower surface of the wing much further forward and require substantial diverter modification to prevent a pinched off channel.

Bifurcated Inlet Shoulder Radius Study

TCA W/B/N/D OVERFLOW Analysis: Surface Lofts

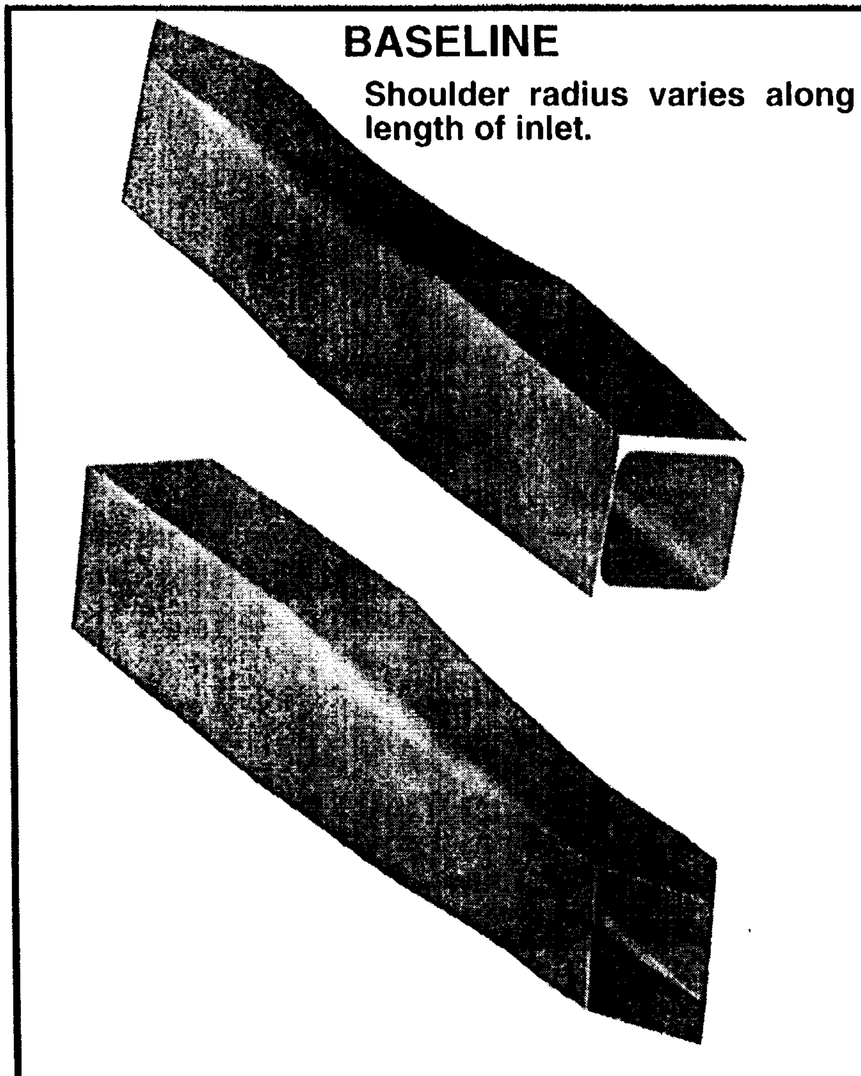

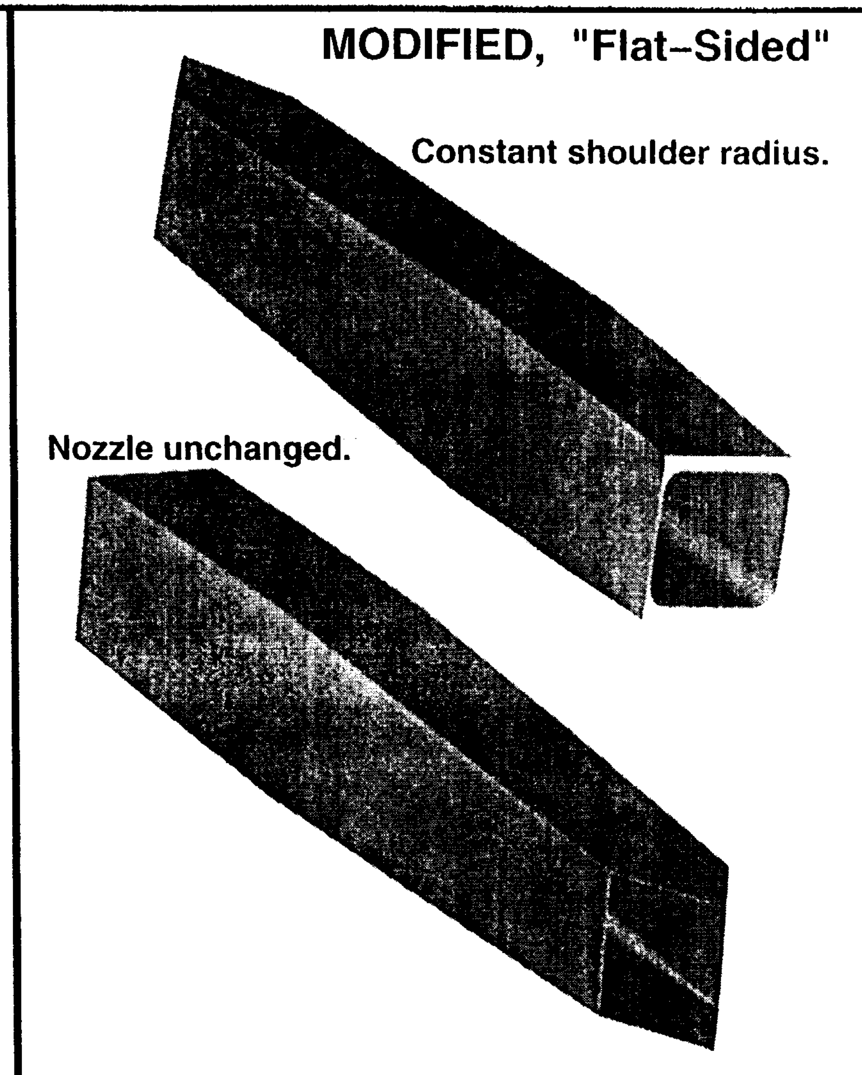

Bifurcated Inlet Shoulder Radius Study

TCA W/B/N/D OVERFLOW Analysis: Area Distribution

The relatively linear rate of area growth of the modified bifurcated inlet is evident in this figure. Both the baseline and the flat-sided have the initial growth associated with the front of the inlet, but the baseline area growth slows down considerably aft of this point before accelerating rapidly further aft to reach the maximum area. This shape resulted in the characteristic double positive pressure field observed on the wing lower surface for this configuration. The third area distribution curve is for a modified nacelle that was used to model the PTC nozzle configuration (will be discussed later).

Bifurcated Inlet Shoulder Radius Study

TCA W/B/N/D OVERFLOW Analysis: Area Distribution

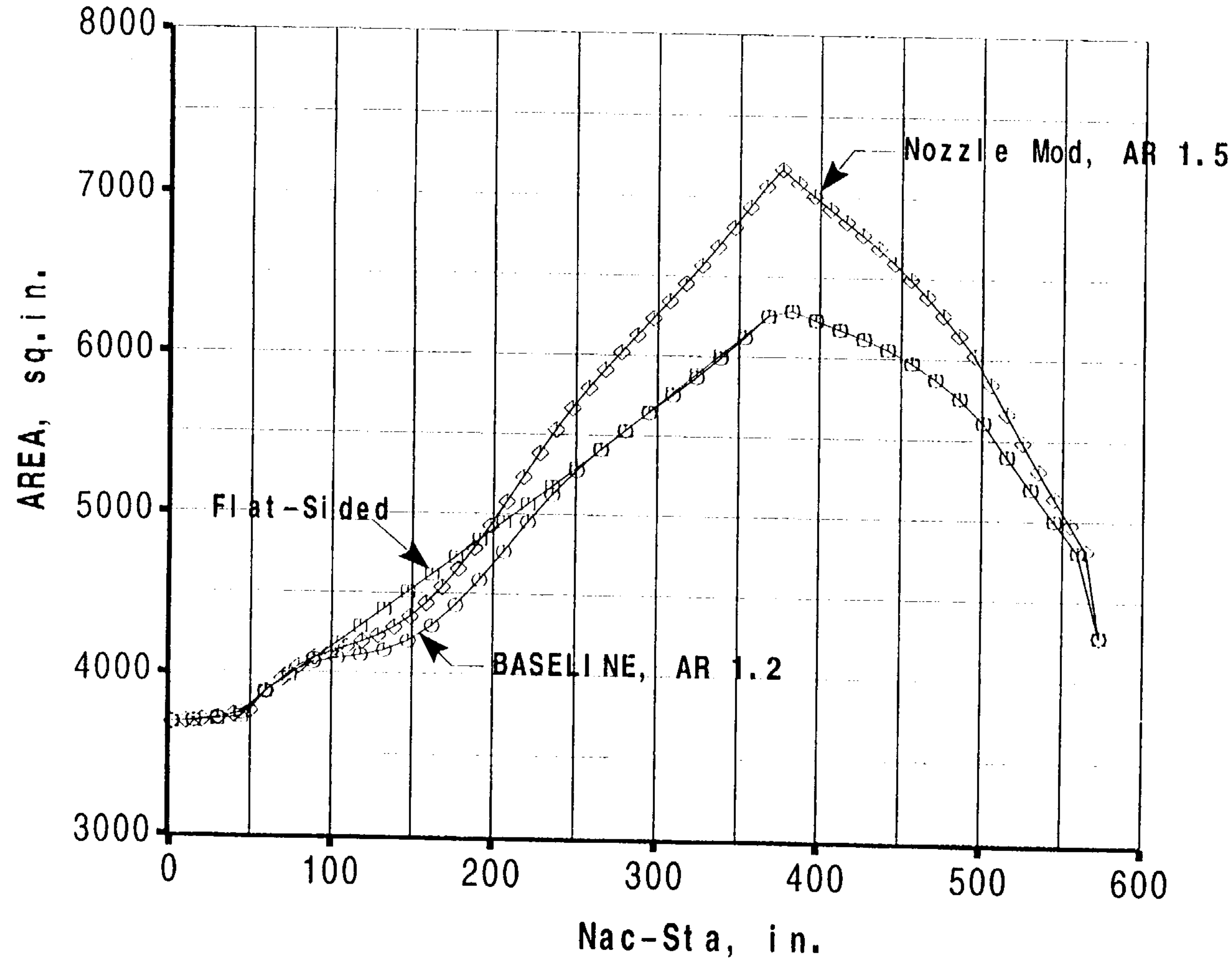

AR = W/H_{nozzle} @ takeoff

Bifurcated Inlet Shoulder Radius Study

TCA W/B/N/D OVERFLOW Analysis: Wing Lower Surface Pressure
Mach 2.4, $\alpha = 3$ deg, $Re_{MAC} = 6.4$ million (WT)

The diverter planform shape for the flat-sided configuration can be seen in this figure. The impact of the nearly doubled included-angle diverters was clearly evident. Both inboard and outboard nacelles had detached shocks with significantly larger high pressure regions at the diverter leading edge than on the baseline (on the baseline the inboard diverter shock remained attached). The effect of the flat sides of the modified nacelle are also evident in this figure, primarily as a much reduced area of favorable pressure interference between the nacelles compared to the baseline installation. The flat-sided nacelle in addition had somewhat lower positive pressure regions inboard of the inboard nacelle and outboard of the outboard nacelle.

Bifurcated Inlet Shoulder Radius Study

TCA W/B/N/D OVERFLOW Analysis: Wing Lower Surface Pressure
Mach 2.4, $\alpha = 3$ deg, $Re_{MAC} = 6.4$ million (WT)

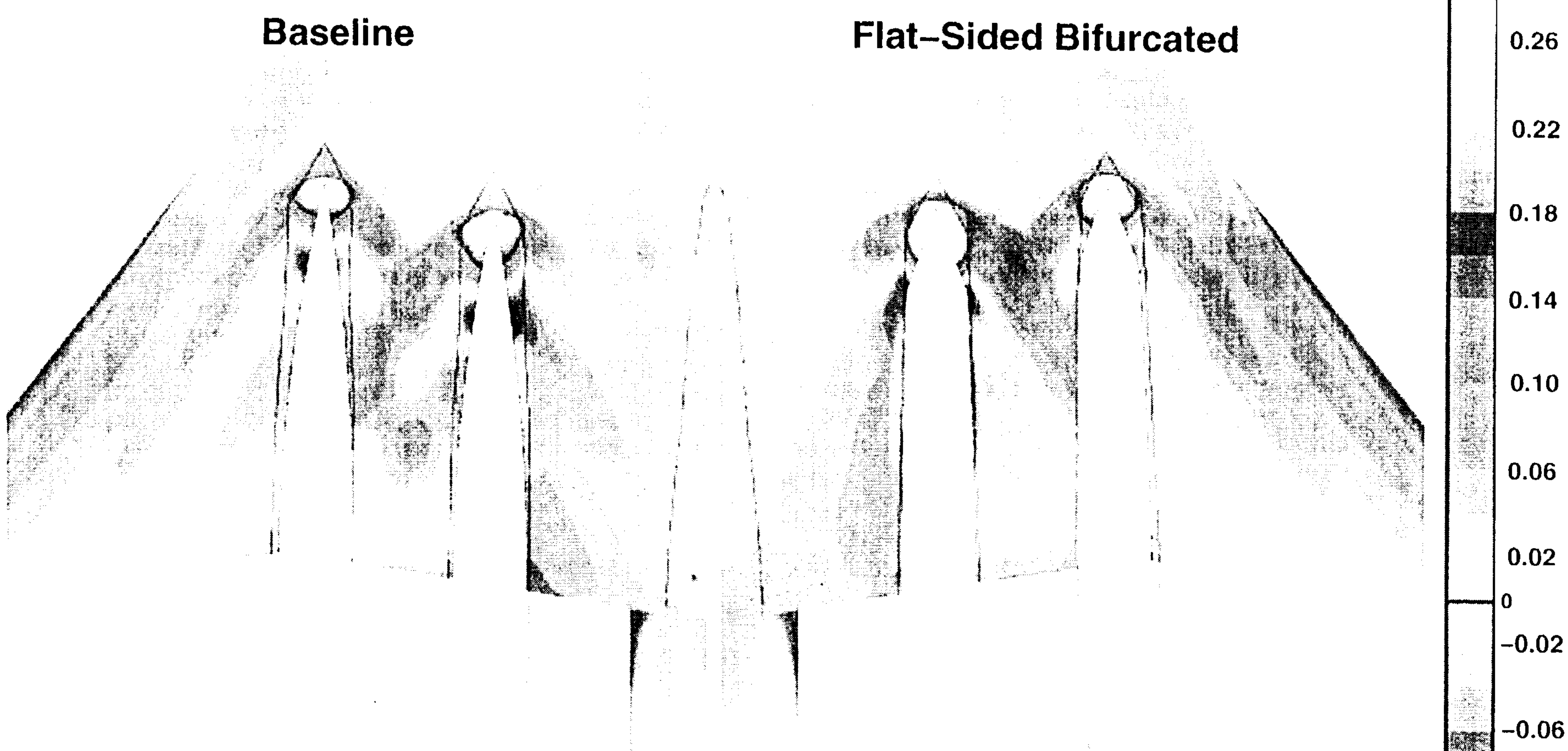

- Diverter angle nearly doubled (from 11 deg) due to lack of channel relief.
- Both inboard and outboard **diverter shocks detached**.
- Double positive pressure signature eliminated.

Bifurcated Inlet Shoulder Radius Study

TCA W/B/N/D OVERFLOW Analysis: Inboard Nacelle Surface Pressure
Mach 2.4, $\alpha = 3$ deg, $Re_{MAC} = 6.4$ million (WT)

This figure and the next show the inboard and outboard nacelle surface pressure results for the baseline and flat-sided nacelle installations. Both inboard and outboard modified nacelles had strong, detached shocks at the diverter leading edges. As has been noted in the original study of the baseline bifurcated nacelle, the inboard installation was just barely adequate in terms of keeping the diverter shock out of the inlet (as long as the shock was attached). The flat-sided nacelle installation required sliding the diverter leading edge forward in order to reduce the diverter angle; the angle was still double the baseline diverter angle. Even if the shock had remained attached in the flat-sided solution it would enter the inlet. The problem was compounded by the increased diverter angle leading to a detached shock that disrupted the inlet flowfield to an even larger extent. These flowfield effects could be inferred (without an OVERFLOW solution) by simple observation of the diverter geometry. However, the goal of this study of the flat-sided nacelle was to assess the effect of the large amount of shoulder carving that was applied to the baseline (and removed on the flat-sided). So, the flat-sided nacelle would not be used as a real installation but was a useful tool for furthering our knowledge base for installing bifurcated inlets. The larger diverter shock strength of the flat-sided installation does, however, confuse the comparison of the nacelle shaping as these increased pressures lead to beneficial lift increases on the wing and penalizing drag increases on the nacelle. This is discussed in more detail below.

Bifurcated Inlet Shoulder Radius Study

TCA W/B/N/D OVERFLOW Analysis: Inboard Nacelle Surface Pressure
Mach 2.4, α = 3 deg, Re_{MAC} = 6.4 million (WT)

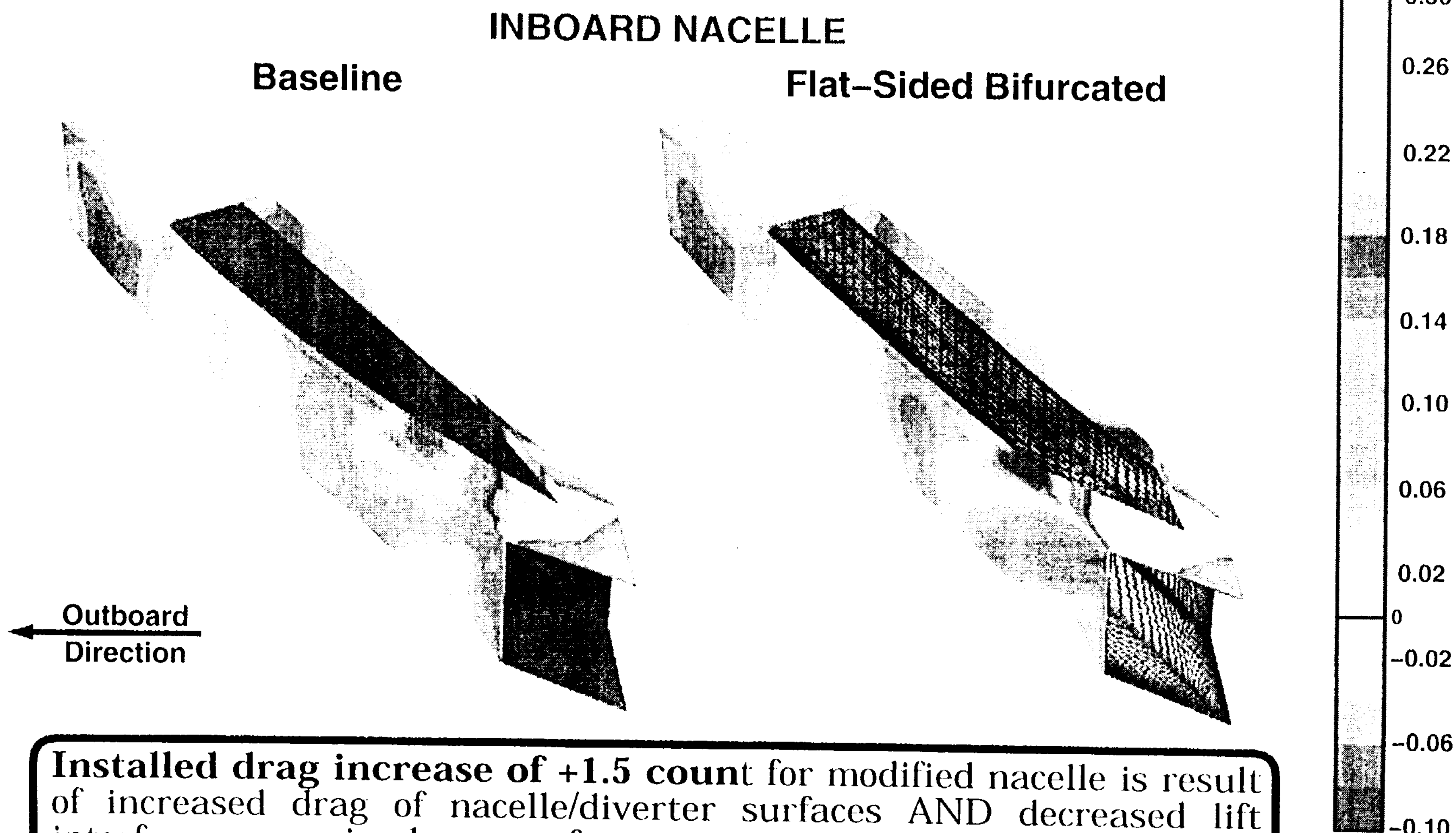

Installed drag increase of +1.5 count for modified nacelle is result of increased drag of nacelle/diverter surfaces AND decreased lift interference on wing lower surface.

Bifurcated Inlet Shoulder Radius Study

TCA W/B/N/D OVERFLOW Analysis: Outboard Nacelle Surface Pressure
Mach 2.4, α = 3 deg, Re_{MAC} = 6.4 million (WT)

See text for previous figure.

Bifurcated Inlet Shoulder Radius Study

TCA W/B/N/D OVERFLOW Analysis: Outboard Nacelle Surface Pressure
Mach 2.4, $\alpha = 3$ deg, $Re_{MAC} = 6.4$ million (WT)

OUTBOARD NACELLE

Baseline — Flat–Sided Bifurcated

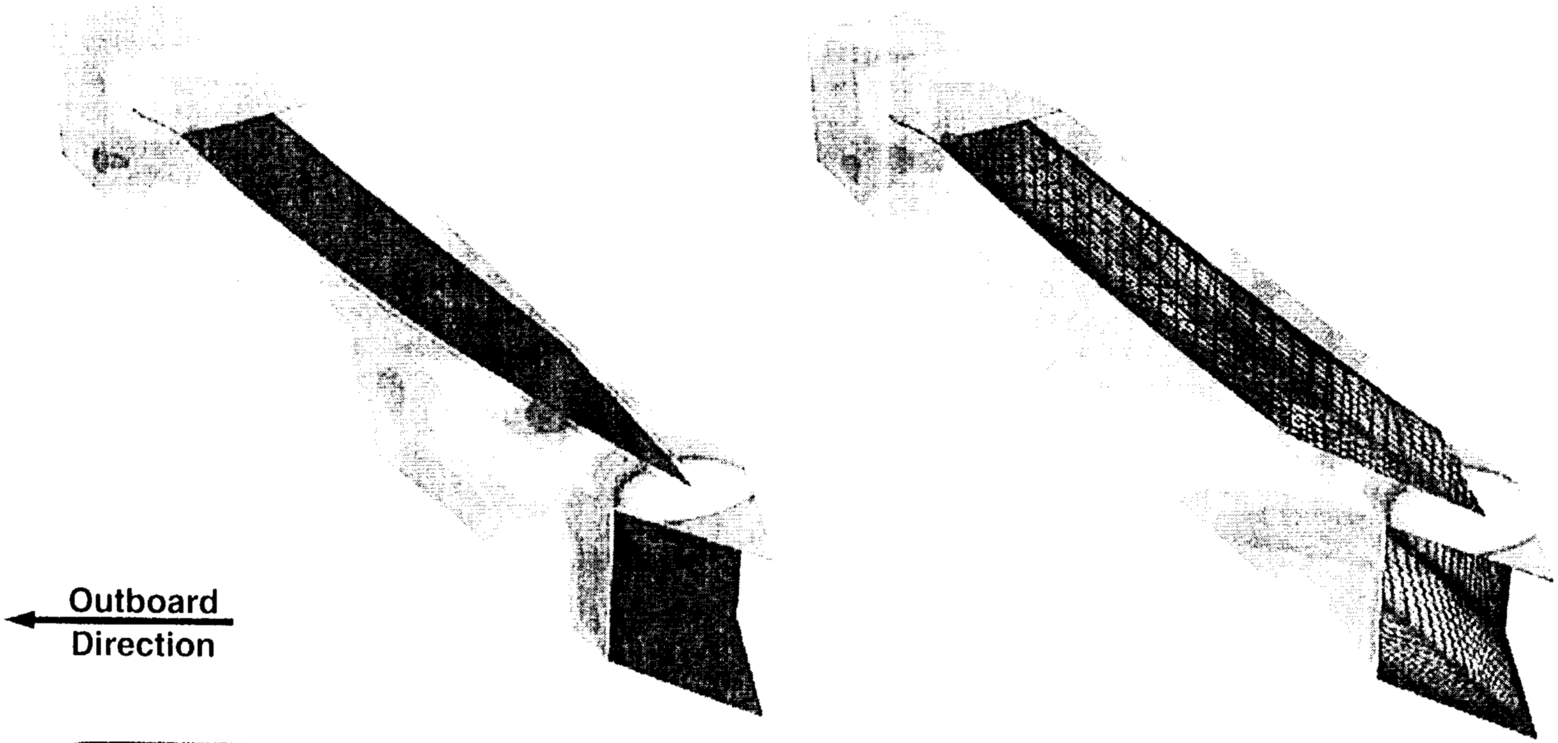

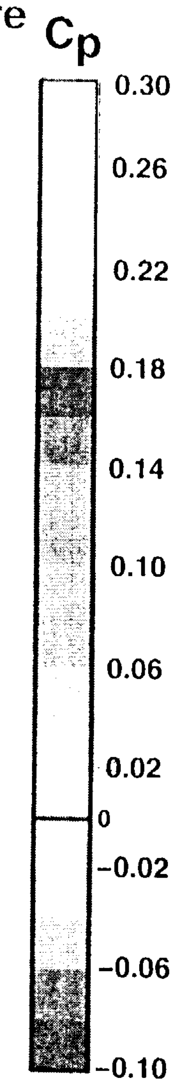

Isolated nacelle drag of flat–sided was 0.27 counts less than baseline (one nacelle). Drag of installed nacelle surfaces was same for both configurations.

Bifurcated Inlet Shoulder Radius Study

TCA W/B/N/D OVERFLOW Analysis: PAI Force Increments Mach 2.4, Re_{MAC} = 6.4 million (WT)

Near the cruise condition, the flat-sided nacelle had an installed drag ~ 1.5 counts higher than the baseline. This figure compares the baseline and modified nacelle force increments. The plot on the right confirms the drag increase of the flat-sided installation over the baseline of 1.5 counts at cruise lift. The plots on the left show the nacelle/diverter drag and lift increments at constant angle of attack for the baseline bifurcated and modified nacelles. The nacelle/diverter drag increment was broken down into pressure and friction components. The results indicated a slightly favorable installation for the modified nacelle in terms of the friction drag that was outweighed by the pressure component, resulting in the total being higher for the modified. The friction drag result was primarily the result of the diverter for the flat-sided installation cutting out larger portions of the wing and nacelle due the enlarged planform. The pressure drag results were reversed from the isolated drag results. An analysis of the isolated nacelle had shown that the flat-sided nacelle had a drag of 0.27 counts less than the baseline (one nacelle). Examination of the drag of individual components revealed the source of this reversal. The drag of the nacelle surfaces only was found to be very nearly the same for the baseline bifurcated and modified installations. The erasure of the isolated drag reduction of the modified nacelles was probably due to the higher pressures generated by the diverters discussed earlier. These pressures spread onto the nacelle forecowl and increase the pressure drag.

The lower left plot indicated that, despite the higher pressures generated by the modified installation diverters, the nacelle/diverter lift increment was less than the baseline level. This was attributed to the change in the nacelle shape: the double positive pressure signature of the baseline bifurcated appeared to result in an increased lift interference component.

Bifurcated Inlet Shoulder Radius Study

TCA W/B/N/D OVERFLOW Analysis: PAI Force Increments
Mach 2.4, Re_{MAC} = 6.4 million (WT)

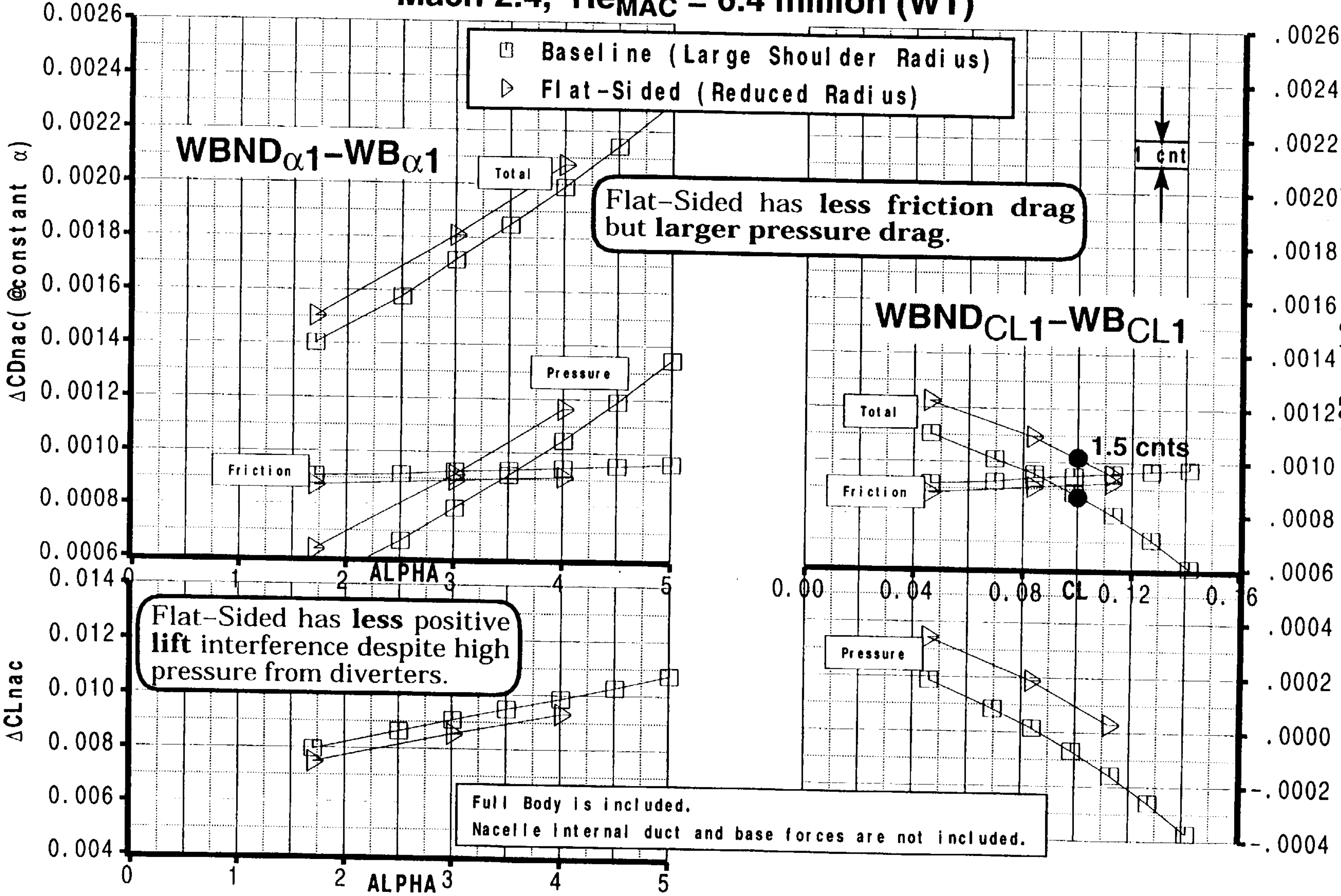

Bifurcated Inlet Shoulder Radius Study

TCA W/B/N/D OVERFLOW Analysis: Diverter Drag
Mach 2.4, Re_{MAC} = 6.4 million (WT)

This figure revealed the reason for the remainder of the drag increase of the straight sided modification. The modified installation resulted in a significantly increased pressure drag for the inboard: 1.1 counts at $\alpha = 3$ degrees. This was due to the increased diverter angle and resulting stronger shock. The outboard diverter drag also increased but to a lesser extent.

The final evaluation of the nacelle shaping applied to the baseline bifurcated (large shoulder radius) was that it was beneficial in several ways:
1) it allowed a diverter installation with included angles equivalent to a axisymmetric inlet installation which lowers drag, and
2) allows a inlet distortion free installation, and
3) produces a nacelle pressure field that increases the beneficial lift interference on the wing lower surface.

Bifurcated Inlet Shoulder Radius Study

TCA W/B/N/D OVERFLOW Analysis: Diverter Drag
Mach 2.4, Re_{MAC} = 6.4 million (WT)

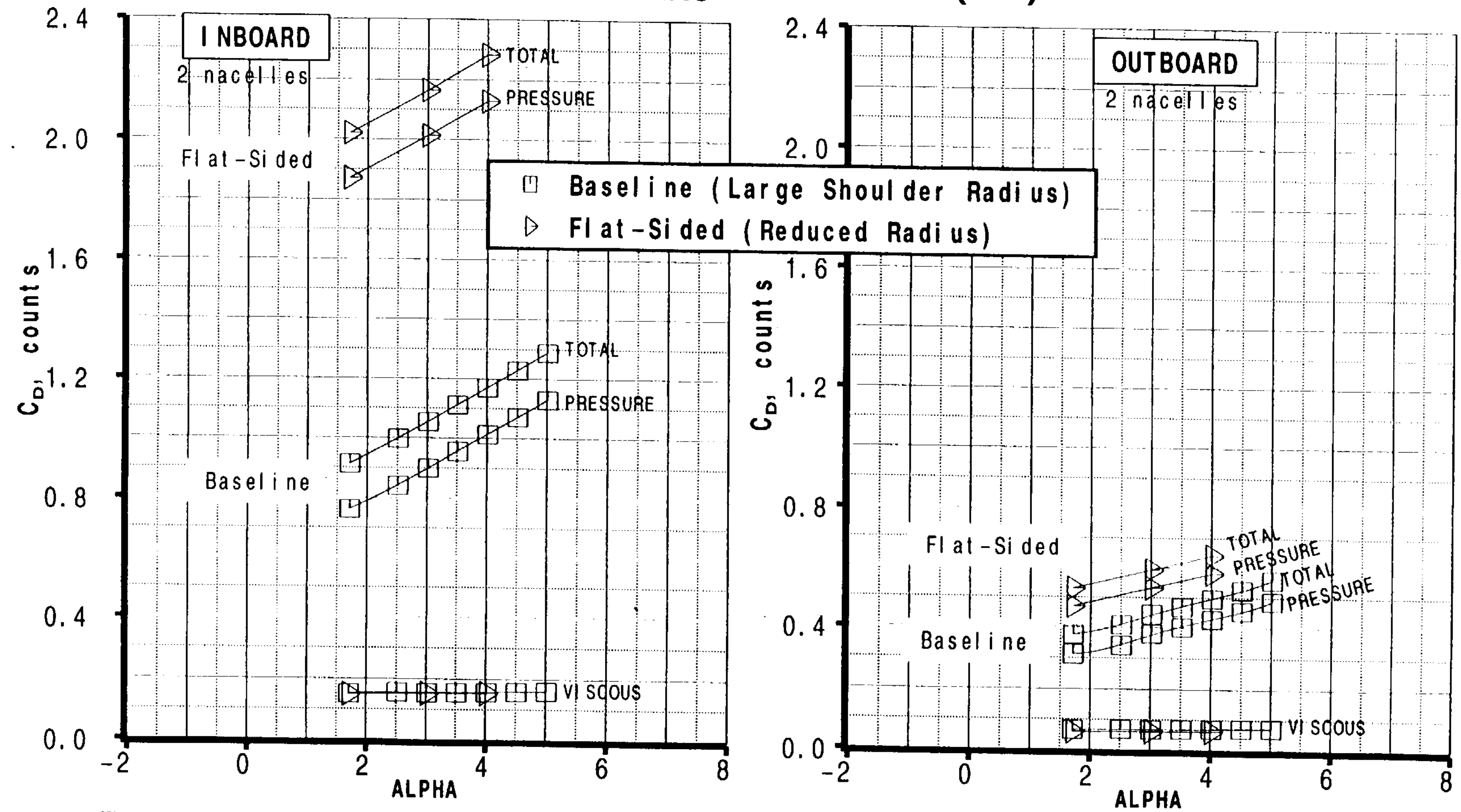

Drag increase on **inboard diverter** comprises most of total drag difference.

Bifurcated Inlet As–Tested Configuration Study

TCA W/B/N/D BSWT644 Test Data: Drag Polar
Mach 2.4, Re_{MAC} = 14.3 million, TCA Model 2b

Analysis of the BSWT 644 wind tunnel configuration has started in order to resolve the drag difference being measured in BSWT between the bifurcated and the axisymmetric nacelles. Three tasks are planned,

1) analysis of the wind tunnel internal duct (slightly different than the baseline CFD analysis duct),
2) parametric variation of the lip bevel to assess the potential for this being a cause of drag variability, and
3) analysis of wind tunnel nacelle external contour measurements.

Bifurcated Inlet As-Tested Configuration Study

TCA W/B/N/D BSWT644 Test Data: Drag Polar
Mach 2.4, Re_{MAC} = 14.3 million, TCA Model 2b

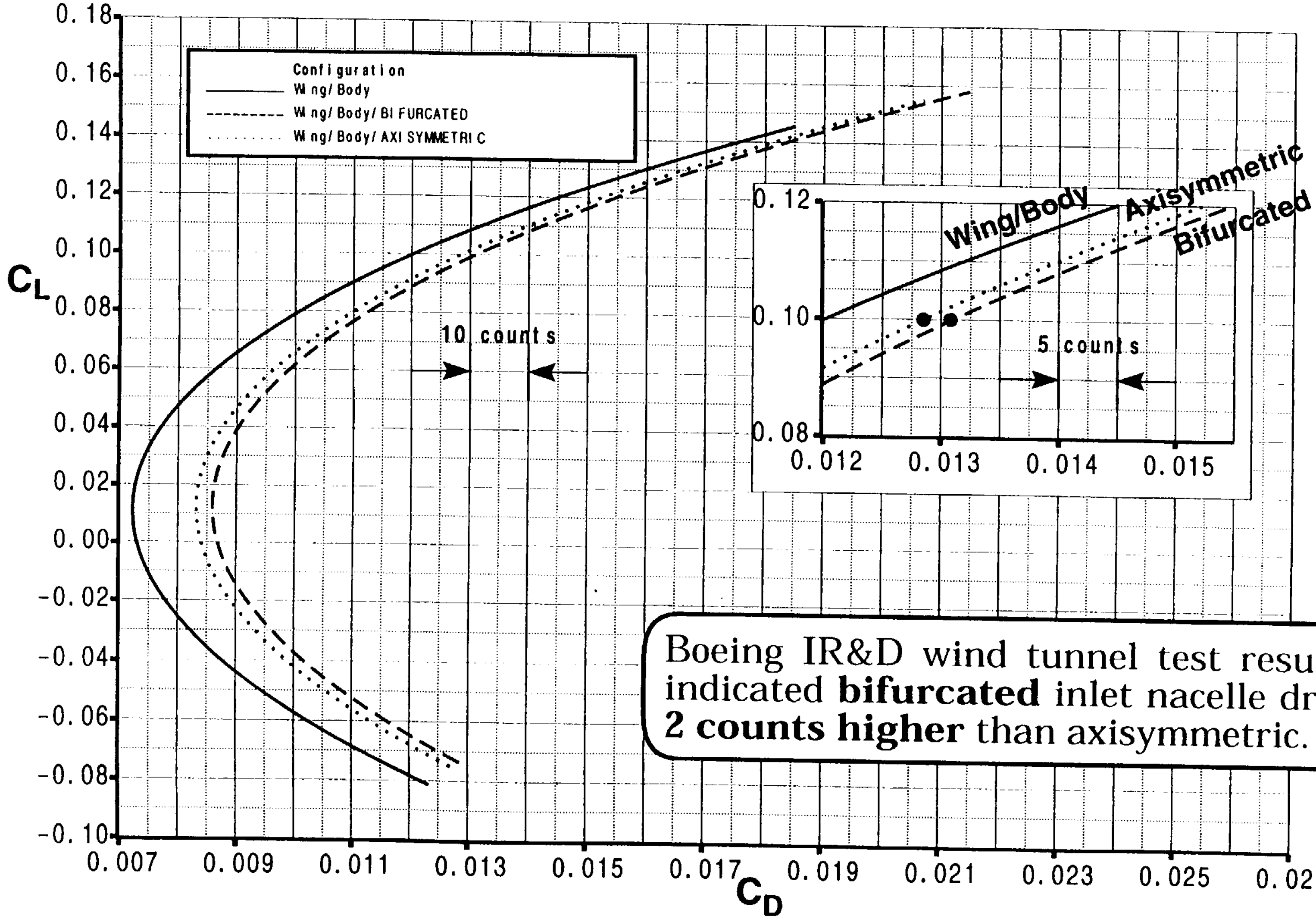

Boeing IR&D wind tunnel test results indicated **bifurcated** inlet nacelle drag **2 counts higher** than axisymmetric.

Bifurcated Inlet As–Tested Configuration Study

TCA W/B/N/D OVERFLOW Analysis: Inboard Nacelle Symmetry Plane Mach
Mach 2.4, α = 3 deg, Re_{MAC} = 6.4 million

The bifurcated nacelle wind tunnel internal geometry was analyzed using OVERFLOW. These analyses were conducted at the LaRC unitary test condition which results in a Reynolds Number about half that obtained in BSWT. This direction was taken in order to avoid the expense of building another grid for a study that was expected to reveal pressure drag discrepancies only.

The wind tunnel geometry was machined with a kink in the internal geometry as a result of machining requirements for the two parts which made up the nacelle. The geometry was analyzed both isolated and installed at wind tunnel Reynolds number, and compared with the baseline bifurcated nacelle OVERFLOW result. The figure shows a pressure distribution on the centerline of the inboard installed nacelle. The location of the kink in the wind tunnel model duct can be identified by the stronger shock from the lower surface shock from the lower surface of the nacelle about 10% aft of the nacelle LE. This shock reflected through out the length of the duct. The wind tunnel duct had a slightly higher drag (due entirely to pressure drag) and a slightly smaller negative lift value. The wind tunnel data is corrected only for the skin friction of the duct so both of these pressure force effects would have an effect on the data. The outboard nacelle Mach contours are shown in Figure V. The lift of the duct was nearly identical for the two configurations but the wind tunnel duct again had higher drag (and again nearly all pressure drag). In conclusion, it appears that in comparing the wind tunnel data to the CFD analyses, that 0.4 counts should be subtracted from the wind tunnel drag levels to account for internal duct modeling differences.

Bifurcated Inlet As–Tested Configuration Study

TCA W/B/N/D OVERFLOW Analysis: Inboard Nacelle Symmetry Plane Mach Contours

Mach 2.4, $\alpha = 3$ deg, $Re_{MAC} = 6.4$ million

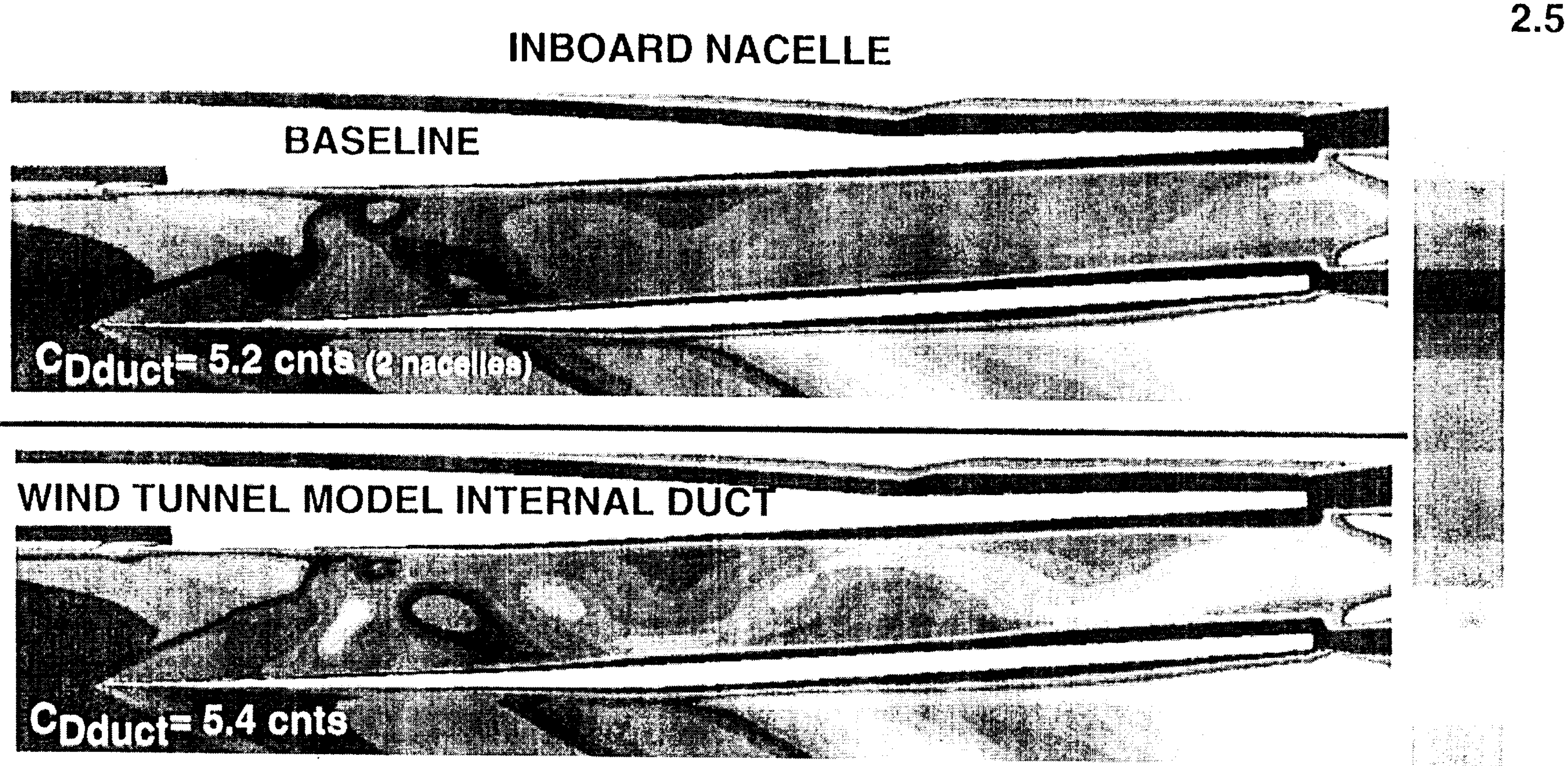

Drag increase of 0.4 counts (inboard plus outboard) for the as–tested internal duct (primarily pressure drag).

Bifurcated Inlet As–Tested Configuration Study

TCA W/B/N/D OVERFLOW Analysis: Outboard Nacelle Symmetry Plane Mach
Mach 2.4, $\alpha = 3$ deg, $Re_{MAC} = 6.4$ million

See text for previous figure.

Bifurcated Inlet As–Tested Configuration Study

TCA W/B/N/D OVERFLOW Analysis: Outboard Nacelle Symmetry Plane Mach Contours
Mach 2.4, α = 3 deg, Re_{MAC} = 6.4 million

OUTBOARD NACELLE

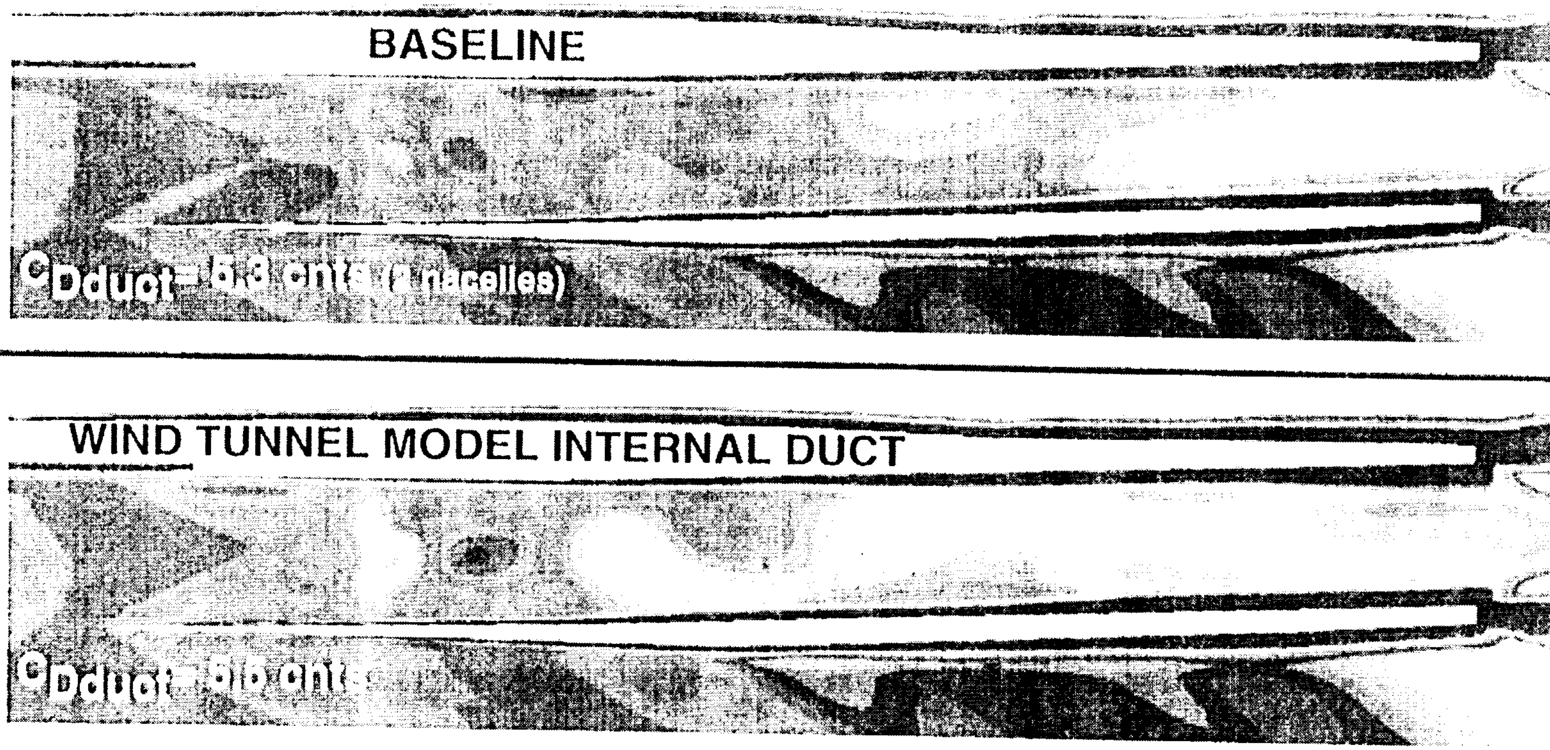

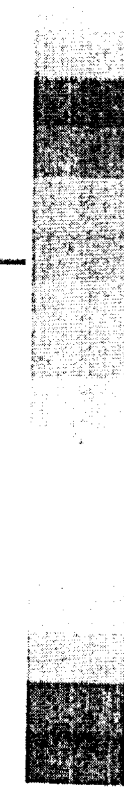

Manufacturing limitations made construction of baseline bifurcated duct impossible. Kink at X/C ~ 0.1 in as–tested duct results in **increased shock strength** for entire length of duct.

Bifurcated Inlet As–Tested Configuration Study

TCA W/B/N/D OVERFLOW Analysis: Nacelle Thickness Variations Dimensions in inches

This figure shows two lip bevel variations that were generated to approximate the actual wind tunnel parts (the actual wind tunnel model parts do not, of course, have infinitely sharp leading edges as shown in this schematic). The nacelle loft lines were not machined near the leading edges (the metal becomes too thin to tolerate the cutter forces). As a result, an over–tolerance line was cut, and the resulting part hand worked down to the desired line. However, as the model scale was so small (1.675%), very small differences in model geometry would translate into significant full scale changes. Measurements were made on the nacelle geometry during the test which indicated a thickness of 1.223 inches at 6 inches aft of the leading edge. The thickness should be 0.398 inches at this point. The nacelles were reworked to a thickness of 0.45 inches and retested in the wind tunnel. These variations from the baseline were analyzed on both an isolated nacelle and an installed nacelle.

Bifurcated Inlet As–Tested Configuration Study

TCA W/B/N/D OVERFLOW Analysis: Nacelle Thickness Variations
Dimensions in inches

Wind tunnel model wall thickness measured 0.1 inches back from leading edge.

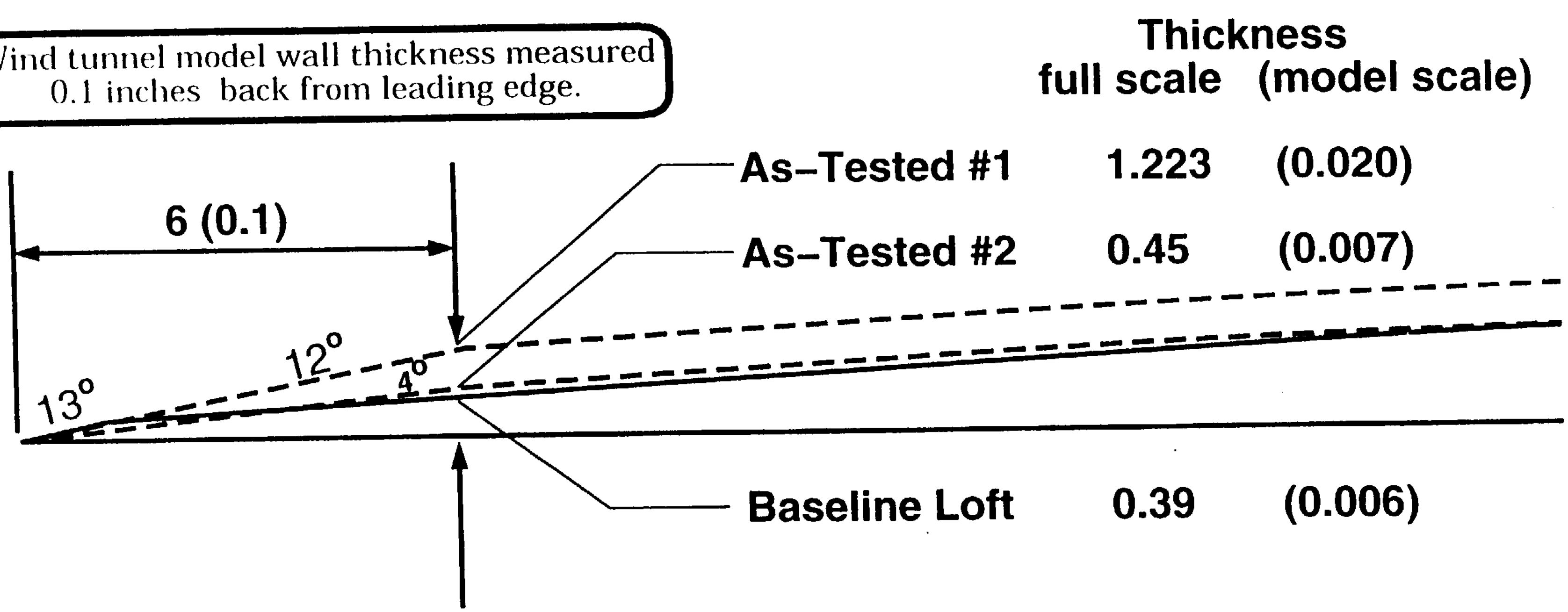

Baseline CFD grid modified to model measured nacelle thickness.

Bifurcated Inlet As–Tested Configuration Study

TCA W/B/N/D OVERFLOW Analysis: Inboard Nacelle Surface Pressure
Mach 2.4, $\alpha = 3$ deg, $Re_{MAC} = 6.4$ million

The installed analysis of the 1.223 inch geometry indicated a drag increase of 1.1 counts relative to the bifurcated inlet baseline. The drag increase on the nacelle surfaces was 1.24 counts but the wing incurred a lift benefit alleviating some of the nacelle drag penalty. This geometry was a significant change from the baseline, and a large drag penalty was expected. This figure and the next (nacelle inboard and outboard surface pressure contours) show the effect of this thicker nacelle with it's large bevel. While the pressures on the baseline bevel are slightly higher, the new bevel had similar pressures over a much larger area. The reflected shock on the inboard nacelle is also of higher pressure due to the larger bevel.

The installed analysis of the 0.45 inch geometry indicated a drag increase of less than 0.05 counts relative to the baseline. The geometry was a moderate change to the baseline, however the bevel angle was significantly less which contributed to the small increase in drag. The isolated nacelle analysis predicted a similar drag level (0.04 counts for four nacelles). It can be seen that the bevel effect is much less for this geometry. While the size of the bevel is readily apparent, the pressures on the bevel are markedly less than for the baseline.

These OVERFLOW results indicate a significant drag penalty for the original as tested wind tunnel model geometry (~ 1 count). However, in the BSWT test, after the inlet was handworked to have a smaller bevel angle, no drag change was measured. This is in contrast to the OVERFLOW results which indicated that the sharpened geometry had nearly equivalent drag to the baseline (or, 1 count less than the original wind tunnel geometry). These results are still being analyzed, but do indicate the possibility of the lip bevel being another source of uncertainty in the wind tunnel measured bifurcated nacelle drag relative to the baseline results obtained from OVERFLOW.

Bifurcated Inlet As–Tested Configuration Study

TCA W/B/N/D OVERFLOW Analysis: Inboard Nacelle Surface Pressure
Mach 2.4, α = 3 deg, Re_{MAC} = 6.4 million

INBOARD NACELLE

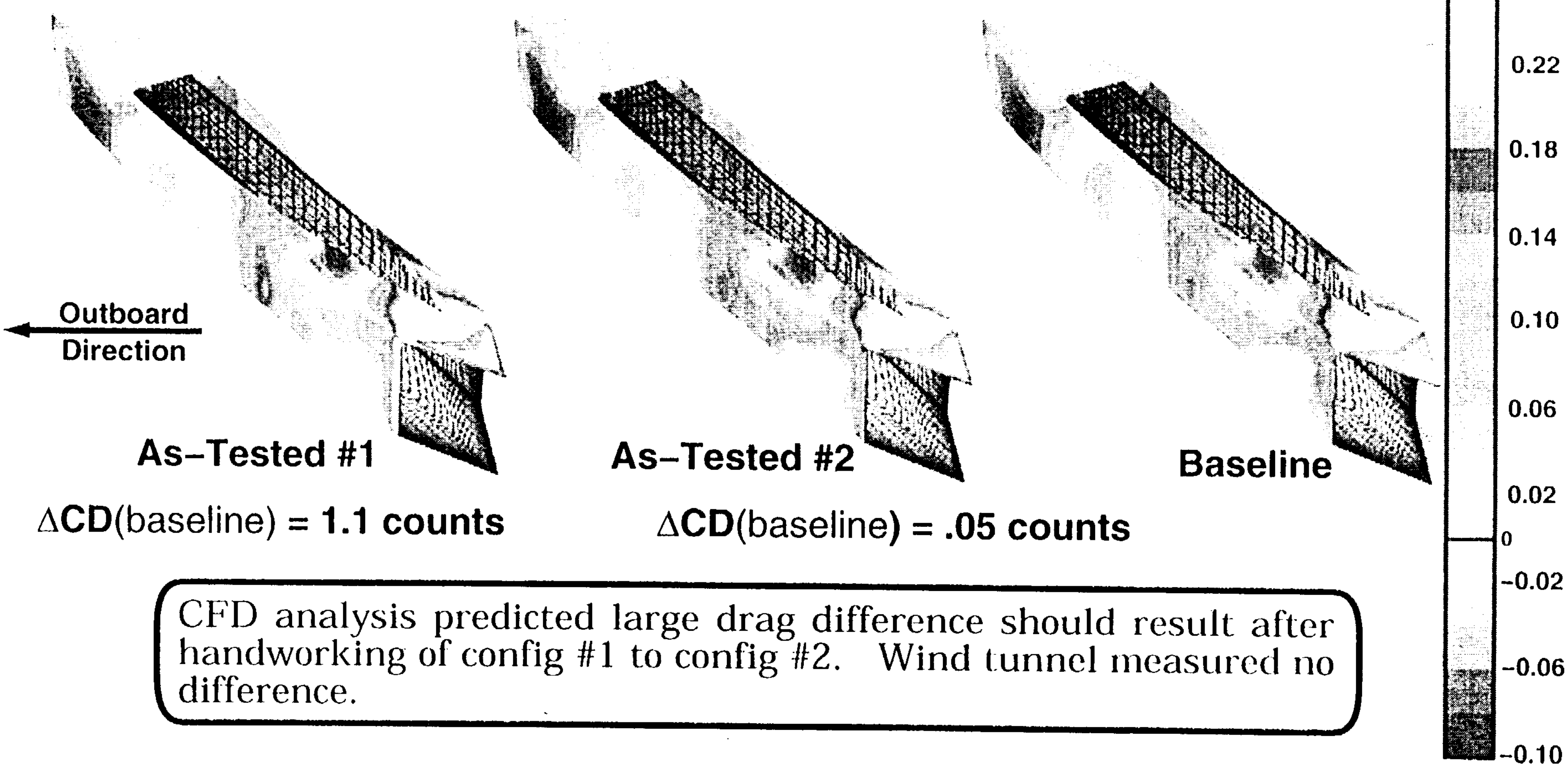

Δ**CD**(baseline) = **1.1 counts**

Δ**CD**(baseline) = **.05 counts**

CFD analysis predicted large drag difference should result after handworking of config #1 to config #2. Wind tunnel measured no difference.

Bifurcated Inlet As–Tested Configuration Study

TCA W/B/N/D OVERFLOW Analysis: Outboard Nacelle Surface Pressure
Mach 2.4, $\alpha = 3$ deg, $Re_{MAC} = 6.4$ million

See text for previous figure.

Bifurcated Inlet As–Tested Configuration Study

TCA W/B/N/D OVERFLOW Analysis: Outboard Nacelle Surface Pressure
Mach 2.4, $\alpha = 3$ deg, $Re_{MAC} = 6.4$ million

OUTBOARD NACELLE

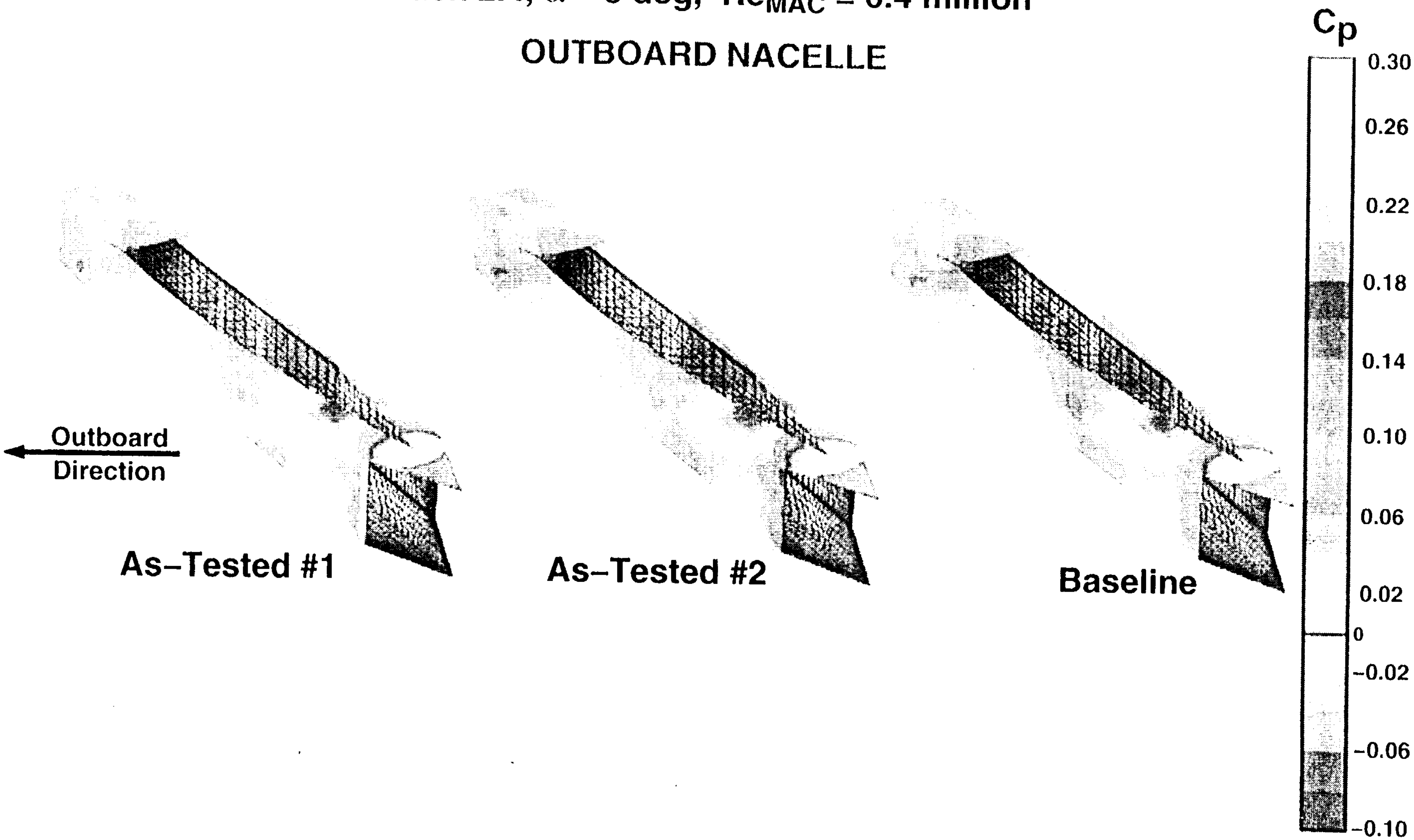

Bifurcated Inlet As–Tested Configuration Study

TCA W/B/N/D OVERFLOW Analysis: Wing Lower Surface Pressure
Mach 2.4, α = 3 deg, Re_{MAC} = 6.4 million

The effect of the larger bevel of the wind tunnel configuration #1 on the wing lower surface is also apparent where the higher pressure region spreads out both laterally and forward in the nacelle footprint. Higher pressure regions are also seen on the wing lower surface between the nacelles. The pressure contours for wind tunnel configuration #2 were very similar to the baseline.

Bifurcated Inlet As–Tested Configuration Study

TCA W/B/N/D OVERFLOW Analysis: Wing Lower Surface Pressure

Mach 2.4, $\alpha = 3$ deg, $Re_{MAC} = 6.4$ million

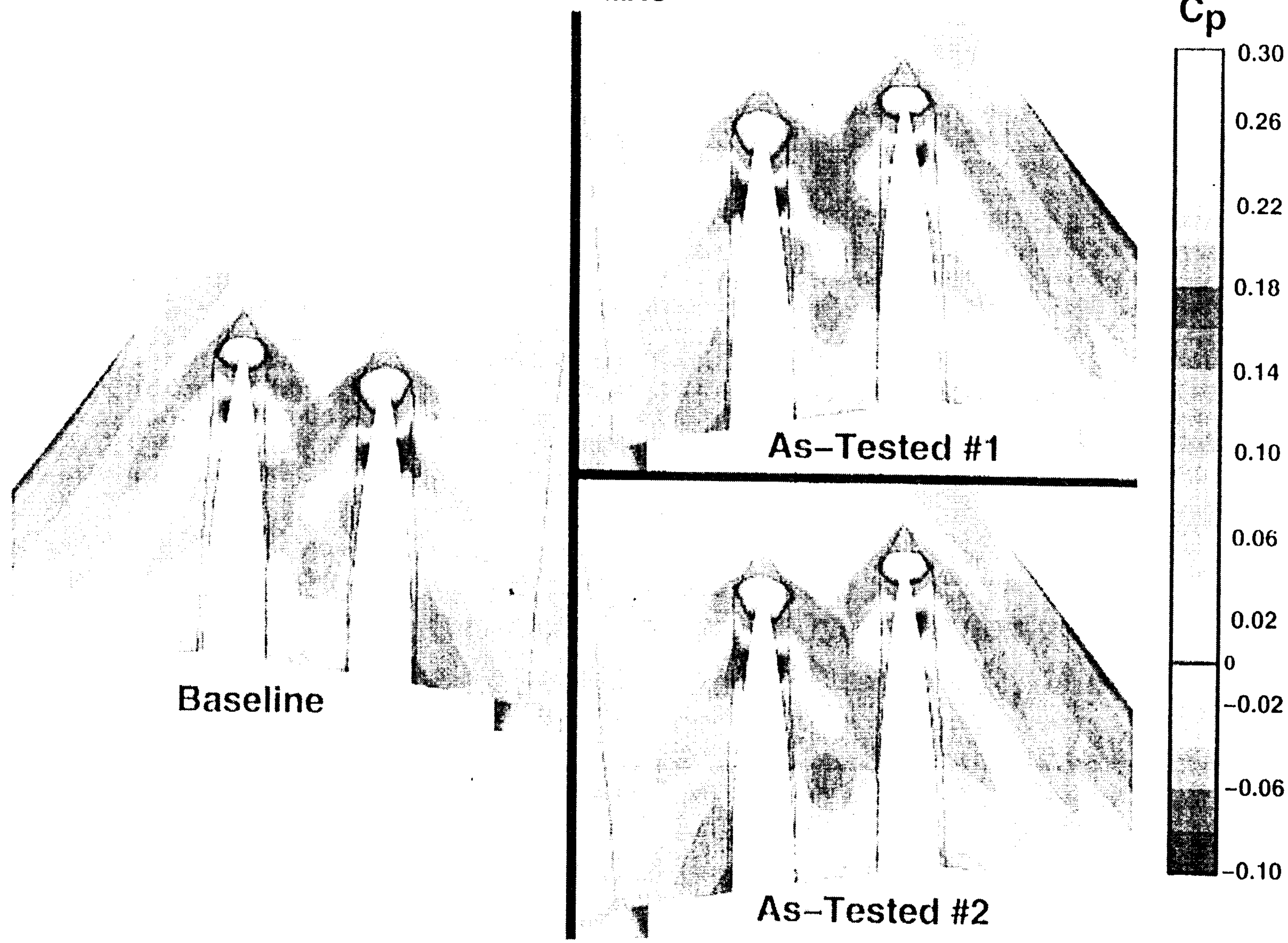

Bifurcated Inlet As–Tested Configuration Study

TCA W/B/N/D OVERFLOW Analysis: WT Model QA Variation fom Loft Dimensions in Full Scale Inches

The final phase of the as–tested configuration study has been an analysis of the quality assurance (QA) laser survey measurements of the nacelle surfaces. The results for the inboard nacelle survey are shown in the figure. Initial observation of the points indicated that they were both translated and rotated away from the baseline loft surface. This could be the result of an inaccurate reference point for the survey, or an inaccurate location of the nacelle. In order to assess the variation of the wind tunnel model from the loft, the distance from each QA point to the loft was calculated. An optimizer was then run to rotate and translate the nacelle in order to minimize the root–sum–square of all the QA point distances; the resulting coordinate transformation is shown in the figure. The resulting distances of each QA point from the loft are color coded. Although the scale is in absolute inches, observation of the points reveals that they are ALL internal relative to the loft. There is also a trend of small variation at the most aft points, and large (~1 inch) variations near the nacelle lip. Modification of the OVERFLOW grid to match these points will require a reduction in the capture area, which will increase the nacelle forecowl angle, and increase drag. This analysis is in progress.

Bifurcated Inlet As–Tested Configuration Study

TCA W/B/N/D OVERFLOW Analysis: WT Model QA Variation fom Loft
Dimensions in Full Scale Inches

Minimize RSS variation	Trans.	Rot., deg
X	–.014	–.155
Y	+.131	+.276
Z	+.222	–.154

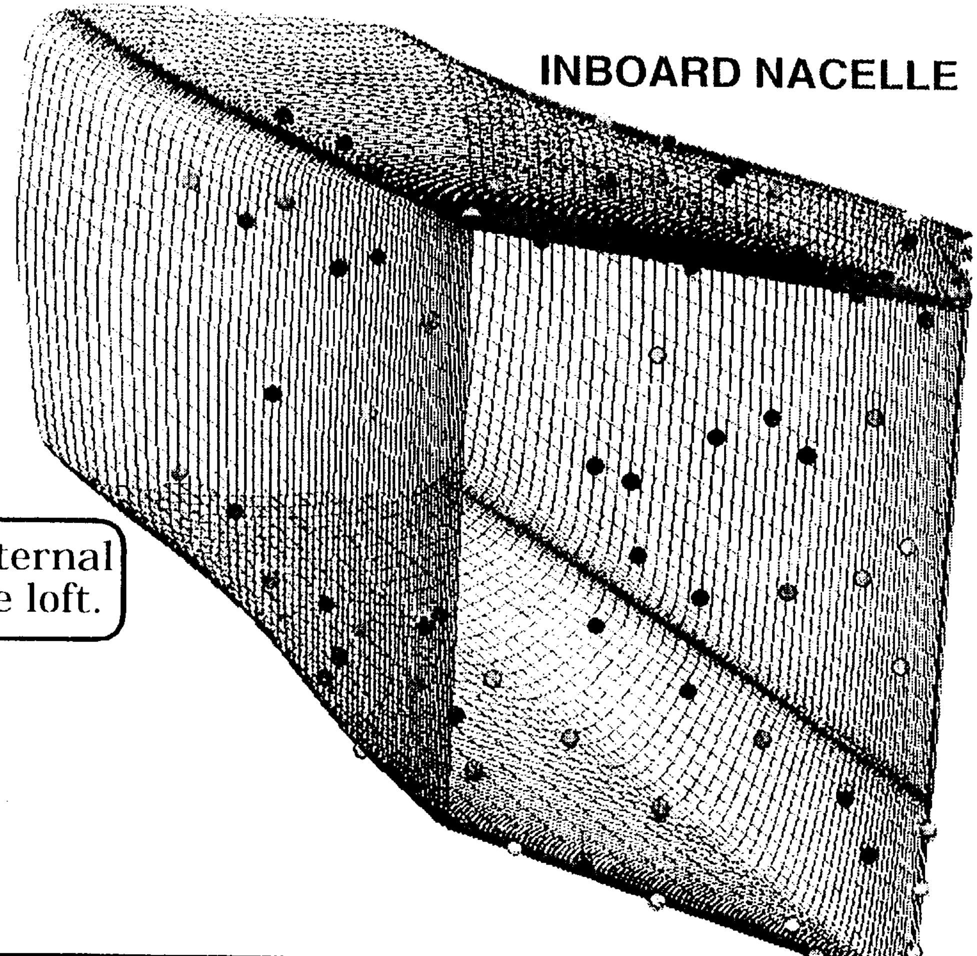

QA points are **all** internal relative to the baseline loft.

CFD grid modification to model QA points requires reducing the capture area, increasing nacelle forecowl angle, and increasing nacelle drag. Analysis in progress.

Bifurcated Inlet Bevel Angle Study

TCA W/B/N/D OVERFLOW Analysis: Angle Variation
Dimensions in Inches Full Scale (Model Scale=0.01675)

Several variations of the nacelle lip bevel were analyzed. The bevel variations were designed by rotating the bevel surfaces about their leading edges to steeper angles (26, 39, 52, and 90 degrees) and one smaller bevel angle (5 degrees bevel angle rather than the 13 degree baseline). A schematic of these bevel configurations is shown in the figure. All variants were analyzed with OVERFLOW on an isolated nacelle at wind tunnel Reynolds number; several were analyzed installed. All CFD analyses to date have modeled infinitely sharp leading edges for the nacelles (as well as, the wing outboard panel). In reality, the wind tunnel model nacelles all have blunt leading edges as the sharpest they are usually filed to is 0.004 inches (quarter inch full scale). As the figure shows, the bifurcated lip bevel is approximately 0.004 inches tall at the base and the 90 degree rotation will provide the worst case blunt lip (entire bevel face on to the flow). It is likely that microscopic observation of the wind tunnel model leading edge would reveal a ragged geometry, i.e., corners chipped off.

Bifurcated Inlet Bevel Angle Study

TCA W/B/N/D OVERFLOW Analysis: Angle Variation
Dimensions in Inches Full Scale (Model Scale=0.01675)

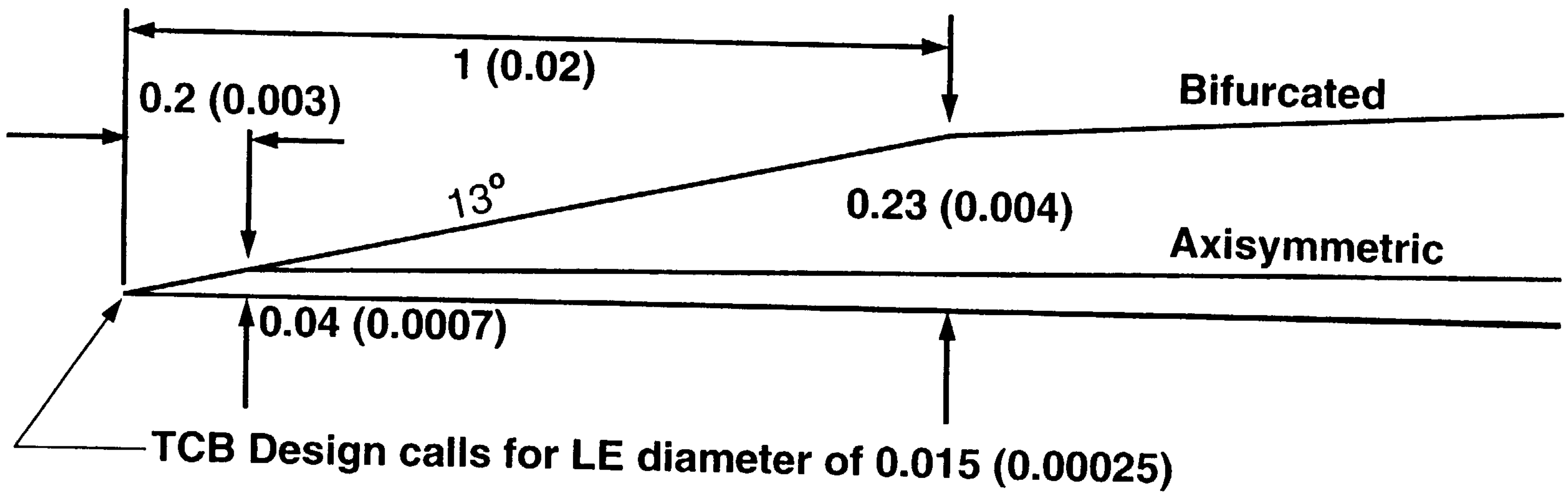

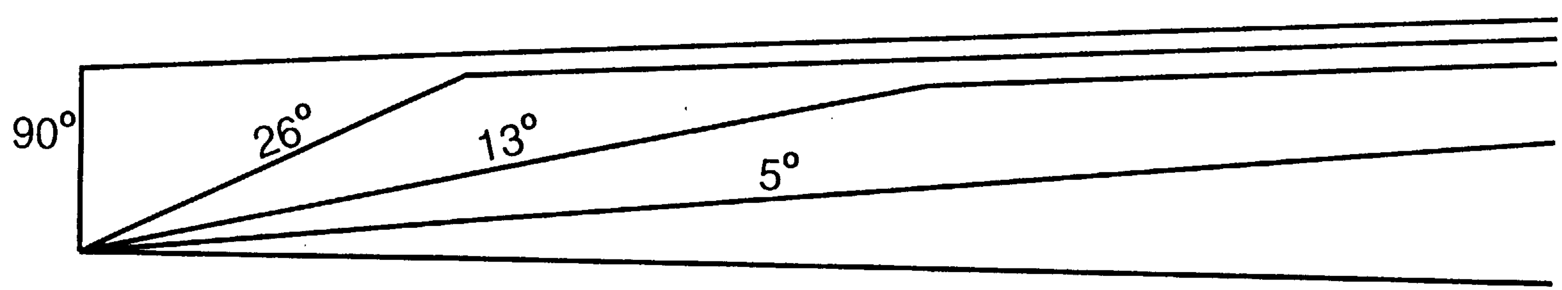

Rotating current bifurcated bevel to 90° models expected wind tunnel model lip geometry (0.004).

Bifurcated Inlet Bevel Angle Study

TCA W/B/N/D OVERFLOW Analysis: Drag Variation
Mach 2.4, $\alpha = 3$ deg, $Re_{MAC} = 6.4$ million

The figure shows a comparison of the incremental drag (from the baseline) of the various bevel angles analyzed. As expected, the drag increments were quite small (on the order of 0.2 counts or less for four nacelles) for bevel angles less than 90 degrees. The shock detachment angle shown was the handbook value for an unswept wedge. The drag increments shown for the isolated nacelle analyses were for the entire nacelle (lip bevel plus forecowl plus nozzle). The drag increment for the one installed case included the entire nacelle, as well as, the positive lift interference effect on the wing lower surface due to increased lip bevel pressures. Initially the blunt bevel was modeled with three points on bevel surface, similar to the baseline. Examination of the OVERFLOW solution in the bevel region indicated that the stand–off shock had not been captured accurately. Several solutions with increased grid density on the bevel were run: one with 9 points and one with 15 points. The pressure drag for the bevel surface increases from the baseline to the blunt by 0.4 counts (for one nacelle). The bevel base in these models was 0.2 inches high. This corresponds to 0.0034 inches model scale. Sharp lips (or leading edges) have generally been worked to achieve a 0.004 inch thickness on HSCT wind tunnel models. This would indicate that the CFD solutions completed to date (which all have infinitely sharp leading edges) could be low relative to test data by greater than 1.6 counts. However, examination of the viscous drag components revealed that there is a decrease in friction drag on the front part of inlet due to the disturbance caused by the stand–off shock that ameliorates the pressure drag increase somewhat. This analysis highlights another possible source of discrepancy between the axisymmetric and bifurcated inlet nacelles tested in BSWT644. The axisymmetric inlet nacelles have "over–sharpened" inlet lips that are estimated to be as thin as 0.002 inches. This could have lead to a lip drag that was as much as 0.7 counts less than the bifurcated.

Bifurcated Inlet Bevel Angle Study

TCA W/B/N/D OVERFLOW Analysis: Drag Variation
Mach 2.4, $\alpha = 3$ deg, $Re_{MAC} = 6.4$ million

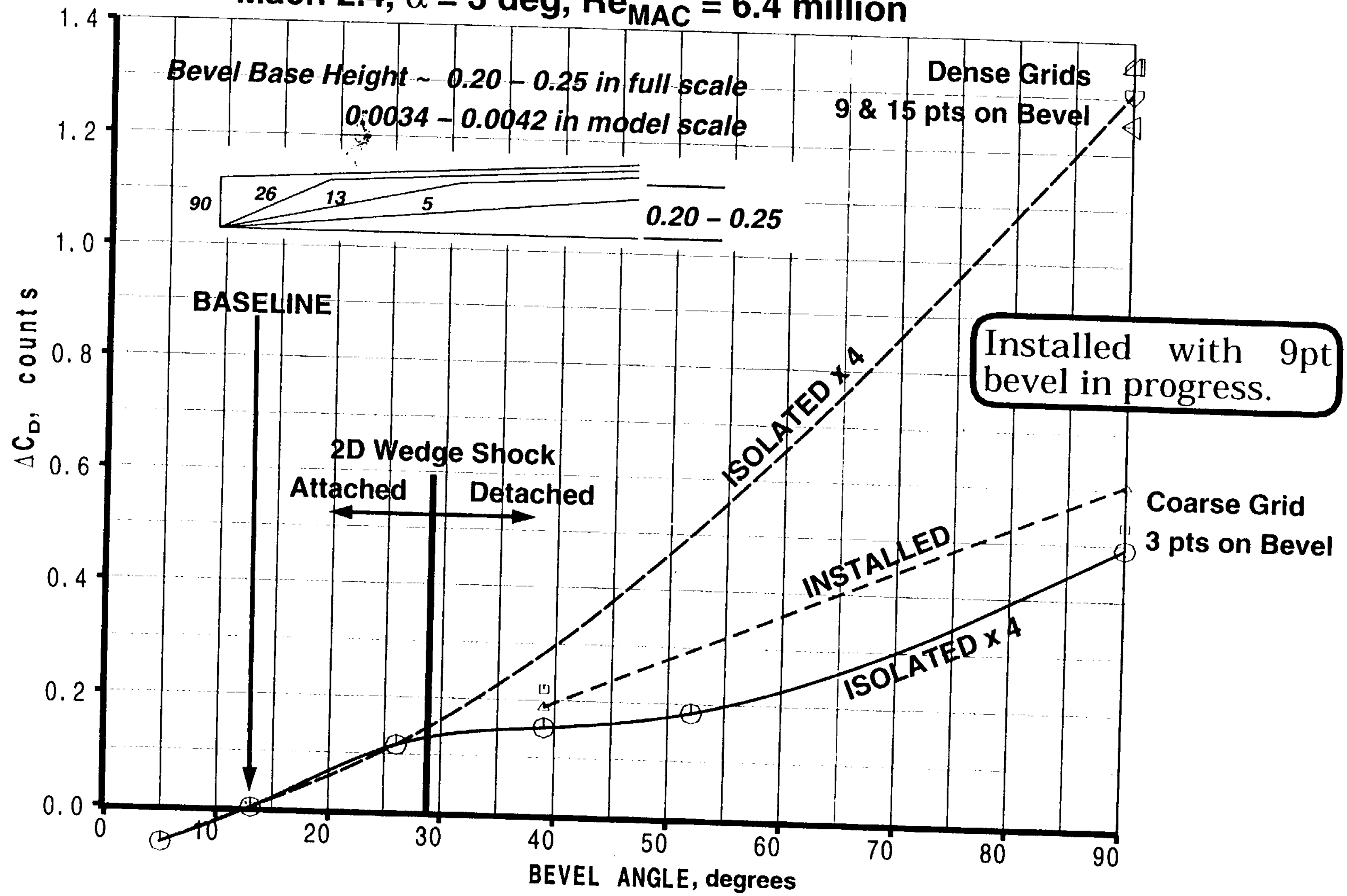

Bifurcated Inlet Bevel Angle Study

TCA W/B/N/D OVERFLOW Analysis: Flow Field Pressure at Lip
Mach 2.4, $\alpha = 3$ deg, $Re_{MAC} = 6.4$ million

Initially the blunt bevel was modeled with three points on bevel surface, similar to the baseline. Examination of the OVERFLOW solution in the bevel region (all isolated analyses) indicated that the stand-off shock had not been captured accurately. Several solutions with increased density on bevel were run. A solution with 9 points and one with 15 points (and an increased density internal grid) are shown in the figure. The 9 point model appears to be sufficient for capturing an accurate stand-off shock and maximum bevel surface pressure.

Bifurcated Inlet Bevel Angle Study

TCA W/B/N/D OVERFLOW Analysis: Flow Field Pressure at Lip

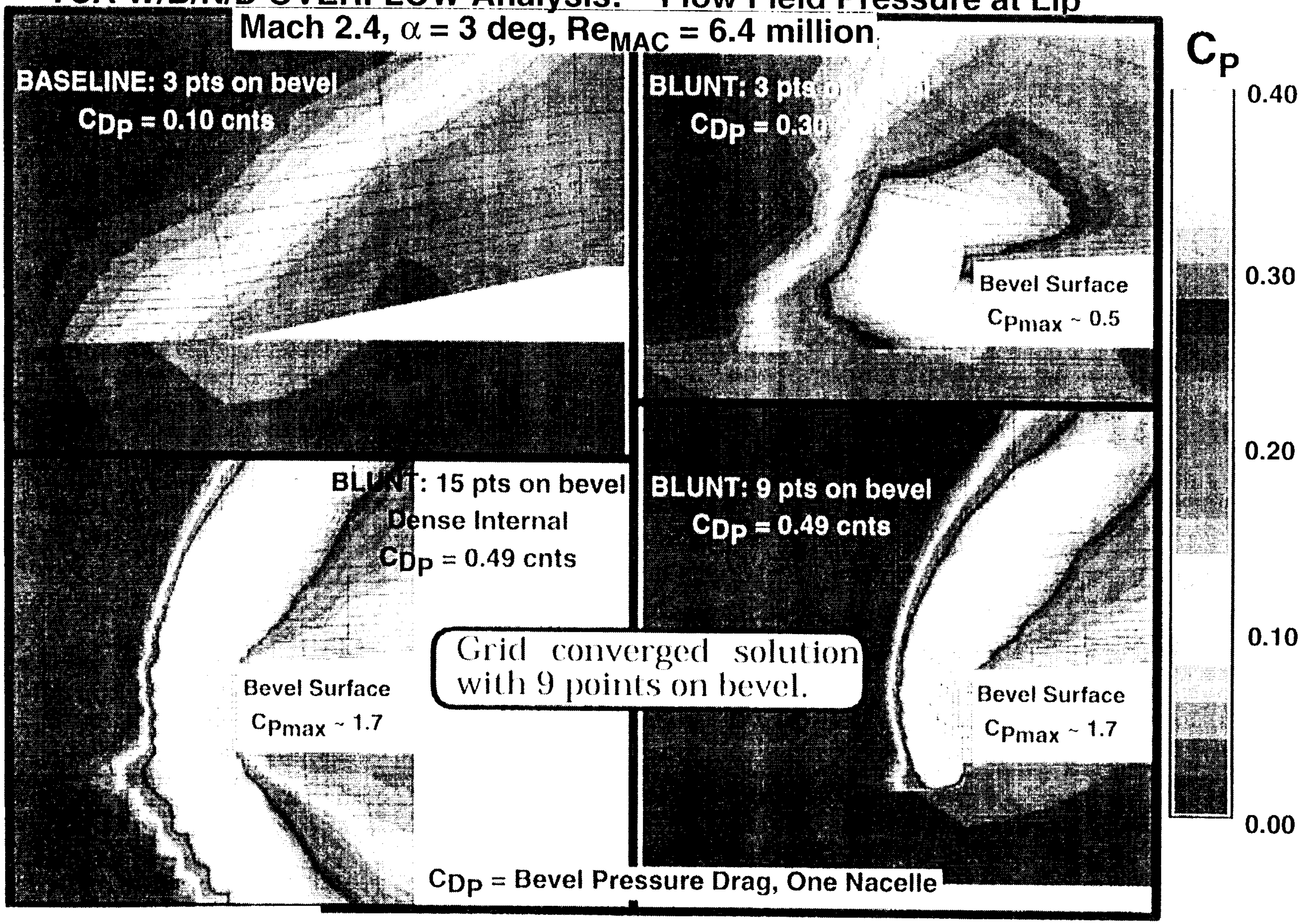

Nozzle Width Study

TCA W/B/N/D OVERFLOW Analysis: Baseline, PTC, Modified Lofts

The nozzle aspect ratio (width/height) has been increased to address noise problems at take–off; the new nozzle design was incorporated on the PTC nacelle installation (middle figure). The engine was unchanged so that it was necessary to retain the same nacelle height. The baseline bifurcated nacelle on the TCA (left figure) was stretched along the nacelle y axis to model this change and assess the impact of the wider nacelle. The baseline bifurcated nacelle as analyzed last year had a take–off nozzle aspect ratio of 1.2. It was modified to match the PTC nacelle take–off nozzle aspect ratio of 1.5; modification resulted in maximum area increase from 6300 to 7200 in^2.

Nozzle Width Study

TCA W/B/N/D OVERFLOW Analysis: Baseline, PTC, Modified Lofts

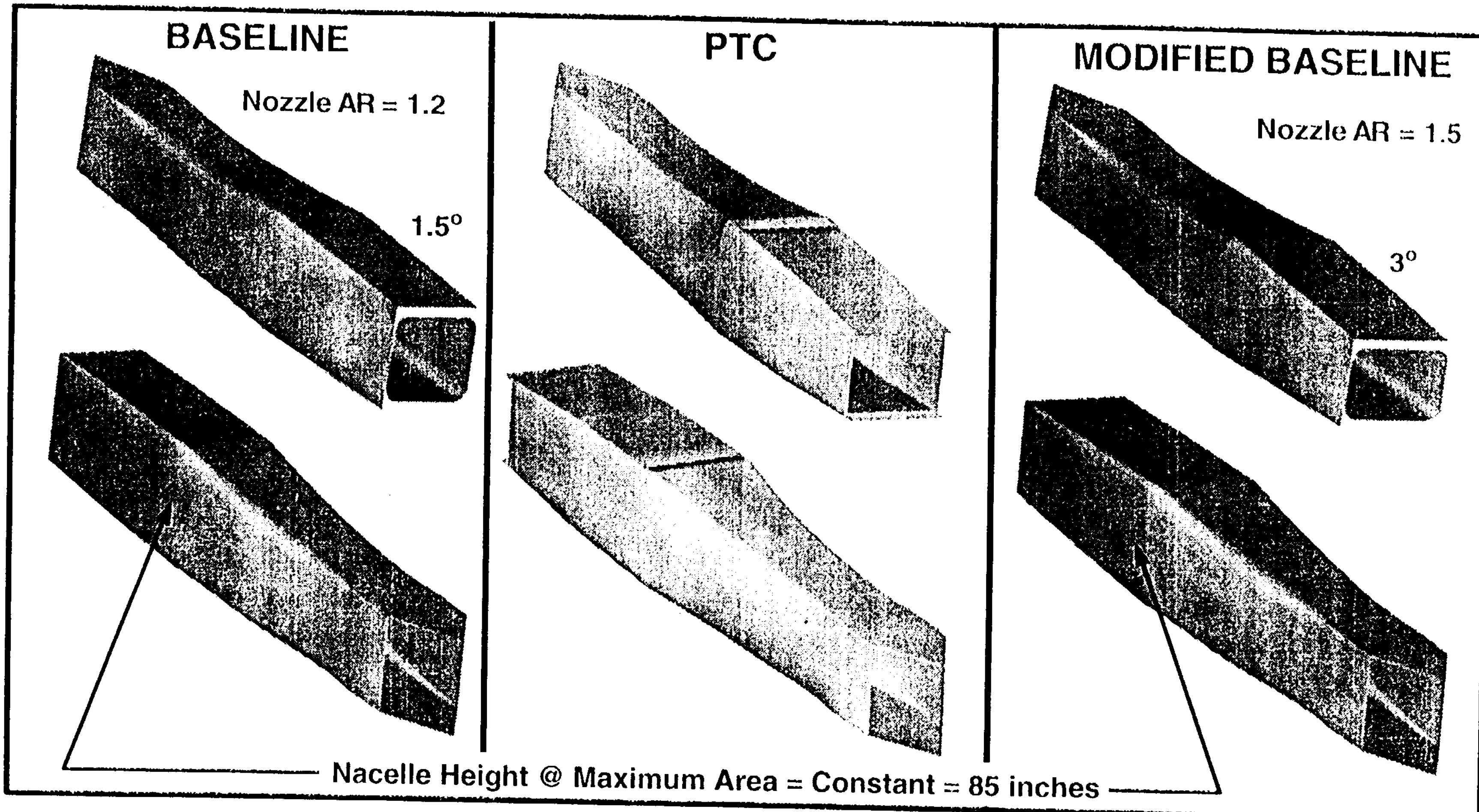

Current baseline bifurcated grid was stretched in Y only to model wider PTC nozzle. Inlet capture geometry was not changed.

Nozzle Width Study

TCA W/B/N/D OVERFLOW Analysis: PAI Force Increments
Mach 2.4, Re_{MAC} = 6.4 million

An OVERFLOW analysis of the isolated AR1.5 nacelle indicated an increase in drag over the baseline of +0.81 counts (for one nacelle). This was evenly split between the forecowl and the nozzle (+0.41 counts on the forecowl, +0.40 counts on the nozzle). This drag increase was nearly all (90%) due to pressure drag. There were larger forecowl angles on the sides of the nacelle, and larger nozzle angles on the top and bottom (the nozzle angle doubled, 1.5 to 3 degrees). The nacelle drag increment at constant alpha was higher for the modified nacelle as expected, based on the isolated results. The modified bifurcated nacelle drag increment at constant angle of attack is ~3.6 counts higher than the baseline at angle of attack of 3 degrees. This compares favorably with the isolated value for 4 nacelles (3.24 = 4 x 0.81). However, there was a very large increase in positive lift interference that counteracted a large part of the drag increase and the final modified bifurcated installed drag delta was +1.0 count at cruise (CL = 0.1).

Nozzle Width Study

TCA W/B/N/D OVERFLOW Analysis: PAI Force Increments
Mach 2.4, Re_{MAC} = 6.4 million

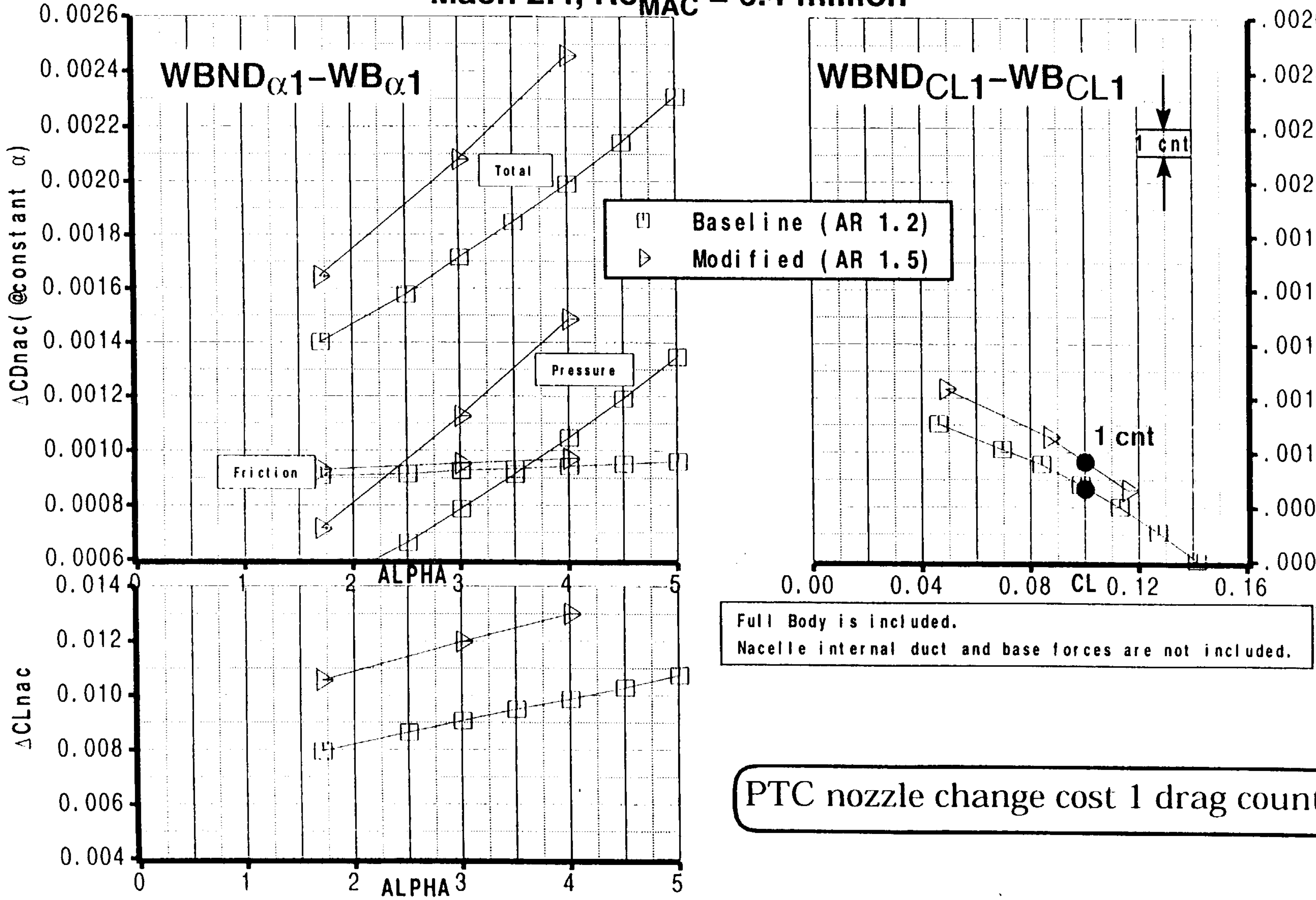

Full Body is included.
Nacelle internal duct and base forces are not included.

PTC nozzle change cost 1 drag count.

Nozzle Width Study

TCA W/B/N/D OVERFLOW Analysis: Wing Lower Surface Pressure Mach 2.4, $\alpha = 3$ deg, $Re_{MAC} = 6.4$ million

The OVERFLOW analysis of the modified bifurcated inlet installed on the TCA has been completed. This geometry was obtained by perturbing the baseline bifurcated so that the maximum area station is equivalent to the PTC nacelle (geometry modifications were discussed in previous activity reports). The wing lower surface pressure contours are shown. The elevated pressure levels due to the larger diverter and nacelle forecowl angles were most noticeable in the region between the nacelles.

Nozzle Width Study

TCA W/B/N/D OVERFLOW Analysis: Wing Lower Surface Pressure

Mach 2.4, $\alpha = 3$ deg, $Re_{MAC} = 6.4$ million

Baseline Bifurcated (AR = 1.2)

Modified Bifurcated (AR=1.5)

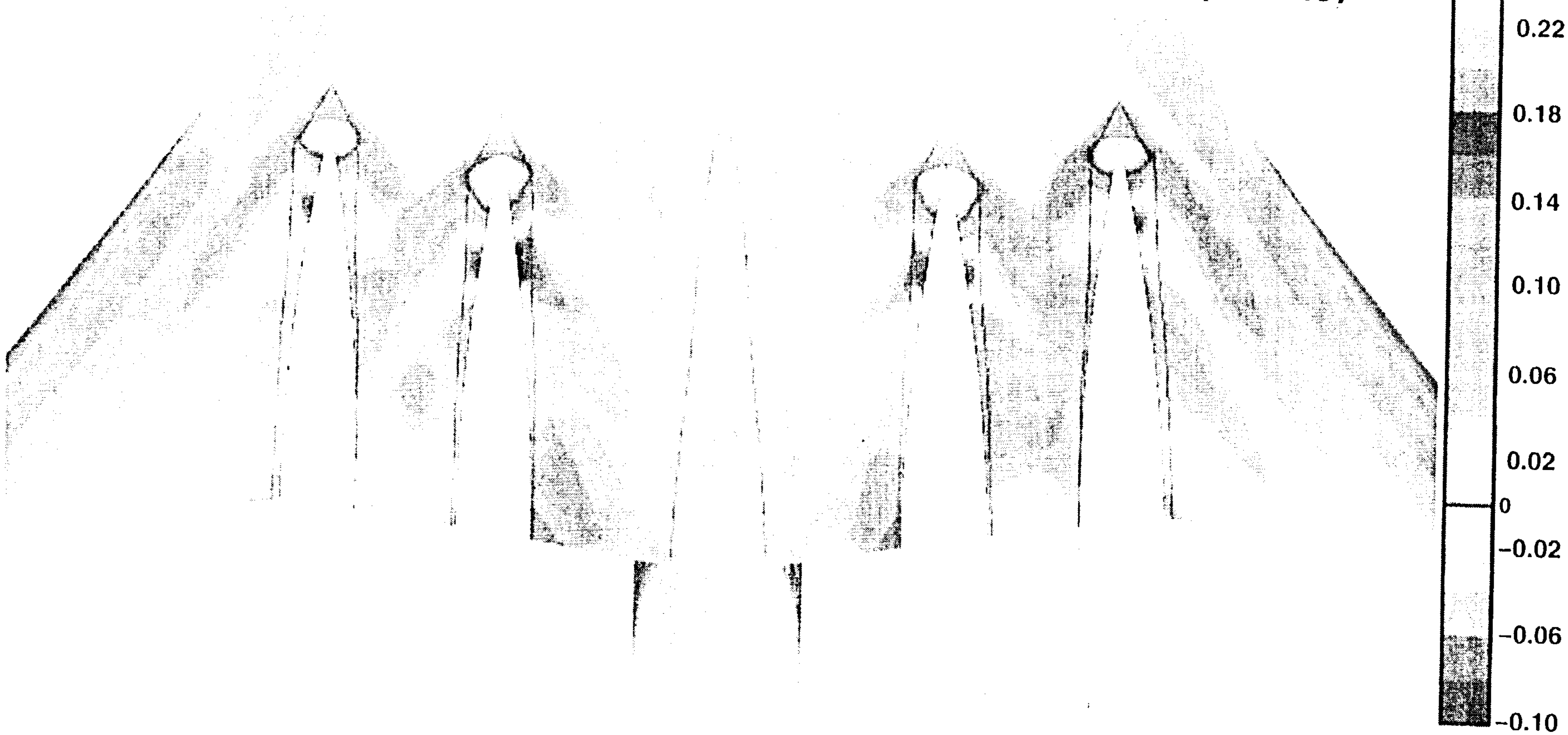

Nozzle Width Study

TCA W/B/N/D OVERFLOW Analysis: Inboard Nacelle Surface Pressure
Mach 2.4, $\alpha = 3$ deg, $Re_{MAC} = 6.4$ million

This figure and the next compare the two nacelles at the inboard and outboard locations respectively. Higher positive pressure levels were seen on both the sides of the nacelle and the diverter. Also, more negative Cp levels were seen on the upper surface of the nozzle; this was the result of the higher nozzle boattail angles (increase from 1.5 to 3 degrees). The isolated nacelle analysis predicted a drag increase for the modified nacelle of 0.81 counts (one nacelle, 0.41 counts on forecowl and 0.40 counts on the nozzle).

Nozzle Width Study

TCA W/B/N/D OVERFLOW Analysis: Inboard Nacelle Surface Pressure
Mach 2.4, $\alpha = 3$ deg, $Re_{MAC} = 6.4$ million

INBOARD NACELLE

Baseline Bifurcated (AR = 1.2) Modified Bifurcated (AR=1.5)

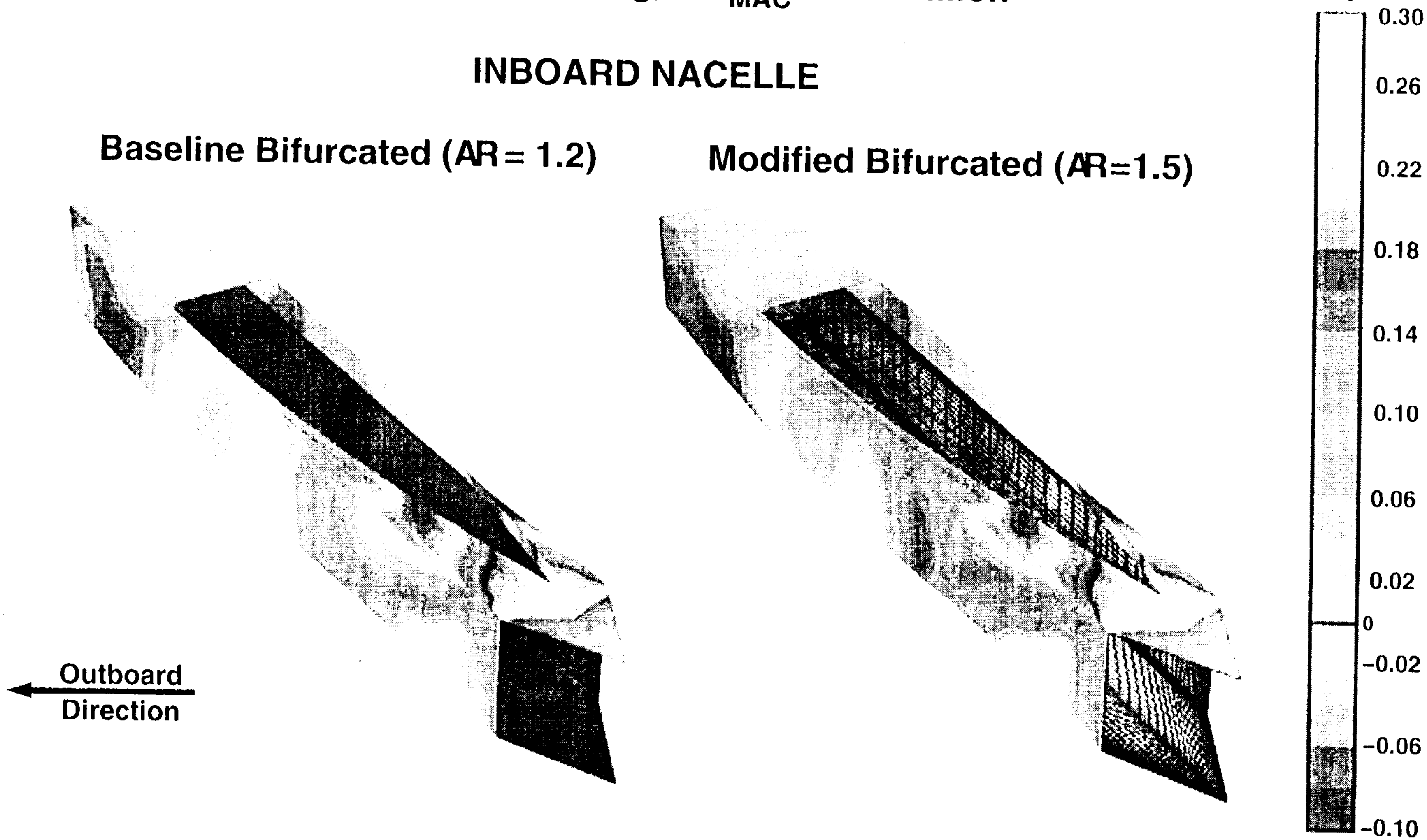

Nozzle Width Study

TCA W/B/N/D OVERFLOW Analysis: Outboard Nacelle Surface Pressure
Mach 2.4, α = 3 deg, Re_{MAC} = 6.4 million

See text for previous figure.

Nozzle Width Study

TCA W/B/N/D OVERFLOW Analysis: Outboard Nacelle Surface Pressure
Mach 2.4, α = 3 deg, Re_{MAC} = 6.4 million

OUTBOARD NACELLE

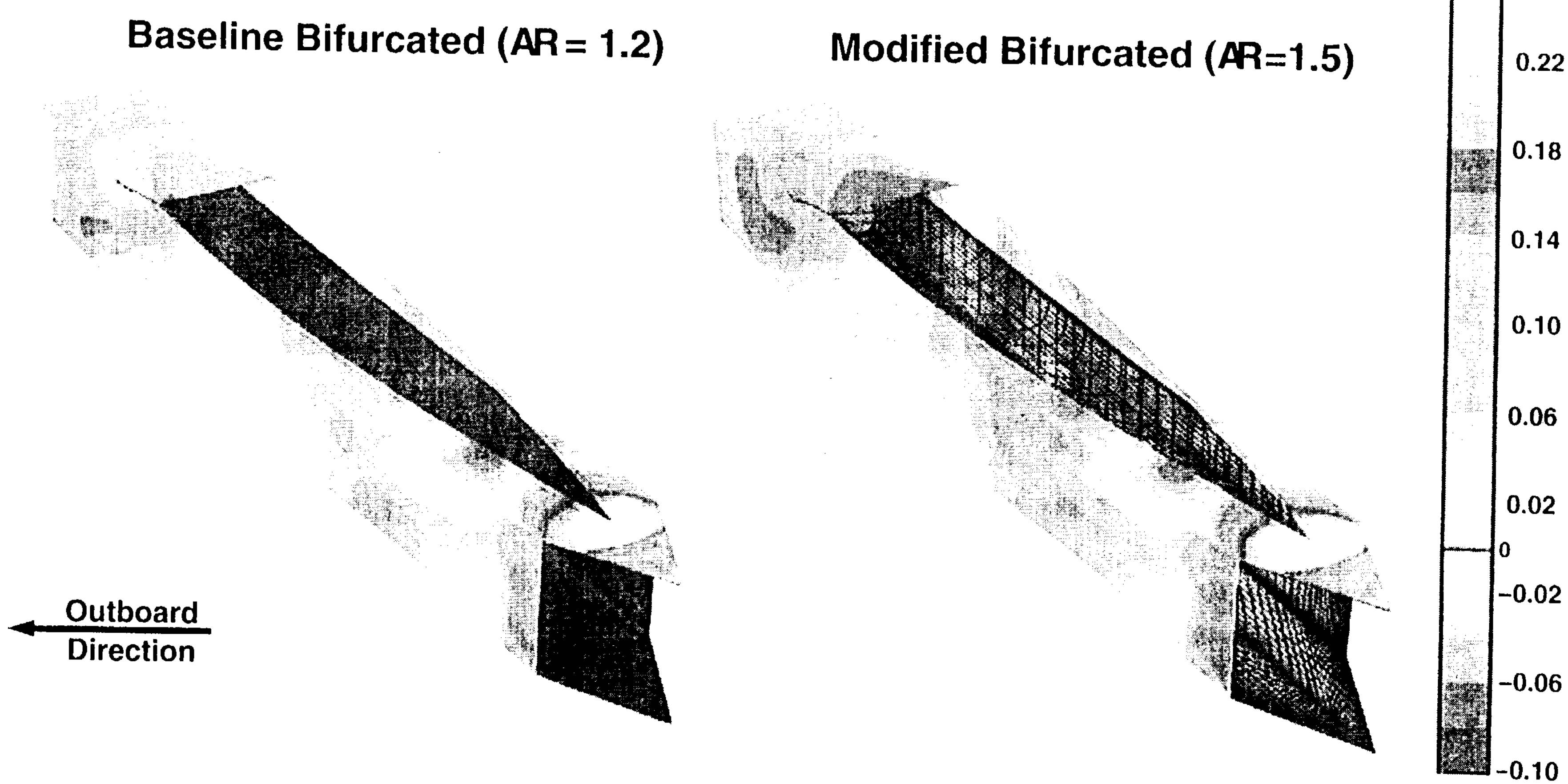

Nacelle Bleed Study

Bifurcated Inlet: Bleed Port Mass Flow Rate Breakdown
Mach 2.4

The figure shows the bleed outflow port locations, the mass flow rate of each port, and the bleed plenum pressure ratio. These data were supplied to NGC for the supercruise bleed flow analysis on the bifurcated installation. These analyses will be conducted at flight Reynolds Number and will be compared to the similar analyses performed last year on the baseline axisymmetric inlet nacelle. The NGC study was still in work and a final report in progress at the time that this current document was assembled; the NGC work shown here has been extracted from monthly summary reports and is a snapshot of current progress.

Nacelle Bleed Study

Bifurcated Inlet: Bleed Port Mass Flow Rate Breakdown
Mach 2.4

- Exact locations of ports are defined in geometry file
- Mach 2.4 Bleed

Port	MFR	P_{bp}/P_{tot}
S1,each,4x	.00254	.154
R1,each,4x	.00254	.154
R2,each,4x	.00106	.262
RS3,each,4x	.00152	.381
C2,each,4x	.00109	.380

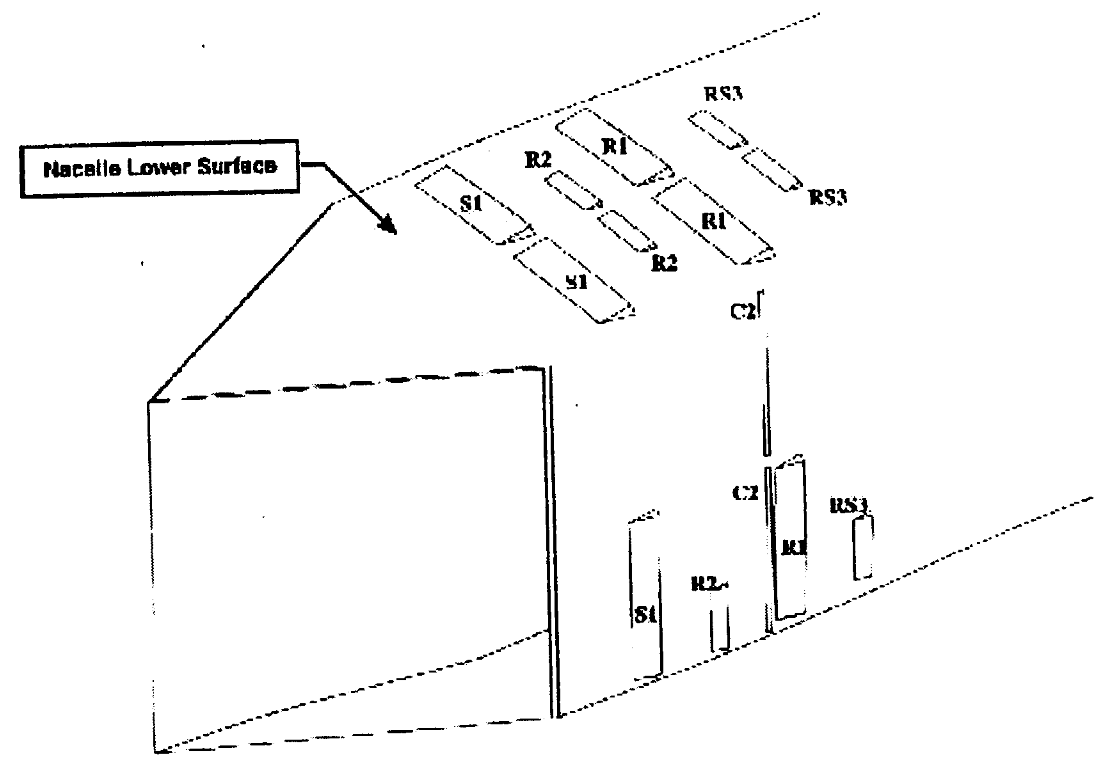

$P_{bp} = P_{bleed-plenum}$

Nacelle Bleed Study
Bifurcated Inlet: Bleed Port Grids

Each of the bleed port doors was modeled by a separate grid block that was embedded in the nacelle grid using chimera block interface methodology.

Nacelle Bleed Study
Bifurcated Inlet: Bleed Port Grids

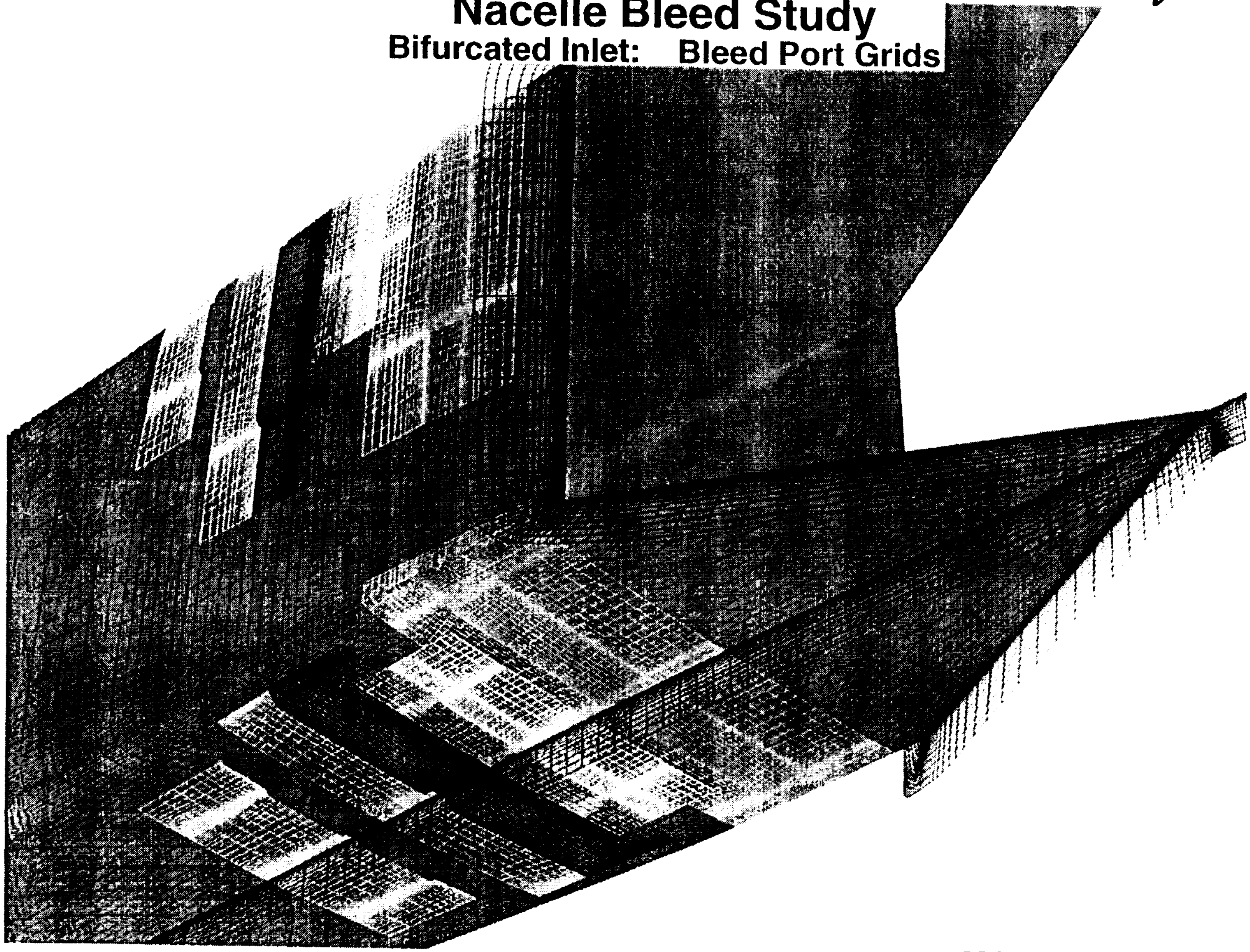

NORTHROP GRUMMAN

Nacelle Bleed Study
Axisymmetric Inlet: Bleed Port Grids

For comparison, the grid topology used in last year's bleed study on the axisymmetric nacelle is shown. The primary difference between the two analyses was that the cowl bleed on the axisymmetric was small enough that it could be captured with a transpiration boundary condition. There was a total of eighteen blocks within the whole geometry. Twelve of the blocks are used for the centerbody bleed ports, three for each port. The port grids are situated within the second nacelle section (blue grid). The cowl bleed ports, modeled with grid clustering for the transpiration boundary condition, are in the nacelle forward section (red grid). All three (blue and red grids, and aft grid is not shown) outer nacelle surface grids are O-mesh topologies. The duct (green) is a slit-O-mesh, where instead of a pole the face is folded over itself. The base grid, which covers the flat nozzle base is not shown. The last grid is the far field block (lower green). It is also an O-mesh topology with each front and end faces collapsed to a pole.

Nacelle Bleed Study
Axisymmetric Inlet: Bleed Port Grids

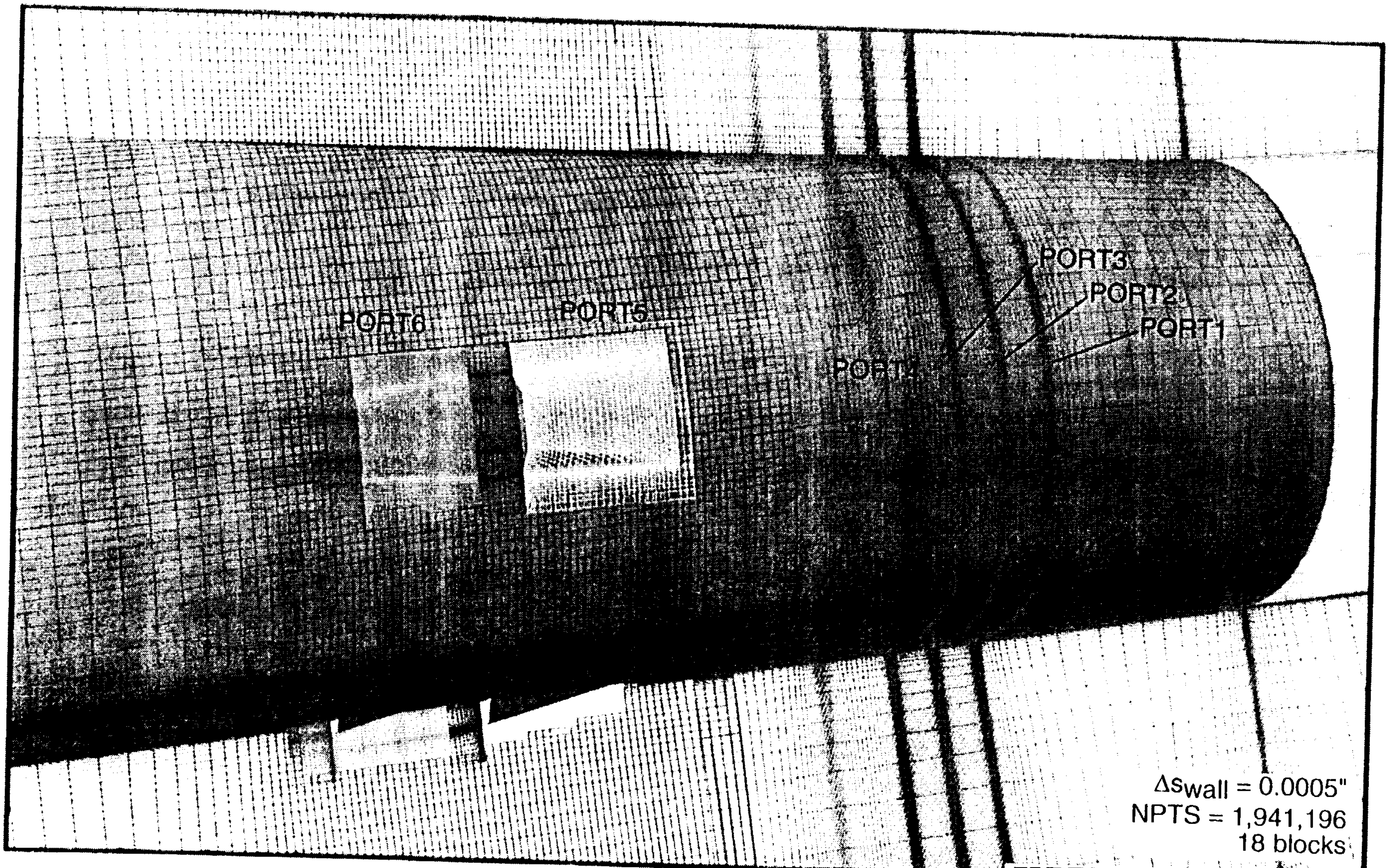

NORTHROP GRUMMAN

Nacelle Bleed Study

Isolated Bifurcated GCNSfv Analysis: Nacelle Surface Pressure

Mach 2.4, Re_{MAC} = 192 million

The bleed port grid blocks were first modeled on the isolated nacelle and solutions ran before doing the installed nacelle. The NPR for each port was adjusted to achieve the desired mass flow rate for that port (the NPR were not significantly different than the propulsion estimates). The bleed exhaust from ports C2 (see previous figure) was small enough to model with transpiration boundary condition; the exhaust from these ports is shown with streamlines arrows at the exit.

Nacelle Bleed Study

Isolated Bifurcated GCNSfv Analysis: Nacelle Surface Pressure
Mach 2.4, ReMAC = 192 million

MFRbleed = 3.5 %

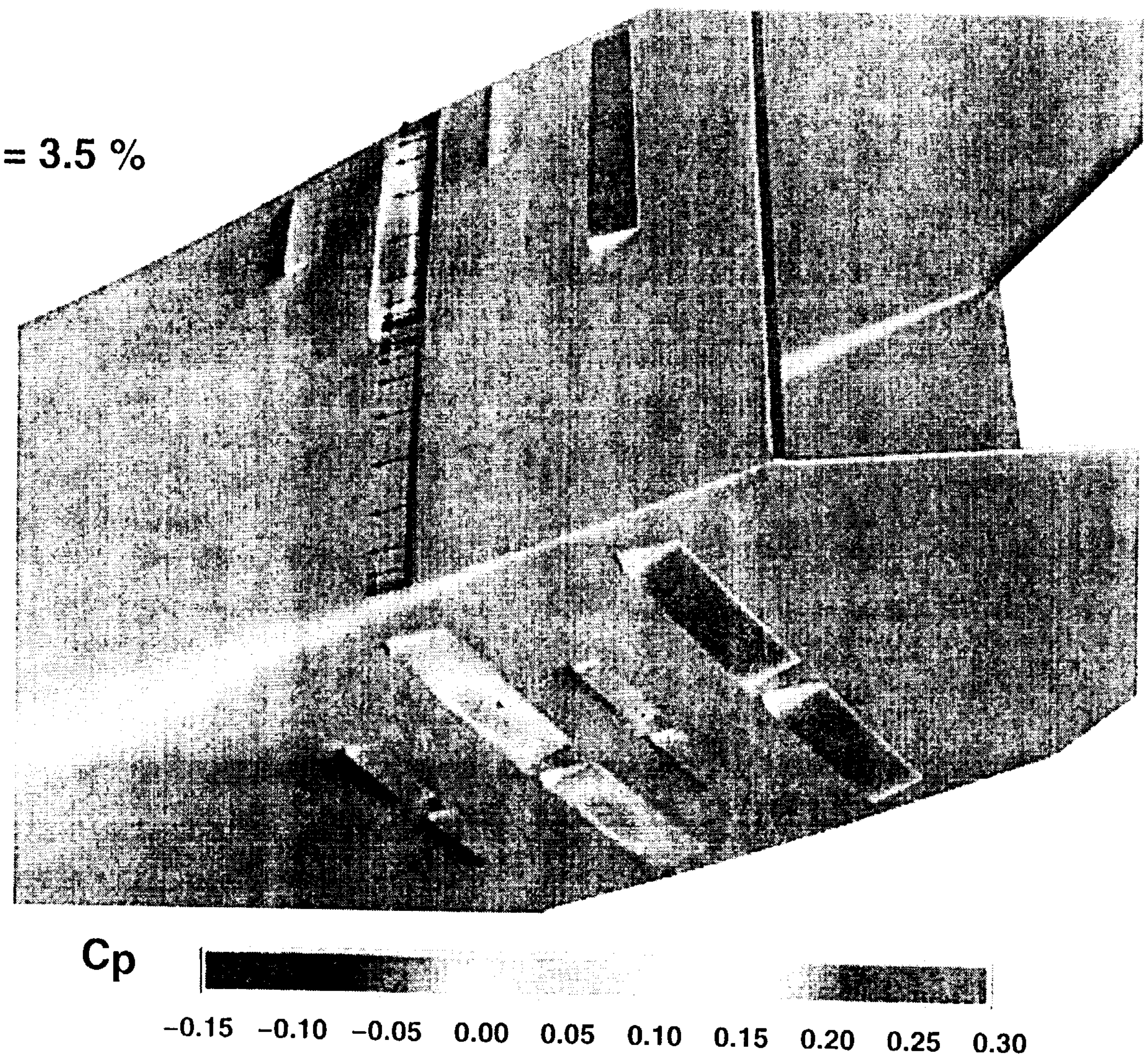

Nacelle Bleed Study

Isolated Axisymmetric GCNSfv Analysis: Nacelle Surface Pressure
Mach 2.4, Re_{MAC} = 192 million

For comparison to the bifurcated isolated solution, last year's solution on the axisymmetric is shown.

Nacelle Bleed Study

Isolated Axisymmetric GCNSfv Analysis: Nacelle Surface Pressure

Mach 2.4, ReMAC = 192 million

MFRbleed = 4.2 %

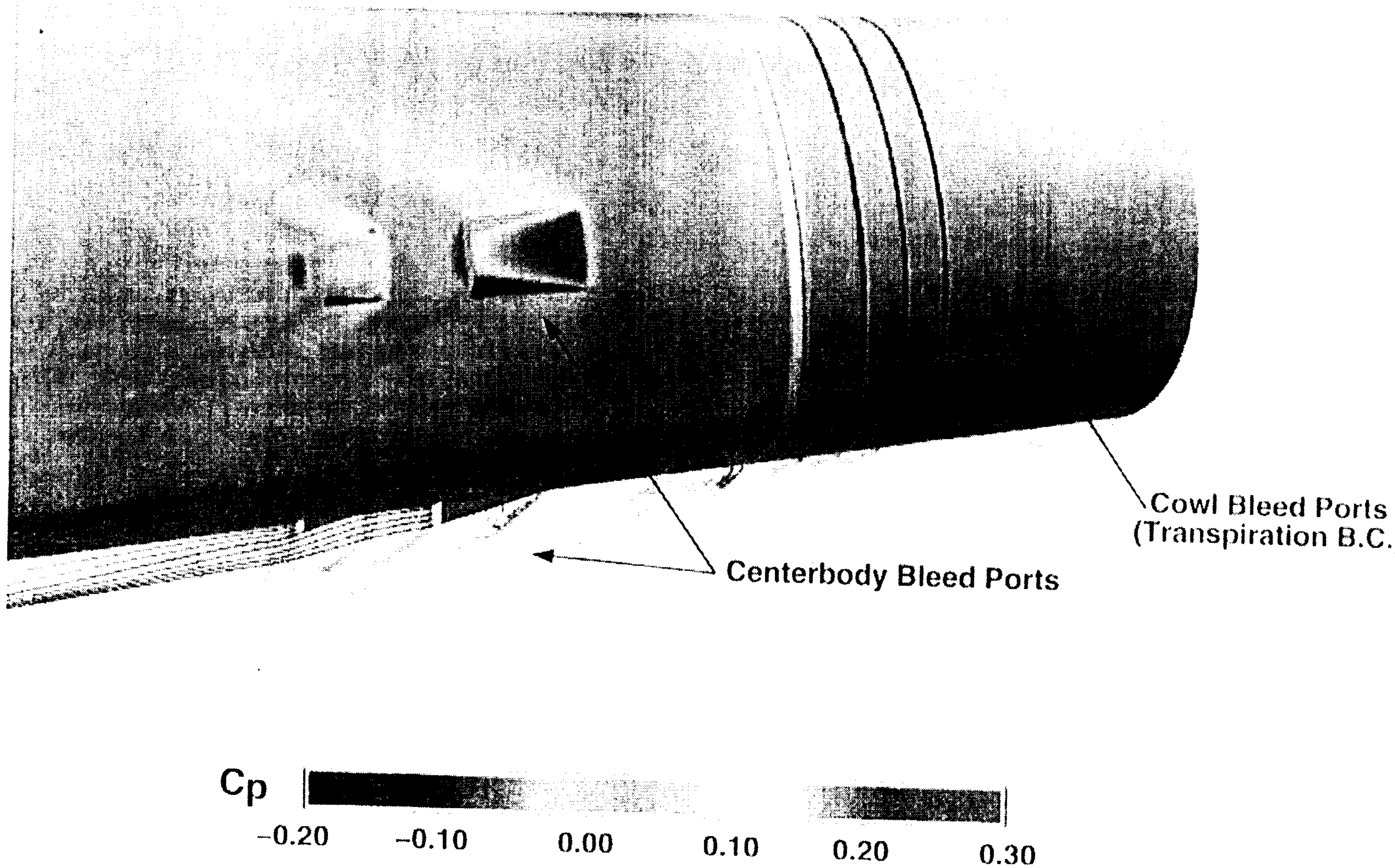

NORTHROP GRUMMAN

Nacelle Bleed Study

TCA W/B/N/D GCNSfv Analysis: Bifurcated Nacelle Surface Pressure
Mach 2.4, $\alpha = 3$ deg ReMAC = 192 million

The bleed port grids and NPR's developed on the isolated nacelle were applied to the installed case. The resulting grid geometry consists of 107 blocks totaling 12.5 million grid points. The figure shows a comparison of the supersonic solutions on the installed nacelle grid with and without the bleed port doors/exhaust. The results are very similar to those from last year's study on the axisymmetric: the doors increase the drag of the nacelle but this is more than made up by the thrust of the exhaust. The bleed has a small effect on wing surface pressures.

Nacelle Bleed Study

TCA W/B/N/D GCNSfv Analysis: Bifurcated Nacelle Surface Pressure

Mach 2.4, α = 3 deg ReMAC = 192 million

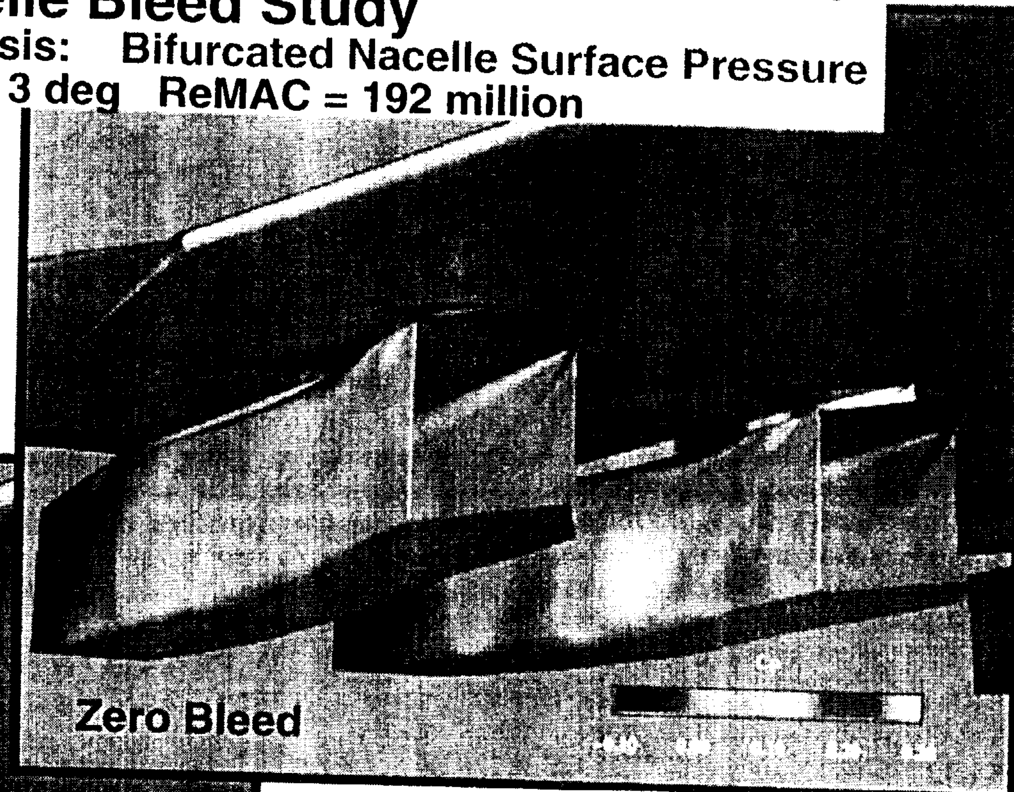

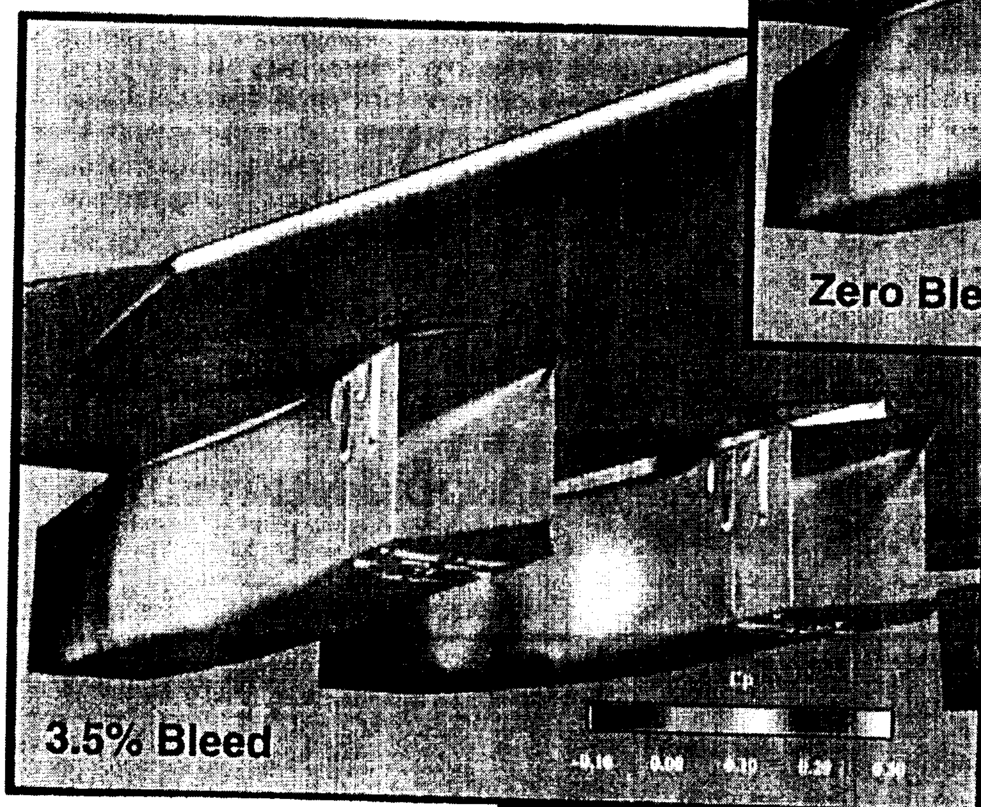

Nacelle Bleed Study

TCA W/B/N/D GCNSfv Analysis: Axisymmetric Nacelle Surface Pressure
Mach 2.4, $\alpha = 3$ deg ReMAC = 192 million

The axisymmetric solutions with and without bleed are shown here for comparison with the bifurcated solutions. As discussed previously, the pressure drag increased on the outer nacelle surface due to bleed port doors. This is clearly evident from the high pressure regions seen on all the centerbody ports on each nacelle. Proof of the cowl bleed port and lower wing surface interaction is seen by the segmented high pressure region on the lower surface of the wing downstream of the diverter leading edge, particularly on the outboard side of the outboard nacelle. Also note the four high pressure stripes on the forward part of each nacelle indicating the four cowl bleed ports.

Nacelle Bleed Study

TCA W/B/N/D GCNSfv Analysis: Axisymmetric Nacelle Surface Pressure
Mach 2.4, $\alpha = 3$ deg ReMAC = 192 million

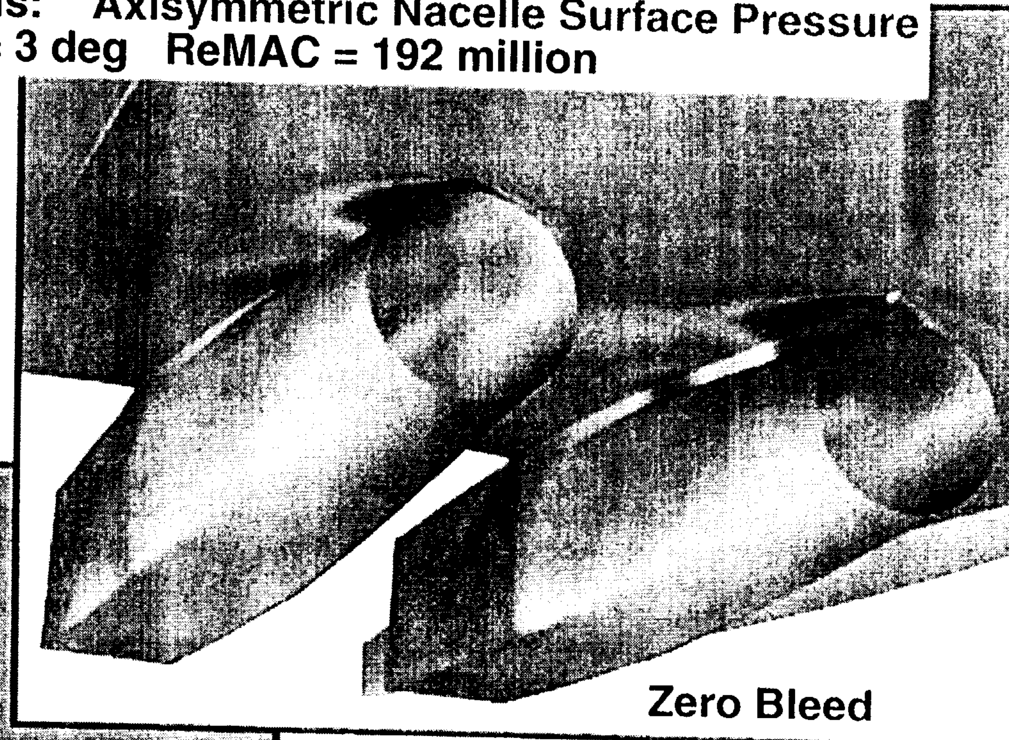

Zero Bleed

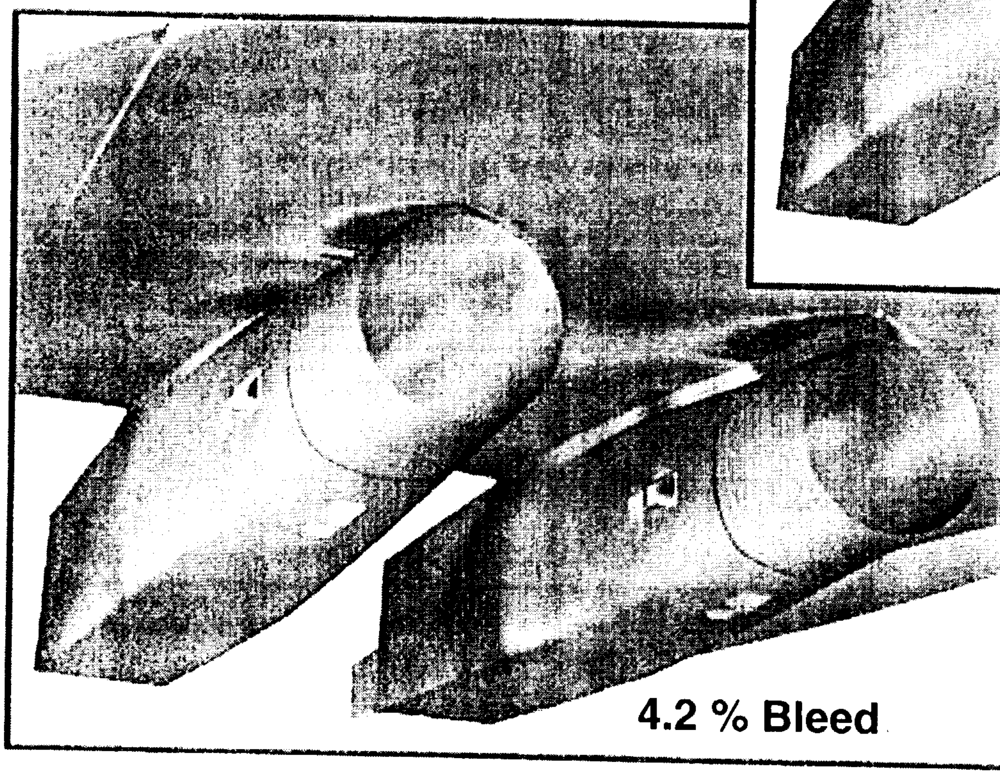

4.2 % Bleed

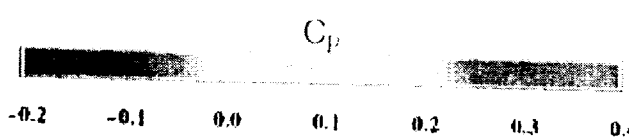

NORTHROP GRUMMAN

Supersonic Cruise Conclusions

OVERFLOW solutions of the bifurcated and the axisymmetric inlet nacelles on the TCA at both wind tunnel and flight conditions indicated that they had equal drag. It appears that the capability to achieve these low drag values with the bifurcated despite its inherent penalty of a larger lip bevel, was due to the large shoulder radius faired in between the inlet lip and the nacelle maximum area station.

Boeing IR&D wind tunnel test 644 in BSWT indicated that the bifurcated had 2 counts more drag than axisymmetric. CFD investigation of the as-tested configuration has found sources for at 1 - 2 counts of this discrepancy. Further analysis is in work (of the QA laser survey points).

The nozzle width increase implemented on the PTC will increase high-speed drag by 1 count.

The NGC bleed study is still in progress. Results to date confirm what was concluded last year in the axisymmetric inlet study. If no accounting is made for the bleed flow internal ducting losses, the blowing bleed ports decrease airplane drag. This is due to the thrust of the bleed exhaust being larger than the drag on the bleed doors.

Supersonic Cruise Conclusions

- CFD predicts bifurcated equal to axi on TCA in WT & flt.
- Bifurcated inlet shoulder contouring beneficial (1.5 cnts)
- BCAG IR&D test bif – axi 2 count discrepancy
  - Internal duct (0.4 cnt)
  - Wall thickness (0 – 1)
  - QA points (~ 1 ?)
  - Blunt lip (.2 – .7)
- PTC nozzle width increase cost 1 count
- Preliminary bleed conclusions(NGC report in progress)
  - Bleed effect on bifurcated trends same as axi
  - ~ –1 count per nacelle with all ports blowing
    - No accounting for bleed plumbing losses
  - Bleed mass flows achievable with design plenum press.

Transonic Cruise and Climb Studies

A brief comparison of the BCA and NGC 1997 results for spillage affects on the axisymmetric nacelle installation are discussed. This is followed by a review of NGC's progress to date on a spillage and bypass study on the bifurcated installation on the TCA. This study was still in progress and a final report in work at the time that this current document was assembled. The review presented here has been assembled from NGC's monthly summaries and represents a snap-shot of work in progress.

The previous study of the axisymmetric nacelle installation at transonic conditions considered only spillage, which is the current design method for dumping the inlet air flow that the engine doesn't need. This year a parametric study was initiated with NGC to trade spillage vs bypass on the bifurcated inlet and determine effects on external aerodynamic characteristics.

Transonic Cruise and Climb Studies

- Axisymmetric Inlet Spillage, Flight vs WT Rey. No.
- NGC spill vs bypass: isolated bifurcated nacelle
- NGC spill vs bypass: installed bifurcated nacelle

Transonic Cruise Spillage, Flight vs WT Reynolds No.

TCA W/B/N/D CFD Analysis: Wing Lower Surface Pressure

Re_{MAC} = 163 million   Mach 0.9, α = 4 deg Re_{MAC} = 11.0 million

NGC - GCNSfv   BCAG - OVERFLOW

Wing lower surface pressure distributions are shown with and without spilling for the axisymmetric nacelle installation on the TCA (the flow through duct actually spills a small amount also, ~ 5%). The figures on the left are from NGC GCNSfv solutions at flight conditions; on the right are BCA OVERFLOW solutions at wind tunnel Reynolds Number. The pressure contours are very similar for the two codes/Reynolds Numbers. The transonic solutions have proven to be very difficult to converge. Based on the similarity between the results it may be beneficial to run at wind tunnel Reynolds Number in order to conserve computer hours and user wall clock hours (wind tunnel ~ 100 C90 hours, flight ~ 300 hours).

Transonic Cruise Spillage, Flight vs WT Reynolds No.

TCA W/B/N/D CFD Analysis: Wing Lower Surface Pressure

Re_{MAC} = 163 million Mach 0.9, α = 4 deg Re_{MAC} = 11.0 million

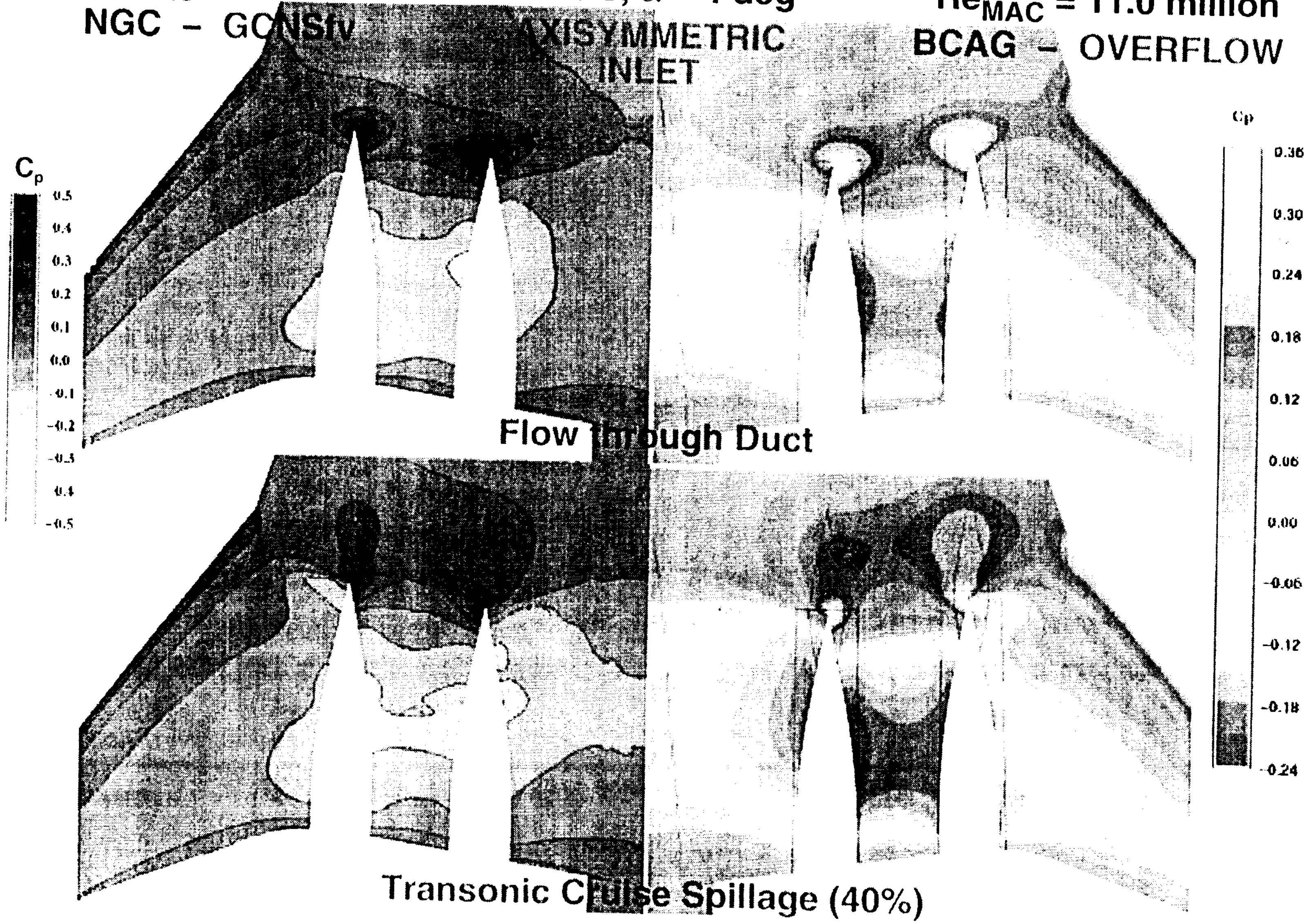

Transonic Climb Spillage, Flight vs WT Reynolds No.

TCA W/B/N/D CFD Analysis: Wing Lower Surface Pressure

Re_{MAC} = 300 million Mach 1.20, α = 4 deg Re_{MAC} = 11.0 million

NGC - GCNSfv BCAG - OVERFLOW

The wing lower surface pressure contours compared favorably between the NGC and BCA solutions at Mach 1.2 also.

Transonic Climb Spillage, Flight vs WT Reynolds No.

TCA W/B/N/D CFD Analysis: Wing Lower Surface Pressure

Re_{MAC} = 300 million Mach 1.20, α = 4 deg Re_{MAC} = 11.0 million

NGC – GCNSfv AXISYMMETRIC INLET BCAG – OVERFLO

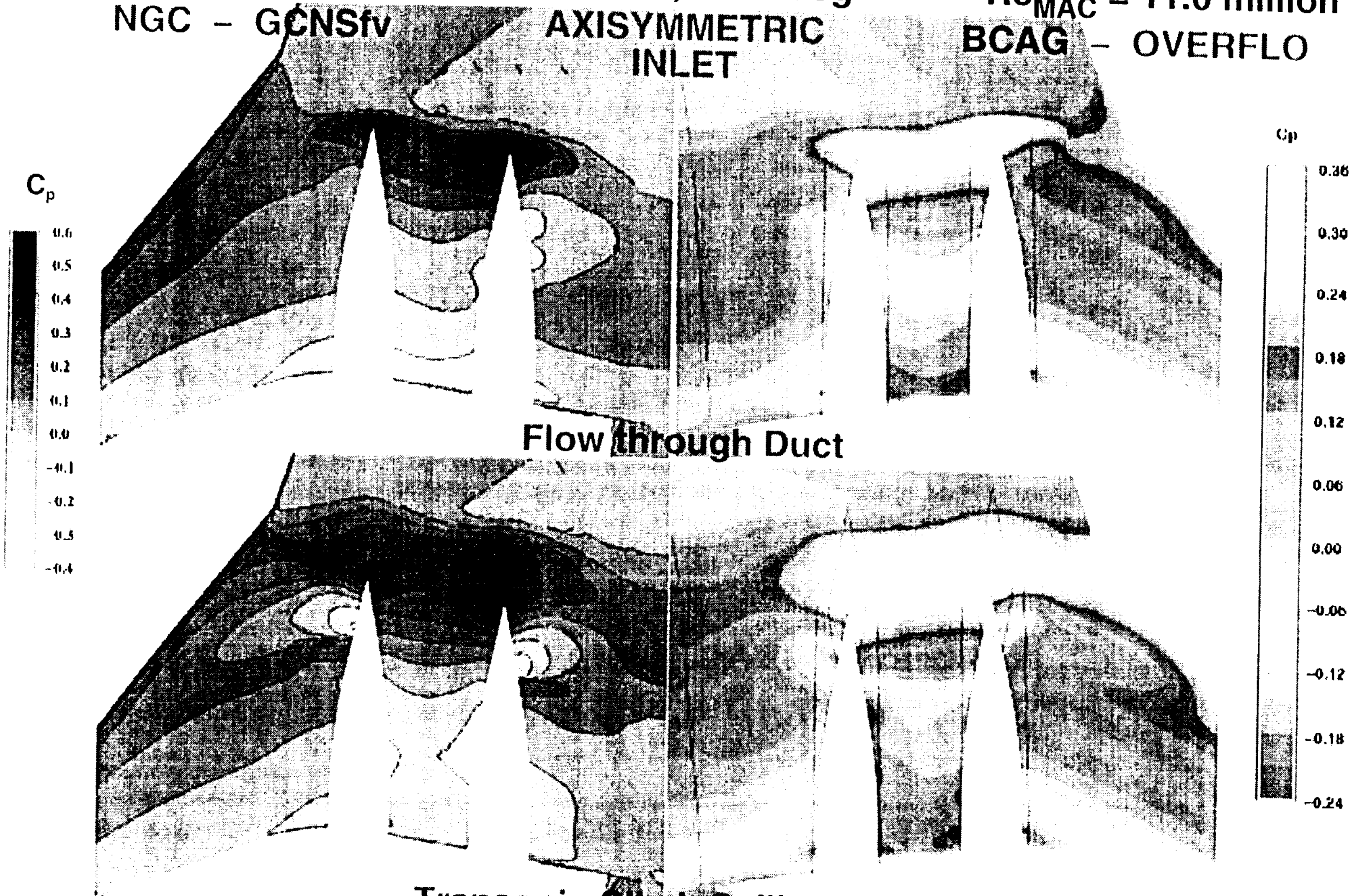

Transonic Climb Spillage (35%)

Bifurcated Inlet Spillage / Bypass Study
TCA W/B/N/D CFD Analysis: Conditions

The range of spillage/bypass conditions for the bifurcated inlet study are shown. The transonic cruise conditions will vary from the nominal (current design values) of 40% spillage/ zero bypass to the minimum spillage condition of 14% spillage/ 26% bypass. The transonic climbout (Mach 1.2) conditions will vary in the study from 34% spillage/ zero bypass to 14% spillage/ 20% bypass.

Bifurcated Inlet Spillage / Bypass Study

TCA W/B/N/D CFD Analysis: Conditions

FLIGHT: nominal / 2D–bifurcated inlet

Condition	Mach	Altitude	α	MFRspill	MFRbypass	MFRbleed	Eta
Supersonic Cruise	2.4	57,000ft	3.0	0.0	0.0	.035	0.930
Subsonic Cruise	0.90	40,000	3.7	0.408	0.0	.003*	0.970
Transonic Climb	1.2	32,000	3.7	0.343	0.0	.010*	0.966
Transonic Climb	1.8	42,000	3.7	0.042	0.118	.024*	0.937

*assume zero for this study

FLIGHT: min spillage / 2D–bifurcated inlet

Condition	Mach	Altitude	α	MFRspill	MFRbypass	MFRbleed	Eta
Subsonic Cruise	0.90	40,000	3.7	0.146	0.265	.003*	0.964
Transonic Climb	1.2	32,000	3.7	0.139	0.206	.010*	0.964

MFR=Mass Flow Ratio, normalized by inlet capture flow.

Alip = 3687.95 in^2

Eta=Pressure recovery at fan face.

Compression Ramp: Positions supplied in geometry files.

Bifurcated Inlet Spillage / Bypass Study

TCA W/B/N/D CFD Analysis: Bypass Door & Duct Geometry

The bypass door geometry and location are shown in this figure. The bypass doors are located just in front of the engine face and are placed on the sides and bottom of the nacelle (the top is covered by the diverter). The compression ramps at the front of the inlet are in the transonic condition position.

Bifurcated Inlet Spillage / Bypass Study

TCA W/B/N/D CFD Analysis: Bypass Door & Duct Geometry

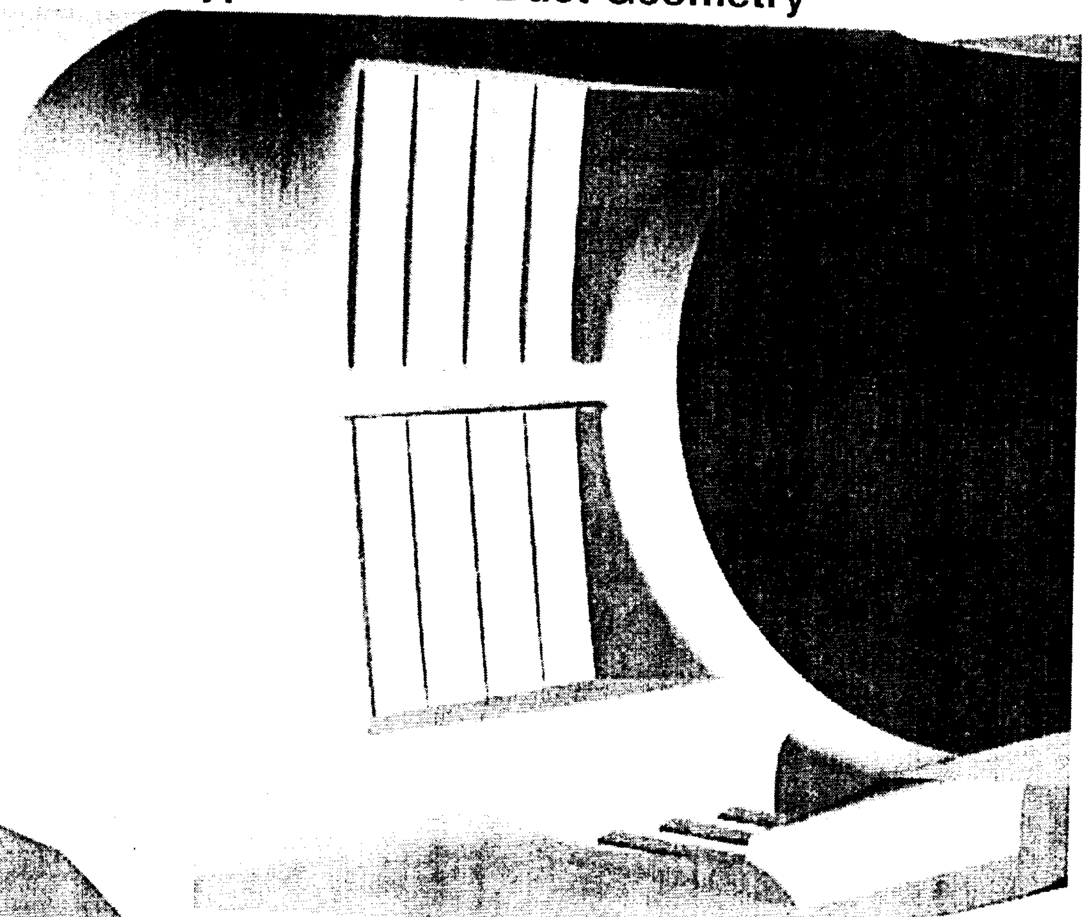

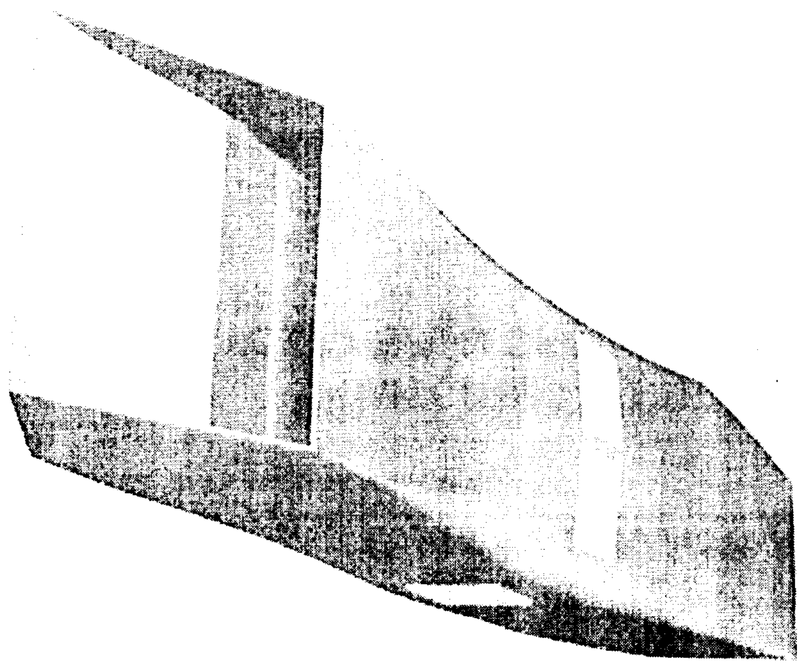

Bifurcated Inlet Spillage / Bypass Study

TCA W/B/N/D CFD Analysis: Bypass Door & Duct Gridding

The actual door angle required for the maximum bypass case was unknown, requiring varying the door angle and measuring the mass flow rate. In addition, several intermediate door positions are planned (between zero bypass and max bypass). This required developing a gridding scheme that would allow for the doors to be rotated to new positions relatively easily. The approach taken was to grid each door individually.

Bifurcated Inlet Spillage / Bypass Study
TCA W/B/N/D CFD Analysis: Bypass Door & Duct Gridding

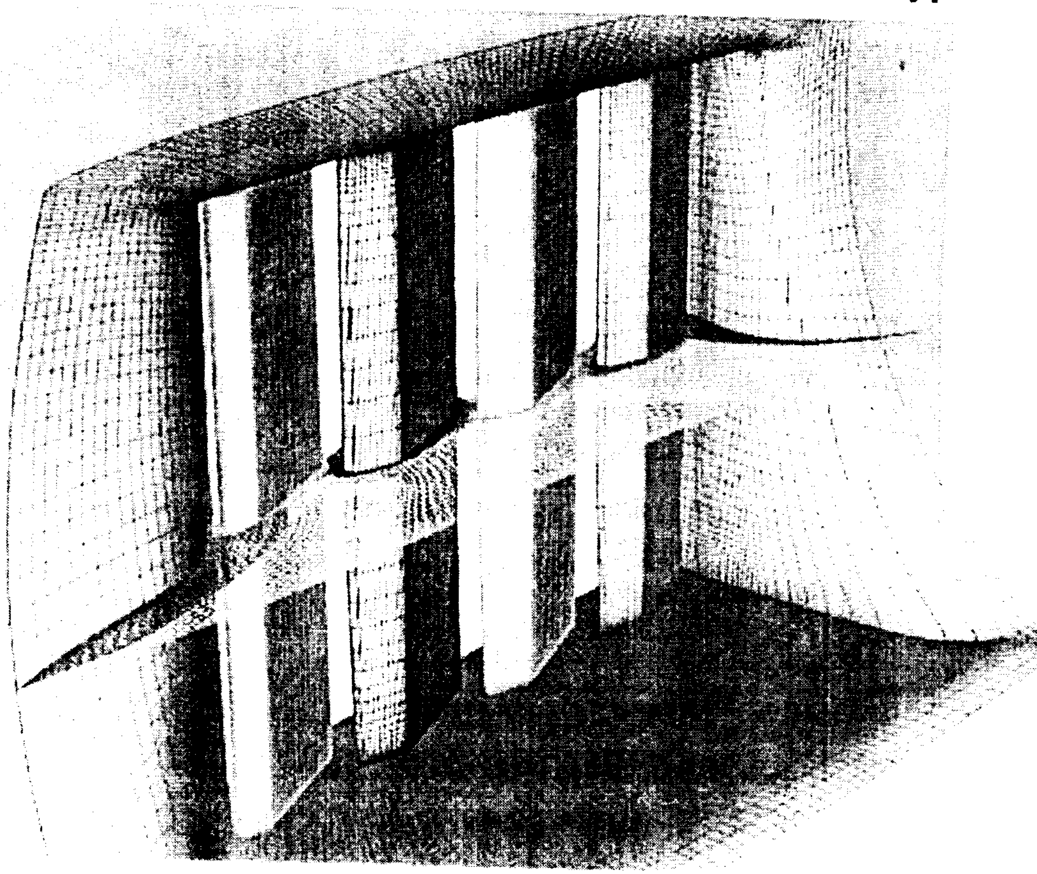

Inside view of one bypass duct

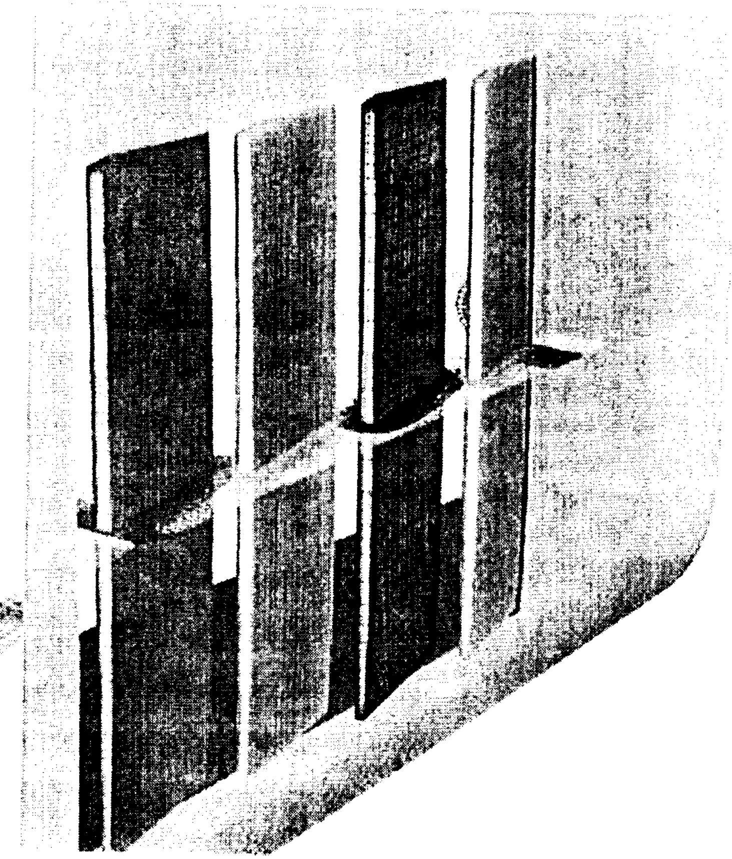

Outside view of nacelle with bypass doors

NORTHROP GRUMMAN

Bifurcated Inlet Spillage / Bypass Study

Isolated CFD Analysis: Nacelle Surface Pressure

Mach 0.90, Re_{MAC} = 163 million (h=40,000 ft)

The bypass grid and solution strategy was exercised on the isolated bifurcated nacelle before installation on the TCA. An estimate of the bypass door angle (for maximum bypass) of 12 degrees was used. The surface pressure coefficient distribution is shown. The effect of the spillage is evident in the low pressures at the cowl lip (blue). The bypass doors have a high pressure at the most forward door, followed by a low pressure region aft of the doors. Note that the bypass is not even close to the desired maximum value (7% vs. 26%).

Bifurcated Inlet Spillage / Bypass Study

Isolated CFD Analysis: Nacelle Surface Pressure

Mach 0.90, Re_{MAC} = 163 million (h=40,000 ft)

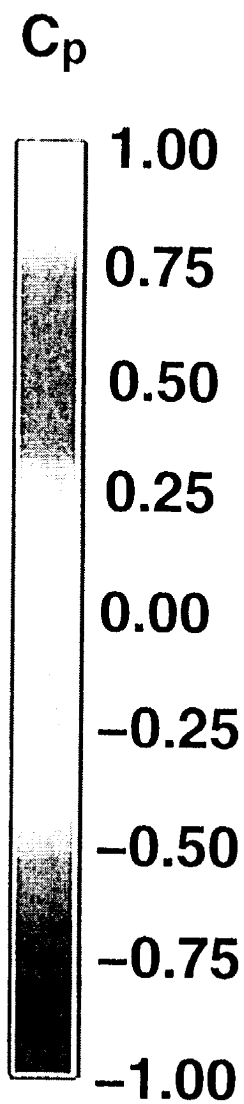

Bypass Doors: 12 deg

MFRengine = 0.60
MFRspill = 0.33
MFRbypass = 0.07

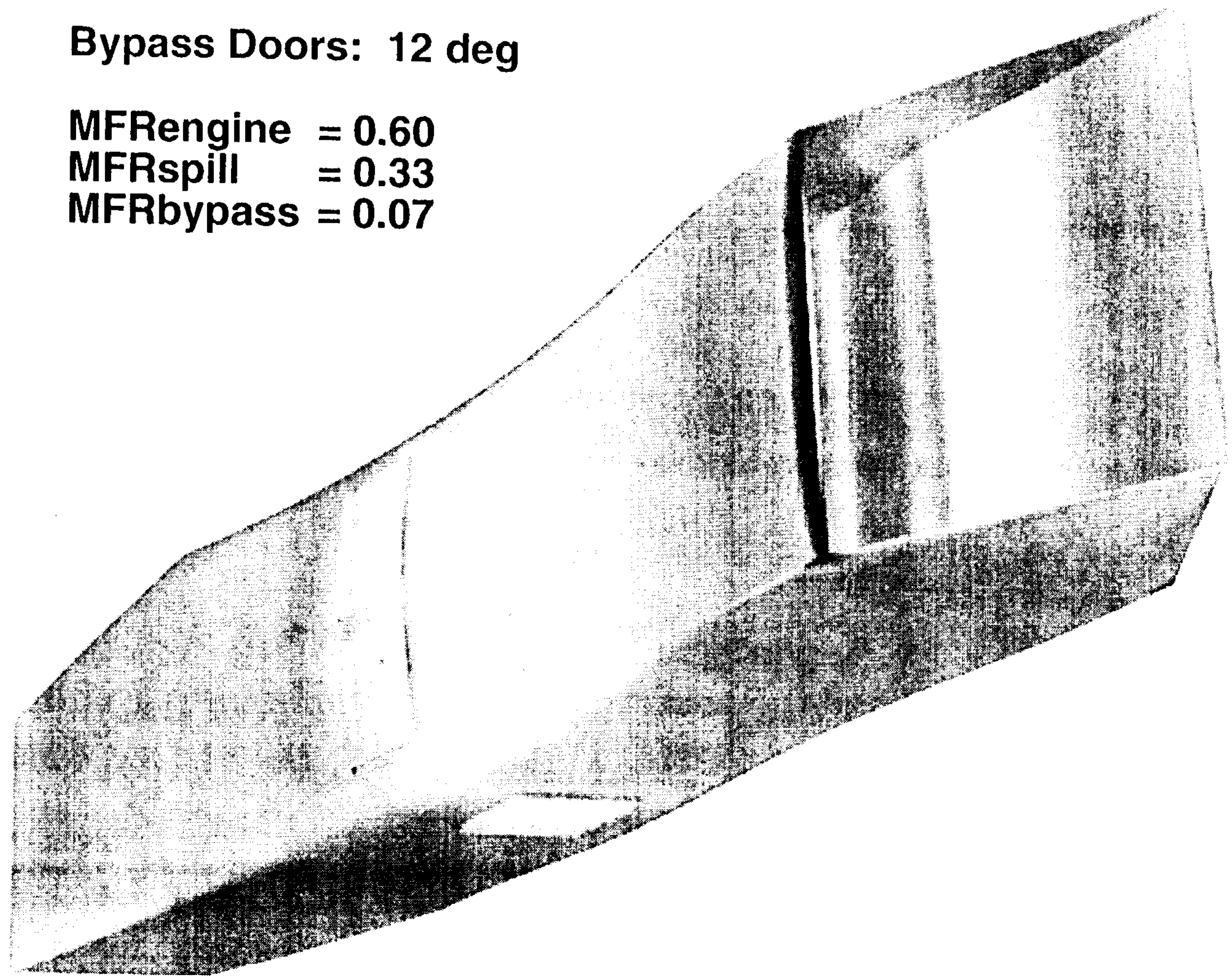

Bifurcated Inlet Spillage / Bypass Study

Isolated CFD Analysis: Nacelle Surface Pressure

Mach 1.20, Re_{MAC} = 304 million (h=32,000 ft)

A similar isolated nacelle analysis was performed at Mach 1.2 with the 12 degree bypass door angle. The results were similar to the Mach 0.90 case with both the spillage and bypass flow effects evident in the pressure distributions. The bypass was again much lower than the maximum desired value (6% vs. 20%).

Bifurcated Inlet Spillage / Bypass Study

Isolated CFD Analysis: Nacelle Surface Pressure

Mach 1.20, Re_{MAC} = 304 million (h=32,000 ft)

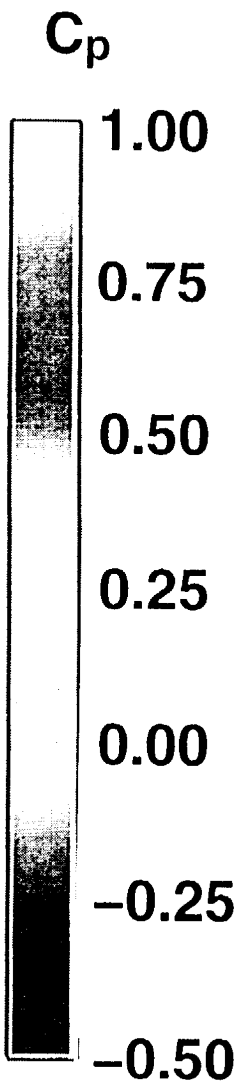

Bypass Doors: 12 deg

MFRengine = 0.65
MFRspill = 0.29
MFRbypass = 0.06

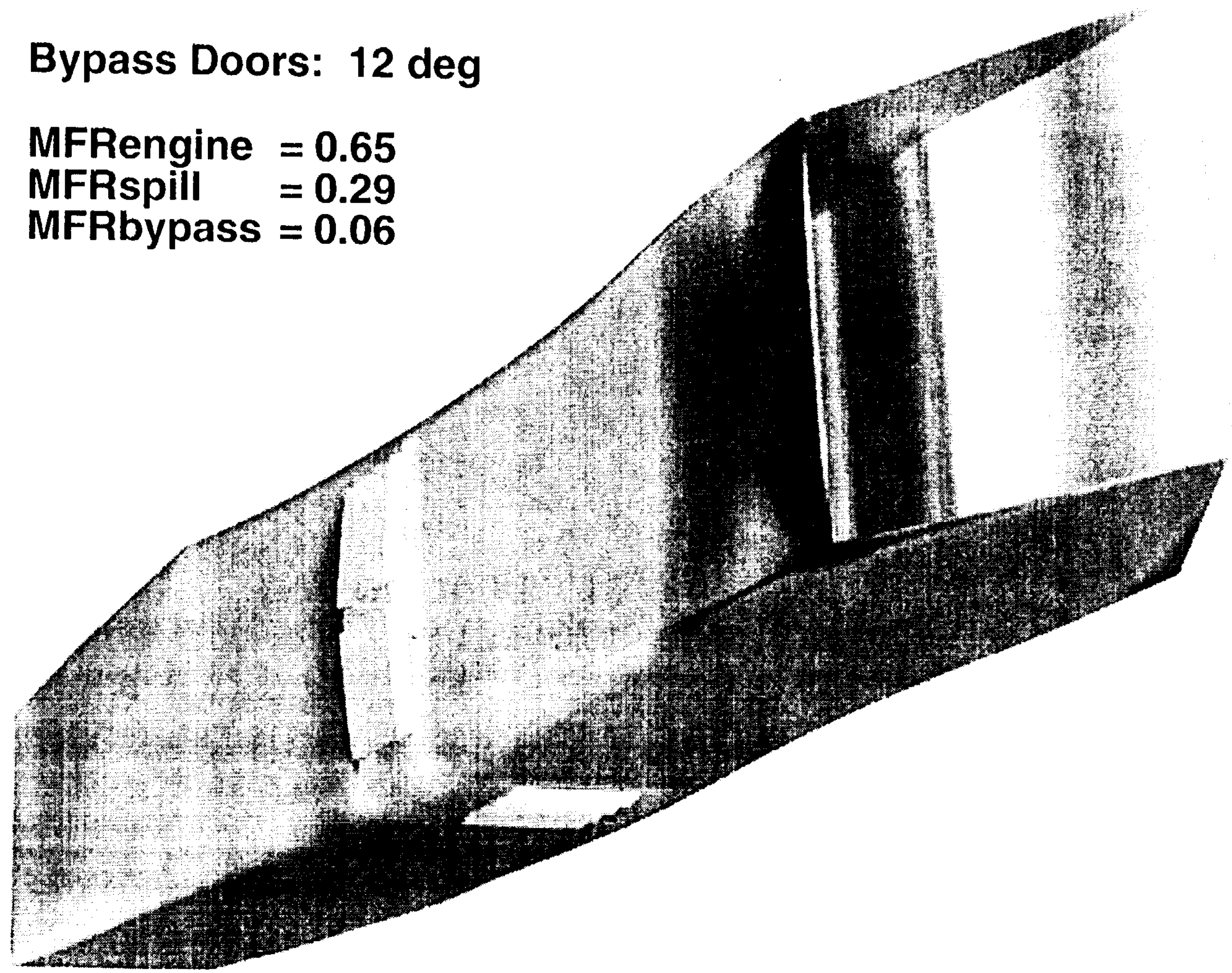

Bifurcated Inlet Spillage / Bypass Study

Isolated CFD Analysis: Inlet Mach Contours

Mach 0.90, Re_{MAC} = 163 million (h=40,000 ft)

Bypass Doors: 12 deg

MFRengine	=	0.60
MFRspill	=	0.33
MFRbypass	=	0.07

The Mach Number distribution through the duct is illustrated in this figure. This is a top view of a waterline cut through the center of the lower/side bypass duct (note the inset figure for orientation). The flow is locally sonic as it turns the sharp corner of the ramp, supersonic around the cowl lip, and sonic near the bypass exit. The flow remains subsonic through the inlet duct, however, it approaches Mach 0.90 in the throat region.

Bifurcated Inlet Spillage / Bypass Study

Isolated CFD Analysis: Inlet Mach Contours

Mach 0.90, Re_{MAC} = 163 million (h=40,000 ft)

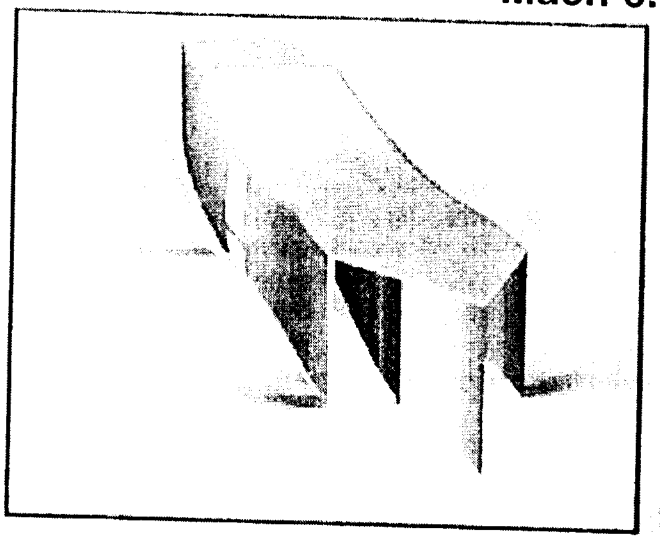

Bypass Doors: 12 deg

MFRengine = 0.60
MFRspill = 0.33
MFRbypass = 0.07

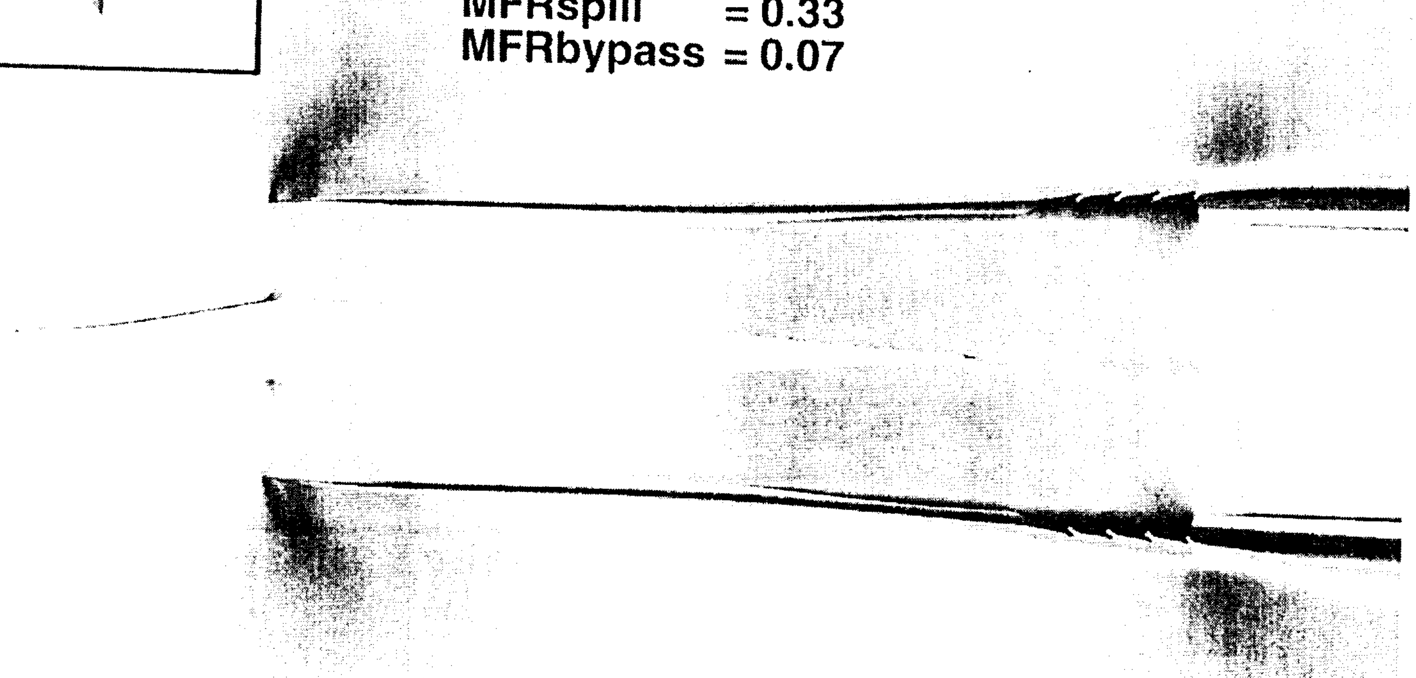

NORTHROP GRUMMAN

Bifurcated Inlet Spillage / Bypass Study

Isolated CFD Analysis: Inlet Mach Contours

Mach 1.20, Re_{MAC} = 304 million (h=32,000 ft)

Bypass Doors: 12 deg

MFRengine	=	0.65
MFRspill	=	0.29
MFRbypass	=	0.06

Mach Number contours on a waterline cut through the center of the lower/side bypass duct for Mach 1.2 are shown. The bow shock shock of the compression ramp creates subsonic flow entering the inlet duct. However, at the same location in the previous Mach 0.90 case where the flow approaches Mach 0.90, the flow in this case goes supersonic until it is downstream of the throat, where it then goes through a normal shock, at the same time separating the wall boundary layer. The choked inlet duct is clearly the reason for the low bypass flow rate: the inlet simply won't take any more flow.

Bifurcated Inlet Spillage / Bypass Study

Isolated CFD Analysis: Inlet Mach Contours

Mach 1.20, Re_{MAC} = 304 million (h=32,000 ft)

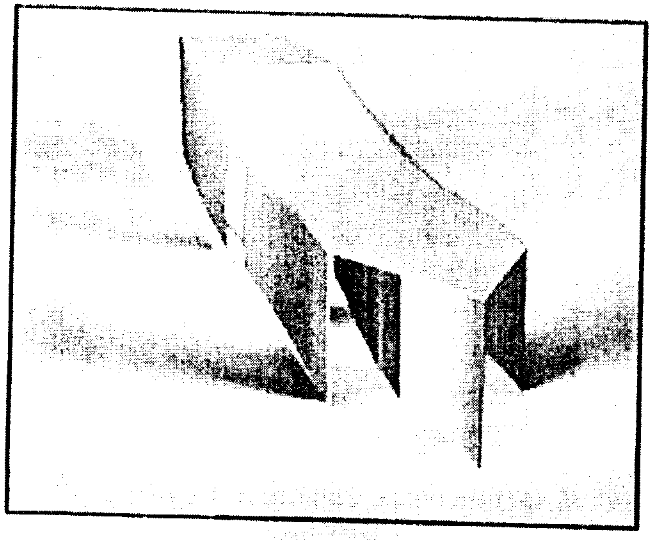

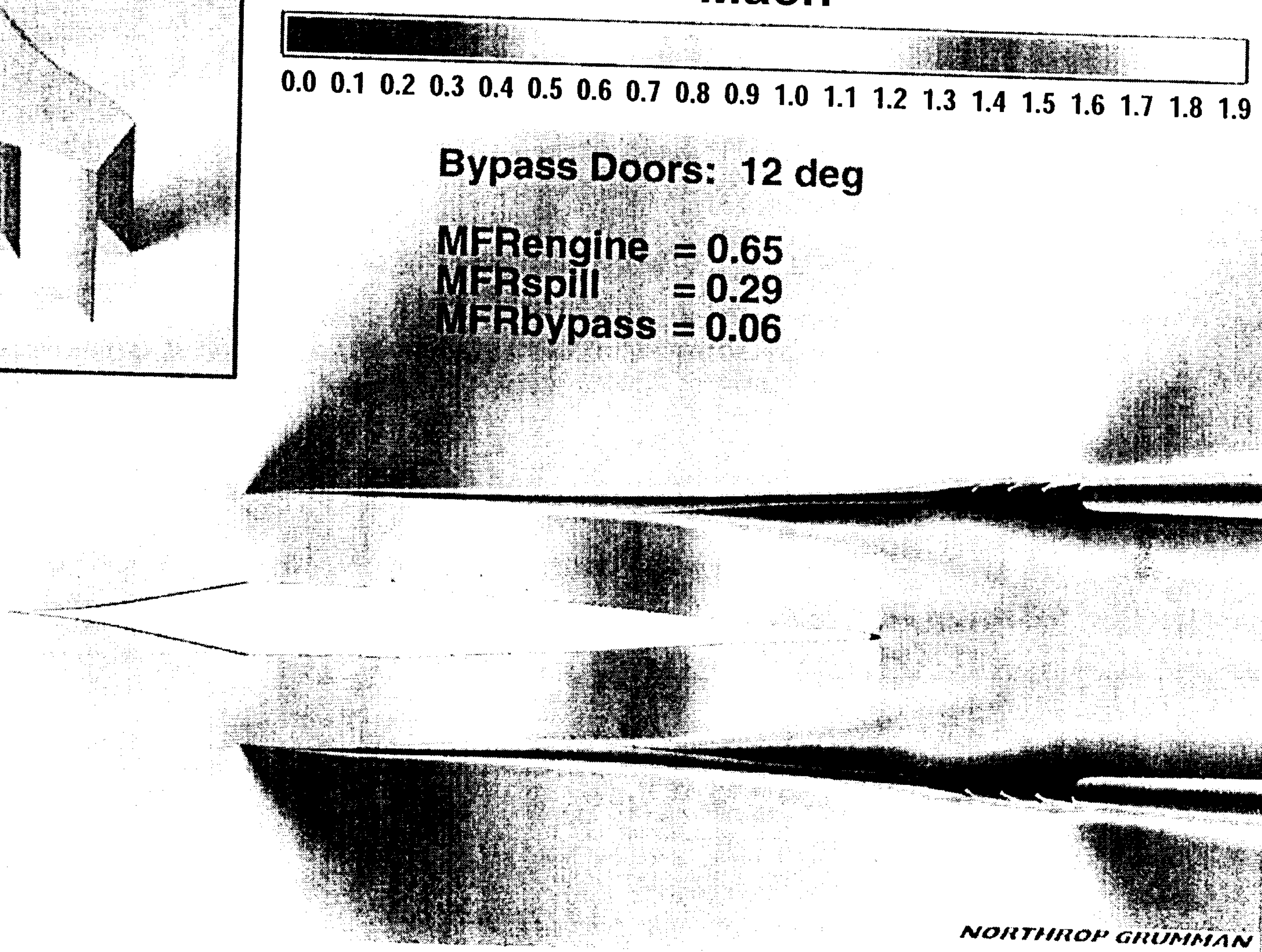

NORTHROP GRUMMAN

Bifurcated Inlet Spillage / Bypass Study

Isolated CFD Analysis: Door Flow Mach Number and Streamlines

Mach 0.90, Re_{MAC} = 163 million (h=40,000 ft)

The flow through the bypass doors for the Mach 0.90 case is shown. As noted earlier the bypass flow rate was much less than expected although the inlet duct was not choked. Part of the reason is evident in this figure. Note the significant separation on the backside (outside) of the bypass doors. The resulting "vena contracta" reduces the effective flow area considerably, contributing to the lower than expected bypass flow rates.

Bifurcated Inlet Spillage / Bypass Study

Isolated CFD Analysis: Door Flow Mach Number and Streamlines

Mach 0.90, Re_{MAC} = 163 million (h=40,000 ft)

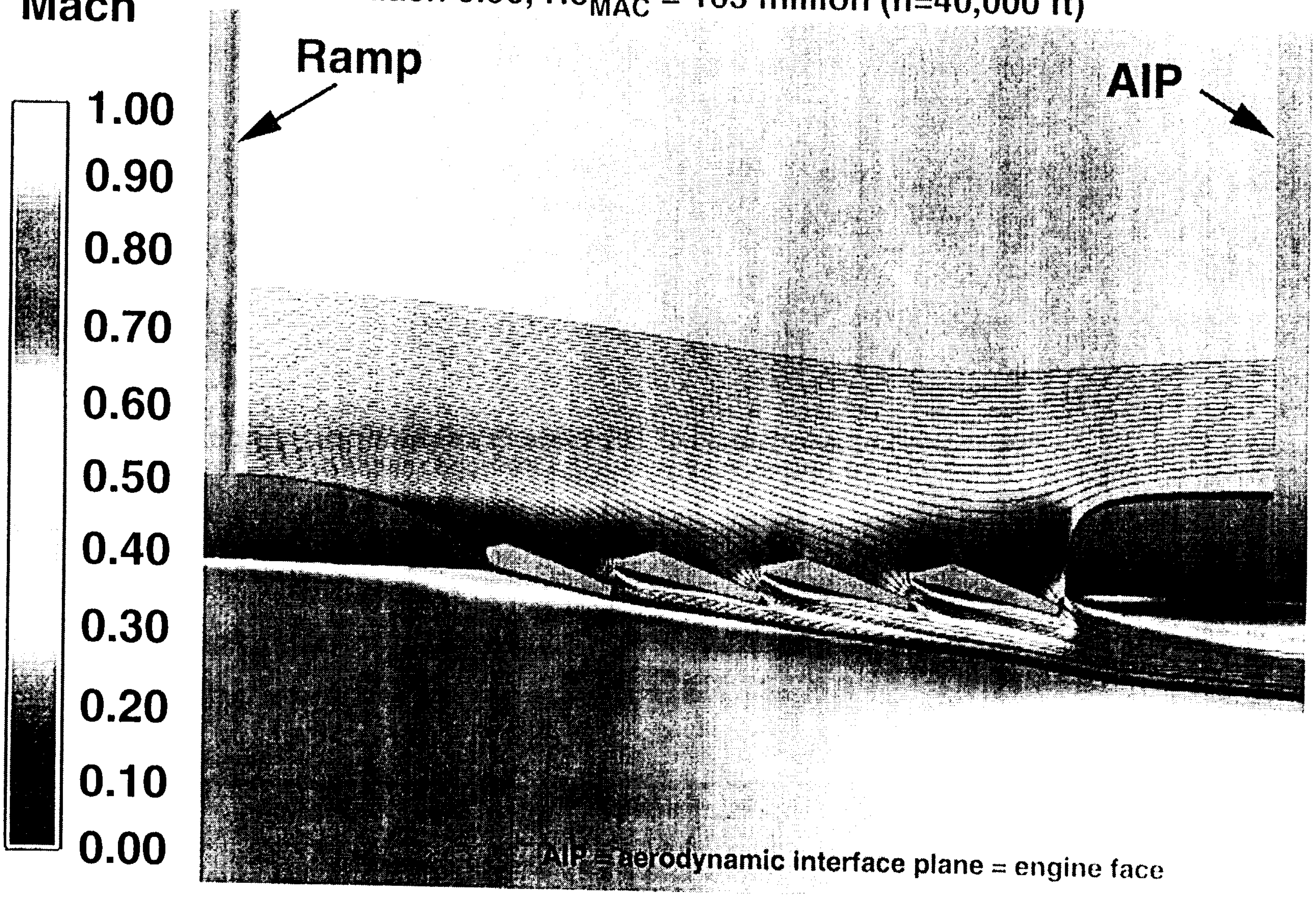

Bifurcated Inlet Spillage / Bypass Study

Isolated CFD Analysis: Modified Door Geometry

A new door geometry was lofted with an elliptical nose shape to address the separation problem. The modified and original geometries are compared in the figure.

Bifurcated Inlet Spillage / Bypass Study

Isolated CFD Analysis: Modified Door Geometry

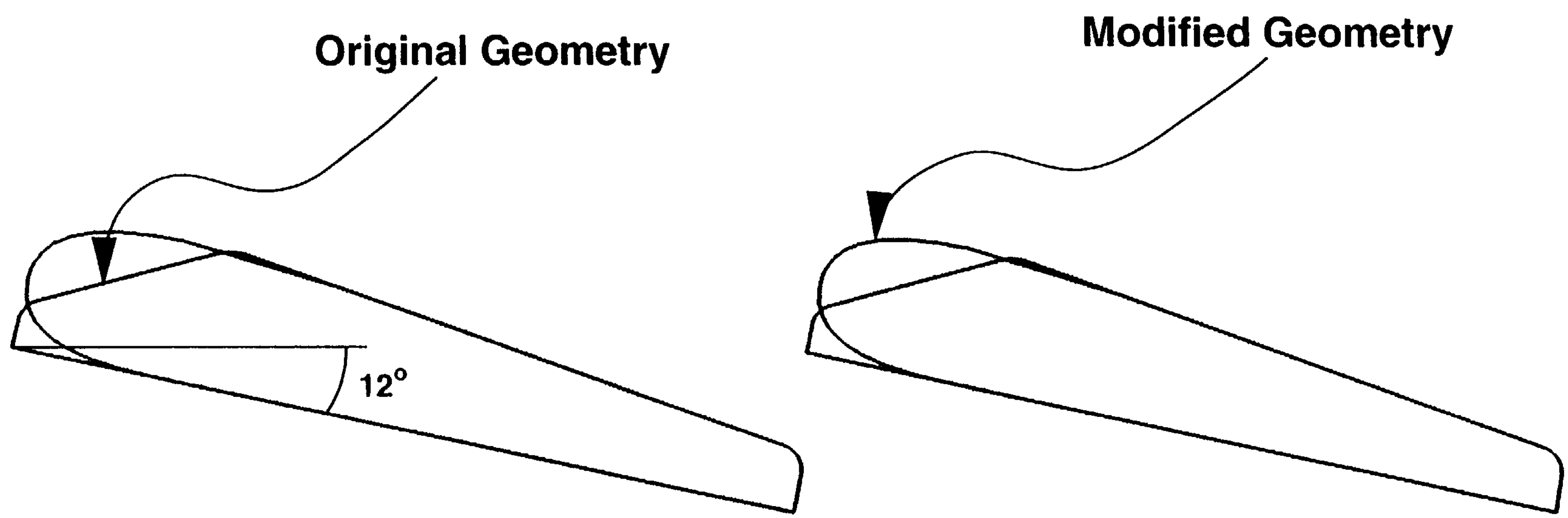

Bifurcated Inlet Spillage / Bypass Study

Isolated CFD Analysis: Inlet Mach Contours

Mach 0.90, Re_{MAC} = 163 million (h=40,000 ft)

Bypass Doors: 12 deg, Modified Geometry

MFRengine	=	0.60
MFRspill	=	0.30
MFRbypass	=	0.10

Rerunning the isolated nacelle analysis at Mach 0.90 with the modified door geometry increased the bypass mass flow rate from 7 % to 10 %. However, as the figure shows the inlet duct was now choked.

Bifurcated Inlet Spillage / Bypass Study

Isolated CFD Analysis: Inlet Mach Contours

Mach 0.90, Re_{MAC} = 163 million (h=40,000 ft)

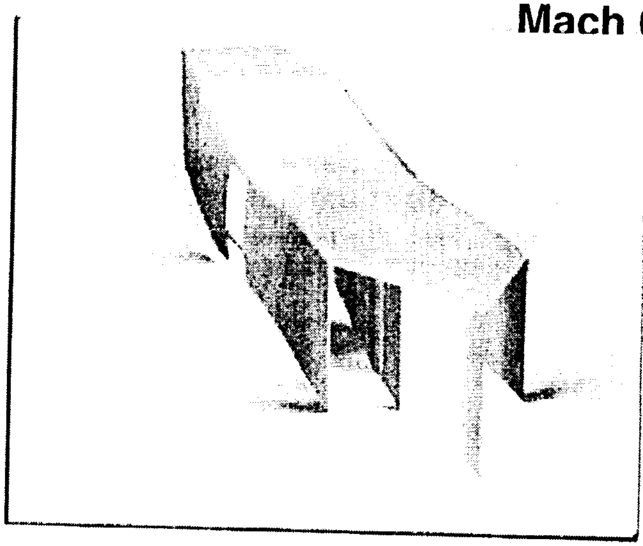

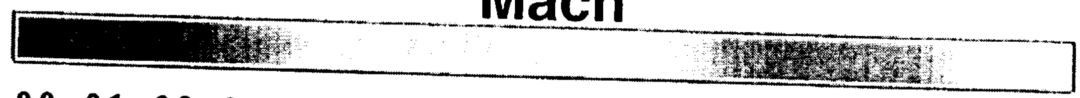

Bypass Doors: 12 deg, Modified Geometry

MFRengine = 0.60
MFRspill = 0.30
MFRbypass = 0.10

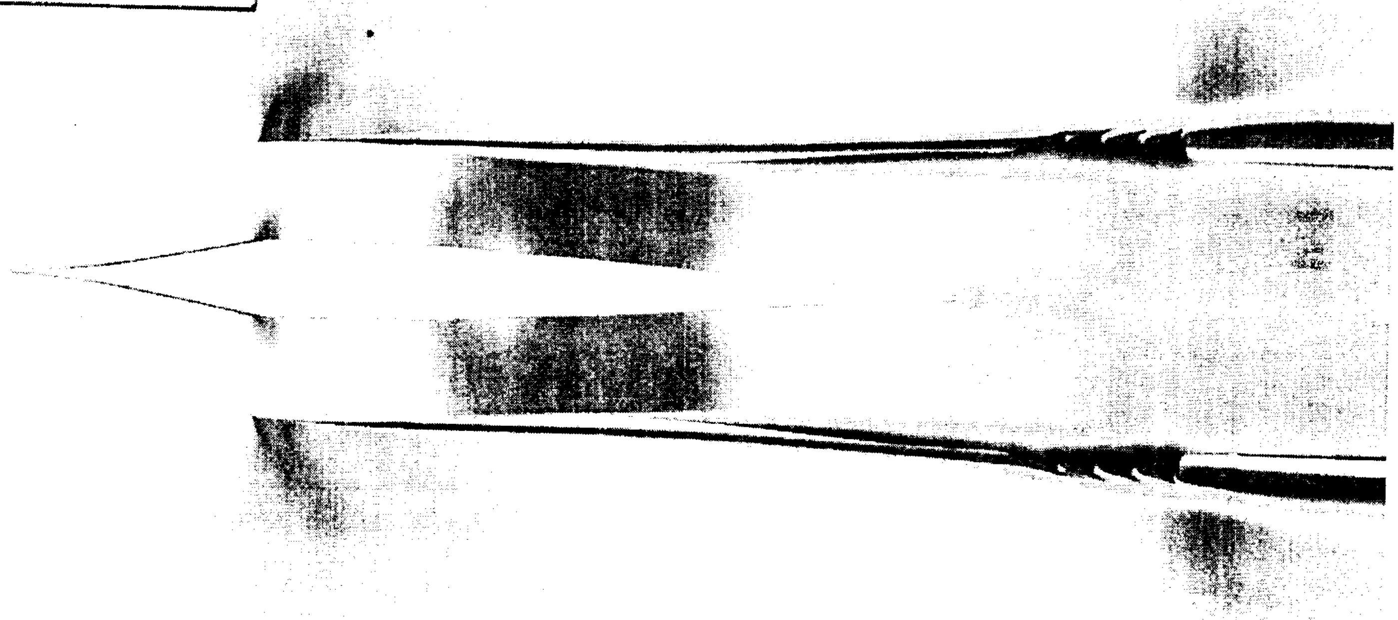

NORTHROP GRUMMAN

Bifurcated Inlet Spillage / Bypass Study

Isolated CFD Analysis: Inlet Mach Contours

Mach 0.90, Re_{MAC} = 163 million (h=40,000 ft)

Bypass Doors: 12 deg, Original Geometry

Ramp: Collapsed

MFRengine	=	0.60
MFRspill	=	0.29
MFRbypass	=	0.11

Another geometry modification to the original isolated analysis was made to try to achieve higher inlet capture mass flow rate. In the case shown here the inlet compression ramp was collapsed even further than its transonic design condition. This unchoked the inlet duct and allowed an increase in the bypass mass flow rate from 7 % to 11 %.

Bifurcated Inlet Spillage / Bypass Study

Isolated CFD Analysis: Inlet Mach Contours

Mach 0.90, Re_{MAC} = 163 million (h=40,000 ft)

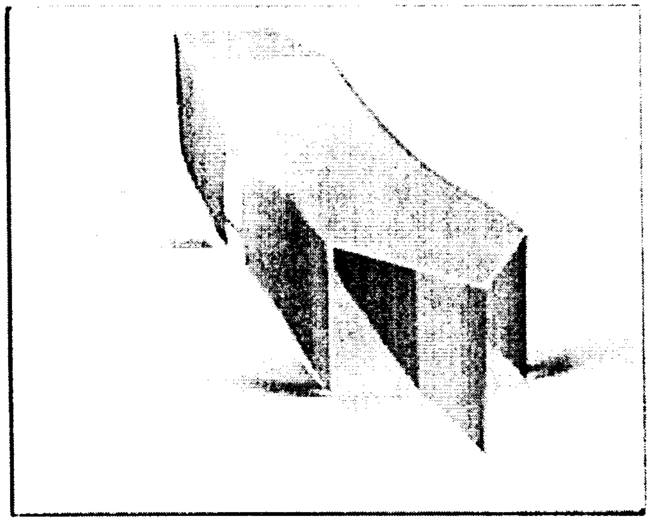

Mach

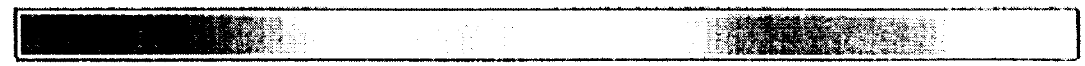

Bypass Doors: 12 deg, Original Geometry
Ramp: Collapsed
MFRengine = 0.60
MFRspill = 0.29
MFRbypass = 0.11

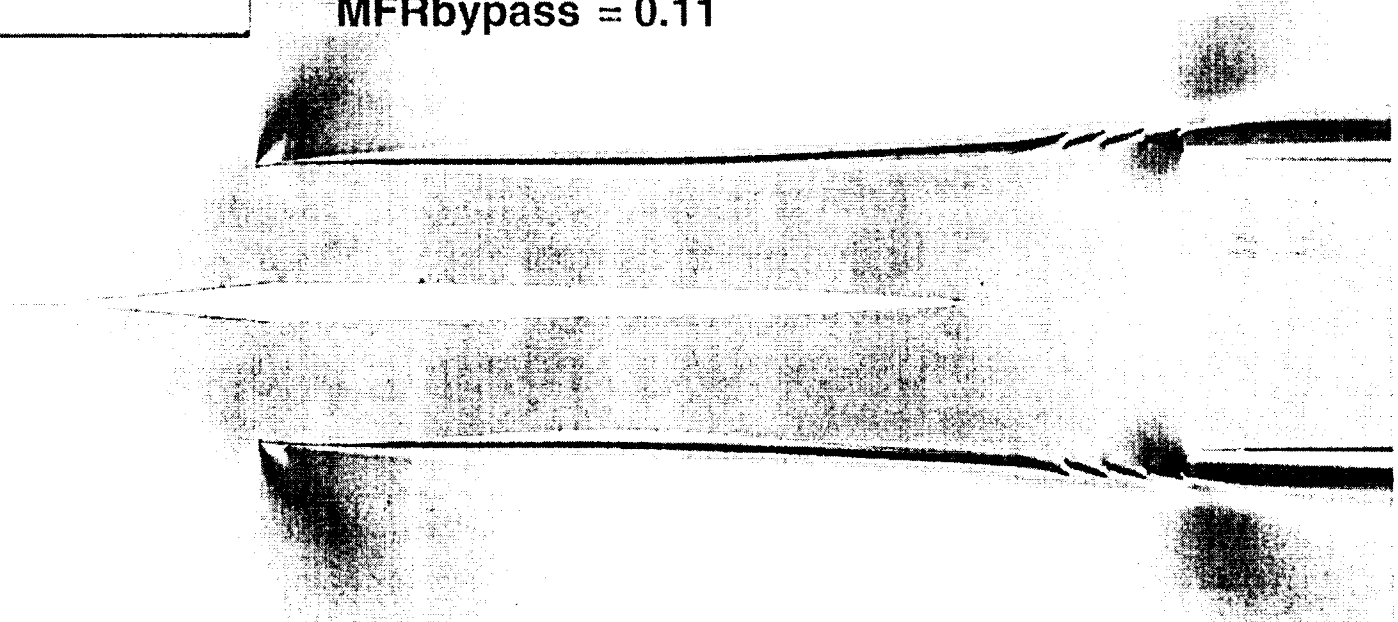

NORTHROP GRUMMAN

Bifurcated Inlet Spillage / Bypass Study

Isolated CFD Analysis: Inlet Mach Contours

Mach 0.90, Re_{MAC} = 163 million (h=40,000 ft)

Bypass Doors: 20 deg, Original Geometry

Ramp: Collapsed

MFRengine	=	0.60
MFRspill	=	0.22
MFRbypass	=	0.18

A third modification of the baseline Mach 0.90 run was made with the original door geometry opened up to 20 degrees and the fully collapsed ramp. As seen in the figure the bypass flow rate was increased considerably from 7 % to 18 %.

Bifurcated Inlet Spillage / Bypass Study

Isolated CFD Analysis: Inlet Mach Contours

Mach 0.90, Re_{MAC} = 163 million (h=40,000 ft)

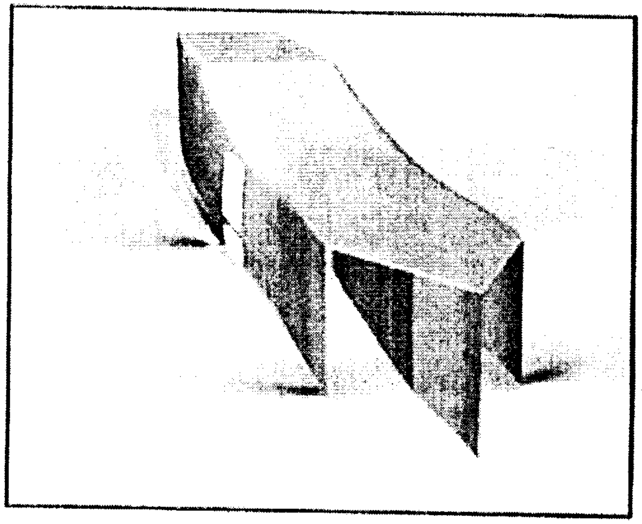

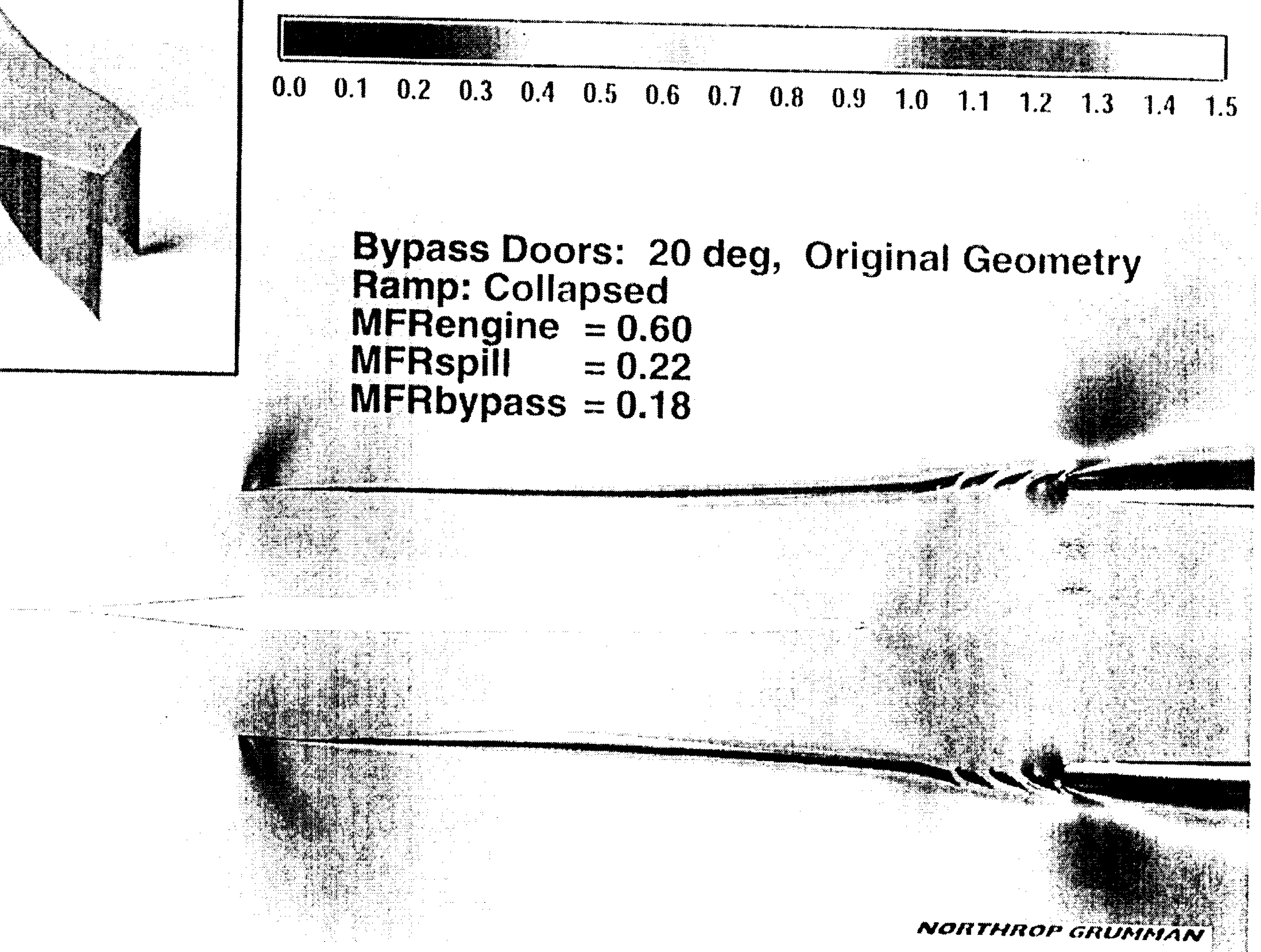

Bifurcated Inlet Spillage / Bypass Study

Isolated CFD Analysis: MFR vs. Bypass Door Angle

Mach 0.90, Re_{MAC} = 163 million (h=40,000 ft)

Ramp: Collapsed

The relationship of the bypass MFR to the bypass door angle for the Mach 0.90 case is shown. With the collapsed ramp and the modified door geometry opened to 20 degrees the highest bypass flow rate of 21 % was achieved.

Bifurcated Inlet Spillage / Bypass Study

Isolated CFD Analysis: MFR vs. Bypass Door Angle

Mach 0.90, Re_{MAC} = 163 million (h=40,000 ft)

Ramp: Collapsed

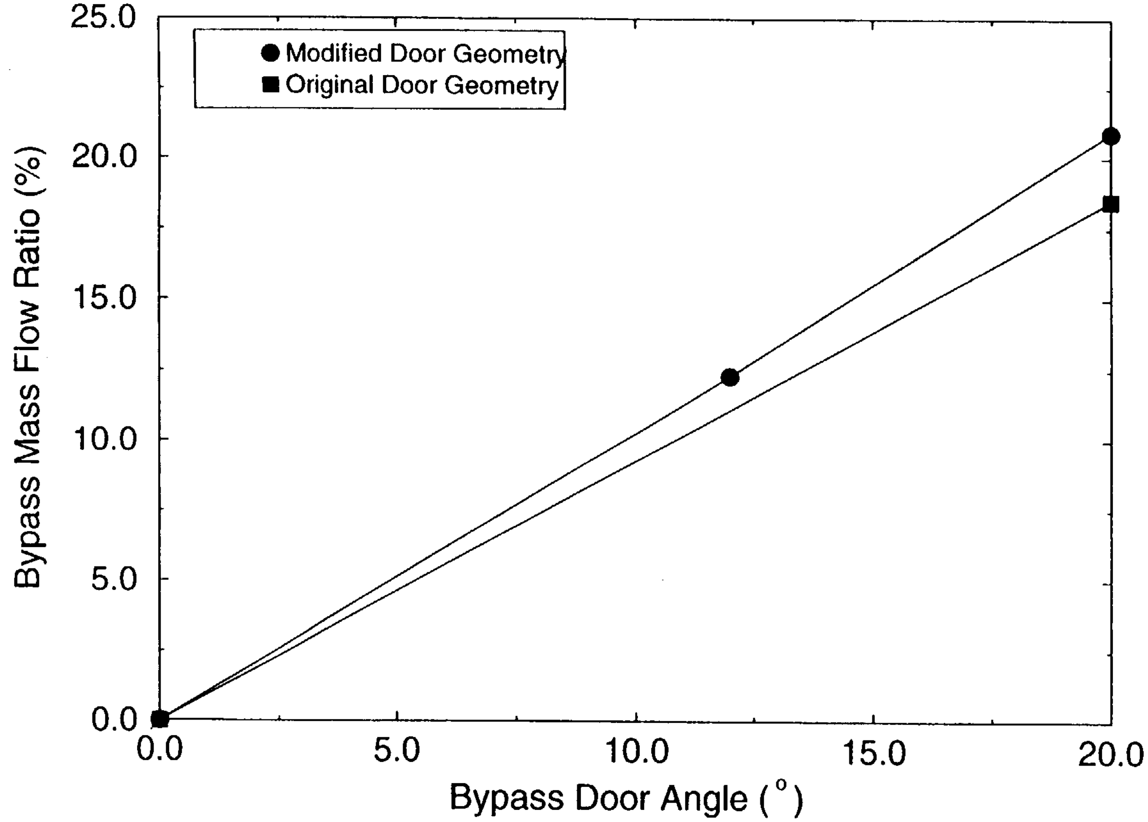

Bifurcated Inlet Spillage / Bypass Study

Isolated CFD Analysis: MFR vs. Bypass Door Angle

Mach 1.20, Re_{MAC} = 304 million (h=32,000 ft)

Ramp: Collapsed

The bypass mass flow rate as a function of bypass door angle for the Mach 1.20 case is shown. The effect of the modified door geometry is dramatic, increasing the bypass MFR from 10 % to 16% at 12 degree door angle. Beyond this door angle, the geometry with the modified doors, flows so well that the inlet duct chokes again, limiting the maximum bypass flow rate to ~ 18 %.

Bifurcated Inlet Spillage / Bypass Study

Isolated CFD Analysis: MFR vs. Bypass Door Angle

Mach 1.20, Re_{MAC} = 304 million (h=32,000 ft)

Ramp: Collapsed

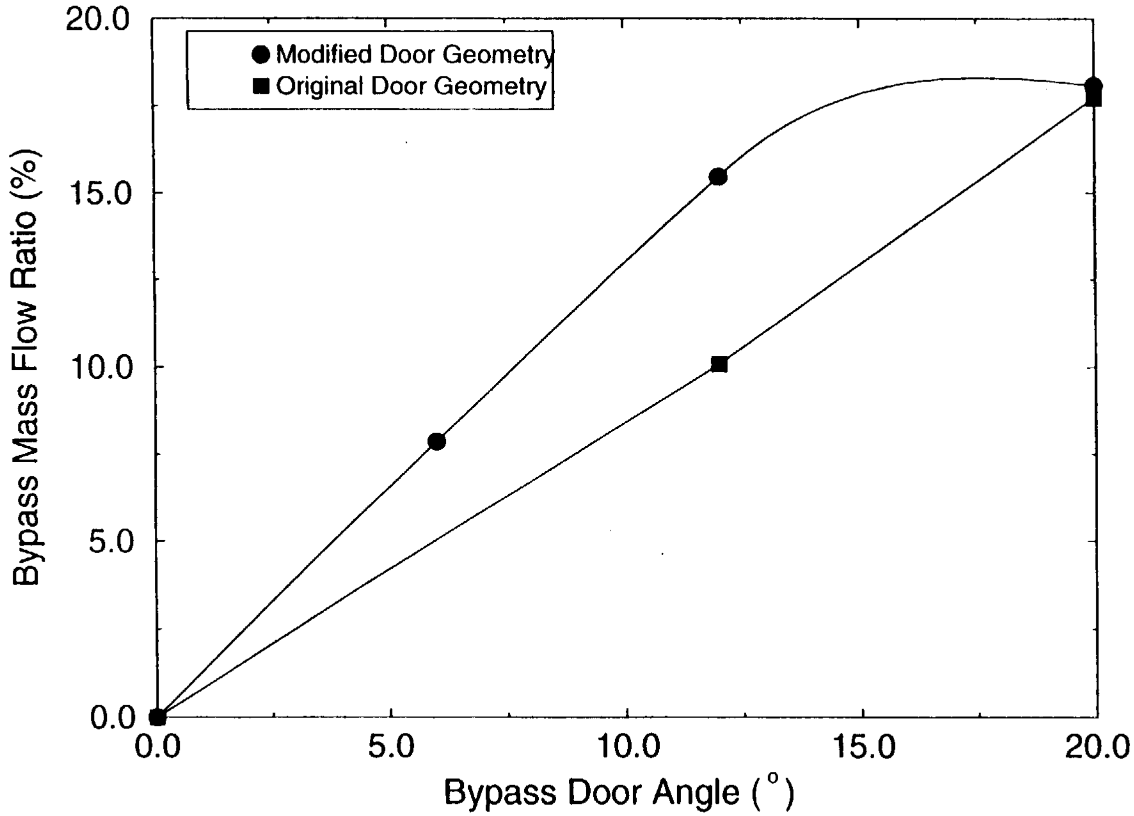

Bifurcated Inlet Spillage / Bypass Study

Isolated CFD Analysis: $CD_{nacelle}$ vs. MFR_{bypass}

Mach 0.90, Re_{MAC} = 163 million (h=40,000 ft)

The nacelle external drag as a function of the bypass mass flow rate is shown for the Mach 0.90 isolated nacelle cases; the external drag excludes the inlet compression ramp and inlet internal surfaces. The drag increases linearly from 1.57 counts to 2.81 counts as the bypass MFR increases from zero to 21 %. As the bypass flow increases the spillage decreases; decreased spillage reduces the beneficial lip suction induced by the spill flow as it expands around the nacelle leading edge. Note that two different drag levels were obtained at zero bypass for the original and collapsed ramp geometries. This drag level difference is discussed in the following two figures.

Bifurcated Inlet Spillage / Bypass Study

Isolated CFD Analysis: $CD_{nacelle}$ vs. MFR_{bypass}

Mach 0.90, Re_{MAC} = 163 million (h=40,000 ft)

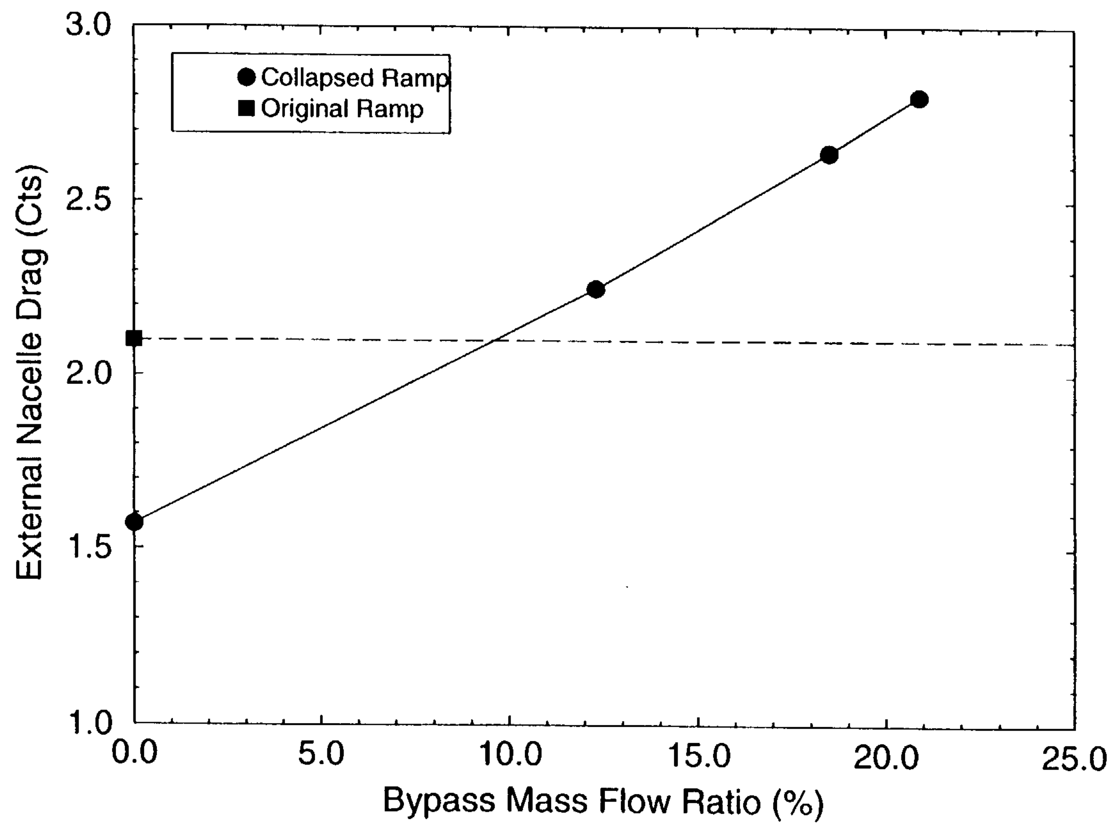

Bifurcated Inlet Spillage / Bypass Study

Isolated CFD Analysis: Inlet Mach Contours

Mach 0.90, Re_{MAC} = 163 million (h=40,000 ft)

Bypass Doors: 0 deg

Ramp: Original

MFRengine	=	0.60
MFRspill	=	0.40
MFRbypass	=	0.0

The zero bypass isolated Mach 0.90 case with the original ramp is shown here; the following figure shows the same case with the collapsed ramp. The lower drag of the collapsed ramp case is evidently due to the increased lip suction (larger high Mach region) at the nacelle leading edge. Apparently the increased wedge angle of the original ramp imparts a flow angularity to the flow field, thereby reducing the amount of turning that must occur at the nacelle lip.

Bifurcated Inlet Spillage / Bypass Study

Isolated CFD Analysis: Inlet Mach Contours

Mach 0.90, Re_{MAC} = 163 million (h=40,000 ft)

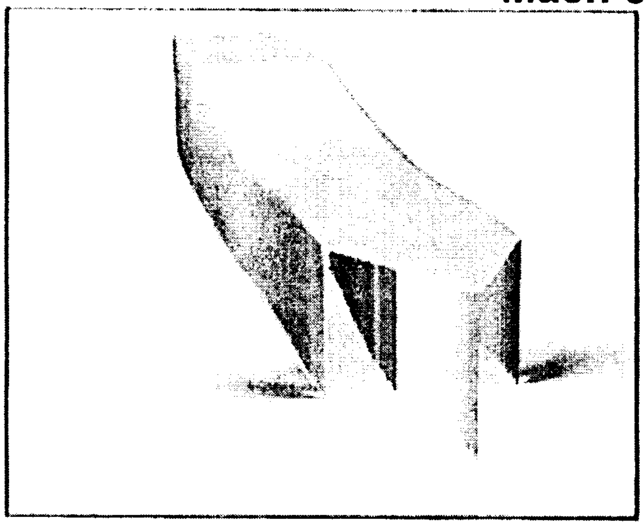

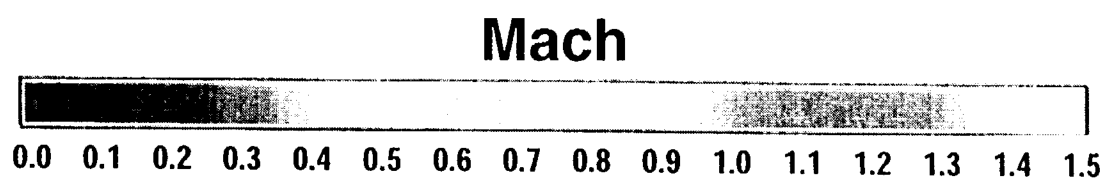

Bypass Doors: 0 deg
Ramp: Original
MFRengine = 0.60
MFRspill = 0.40
MFRbypass = 0.0

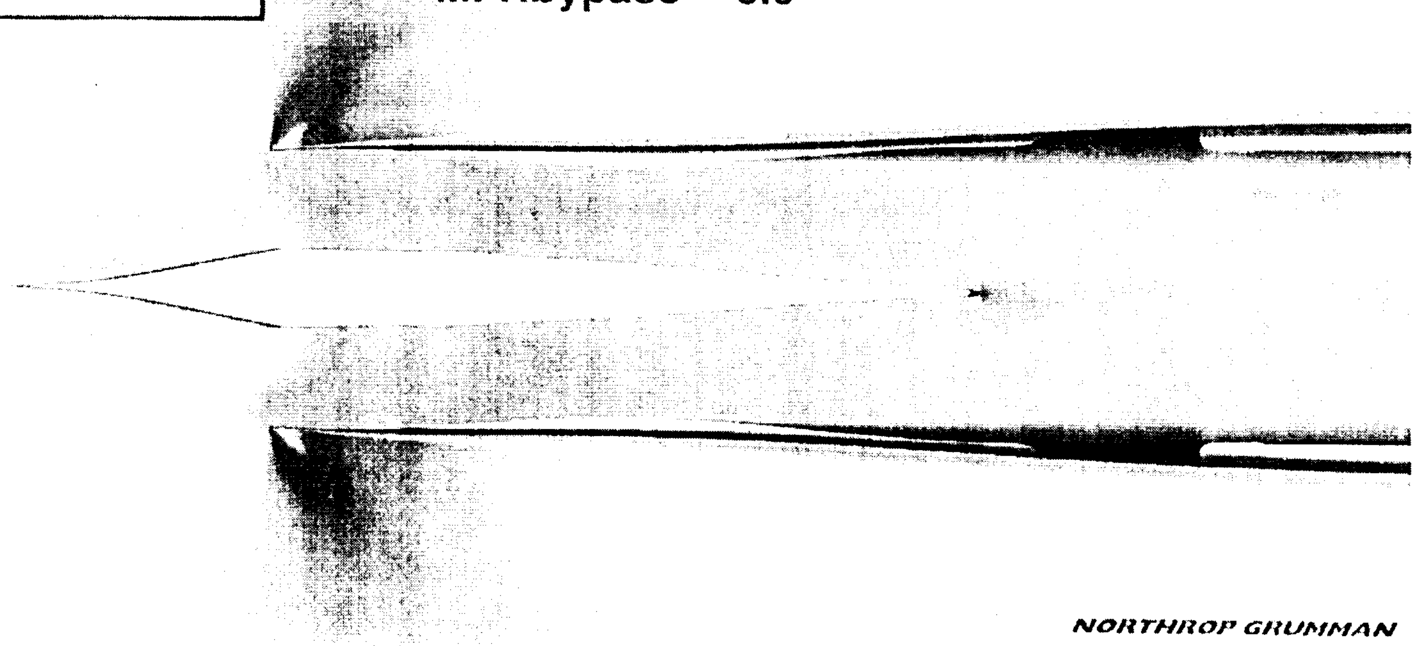

NORTHROP GRUMMAN

Bifurcated Inlet Spillage / Bypass Study

Isolated CFD Analysis: Inlet Mach Contours

Mach 0.90, Re_{MAC} = 163 million (h=40,000 ft)

Bypass Doors: 0 deg

Ramp: Collapsed

MFRengine	=	0.60
MFRspill	=	0.40
MFRbypass	=	0.0

See text for previous page.

Bifurcated Inlet Spillage / Bypass Study

Isolated CFD Analysis: Inlet Mach Contours

Mach 0.90, Re_{MAC} = 163 million (h=40,000 ft)

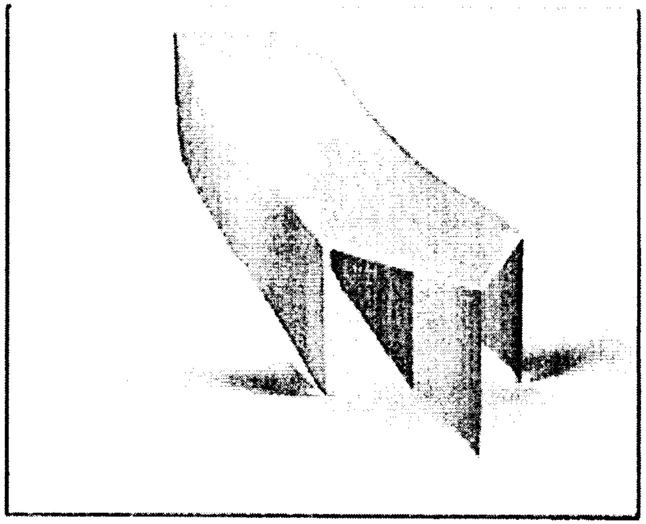

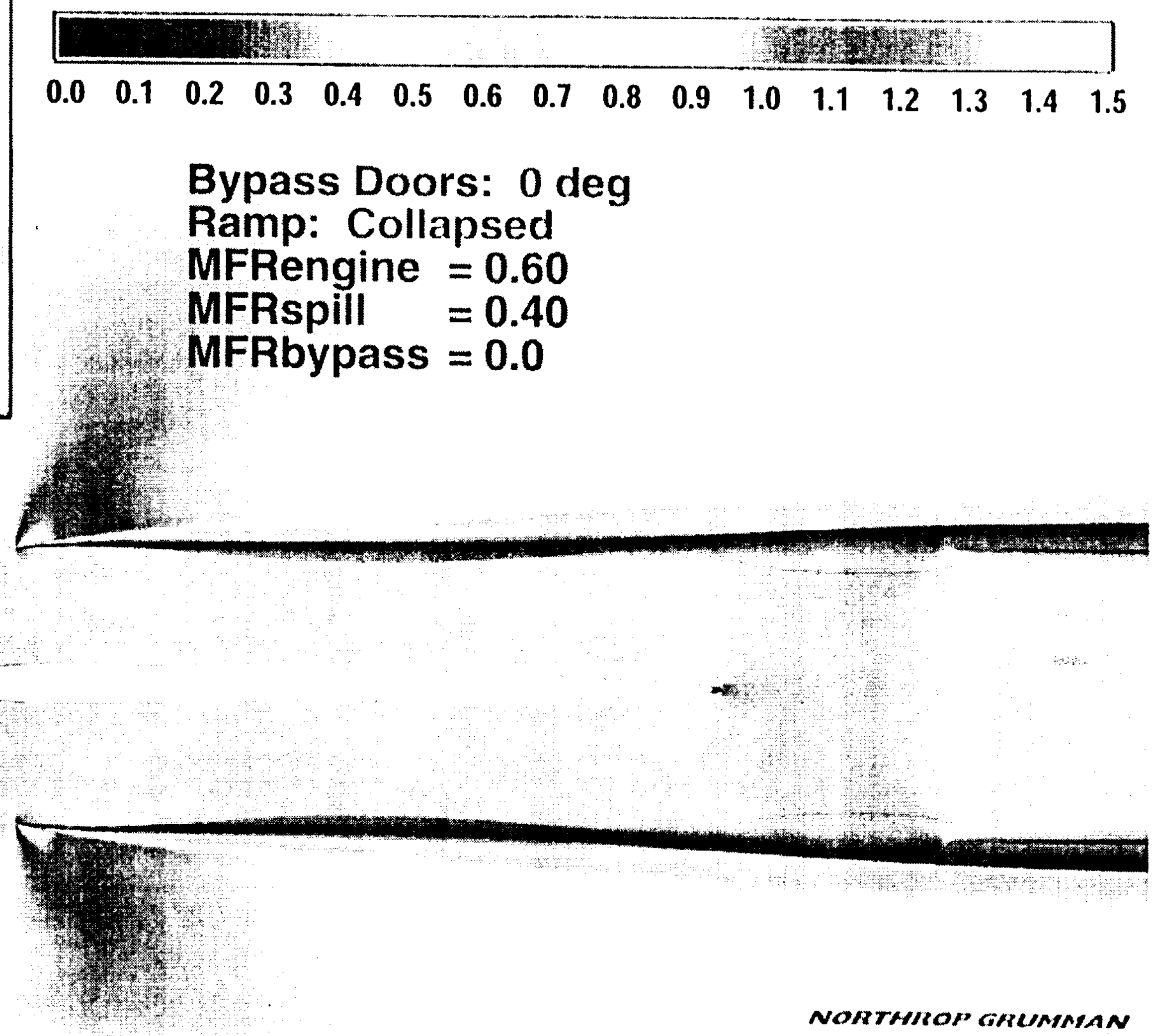

NORTHROP GRUMMAN

Bifurcated Inlet Spillage / Bypass Study

Isolated CFD Analysis: $CD_{nacelle}$ vs. MFR_{bypass}

Mach 1.20, Re_{MAC} = 304 million (h=32,000 ft)

The external nacelle drag for the isolated Mach 1.20 case is shown here as a function of bypass mass flow rate. The drag increases linearly up to MFR = 15%; beyond which the drag increased sharply. The drag increase is the combined effect of losing lip suction as the spillage decreases, and penetration of the bypass doors into the external flow.

Bifurcated Inlet Spillage / Bypass Study

Isolated CFD Analysis: $CD_{nacelle}$ vs. MFR_{bypass}

Mach 1.20, Re_{MAC} = 304 million (h=32,000 ft)

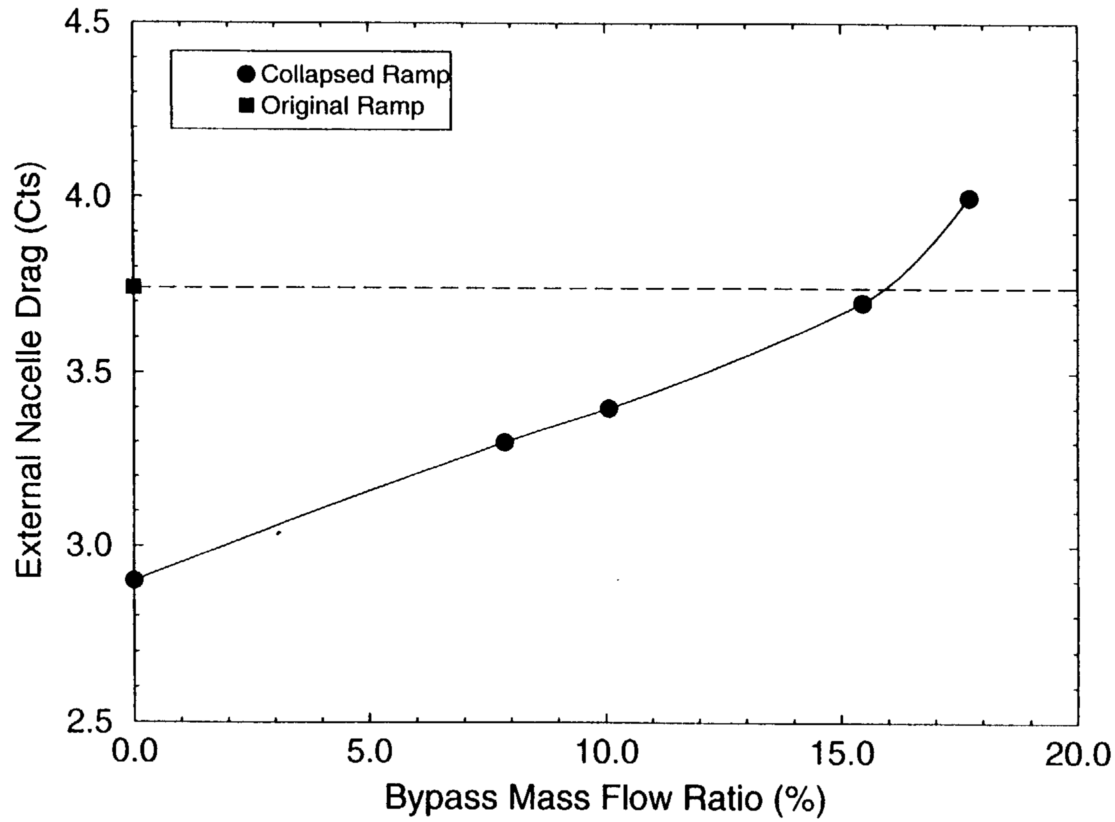

Bifurcated Inlet Spillage / Bypass Study

TCA W/B/N/D CFD Analysis: Surface Pressure Distribution

Mach 1.20, Re_{MAC} = 304 million (h=32,000 ft)

Zero Bypass (MFRspill = 35 %)

The zero bypass installed nacelle Mach 1.20 case has been completed. Surface pressure contours are shown in the figure. The spillage at the cowl lip (low pressure region) and the high pressure region on the wing lower surface as seen in the BCA wind tunnel Reynolds Number analysis done in 1997 are clearly evident. This run took 268 cpu-hours.

Bifurcated Inlet Spillage / Bypass Study

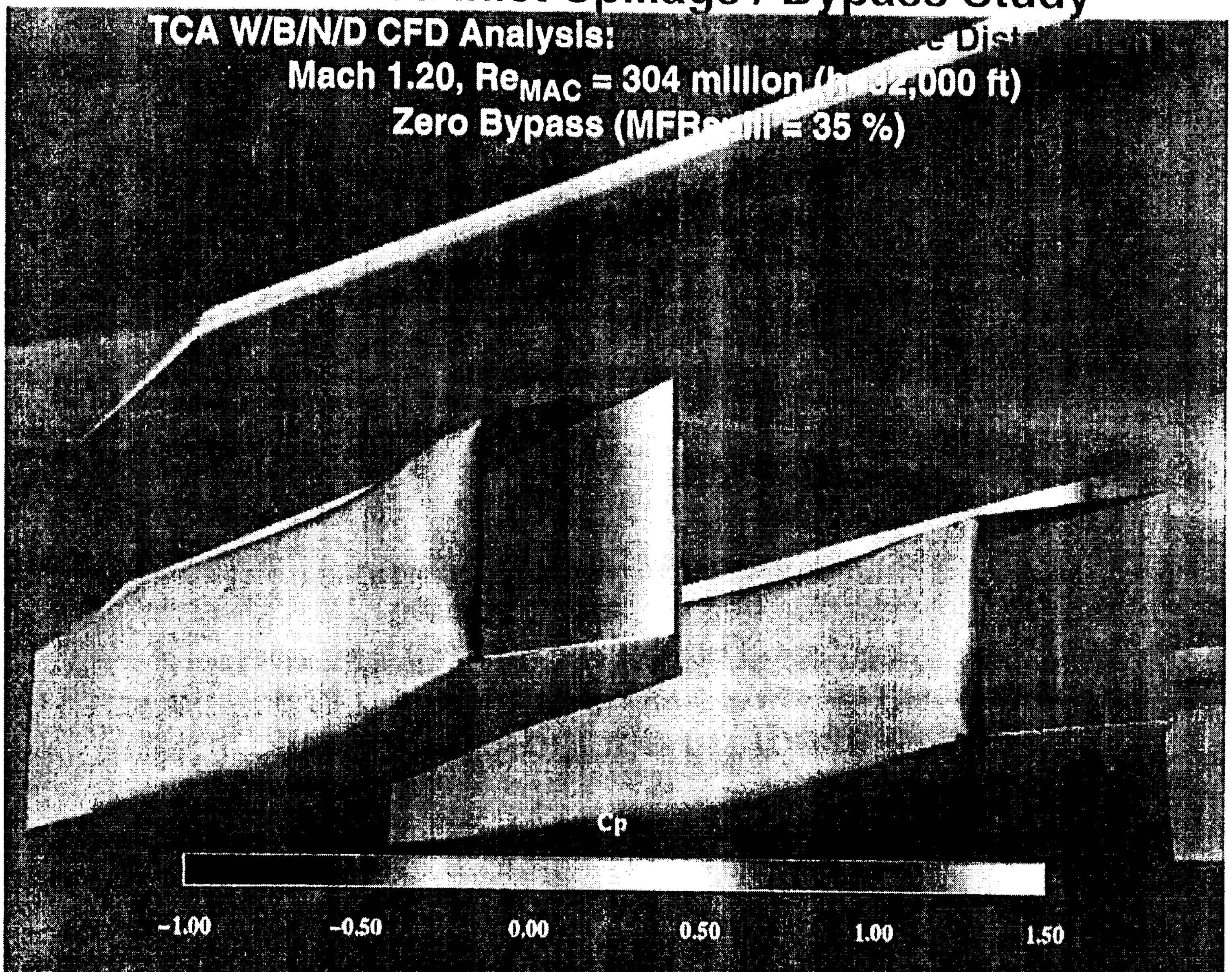

Bifurcated Inlet Spillage / Bypass Study

TCA W/B/N/D CFD Analysis: Surface Pressure Distribution

Mach 1.20, Re_{MAC} = 304 million (h=32,000 ft)

Bypass Doors: 12 deg

PRELIMINARY (convergence not complete)

The surface pressure distribution for the 12 degree bypass door case is shown. This case is 60% converged (it is estimated that completion will require 550 cpu-hours). Comparison with the zero bypass case indicates the same trends as seen on the isolated nacelle: reduced low pressure at nacelle lip due to reduced spillage, increased pressure near bypass doors. In addition, a region of increased pressure on the wing lower surface just above the bypass doors is evident that was not present in the zero bypass case.

Bifurcated Inlet Spillage / Bypass Study

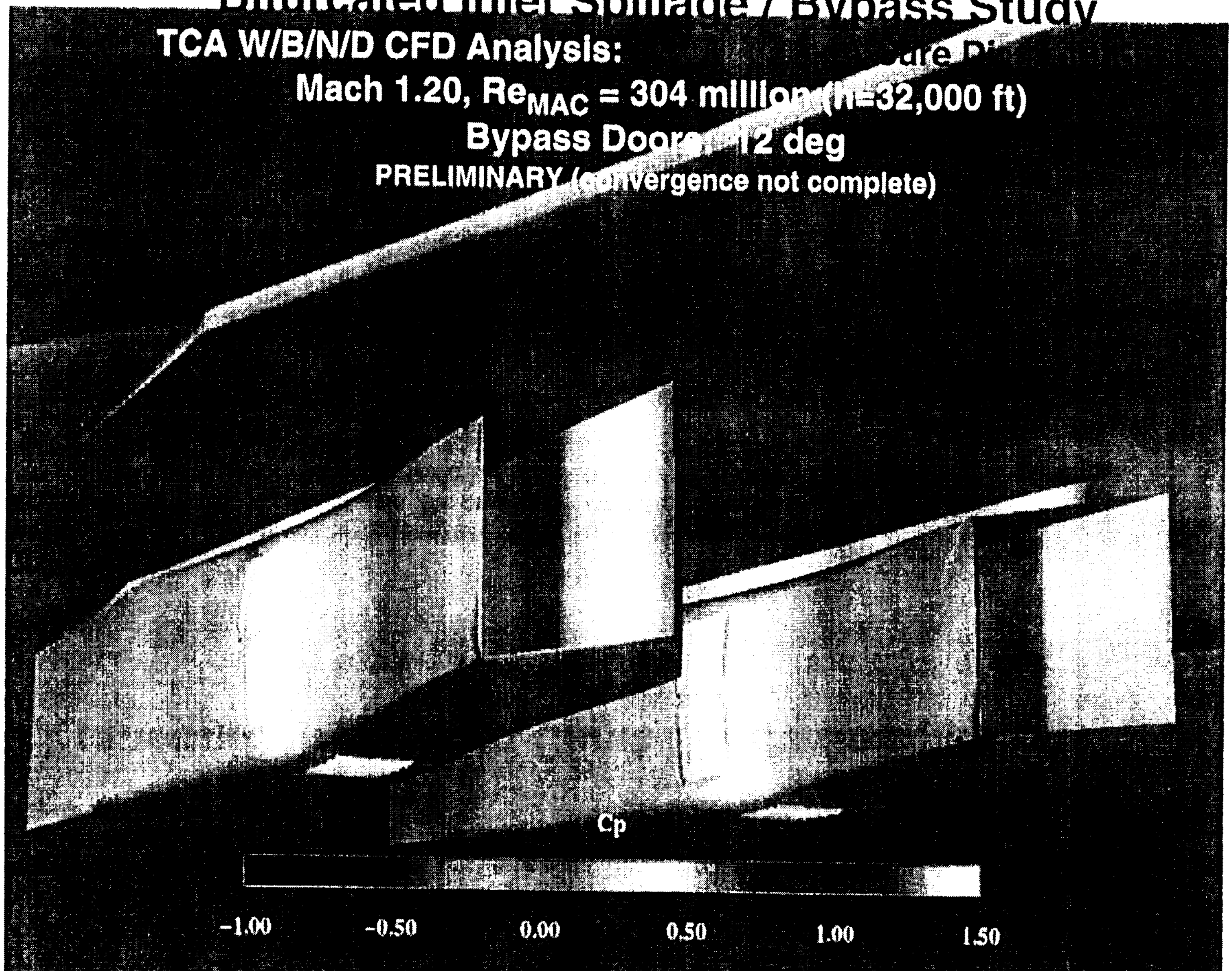

NORTHROP GRUMMAN

Transonic Cruise and Climb Study Conclusions

The transonic results for the installed axisymmetric nacelle done with different grids, different codes, and at different Reynolds Numbers yielded very similar results. When NGC completes the bifurcated analysis a similar comparison can be made to the BCA bifurcated results.

The bifurcated inlet/ramp system as designed is clearly not adequate for anything but very low bypass rates. In order to obtain a bypass mass flow rate close to the propulsion designated maximum it was necessary to collapse the compression ramp to an unrealistic width. In addition, the bypass doors were redesigned to remove corners at the leading edge that were separating the flow and limiting the flow rate.

The relationship between bypass mass flow rate and nacelle drag has been investigated on the isolated bifurcated nacelle: the drag increases as the bypass MFR increases due to reduced spillage lip suction.

The NGC spillage/bypass study on the installed bifurcated is in progress.

Transonic Cruise and Climb Study Conclusions

- Axi inlet spilling effects very similar at WT(BCAG–OVERFLOW) and flight conditions(NGC–GCNS)
  - NGC flight analysis of spilling bifurcated inlet in progress
- Baseline bifurcated inlet/ramp system designed to spill, NOT bypass
  - Ramp and door modifications required to reach required MFR_{bypass}
- Isolated nacelle drag increases when bypass increased
  - Less spillage means less lip suction
- NGC analysis of installed bifurcated with bypass in progress

Plans

The funding level for 1999 is somewhat uncertain at this time, but these tasks are currently expected to be completed.

Plans

- Bifurcated as–tested QA point analysis
- Complete blunt lip analysis
- Implement / assess S–A turb model mods on WBND
- Alternate nacelle / diverter designs
    - Wave–rider inlet
- Archive multi–year PAI analysis effort

Improvements to the Unstructured Mesh Generator MESH3D

Scott D. Thomas, Raytheon ITSS

Timothy J. Baker, Princeton University

Susan E. Cliff, NASA Ames Research Center

February 9, 1999

AIRPLANE Advantages

CAD → MESH3D → AIRPLANE

- Robust and accurate Euler flow solver.
- Has been extensively validated.
- Handles complete, complex geometries.
- Multiple platforms, vector and parallel.
- There is a path to Navier–Stokes.

Chart 2: AIRPLANE Advantages

The AIRPLANE process starts with an aircraft geometry stored in a CAD system. The surface is modeled with a mesh of triangles and then the flow solver produces pressures at surface points which may be integrated to find forces and moments.

Why AIRPLANE? The biggest advantage is that the grid generation bottleneck of the CFD process is eliminated when an unstructured tetrahedral mesh is used. MESH3D is the key to turning around the first analysis of a CAD geometry in days instead of weeks.

The flow solver part of AIRPLANE has proven to be robust and accurate over a decade of use at NASA. It has been extensively validated with experimental data and compares well with other Euler flow solvers. AIRPLANE has been applied to all the HSR geometries treated at Ames over the course of the HSR program in order to verify the accuracy of other flow solvers.

The unstructured approach makes handling complete and complex geometries very simple because only the surface of the aircraft needs to be discretized, i.e. covered with triangles. The volume mesh is created automatically by MESH3D.

AIRPLANE runs well on multiple platforms. Vectorization on the Cray Y–MP is reasonable for a code that uses indirect addressing. Massively parallel computers such as the IBM SP2, SGI Origin 2000, and the Cray T3E have been used with an MPI version of the flow solver and the code scales very well on these systems. AIRPLANE can run on a desktop computer as well.

AIRPLANE has a future. The unstructured technologies developed as part of the HSR program are now targeting high Reynolds number viscous flow simulation. The pacing item in this effort is Navier–Stokes mesh generation.

AIRPLANE Advantages

$$\text{CAD} \longrightarrow \text{MESH3D} \longrightarrow \text{AIRPLANE}$$

- Robust and accurate Euler flow solver.
- Has been extensively validated.
- Handles complete, complex geometries.
- Multiple platforms, vector and parallel.
- There is a path to Navier–Stokes.

Baseline TCA: AIRPLANE Solution

Mach 2.4 $\alpha = 3.6$

Replace this chart with a color picture showing the surface mesh and color Cp function on the surface of the baseline TCA nacelles, diverters, and the lower surface of the wing.

The mesh for this case was generated by MESHPLANE, the precursor to MESH3D.

The picture illustrates that AIRPLANE can handle complete, complex geometries.

Chart 3: Baseline TCA: AIRPLANE Solution, Mach 2.4, α=3.6

This color picture shows the surface mesh and color Cp function on the surfaces of the TCA nacelles, diverters, and the lower surface of the wing.

The mesh for this case was generated by MESHPLANE, the precursor to MESH3D. The picture illustrates that AIRPLANE can handle complete, complex geometries.

The AIRPLANE process used today at NASA is the result of efforts initiated by Antony Jameson and Tim Baker, and it has been augmented by several other contributors.

References (taken from AIRPLANE source code):

(1) A.Jameson,T.J.Baker and N.J.Weatherill,"Calculation of Inviscid Flow over a Complete Aircraft",AIAA Paper 86-0103,January 1986.
(2) A. Jameson and T. J. Baker, "Improvements to the Aircraft Euler Method", AIAA Paper 87-0452, January 1987.
(3) A. Jameson, "Computational Transonics", Comm. Pure Appl. Math., Vol. 16, 1988, pp. 507-549.
(4) A. Jameson, "Computational Aerodynamics for Aircraft Design", Science, Vol. 245, 1989, pp. 361-371.
(5) T. J. Baker, "Three Dimensional Mesh Generation by Triangulation of Arbitrary Points Sets", AIAA Paper 87-1124-CP, June 1987.
(6) T. J. Baker, "Developments and Trends in Three-Dimensional Mesh Generation", Appl. Num. Math. 5, 1989, pp. 275-304.
(7) T. J. Baker, "Construction of Tetrahedral Meshes Around Complex Three Dimensional Shapes", Conference on Supercomputing in Fluid Flow, Lowell, Mass., October 1989.

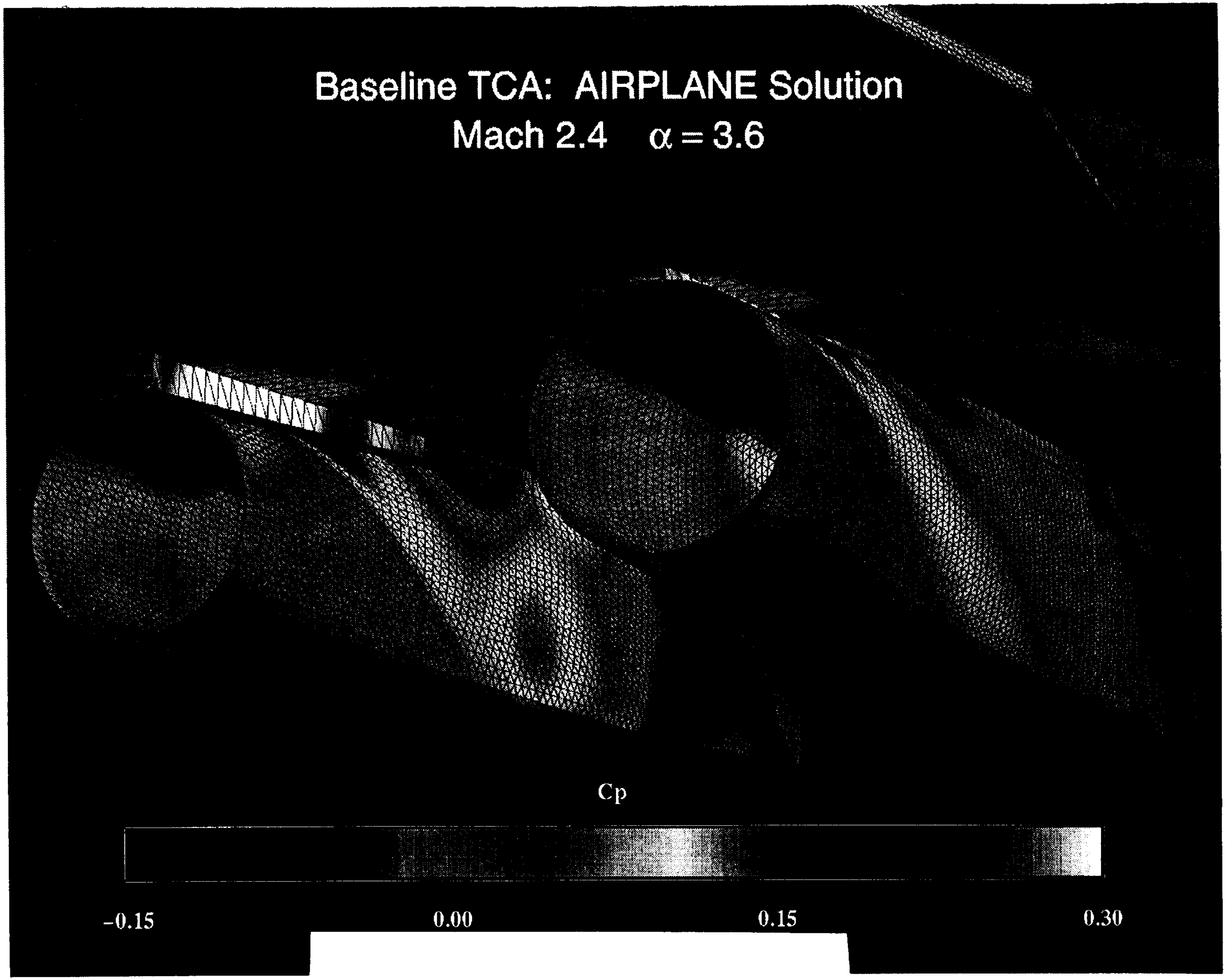
Baseline TCA: AIRPLANE Solution
Mach 2.4 α = 3.6
Cp
-0.15
0.00
0.15
0.30

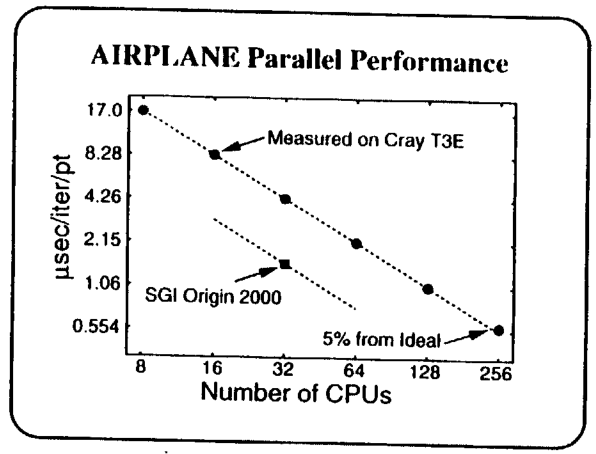

Chart 4: AIRPLANE Parallel Performance

The MPI version of AIRPLANE requires 2^N, a power of two, processors, because it uses recursive bisection to create subdomains. Measurements show that AIRPLANE performance for large problems scales nearly ideally on the IBM SP2, the SGI Origin 2000, and the Cray T3E.

In the figure, the number of microseconds per iteration per mesh point is shown against the number of processing elements (CPUs) on a log–log scale. Measured values for a Cray T3E, jsimpson.gsfc.nasa.gov, are listed on the left of the figure. Ideal performance is shown with a dashed line, obtained by successively dividing the 8–CPU performance by 2. AIRPLANE was applied to a mesh of over 800,000 points. The residual smoothing option was turned on, and smoothing communication was lagged at subdomain boundaries. Scaling is nearly ideal and there is less than 5% difference from the ideal figure at the top end.

One symbol is shown for the SGI Origin 2000 (O2K), steger.nas.nasa.gov, for 32 CPUs. Performance on the O2K is known to scale very well with the number of CPUs.

A typical mesh has about 800,000 points. It takes one to three wall seconds per iteration to run the flow solver, and one to two thousand iterations to obtain a typical steady solution. Thus it is possible to run an alpha sweep of a dozen points in one day.

Information on MPI may be found at URL: http://www.mcs.anl.gov/mpi/mpich/index.html.

AIRPLANE Parallel Performance

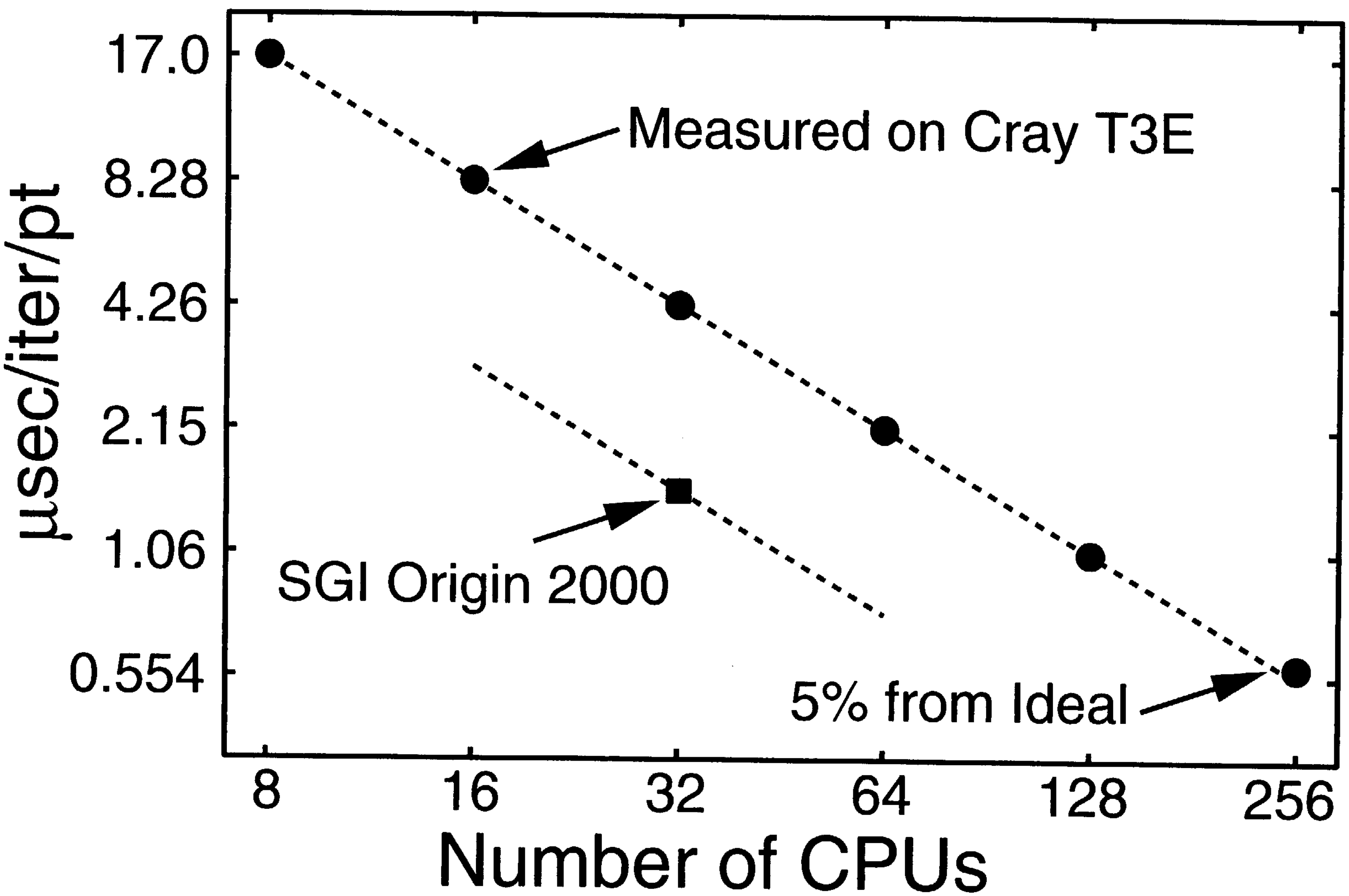

AIRPLANE/SYN107–MB Comparison

Replace this chart with a color picture showing a comparison of an AIRPLANE mesh generated by MESH3D and a multi-block grid for SYN107–MB generated by Gridgen (Mark Rimlinger).

The geometry is the PTC and the figure shows a cut through a constant Y plane (a waterline cut) through all the faces of the unstructured tetrahedra and all the faces of the structured hexahedra.

The picture illustrates that AIRPLANE can handle complete, complex geometries, and reminds that it is used to check other Euler flow computations.

Chart 5: AIRPLANE/SYN107–MB Comparison

This color picture shows a comparison of an AIRPLANE mesh generated by MESH3D and a multi–block grid for SYN107–MB which was assembled manually by Mark Rimlinger using Gridgen.

The geometry is the PTC (Preliminary Technology Concept) with canard, and the figure shows a cut through a constant Y plane (a waterline cut) through all the faces (triangles) of the unstructured tetrahedra and all the faces (quadrilaterals) of the structured hexahedra. The plane cuts through the middle of the canard, and it passes over the wing and under the horizontal tail.

The picture illustrates that AIRPLANE can handle complete, complex geometries and it is used to check other Euler flow computations.

Clustering of points near the tips of the canard, wing, and tail are evident in the structured grid, and this clustering gradually relaxes in the span direction off the tips. Without the H–topology constraint, the unstructured mesh is able to coarsen much sooner.

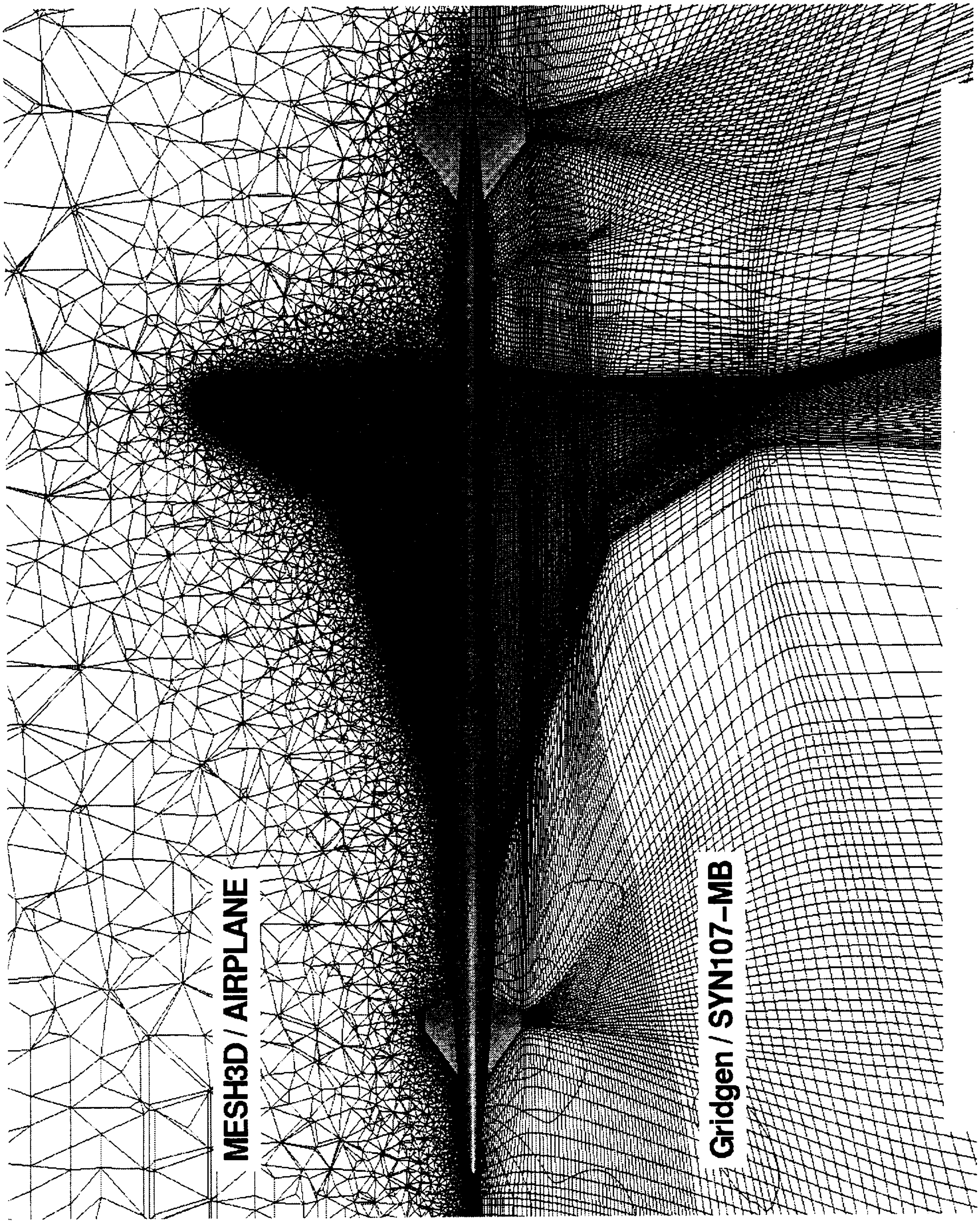
MESH3D / AIRPLANE
Gridgen / SYN107–MB

MESH3D

- Automatic tetrahedral mesh generation method.
- Based on a constrained Delaunay algorithm.
- Exploits edge/face swapping technique to establish boundary surfaces.
- Requires a surface mesh which can be obtained from GridTool/VGRID or Gridgen.

Chart 6: MESH3D

The computer program MESH3D creates a volume mesh of tetrahedra that conforms to a prescribed surface triangulation. The Delaunay requirement means that no mesh point may be inside any tetrahedron's circumsphere, and this leads to a regular mesh away from the boundary surface. The meshing algorithm is based on a constrained Delaunay technique that exploits edge/face swapping to establish the boundary surface triangulation within a volume mesh. The combination of circum–center point insertion and a sliver detection and removal strategy then generates a high quality tetrahedral mesh with a smooth gradation in cell size. MESH3D has proven to be very robust and is currently being used to generate meshes for use by the AIRPLANE code.

Baker, T.J. "Triangulations, Mesh Generation and Point Placement Strategies", in Frontiers of Computational Fluid Dynamics 1994, (ed. Caughey and Hafez), pub. J. Wiley and Sons.

Baker, T.J. and Vassberg, J.C. "Tetrahedral Mesh Generation and Optimization", Proc. 6th International Conference on Numerical Grid Generation, pub ISGG, pp337–349, 1998.

The following surface terms will be used in this report:

Geometry: The representation of a surface in the manner native to an unspecified CAD system, e.g. NURBS.
Mesh: A list of (x,y,z) points and a list of triangular faces, where each face is represented by three integer index values that refer to the point list, one per vertex, and a fourth integer that is the component number of which the face is a part.
Grid: NB structured NJ by NK three dimensional patches, i.e. ((((xyz(m,j,k,n),m=1,3),j=1,NJ(n)),k=1,NK(n)),n=1,NB).
Modeling: A CAD geometry is approximated with a mesh or grid by applying a tool like GridTool/VGRID or Gridgen.

MESH3D

- Automatic tetrahedral mesh generation method.
- Based on a constrained Delaunay algorithm.
- Exploits edge/face swapping technique to establish boundary surfaces.
- Requires a surface mesh which can be obtained from GridTool/VGRID or Gridgen.

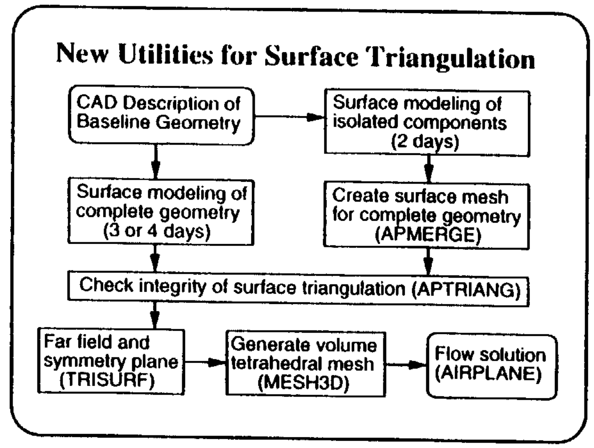

Chart 7: New Utilities for Surface Triangulation

Although tetrahedral mesh generation using MESH3D is a fully automated procedure, the user must first generate a surface triangulation. GridTool/VGRID and, more recently, Gridgen have been used to generate surface triangulations from CAD data, but both surface meshers still require a significant degree of user activity to create good quality surface triangulations.

The two new utilities APMERGE and APTRIANG aid the user in creating a baseline surface triangulation. The program APMERGE provides automated merging and assembly of a surface triangulation for a geometry formed by the intersection of a series of individual components. In other words, once the user has created surface triangulations of the individual parts, the generation of a surface triangulation for the complete configuration is possible without any further action by the user aside from defining the position and orientation of each component.

The program APTRIANG provides a comprehensive check on the integrity of the surface triangulation. In particular the triangulation is checked to see if it forms a closed manifold (i.e. whether it is water tight), whether there are any duplicate points and whether all normals point outward. It can also remove unused or redundant points and adjust all surface normals to be consistently oriented.

TRISURF is used prior to MESH3D to create surface triangulations of the symmetry plane and the far field boundaries. The output from TRISURF which consists of the complete surface triangulation (aircraft configuration, symmetry plane, and far field boundaries) can then be used as input to MESH3D.

New Utilities for Surface Triangulation

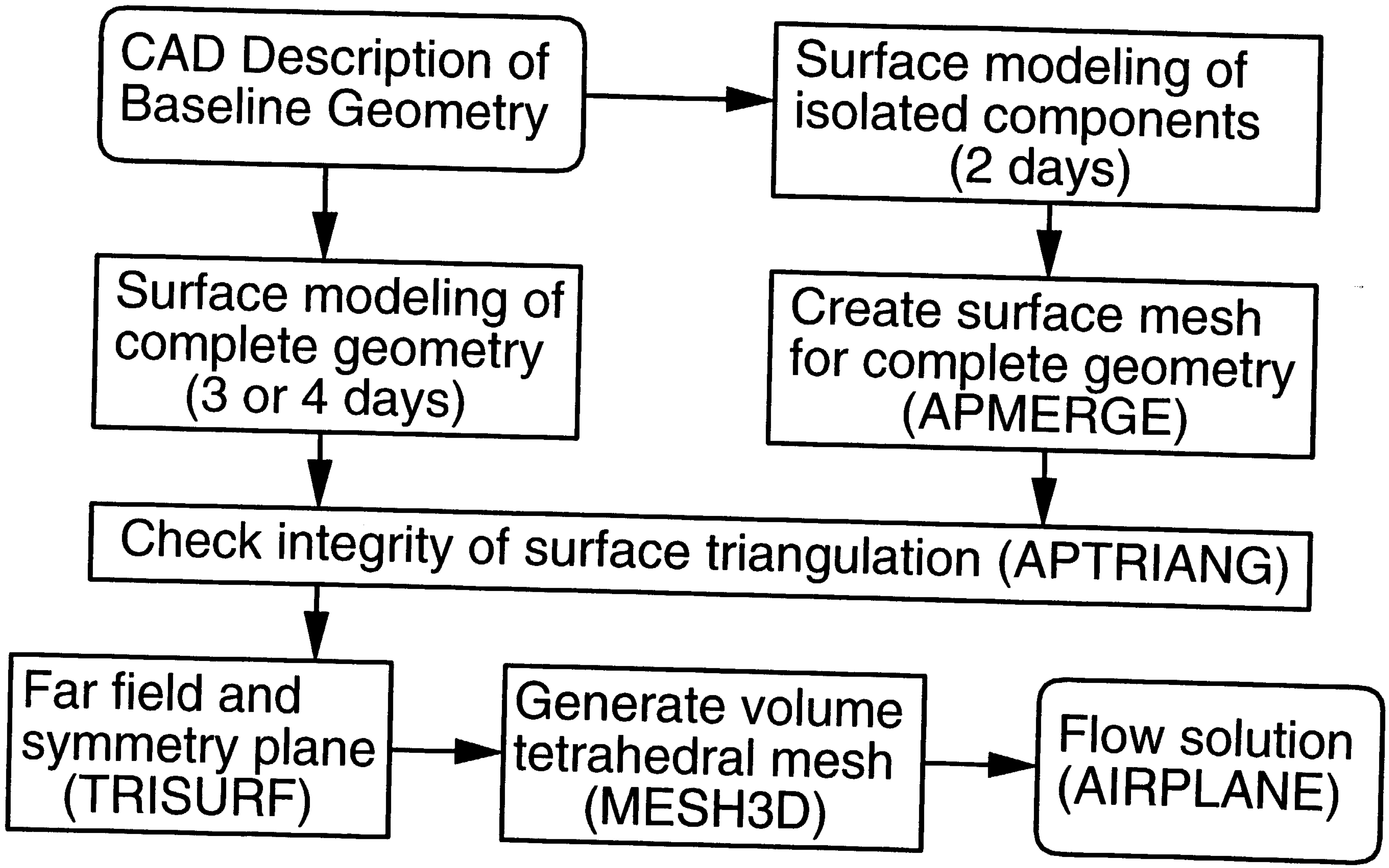

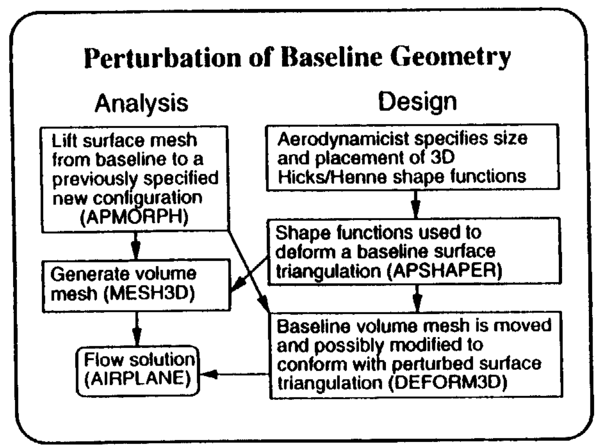

Chart 8: New Utilities for Perturbation of Baseline Geometry

The three new utilities (APMORPH, APSHAPER, and DEFORM3D) automate the generation of surface and volume triangulations for configurations which arise from perturbations of the baseline geometry.

APMORPH provides automated morphing of a given surface triangulation onto a slightly perturbed geometry. This is particularly useful when the user wishes to obtain an AIRPLANE flow solution on two different configurations using almost identical meshes. Any systematic bias in the computation will then affect each solution in essentially the same way so that incremental changes in the aerodynamic performance of the two configurations will be predicted with very high accuracy.

APSHAPER facilitates the application of AIRPLANE as a design tool. The user first defines the size and placement of Hicks/Henne shape functions on the surface of the configuration. APSHAPER then deforms the baseline surface triangulation to fit the perturbed geometry. At this point the user can, if desired, run MESH3D to generate the volume mesh. Alternatively, the user will have the option of running the program DEFORM3D to perturb a baseline volume mesh so that it conforms with the perturbed surface triangulation that was created either by APSHAPER or by APMORPH.

Perturbation of Baseline Geometry

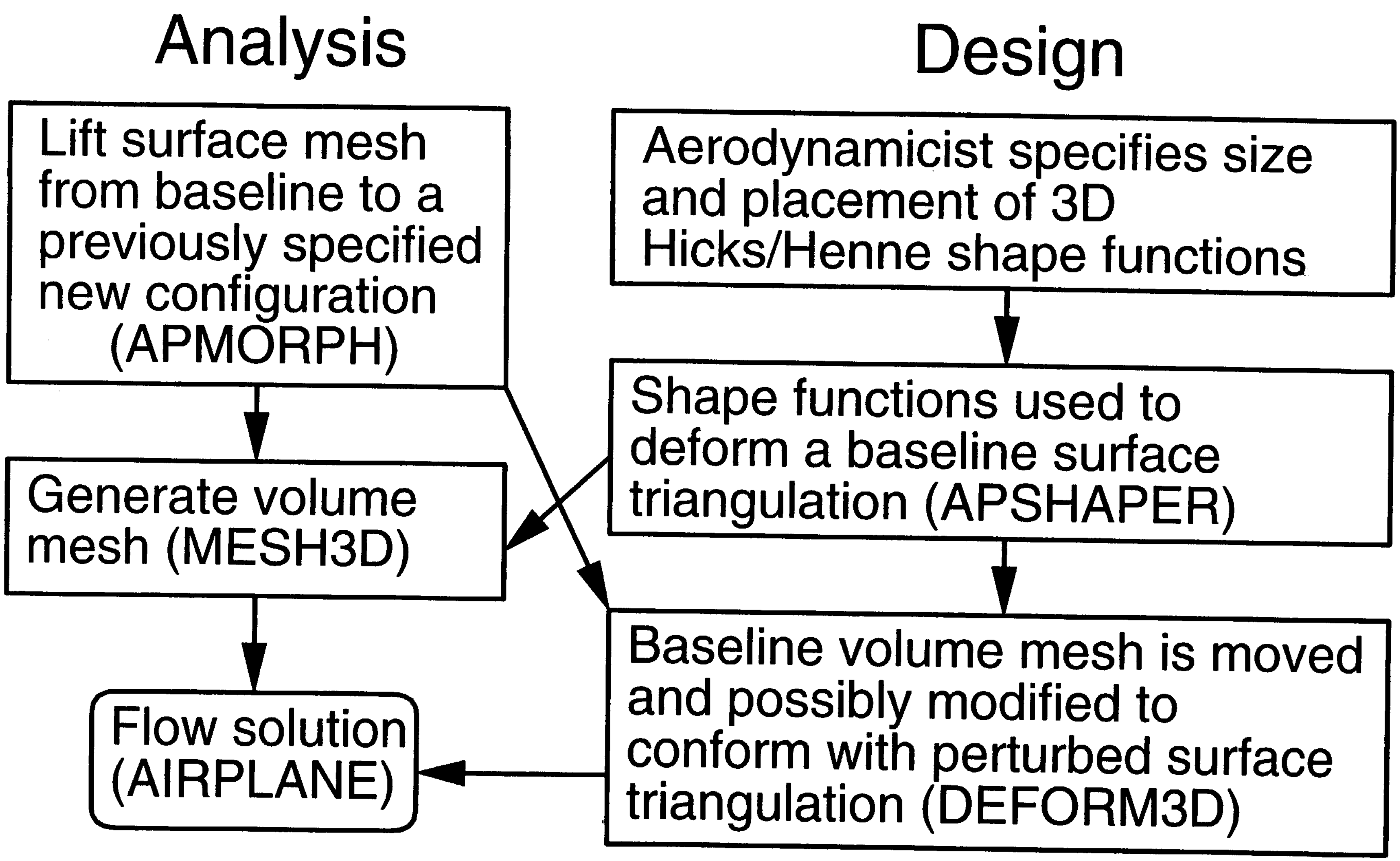

APTRIANG

A tool for surface mesh examination and manipulation.

File types: PLOT3D, FAST, TRISURF, AIRPLANE, VGRID, Gridgen

Examines: Physical extent of points, edges, faces.
Finds edges used more than twice.
Computes surface area and volume.
Locates holes and gaps in the mesh.

Manipulates: Joins components with unique point list.
Orients faces with consistent normals.
Snaps points to the symmetry plane.
Eliminates unused points and faces.
Forms a mesh from a structured grid.

Chart 9: APTRIANG -- A tool for surface mesh examination and manipulation.

This is a tool for structured surface grid or unstructured (triangulated) surface mesh examination and manipulation. It can read or write several types of files: PLOT3D, FAST, TRISURF, AIRPLANE, GridTool/VGRID, and Gridgen. The program is text oriented, that is, it uses an ASCII command line interface. A mesh and its attributes can be visualized by writing FAST files and then applying a graphics program like FAST. A FAST file of edges colored by repeat count can graphically pinpoint holes.

Tables of properties that can be generated include lists of x,y,z extrema of points, edges, and faces. Component-wise and total surface areas and enclosed volumes can be obtained. The program checks for edges used more than twice and locates holes in the surface and gaps between components. A message indicates whether the triangulation is likely to form a water-tight surface.

Certain mesh properties can be manipulated, and small problems can be corrected. Components in multiple files can be joined together provided they match at points along their edges, and they can be removed or renumbered. A unique point list may be generated and redundant points and faces can be removed. Points near the symmetry plane may be snapped to lie exactly on it (Z=0). Surface normals can be reversed and a consistent direction of surface normals can be enforced among all neigboring triangles.

An unstructured mesh can be derived from each structured surface grid quadrilateral face three ways: (1) regular subdivision, (2) taking the shorter of the two diagonals, or (3) adding a midpoint and forming four triangles around the perimeter.

APTRIANG can process penetrating surfaces but neither detects nor corrects this kind of pathology. The other MESH3D tools for handling components that cross over themselves or through each other are APMERGE and APSHAPER.

APTRIANG

A tool for surface mesh examination and manipulation.

File types: PLOT3D, FAST, TRISURF, AIRPLANE, VGRID, Gridgen

Examines:
- Physical extent of points, edges, faces.
- Finds edges used more than twice.
- Computes surface area and volume.
- Locates holes and gaps in the mesh.

Manipulates:
- Joins components with unique point list.
- Orients faces with consistent normals.
- Snaps points to the symmetry plane.
- Eliminates unused points and faces.
- Forms a mesh from a structured grid.

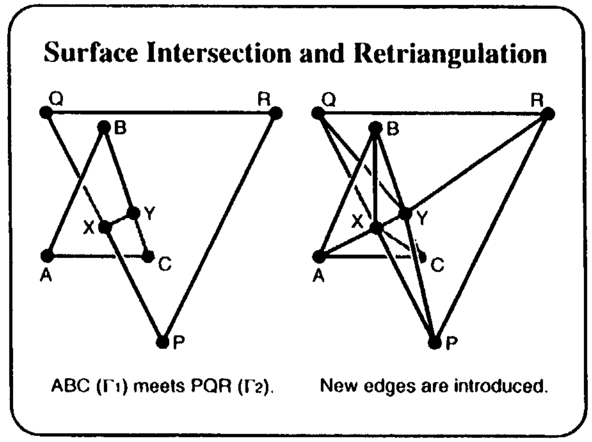

Chart 10: Surface Intersection and Retriangulation

The utility APMERGE examines a collection of N surface triangulations $\{\Gamma_k \mid k=1,...,N\}$ to find all intersections between the different surfaces. The algorithm proceeds by checking every edge from surface Γ_1 with every triangle from the remaining surfaces, then checks the remaining surfaces until all intersections are found. The computation is formally O(N^2) (order N squared) but a simple proximity check filters out the majority of edges and triangles, leaving the computationally intensive determination of an intersection point to be carried out for a substantially smaller number of edges and triangles.

End-to-end sequences of edges at the intersections of multiple surfaces are used to clip away those triangles that ought not to be included in the surface of the aircraft. In other words, only the triangles that will be wetted by the flow field are retained.

A typical situation is illustrated in the figure. Edge BC of triangle ABC on surface Γ_1 intersects triangle PQR on surface Γ_2, and edge PQ of triangle PQR intersects triangle ABC. After finding the two intersection points X and Y, new edges are introduced into each triangle to obtain a valid retriangulation of the surfaces that contains these intersection points. There are a number of different cases to consider. For example, two edges of triangle ABC may intersect the face of triangle PQR, or the intersection point X may lie on the edge AB. A more pathological case occurs when the edges of two triangles, one from each of two different surfaces, are coincident. APMERGE is being implemented to handle all these possible cases and extract a valid retriangulation of the surfaces that contains a sequence of edges comprising their intersection.

Surface Intersection and Retriangulation

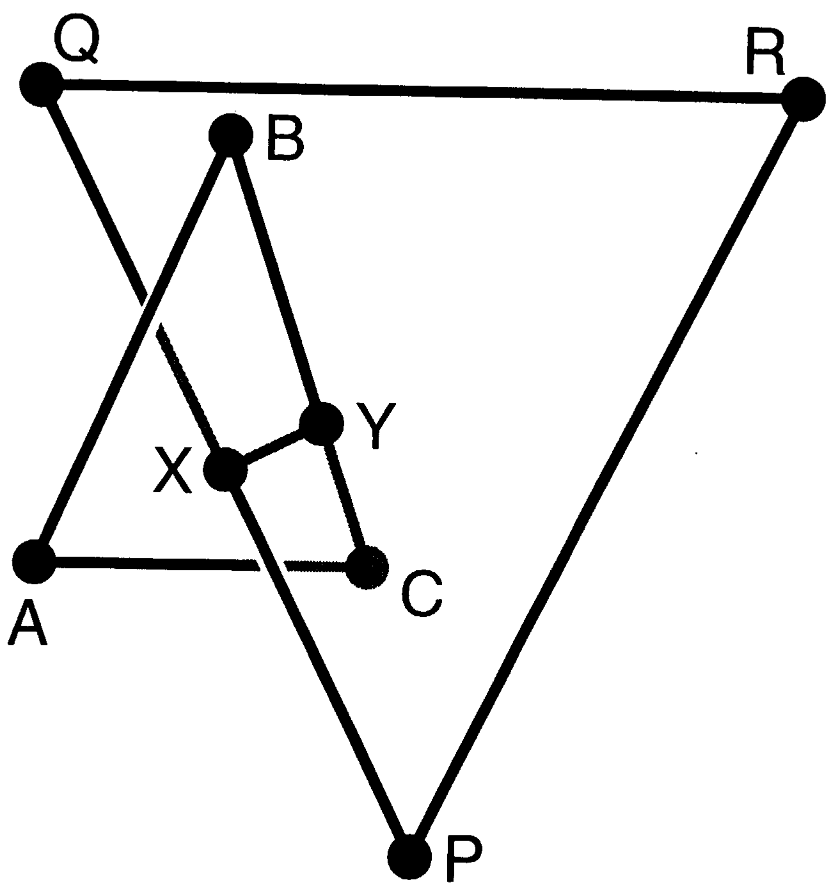

ABC (Γ_1) meets PQR (Γ_2).

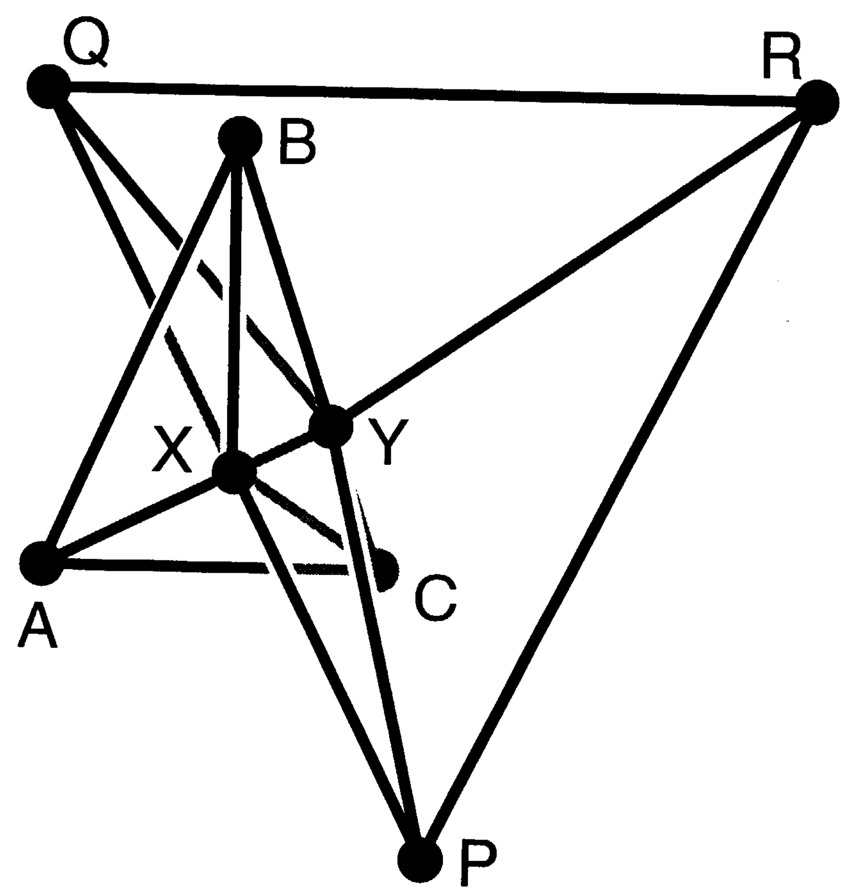

New edges are introduced.

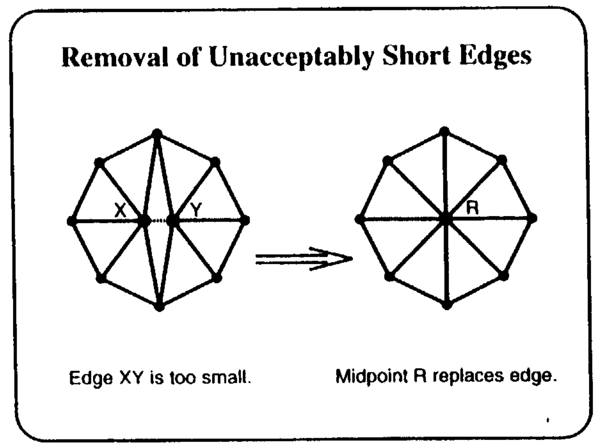

Chart 11: Removal of Unacceptably Short Edges

If the intersection point of edge PQ with triangle ABC (previous figure) lies close to an edge or vertex of triangle ABC then the quality of the retriangulation will be extremely poor. A post–processing step is therefore applied to remove any unacceptably small edges that have been created as a result of the retriangulation procedure. Suppose (present figure) that edge XY should be removed. Let R be the mid–point of edge XY and allow this edge to collapse onto point R so that all other edges that were incident to either X or Y are now incident to R.

The quality of the resulting triangulation can be further enhanced by using diagonal swapping to reduce the number of edges incident to R and thus improve the triangle aspect ratio (but not in the present figure). Care must be taken to ensure that no intersection edges are removed by diagonal swapping. Similarly, only those surface edges with dihedral angles close to 180 degrees should be swapped.

Removal of Unacceptably Short Edges

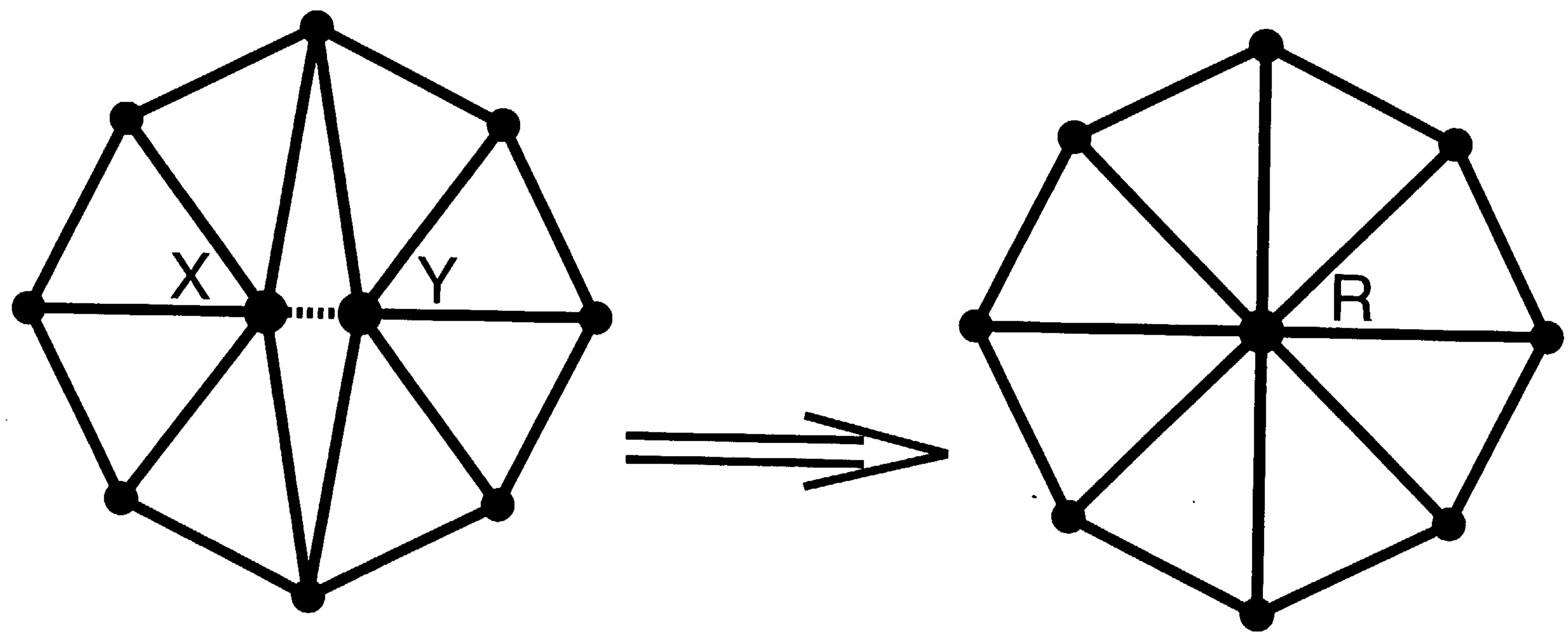

Edge XY is too small. Midpoint R replaces edge.

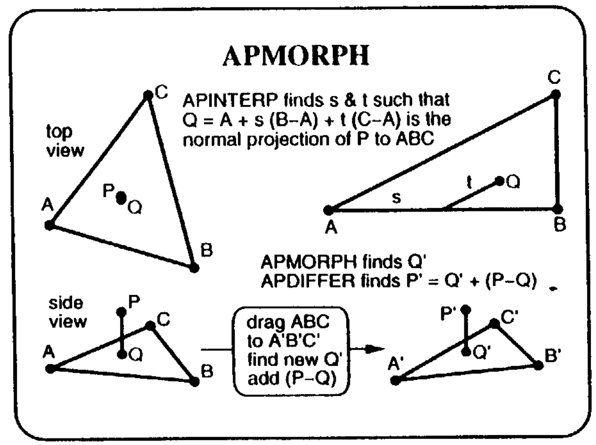

Chart 12: APMORPH -- Actually a combination of APTRIANG, APINTERP, APMORPH, and APDIFFER

Surface mesh generation can take days to accomplish. The following approach to surface mesh perturbation can be done in minutes.

If baseline geometry is modeled by both an unstructured mesh as well as a structured grid, then an association can be made between the mesh and the grid. If the structured surface grid is perturbed during design and still has the same dimensions and topology as the baseline grid, then the mesh with the baseline grid can be exploited to remap the old unstructured mesh to a new mesh that closely matches the perturbed grid resulting from design. The two meshes connect exactly the same way (same set of edges and faces).
A detailed explanation follows.

The baseline grid is turned into a 4:1 unstructured mesh by making four triangles per quadrilateral, using APTRIANG. A program called APINTERP finds, for the nth baseline mesh point P, the index IFACE(n) of the closest triangle ABC of the 4:1 mesh together with a pair of scalars (s(n),t(n)) which are interpolation coefficients for the closest point Q in ABC. In most cases Q is inside ABC and (P–Q) is normal to the plane of ABC. The nearest Q does not have to be a normal projection, however. The list of triples (IFACE(n),s(n),t(n)) as n ranges over the baseline mesh points is applied by a program called APMORPH to a 4:1 mesh derived from the new design grid to obtain a new list of points Q'. Finally, the difference (P–Q) is added back to Q' for each n. This final step allows the morphing process to preserve the original mesh if the design grid is identical to the baseline grid. Since (P–Q) is not scaled or rotated in any way this can introduce noise which is usually expected to be small. There is no guarantee that the new mesh will precisely match a CAD geometry corresponding to the new design grid, but the result is quickly obtained and should still be useful.

APMORPH

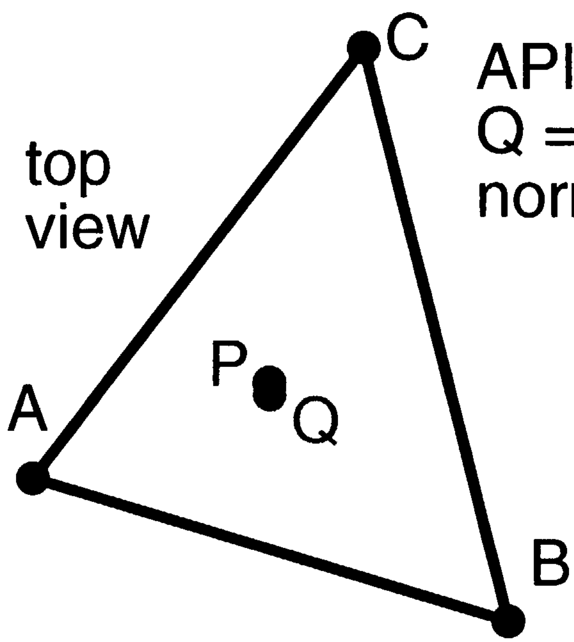

APINTERP finds s & t such that
Q = A + s (B–A) + t (C–A) is the
normal projection of P to ABC

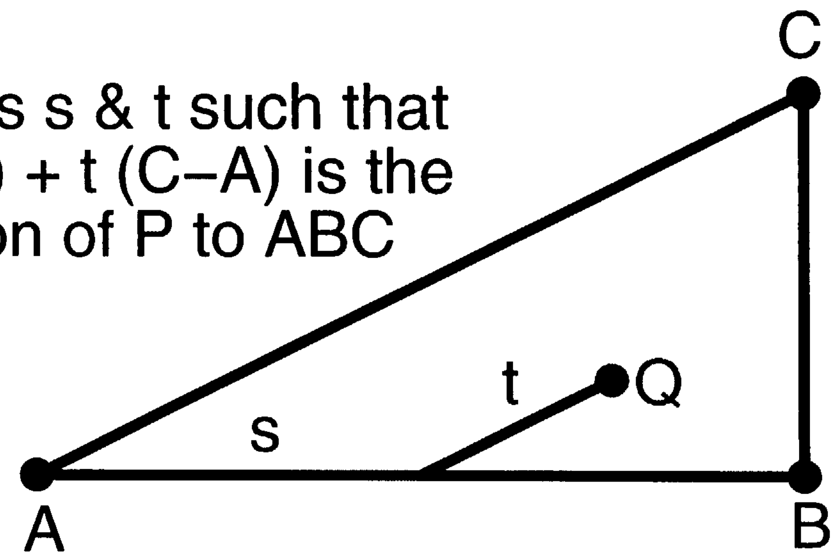

APMORPH finds Q’
APDIFFER finds P’ = Q’ + (P–Q)

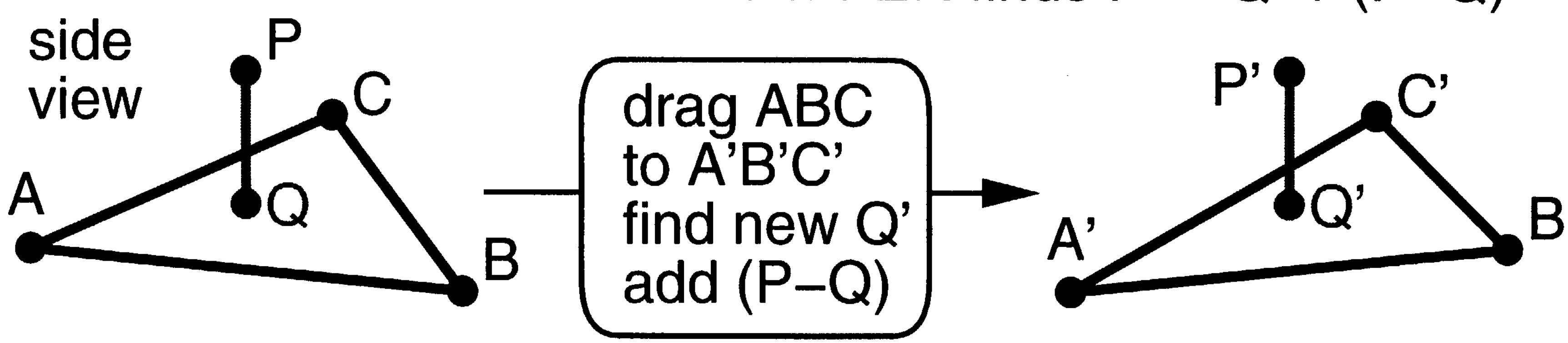

APSHAPER

- A tool for applying Hicks/Henne shape functions directly to a surface mesh, first implemented for a boxed wing.
- Surface is parameterized by (u,v) in the unit square, leading and trailing edges are found automatically.
- Two dimensional shape functions are products of one dimensional functions: $f(u,v) = c \times g(u) \times h(v)$.
- Shape functions are applied independently to upper and lower surfaces, followed by twist.
- Thickness is computed at every point to alert the user of upper–lower surface penetration.

Chart 13: APSHAPER

APSHAPER is a tool for applying Hicks/Henne shape functions directly to an unstructured surface mesh. This provides a way to use an existing surface mesh with AIRPLANE as a design tool. The program is currently in development. APSHAPER is first being applied to the surface of a wing inside a Cartesian box: $xmin <= x <= xmax$. $ymin <= y <= ymax$, $zmin <= z <= zmax$. For each point $P=(x,y,z)$ of the surface mesh, the program finds the leading edge xle and trailing edge xte, each of which may be on an edge between two other mesh points. The values (u,v) in $[0,1]x[0,1]$, $u=(x-xle)/(xte-xle)$, chordwise, and $v=(z-zmin)/(zmax-zmin)$, spanwise, are assigned to the point and a determination is made whether the point belongs to the upper or lower surface.

The user defines the size and placement of Hicks/Henne shape functions depending on u and v. Each shape function f(u,v) is a product of amplitude c, chordwise function g(u) and spanwise function h(v). Functions are applied incrementally at every point for the upper and then the lower surfaces, then twist is applied.

The thickness at every point is computed, new surface files are written, and extrema are listed. Negative thickness is an indication of a flaw in the application of the shape functions. Upper–lower surface penetration can be visualized with FAST using the thickness function.

The perturbed surface may be used to generate a new mesh with MESH3D. If a volume mesh already exists for the original mesh it will be quicker to apply DEFORM3D. Another alternative is to apply APSHAPER to a wing alone, then APMERGE to join it to a fuselage, then MESH3D.

APSHAPER

- A tool for applying Hicks/Henne shape functions directly to a surface mesh, first implemented for a boxed wing.
- Surface is parameterized by (u,v) in the unit square, leading and trailing edges are found automatically.
- Two dimensional shape functions are products of one dimensional functions: $f(u,v) = c \times g(u) \times h(v)$.
- Shape functions are applied independently to upper and lower surfaces, followed by twist.
- Thickness is computed at every point to alert the user of upper–lower surface penetration.

Volume Mesh Deformation

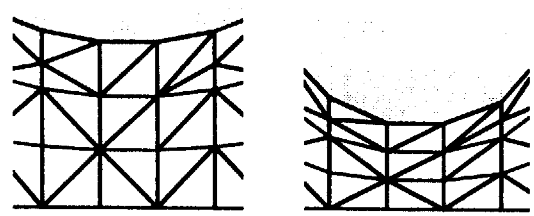

The computer program DEFORM3D will perturb a volume mesh based on a perturbation of its surface mesh.

Chart 14: Volume Mesh Deformation

The computer program DEFORM3D will perturb a volume mesh based on a perturbation of its surface mesh.

Small perturbations of the flow domain can be accomplished by simply relaxing the mesh points according to a suitable physical model. One popular approach is based on a spring analogy that treats the edges of the mesh as a network of springs connected at its mesh points. The equilibrium position (i.e. position of lowest potential energy) determines the new position of the mesh points induced by the boundary deformation. Other models have been proposed (e.g. treating the flow domain as an elastic solid) but eventually all of these models break down when extreme deformation causes excessive distortion of the tetrahedral shape.

One can monitor the degree of distortion for each tetrahedron by considering a 3x3 matrix **T0** formed by assembling three vectors, each of which represents an edge of the tetrahedron. If **T1** represents the equivalent matrix for the tetrahedron after mesh movement then we can write **T1** = **M T0** where **M** assumes the role of a shape transformation matrix. The polar decomposition theorem permits us to write **M** = **P U** where **U** is a unitary matrix representing pure rotation and **P** is positive semi–definite matrix whose eigenvalues represent modes of pure dilatation. These eigenvalues, which are the positive square roots of the eigenvalues of **M M^T (M** times its transpose) provide a useful measure of cell distortion.

Volume Mesh Deformation

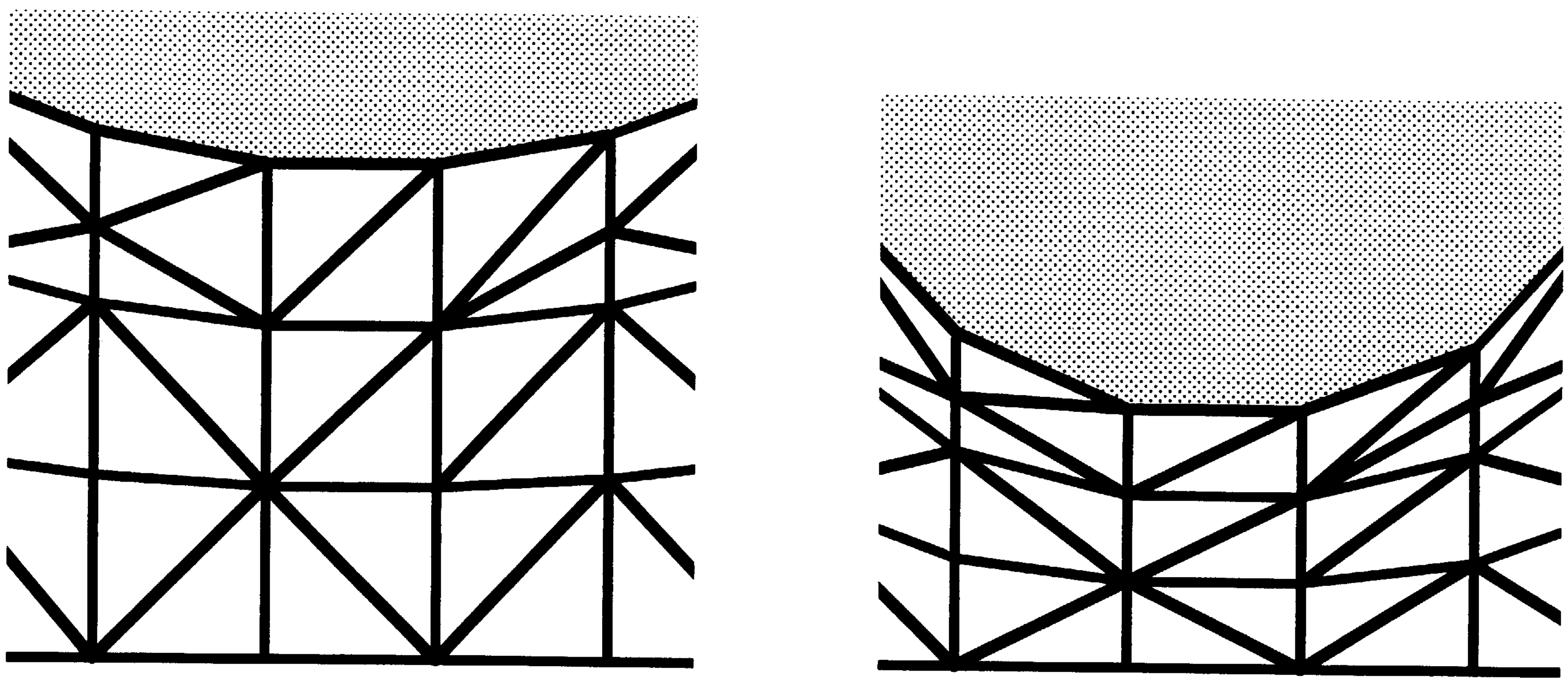

The computer program DEFORM3D will perturb a volume mesh based on a perturbation of its surface mesh.

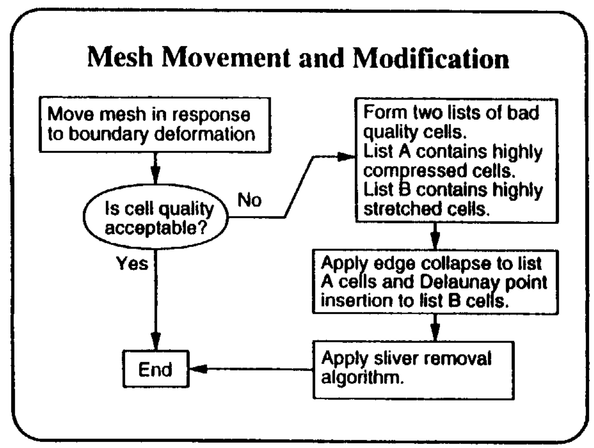

Chart 15: Volume Mesh Movement and Modification

If the mesh has suffered unacceptable distortion as a result of mesh movement, remedial action is taken to restore mesh quality. Mesh coarsening is applied to those regions of the mesh that have been excessively compressed (i.e. one or more of the eigenvalues of **M M**^T is much less than unity). Mesh enrichment is applied to those regions that have been excessively stretched (i.e. one or more of the eigenvalues of **M M**^T is much larger than unity). A three dimensional version of the edge collapse procedure is used to achieve mesh coarsening, and the Delaunay point insertion algorithm is exploited to effect mesh enrichment.

Baker, T.J. and Cavallo, P.A. "Dynamic Adaptation for Deforming Tetrahedral Meshes", Abstract submitted to the 14th AIAA CFD Conference, Norfolk, VA, June 1999.

Mesh Movement and Modification

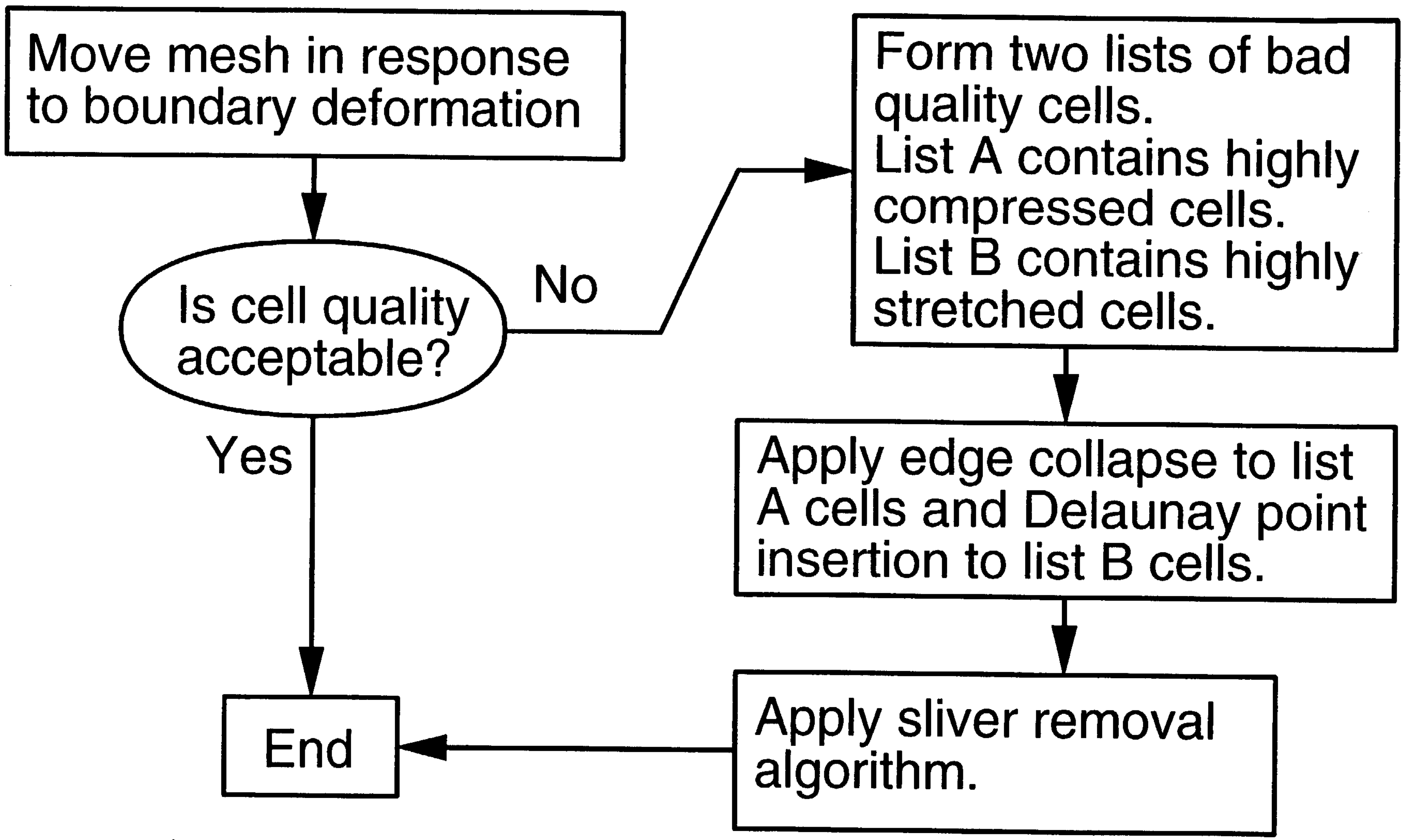

Navier–Stokes Mesh Generation

- Highly stretched tetrahedral meshes in the boundary layer.
- Refinement of Euler type tetrahedral mesh (points placed normal to surface).
- Layers of tetrahedra are developed by successive subdivision of the Euler type tetrahedra.
- Standard isotropic refinement of points outside the boundary layer.
- Isotropic refinement in corner regions and along salient edges is an option.

Chart 16: Navier–Stokes Mesh Generation

Work is underway to create highly stretched tetrahedral meshes suitable for the solution of Reynolds Averaged Navier–Stokes (RANS) equations for high Reynolds numbers. There is an increasing body of empirical and theoretical evidence to support the view that accurate resolution of boundary layers and wakes is possible on stretched tetrahedral meshes provided the cells are well shaped and have a layered appearance. This can be achieved by exploiting a modified form of the constrained Delaunay algorithm.

In order to maintain a robust and efficient procedure it is necessary to create an Euler type mesh and then subsequently refine this initial mesh in the viscous regions. The first set of points is inserted normal to the boundary in order to create a layered series of tetrahedra whose aspect ratio is approximately one. Outside of this region points are inserted by the standard isotropic refinement procedure.

Navier–Stokes Mesh Generation

- Highly stretched tetrahedral meshes in the boundary layer.
- Refinement of Euler type tetrahedral mesh (points placed normal to surface).
- Layers of tetrahedra are developed by successive subdivision of the Euler type tetrahedra.
- Standard isotropic refinement of points outside the boundary layer.
- Isotropic refinement in corner regions and along salient edges is an option.

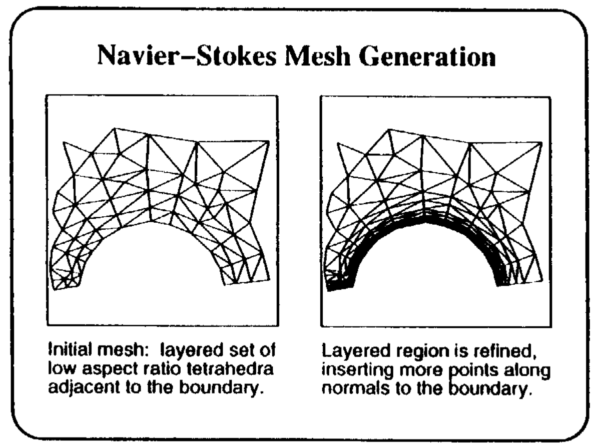

Chart 17: Navier–Stokes Mesh Generation

The initial mesh consists of a layered set of low aspect ratio tetrahedra adjacent to the boundary surface and any pre–specified wake surfaces. The mesh in the layered regions is then refined by inserting more points along the normals to the boundary. The point distribution along these normals is successively refined until the mesh increment normal to the boundary is sufficiently small and enough points and cells lie within the boundary layer region.

Navier–Stokes Mesh Generation

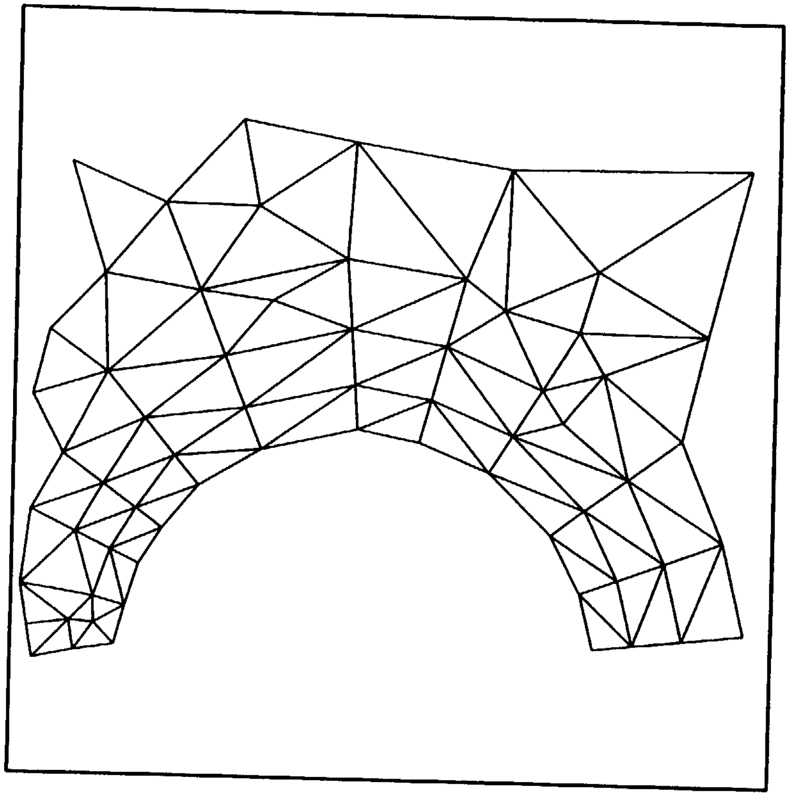

Initial mesh: layered set of low aspect ratio tetrahedra adjacent to the boundary.

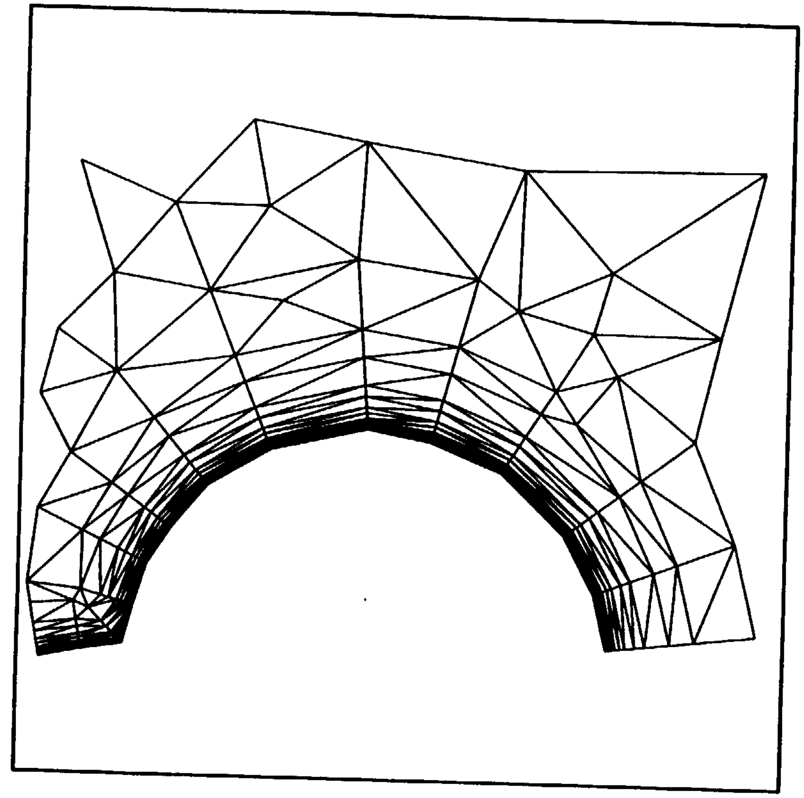

Layered region is refined, inserting more points along normals to the boundary.

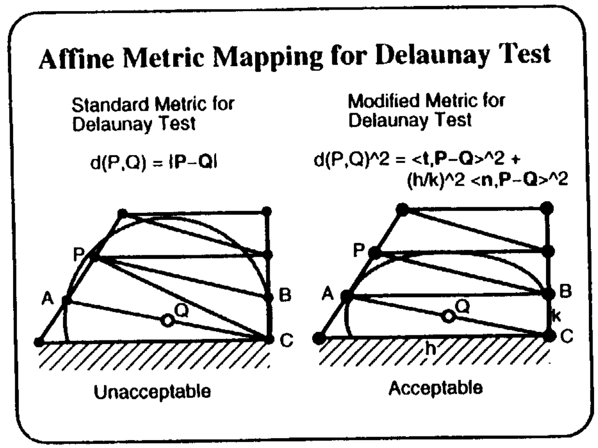

Chart 18: Affine Mapping of Metric for the Delaunay Test

In regions where the boundary layer surface is concave it is possible for the Delaunay algorithm to generate tetrahedra whose connectivity is unacceptable. This could be avoided by explicitly creating a structured layer of tetrahedra near the boundary surface. An alternative approach, that appears to be more robust, is based on modifying the metric used in the Delaunay test. Let **P** and **Q** be the position vectors of the points P and Q. The standard metric for the Delaunay in-sphere test is based on the Euclidean metric

$$d(P,Q) = |\mathbf{P}-\mathbf{Q}|$$

and is applied to determine whether a point P is inside the circumsphere of tetrahedron ABCD with circum-center Q. In its standard form the in-sphere test would consider point P inside tetrahedron ABCD and remove this tetrahedron creating the unacceptable arrangement of tetrahedra shown on the left of the figure (to simplify the drawing, point D is not shown).

The approach we have adopted is based on an affine mapping of the metric that has the effect of replacing the circum-sphere centered at Q by a flattened sphere, i.e. an ellipsoid, that does not contain point P. Let **n** denote the unit surface normal, then the inner product $\langle \mathbf{n},\mathbf{P}-\mathbf{Q}\rangle$ represents the oriented distance along the normal direction from Q to P. Let **t** denote a unit tangent for which $\langle \mathbf{n},\mathbf{t}\rangle=0$ and, for some scalars a and b, $\mathbf{P} = \mathbf{Q} + a\mathbf{n} + b\mathbf{t}$. If h and k are the local mesh increments, respectively parallel and normal to the surface, then the modified metric for the Delaunay in-sphere test has the form

$$d(P,Q)^2 = \langle \mathbf{t},\mathbf{P}-\mathbf{Q}\rangle^2 + (h/k)^2 \langle \mathbf{n},\mathbf{P}-\mathbf{Q}\rangle^2.$$

Affine Metric Mapping for Delaunay Test

Standard Metric for Delaunay Test

$$d(P,Q) = |\mathbf{P}-\mathbf{Q}|$$

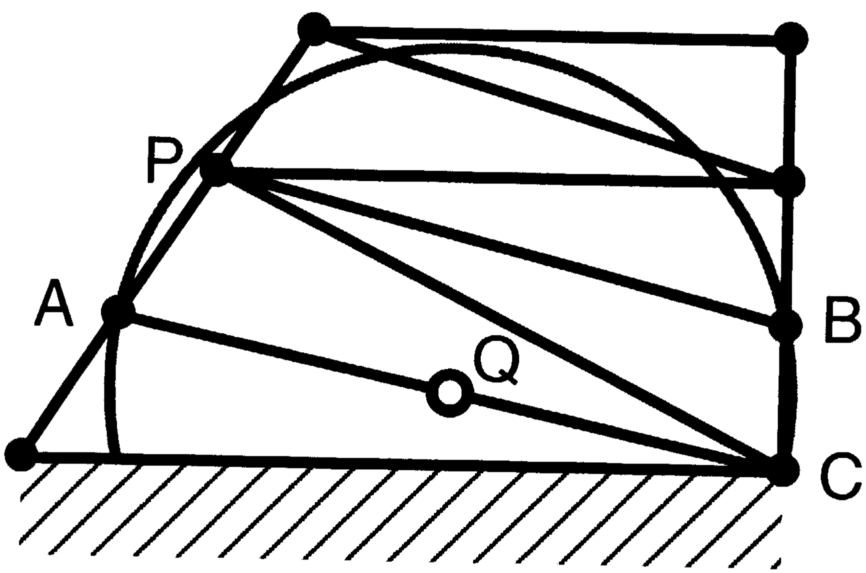

Unacceptable

Modified Metric for Delaunay Test

$$d(P,Q)^2 = \langle \mathbf{t},\mathbf{P}-\mathbf{Q}\rangle^2 + (h/k)^2 \langle \mathbf{n},\mathbf{P}-\mathbf{Q}\rangle^2$$

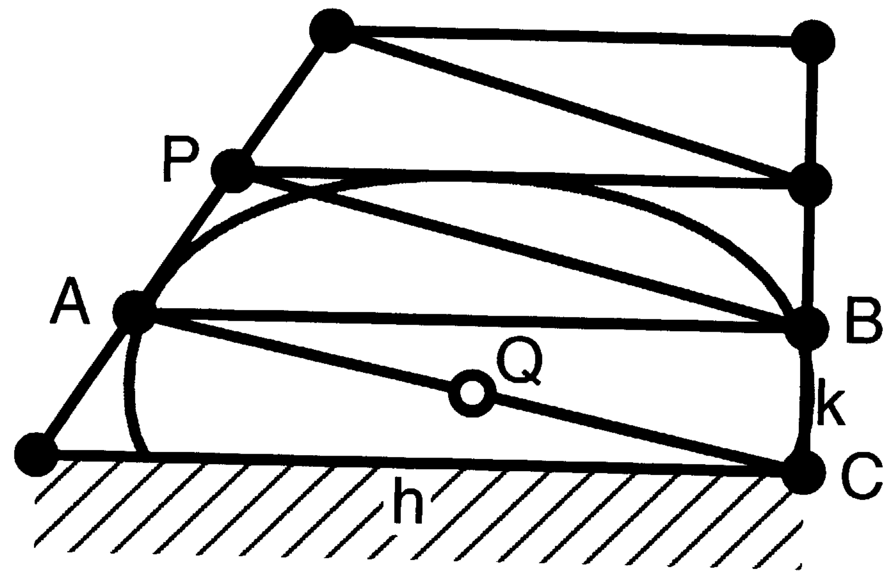

Acceptable

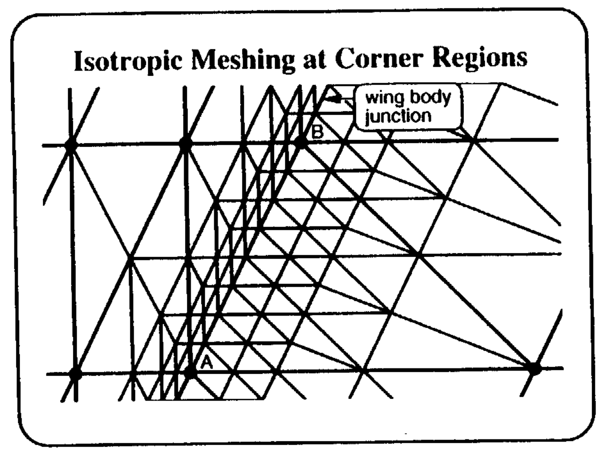

Chart 19: Isotropic Meshing at Corner Regions

In corner regions (e.g. wing body junctions) or at salient edges (e.g. wing trailing edges, wing tips, etc.) the usual boundary layer assumptions break down and an anisotropic mesh may not be appropriate. The user therefore has the option of allowing isotropic refinement of the mesh in regions wherever there is an abrupt change in angle between neighboring surface normals. The procedure requires refinement and hence a modification of the surface triangulation. To preserve the conformity of the surface triangulation, surface triangles and their adjacent tetrahedra are refined using straightforward edge splitting.

Isotropic Meshing at Corner Regions

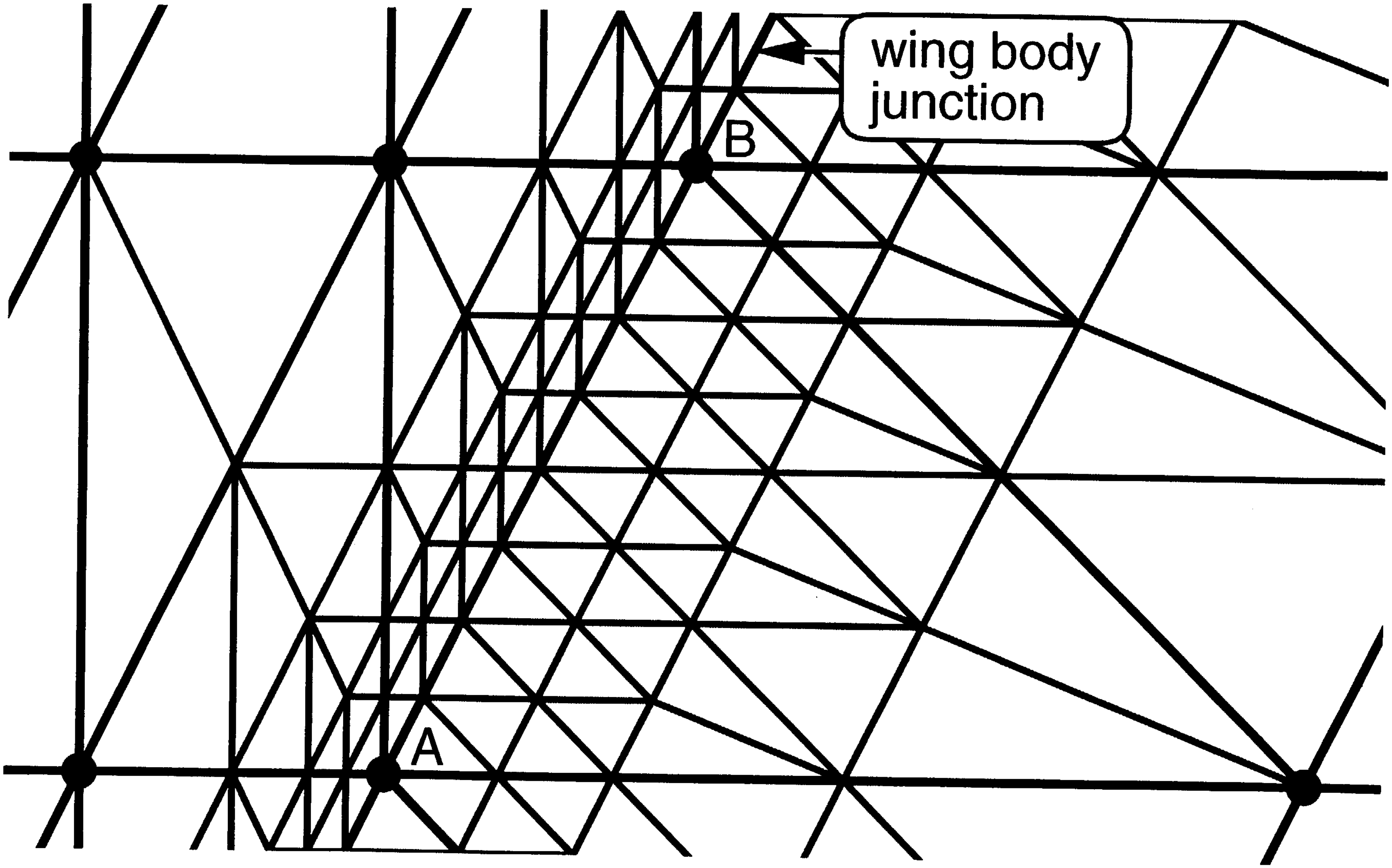

Conclusion

✓	MESH3D	Robust for Euler meshes
✓	APTRIANG	Ready now, room to grow
➾	APMERGE	Under development, FY99
✗	APMORPH	Has been proven to work
➾	APSHAPER	Under development, FY99
➾	DEFORM3D	Under development, FY99
☛	Navier–Stokes	Under development, FY99

Chart 20: Conclusion

✓ (product) MESH3D: once a good surface mesh is supplied, the volume mesh for an Euler flow solver is automatic.

✓ (product) APTRIANG is now a useful tool for assessing, correcting, and assembling a surface mesh, and it could do more.

➾ (writing) APMERGE will simplify surface mesh generation by automatically intersecting component surfaces.

✗ (pilot) APMORPH can be used to perturb a satisfactory surface mesh, saving significant labor time.

➾ (writing) APSHAPER will be a useful addition to the design process and will be useful in combination with APMERGE.

➾ (writing) DEFORM3D will speed up volume mesh generation by deforming an existing mesh.

☛ (alpha) Navier–Stokes mesh generation is needed to carry out viscous flow simulation.

Conclusion

✓	MESH3D	Robust for Euler meshes
✓	APTRIANG	Ready now, room to grow
✒	APMERGE	Under development, FY99
✗	APMORPH	Has been proven to work
✒	APSHAPER	Under development, FY99
✒	DEFORM3D	Under development, FY99
☛	Navier–Stokes	Under development, FY99

Assessment of CFD Predictions of Flat Plate Skin Friction

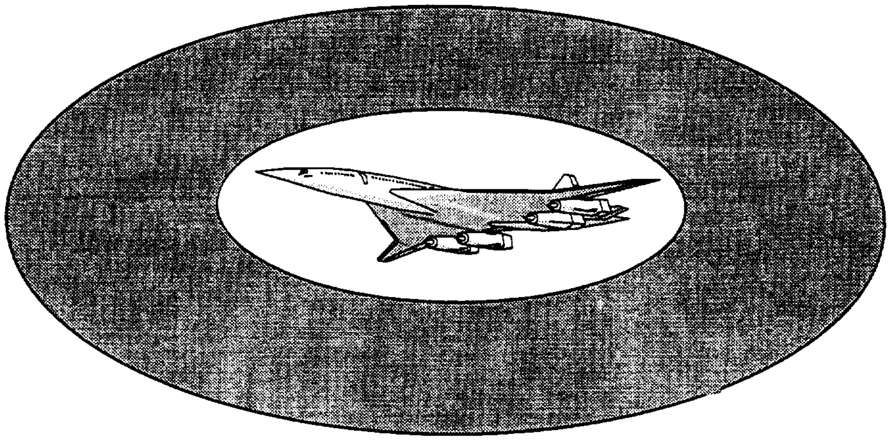

HSR Airframe Technical Review

Los Angeles, California
February 9 - February 11, 1998

Robert M. Kulfan
Boeing Commercial Airplane Group

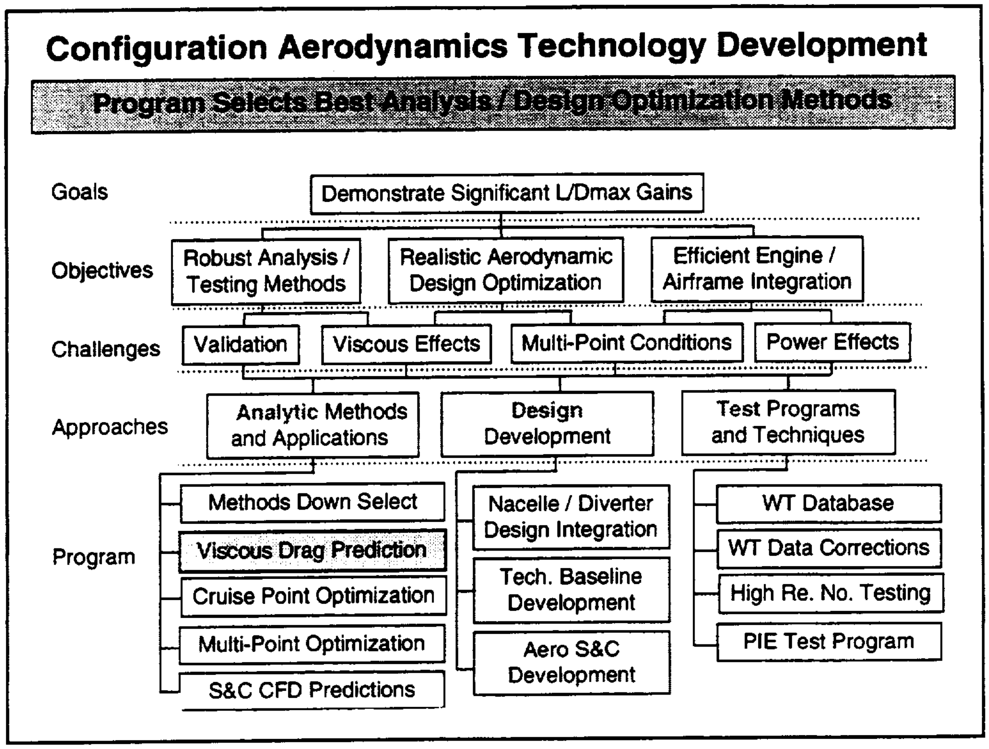

The assessment of the CFD flat plate fully turbulent flow skin friction predictions is an element of the "Viscous Drag Prediction" technology development element shown in the Configuration Aerodynamics program on a page shown in this figure.

Topics

- Variations in Viscous Drag Predictions
- Resolution Strategy
- Flat Plate Skin Friction Comparison Database
- BLB-PW CFL3D Predictions
- BCA Overflow Predictions
- Ames OVERFLOW Predictions
- Conclusions

Recent CFD validation studies have shown significant variations in viscous drag predictions between the various methods used by the NASA and industry HSCT organizations. The methods include Navier Stokes CFD codes in which the viscous forces are part of the solutions, and predictions obtained from the different fully turbulent flow flat plate skin friction drag equations used by the various organizations.

In this paper, the variation of these viscous drag predictions will be shown. The strategy developed to resolve these differences will be discussed. The first step in the resolution strategy was the development of a skin friction database for flat plate fully turbulent flow. This database will be briefly reviewed. The comparisons of CFD skin friction prediction by Boeing Phantom Works Long Beach - , BPW-LB, by Boeing Commercial Aircraft aerodynamics, BCA, and by NASA Ames will be reviewed.

The study conclusions will be summarized.

Comparison of Predicted Viscous Drags From Various CFD Codes for the TCA Wing/Body Configuration

$M_\infty = 2.4$, $C_L = 0.1$, $R_e = 6.36 \times 10^6$

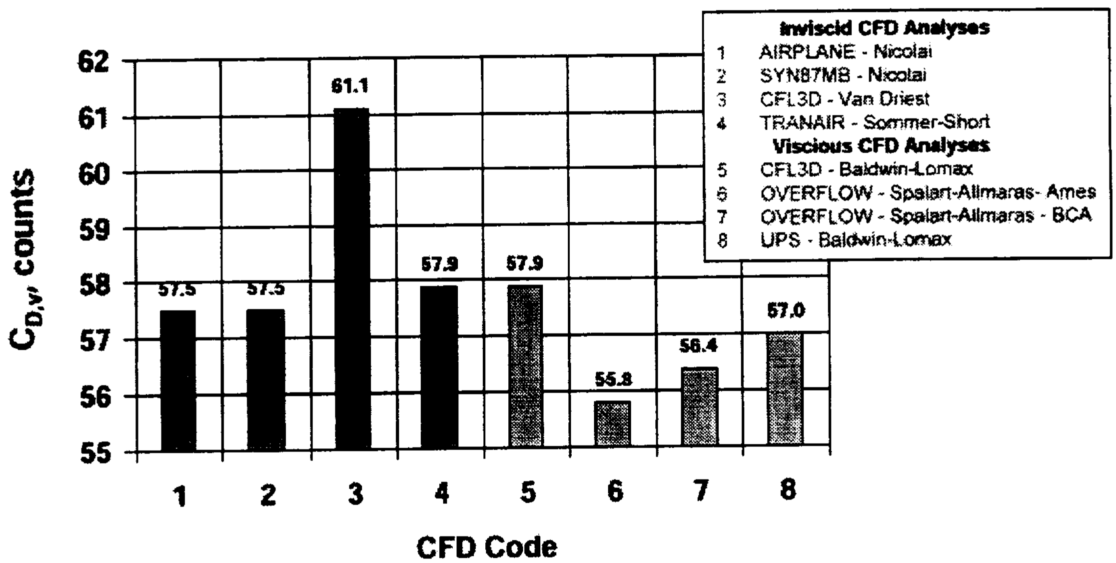

This figure illustrates the variations in viscous drag predictions for the TCA wind tunnel model wing plus body configuration. There are significant variations in flat plate theory predictions used in the inviscid CFD analyses as well as the CFD predictions obtained with the viscous analyses.

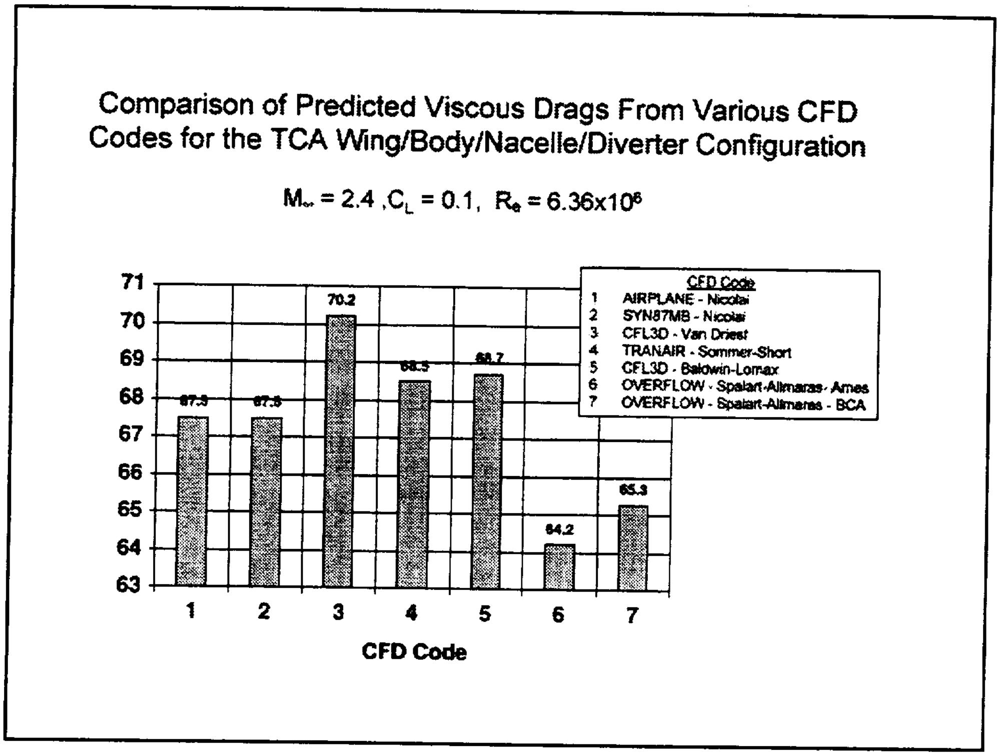

This figure shows similiar comparisons for the wing plus body plus nacelle configuration. There is seen to be a three drag count variation in the flat plate predictions corresponding to the inviscid analyses, (numbers 1 through 4). The BLB-PW CFD predictions using CFL3D appear to match the flat plate theory predictions. The OVERFLOW predictions of BCA and Ames predict significantly lower drag levels.

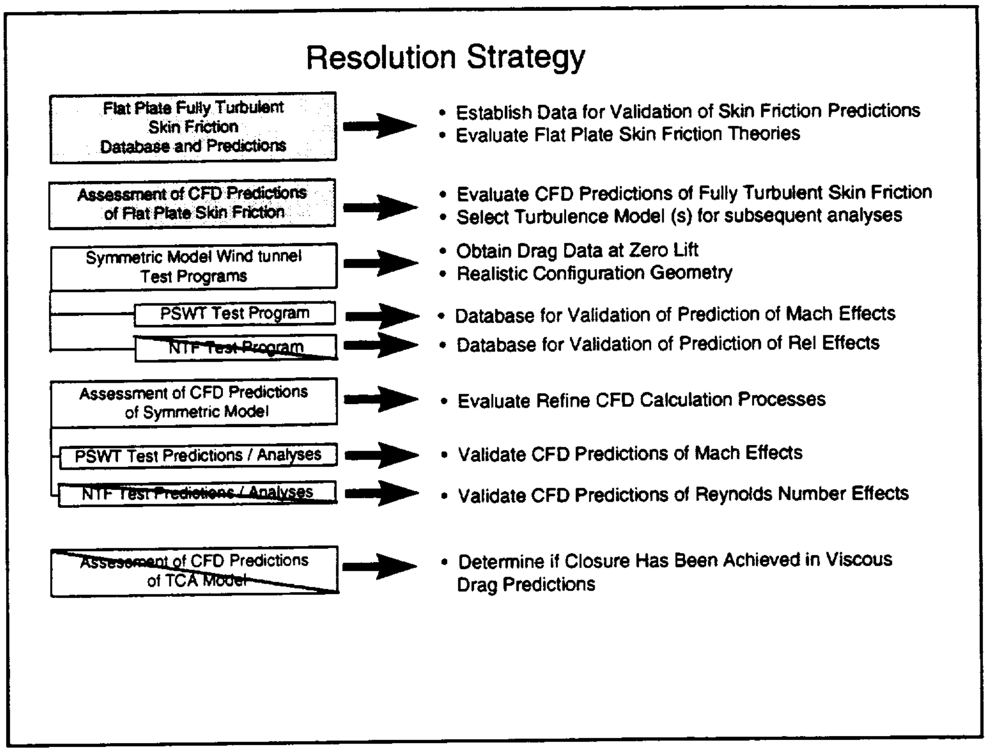

This illustrates the strategy that was developed to resolve the viscous drag prediction differences. This consisted of a series of sequential activities:

• Establish a database of fully turbulent flow flat plate skin friction data to be used for the validation of the corresponding CFD predictions. Flat plate prediction methods were assessed. A modified flat plate skin friction prediction method was developed that accurately represents the mean of the test data and captures both the Reynolds number and Mach number variations of this mean.

• The second step includes the comparison of the CFD predictions of fully turbulent flow flat plat viscous drag with the mofified flat plate theory. The results of this activity is the subject of this paper.

• A symmetric model representation of the HSR TCA configuration was defined and will be fabricated and tested to obtain data for validation of CFD viscous drag predictions on an HSR type configuration, Supersonic tests are planned in the Boeing Polysonic Wind Tunnel to obtain supersonic drag data at moderate Reynolds numbers The model was also planned to be tested in the NASA Langley NTF tunnel to obtain data for a wide range of Reynolds numbers.

• The final element is to recalculate the drag of the TCA to see if the variations between the theories has vanished and the theory predicts the test results.

•The elements that are crossed out have been canceled by reduction in program funding

Why the Interest in Flat Plate Turbulent Boundary layers ?

- First Step in Evaluating Navier Stokes Prediction Methods
- Help Sort Out Appropriate Turbulence Models
- Good Estimate of Viscous Drag of HSCT Type Configurations (Easy, Quick , Robust and Accurate)
- PD Drag Prediction Methods
- Extrapolation of Wind Tunnel Data to Flight Conditions
- δ Predictions Used to Size Diverter Height
- δ^* plus CF Predictions Used to Calculate Spillage and Internal Drag of Flow-Through Nacelles
- Quick Estimate of Surface Temperature
- Provides Physical Insight into Viscous Flow Characteristics

It is felt that the first step in validating the viscous drag predictions of any Navier Stokes code is to make sure that predictions of the local and average skin friction drag and boundary layer must match the "simple" flat plate measured test data over the range of Mach numbers and Reynolds for which the codes will be used. This process will help to evaluate the applicability of of the various turbulence models.

Because HSCT configurations have rather thin wings, slender bodies and low cruise lift coefficients, experience has shown that flat plate skin friction calculations provide good estimates of the viscous drag of HSCT type configurations. The predictions are easy, quick, robust and quite accurate.

The current PD viscous drag prediction methods are based on flat plate skin friction drag calculations. Currently wind tunnel data is extrapolated to flight conditions using flat plate friction drag predictions.

Flat plate estimates of the boundary layer thickness are used as the preliminary criteria for specifying the boundary layer diverter height for the HSCT nacelle installations. Boundary layer displacement thickness predictions together with CF calculations are used to calculate the spillage and internal drag of wind tunnel flow though nacelles.

Local skin friction calculations corrected for local dynamic pressure effects can be used to estimate local surface temperatures.

The boundary layer thickness information presented in this note also provides some physical insight in to the fundamental features of turbulent flat plate flow.

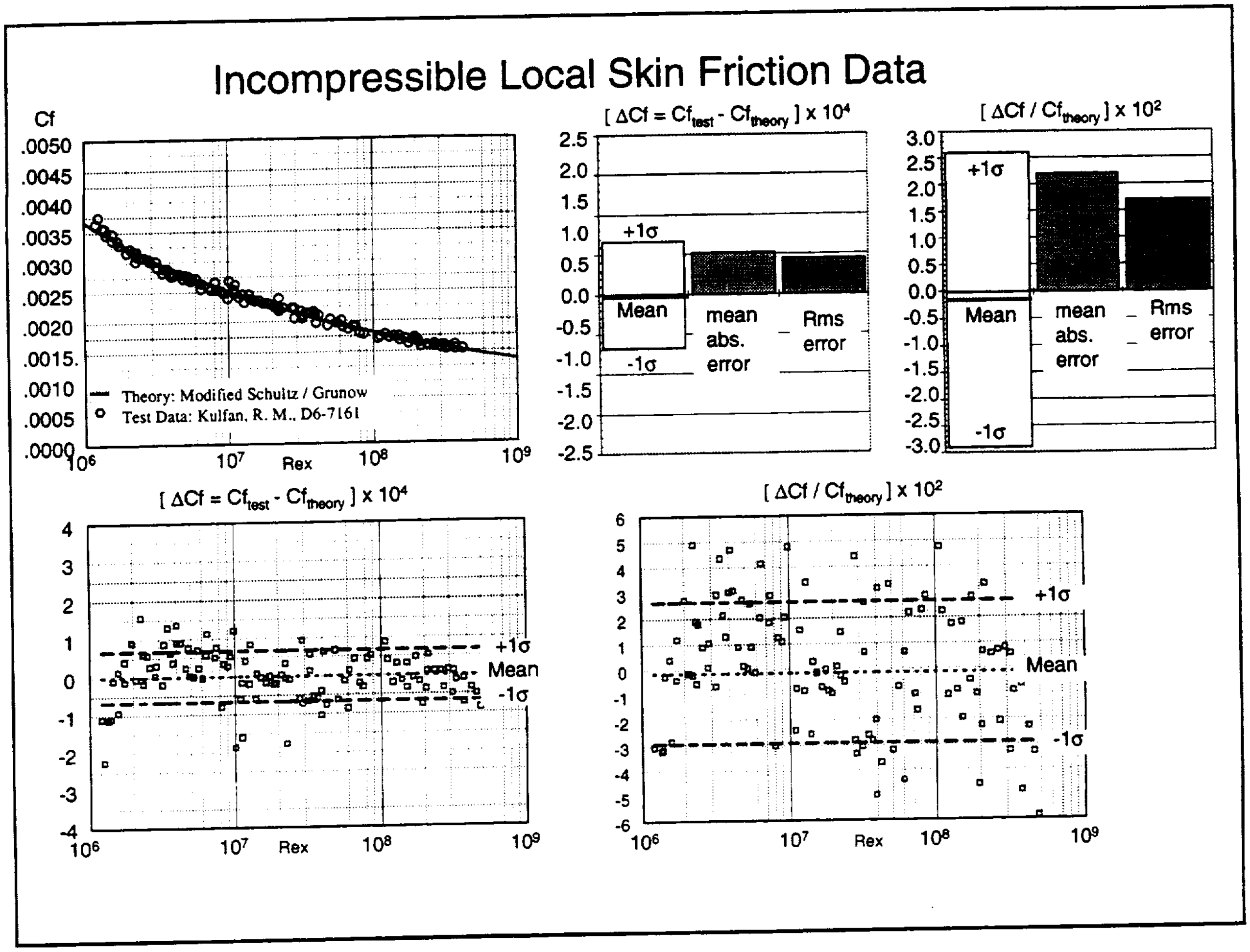

Flat plate skin friction data was obtained from a number of experimental sources. These data cover a wide range of Mach numbers and Reynolds numbers. Comparisons were made with various flat plate theories to select the theory that most closely matches the test data. The results of these assessments are presented in the Reference shown below.

The flat plate theories are based on the reference temperature method. This method assumes that the incompressible skin friction equations apply to supersonic Mach numbers provided that the density and viscosity are calaculate at some reference temperature that represents the variation of temperature across the boundary layer.

This figure shows the comparison of the modified Shultz / Grunow equation with incompressible test data. Statistical analysis of the differences between the test data and corresponding Cf predictions shows that the mean of the differences is $\Delta Cf = -.000000671$ which corresponds to an average difference of 0.13% .The standard deviation of data about the mean is approximately 0.7 counts of drag ($\Delta Cf = 0.000067$) which corresponds to 2.8% of the corresponding predicted value.

The modified Shultz / Grunow equation therefore appears to provide an accurate estimate of incompressible local skin friction coefficient over the entire range of Reynolds Numbers covered by the test data.

Reference: Kulfan, R. M., "Historic background on flat plate turbulent flow skin friction and boundary layer growth", HSR Airframe Technical Review, Feb 1998

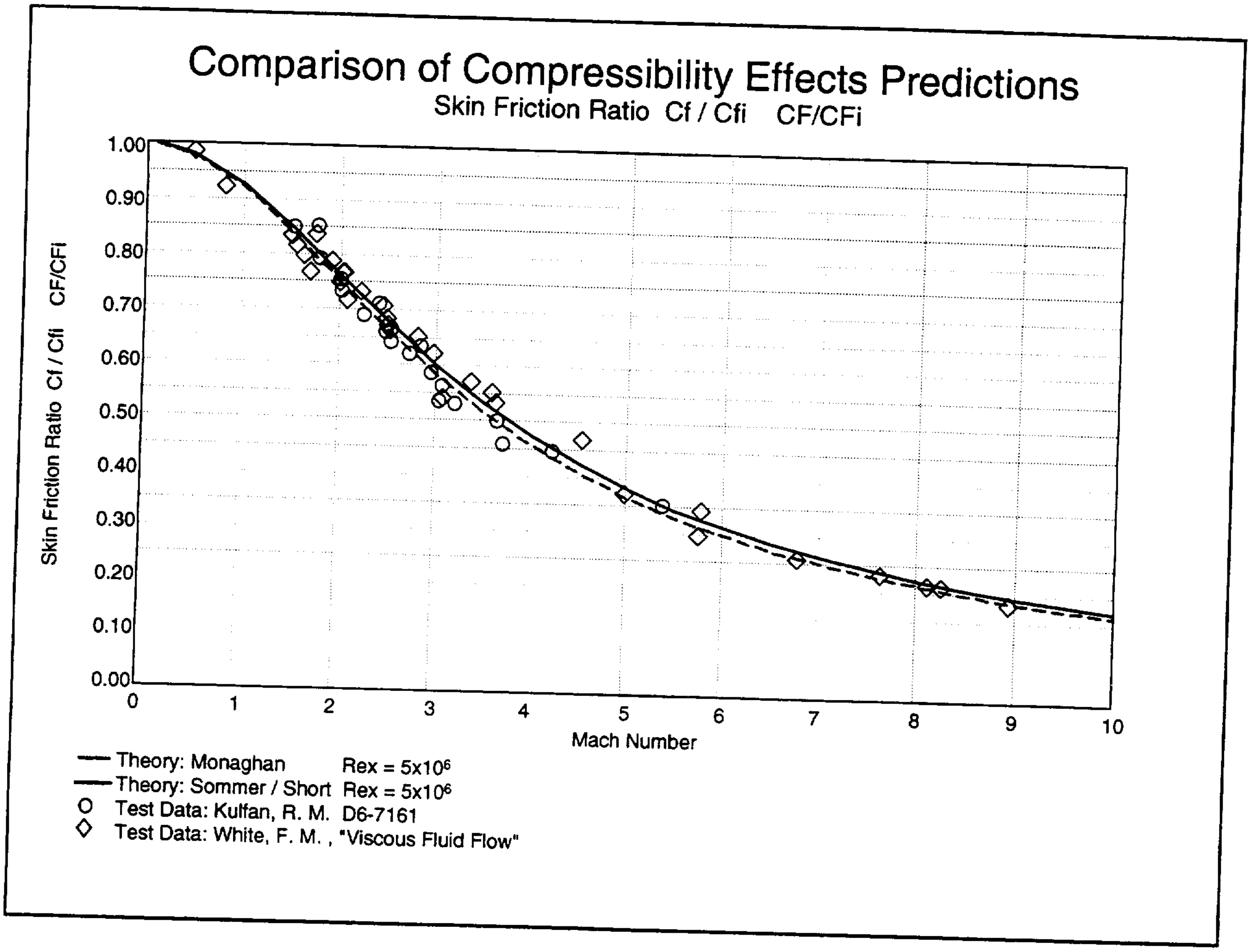

This figures shows some of the compressible flow skin friction datya used to validate the flatplate theories. This compares the compressible skin friction predictions obtained using two commonly used T* methods, the Monaghan T* and the Sommer-Short T* method.

The Sommer-Short T* equation results in compressible skin friction values consistently higher than predicted using the Monaghan method. It was for this reason that the Boeing US SST program switched from the Monaghan method to the Sommer-Short method.

The full scale SST performance predictions were obtained from wind tunnel data corrected to full scale conditions. Wind tunnel skin friction drag is higher than the full scale conditions. Using higher skin friction values calculated by the Sommer -Short method resulted larger skin friction corrections. This resulted in higher L/D assessments for the SST.

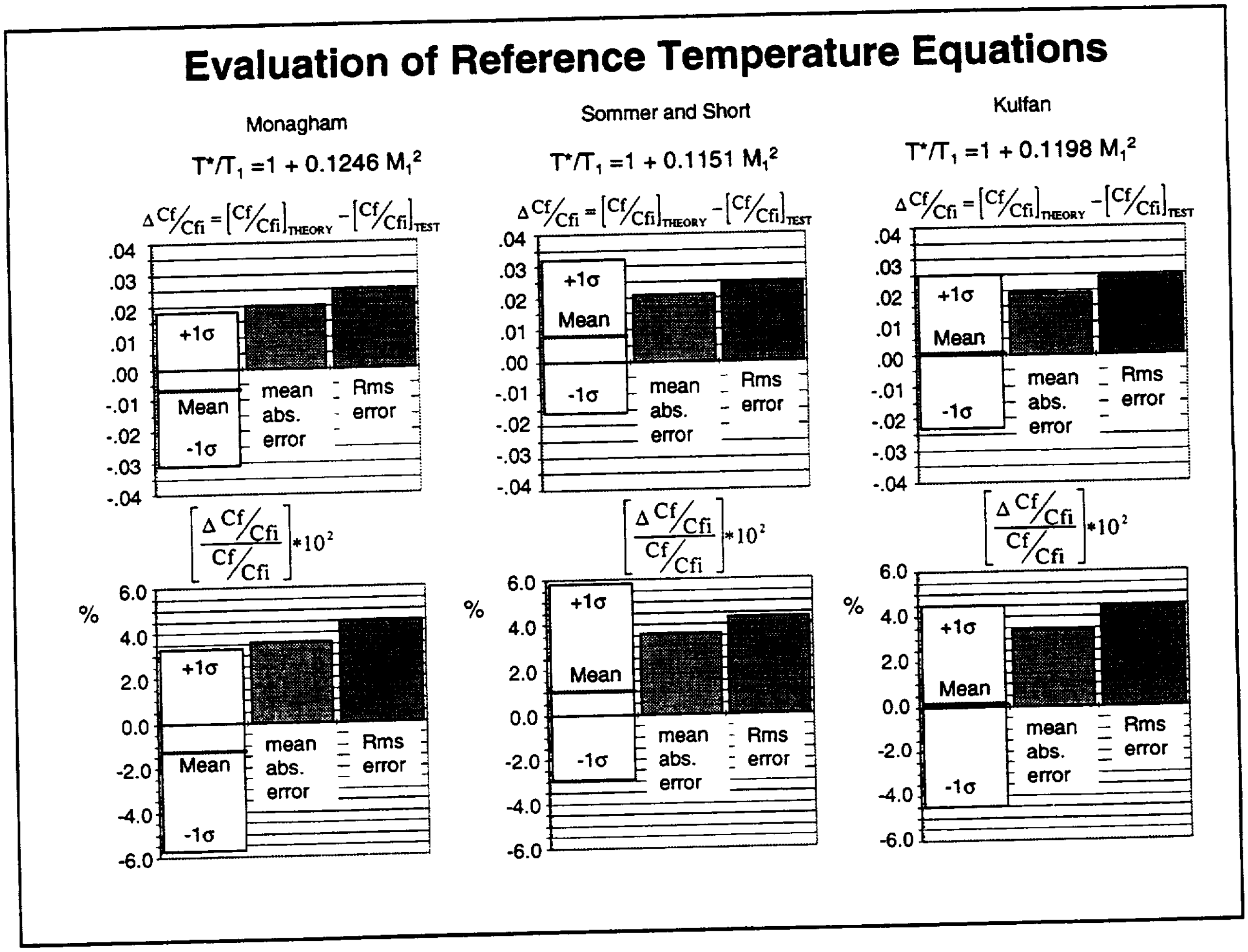

Statistical analyses were made of the differences between Cf predictions and the corresponding test data as shown in this figure . The theoretical predictions were obtained using three different T* equations.

The "scatter" in the test - theory increments are essentially equal. The mean of the differences between the test and theory, however differs between the predictions obtained using the different T* equations.

The "mean" of the theory - test differences obtained using the Monaghan T* equation is approximately 1% low. The "mean" of the theory - test differences obtained using the Sommer-Short T* equation is approximately 1% high. The constant for the Kulfan T* equation was therefore chosen to be the average of the Sommer-Short and the Monaghan constants.

This essentially resulted in a mean error between the test data and the theoretical predictions of zero.

The test data scatter about the mean has a standard deviation of about 4.5%. This large scatter is in part due to the variations of Reynolds number of the test data. The Reynolds number for the test data 10^6 to 10^7.

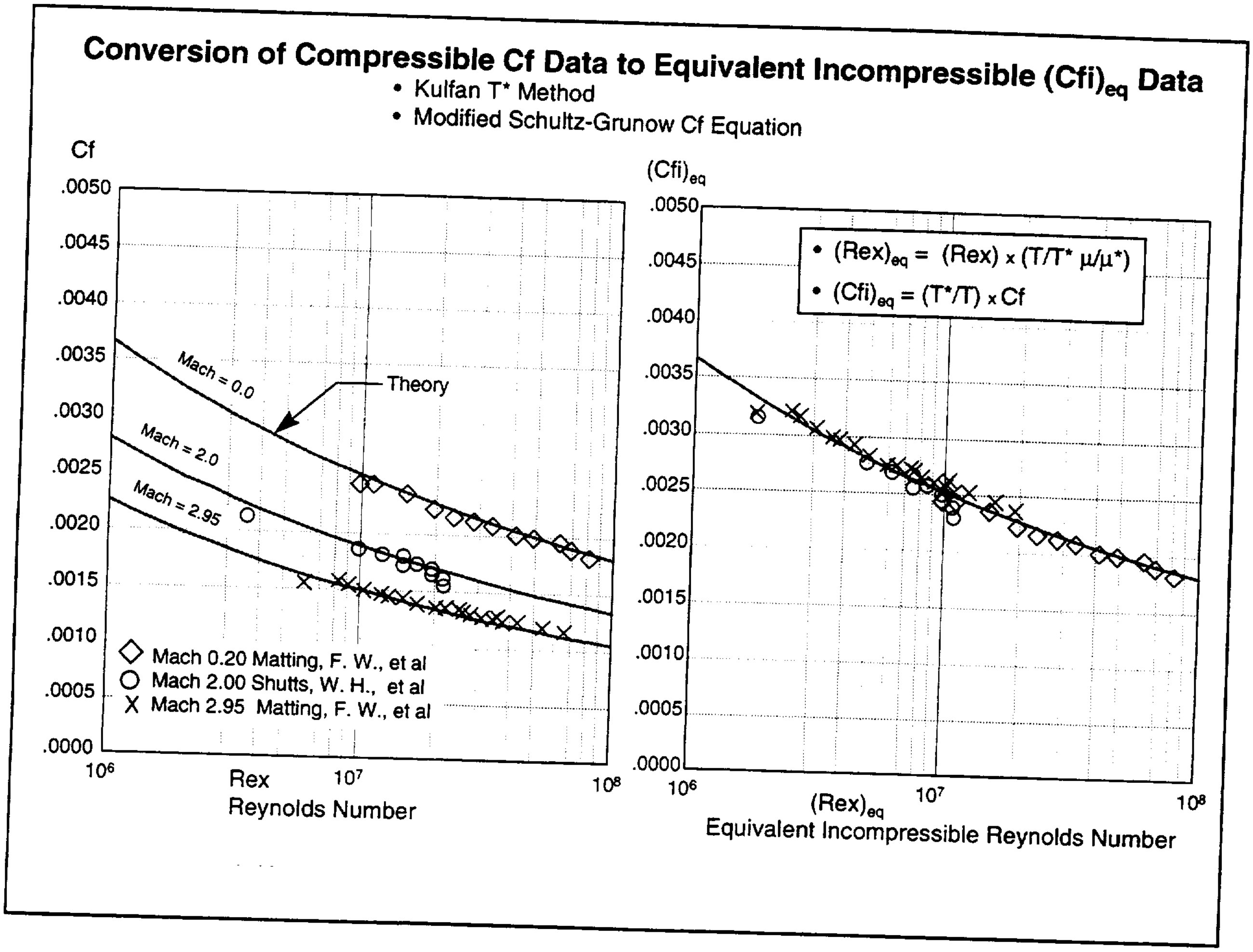

The T* equations can also be used to convert the compressible skin friction to equalivent incompressible data. This transformation procedure, as shown in the Figure, "collapses" all of the test data about the incompressible skin friction curve. This approach can provide a convenient means to assess the accuracy of the theoretical methods to account for compressibility effects simultaneously over a range of Mach numbers and Reynolds numbers.

Conclusions - Flat Plate Database Developemnt

- Modified Incompressible Equations and Improved T*/T Method Predict "Mean" of Available Flat Plate Skin Friction Drag Measurements
- New Methods Presented That Appear to Provide Good Estimates of Boundary layer Thickness and Displacement Thickness
- Compressibility Effects Have Very Little Effect on The Shape or Height of the Turbulent Flat Plate Velocity Profile.
- Boundary Layer Displacement Thickness Increases Rapidly With Mach Number
- Comparisons of Navier Stokes CFD Predictions of Flat Plate Turbulent Skin Friction Drag and Boundary Layer Growth, With the Test Data and / or Theory Presented in This paper, is considered to be a Necessary and Vital Step to Validating the Codes For HSCT Viscous Drag Predictions .
- Need Additional / Quality Experimental CF Data:
  - Locate Available Existing Data
  - Symmetric Model Tests
  - Segmented Axisymmetry Body of Revolution
  - Utilize TU-144 Flight Test Data
  - ???

The modified incompressible CF equations and the improved T* equation presented in the reference paper appeared to consistently match the test better than the other flat plate CF methods currently in use on the HSCT program. It was recommended that the methods presented there, be adapted as the official HSCT flat plate calculation methods.

The boundary layer thickness, and displacement thickness calculations methods presented in that paper seem to be validated by the existing data.

Compressibility effects were shown to have little effect on either the shape or height of a turbulent boundary layer. The displacement thickness however varies rapidly with increasing Mach number.

A modified Shultz / Grunow incompressible local skin friction equation and the modified Prandtl / Schlichting average skin friction were used with the Kulfan T* equation in the studies reported in this paper to evaluate the CFD predictions of fully turbulent flow flat plate skin friction drag.

BPW-LB Skin Friction Analyses Analyses

- Code: CFL3D
- Average Skin Friction, CF
- Turbulence Models:
  - Baldwin - Lomax
  - Spalart - Allmaras
  - Menter's SST
- Mach Numbers:
  - 0.5
  - 1.5
  - 2.25
  - 2.5
- Reynolds Number:
  - 10^6 to 200 x 10^8

The BPW-LB average skin friction predictions were made using CFL3D and a number of turbulence models for a range of Mach numbers and Reynolds as shown in the figure.

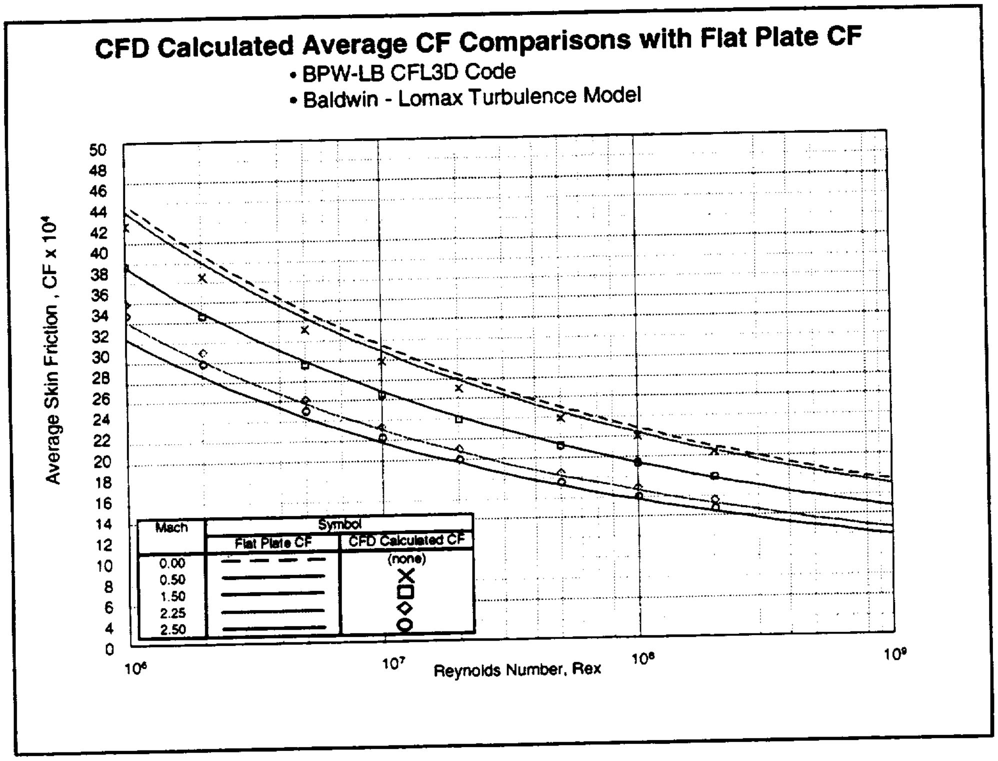

This compares average skin friction predictions obtained using the Baldwin - Lomax turbulence model, with the flat plate predictions.The Calculations were made for Mach = 0.5, 1.5, 2.25 and 2.5

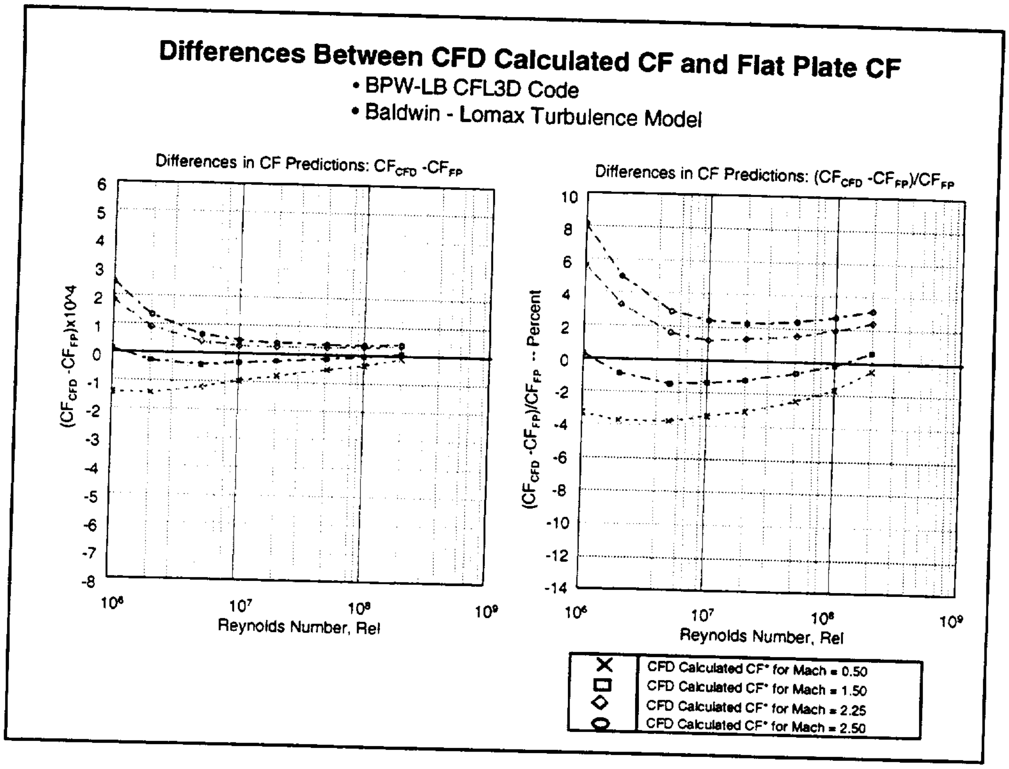

This shows the differences between the CFL3D predictions and the flat plate theory both as incremental differences, and differences in percent.

The differences in the predictions are quite Mach number dependent.

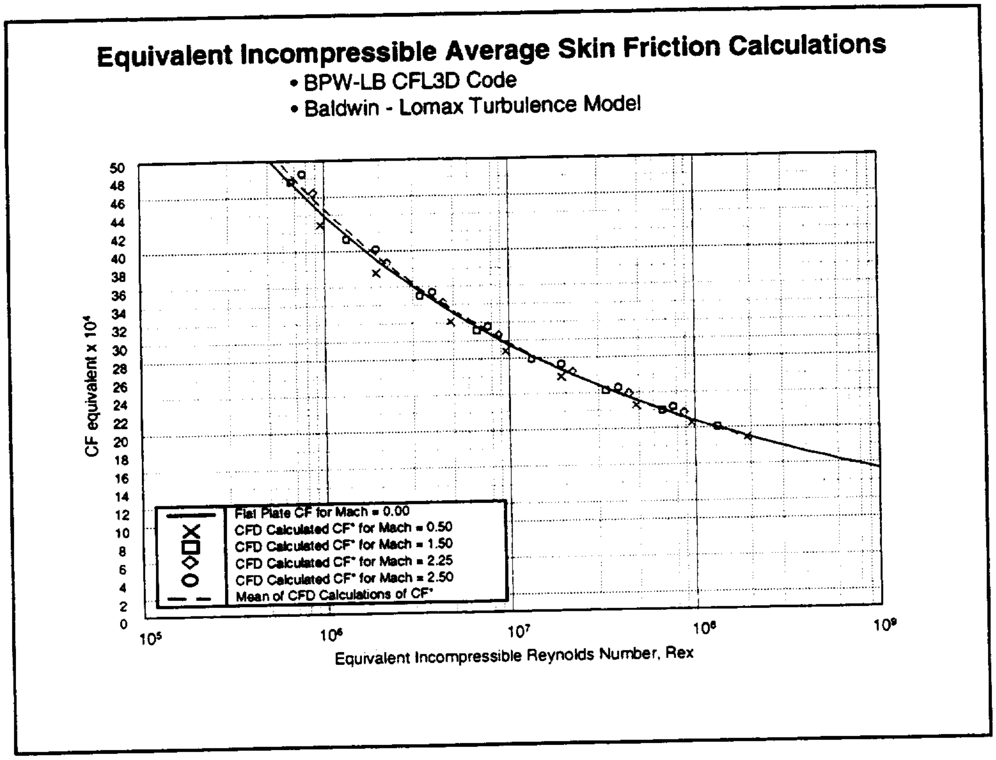

The Kulfan T* equation was used to transform the CFL3D predictions to incompressible skin friction data. The dash red line in this picture is the mean of the CFL3D predictions. It appears that the CFL3D predictions with the Baldwin-Lomax turbulence matched the flat plate predictions and the variation of Cf with Reynolds number

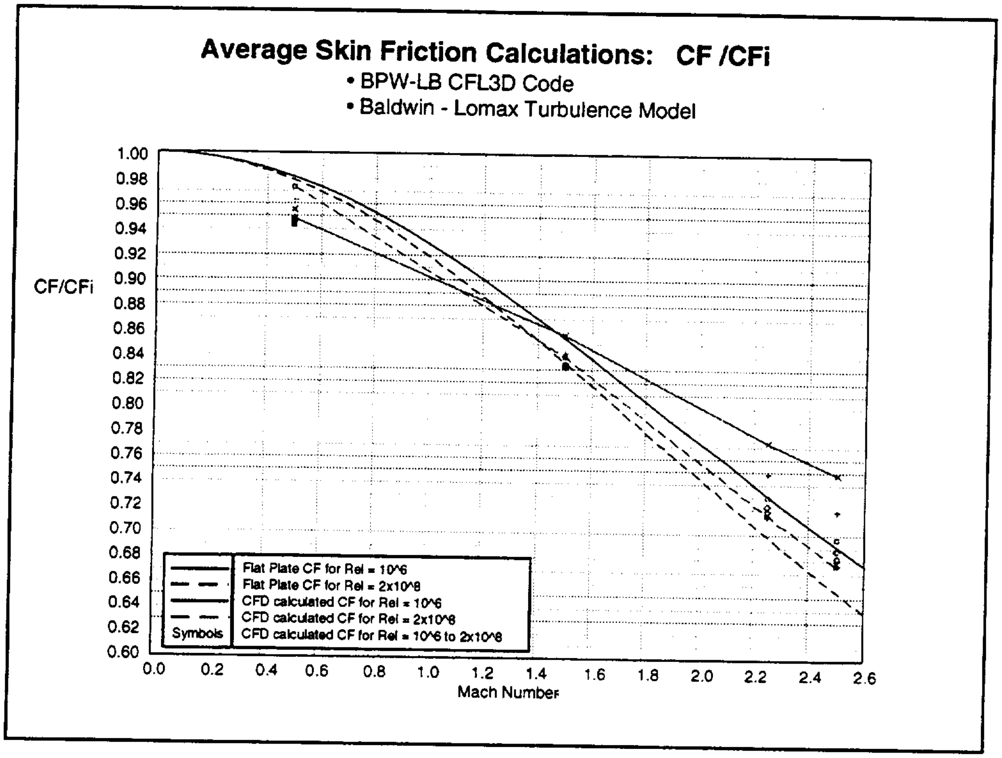

Average Skin Friction Calculations: CF /CFi
• BPW-LB CFL3D Code
• Baldwin - Lomax Turbulence Model
CF/CFi
Mach Number
Flat Plate CF for Rel = 10^6
Flat Plate CF for Rel = 2x10^8
CFD calculated CF for Rel = 10^6
CFD calculated CF for Rel = 2x10^8
Symbols
CFD calculated CF for Rel = 10^6 to 2x10^8

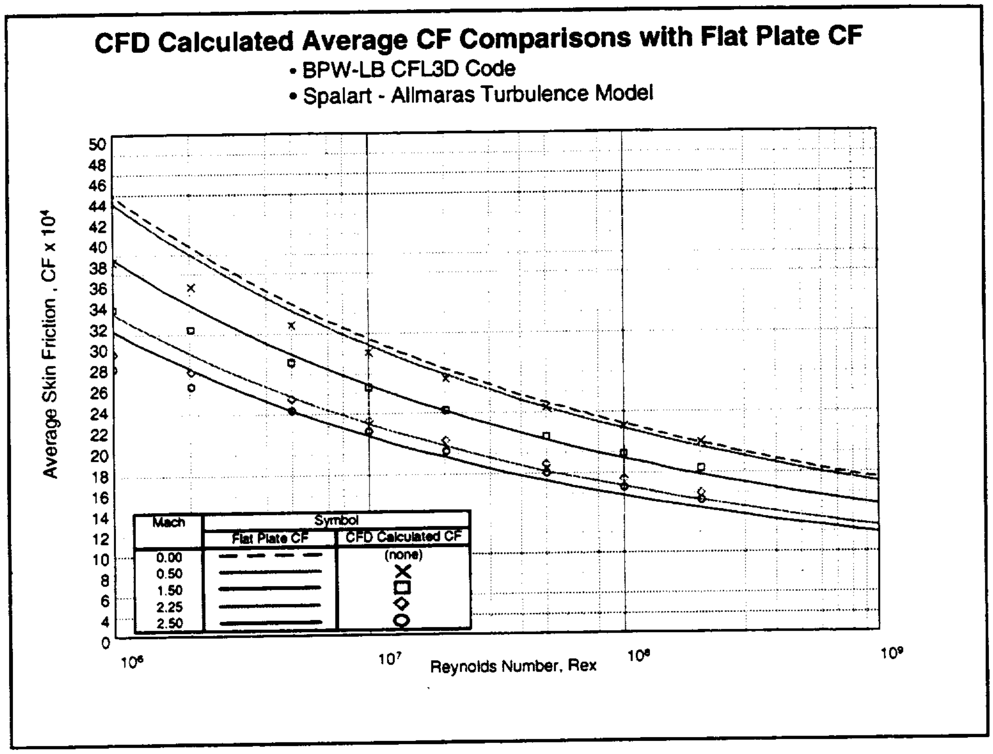
CFD Calculated Average CF Comparisons with Flat Plate CF
• BPW-LB CFL3D Code
• Spalart - Allmaras Turbulence Model
Average Skin Friction, CF x 10⁴
Reynolds Number, Rex
Mach
Symbol
Flat Plate CF
CFD Calculated CF
0.00
0.50
1.50
2.25
2.50
(none)

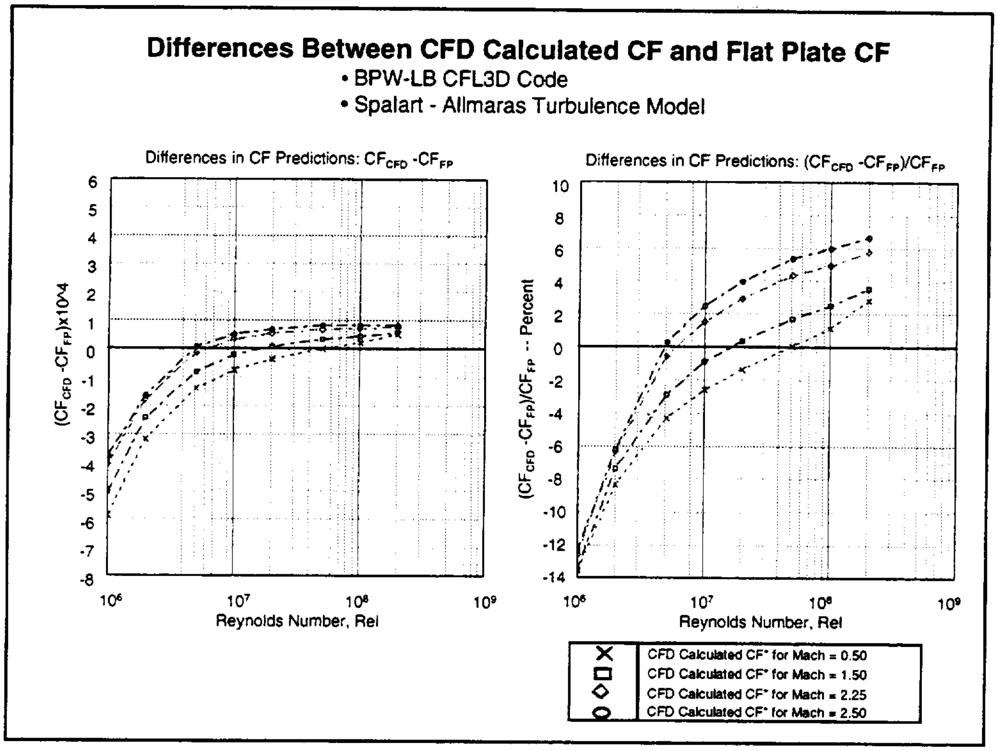
Differences Between CFD Calculated CF and Flat Plate CF
• BPW-LB CFL3D Code
• Spalart - Allmaras Turbulence Model
Differences in CF Predictions: CFCFD -CFFP
(CFCFD -CFFP)x10^4
Reynolds Number, Rel
Differences in CF Predictions: (CFCFD -CFFP)/CFFP
(CFCFD -CFFP)/CFFP -- Percent
Reynolds Number, Rel
CFD Calculated CF* for Mach = 0.50
CFD Calculated CF* for Mach = 1.50
CFD Calculated CF* for Mach = 2.25
CFD Calculated CF* for Mach = 2.50

Equivalent Incompressible Average Skin Friction Calculations

- BPW-LB CFL3D Code
- Spalart - Allmaras Turbulence Model

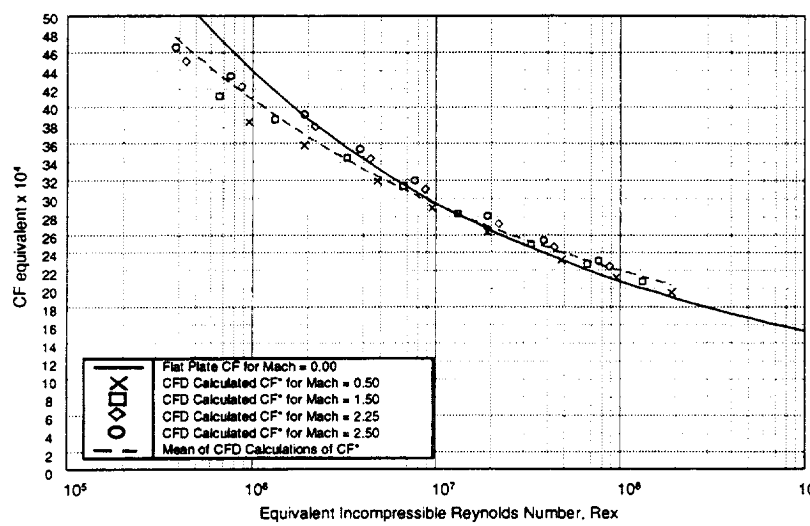

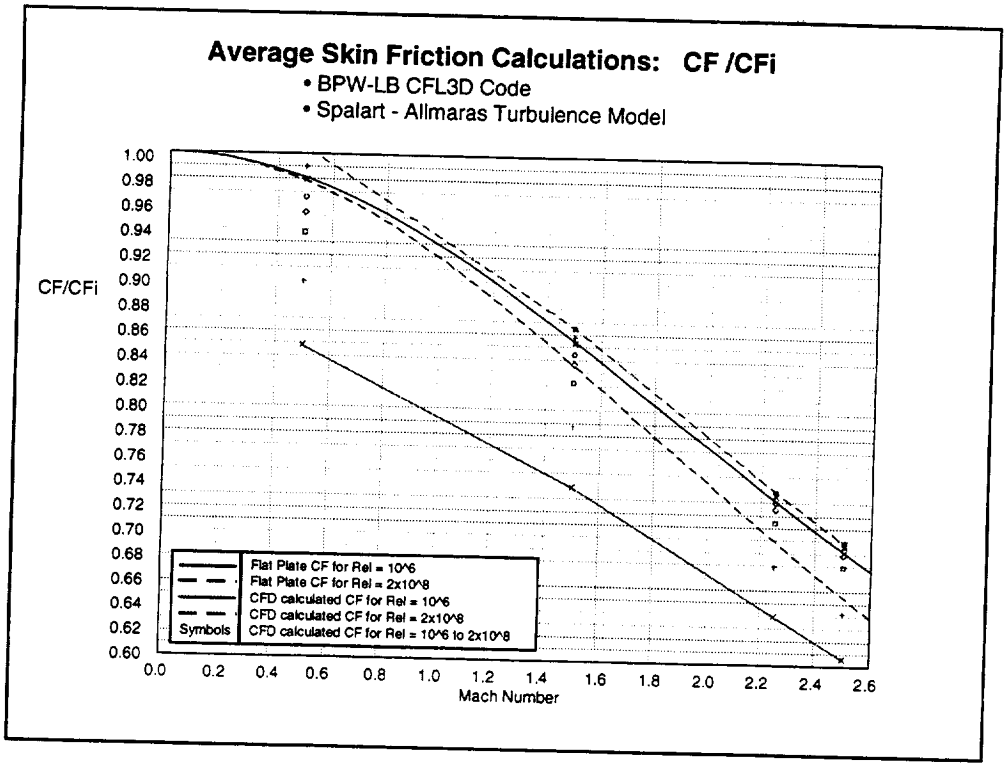
Average Skin Friction Calculations: CF /CFi
• BPW-LB CFL3D Code
• Spalart - Allmaras Turbulence Model
CF/CFi
1.00
0.98
0.96
0.94
0.92
0.90
0.88
0.86
0.84
0.82
0.80
0.78
0.76
0.74
0.72
0.70
0.68
0.66
0.64
0.62
0.60
0.0
0.2
0.4
0.6
0.8
1.0
1.2
1.4
1.6
1.8
2.0
2.2
2.4
2.6
Mach Number
Flat Plate CF for Rel = 10^6
Flat Plate CF for Rel = 2x10^8
CFD calculated CF for Rel = 10^6
CFD calculated CF for Rel = 2x10^8
Symbols
CFD calculated CF for Rel = 10^6 to 2x10^8

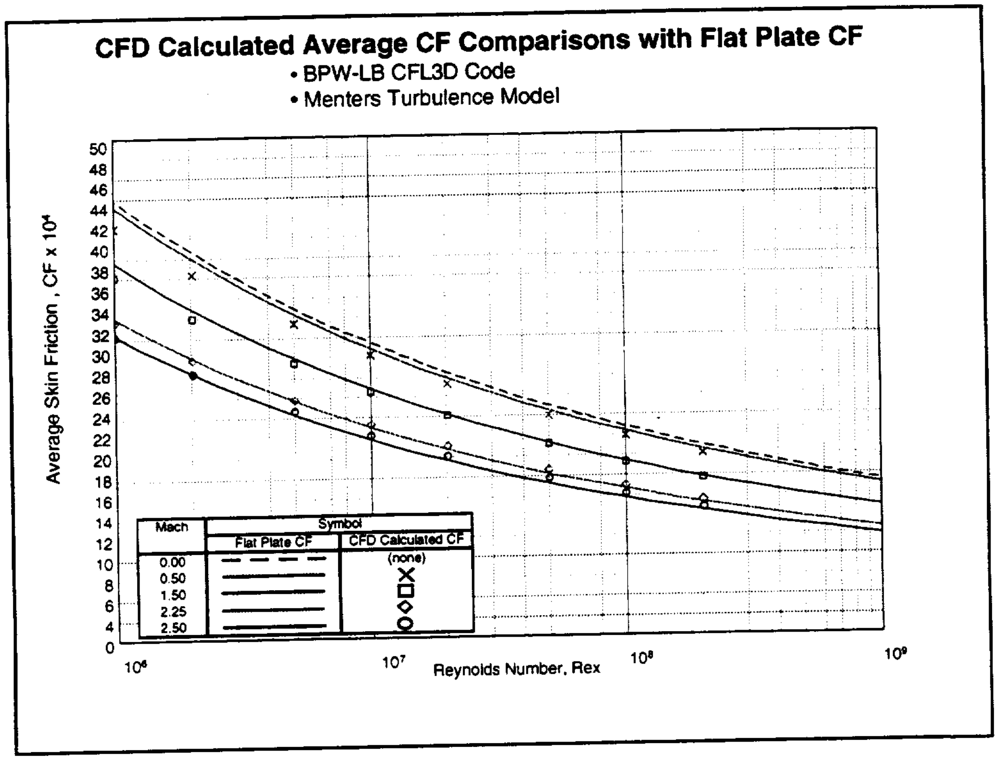

CFD Calculated Average CF Comparisons with Flat Plate CF
• BPW-LB CFL3D Code
• Menters Turbulence Model
Average Skin Friction, CF x 10⁴
Reynolds Number, Rex
Mach
Symbol
Flat Plate CF
CFD Calculated CF
0.00
0.50
1.50
2.25
2.50
(none)

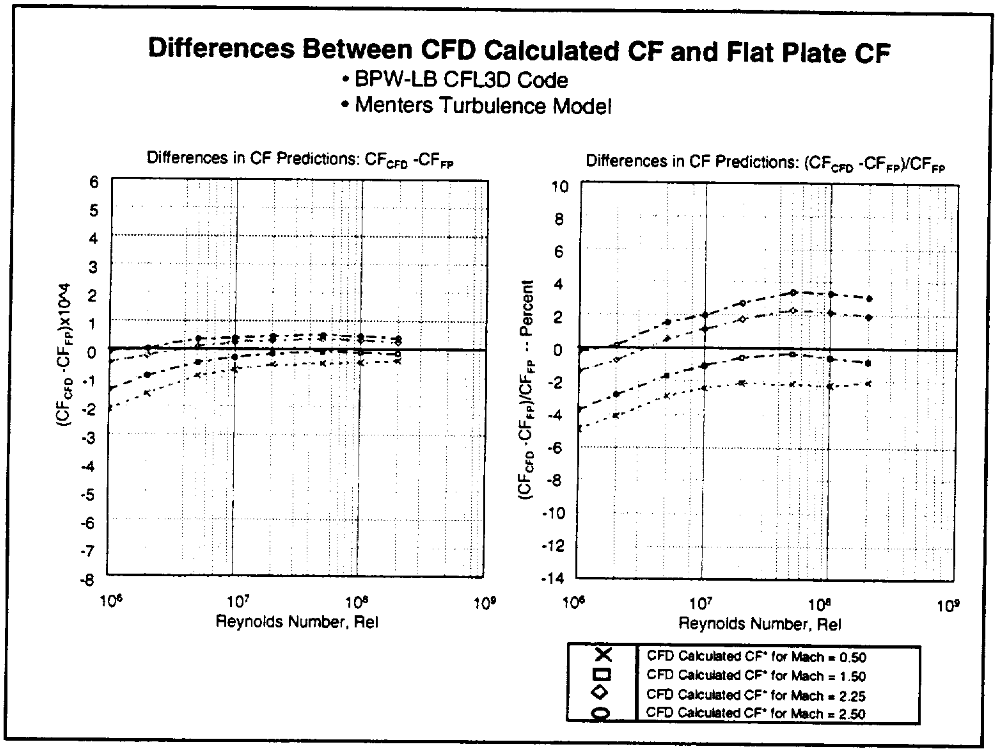
Differences Between CFD Calculated CF and Flat Plate CF
• BPW-LB CFL3D Code
• Menters Turbulence Model
Differences in CF Predictions: CFCFD -CFFP
(CFCFD -CFFP)x10^4
Reynolds Number, Rel
Differences in CF Predictions: (CFCFD -CFFP)/CFFP
(CFCFD -CFFP)/CFFP -- Percent
Reynolds Number, Rel
CFD Calculated CF* for Mach = 0.50
CFD Calculated CF* for Mach = 1.50
CFD Calculated CF* for Mach = 2.25
CFD Calculated CF* for Mach = 2.50

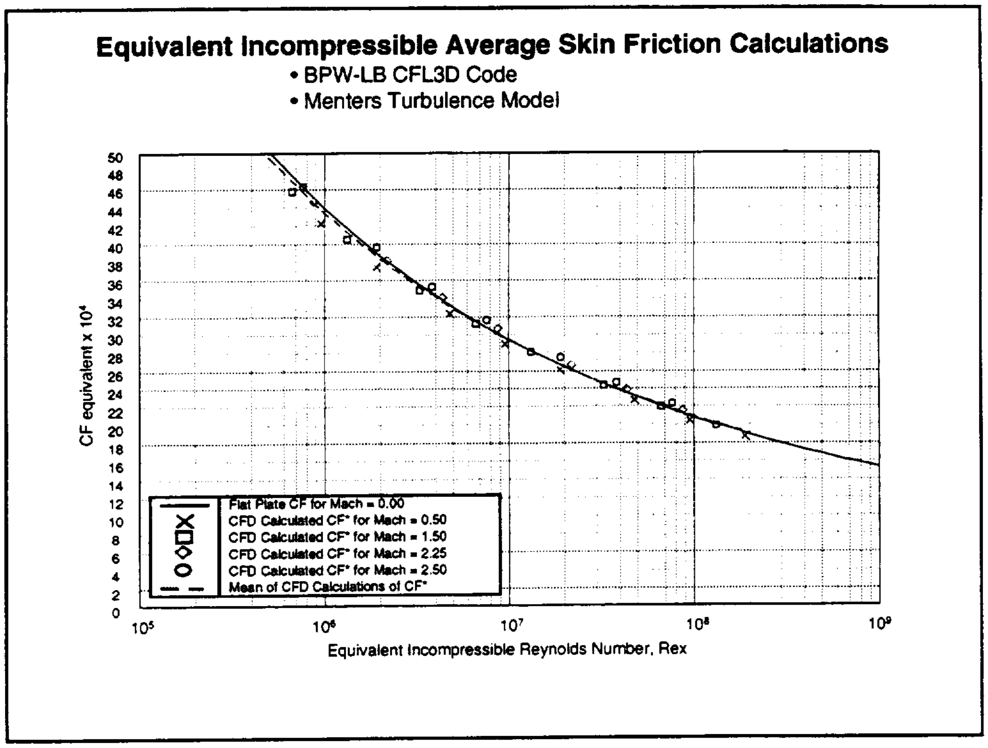

Equivalent Incompressible Average Skin Friction Calculations
• BPW-LB CFL3D Code
• Menters Turbulence Model
CF equivalent x 10⁴
Equivalent Incompressible Reynolds Number, Rex
Flat Plate CF for Mach = 0.00
CFD Calculated CF* for Mach = 0.50
CFD Calculated CF* for Mach = 1.50
CFD Calculated CF* for Mach = 2.25
CFD Calculated CF* for Mach = 2.50
Mean of CFD Calculations of CF*

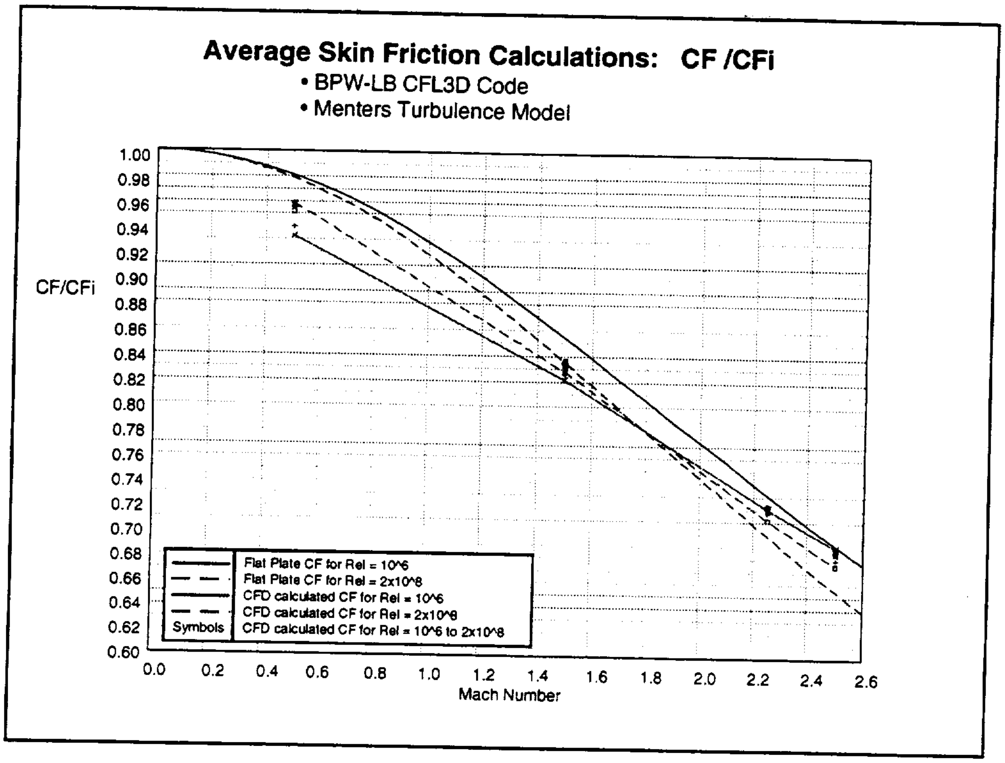

Average Skin Friction Calculations: CF /CFi
• BPW-LB CFL3D Code
• Menters Turbulence Model
CF/CFi
1.00
0.98
0.96
0.94
0.92
0.90
0.88
0.86
0.84
0.82
0.80
0.78
0.76
0.74
0.72
0.70
0.68
0.66
0.64
0.62
0.60
0.0
0.2
0.4
0.6
0.8
1.0
1.2
1.4
1.6
1.8
2.0
2.2
2.4
2.6
Mach Number
Flat Plate CF for Rel = 10^6
Flat Plate CF for Rel = 2x10^8
CFD calculated CF for Rel = 10^6
CFD calculated CF for Rel = 2x10^8
Symbols
CFD calculated CF for Rel = 10^6 to 2x10^8

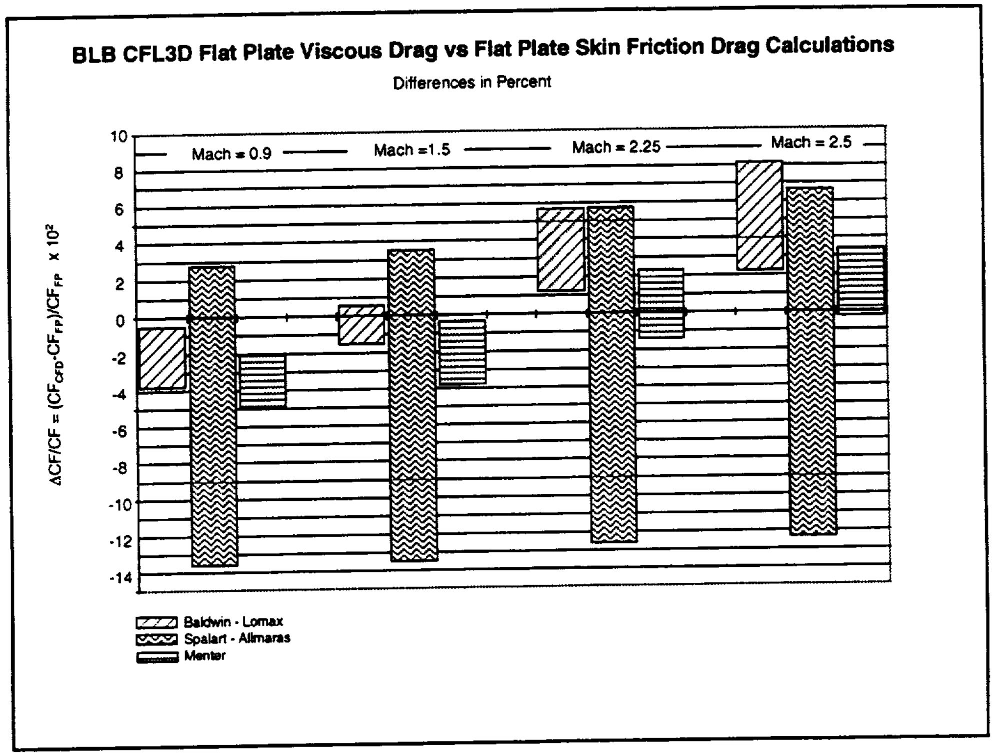
BLB CFL3D Flat Plate Viscous Drag vs Flat Plate Skin Friction Drag Calculations
Differences in Percent
Mach = 0.9
Mach =1.5
Mach = 2.25
Mach = 2.5
$\Delta CF/CF = (CF_{CFD}-CF_{FP})/CF_{FP} \times 10^2$
10
8
6
4
2
0
-2
-4
-6
-8
-10
-12
-14
Baldwin - Lomax
Spalart - Allmaras
Menter

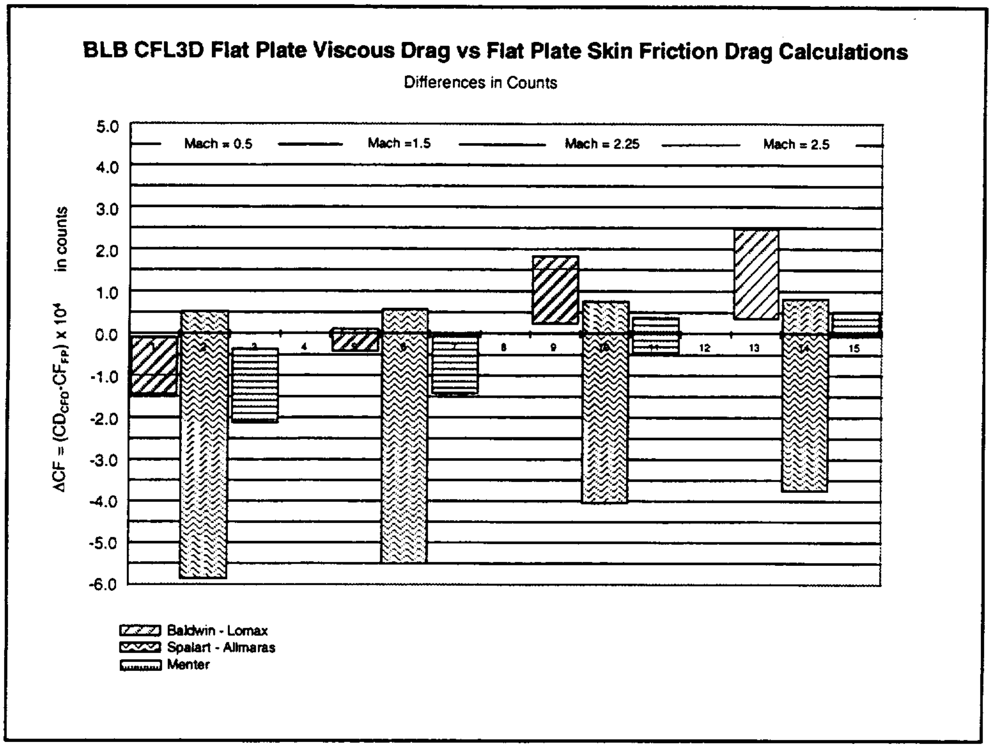
BLB CFL3D Flat Plate Viscous Drag vs Flat Plate Skin Friction Drag Calculations
Differences in Counts
Mach = 0.5
Mach =1.5
Mach = 2.25
Mach = 2.5
5.0
4.0
3.0
2.0
1.0
0.0
-1.0
-2.0
-3.0
-4.0
-5.0
-6.0
ΔCF = (CD_CFD-CF_FP) x 10^4 in counts
1 2 3 4 5 6 7 8 9 10 11 12 13 14 15
Baldwin - Lomax
Spalart - Allmaras
Menter

BAC Skin Friction Analyses Analyses

- Code: OVERFLOW
- Local Skin Friction, Cf
- Average Skin Friction, CF
- Turbulence Models:
  - * Baldwin - Lomax
  - * Spalart - Allmaras
  - * Menter's SST
  - * Baldwin - Barth
  - * k - e
  - * k - w
- Grid vertical spacing variations
- Mach Numbers:
  - * 0.9
  - * 2.4
- Reynolds Number:
  - * 10^5 to 6×10^6
  - * 10^5 to 200×10^8

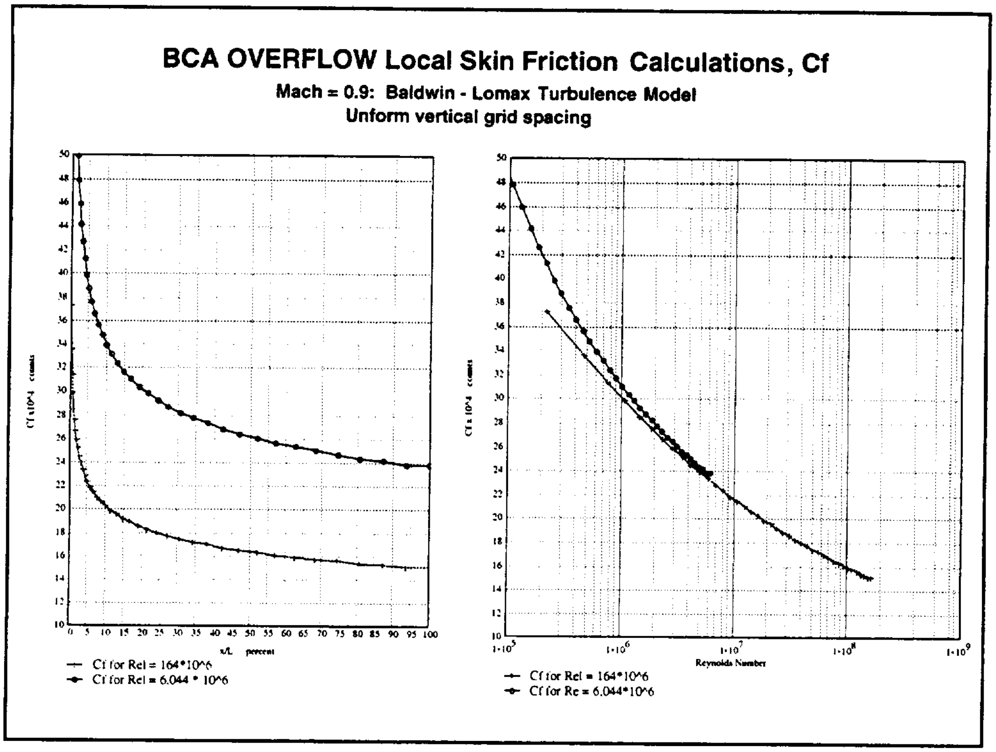
BCA OVERFLOW Local Skin Friction Calculations, Cf
Mach = 0.9: Baldwin - Lomax Turbulence Model
Unform vertical grid spacing
x/L percent
Cf for Rel = 164*10^6
Cf for Rel = 6.044 * 10^6
Reynolds Number
Cf for Rel = 164*10^6
Cf for Re = 6.044*10^6

BCA OVERFLOW Local Skin Friction Calculations, Cf

Mach = 2.4: Bladwin - Lomax Turbulence Model

Unform vertical grid spacing

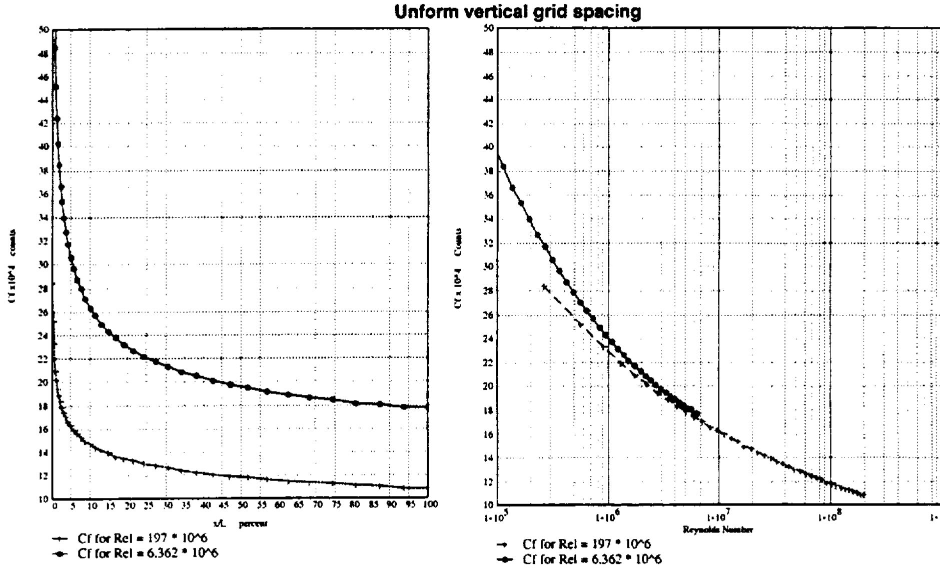

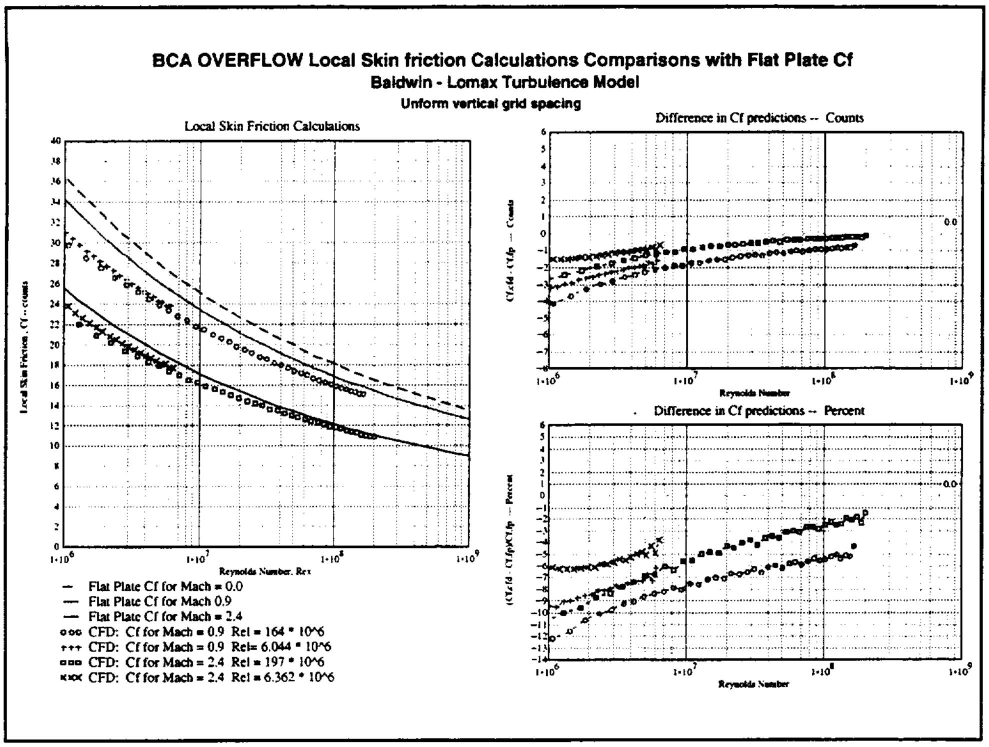
BCA OVERFLOW Local Skin friction Calculations Comparisons with Flat Plate Cf
Baldwin - Lomax Turbulence Model
Unform vertical grid spacing
Local Skin Friction Calculations
Difference in Cf predictions -- Counts
Difference in Cf predictions -- Percent
Reynolds Number, Rex
Reynolds Number
— Flat Plate Cf for Mach = 0.0
— Flat Plate Cf for Mach 0.9
— Flat Plate Cf for Mach = 2.4
ooo CFD: Cf for Mach = 0.9 Rel = 164 * 10^6
+++ CFD: Cf for Mach = 0.9 Rel= 6.044 * 10^6
□□□ CFD: Cf for Mach = 2.4 Rel = 197 * 10^6
xxx CFD: Cf for Mach = 2.4 Rel = 6.362 * 10^6

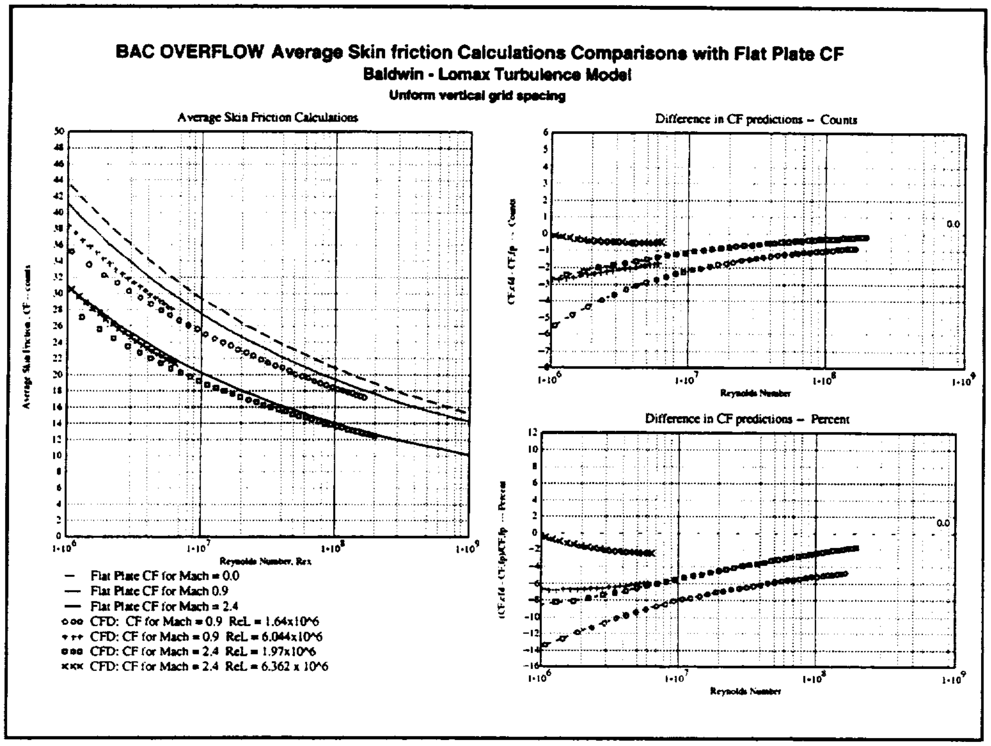
BAC OVERFLOW Average Skin friction Calculations Comparisons with Flat Plate CF
Baldwin - Lomax Turbulence Model
Uniform vertical grid spacing
Average Skin Friction Calculations
Difference in CF predictions -- Counts
Difference in CF predictions -- Percent
Reynolds Number, Rex
Reynolds Number
Flat Plate CF for Mach = 0.0
Flat Plate CF for Mach 0.9
Flat Plate CF for Mach = 2.4
CFD: CF for Mach = 0.9 ReL = 1.64x10^6
CFD: CF for Mach = 0.9 ReL = 6.044x10^6
CFD: CF for Mach = 2.4 ReL = 1.97x10^6
CFD: CF for Mach = 2.4 ReL = 6.362 x 10^6

BCA OVERFLOW Local Skin Friction Calculations, Cf

Mach = 0.9: Spalart - Allmaras Turbulence Model
Unform vertical grid spacing

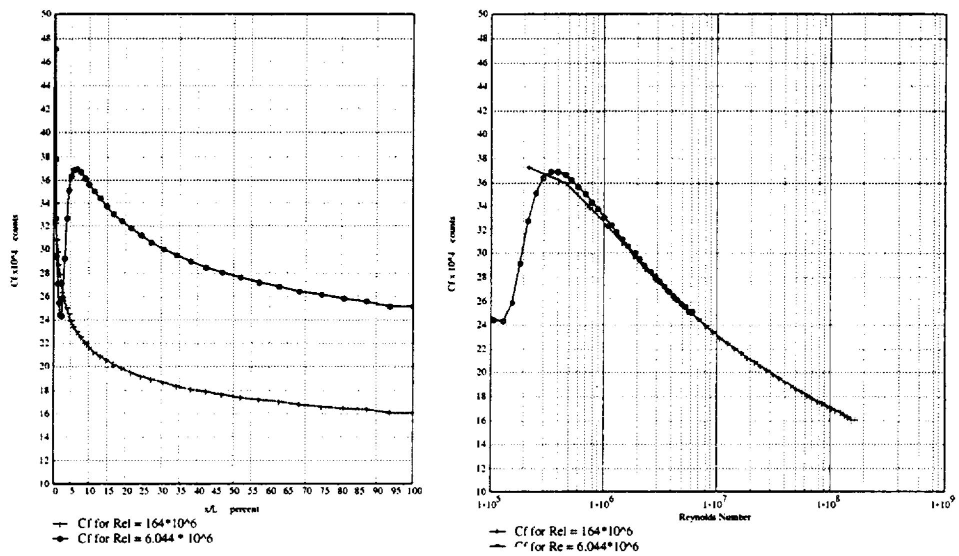

BCA OVERFLOW Local Skin Friction Calculations, Cf

Mach = 2.4: Spalart - Allmaras Turbulence Model

Unform vertical grid spacing

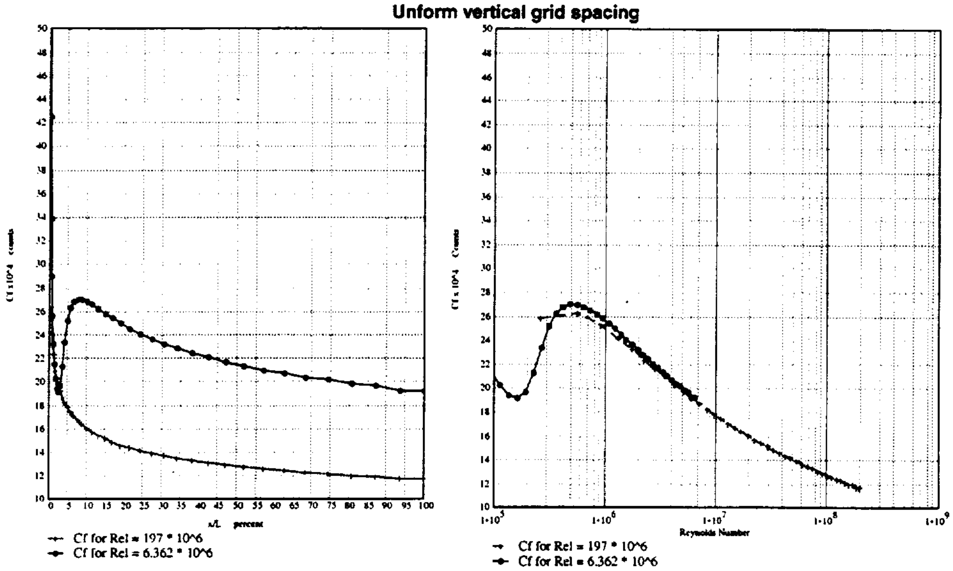

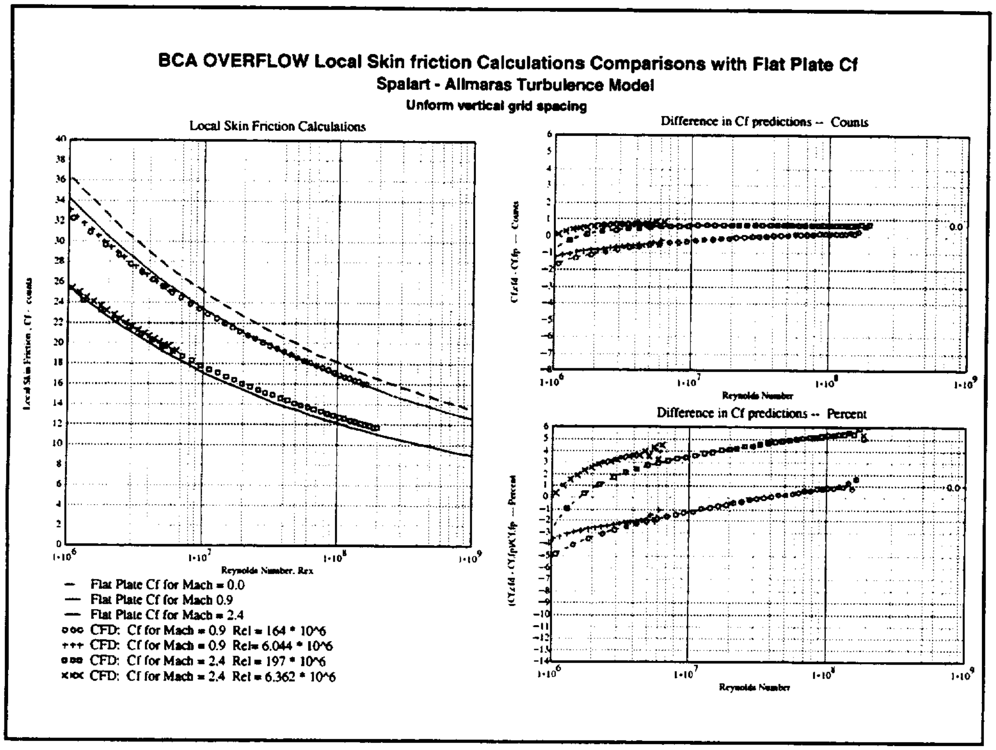

BCA OVERFLOW Local Skin friction Calculations Comparisons with Flat Plate Cf
Spalart - Allmaras Turbulence Model
Uniform vertical grid spacing
Local Skin Friction Calculations
Difference in Cf predictions -- Counts
Difference in Cf predictions -- Percent
Reynolds Number, Rex
Reynolds Number
— Flat Plate Cf for Mach = 0.0
— Flat Plate Cf for Mach 0.9
— Flat Plate Cf for Mach = 2.4
ooo CFD: Cf for Mach = 0.9 Rel = 164 * 10^6
+++ CFD: Cf for Mach = 0.9 Rel= 6.044 * 10^6
ooo CFD: Cf for Mach = 2.4 Rel = 197 * 10^6
xxx CFD: Cf for Mach = 2.4 Rel = 6.362 * 10^6

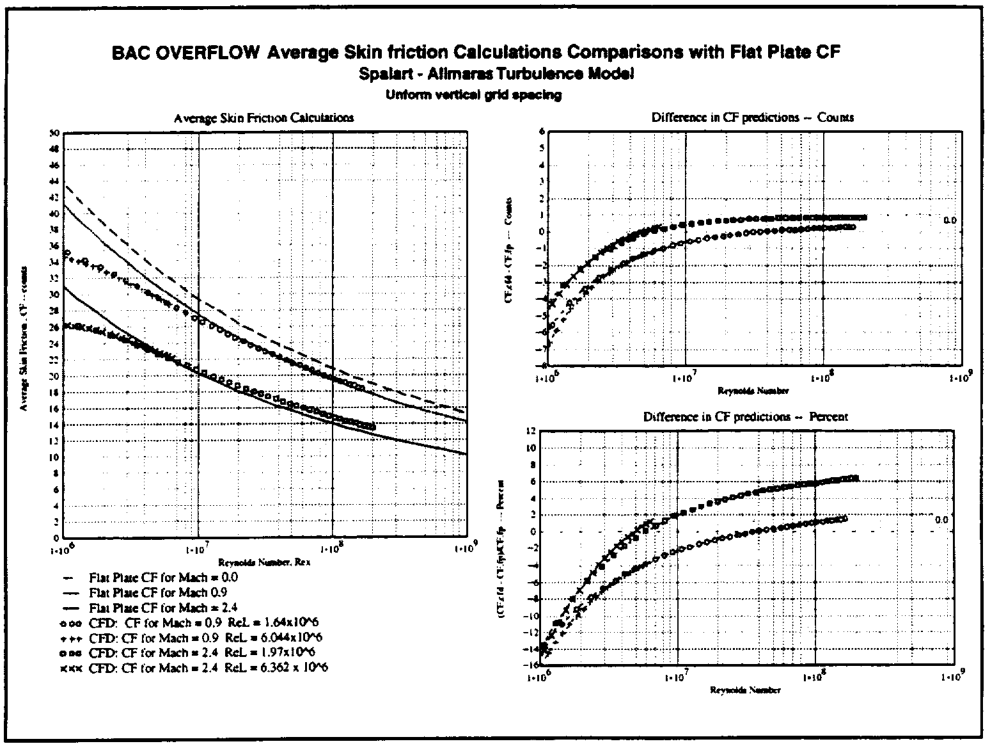
BAC OVERFLOW Average Skin friction Calculations Comparisons with Flat Plate CF
Spalart - Allmaras Turbulence Model
Unform vertical grid spacing
Average Skin Friction Calculations
Difference in CF predictions -- Counts
Difference in CF predictions -- Percent
Reynolds Number, Rex
Reynolds Number
0.0
Flat Plate CF for Mach = 0.0
Flat Plate CF for Mach 0.9
Flat Plate CF for Mach = 2.4
CFD: CF for Mach = 0.9 ReL = 1.64x10^6
CFD: CF for Mach = 0.9 ReL = 6.044x10^6
CFD: CF for Mach = 2.4 ReL = 1.97x10^6
CFD: CF for Mach = 2.4 ReL = 6.362 x 10^6

BCA OVERFLOW Local Skin Friction Calculations, Cf

Mach = 0.9: Menter's Turbulence Model
Unform vertical grid spacing

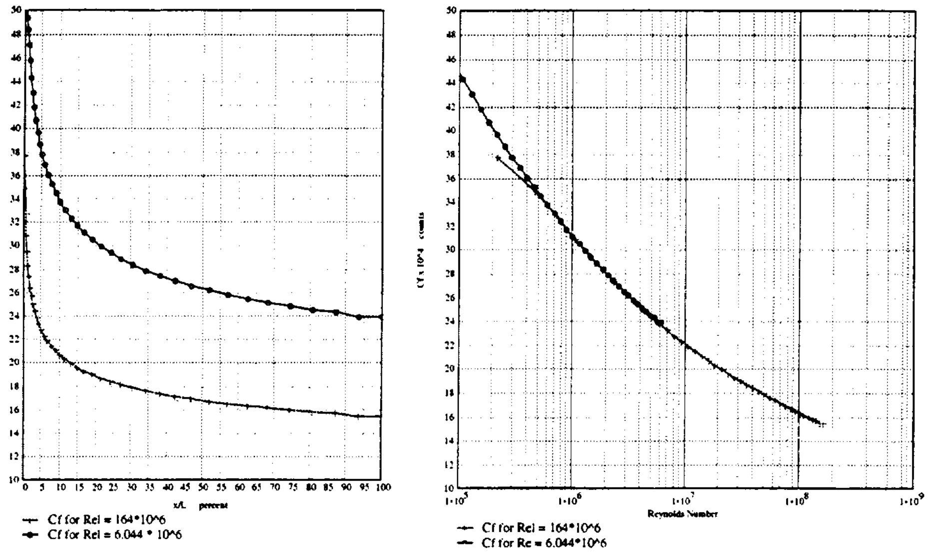

BCA OVERFLOW Local Skin Friction Calculations, Cf

Mach = 2.4: Menter's Turbulence Model

Unform vertical grid spacing

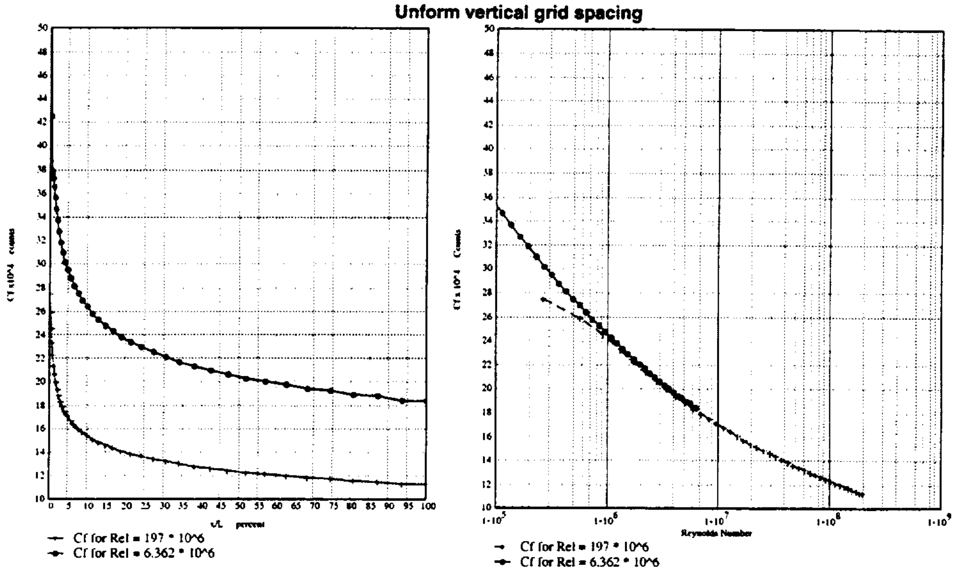

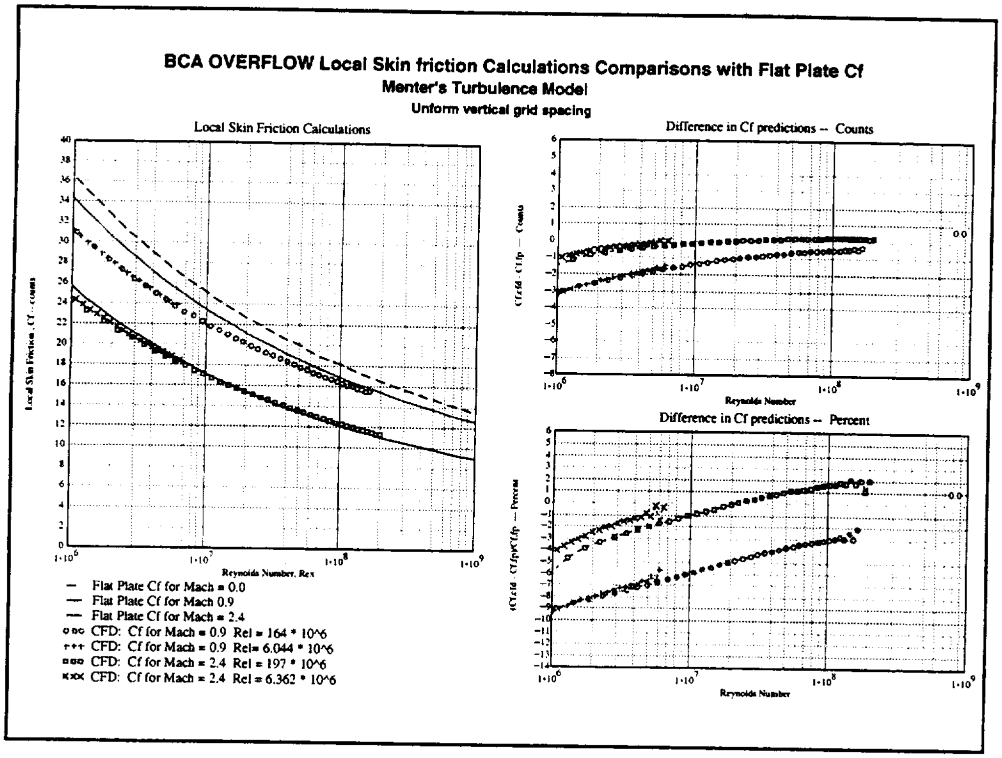
BCA OVERFLOW Local Skin friction Calculations Comparisons with Flat Plate Cf
Menter's Turbulence Model
Unform vertical grid spacing
Local Skin Friction Calculations
Local Skin Friction, Cf - counts
Reynolds Number, Rex
— Flat Plate Cf for Mach = 0.0
— Flat Plate Cf for Mach 0.9
— Flat Plate Cf for Mach = 2.4
ooo CFD: Cf for Mach = 0.9 Rel = 164 * 10^6
+++ CFD: Cf for Mach = 0.9 Rel= 6.044 * 10^6
□□□ CFD: Cf for Mach = 2.4 Rel = 197 * 10^6
xxx CFD: Cf for Mach = 2.4 Rel = 6.362 * 10^6
Difference in Cf predictions -- Counts
Cfcfd - Cffp — Counts
Reynolds Number
Difference in Cf predictions -- Percent
(Cfcfd - Cffp)/Cffp — Percent
Reynolds Number

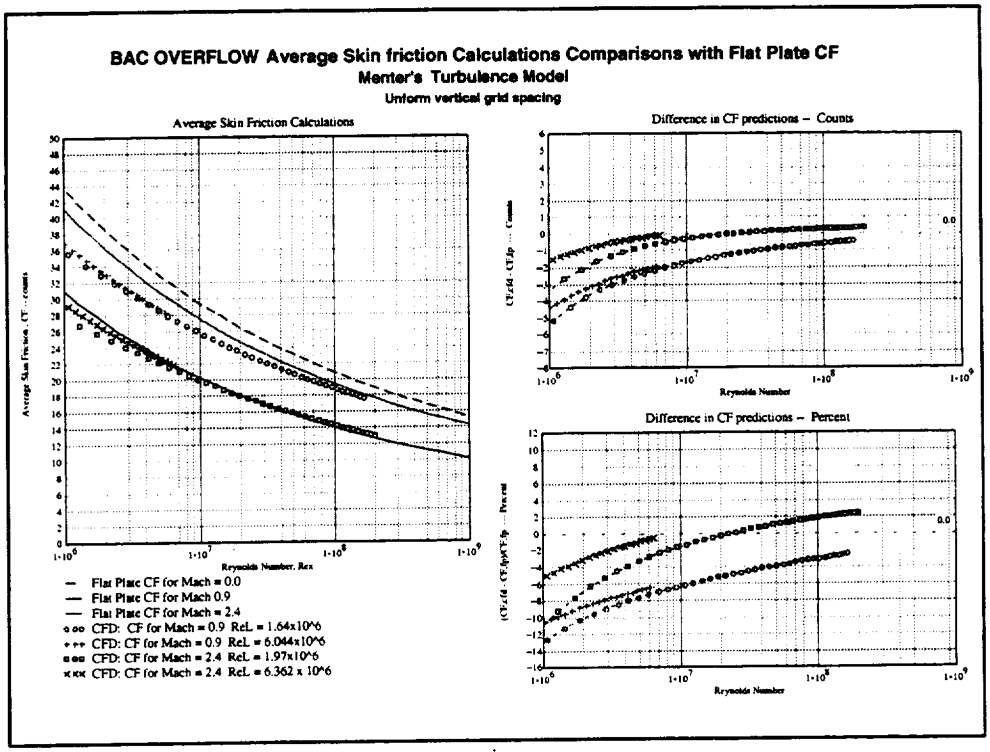
BAC OVERFLOW Average Skin friction Calculations Comparisons with Flat Plate CF
Menter's Turbulence Model
Unform vertical grid spacing
Average Skin Friction Calculations
Difference in CF predictions – Counts
Difference in CF predictions – Percent
Reynolds Number, Rex
Reynolds Number
Flat Plate CF for Mach = 0.0
Flat Plate CF for Mach 0.9
Flat Plate CF for Mach = 2.4
CFD: CF for Mach = 0.9 ReL = 1.64x10^6
CFD: CF for Mach = 0.9 ReL = 6.044x10^6
CFD: CF for Mach = 2.4 ReL = 1.97x10^6
CFD: CF for Mach = 2.4 ReL = 6.362 x 10^6

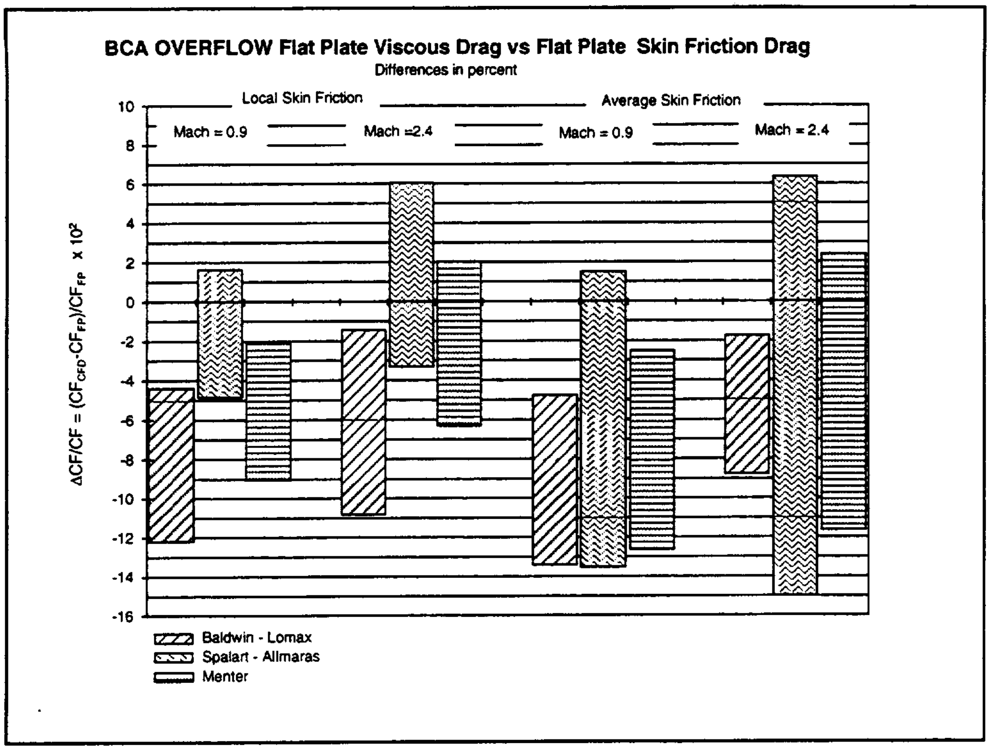

BCA OVERFLOW Flat Plate Viscous Drag vs Flat Plate Skin Friction Drag
Differences in percent
Local Skin Friction
Average Skin Friction
Mach = 0.9
Mach =2.4
Mach = 0.9
Mach = 2.4
ΔCF/CF = (CF_CFD-CF_FP)/CF_FP x 10²
10
8
6
4
2
0
-2
-4
-6
-8
-10
-12
-14
-16
Baldwin - Lomax
Spalart - Allmaras
Menter

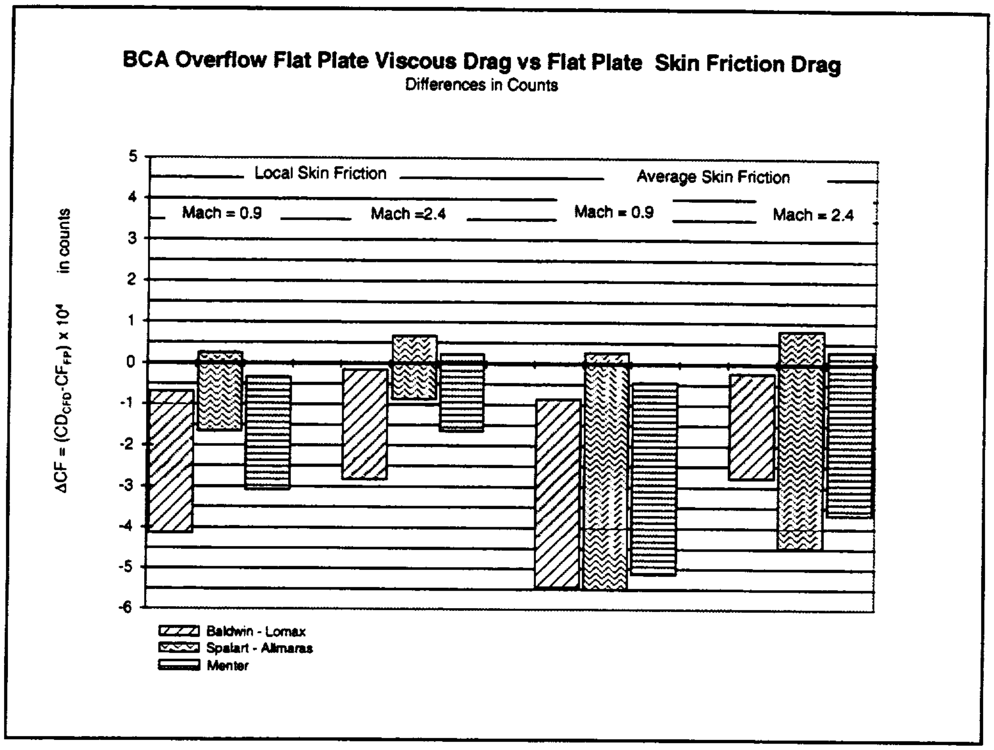
BCA Overflow Flat Plate Viscous Drag vs Flat Plate Skin Friction Drag
Differences in Counts
Local Skin Friction
Average Skin Friction
Mach = 0.9
Mach =2.4
Mach = 0.9
Mach = 2.4
ΔCF = (CDCFD-CFFP) x 10⁴ in counts
5
4
3
2
1
0
-1
-2
-3
-4
-5
-6
Baldwin - Lomax
Spalart - Allmaras
Menter

ARC Analyses

Code: OVERFLOW

Local Skin Friction, Cf

Average Skin Friction, CF

Turbulence Models:
* Spalart - Allmaras
* Menter's SST

Mach Numbers:
* 0.5
* 0.9
* 1.5
* 2.0
* 2.4

Reynolds Number:
* 10^5 to 6×10^6
* 10^5 to 200×10^8

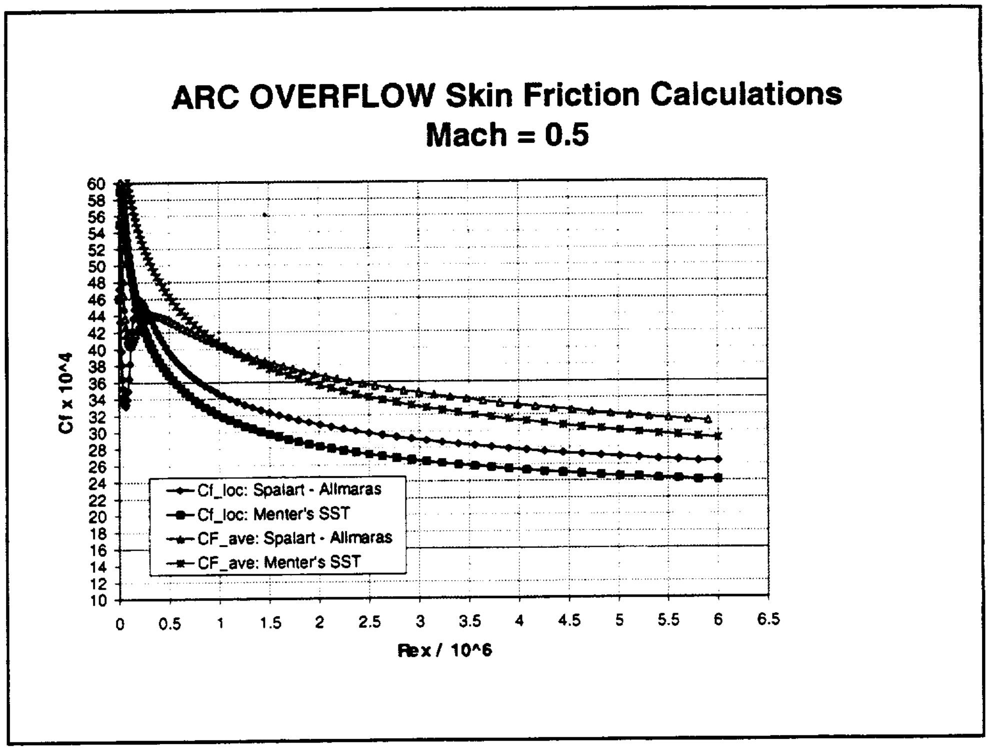

ARC OVERFLOW Skin Friction Calculations
Mach = 0.5
Cf x 10^4
Rex / 10^6
Cf_loc: Spalart - Allmaras
Cf_loc: Menter's SST
CF_ave: Spalart - Allmaras
CF_ave: Menter's SST

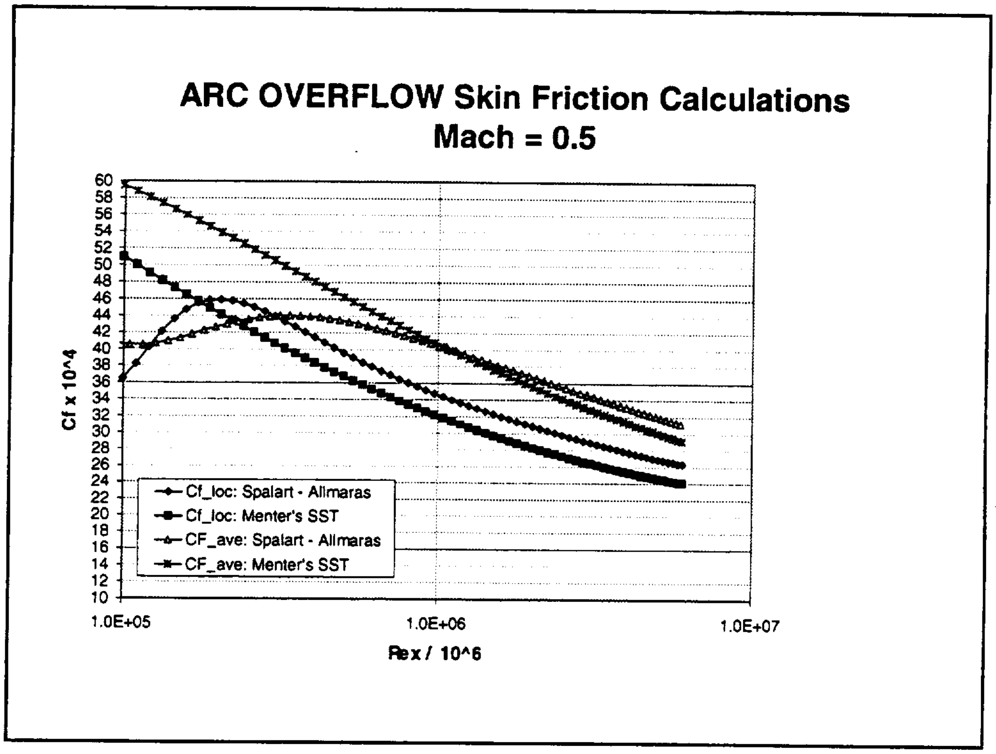
ARC OVERFLOW Skin Friction Calculations
Mach = 0.5
Cf x 10^4
Rex / 10^6
1.0E+05
1.0E+06
1.0E+07
Cf_loc: Spalart - Allmaras
Cf_loc: Menter's SST
CF_ave: Spalart - Allmaras
CF_ave: Menter's SST

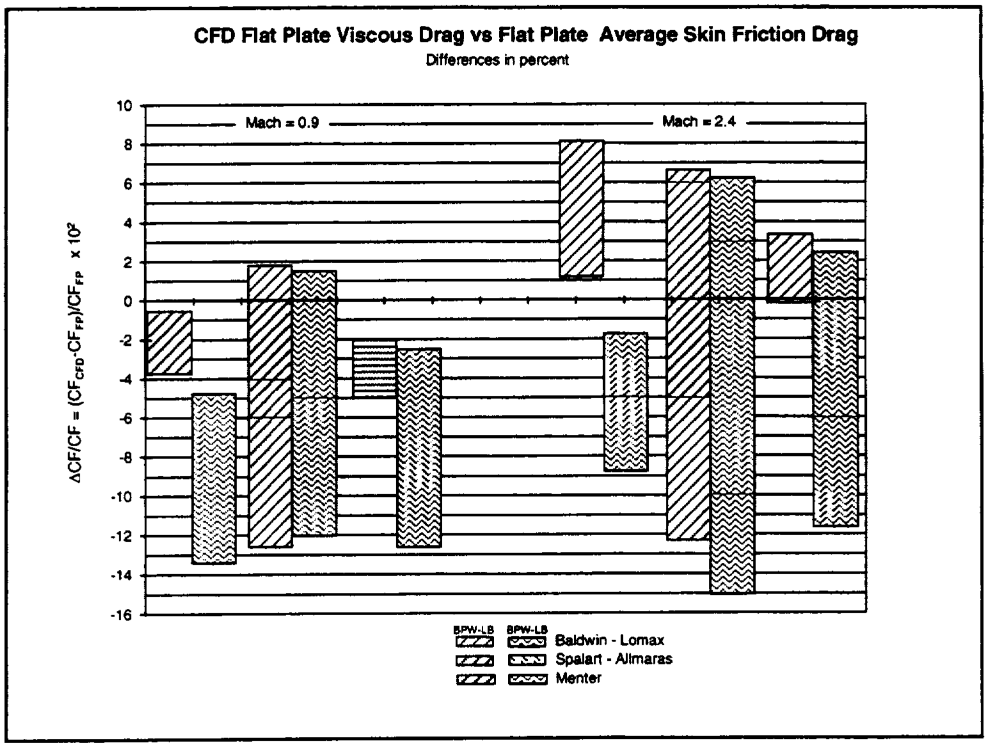

CFD Flat Plate Viscous Drag vs Flat Plate Average Skin Friction Drag
Differences in percent
Mach = 0.9
Mach = 2.4
10
8
6
4
2
0
-2
-4
-6
-8
-10
-12
-14
-16
ΔCF/CF = (CF_CFD-CF_FP)/CF_FP x 10²
BPW-LB
BPW-LB
Baldwin - Lomax
Spalart - Allmaras
Menter

Conclusions

- Modified incompressible CF equations and improved T*/T method predict "mean" of available flat plate skin friction drag measurements
- BPW-LB CDL3D And BCA OVERFLOW CF predictions with the Spalart - Allmaras Turbulence Model are consistent and show a large difference in the variation of CF with Reynolds Number compared to the flat plate CF predictions
- The Spalart - Allmaras Cf predictions indicate a laminar to turbulent transition characteristic. This is the source of the large Reynolds Number variations
- The BPW-LB CFL3D CF predictions agree better with the flatp plate theory, and therfore also the test data, then the BAC OVERFLOW predictions
- Menter's SST slightly underpredicts CF at low Mach Numbers, But overall best predicts flat plate fully turbulent flow CF
- BAC OVERFLOW results include:
  - CFD skin friction predictions vary with vertical grid spacing scheme.
  - "constant grid spacing" near the wall, CF predictions appear better than "stretched grid spacing" predictions
- Initial assessment of ARC OVERFLOW predictions show significant differences in the predictions using the Spalart- Almaras and the Menter SST Turbulence Models
- Additional effort is necessary to understand and resolve the CF prediction differences

The conclusions of this study are shown in the Figure.

Progress Toward Viscous Drag Calculations (Part I)

Flow Over Flat Plate with No Pressure Gradient

Hamid Jafroudi
Alpha STAR Corporation
Long Beach, CA

Raul Mendoza
Peter Hartwich
Shreekant Agrawal
The Boeing Company
Phantom Works
Long Beach, CA

NASA/ Industry HSR Airframe Review
Anaheim, California
February 8 -11, 1999

Alpha STAR CORPORATION

BOEING

Progress Toward Viscous Drag Calculations

High Speed Aerodynamics, Long Beach

ABSTRACT

A systematic prediction capabilities of a state-of-the-art Navier-Stokes solver employed in HSR program for viscous drag for flow with and without pressure gradient was assumed and a computational database was built. The study of the viscous drag prediction capability of the CFL3D Navier-Stokes solver was conducted at Boeing Long Beach in two phases. In the firstphase, Navier-Stokes solutions were correlated with experimental data for flows over a flat plate without pressure gradients. In the second phase, flows with pressure gradients were considered by examining the TCA symmetric wing/body configuration. The High Speed Research (HSR), Configuration Aerodynamics community has proposed a Technical Concept Airplane (TCA) symmetrical wing/body configuration in an effort to obtain a computational database for validation of viscous drag for wind-tunnel and fligh Reynolds numbers. This model was also selected because wind-tunnel data become available for comparison in the near future. The study was performed for several turbulence models and the flow conditions (M_∞ = 0.31 to 2.40 at wind-tunnel and flight Reynolds numbers) were chosen such that they bracketed the transonic and supersonic cruise Mach numbers of an HSCT aircraft.

Alpha STAR CORPORATION

BOEING

Outline

The outline of my talk will be as followed: First, the objective of the study will be given. The approach to this analysis will be described. Then some brief background will be introduced. The computational grid and grid topology will be discussed. The turbulence models are used for this study are described. The computational and empirical results will be presented. Finally, the summary of the analysis will be given.

Flat Plate with No Pressure Gradient

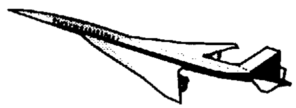

High Speed Aerodynamics, Long Beach

Outline

- Objective
- Introduction
- Method of solution
- Computational grid
- Turbulence models
- Computational results
- Summary

Alpha STAR CORPORATION

BOEING

Flat Plate with No Pressure Gradient

High Speed Aerodynamics, Long Beach

Objective

The primary objective of this study was to evaluate the viscous-drag prediction capability of the different Navier-Stokes codes employed in the HSR program. This study was prompted as a result of significance differences observed between various estimate in viscous-drag predictions. In addition, the study provides a computational database for correlation with experimental database for viscous-drag over a wide range of subsonic to supersonic speeds. The flat plate boundary-layer flows isolate skin-friction drag from other components of drag encountered in practical flows. To make the results of this study more relevent to the practitioner, flows with pressure gradient are considered in the second part of this presentation, that is the flow over TCA symmetric wing/body configuration.

Alpha STAR CORPORATION

BOEING

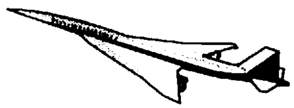

Flat Plate with No Pressure Gradient

High Speed Aerodynamics, Long Beach

Objective

- To provide a computational database
  - smooth adiabatic flat plate with no pressure gradient
  - subsonic to supersonic Mach numbers
  - wide range of Reynolds numbers
  - several turbulence models

Alpha STAR CORPORATION

BOEING

Flat Plate with No Pressure Gradient

Introduction

There is much confidence that Euler solutions tend to overpredict wave drag, and Navier-Stokes solutions for viscous flows predict the pressure drag quite accurately. This is concluded from comparisons with wind-tunnel data. However, for viscous drag predictions, there are discrepencies among the Navier-Stokes solutions as well as between Computational Fluid Dynamics (CFD) results and wind-tunnel data. This spurned the current systematic study of the viscous drag prediction capability of Navier-Stokes codes.

Kulfan has compiled local and average skin-friction data from numerous wind-tunnel test data. In the process of extracting the data, statistical analyses were performed between the test data and the corresponding predictions of various fully turbulent flat plate skin-friction prediction methods. After a thorough analysis, and a critical evaluation of several empirical correlation formulae for compressible boundary layer flows, Kulfan proposed a skin-friction correlation that appears to work very well over a wide range of Mach and Reynolds numbers. These correlations are currently being used to calibrate the skin-friction prediction capabilities of CFL3D code.

Flat Plate with No Pressure Gradient

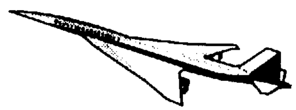

High Speed Aerodynamics, Long Beach

Introduction

- First step in evaluating Navier-Stokes based viscous drag prediction methods
- Help sort out appropriate turbulence models
- Good estimate of viscous drag of HSCT type configurations
- Asembly of a database in 1960 from selected experiments
- Extrapolation of wind-tunnel data to flight conditions
- Boundary layer porofile data measurements

Alpha STAR CORPORATION

BOEING

Flat Plate with No Pressure Gradient

Method of Solution

A systematic study of the viscous-drag prediction capability of the CFL3D based Navier-Stokes solver was conducted at Boeing Long Beach in two phases. In the first phase, 2-D subsonic to supersonic Navier-Stokes solutions were correlated with the experimental data for compressible turbulent flows over a flat plate without pressure gradients. In the second phase of this study, flows with pressure gradient were considered by examining the TCA symmetric wing/body configuration. This configuration was selected because wind-tunnel test data would become available for comparison in the near future.

Flat Plate with No Pressure Gradient

Method of Solution

- Use CFL3D developed by NASA Langely and modified by Boeing
  - Navier-Stokes formulation
  - several turbulence models
  - obtain computational skin-friction

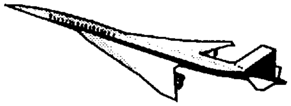

Flat Plate with No Pressure Gradient

High Speed Aerodynamics, Long Beach

CFL3D Features

The CFL3D code is based on time-dependent conservation law form of the Reynolds-averaged Navier-Stokes formulations. The spatial discretization involves a finite volume approach. Upwind-biased differencing is applied to the inviscid flux terms. The upwinding is based on either the Van Leer flux-vector splitting or Roe flux-differencing splitting. Central differences used for shear stress and heat transfer terms. The time advancement is implicit with the ability to solve steady and unsteady cases. Multigrid and mesh sequencing are also available for convergence acceleration. Numerous turbulence models with different levels of complexity are available in the code. The turbulence models are zero-, one-, and two-equation models. In grid topology, a domain decomposition using C-O continuous, patched, interface and overlapped/embedded grid are implemented in the code.

Alpha STAR CORPORATION

BOEING

Flat Plate with No Pressure Gradient

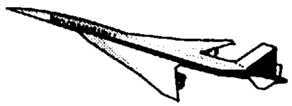

High Speed Aerodynamics, Long Beach

CFL3D Features

- Time-dependent conservation law form of the Reynolds-averaged Navier-Stokes equations
- Finite volume discretization at cell centers
- Upwind-biased convective/pressure term differencing using either Van Leer flux-vector-splitting or Roe flux-differencing-splitting
- Central-differencing of dissipative terms with several turbulence models

Alpha STAR CORPORATION BOEING

Flat Plate with No Pressure Gradient

CFL3D Features (continued)

- Spatial 3-factor implicit algorithm with either 5x5 block inversion or diagonal inversions applicable to steady and unsteady flows
- FAS multigrid acceleration for both steady and unsteady flows
- Local solution refinement via embedded meshes
- Domain decomposition using continuous, patched, interfaces and overlapped/embedded grids through chimera scheme
- Boundary conditions over subsets of block faces

Alpha STAR CORPORATION

BOEING

Local and Average Skin-Friction Coefficients

The local skin-friction coefficient is defined as the ratio of shear stress at the surface to the dynamic pressure

$$C_f = \frac{\tau_w}{0.5\,\rho_\infty U_\infty^2}$$

Where τ_w = Local shearing stress at the surface

The average skin-friction coefficient is defined as the integral of local skin friction along the flat plate

$$C_F = \frac{1}{X}\int_0^X C_f \, dX$$

Using the modified Schultz-Grunow equation for incompressible flow and an appropriate reference temperature approach, the compressible local and average skin-friction become:

$$C_f = 0.295\,\frac{T_\infty}{T^*}\,[\log(Re_x \frac{T_\infty}{T^*} \frac{\mu_\infty}{\mu^*})]^{-2.45}$$

and

$$C_F = 0.463\,\frac{T_\infty}{T^*}\,[\log(Re_x \frac{T_\infty}{T^*} \frac{\mu_\infty}{\mu^*})]^{-2.60}$$

Flat Plate with No Pressure Gradient

Local and Average Skin-Friction Coefficient (Definition)

- Local skin-friction coefficient

$$C_f = \frac{\tau_w}{0.5\,\rho_\infty\,U_\infty^2}$$

Where τ_w = local shearing stress at the surface

- Average skin-friction coefficient

$$C_F = \frac{1}{X}\int_0^X C_f\,dX$$

Flat Plate with No Pressure Gradient

Reference Temperature Approach

Incompressible skin-friction equations can be used to calculate compressible skin friction if an "appropriate" reference temperature is used to calculate ρ and μ in the equations:

The modified Schultz-Grunow equation is used for computation of incompressible local skin-friction as foloow:

$$Cfi = 0.295\,[\log(Re_x)]^{-2.45}$$

The Reynolds number correction calculated using the Southerland viscosity equation

$$\frac{\mu_\infty}{\mu^*} = \left(\frac{T_\infty}{T^*}\right)^{3/2} \frac{T^* + S}{T_\infty + S} \qquad (S = 198.7\ R^{o})$$

And the compressible local skin-friction can be written as

$$Cf = 0.295\,\frac{T_\infty}{T^*}\,[\log(Re_x\,\frac{T_\infty}{T^*}\,\frac{\mu_\infty}{\mu^*})]^{-2.45}$$

Flat Plate with No Pressure Gradient

Reference Temperature Approach

Incompressible skin-friction equations can be used to calculate compressible skin-friction if an "appropriate" reference temperature is used to calculate ρ and μ in the equations:

- Modified Schultz-Grunow equation

  $Cfi = 0.295\,[\log(Re_x)]^{-2.45}$

- The Reynolds number correction calculated using the Southerland viscosity equation

  $$\frac{\mu_\infty}{\mu^*} = \left(\frac{T_\infty}{T^*}\right)^{3/2} \frac{T^* + S}{T_\infty + S} \qquad (S = 198.7\ R^o)$$

- Compressible skin-friction

  $$Cf = 0.295\ \frac{T_\infty}{T^*}\left[\log\left(Re_x \frac{T_\infty}{T^*}\frac{\mu_\infty}{\mu^*}\right)\right]^{-2.45}$$

Alpha STAR CORPORATION

BOEING

Local and Average Skin-Friction Coefficients

Compressible local skin-friction coefficient

$$C_f = 0.295 \quad \frac{T_\infty}{T^*} \left[\log\left(Re_x \frac{T_\infty}{T^*} \frac{\mu_\infty}{\mu^*}\right)\right]^{-2.45}$$

Compressible average skin-friction coefficient

$$C_F = 0.463 \quad \frac{T_\infty}{T^*} \left[\log\left(Re_x \frac{T_\infty}{T^*} \frac{\mu_\infty}{\mu^*}\right)\right]^{-2.60}$$

Flat Plate with No Pressure Gradient

Local and Average Skin-Friction Coefficient (Empirical)

- Compressible local skin-friction coefficient

$$C_f = 0.295 \frac{T_\infty}{T^*} \left[\log\left(Re_x \frac{T_\infty}{T^*} \frac{\mu_\infty}{\mu^*}\right)\right]^{-2.45}$$

- Compressible average skin-friction coefficient

$$C_F = 0.463 \frac{T_\infty}{T^*} \left[\log\left(Re_x \frac{T_\infty}{T^*} \frac{\mu_\infty}{\mu^*}\right)\right]^{-2.60}$$

Flat Plate with No Pressure Gradient

Reference Temperature Empirical Formula

According to the mean-enthalpy concept, incompressible skin-friction relationships can be extended to compressible flow if an appropriate reference temperature is used. The reference temperature approach is used in order to use the incompressible skin-friction relationships. This means that assuming that compressible turbulent skin-friction drag could be obtained using well known incompressible skin-friction equations by evaluation all of the fluid properties that appear in the incompressible equations at some appropriate reference temperature. For an adiabatic wall conditions the reference temperature equation can be written in the following form:

$$\frac{T^*}{T_\infty} = 1 + Kr \,.\, r\,(\gamma - 1)\; M_\infty^{\;2}$$

Where γ is the ratio of specific heats, r is a temperature recovery factor, M_∞ is freestream Mach number, T_∞ and T^* are freestream and reference temperatures, respectively. Kr is a constant and will be determined empirically. Three different models are proposed in order to calculate the reference temperature. These formulae are shown below:

$$\frac{T^*}{T_\infty} = 1 + 0.1198\, M_\infty^{\;2} \qquad \text{Kulfan}$$

$$\frac{T^*}{T_\infty} = 1 + 0.1151\, M_\infty^{\;2} \qquad \text{Sommer and Short}$$

$$\frac{T^*}{T_\infty} = 1 + 0.1246\, M_\infty^{\;2} \qquad \text{Monaghan}$$

Flat Plate with No Pressure Gradient

Reference Temperature Empirical Formulae

For adiabatic wall conditions, the reference temperature equation can be written as

- $\dfrac{T^*}{T_\infty} = 1 + Kr \, . \, r \, (\gamma - 1) \; M_\infty^{\;2}$
  - Kulfan $\dfrac{T^*}{T_\infty} = 1 + 0.1198 \, M_\infty^{\;2}$
  - Sommer and Short $\dfrac{T^*}{T_\infty} = 1 + 0.1151 \, M_\infty^{\;2}$
  - Monaghan $\dfrac{T^*}{T_\infty} = 1 + 0.1246 \, M_\infty^{\;2}$

Where γ is the ratio of specific heats, r is a temperature recovery factor and Kr is a constant and will be determined empirically.

Velocity Profile Approximation

Velocity profile in turbulent boundary Layer can be approximated based on power law relation of the form as:

$$\frac{u}{U_\infty} = \left(\frac{y}{\delta}\right)^{1/N} \qquad \text{for } y \leq \delta$$

$$\frac{u}{U_\infty} = 1 \qquad \text{for } y \geq \delta$$

Where

u = Velocity at the height y from the wall

U_∞ = Free stream velocity

δ = Boundary layer thickness

Using experimental velocity profile can determine the value of reciprocal exponent N.

Flat Plate with No Pressure Gradient

Velocity Profile Approximation

- Velocity profile in turbulent boundary Layer can be approximated based on power law as:

$$\frac{u}{U_\infty} = \left(\frac{y}{\delta}\right)^{1/N} \qquad \text{for} \quad y \leq \delta$$

$$\frac{u}{U_\infty} = 1 \qquad \text{for} \quad y \geq \delta$$

Where

u = Velocity at the height y from the wall

U_∞ = Free stream velocity

δ = Boundary layer thickness

Flat Plate with No Pressure Gradient

Mach Numbers and Reynolds Numbers

A series of computational runs for turbulent boundary layer were performed on smooth adiabatic flat plate with no pressure gradient and for subsonic to supersonic Mach numbers. The range of Reynolds and Mach numbers are listed in Table. The range of Reynolds and Mach numbers were selected such that to cover the transonic and supersonic cruise Mach number of HSCT aircraft.

Flat Plate with No Pressure Gradient

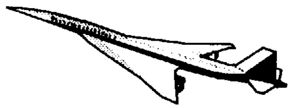

High Speed Aerodynamics, Long Beach

Mach Numbers and Reynolds Numbers

M_∞	$Re_x \times 10^{-6}$
0.31	6.78
0.50	1, 5, 10, 50, 100
1.50	1, 5, 10, 50, 100
2.25	1, 5, 10, 50, 100
2.50	1, 5, 10, 50, 100

Alpha STAR CORPORATION

BOEING

Flat Plate with No Pressure Gradient

High Speed Aerodynamics, Long Beach

CPU Timing On HP Platform

The CPU time for all three turbulence models and four levels of mesh are listed in Table. The table shows that the CPU time for one-, and two-equations turbulence models of Spalart-Allmaras and Menter's k-ω SST are comparable, whereas the zero-order equation of Baldwin-Lomax turbulence model uses less CPU time for the same conditions as the other two turbulence models.

Alpha STAR CORPORATION

BOEING

CPU Timing for Flat Plate with No Pressure Gradient

CPU Timing On HP Platform

Grid	Turbulence Model		
	Baldwin-Lomax	Spalart-Allmaras	Menter's k-Omega SST
Coarse 17 x 25	45 Sec.	82 Sec.	84 Sec.
Medium 1 33 x 49	420 Sec.	580 Sec.	586 Sec.
Medium 2 65 x 97	1130 Sec.	1410 Sec.	1480 Sec.
Fine 129 x 193	6679 Sec.	7570 Sec.	8100 Sec.

Flat Plate with No Pressure Gradient

Computational Grid

In grid topology, a single zone grid was used for the computations. The flat plate length was normalized to unity such that, the leading and trailing edges were located at the coordinate X = 0.0 and X = 1.0, respectively. Four levels of grid are used for grid sensitivity study. These are coarse mesh (17 x 25), medium 1 mesh (33 x 49), medium 2 mesh (65 x 97), and fine mesh (129 x 193). The grid is uniformly distributed in the streamwise (X-direction) direction and exponentially in the narmal (Z - direction) direction to the edge of boundary layer and uniformly after that to the the upper bound.

Flat Plate with No Pressure Gradient

Computational Grid

- Single zone grid
  - Number of coarser grids for mesh sequencing
  - Mesh sequencing for global grid
  - Uniform in streamwise direction
  - Exponential in normal direction
  - CFL3D grid format

Flat Plate with No Pressure Gradient

Computational Grid (continued)

- Mesh sequencing
  - Coarse mesh 17 x 25 = 425
  - Medium 1 mesh 33 x 49 = 1617
  - Medium 2 mesh 65 x 97 = 6305
  - Fine mesh 129 x 193 = 24897

Computational Grid (continued)

The streamwise (X-direction) and normal (Z-direction) direction grids are shown in the following Figures for turbulent flows over flat plate.

Single Zone Grid for Flat Plate with No Pressure Gradient

High Speed Aerodynamics, Long Beach

Streamwise Direction Grid

Fine Mesh 129 x 193

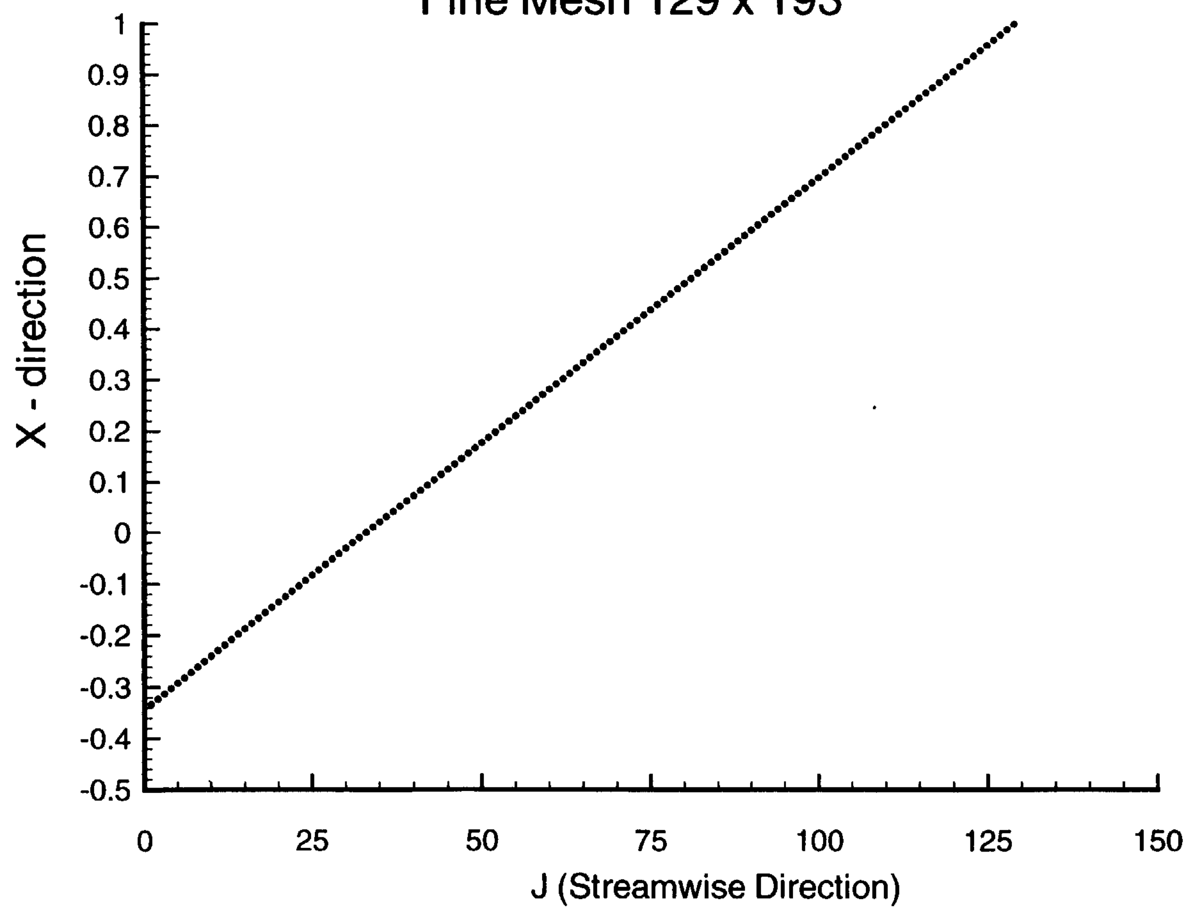

Alpha STAR CORPORATION

BOEING

Single Zone Grid for Flat Plate with No Pressure Gradient

High Speed Aerodynamics, Long Beach

Streamwise Direction Grid

Fine Mesh 129 x 193

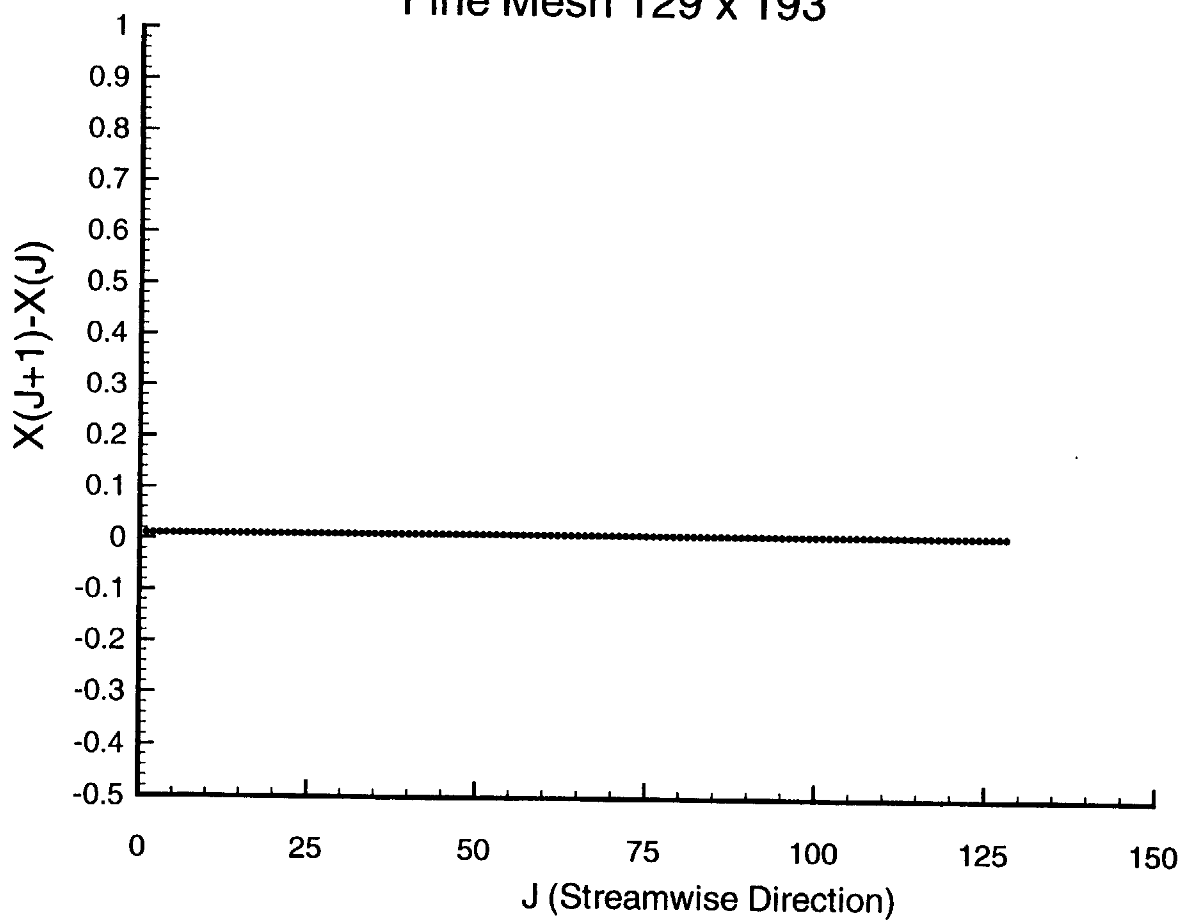

Alpha STAR CORPORATION

BOEING

Single Zone Grid for Flat Plate with No Pressure Gradient

High Speed Aerodynamics, Long Beach

Normal Direction Grid

Fine Mesh 129 x193

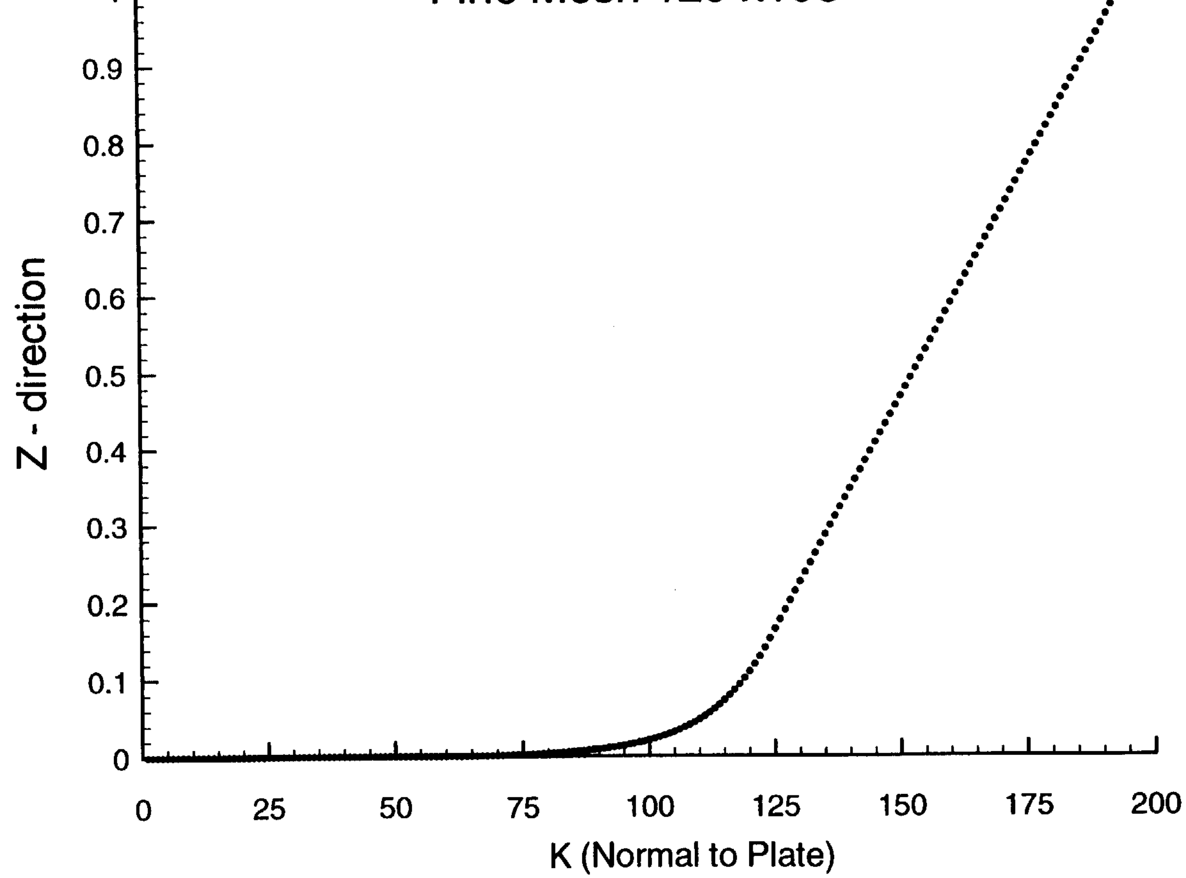

Alpha STAR CORPORATION

BOEING

Single Zone Grid for Flat Plate with No Pressure Gradient

High Speed Aerodynamics, Long Beach

Normal Direction Grid

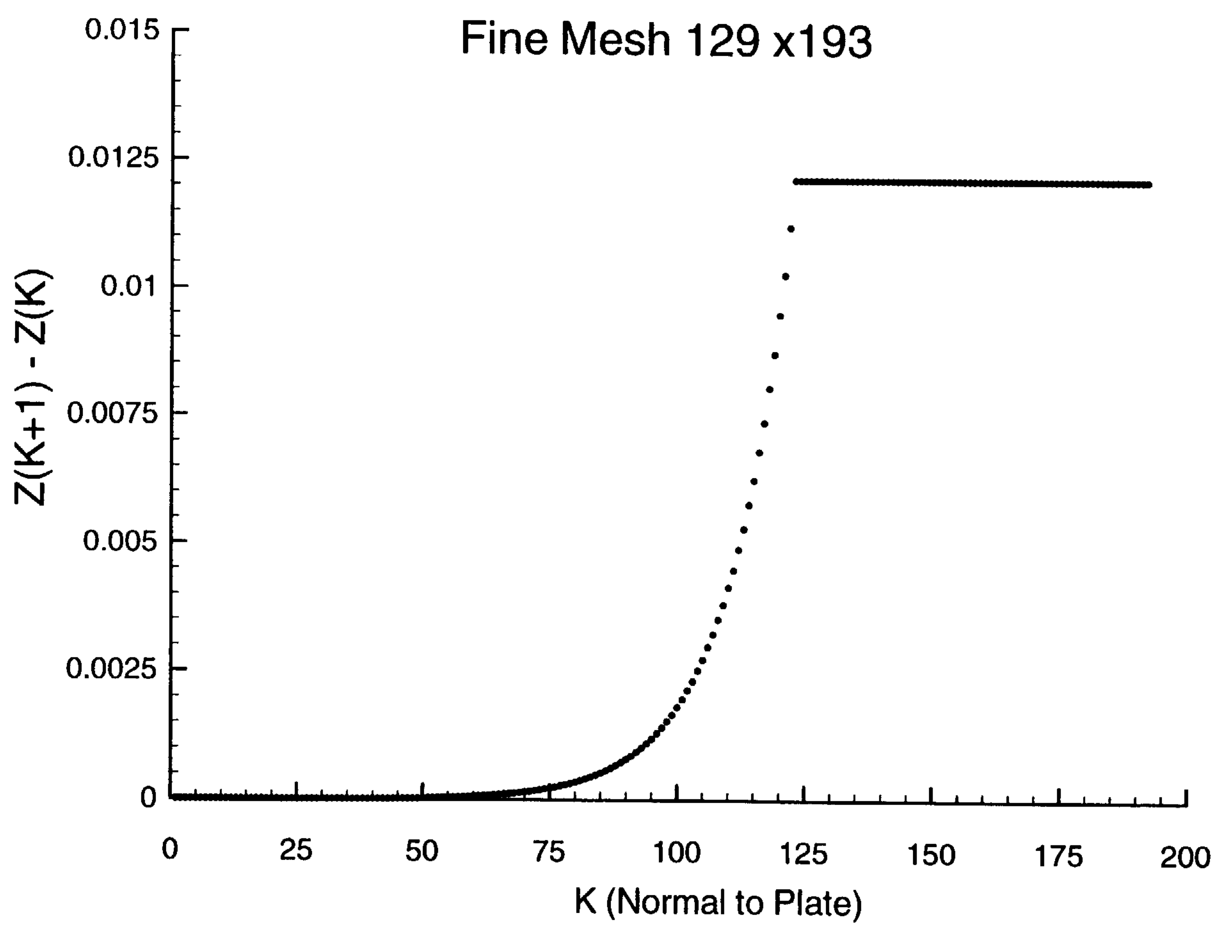

Alpha STAR CORPORATION

BOEING

Computational Grid (continued)

The computational grids are shown in the following Figures for the coarse, medium 1, medium 2, and the fine grid, respectively.

Flat Plate with No Pressure Gradient

Computational Grid

Coarse Mesh 17 x 25

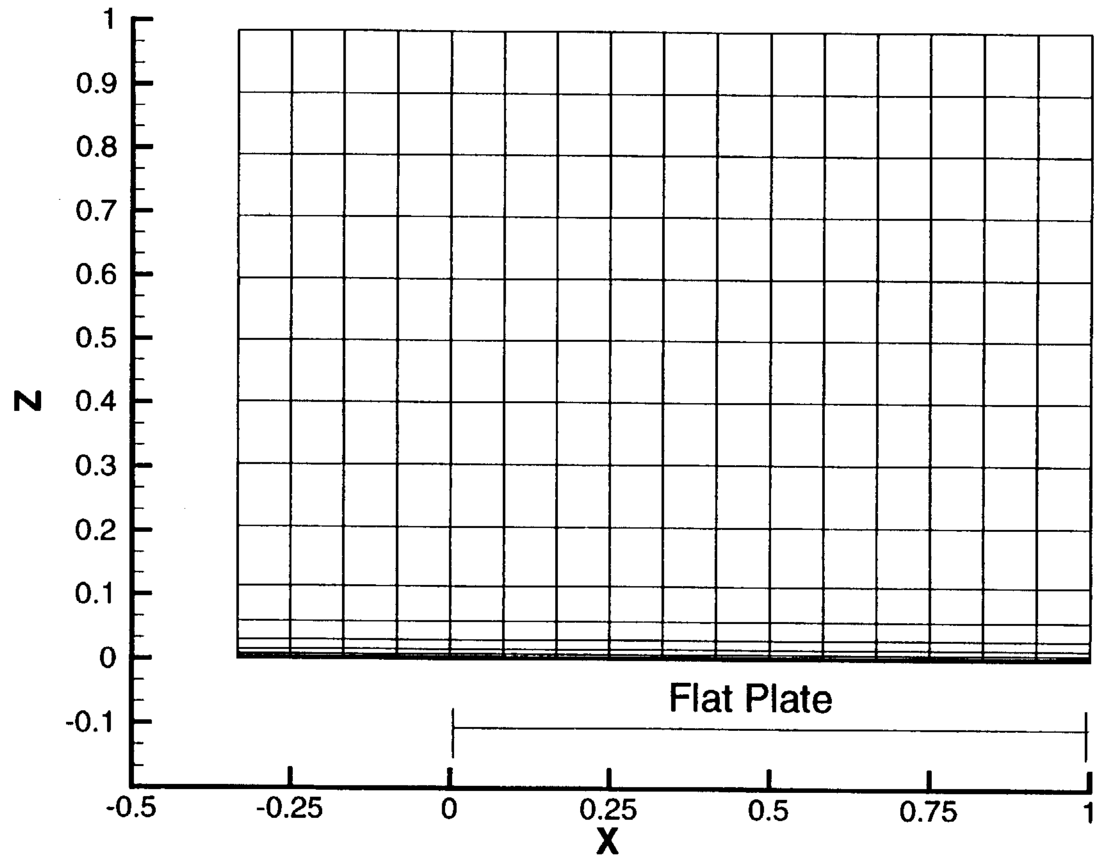

Flat Plate with No Pressure Gradient

High Speed Aerodynamics, Long Beach

Computational Grid
Medium 1 Mesh 33 x 49

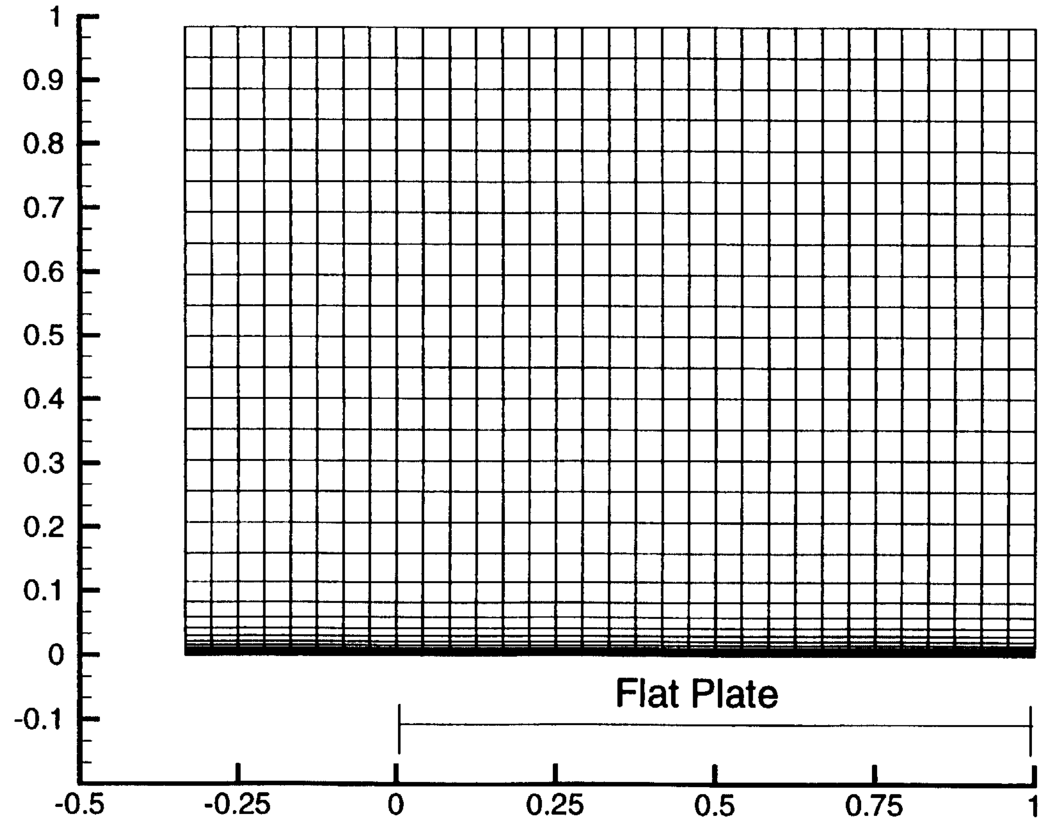

Alpha STAR CORPORATION

BOEING

Flat Plate with No Pressure Gradient

High Speed Aerodynamics, Long Beach

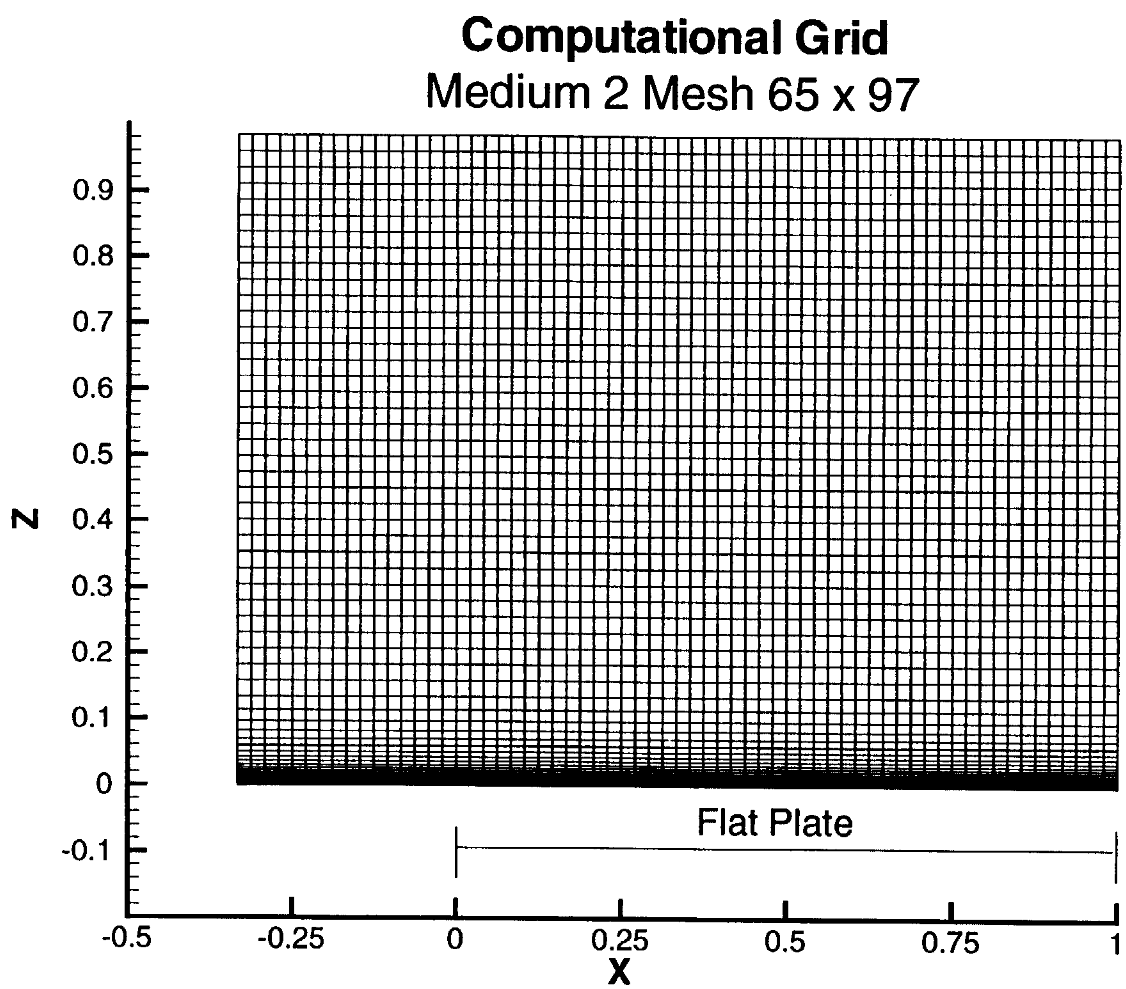

Alpha STAR CORPORATION

Flat Plate with No Pressure Gradient

High Speed Aerodynamics, Long Beach

Computaional Grid

Fine Mesh 129 x 193

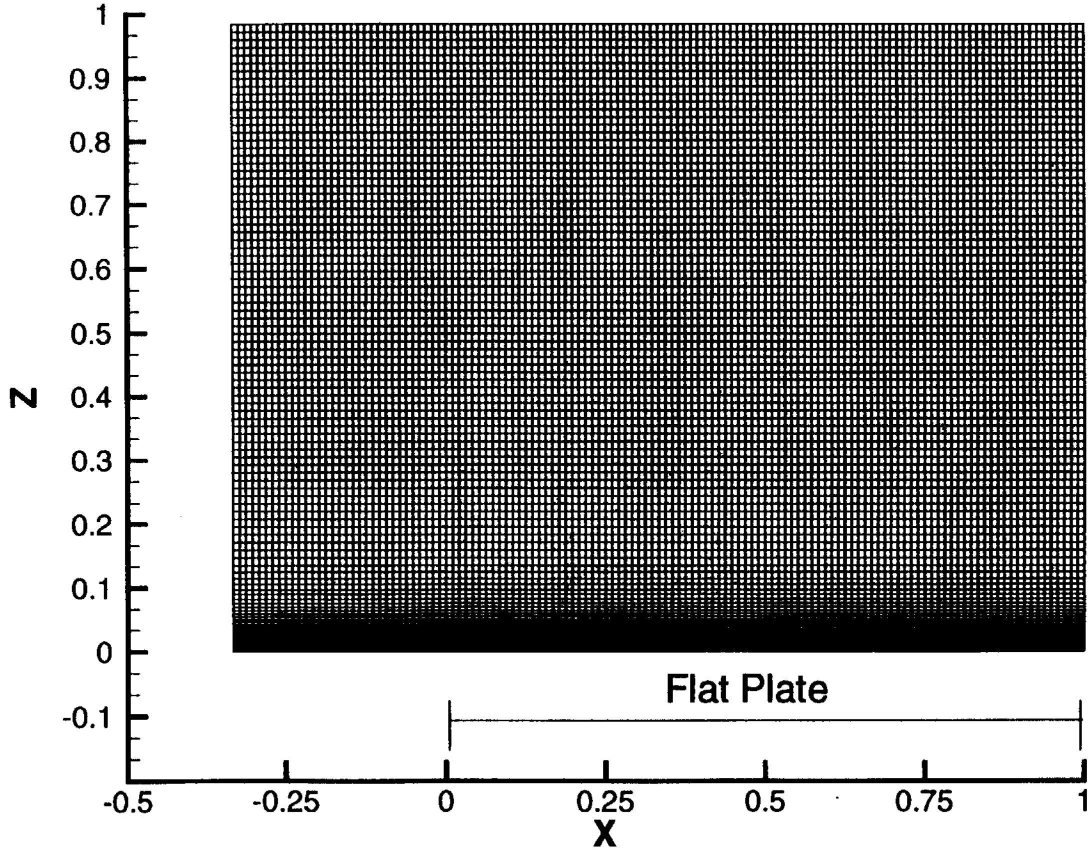

Alpha STAR CORPORATION

BOEING

Turbulence Model Equations

CFL3D has several turbulence capability. Three turbulence models of different levels of complexity are being used for the computation of CFL3D solver. The first turbulence model which is widely used in CFD community is zero-equation model. The model is based on Baldwin-Lomax model which is algebraic model. The second model is one- equation model based on Spalarat-Allmaras model. This model solve the eddy viscosity as a single field equation. The third model is two-equation model based on Menter's k- ω shear stress transpor (SST) model. The model solves two equation simultaneously in terms of turbulence kinetic energy and rotational velocity or vorticity.

Flat Plate with No Pressure Gradient

Turbulence Model Equations

- Zero - equation model
  - Baldwin - Lomax
- One - equation model
  - Spalart - Allmaras
- Two - equation model
  - Menter's k - ω SST

Flat Plate with No Pressure Gradient

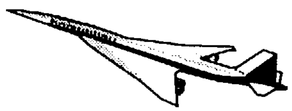

High Speed Aerodynamics, Long Beach

Computational Results

A series of computational runs for turbulent boundary layer flow were performed on a adiabatic flat plate with no pressure gradient for subsonic to supersonic Mach number. The flow conditions ($M_\infty = 0.50$, 1.50, 2.25, and 2.50 at $Re = 1 \times 10^6$, 5×10^6, 10×10^6, 50×10^6, and 100×10^6) were chosen such that they bracketed the transonic and supersonic cruise Mach numbers of an HSCT aircraft. The computational results are compared with empirical skin-friction correlations by Sommer and Short, Kulfan, and Monaghan.

A typical residual and drag coefficient convergence summary are plotted for Baldwin-Lomax, Spalarat-Allmaras, and Menter's k-ω SST turbulence models.

Alpha STAR CORPORATION

BOEING

Flat Plate with No Pressure Gradient

High Speed Aerodynamics, Long Beach

Computational Results

- Residual and drag coefficient convergence cistories
- Local skin-friction coefficient versus Reynolds number
- Average skin-friction coefficient versus Reynolds number
- Local skin-friction coefficient versus Mach number
- Average skin-friction coefficient versus Mach number

Alpha STAR CORPORATION

BOEING

Residual Convergence Summary for Flat Plate with No Pressure Gradient

Baldwin-Lomax Turbulence Model
CFL3D, $M_\infty = 0.50$, $Re_x = 1 \times 10^6$

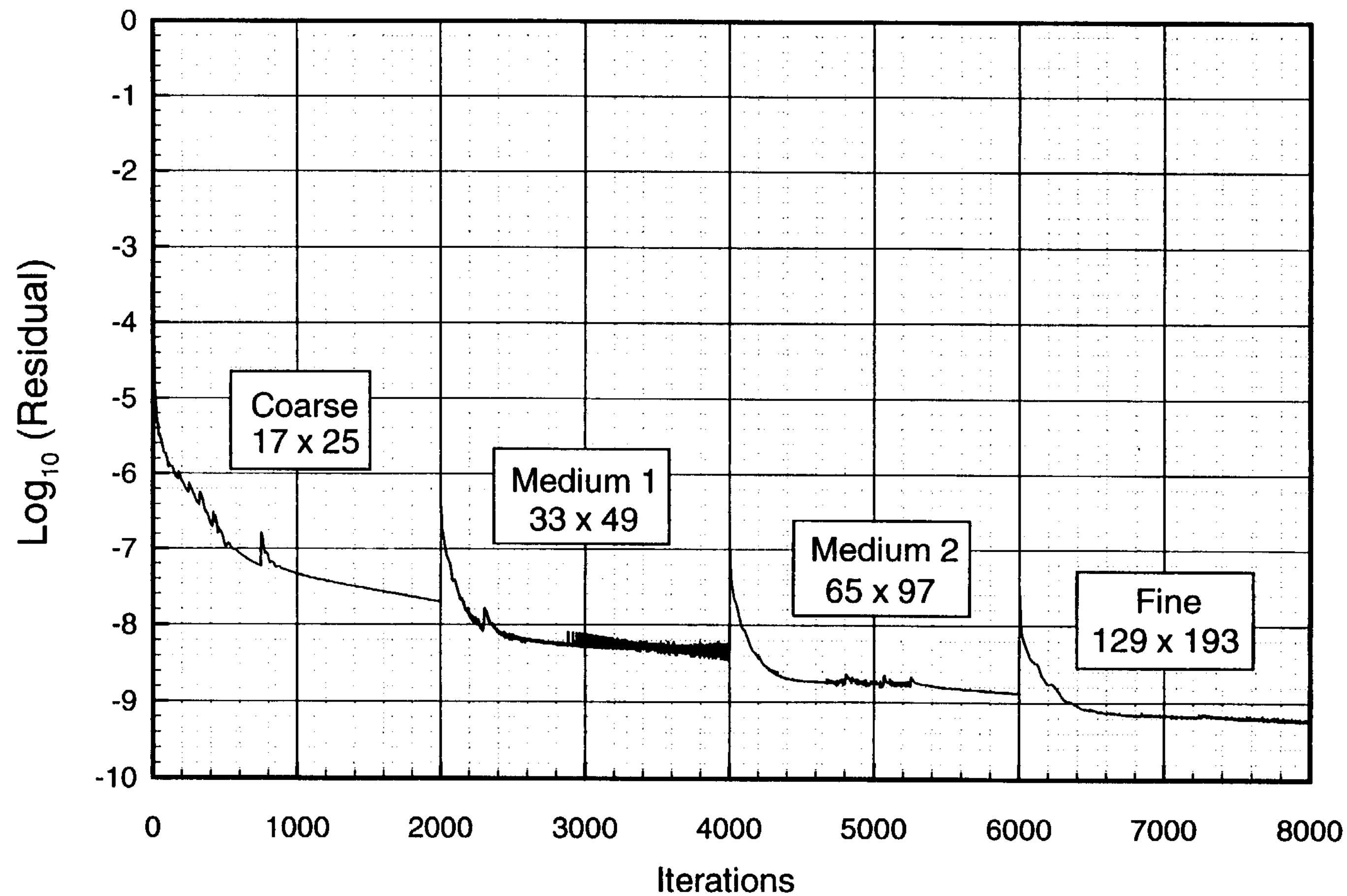

Alpha STAR CORPORATION

BOEING

Drag Convergence Summary for Flat Plate with No Pressure Gradient

High Speed Aerodynamics, Long Beach

Baldwin-Lomax Turbulence Model
CFL3D, $M_\infty = 0.50$, $Re_x = 1 \times 10^6$

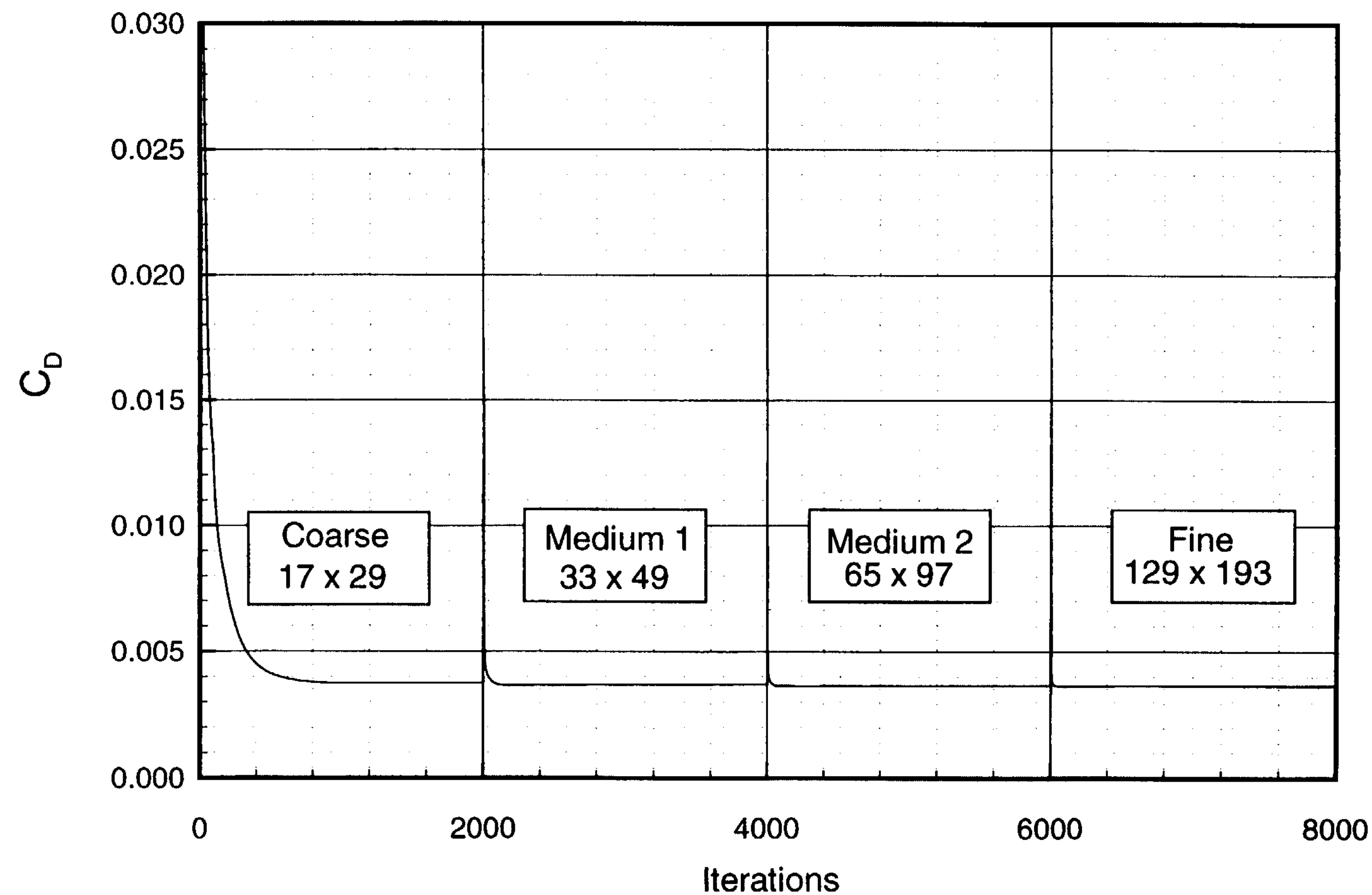

Alpha STAR CORPORATION

BOEING

Residual Convergence Summary for Flat Plate with No Pressure Gradient

High Speed Aerodynamics, Long Beach

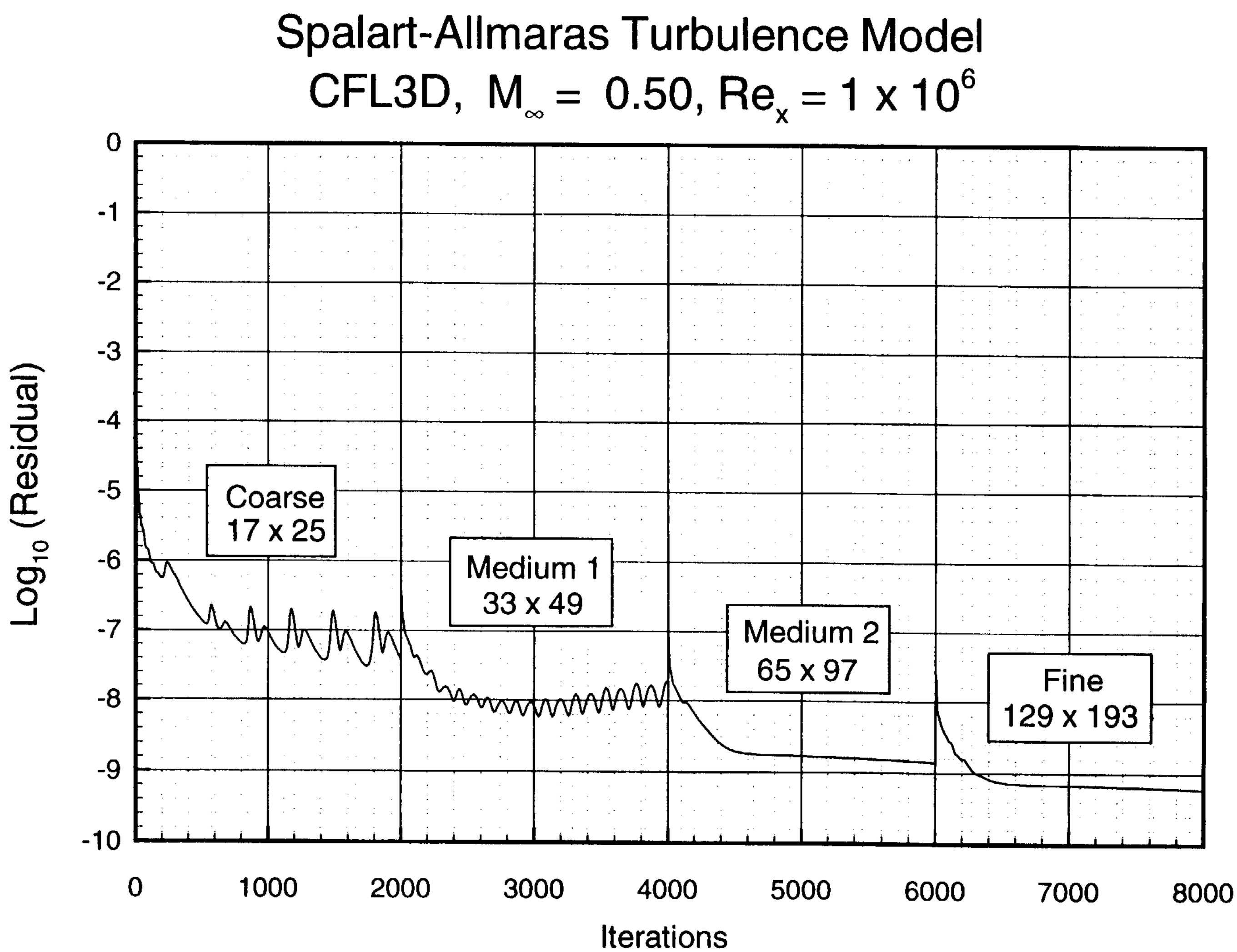

Alpha STAR CORPORATION

BOEING

Drag Convergence Summary for Flat Plate with No Pressure Gradient

Spalart-Allmaras Turbulence Model
CFL3D, $M_\infty = 0.50$, $Re_x = 1 \times 10^6$

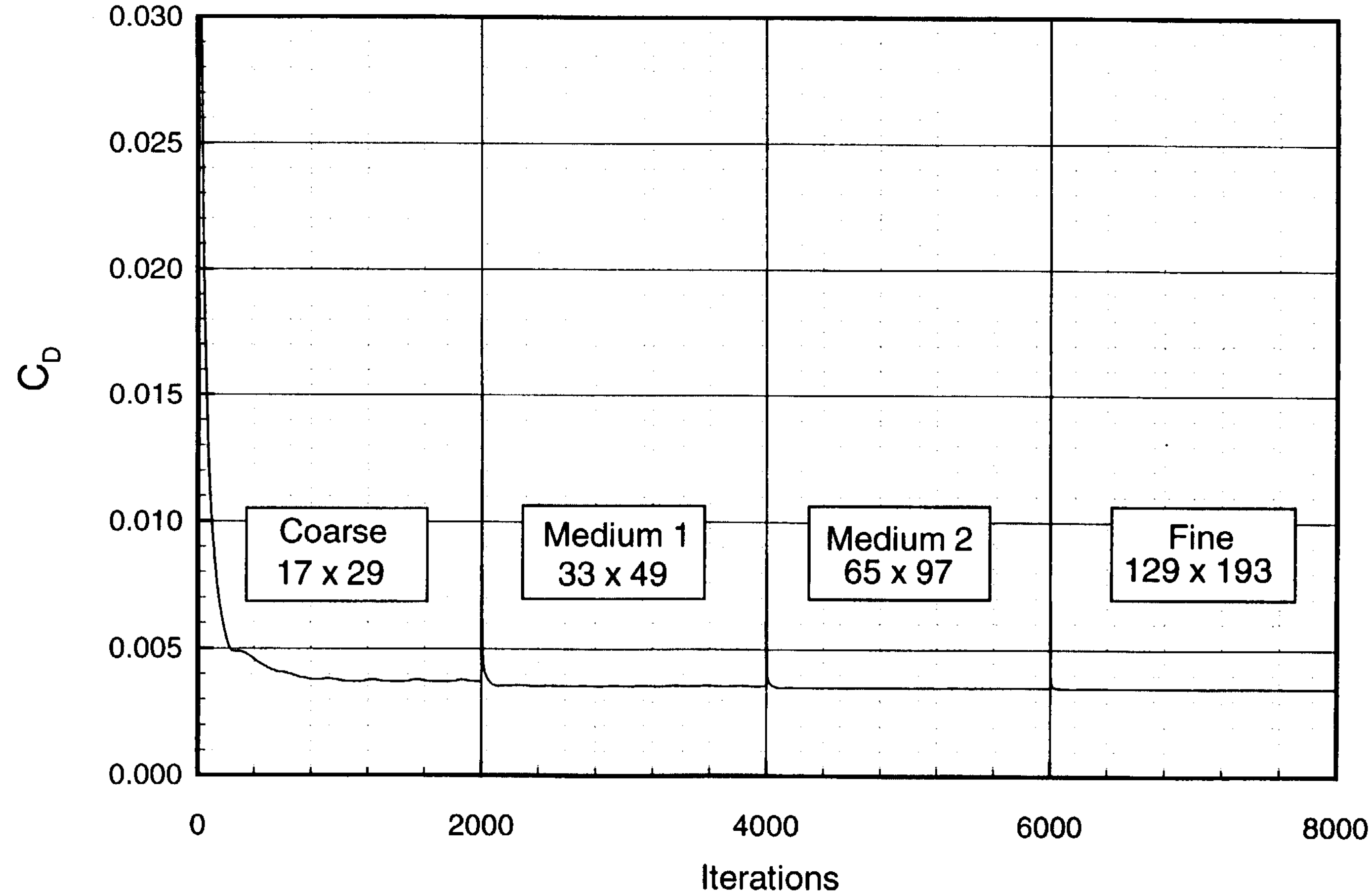

Residual Convergence Summary for Flat Plate with No Pressure Gradient

High Speed Aerodynamics, Long Beach

Menter's k-ω SST Turbulence Model

CFL3D, $M_\infty = 0.50$, $Re_x = 1 \times 10^6$

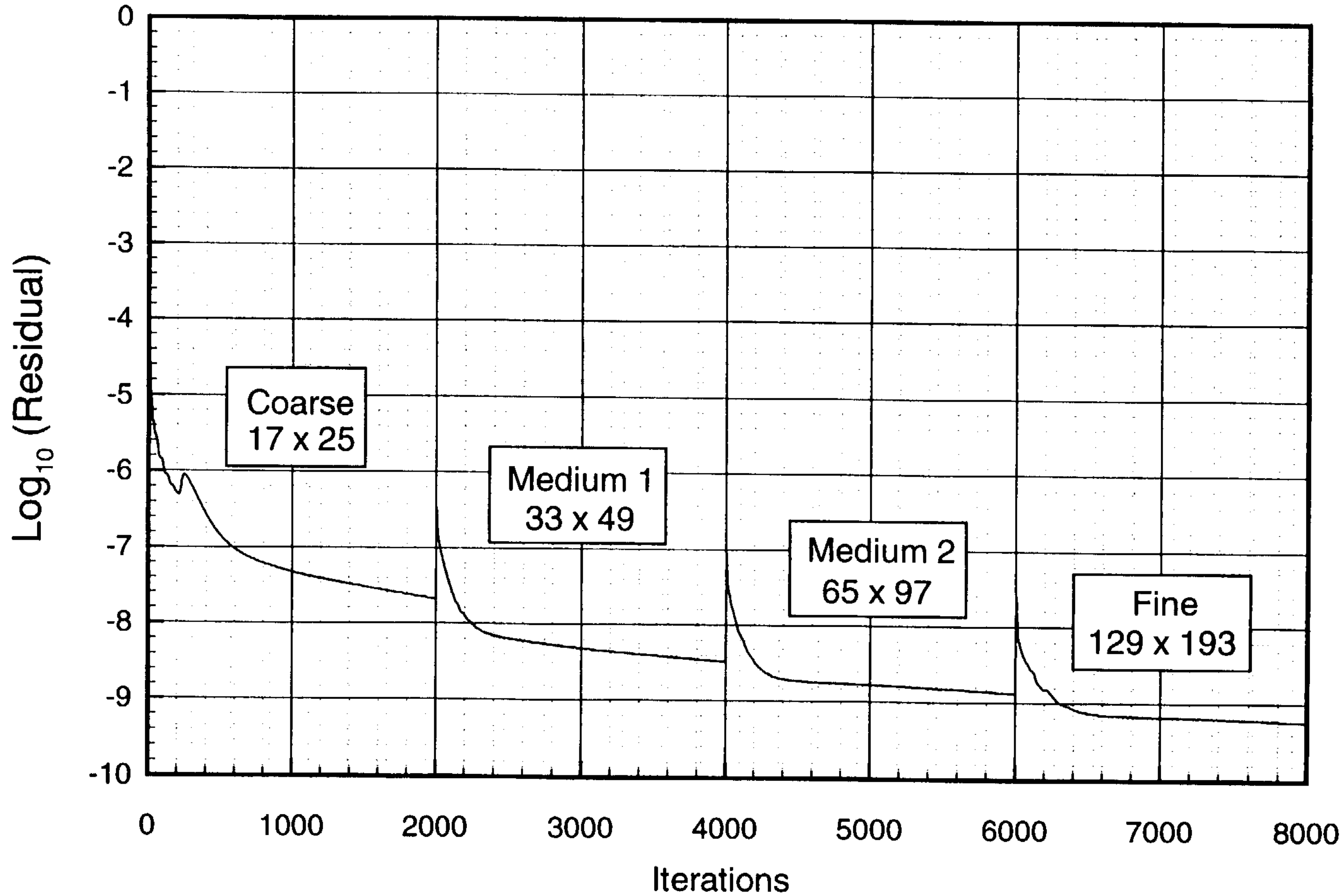

Alpha STAR CORPORATION

BOEING

Drag Convergence Summary for Flat Plate with No Pressure Gradient

High Speed Aerodynamics, Long Beach

Menter's k-ω SST Turbulence Model
CFL3D, $M_\infty = 0.50$, $Re_x = 1 \times 10^6$

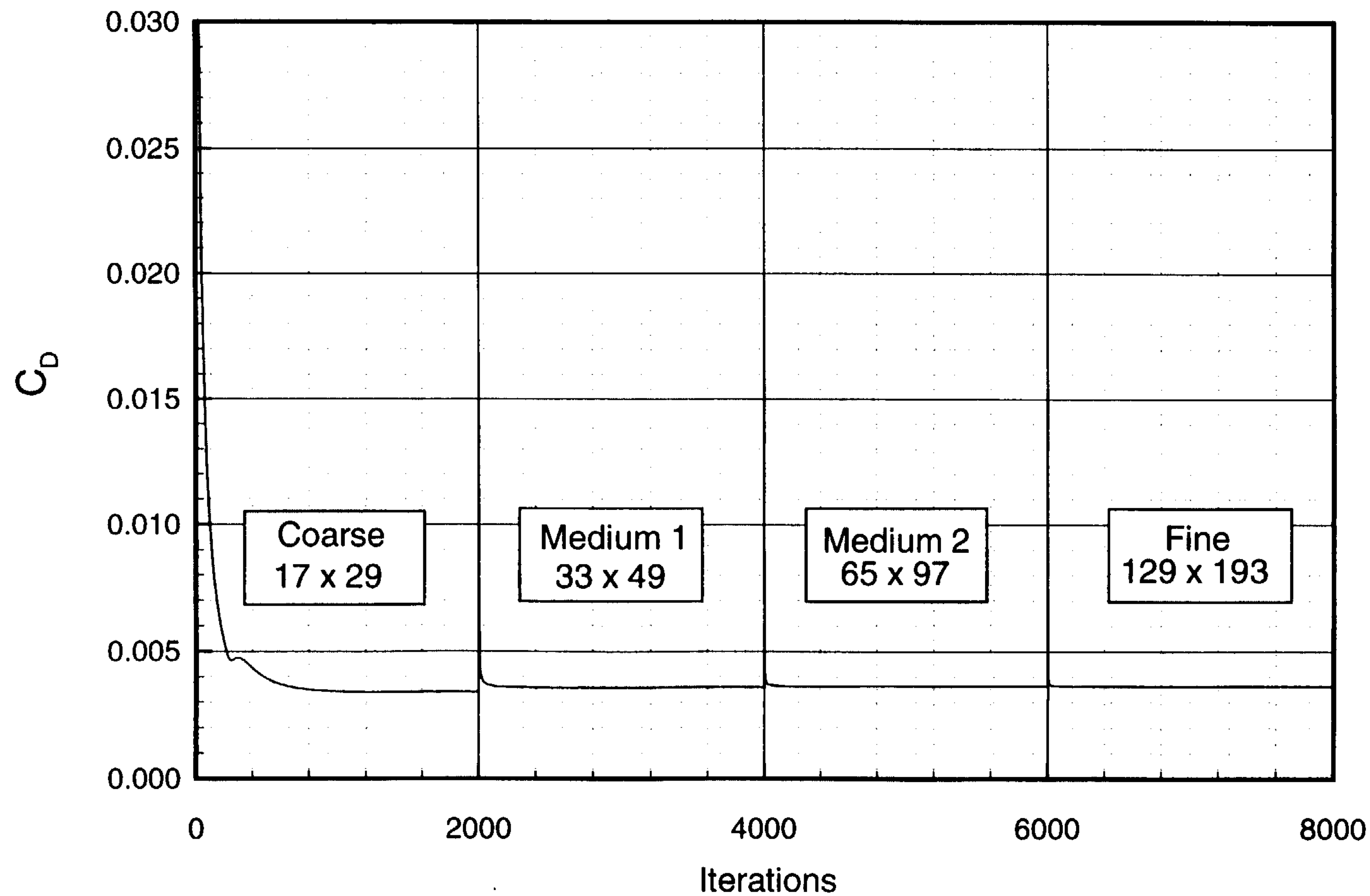

Alpha STAR CORPORATION

BOEING

Computational Results (continued)

The variation of local and average skin-friction with Reynolds number at $M_\infty = 2.50$ are plotted. For this Mach number, the local skin friction results obtained with Baldwin-Lomax and Menter's k-ω SST turbulence models show an acceptable agreement with the empirical data over the entire range of Reynolds numbers considered. The Spalart-Allmaras turbulence model compares reasonably well with the empirically-determined local skin-friction at $Re = 1 \times 10^6$, but slightly overpredicts the empirical values for higher Reynolds numbers.

The results from Baldwin-Lomax predicts considerably higher average skin-friction than any of the empirical methods for $Re < 10 \times 10^6$. This trend is opposite to that observed for Spalart-Allmaras predictions. The average skin-friction values predicted by Menter's k-ω SST model are in good agreement with the empirical data over the full range of Reynolds numbers considered in this study. The results of the other Mach numbers indicate that, in general , the Bladwin-Lomax and SST models both agree reasonably well with the empirical average skin-friction values at $M_\infty = 0.50$, 1.50 for all Reynolds numbers considered. As the Mach number increases to $M_\infty = 2.25$ and 2.50, Menter's SST model shows the best correlation with the empirical data. The Spalart-Allmaras turbulence model, on the other hand, significantly underpredicts the empirical average skin-friction data for low Reynolds numbers ($Re<5x10^6$) at all four Mach number.

The agreement with empirical results improves for higher Reynolds numbers, but the Spalart-Allmaras computations tend to overpredict the empirical data as the Reynolds numbers increases. The Spalart-Allmaras turbulence model has a built-in transition model that simulates a laminar run with reduced local skin-friction immediately downstream of the leading edge. The extend of this region of laminar flow decreases as the free stream Reynolds number oincreases. This explains why the correlation between the Spalart-Allmaras and the empirical results is poor at low Reynolds Number.

Skin Friction for Flat Plate with No Pressure Gradient

High Speed Aerodynamics, Long Beach

CFL3D, Navier-Stokes, 129 x 193 Fine Grid, $M_\infty = 2.50$

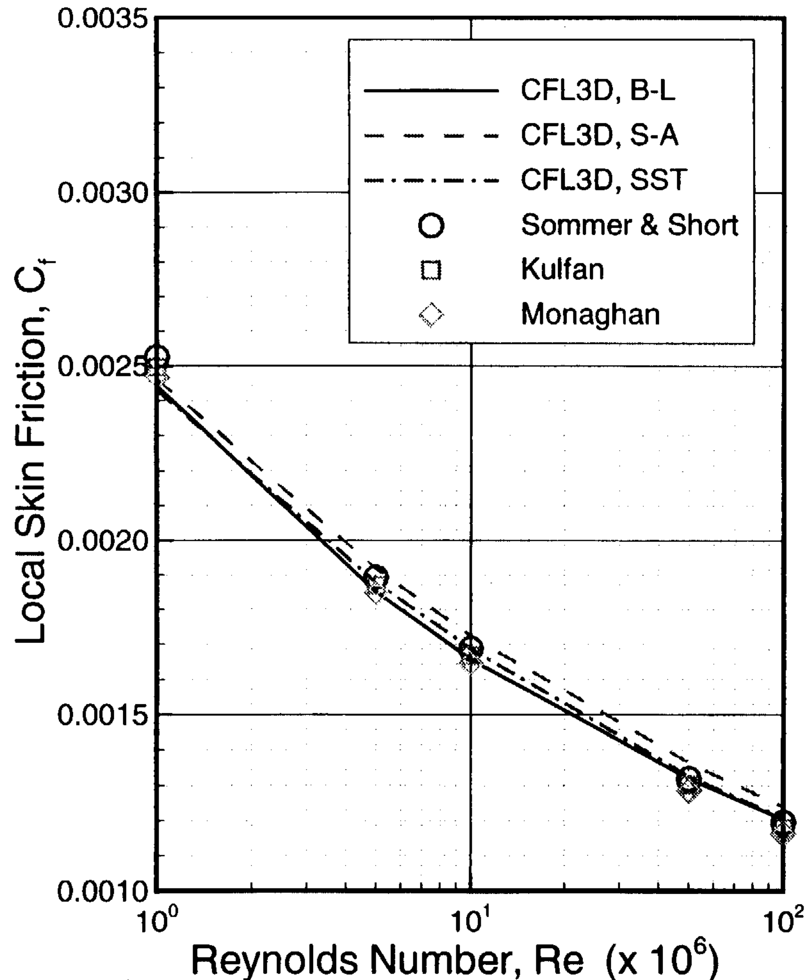

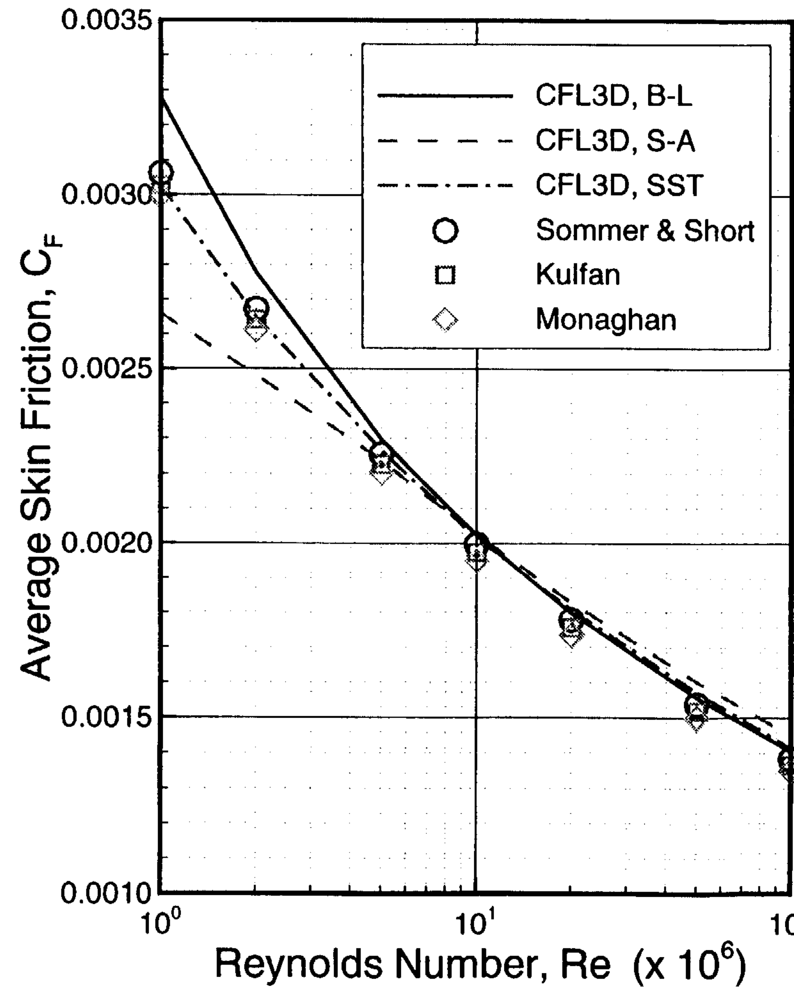

Alpha STAR CORPORATION

BOEING

Flat Plate with No Pressure Gradient

Computational Results (continued)

The variation of local and average skin-friction values at Re = 10×10^6 is shown that for low Mach numbers (M_∞ = 0.5 and 1.5), the Spalart-Allmaras model agrees better with the empirical local skin-friction data than the other two turbulence models. As the Mach number increases, however, the Menter's k-ω SST model seems to be in better agreement with the empirical data. In terms of average skin-friction, all three models show almost the same agreement with the empirical data (except at M_∞=0.5, where the Baldwin-Lomax prediction is slightly lower than the other two turbulence models results)

Skin Friction for Flat Plate with No Pressure Gradient

High Speed Aerodynamics, Long Beach

CFL3D, Navier-Stokes, 129 x 193 Fine Grid, Re = 10×10^6

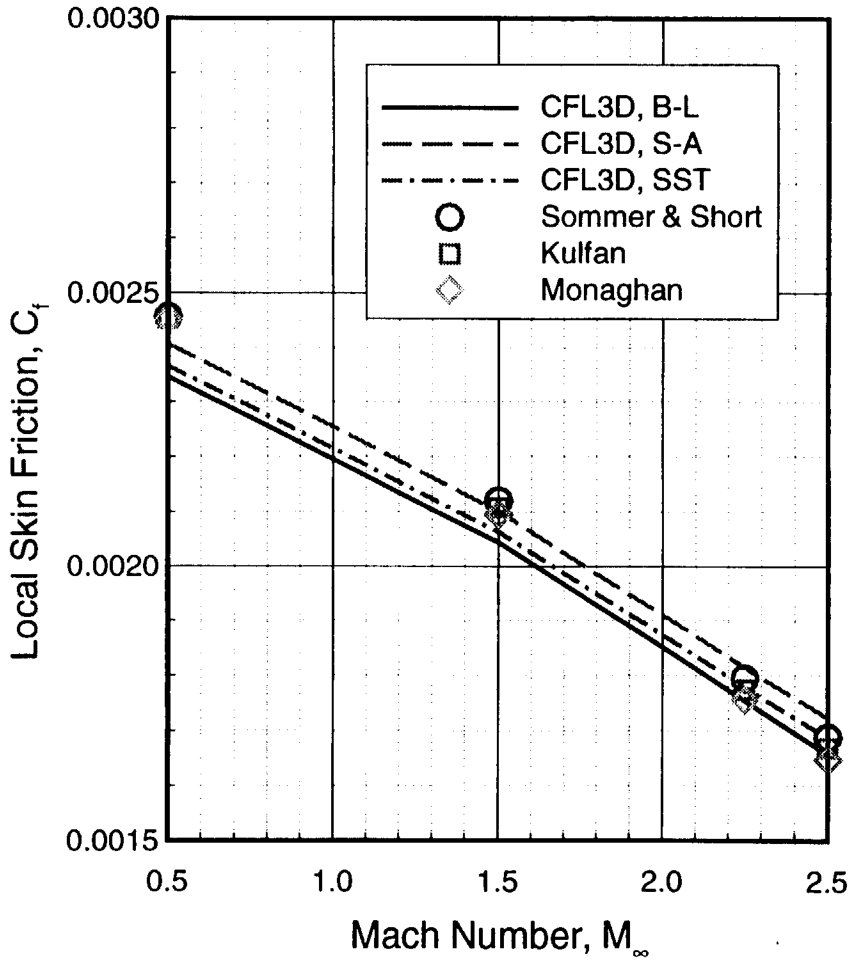

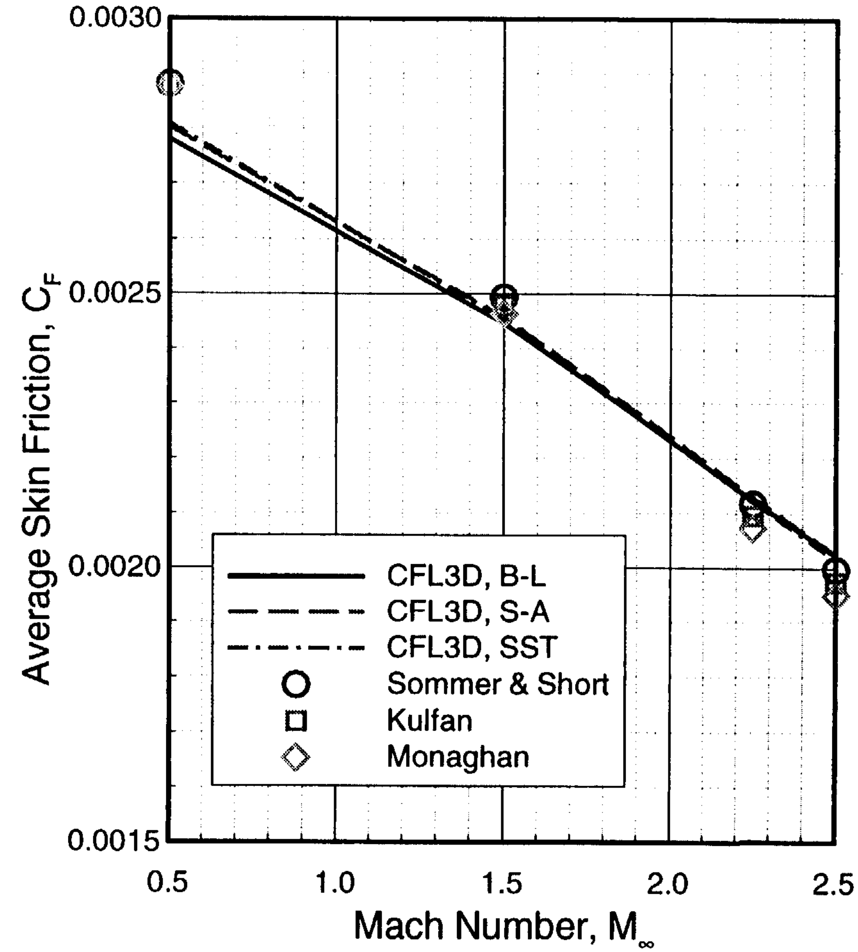

Flat Plate with No Pressure Gradient

High Speed Aerodynamics, Long Beach

Comparison of Local Skin Friction Drag

The variation of computed local skin-friction along the flat plate is presented with the Baldwin-Lomax, Spalart-Allmaras, and Menter's k-ω SST turbulence models. This serves two purposes. First, it helps to explain the trends observed in previous figure as compared to local skin-friction results from SST turbulence model. The Baldwin-Lomax results predict higher local skin-friction near the leading edge. This result correlates well with the larger predicted average skin-friction coefficient, compared to the empirical data and the SST results, for $Re_x < 10 \times 10^6$. The Spalart-Allmaras turbulence model has a built-in transition model which causes a laminar run with reduced local skin-friction immediately downstream of the leading edge. The extent of this region of laminar flow diminishes with increasing freestrem Reynolds number. This expalin why the match between the empirical and the Spalart-Allmaras results improves with increasing Reynolds number.

This figure also indicates that the boundary layer flow is properly resolved in these calculations. Apart from the transitional flow close to the leading edge, all three sets of Navier-Stokes solutions predict closely matching local skin-friction results for the same local Reynolds number.

Alpha STAR CORPORATION

BOEING

Local Skin Friction for Flat Plate with No Pressure Gradient

High Speed Aerodynamics, Long Beach

CFL3D, Navier-Stokes, 129 x 193 Fine Grid, $M_\infty = 2.50$

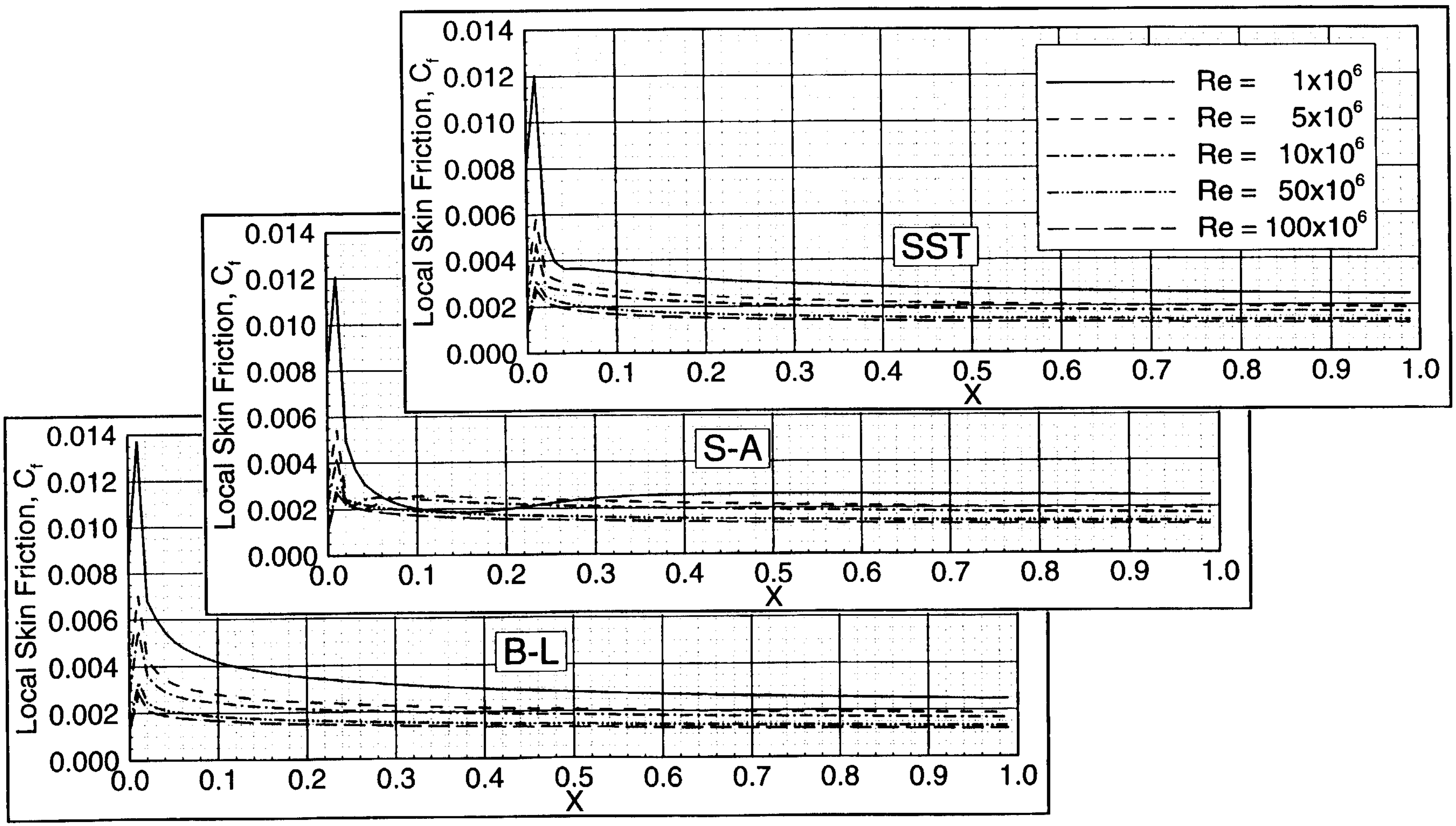

Alpha STAR CORPORATION

BOEING

Effect of Grid Sensitivity

The results from grid convergence study are shown using CFL3D Navier-Stokes solver with the Baldwin-Lomax, Spalart-Allmaras, and Menter's k-ω SST turbulence models. These figures show the variation of local skin-friction at a given local Reynolds number with grid density. The plotting format is chosen such that the results from successive grid refinements should fall on a straight line. This is because CFL3D is formally second-order accurate in space. This means that doubling the grid density (i.e., halving the spatial step size) should yield a fourfold increase in accuracy.

It appears that the results with the Spalart-Allmaras and Menter's k-ω SST models are spatially converged since they roughly fall on a straight line and an asymptotoic value for finite grid density can be estimated. The results for Baldwin-Lomax model appear neither spatially converged nor second-order accuarate. Additional solutions on even finer computational grids were performed. The conclusion was that the coarse grid for Baldwin-Lomax was too coarse, but going to one level finer mesh resolved the asymptotic behaviour of the grid density for zero-order equation turbulence model.

Flat Plate with No Pressure Gradient: Effect of Grid Density

CFL3D, Baldwin-Lomax, $M_\infty = 0.50$

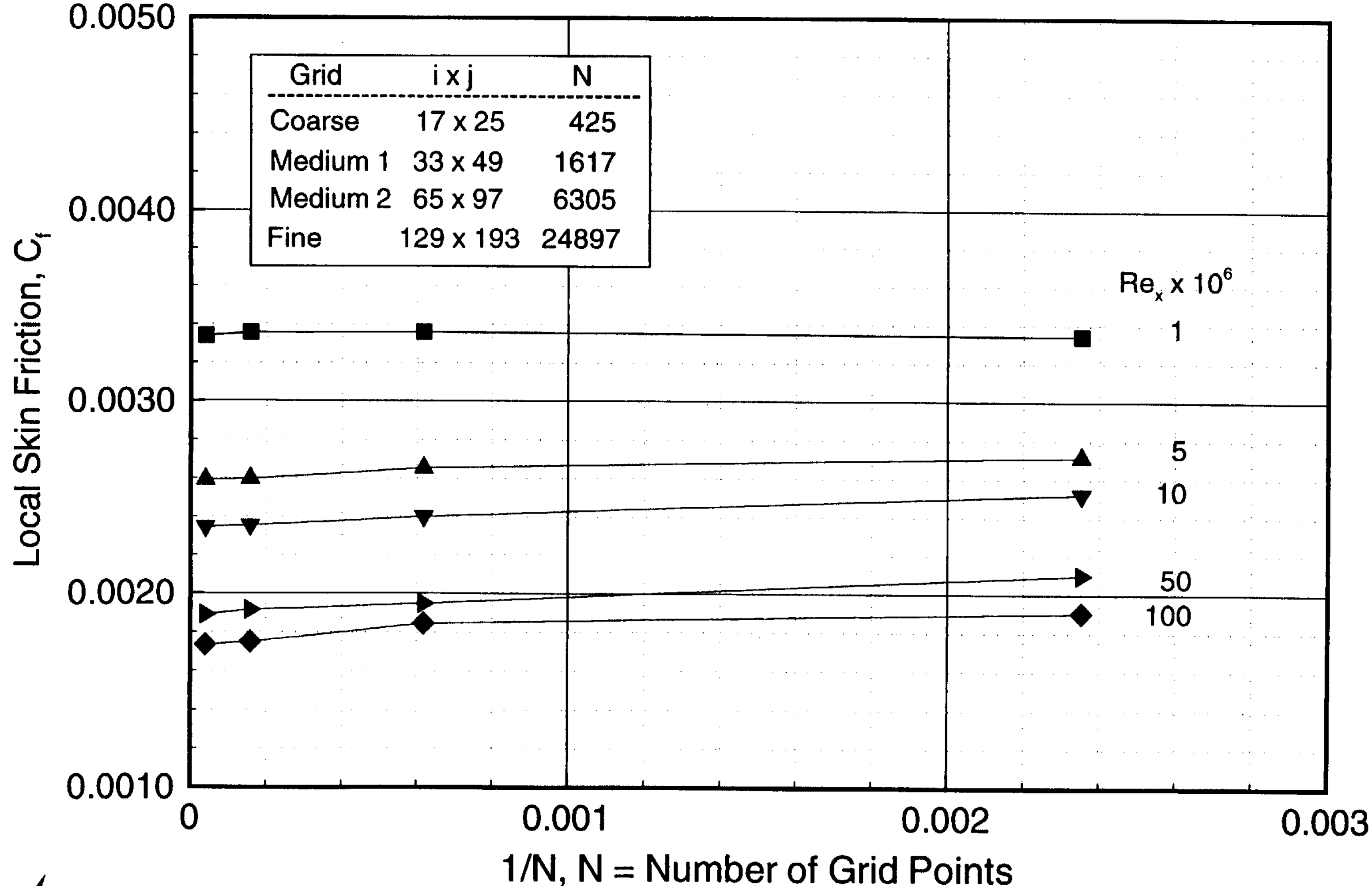

Grid	i x j	N
Coarse	17 x 25	425
Medium 1	33 x 49	1617
Medium 2	65 x 97	6305
Fine	129 x 193	24897

Flat Plate with No Pressure Gradient: Effect of Grid Density

High Speed Aerodynamics, Long Beach

CFL3D, Spalart-Allmaras, $M_\infty = 0.50$

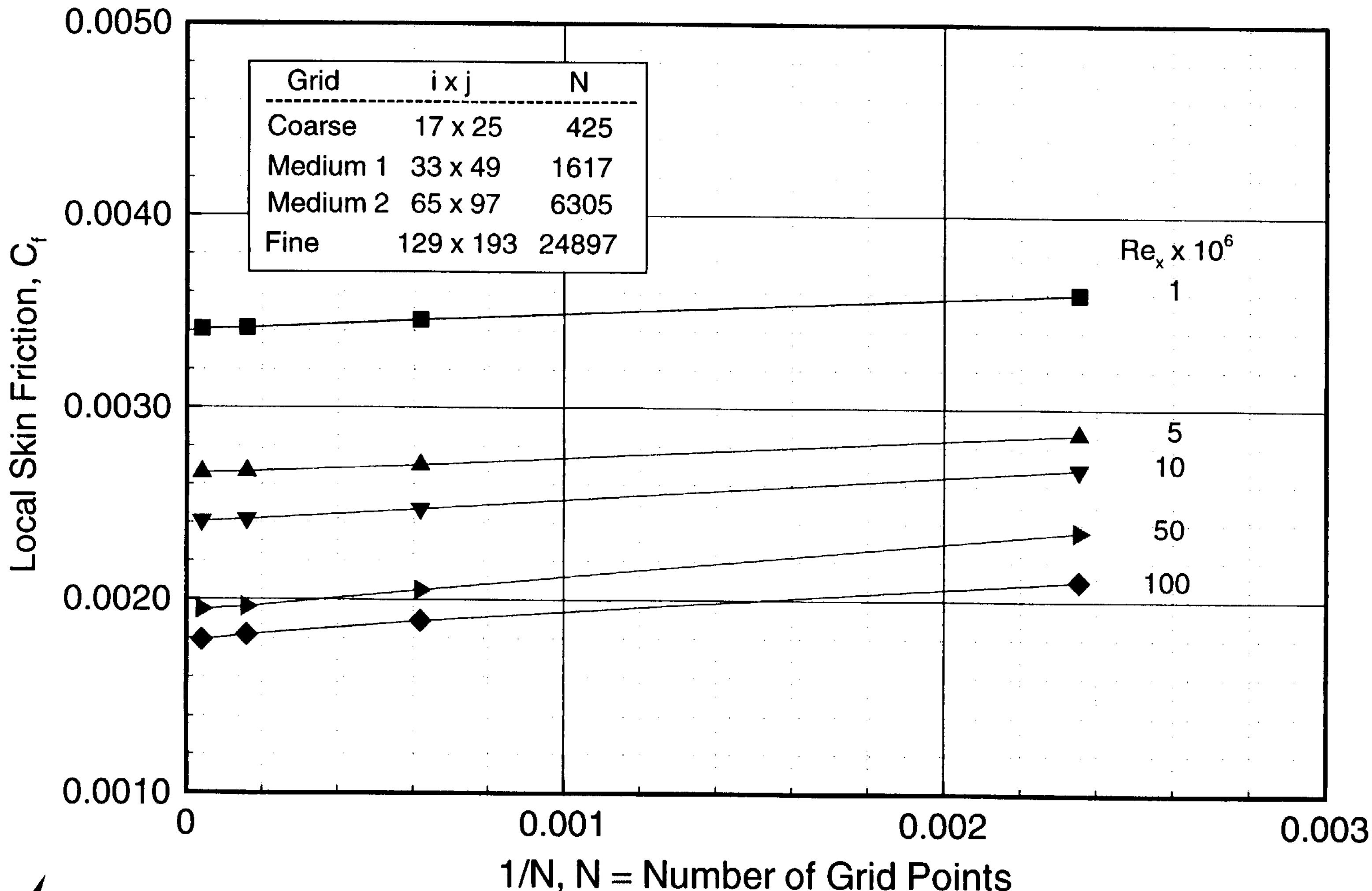

Alpha STAR CORPORATION

BOEING

Flat Plate with No Pressure Gradient: Effect of Grid Density

High Speed Aerodynamics, Long Beach

CFL3D, Menter's k-ω SST, $M_\infty = 0.50$

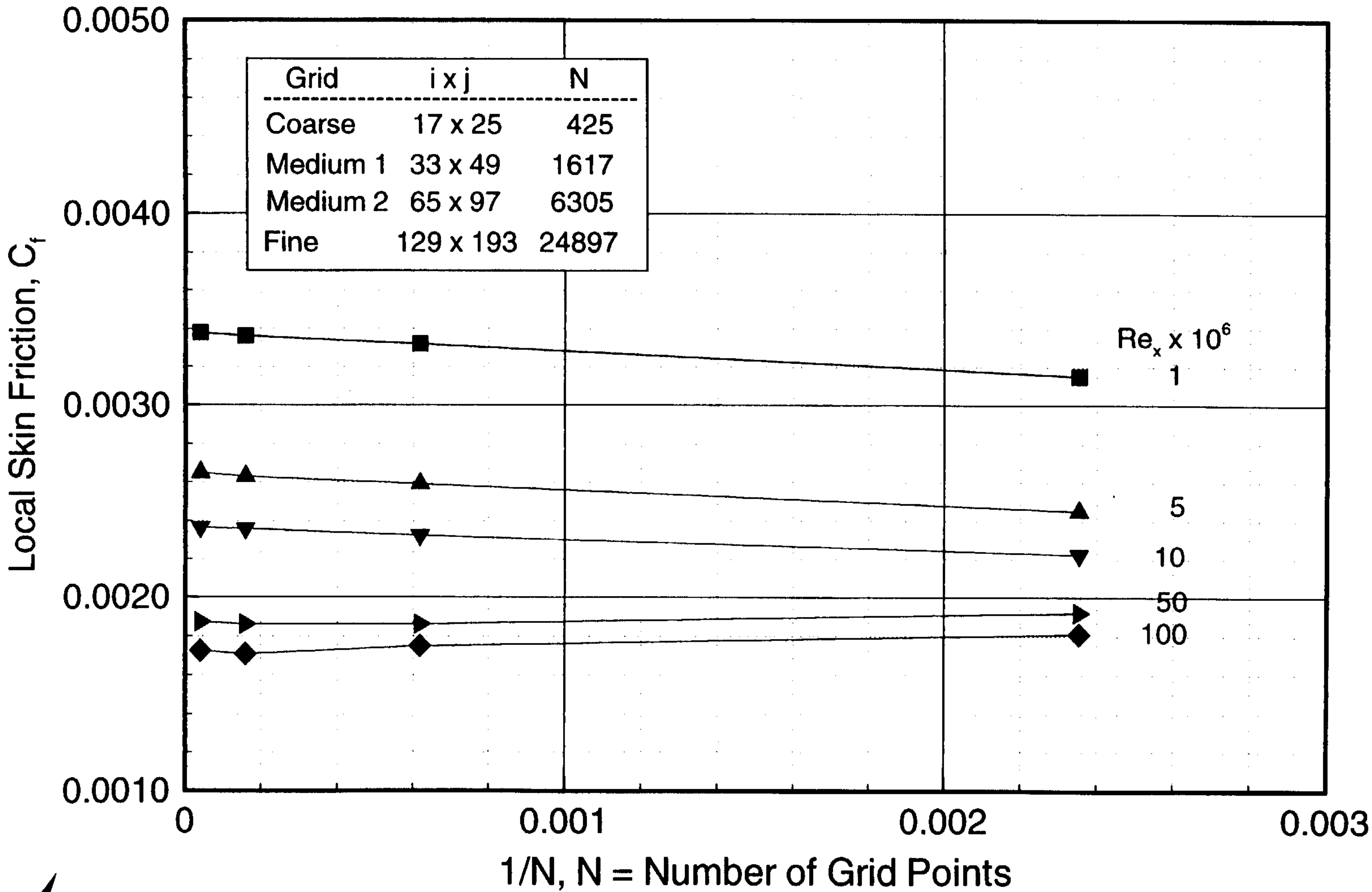

Grid	i x j	N
Coarse	17 x 25	425
Medium 1	33 x 49	1617
Medium 2	65 x 97	6305
Fine	129 x 193	24897

Alpha STAR CORPORATION

BOEING

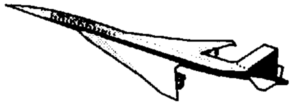

Flat Plat Velocity Profiles

The flat plate computations were performed using three turbulence models. The results of boundary-layer velocity profiles were compared with measurement of Smith and Walker at $M_\infty = 0.31$ and $Re_c = 6.78 \times 10^6$. This results of velocity profiles from Baldwin-Lomax, Spalart-Allmaras, and Menter's k-ω SS turbulence models show good agreement with correlation to experimental data of Smith and Walker.

Alpha STAR CORPORATION

BOEING

Flat Plate with No Pressure Gradient: Velocity Profiles

High Speed Aerodynamics, Long Beach

$M_\infty = 0.31$, $Re_x = 6.78 \times 10^6$, $x = 39.75$ in.

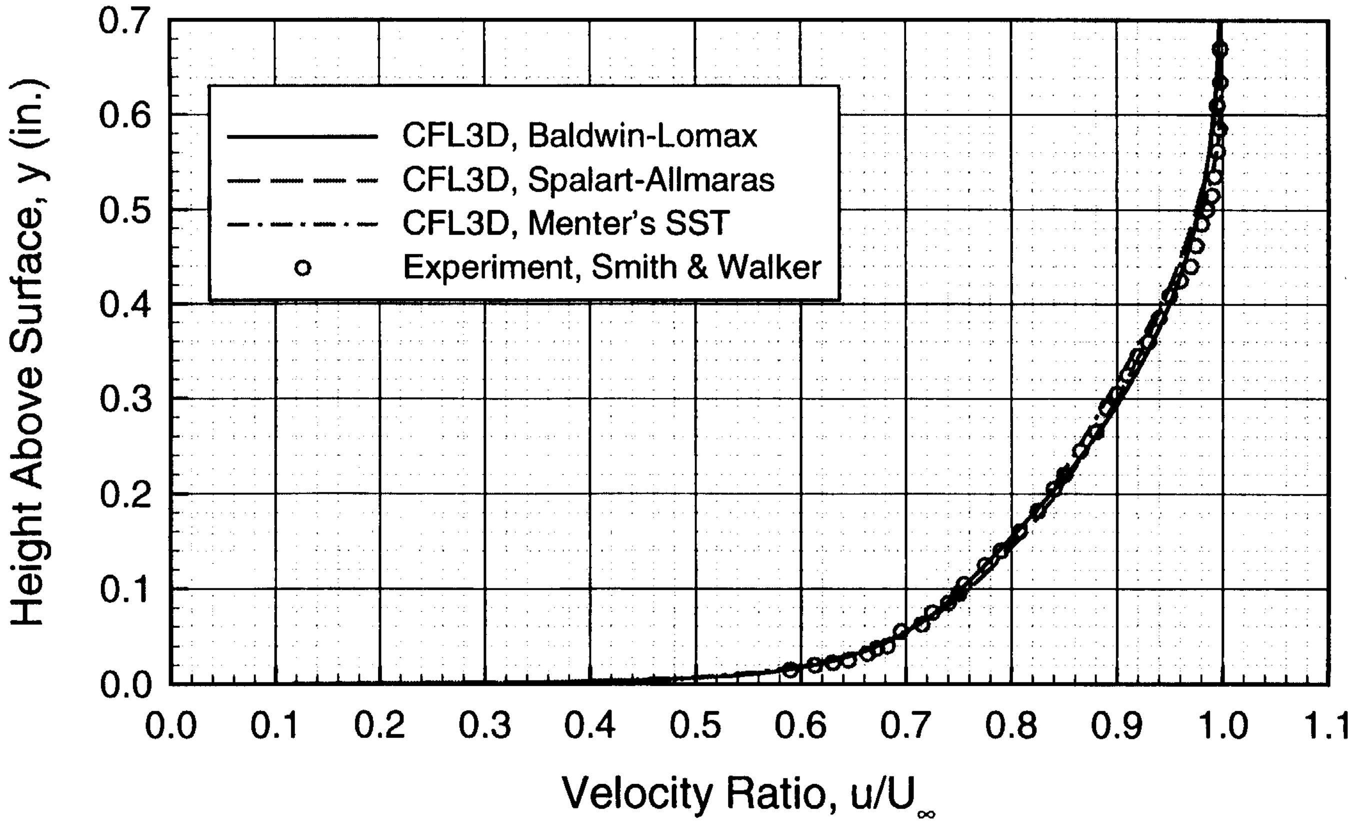

Alpha STAR CORPORATION

BOEING

Summary

A systematic study has been completed to evaluate the viscous drag prediction capability of CFL3D code. A series of computations are performed to validate the experimental local and average skin-friction for comprssible boundary layer flow over smooth adiabatic flat plate with no pressure gradient for subsonic to supersonic cruise Mach number of HSCT aircraft and a wide range of Reynolds numbers.

In the study of grid sensitivity, the coarse grid was too coarse especially for the Baldwin-Lomax turbulence model. A finer grid was generated. By eliminating the coarse mesh results, the C_f data for all three turbulence models are on the straight line and approaches to the asymptotic value of C_f.

The local and average skin friction coefficients were compared with empirical formula of Sommer & Short, Kulfan and Monaghan, for a wide range of Mach and Reynolds numbers. It was shown that for $M_\infty = 0.50$ and 1.50, the Spalart-Allmaras turbulence model is in good agreement with the empirical data, whereas for supersonic Mach numbers, $M_\infty = 2.25$ and 2.50, the Baldwin-Lomax and Menter's k-ω SST turbulence model are in better agreement with empirical data. A similar trend is seen for the average skin friction coefficient (C_F).

The comparison of velocity profiles for $M_\infty = 0.31$ and $Re_x = 6.78 \times 10^6$ and three turbulence models with experimental data of Smith and Walker, shows that the Menter's k-ω SST turbulence model is the best fit to experimental data.

Flat Plate with No Pressure Gradient

Summary

- A series of computations are performed to validate the experimental local and average skin friction for compressible boundary layer flow over smooth adiabatic flat plate with no pressure gradient for subsonic to supersonic Mach numbers and a wide range of Reynolds numbers.
- In the study of grid sensitivity, the coarse grid was too coarse especially for the Baldwin-Lomax turbulence model. A finer grid was generated. By eliminating the coarse mesh results, the C_f data for all three turbulence models are on the straight line and approaches to the asymptotic value of C_f.
- The local and average skin-friction coefficients were compared with empirical formula of Kulfan, Sommer & Short and Monaghan, for a wide range of Mach and Reynolds numbers. It was shown that for $M_\infty = 0.50$ and 1.50, the Spalart-Allmaras turbulence model is in good agreement with the empirical data, whereas for supersonic Mach numbers, $M_\infty = 2.25$ and 2.50, the Baldwin-Lomax and Menter's k-ω SST turbulence model are in better agreement to the empirical data.
- A similar trend is seen for the average skin-friction coefficient (C_F).
- The comparison of velocity profiles for $M_\infty = 0.31$ and $Re_x = 6.78 \times 10^6$ and three turbulences models with experimental data of Smith and Walker show that all three turbulence model agree well with the experimental data.

Progress Toward Viscous Drag Calculations (Part II)

Flow with Pressure Gradient Over TCA Symmetric Wing/Body Configuration

Hamid Jafroudi
Alpha STAR Corporation
Long Beach, CA

Raul Mendoza
Peter Hartwich
Shreekant Agrawal
The Boeing Company
Phantom Works
Long Beach, CA

NASA/ Industry HSR Airframe Review
Anaheim, California
February 8-11, 1999

Alpha STAR CORPORATION

BOEING

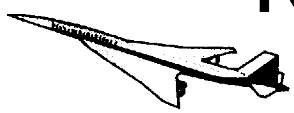

Outline

In the second phase of viscous-drag prediction, the flow with pressure gradient was analyzed. For this study flow over TCA symmetric wing/body configuration was selected. The outline of my talk will be as followed: First, the objective and brief introduction will be given. The approach to this analysis will be described. The computational grid and grid topology will be discussed. The turbulence models used for this study are described. The computational and empirical results will be presented. And finally, the summary of the analysis will be discussed.

TCA Symmetric Wing/Body Configuration

Outline

- Objective
- Introduction
- Method of solution
- Computational grid
- Turbulence models
- Computational results
- Conclusions

Alpha STAR CORPORATION

BOEING

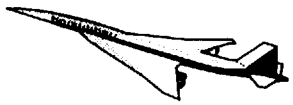

TCA Symmetric Wing/Body Configuration

High Speed Aerodynamics, Long Beach

Objective

In the second phase of viscous drag prediction, flows with pressure gradient are being investigated by analyzing the TCA symmetric winf/body configuration. In this study Euler solutions as well as Navier-Stokes solutions are computed. The turbulence models used are zero-equation model of Baldwin-Lomax and two-equation model of Menter's k- ω SST . The TCA symmetric configuration was analyzed at the zero-angle-of-attack and at both wind-tunnel and flight Reynolds numbers. The effects of Reynolds number on zero-lift drag were studied. The Navier-Stokes solutions were obtained at various free stream Mach numbers. A wide range of Mach numbers were considered for this study ranging from subsonic to supersonic speeds.

Alpha STAR CORPORATION

BOEING

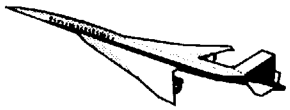

TCA Symmetric Wing/Body Configuration

High Speed Aerodynamics, Long Beach

Objective

- To provide a computational database
  - flow over TCA symmetric wing/body configuration
  - subsonic to supersonic Mach numbers
  - wide range of Reynolds numbers
  - two turbulence models

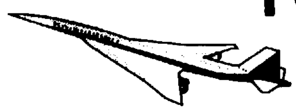

TCA Symmetric Wing/Body Configuration

High Speed Aerodynamics, Long Beach

Introduction

The prediction of viscous drag for HSCT configuration have shown significant dependencies using several CFD codes. Therefore, the High Speed Research (HSR), Configuration Aerodynamics community has proposed a Technical Concept Airplane (TCA) symmetrical wing/body configuration in an effort to obtain a computational database for validation of viscous drag for wind-tunnel and flight Reynolds numbers and a wide range of Mach numbers that covers the subsonic to supersonic range that includes the cruise condition of HSCT aircraft. The viscous drag validation is based on the computaional results of CFL3D Navier-Stokes formulations. The results obtained will be used to support the upcoming wind-tunnel test for the TCA symmetric wing/body model.

In order to accomplish the objective of this task, CFL3D based on Navier-Stokes formulations are used to collect a series of results for the prediction of viscous drag that can be used later for validation of test data. The compuation will concentrate on both Euler and Navier-Stokes modes for a series of Mach numbers in flight and wind-tunnel based on two turbulence models. The turbulence models are zero-order equation of Baldwin-Lomax and two-equation model of Menter's k-ω SST. The results of two model will be compared against the Euler solution. The comparison of results will also include the classical flat plate results of van Driest II method, and Sommer and Short for prediction of skin-friction drag. These method are based on equivalent flat plate skin-friction theory. These method are widely being used for correction to Euler solutions. These formulation requires the freestream Mach number and the Reynolds number and freestream temperature as an inputs.

Alpha STAR CORPORATION

BOEING

TCA Symmetric Wing/Body Configuration

High Speed Aerodynamics, Long Beach

Method of Solution

A systematic study of the viscous-drag prediction capability of the CFL3D based Navier-Stokes solver was conducted at Boeing Long Beach in two phases. In the first phase, 2-D subsonic to supersonic Navier-Stokes solutions were correlated with the experimental data for compressible turbulent flows over a flat plate without pressure gradients. In the second phase of this study, flows with pressure gradients were considered by examining the TCA symmetric wing/body configuration. This configuration was selected because wind-tunnel test data would become available for comparison in the near future.

Alpha STAR CORPORATION

BOEING

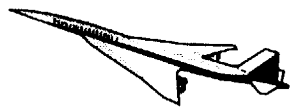

TCA Symmetric Wing/Body Configuration

High Speed Aerodynamics, Long Beach

Method of Solution

- Use CFL3D developed by NASA Langely and modified by Boeing
  - Euler and Navier-Stokes formulations
  - two turbulence models
  - viscous and pressure drag computations

Alpha STAR CORPORATION

BOEING

Computational Grid

A typical volume grid is being used during this study. This is a structured, single zone wing/body grid with a C-O topology. There are a total of 329 point in the streamwise direction and 97 points in the spanwise direction. The grid used for all the Euler calculations had 65 points in the normal direction for a total of 2.1 million points. On the other hand, a different Navier-Stokes grid was used every time the flow conditions changed significanly. The Navier-Stokes grids were constructed from the Euler grid by adding 24 cells in the normal direction and clustering the points near the surface appropriately for different Reynolds numbers. Thus, the Navier-Stokes grids increased to 89 points in the normal direction resulting in a total of 2.8 million points.

The volume grids extend more than five body lengths in all directions, except in the spanwise direction where the grid extends by more than 12 semispans. This type of grid was found to be adequate for all computations performed, including the transonic calculations. A 1.675% model with a closed aftbody was used in the CFD computations.

TCA Symmetric Wing/Body Configuration

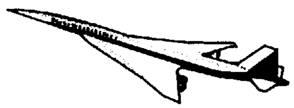

High Speed Aerodynamics, Long Beach

Computational Grid

- Single block with a C-O topology
  - Coarse mesh 83 x 23 x 25 = 47,725
  - Medium mesh 164 x 33 x 49 = 363,825
  - Fine mesh 329 x 89 x 97 = 2,840,257

Alpha STAR CORPORATION

BOEING

Volume Grid for the TCA Symmetric W/B Configuration

High Speed Aerodynamics, Long Beach

Euler: C-O Grid (329 x 65 x 97), 2.1 Million Points
Navier-Stokes: C-O Grid (329 x 89 x 97), 2.8 Million Points

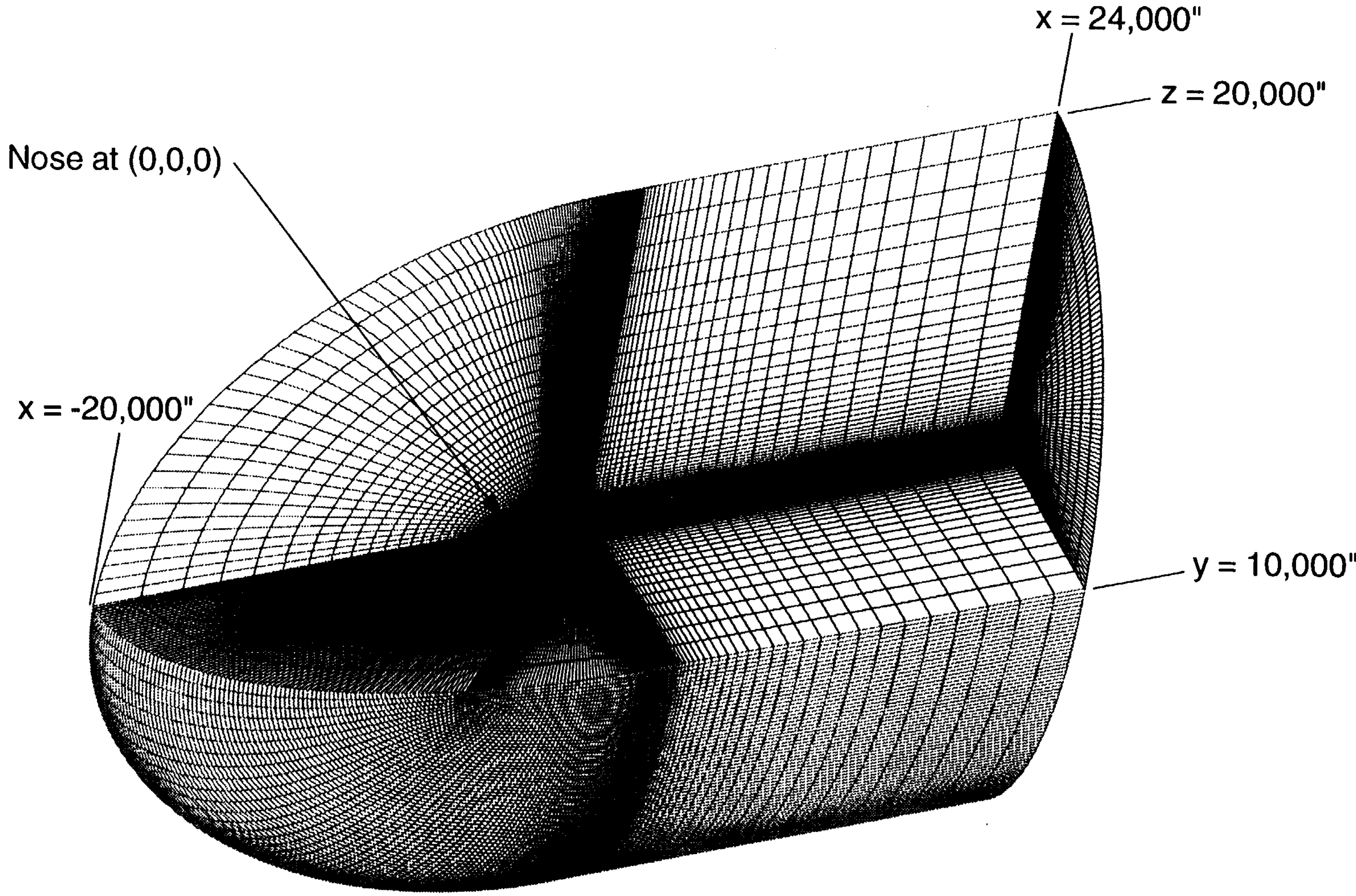

Alpha STAR CORPORATION

BOEING

Turbulence Model Equations

Several turbulence capabilities are built-in to CFL3D state-of-the-art CFD solver. Two turbulence models of different levels of complexity are being used for the computation of CFL3D solver. The first turbulence model which is widely used in CFD community is zero-equation model. The model is based on Baldwin-Lomax model which is algebraic model. The second model is two-equation model based on Menter's k-ω shear stress transport (SST) model. The model solves two equation simultaneously in terms of turbulence kinetic energy and rotational velocity or vorticity.

TCA Symmetric Wing/Body Configuration

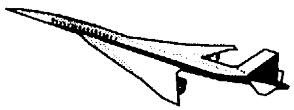

High Speed Aerodynamics, Long Beach

Turbulence Models

- Zero - equation model
  - Baldwin - Lomax
- Two - equation model
  - Menter's k - ω SST

Mach Numbers and Reynolds Numbers

A series of computational runs for turbulent boundary layer were performed over TCA symmetric wing/body for subsonic to supersonic Mach numbers. The range of Reynolds and Mach numbers are listed in Table. The range of Reynolds and Mach numbers were selected such that to cover the transonic and supersonic cruise Mach number of HSCT aircraft.

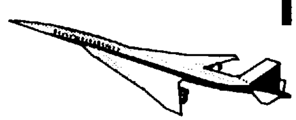

TCA Symmetric Wing/Body Configuration

High Speed Aerodynamics, Long Beach

Mach Numbers and Reynolds Numbers

M_∞	Wind Tunnel $Re_c \times 10^{-6}$	Flight $Re_c \times 10^{-6}$
0.50	6.36	221.2
0.90	6.36	163.3
0.95	6.36	171.9
1.05	6.36	172.8
1.10	6.36	172.8
1.20	6.36	174.7
1.50	6.36	168.1
1.80	6.36	170.0
2.10	6.36	156.7
2.40	6.36	211.7

Alpha STAR CORPORATION

BOEING

Computational Results

A series of computational runs for flow with pressure gradient over TCA symmetric wing/body configuration were performed for subsonic, transonic and supersonic freestream Mach numbers (0.50, 0.90, 0.95, 1.05, 1.10, 1.20, 1.50, 1.80, 2.10, 2.40). The Reynolds numbers chosen is $4\text{x}10^6$/ft or $6.36\text{x}10^6$ based on mean aerodynamic chord for wind-tunnel and a series of flight Reynolds numbers ($221.2\text{x}10^6$, $163.3\text{x}10^6$, $171.9\text{x}10^6$, $172.8\text{x}10^6$, $172.8\text{x}10^6$, $174.7\text{x}10^6$, $168.1\text{x}10^6$, $170.0\text{x}10^6$, and $211.7\text{x}10^6$). Two turbulence models were used for this study. The results include the Euler solution for comparison.

A typical convergence summary are plotted for Menter's k-ω SST turbulence model for the wind-tunnel and the flight Reynolds numbers at subsonic Mach number.

TCA Symmetric Wing/Body Configuration

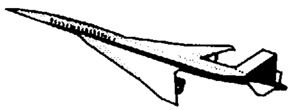

High Speed Aerodynamics, Long Beach

Computational Results

- Summary of convergence history
- Effects of grid sensitivity
- Variation of drag with Mach number at wind-tunnel and flight Reynolds numbers
- Distribution of surface pressure

Alpha STAR CORPORATION

BOEING

Convergence Histories for TCA Symmetric Wing/Body Configuration

High Speed Aerodynamics, Long Beach

CFL3D, N-S, 329 x 89 x 97 C-O Grid, $M_\infty = 0.50$, $Re_c = 6.36 \times 10^6$, $\alpha = 0^\circ$
Menter's k-ω SST Turbulence Model

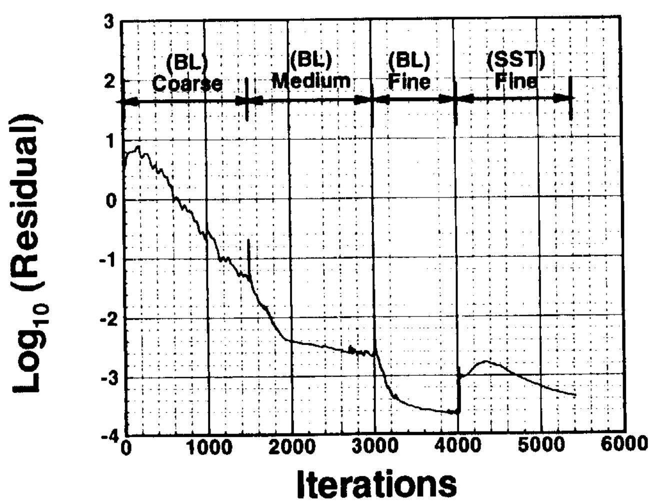

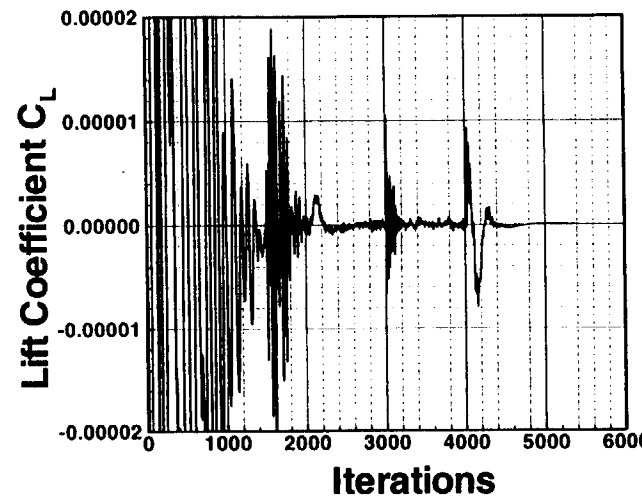

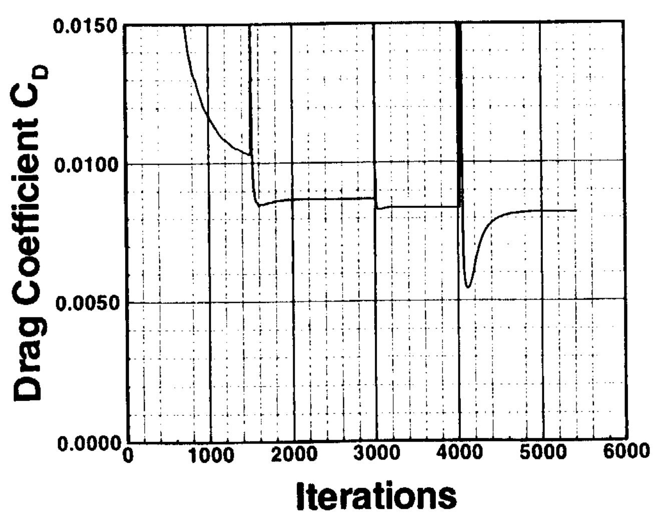

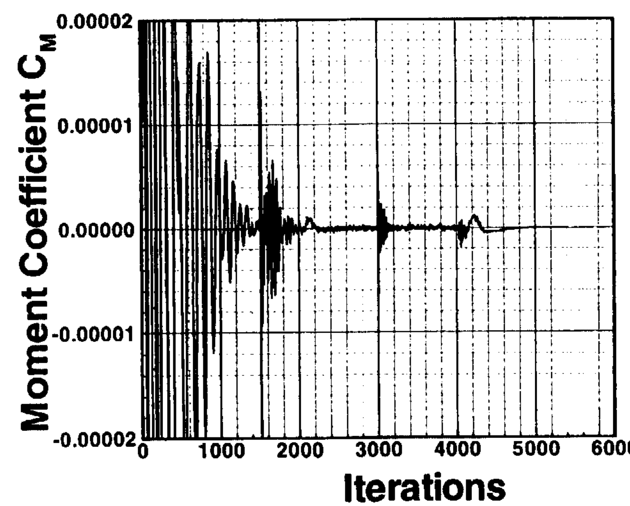

High Speed Aerodynamics, Long Beach

CFL3D, N-S, 329 x 89 x 97 C-O Grid, $M_\infty = 0.50$, $Re_c = 221.2 \times 10^6$, $\alpha = 0°$
Menter's k-ω SST Turbulence Model

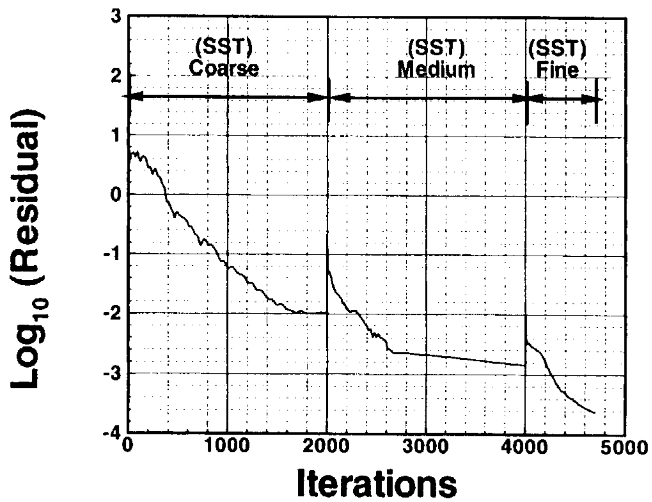

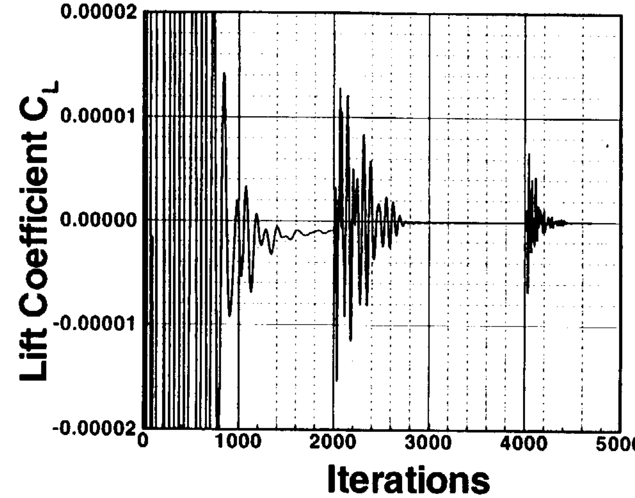

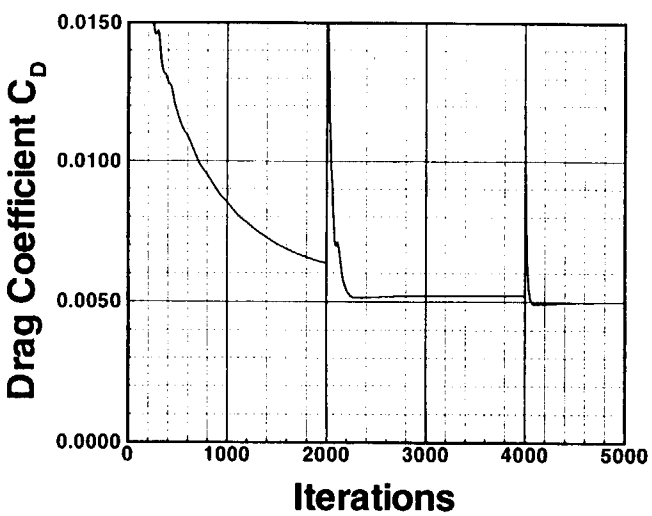

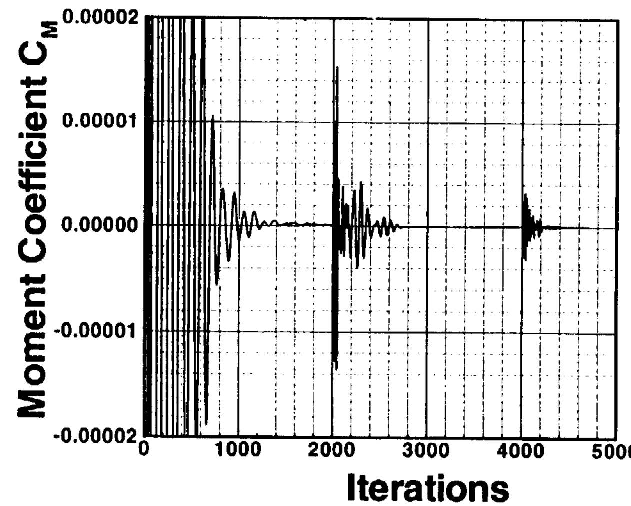

Alpha STAR CORPORATION

BOEING

Computational Results (continued)

A typical results from a grid convergence study are shown using CFL3D with Baldwin-Lomax and Menter's k-ω SST turbulence models. These figures show the variation of total drag coefficient at a given Reynolds number for wind-tunnel and flight and a wide range of Mach numbers. The plotting format is chosen such that the results from successive grid refinement should fall on a straight line. For 3-D flow the drag must be be proportional to the inverse of number of grid points to the power 2/3. It appears that the results of Baldwin-Lomax and Menter's k-ω SST models are spatially converged since they roughly fall on a straight line and an asymptotic value for finite grid density can be estimated.

Total Drag Coefficient: Effect of Grid Density

High Speed Aerodynamics, Long Beach

TCA Symmetric Wing/Body Configuration at $\alpha = 0^\circ$, and $Re_c = 6.36 \times 10^6$
CFL3D, Navier-Stokes, Baldwin-Lomax Turbulence Model

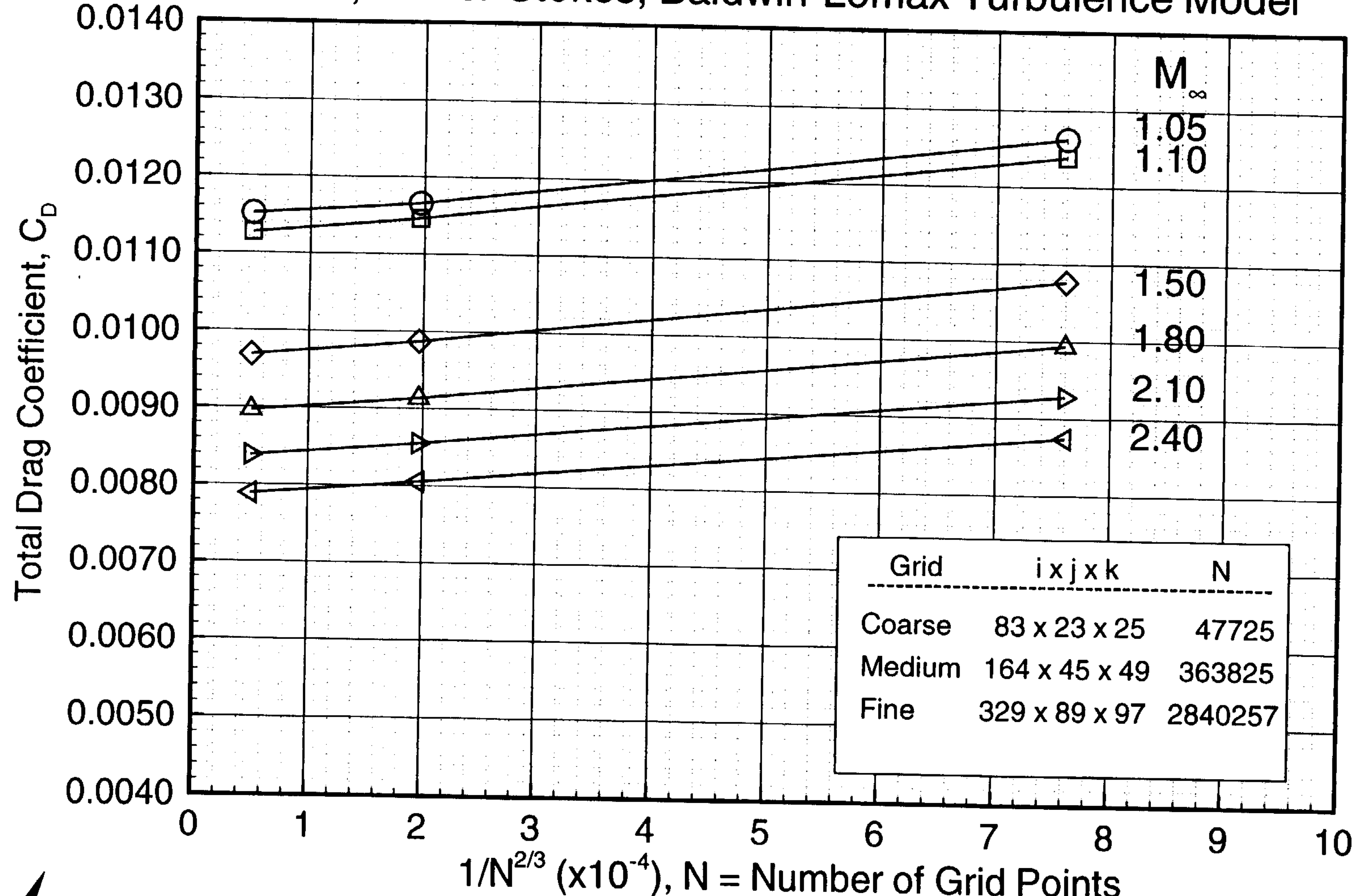

Alpha STAR CORPORATION

BOEING

Total Drag Coefficient: Effect of Grid Density

High Speed Aerodynamics, Long Beach

TCA Symmetric Wing/Body Configuration at $\alpha = 0^{\circ}$, Flight Reynolds Numbers
CFL3D, Navier-Stokes, Menter's k-ω SST Turbulence Model

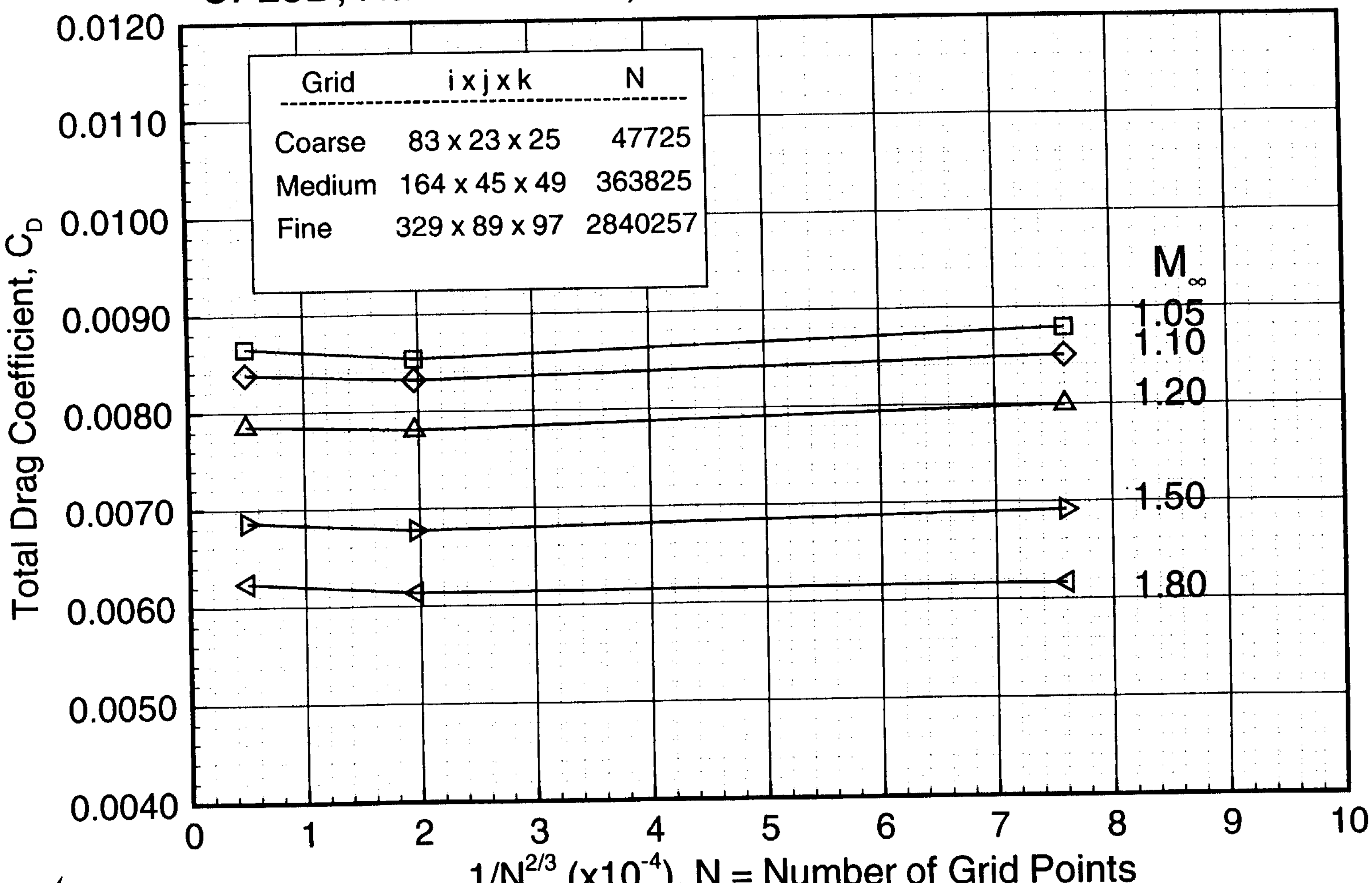

Inha STAR CORPORATION

BOEING

Computational Results (continued)

The variation of pressure, viscous, and total drag with freestraem Mach number are shown in three consequtive figures at the wind-tunnel Reynolds number of $Re_c = 6.36 \times 10^6$. The two Navier-Stokes s olutions (BL and SST) predict similar pressure drag. At the subsonic Mach numbers, the Navier-Stokes solutions show the effect of the boundary layer displacement: higher pressure than the Euler solution, as expected.

The results of viscous drag show that the SST solution has the least drag throughout the Mach number range. The Baldwin-Lomax solution has higher drag, and the shape of the curve matches the SST prediction. The equivalent flat plate methods predict even higher drag, and they do not predict the shift near $M_\infty=1.0$. The close agreement between Baldwin-Lomax and the flat plate predictions is in part due to the assumptions made in the Bladwin-Lomax formulation; namely, that the boundary layer flow is self-similar. These assumptions are compatible with the correlations by van Driest II and by Sommer and Short which are for boundary-layer flows without pressure gradient.

The total drag is shown in here. At subsonic Mach numbers, the SST predictions match the Euler/flat plate predictions better than the B-L predictions. However, this is a fortuitous result of two errors(in C_{Dp} and C_{Dv}) canceling. At supersonic Mach numbers, SST predicts the lowest drag, followed by B-L and the Euler/flat plate predictions.

TCA Symmetric Model: Pressure Drag vs. Mach Number

High Speed Aerodynamics, Long Beach

CFL3D, Euler and Navier-Stokes, 329 x 89 x 97 C-O Grid

$\alpha = 0^\circ$, $Re_c = 6.36 \times 10^6$

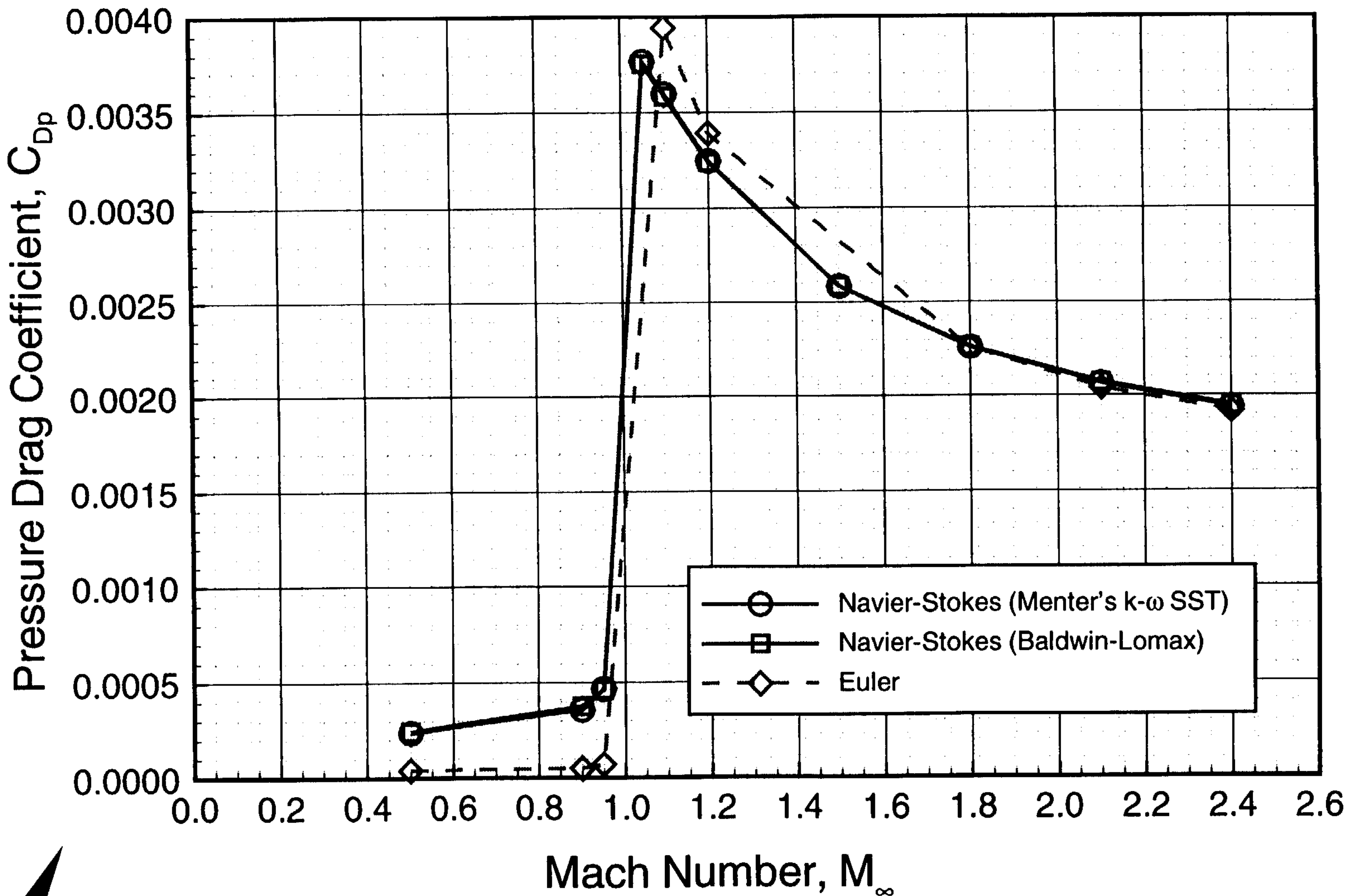

Inha STAR CORPORATION

BOEING

TCA Symmetric Model: Viscous Drag vs. Mach Number

High Speed Aerodynamics, Long Beach

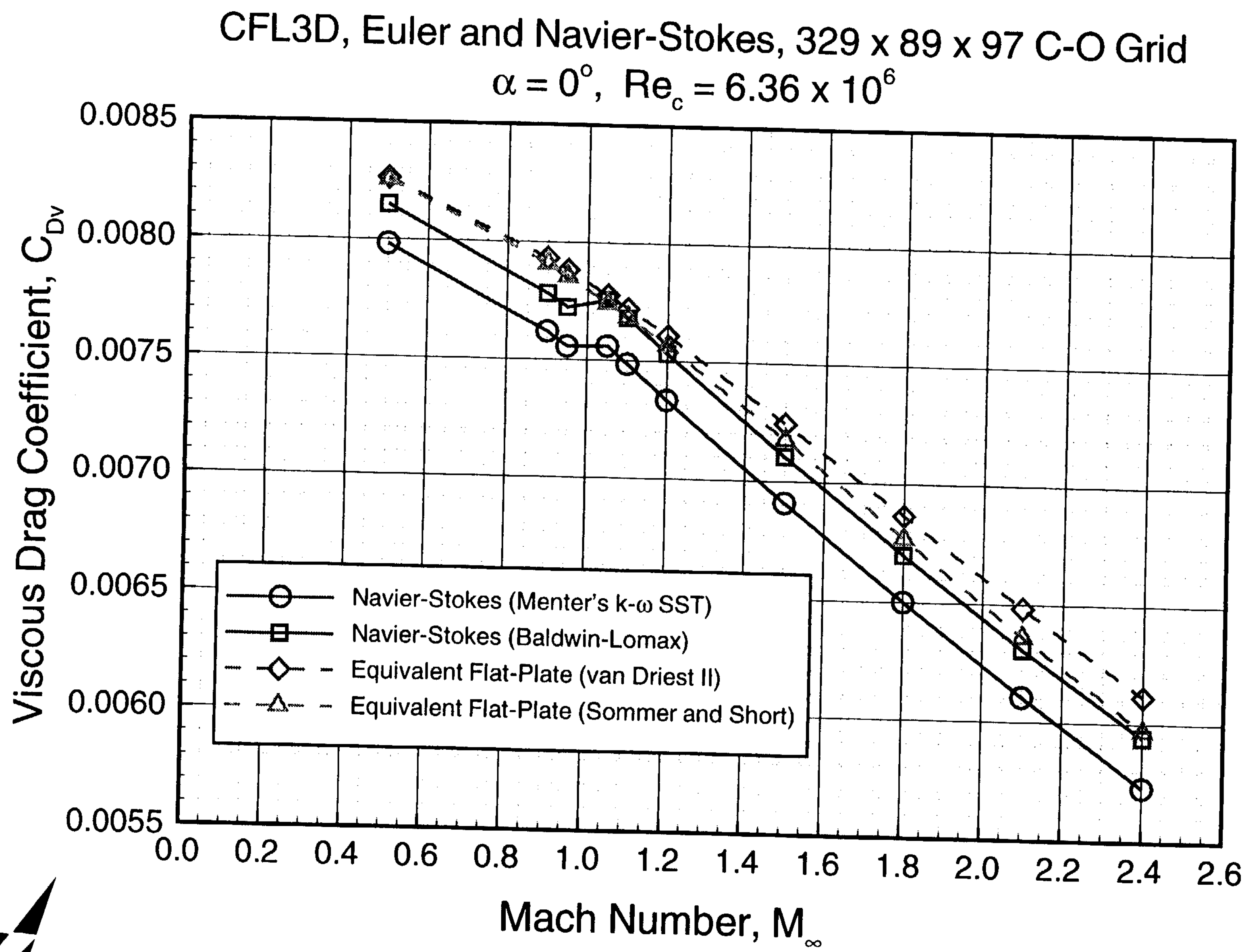

Alpha STAR CORPORATION

BOEING

TCA Symmetric Model: Total Drag vs. Mach Number

High Speed Aerodynamics, Long Beach

CFL3D, Euler and Navier-Stokes, 329 x 89 x 97 C-O Grid
$\alpha = 0^{\circ}$, $Re_c = 6.36 \times 10^6$

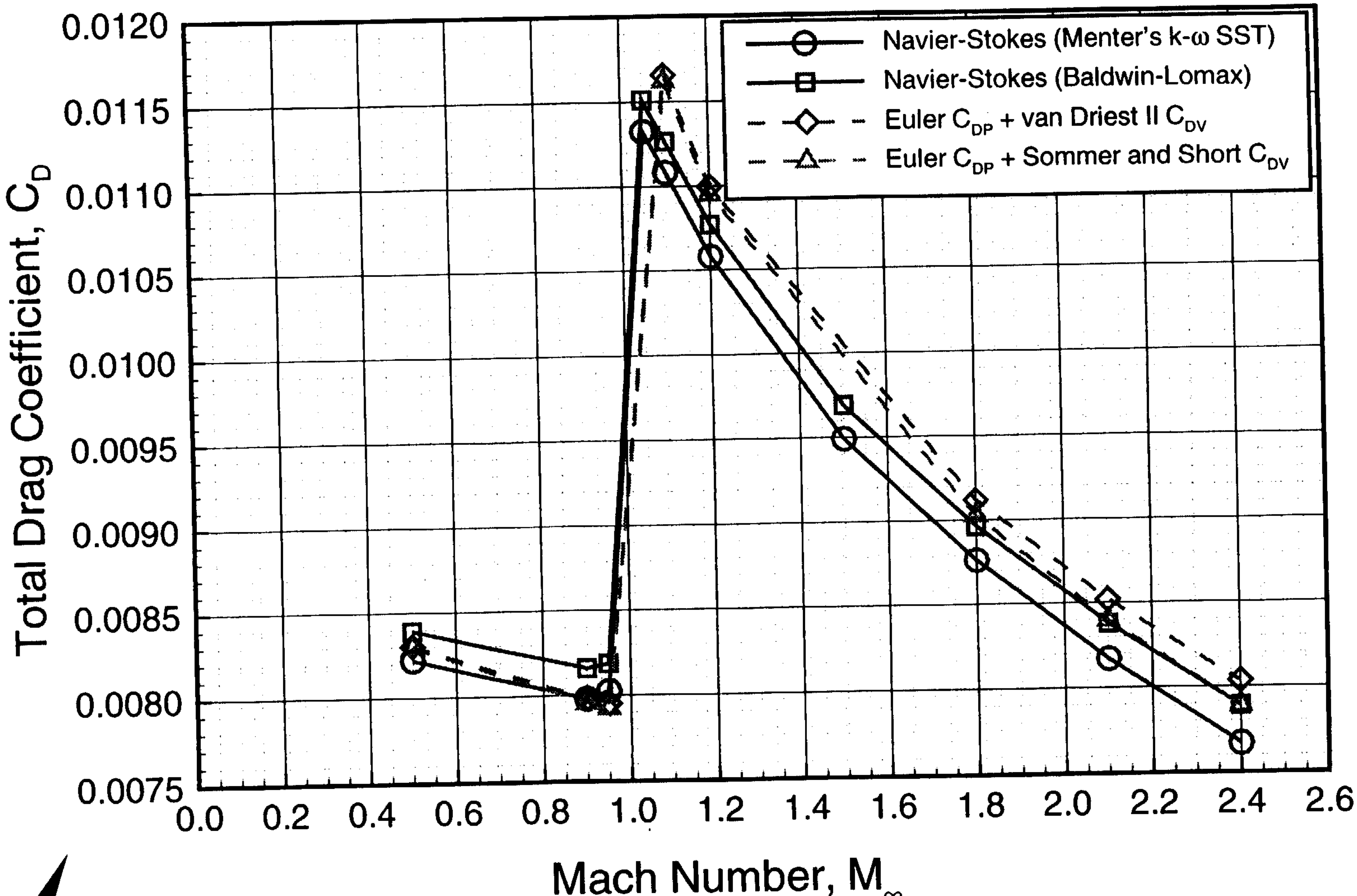

Alpha STAR CORPORATION

BOEING

Computational Results (continued)

The variation of drag with freestream Mach number at the flight Reynolds numbers are shown in a sequence of figures. As it is seen in these figures the trend is similar in pressure drag as for the wind-tunnel Reynolds number. On the other hand, the viscous drag predictions have a different trend than at the wind-tunnel Reynolds number: B-L predicts the highest drag for $M_\infty < 1.4$. The SST model predicts the lower total drag than B-L, but that the two Navier-Stokes predictions are higher than the Euler/flat plate for subsonic Mach numbers and lower for supersonic Mach numbers.

TCA Symmetric Model: Pressure Drag vs. Mach Number

High Speed Aerodynamics, Long Beach

CFL3D, Euler and Navier-Stokes, 329 x 89 x 97 C-O Grid

$\alpha = 0^{\circ}$, Flight Reynolds Numbers

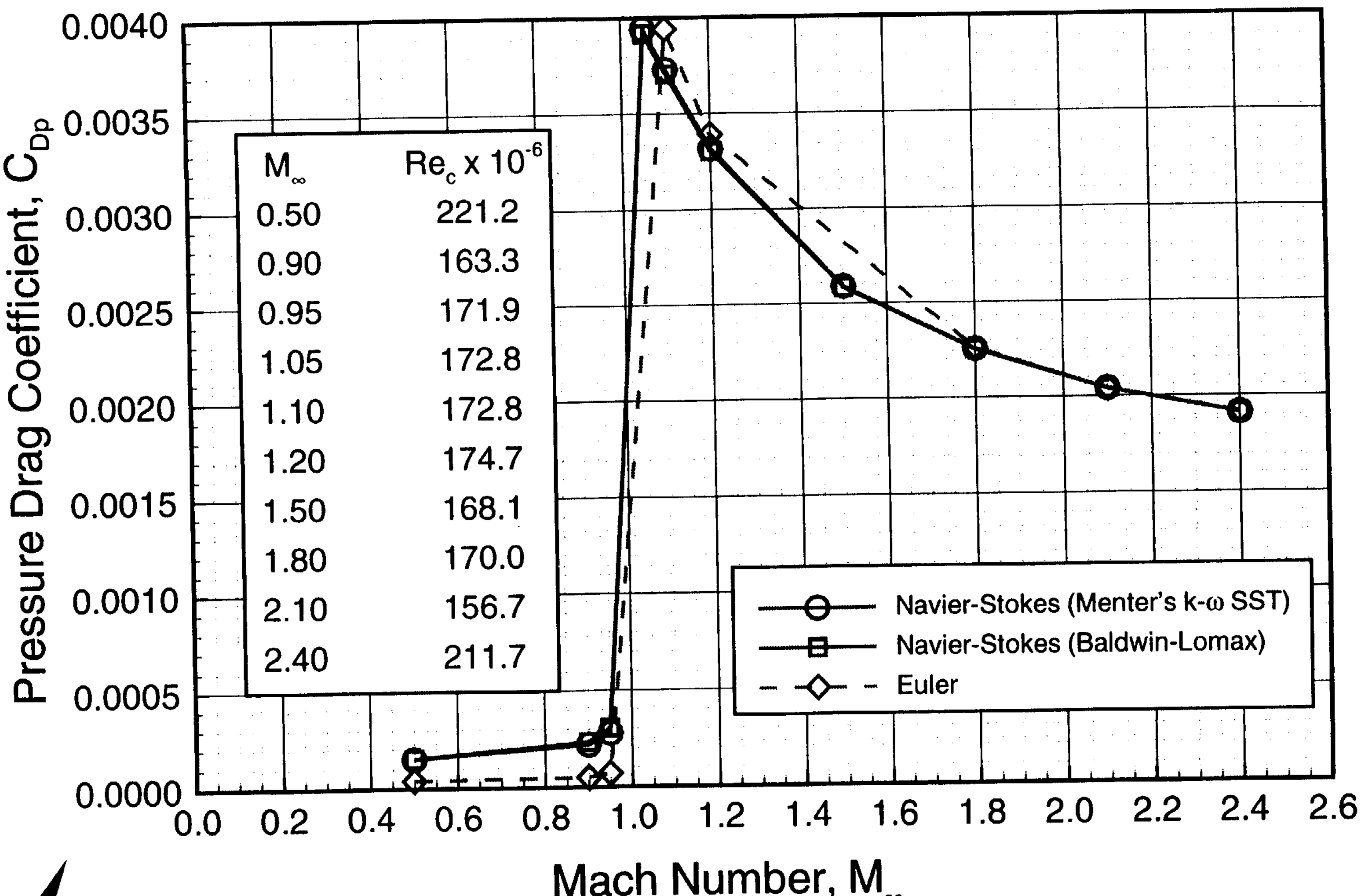

M_∞	$Re_c \times 10^{-6}$
0.50	221.2
0.90	163.3
0.95	171.9
1.05	172.8
1.10	172.8
1.20	174.7
1.50	168.1
1.80	170.0
2.10	156.7
2.40	211.7

Inha STAR CORPORATION

TCA Symmetric Model: Viscous Drag vs. Mach Nu..

High Speed Aerodynamics, Long Beach

CFL3D, Euler and Navier-Stokes, 329 x 89 x 97 C-O Grid

$\alpha = 0^{\circ}$, Flight Reynolds Numbers

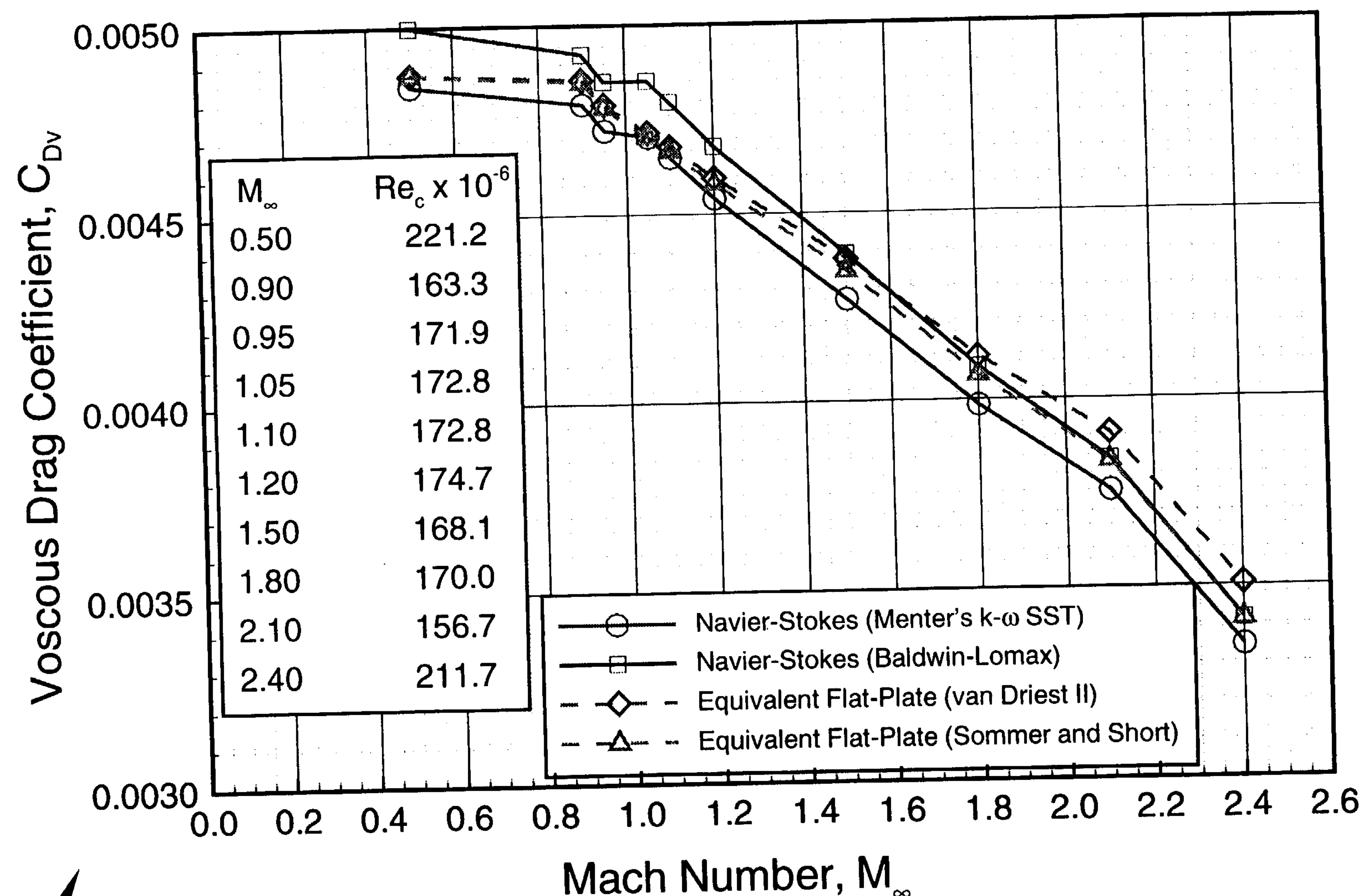

Alpha STAR CORPORATION

BOEING

TCA Symmetric Model: Total Drag vs. Mach Number

High Speed Aerodynamics, Long Beach

CFL3D, Euler and Navier-Stokes, 329 x 89 x 97 C-O Grid

$\alpha = 0^\circ$, Flight Reynolds Numbers

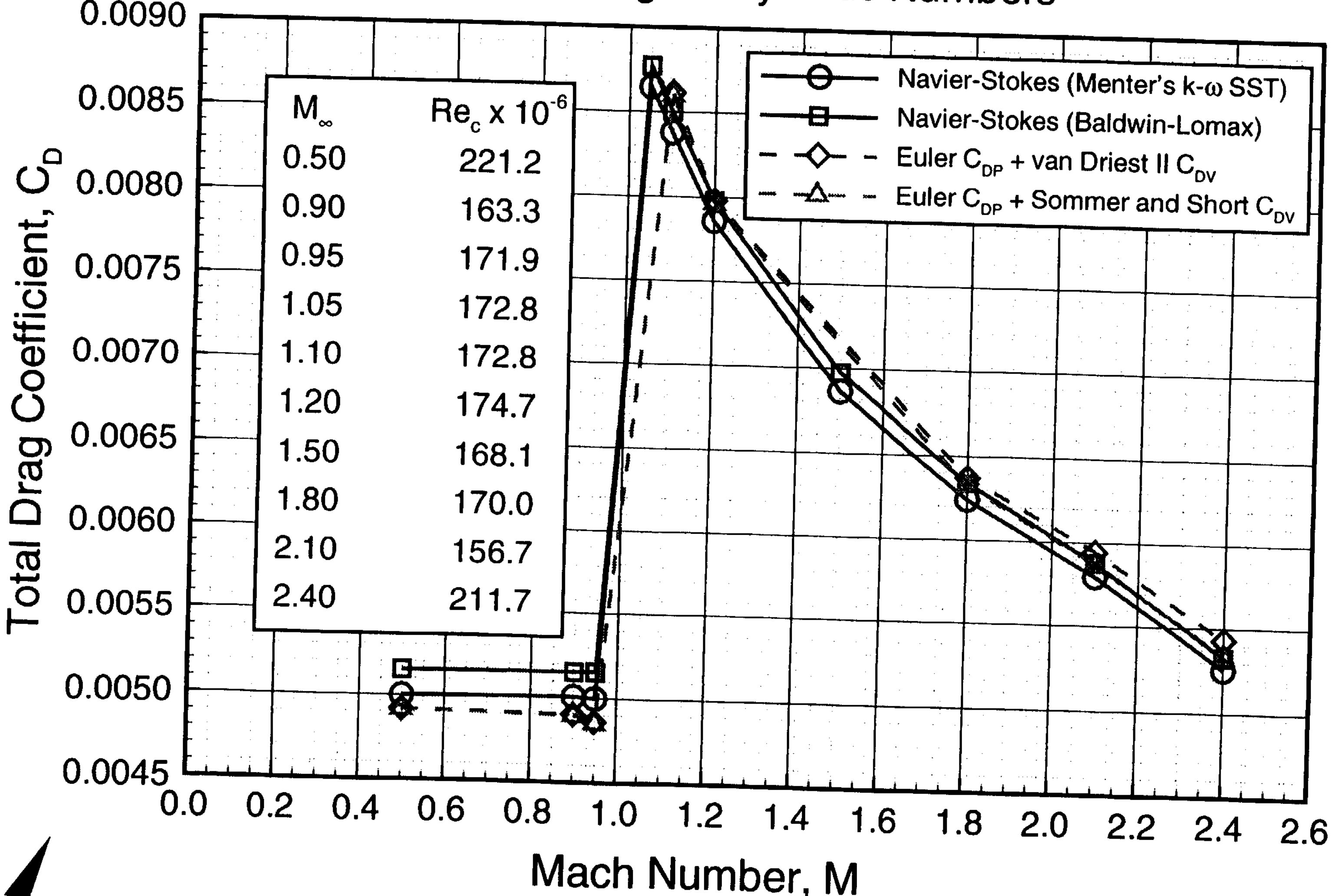

M_∞	$Re_c \times 10^{-6}$
0.50	221.2
0.90	163.3
0.95	171.9
1.05	172.8
1.10	172.8
1.20	174.7
1.50	168.1
1.80	170.0
2.10	156.7
2.40	211.7

...ha STAR CORPORATION

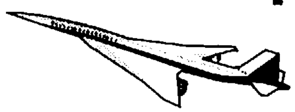

TCA Symmetric Wing/Body Configuration

Computational Results (continued)

The computational surface pressure coefficient (C_p) from CFL3D Navier-Stokes solution using Menter's k-ω SST turbulence model is plotted for a wide range of Mach number and wind-tunnel and flight Reynolds numbers. The results show a good agreement between the computational wind-tunnel and the flight Reynolds numbers.

Alpha STAR CORPORATION

BOEING

Pressure Distribution for the TCA Symmetric Wing/Body Configuration

High Speed Aerodynamics, Long Beach

CFL3D, N-S, 329 x 89 x 97 C-O Grid, $M_\infty = 0.50$, $\alpha = 0^\circ$
Menter's k-ω Turbulence Model

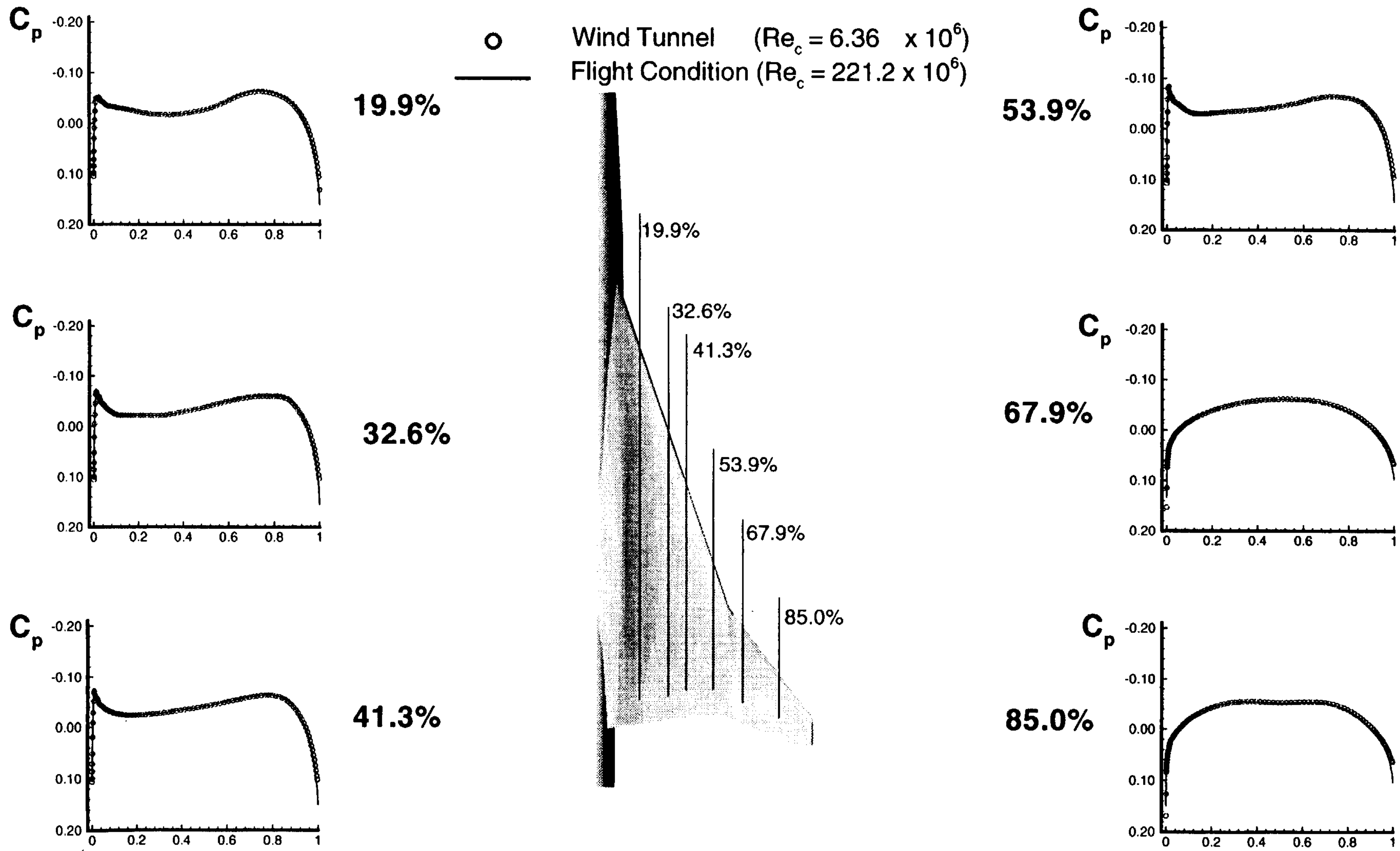

Alpha STAR CORPORATION

BOEING

Computational Results (continued)

The computational results of two turbulence models for the surface pressure coefficients were also compared and plotted for Mach numbers of 0.50, 0.90, 1.10, 1.80, 2.10, and 2.40, respectively, for the computational wind-tunnel Reynolds numbers. These results also show good agreement between the Bladwin-Lomax and Menter's k-ω SST turbulence models. This supports the pressure drag results

Pressure Distribution for the TCA Symmetric Wing/Body Configuration

High Speed Aerodynamics, Long Beach

CFL3D, N-S, 329 x 89 x 97 C-O Grid, $M_\infty = 0.50$, $Re_c = 6.36 \times 10^6$, $\alpha = 0^\circ$

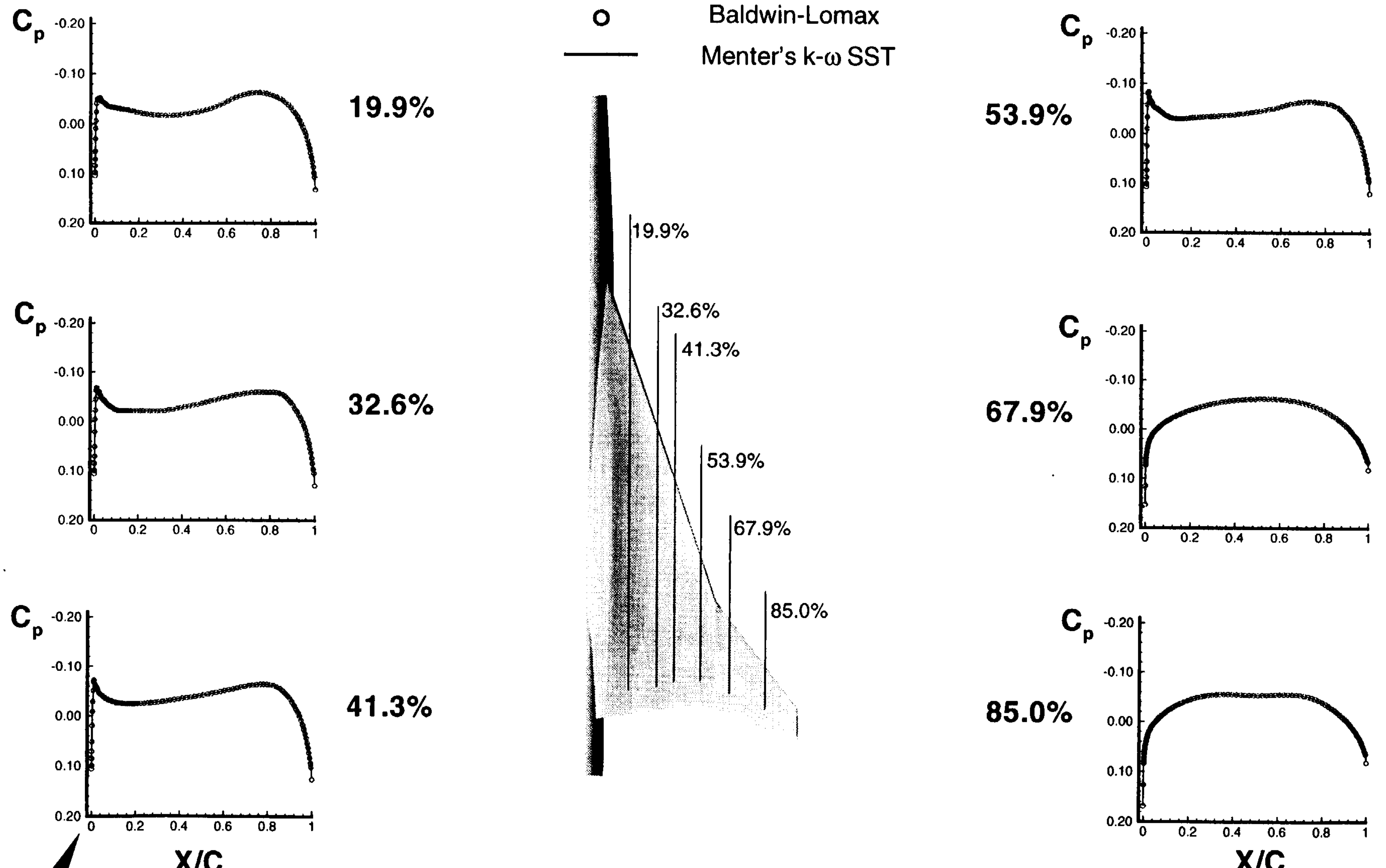

lpha STAR CORPORATION

BOEING

TCA Symmetric Wing/Body Configuration

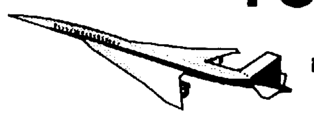

High Speed Aerodynamics, Long Beach

Summary

A series of computational runs were performed for TCA symmetric wing/body configuration at zero angle-of-attack for prediction of viscous drag at subsonic to supersonic Mach numbers both for the wind-tunnel and flight Reynolds numbers and a wide range of Reynolds numbers. The turbulence models of Bladwin-Lomax and Menter's k-ω SST were used. The freestream Mach number chosen for this study are 0.50, 0.90, 1.10, 1.20, 1.50, 180, 2.10, and 2.40. The results obtained for the wind-tunnel (Re_c=6.36x10^6) and the flight Reynolds numbers (Re_c=221.2x10^6, 163.3x10^6, 172.8x10^6, 174.7x10' 168.1x10' 170.0x10^6, 156.7x10^6, and 211.7x10^6).

The results of wind-tunnel and the flight Reynolds numbers for surface pressure coefficients show good agreement for the range of Mach numbers (0.5 - 2.4).

The results of surface pressure coefficients from two turbulence models obtained from CFL3D Navier-Stokes solutions were also compared. The results show good agreement using Baldwin-Lomax and Menter's k-ω .

The results of pressure drag coefficients between two turbulence models show a good agreement with each other for all Mach numbers and both wind-tunnel and flight Reynolds numbers. The results of Euler solutions are under-predicted compared to Navier-Stokes and equivalent flat-plate theory. The viscous and the total drag coefficient are over-predicted using Baldwin-Lomax and van Driedt II and Sommer and Short estimates.

Similar trend is seen for the flight Reynolds numbers for pressure, viscous, and total drag coefficients.

Finally, the wind-tunnel test data are needed to validate the results obtained for the surface pressure coefficients as well as the drag coefficients.

Alpha STAR CORPORATION

BOEING

TCA Symmetric Wing/Body Configuration

High Speed Aerodynamics, Long Beach

Summary

- A series of computational runs were performed for TCA symmetric wing/body configuration at zero angle-of-attack for prediction of viscous drag at subsonic to supersonic Mach numbers both for the wind-tunnel and flight Reynolds numbers and a wide range of Reynolds numbers.
- The results of wind-tunnel and the flight Reynolds numbers for surface pressure coefficients show good agreement for the range of Mach numbers (0.5 - 2.4).
- The results of surface pressure show good agreement using Baldwin-Lomax and Menter's k-ω turbulence models for the wind-tunnel condition.
- Pressure drag coefficients are in good agreement from two turbulence models for both wind-tunnel and the flight Reynolds numbers. Baldwin-Lomax and van Driest II and Sommer & Short predict higher viscous and total drag compared to Menter'sk-ω SST model.
- Similar trend is seen for the flight Reynolds numbers for pressure, viscous, and total drag coefficients.
- Finally, the wind-tunnel test data are needed for validation of surface pressure coefficients and drag.

Alpha STAR CORPORATION

BOEING

***OVERFLOW*: Facts on Friction**

Scott Lawrence
NASA Ames Research Center

Annual Airframe Technical Review
Anaheim, California
February 9-13, 1999

NASA Ames Research Center
February, 1999

This paper presents results of three minor studies into the behavior of the OVERFLOW with respect to the prediction of skin friction drag on wing bodies at cruise Mach number and wind tunnel Reynolds number. The studies include a preliminary assessment of the behavior of the two new 2-equation turbulence models introduced with the latest version of OVERFLOW (v. 1.8f), an investigation into potential improvements in the matrix dissipation scheme currently implemented in OVERFLOW, and an analysis of the observed sensitivity of the code's skin friction predictions to grid stretching at solid surface boundaries.

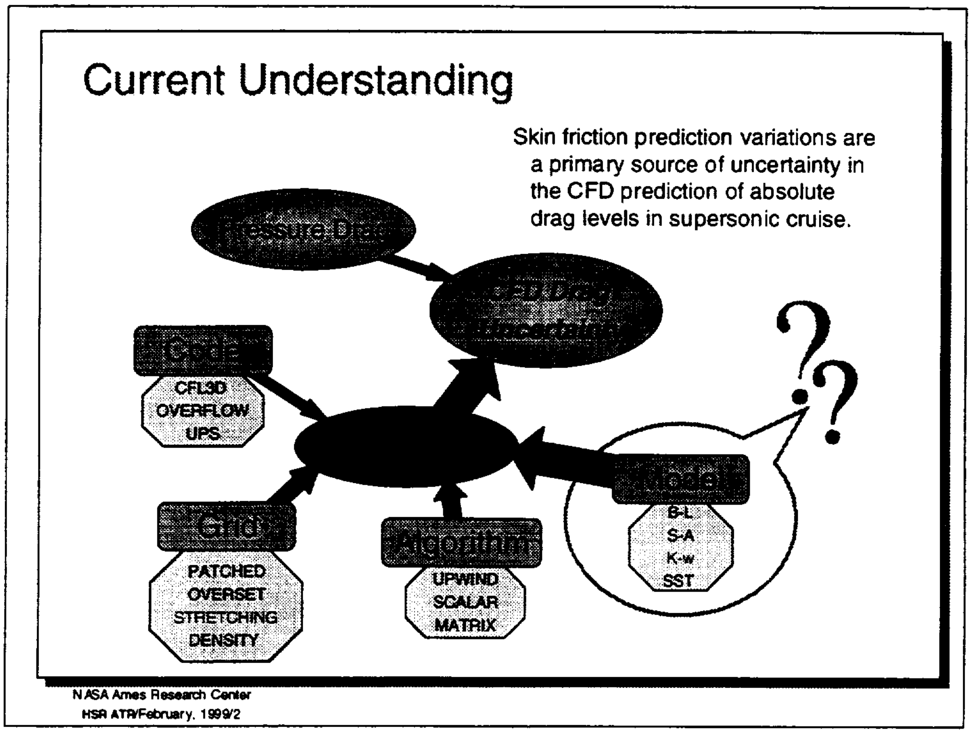

This schematic describes what is believed to be the current understanding of the sources of CFD drag prediction uncertainties, at least for the prediction of cruise Mach number wing/body configuration performance.

For "reasonable" grids and algorithms, pressure drag appears to be relatively consistently predicted, whereas skin friction drag can be quite variable. The factors that might potentially cause this variability are shown as: code, grid, algorithm, and turbulence model. Of these factors, the code itself is not thought to cause uncertainty. Whereas poor choices of grid and algorithm have been found to produce a wide range of skin friction drag estimates, it is the author's belief that the processes currently in use employ choices for these parameters that are suitable to reduce the uncertainty in friction drag predictions to acceptable levels (< 1 count) for wing/body configurations. For these parameters, poor choices can, to some extent, be identified without experimental comparison. For example, using artificial dissipation at the wall gives different results than scaling dissipation down near the wall; in the absence of experimental data, it is reasonable to conclude that the latter results are the more accurate. With a few exceptions (e.g., the low Reynolds number laminar flow produced by the Spalart-Allmaras model) the same cannot be said for the variation associated with the use of different turbulence models. Thus, the choice of turbulence model appears to have become the primary source of uncertainty in CFD drag predictions.

Outline

- New OVERFLOW turbulence models
- Grid-to-Grid comparisons
- Matrix dissipation in OVERFLOW
- Grid stretching analysis
- Summary/Conclusions

NASA Ames Research Center
HSR ATR/February, 1999/3

The outline of the presentation is shown here. The structure is intended to address elements of the previous figure, namely turbulence model, grid, and algorithm effects on friction drag.

OVERFLOW (1.8f) Turbulence Models

Flat Plate Test Case: Mach 2.4 Wind Tunnel Conditions

- New models in OVERFLOW v1.8f:
  - k-ω (Wilcox/Huang)
  - SST (Menter)
- Local skin friction groups into two distinct levels at moderate Re_x
- Average skin friction complicated by low-Re_x behavior

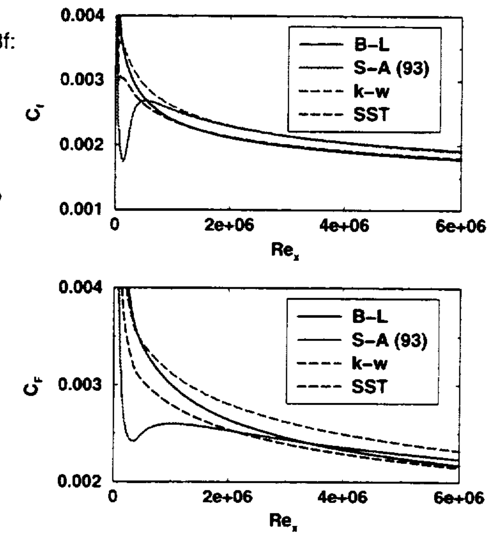

NASA Ames Research Center
HSR ATR/February, 1999/4

The version of OVERFLOW exercised in this study is v1.8f. This version includes two new (to OVERFLOW) 2-eq turbulence models: the k-w model developed by Wilcox and the SST model (Menter), which is a modification of the Wilcox model.

The results shown here, for a Mach 2.4 flat plate, indicate that the two new models produce significantly different local skin friction levels at moderate to high Re. In fact, the k-w model tends to track the local skin friction produced by the Spalart-Allmaras (S-A) model, whereas the SST model tracks the Baldwin-Lomax (B-L) skin friction.

At low Re, there is a wide variation observed between the four models used and this variation has a substantial effect on the behavior of the average skin friction distributions. In particular, the average skin friction generated by the S-A model is severely affected by the laminar run region at low Re. This results in a much lower slope with Reynolds number than any of the other models.

OVERFLOW Turbulence Models: Integrated Drag

TCA Wing/Body: Mach 2.4 Wind Tunnel Conditions

Single-zone C-O grid (modified LB grid), truncated (3148")

New models add uncertainty:

- Spread of 5 counts across model families
- k-ω model notoriously sensitive to freestream turbulence

Total Skin Friction Drag

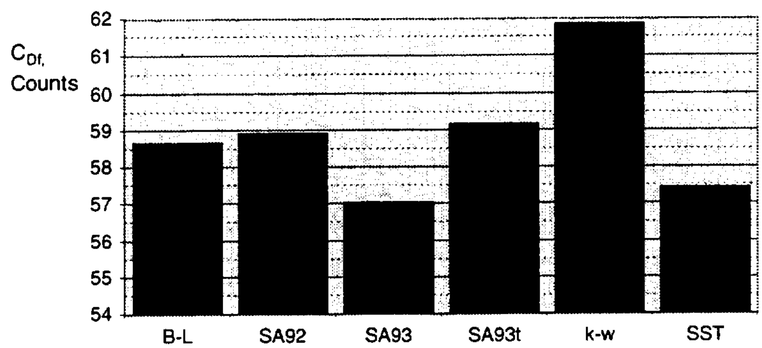

NASA Ames Research Center
HSR ATR/February, 1999/5

This bar chart indicates results of the four turbulence models (plus two modifications of the S-A model) in application to the TCA wing/body. The grid used is a single-zone C-O topology grid truncated at the sting location (x=3148"). The dimensions of the grid are 97x241x65 and the wall spacing provides an average y+ at the surface of approximately 0.7. Stretching was applied beginning at the third point off the surface.

The B-L and S-A (as implemented in OVERFLOW, SA93) models show approximately two counts of variation. This is caused by the presence of the laminar flow region near the wing leading edge over most of the span. Application of the original, or classic, S-A model (SA92), produces fully turbulent flow from the leading edge and similar integrated friction drag to that obtained with the B-L model. Overtripping, as suggested by Spalart, can also be used to cancel the effect of the laminar flow, though this process requires the specification of trip lines within the CFD grid. In addition, results are quite sensitive to a length parameter that must be specified by the user, which limits the usefullness of this approach as a predictive tool.

Note that the variation with turbulence model is increased by virtually an order-of-magnitude with the addition of the 2-eq. models. It should be noted that the k-w model is known to be sensitive to freestream turbulence levels specified in the code. This effect has not been adequately investigated here.

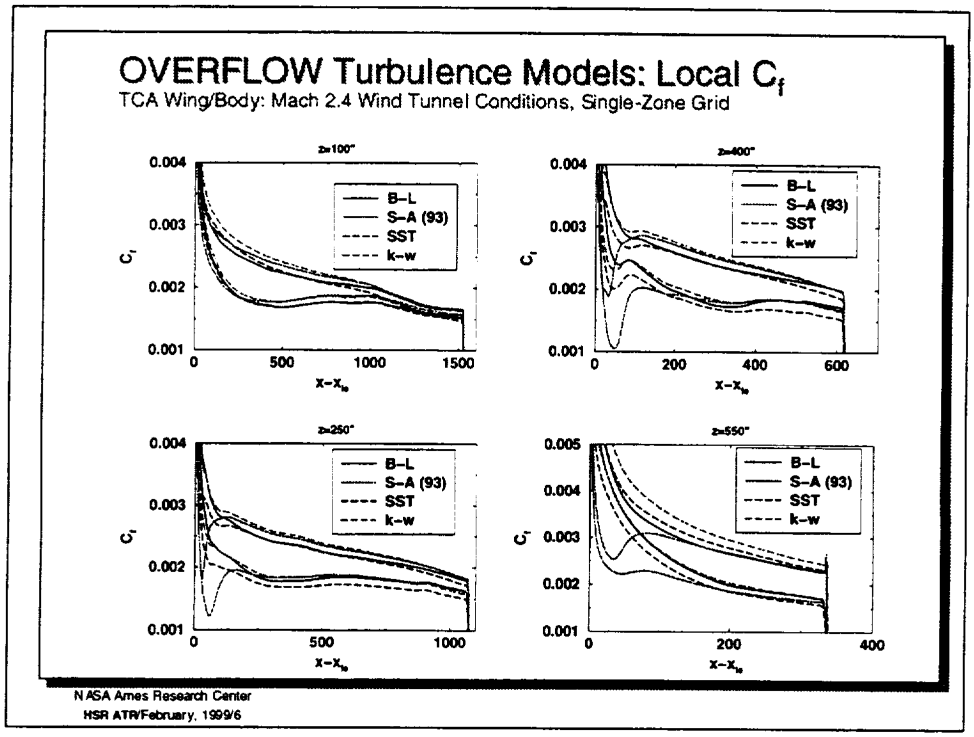

In an attempt to localize the sources of the friction drag differences, local skin friction has been plotted at four equally spaced span stations. Styles are applied in a manner similar to the flat plate case. It is apparent that the local skin friction on the lower surface (higher levels) behaves somewhat flat plate-like in a relative sense. That is, the S-A and k-w models produce similar distributions and the B-L and SST produce similar distributions, but lower than those of the other models. The behavior on the upper surface is more complicated, indicating a variation in the response of the various models to pressure gradient. Also, the outboard section (z=550") is complicated by low Re effects.

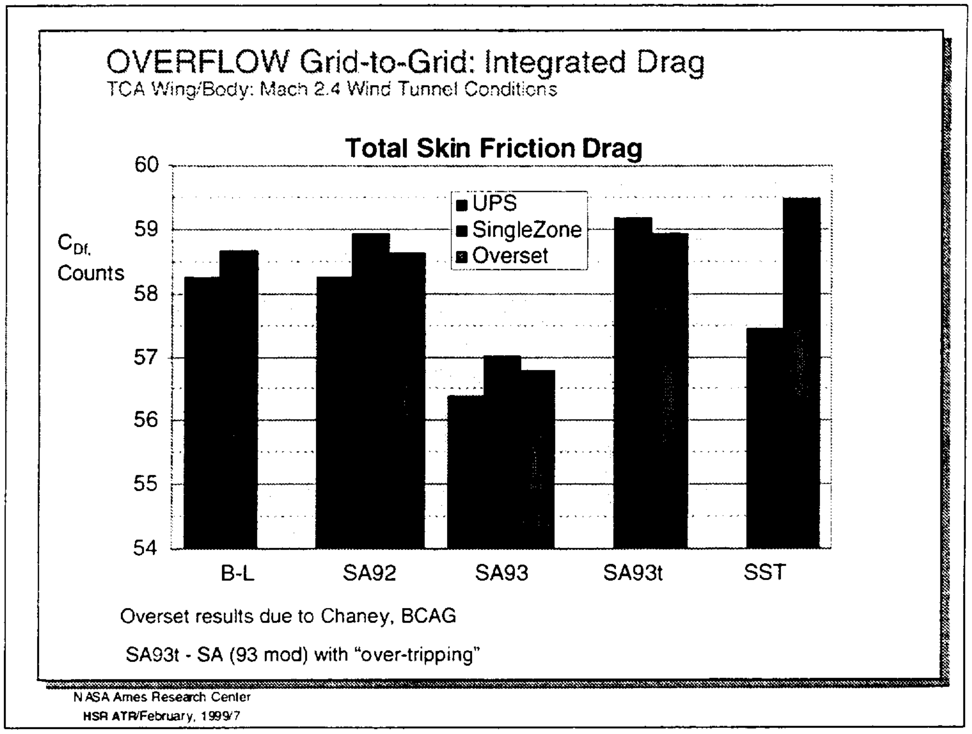

Skin friction drag predictions for the TCA wing/body are shown here for 12 different solution processes. Variables include turbulence model, code, and grid. For each turbulence model, variations tend to be modest (< 1 count of frag), except for the SST model which indicates a significant sensitivity to grid. Overset grid solutions were computed by Chaney at BCAG.

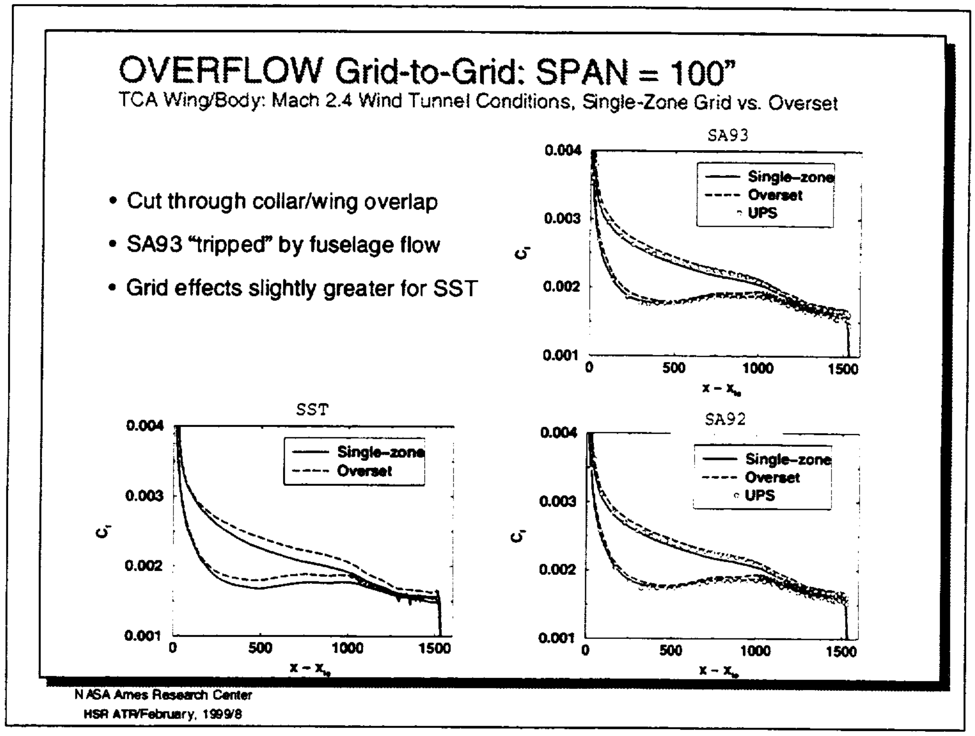

In order to localize the sensitivity to grid observed with the SST model, local skin friction coefficients are plotted at the four span stations previously used. Results are shown here at z=100" for three turbulence models, including the SST model. Some chatter is observed in the overset grid results because this station passes through the wing/collar overlap region. Also of interest is the lack of laminar flow observed in the SA93 results. This is caused by the proximity of the fuselage boundary layer, which provides an influx of "turbulence" sufficient to numerically "trip" the wing boundary layer. Some grid sensitivity is observed in all three plots, but slightly more sensitivity is apparent in the SST distributions.

OVERFLOW Grid-to-Grid: SPAN = 250"

TCA Wing/Body: Mach 2.4 Wind Tunnel Conditions, Single-Zone Grid vs. Overset

- Middle of inboard wing
- SA93 shows laminar region
- Significant grid effects only w/ SST

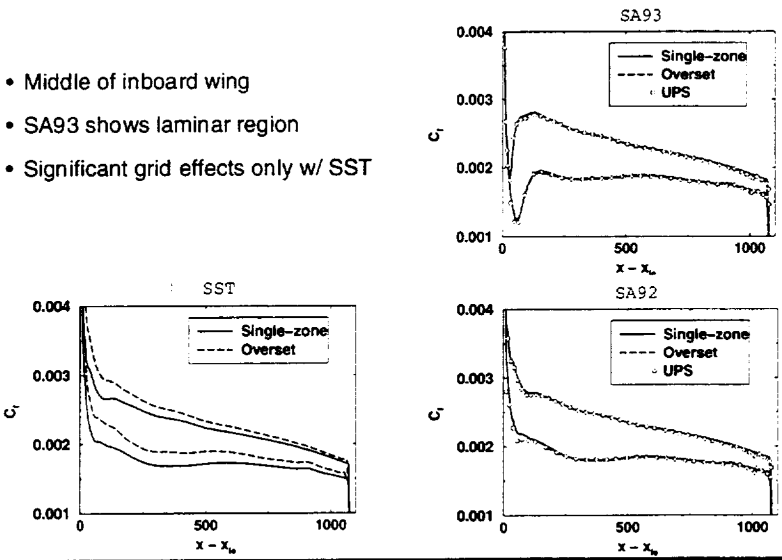

NASA Ames Research Center
HSR ATR/February, 1999/9

At z=250", the grid sensitivity of the SST model appears to be more severe than at the inboard station. The overset result produces high skin friction on both the upper and lower surfaces. Results for the two versions of the S-A model appear to be insensitive to grid and code at this span location. The SA93 model exhibits the characteristic undershoot or laminar flow region near the leading edge on both upper and lower surfaces at this location.

OVERFLOW Grid-to-Grid: SPAN = 400"

TCA Wing/Body: Mach 2.4 Wind Tunnel Conditions, Single-Zone Grid vs. Overset

- Slightly inboard of wing break
- Reduced grid effects on aft lower surface (SST model)
- SA92 and SA93 show good grid-to-grid and code-to-code agreement

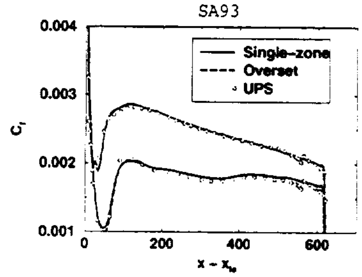

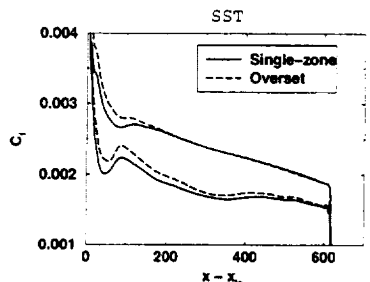

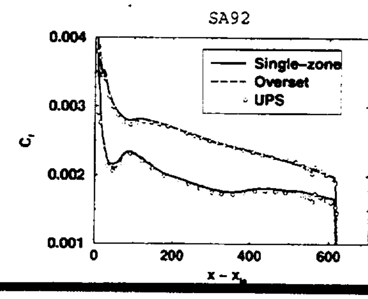

NASA Ames Research Center
HSR ATR/February, 1999/10

Near the outer edge of the inboard wing section, the grid sensitivity of the SST model is more modest, especially on the lower surface. Again, little grid or code sensitivity is observed with either S-A model.

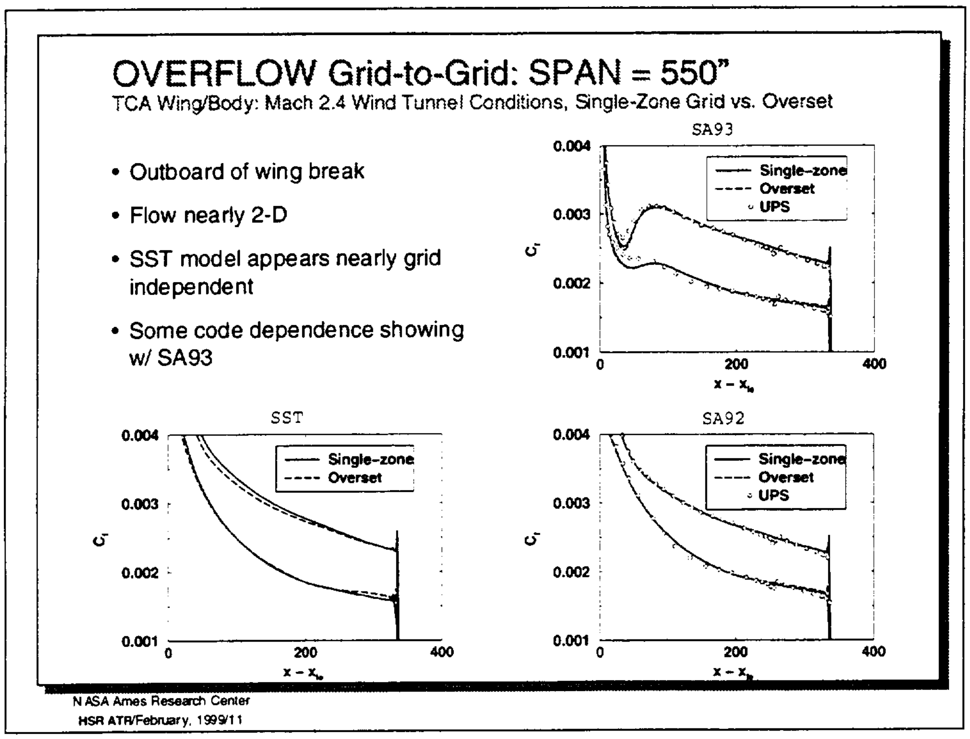

Finally, on the outboard wing, the grid sensitivity of the SST model is nearly gone. Some sensitivity to code (or grid) is observed with the SA93 model, but it is of a relatively small magnitude and is limited to a relatively small area.

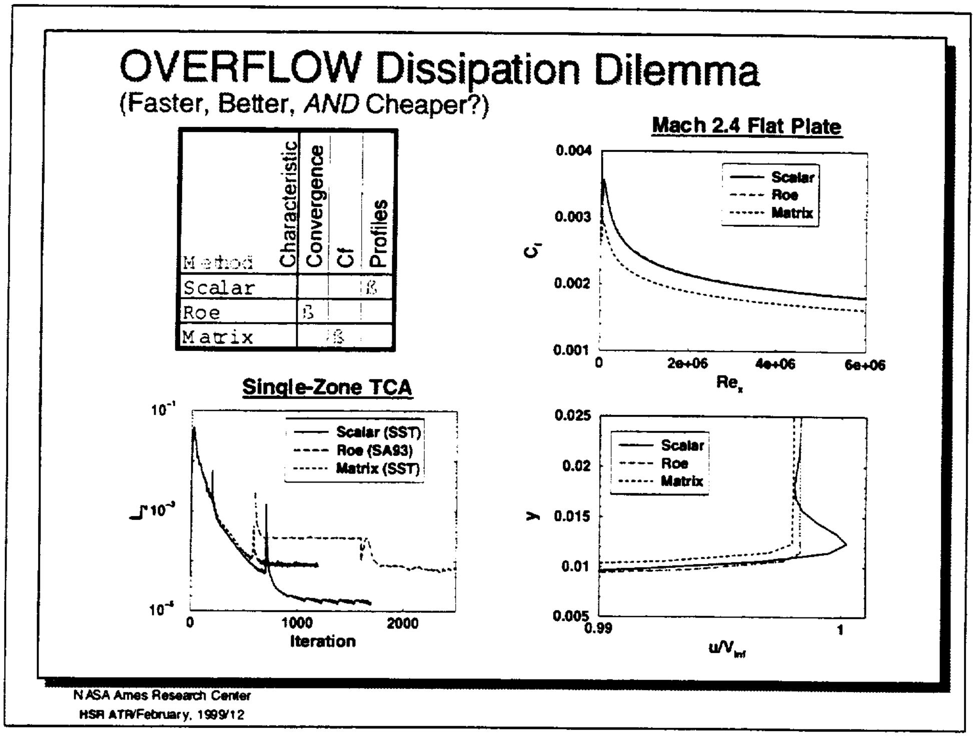

The OVERFLOW code provides essentially three algorithm dissipation options. In terms of three criteria of interest in the HSR program, none of the algorithm options is entirely satisfactory. Each has a critical drawback: the scalar dissipation method produces velocity profiles with overshoots near the boundary-layer edge, the upwind method has convergence problems in many cases, and the matrix dissipation tends to produce skin friction significantly lower than the other methods.

The matrix dissipation scheme is similar to the scalar method in that a second/fourth dissipation operator is applied. However, it is applied to a difference of flux-like terms rather than conserved variable-like terms. With the scalar dissipation method, the user is given the option of modulating the dissipation near the wall to lessen its impact on the flow at the wall and, thus, the skin friction. This has been found to be critical to obtaining accurate friction drag estimates from OVERFLOW. In the present version of OVERFLOW, the matrix dissipation scheme has no such option.

MODIFIED Matrix Dissipation
Mach 2.4 Flat Plate

SMOO = 1 option added (analogous to Scalar method)

- Upwind-like behavior for Cf and profiles
- Convergence behavior uncertain

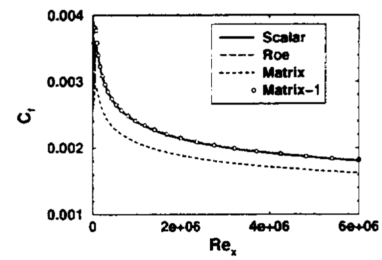

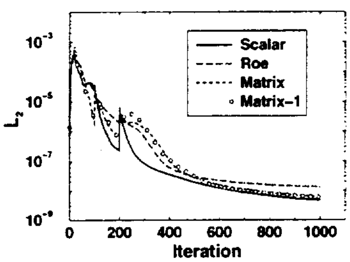

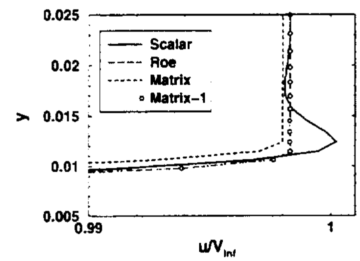

NASA Ames Research Center
HSR ATR/February, 1999/13

If an option is implemented for the matrix dissipation method analogously to what is done for the scalar dissipation, results are obtained as shown here. Skin friction results are observed to align with the scalar and Roe results, and velocity profiles are obtained which are virtually indistinguishable from those obtained using Roe. Convergence histories with the modified matrix method (Matrix-1) are similar to those obtained with the original matrix scheme. However, the convergence histories for the flat plate problem don't provide a good example of the problems that can be experienced with the Roe scheme.

Preliminary calculations using Matrix-1 on the TCA wing/body indicate that the skin friction and profiles are improved in that case as well; however, it was observed to be somewhat less robust than the scalar method and the Roe method, so further work is required.

OVERFLOW Pseudo-Finite-Volume

Effect of Volume Averaging on Grid Sensitivity

Simple Flat Plate Example (neglecting streamwise averaging)

For stress at secondary point 2:

$$\left.\frac{\partial u}{\partial y}\right)_2 = \frac{u_{3'} - u_{2'}}{\Delta y}$$

OVERFLOW: $\Delta y^* = (\Delta y_{2'} + \Delta y_{3'})/2 = (\Delta y_3 + 2\Delta y_2 + \Delta y_1)/4$

$$\Delta y^* = \Delta y + (\gamma - 1)\,\Delta y/4$$

For stress at secondary point 3:

OVERFLOW:

$$\Delta y^* = \gamma\Delta y + (\gamma - 1)^2\,\Delta y/4$$

There is a sensitivity to stretching (γ) everywhere, but especially at points where there is a sharp change in stretching.

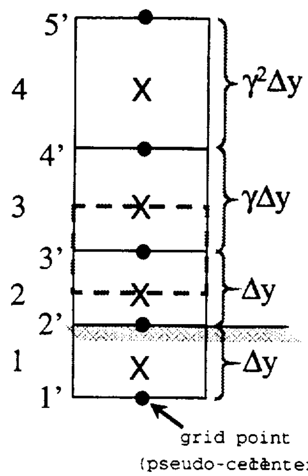

NASA Ames Research Center
HSR ATR/February, 1999/14

Finally, the sensitivity of OVERFLOW skin friction drag predictions to grid stretching at the wall has been known for several years. However, the underlying cause of the sensitivity has not been clearly understood. In attempt to provide a better understanding of the problem, a simple analysis was undertaken using a flat plate example.

The pseudo-finite-volume approach taken by OVERFLOW applies flux conservation to implied volumes (shown as dashed red line) for which geometry information is determined using averages of the geometries of the surrounding "true" volumes. As a result, for the evaluation of the shear stress at the pseudo-cell face, an average of Δy from the surrounding grid cells is effectively used rather than the actual Δy that would be used in a more formal finite-volume approach. The error introduced through this approximation is proportional to $(\gamma-1)^2$ in regions where the growth factor, γ, is constant. This is a relatively modest error as long as γ is small ($1 < \gamma < 1.2$).

The real problem occurs at the wall where the grid is effectively reflected to get boundary information. As such, $\gamma = 1$ at the wall, which introduces a discontinuity in γ, and the error in Δy incurred by averaging increases by a factor of $1/(\gamma-1)$. The error can be reduced again by extrapolating into the wall rather than reflecting, but the error is not completely eliminated without changing the way the fluxes are evaluated. It is not clear at this time, to what extent the code needs to be modified to address this problem.

Conclusions

OVERFLOW's new turbulence models add to existing uncertainty in CFD friction drag predictions

- models produce significantly different flat-plate C_f distributions
  - ➡experimental comparison (local or integrated)
- two-equation model(s) appear much more sensitive to grid than Spalart-Allmaras (one-eq.)
  - ➡controlled overset/single grid study

Matrix dissipation can probably be modified (ala scalar) to produce "good" skin friction.

Jacobian averaging is believed to be the source of OVERFLOW's sensitivity to grid stretching.

- ➡move averaging into flux routines

NASA Ames Research Center
HSR ATR/February, 1999/15

Conclusions are drawn from the work presented.

Uncertainty appears to be increased by the new turbulence models available in the new version of OVERFLOW. The uncertainty stems from differences in flat plate skin friction levels, as well as some observed grid sensitivities with the SST model. Presumably, the k-w model would exhibit similar tendencies if applied with the grids used here. It is felt that some of the differences in flat plate skin friction predictions could be sorted out through the use of experimental data, such as existing flat plate local skin friction and/or integrated skin friction through the symmetric model test. The source of the grid sensitivity of the 2-eq. models could be identified with controlled grid studies involving overset and single-zone grids on a simple geometry.

It is believed that modifications to the matrix dissipation method currently implemented in OVERFLOW could be effectively applied to correct skin friction underpredictions, though further work is needed to establish exactly how the modifications could be applied to maximize the robustness of the resulting algorithm.

Finally, simple analysis indicates that the sensitivity displayed by OVERFLOW to grid stretching at the wall is caused by the volume averaging used. The solution to the problem appears to involve moving the averaging into the flux routines to provide "flux-specific" averaging, though the performance penalty that would be incurred is unknown.

HSR Airframe Workshop, February 8-11, 1999
Task 32 - Configuration Aerodynamics

Canard Effectiveness Predictions

Doug Wilson	Boeing
Greg Stanislaw	Boeing
Servando Flores	Boeing
Max Kandula	Dynacs Eng.
Gerald Fargo	Dynacs Eng.
Anthony Saladino	Dynacs Eng.

Text for Outline

This page intentionally left blank.

Outline

- Background
- Objectives
- Approach
- Methodology
- Results:
  - Flow Visualization
  - Forces/Moments for Isolated Planforms
  - Forces/Moments for Installed Canard
- Conclusions & Lessons Learned

Text for Background

This study grew from a fusion of related studies planned by the High-Speed Configuration Aerodynamics ITD Team (CA), and the Technology Integration (TI) team. The High Lift (HL) team also lent support as the study took place, to extend the study into the low-Mach regimes which actually establish the control surface sizes. In addition to providing data for a configuration decision on what planform to use for the canard, this study provided a test case for the application of current CFD tools to prediction of control effectiveness at high CL. As such, both the methodology and results are applicable to similar planforms used for vertical and horizontal tails.

The results were intended to support various other analyses such as the canard position study being performed at Boeing Phantom Works-Long Beach and the CFD validation studies planned to utilize the aft-body closure test data to be obtained in 1999.

Background

- Canard is used for:
  - control
  - trim
  - structural mode control.
- Controls are typically sized by low-speed CLmax.
- TI wants to optimize canard planform.
- S&C needs planform and Mach effects on CLmax.
- S&C is interested in how to use CFD at <u>high AoA</u>.
- Results are applicable to horizontal and vertical tails.
- Study was supported by CA, TI, HL ITD's.

Text for Objectives

The objectives are listed on the following slide. They include both configuration development objectives (planform effects) and CFD application objectives (demonstration and selection of methods).

Objectives

- Determine maximum control effectiveness and trim efficiency of two canard planforms.
- Determine elevator effectiveness on both planforms (for structural mode control)
- Determine whether isolated results predict installed behavior.
- Compare Euler and Navier-Stokes solutions (to support other canard-wing-body analyses).
- Evaluate effect of Mach number and Reynolds number on canard effectiveness.

Text for Approach

The objectives were addressed with an interwoven matrix of analyses. Since it was desired to tie in with other HSR high-speed canard integration studies, the "PTC Canard on TCA Wing/Body" configuration was utilized.

One crucial aspect of the approach involved using a consistent method (CFD code, turbulence model, grid) for obtaining the Navier-Stokes solutions so that effects of planform, Mach and Reynolds number could be obtained.

Another part of the strategy involved scoping the problem so that the isolated planform studies could be run on the SGI-R10000 workstation available in-house at Dynacs Engineering. This consideration entered into the decision to do much of the analysis on an isolated planform rather than an installed canard, and also in selecting the highest Reynolds number considered. Most of the installed w/b/c analyses were performed on the NASA Cray C-90.

The reasons for focusing on the Mach 0.9 case rather than a lower Mach number were: (1) the TI study focused on high-speed trim drag and canard effectiveness as a structural mode controller, (2) the numerical problem was known to be more amenable to solution at the higher Mach number, and (3) known related studies would also be in this speed regime.

Approach

- Select planforms based on TI feasibility study.
- Analyze isolated planforms with Euler & Navier-Stokes codes.
- Choose method for installed analyses based on isolated results.
- Use same geometry as other "PTC-on-TCA" studies.
- Size problem to fit on SGI-R10000 workstation.
- Focus on transonic case (M=0.9).
- Evaluate selected conditions at low speed (M=0.24).

Text for Methodology

It was desired to use a common method which could be applied to all of the analyses needed to meet the various objectives. A grid was developed for the isolated planform which would provide a y+ of 2 for the highest Re considered. This same grid was used for the lower Re N-S solutions and the Euler solutions.

The OVERFLOW code was used for all analyses with the default ARC3D algorithm. Initially the Spalart-Allmaras turbulence model was used, but it was found to have convergence difficulties at high angles of attack with a deflected elevator. The Baldwin-Barth model was then used, and most of the cases already run with S-A were re-run with B-B to obtain a consistent set of results. It was not possible to obtain a converged Euler solution at high angle of attack for the Canard-2 planform at Mach 0.24 using the ARC3D algorithm, so the LU-SGS/Roe algorithm was tried. This algorithm converged, but resulted in very high CL's, and the data are not presented.

Run times on the SGI-R10000 were approximately 10.8 hours for a isolated N-S solution and 3.6 hours for an isolated Euler solution. The installed w/b/c N-S solution took approximately 40 hours on the SGI R-10000, or 7 hours on the Cray C-90.

Methodology

- OVERFLOW code used for Euler and N-S solutions.
- Spalart-Allmaras turbulence model used initially, but did not converge on some cases; switched to Baldwin-Barth.
- ARC3D central-difference algorithm (default) was used; did not converge for some low-Mach Euler solutions.
- LU-SGS/Roe algorithm was tried for low-Mach Euler to improve convergence, but results appeared questionable.
- Grid for isolated planform (similar for installed canard):
  - 245c x 59s x 55n (N-S, same for all Re)
  - 245c x 59s x 38n (Euler)
- Y+ = ~2 at Re = 10E6 (based on canard MAC)

Text for Installed Geometry

The canard surface was installed on the TCA wing/body in the location used for the "TCA Canard Integration Test" (LaRC UPWT 1705). Details of the installation and CFD model are discussed later with the installed results.

Exposed geometry of the installed canard is given below:

Installed Canard Geometry (Exposed)

Item	Baseline canard	Canard-2
semi-span, in.	199.69	286.74
surface area, ft^2	223.70	220.62
aspect ratio	1.238	2.588
taper ratio	0.275	0.30
leading edge sweep, deg.	54.2	40
trailing edge sweep, deg.	-25.3	0
MAC, in.	170.74	89.69
root chord, in.	241.77	170.3

Installed Geometry

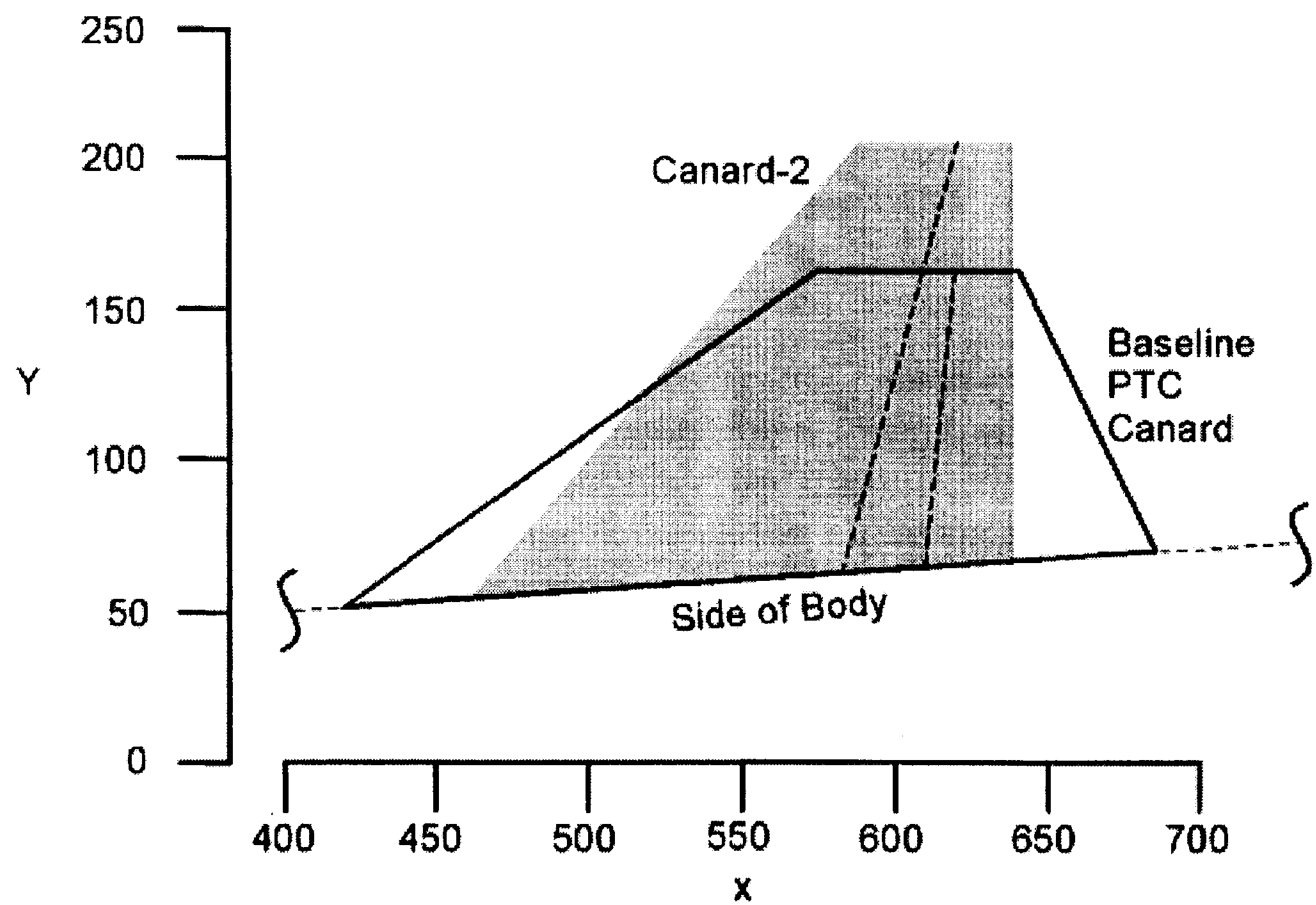

Text for Isolated Geometry

The isolated geometry was intended to be equivalent to the nominal exposed installed geometry so direct comparisons of installed and isolated characteristics could be made. However, some unintentional differences appeared in the geometry used for the isolated analyses. Most significantly, the isolated planforms had a somewhat higher aspect ratio than the exposed installed canards: 9% greater for the Baseline, and 4% greater for Canard-2.

The isolated geometry is listed below:

Isolated Canard Geometry

Item	Baseline Canard	Canard-2
span, in.	239.16	316.38
surface area, ft^2	294.40	257.96
aspect ratio	1.349	2.695
taper ratio	0.23	0.28
leading edge sweep, deg.	54.2	40
trailing edge sweep, deg	-23.5	0
MAC, in.	200.9	129.3
root chord, in.	288.88	182.74

Isolated Geometry

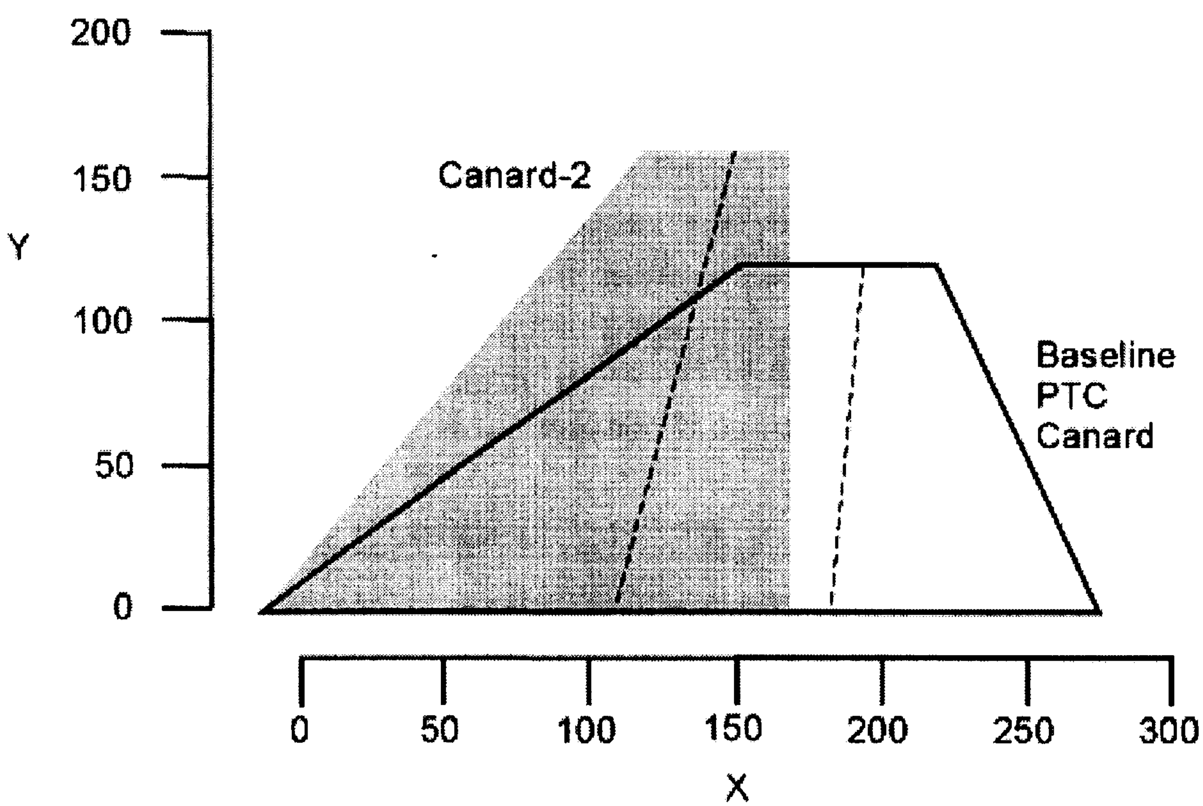

Text for Surface Pressures on Baseline

The following figure shows surface pressures on the Baseline planform at 4 deg. and 30 deg. angles of attack, for both the the Navier-Stokes and Euler solutions. The pressure patterns predicted by both solvers are similar, though it can be seen that the Euler solution displays slightly stronger gradients, particularly in the vicinity of the leading-edge vortex. The Spalart-Allmaras turbulence model was used for the N-S solutions in this figure.

Surface Pressures on Isolated Baseline Canard

M=0.9, α=4 and 30°, Re=10E6
OVERFLOW Code

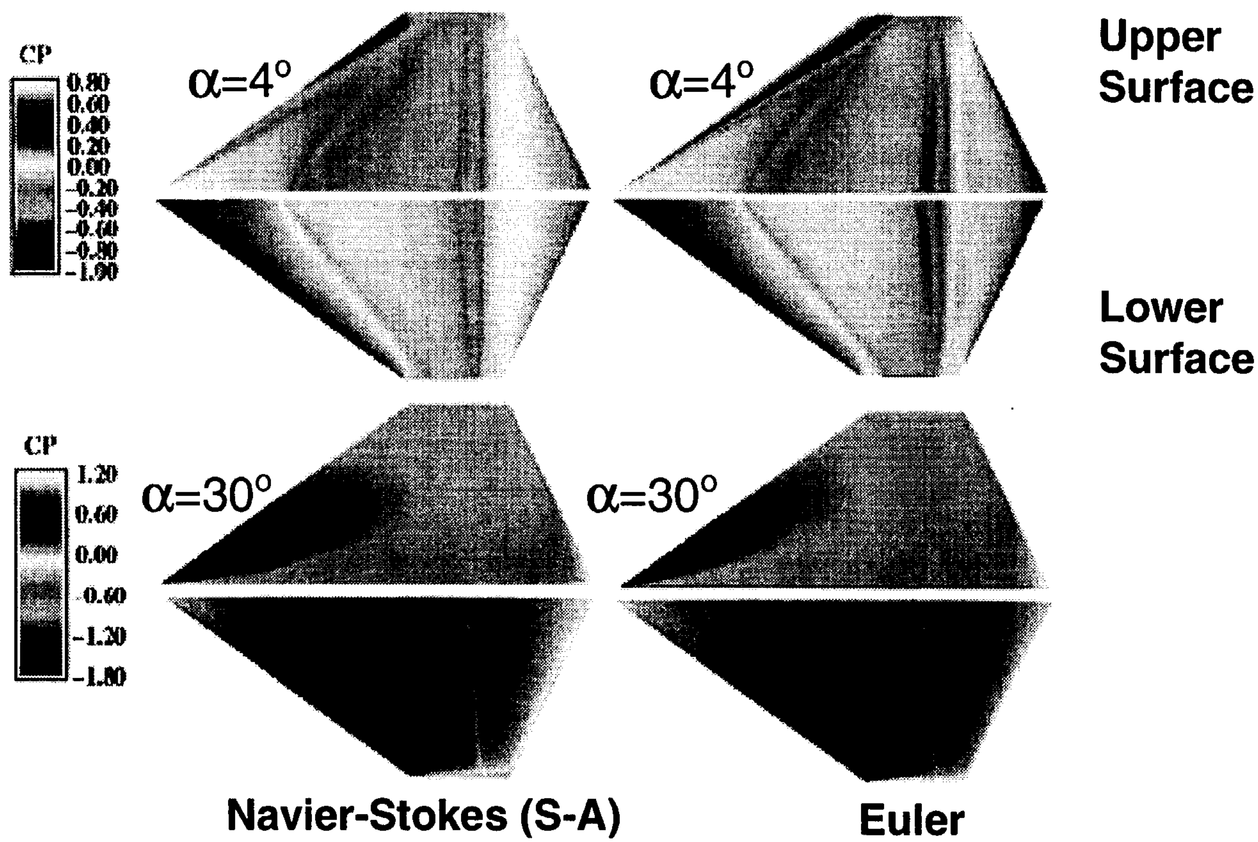

Text for Surface Streamlines on Baseline

The surface streamlines on the Baseline planform show the formation of the leading edge vortex. The Navier-Stokes solution shows evidence of vortex breakdown at the 30 deg. AoA condition, while the Euler solution is still well organized.

Off-Surface Streamlines for Isolated Baseline Canard

M=0.9, α=4 and 30°, Re=10E6
OVERFLOW Code
(upper surface shown)

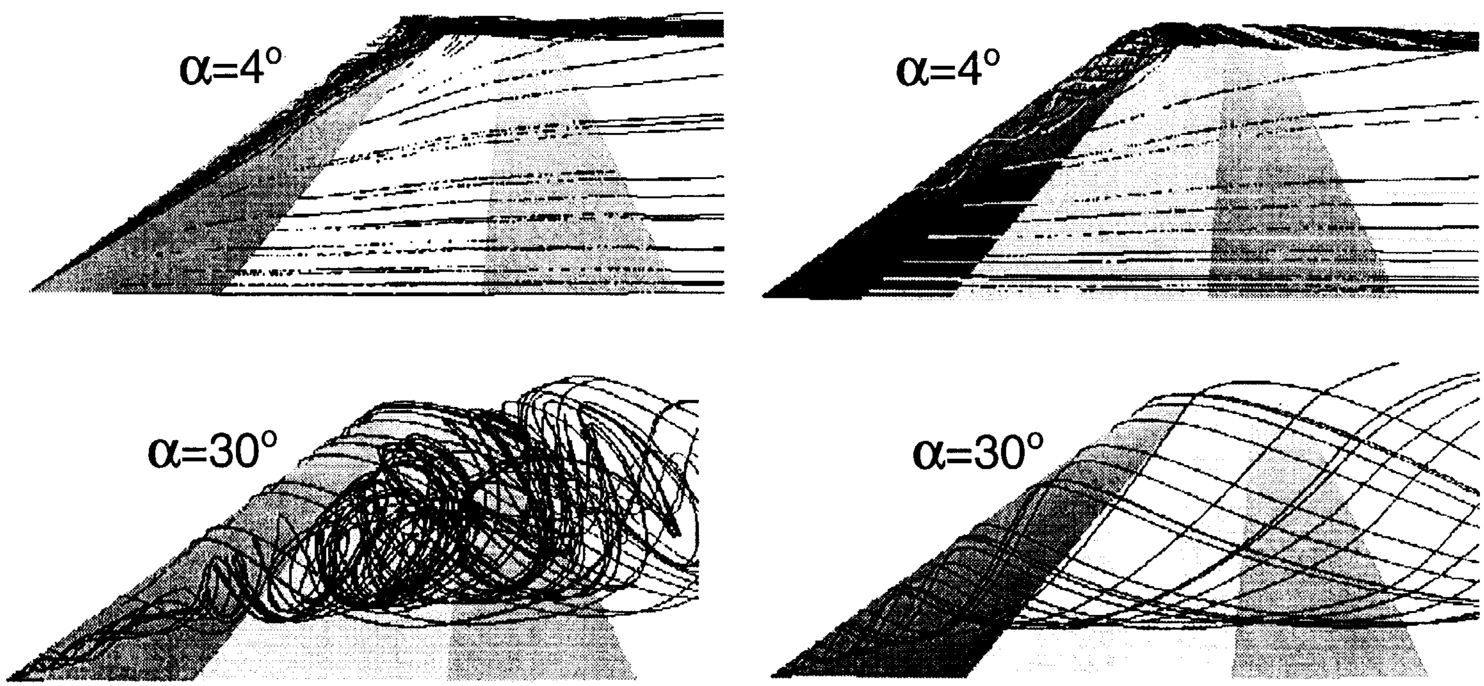

Navier-Stokes (S-A) | Euler

Text for Surface Pressures on Canard 2

The following figure shows surface pressures on the "Canard 2" planform at 4 deg. and 30 deg. angles of attack, for both the Navier-Stokes and Euler solutions. Again, the pressure patterns predicted by both solvers are similar, and again the Euler solution displays slightly stronger gradients, particularly in the vicinity of the leading-edge vortex. The vortex is not as well defined as for the Baseline planform. The Spalart-Allmaras turbulence model was used for the N-S solutions in this figure.

Surface Pressures on Isolated Canard-2 Planform

M=0.9, α=4 and 30°, Re=10E6
OVERFLOW Code

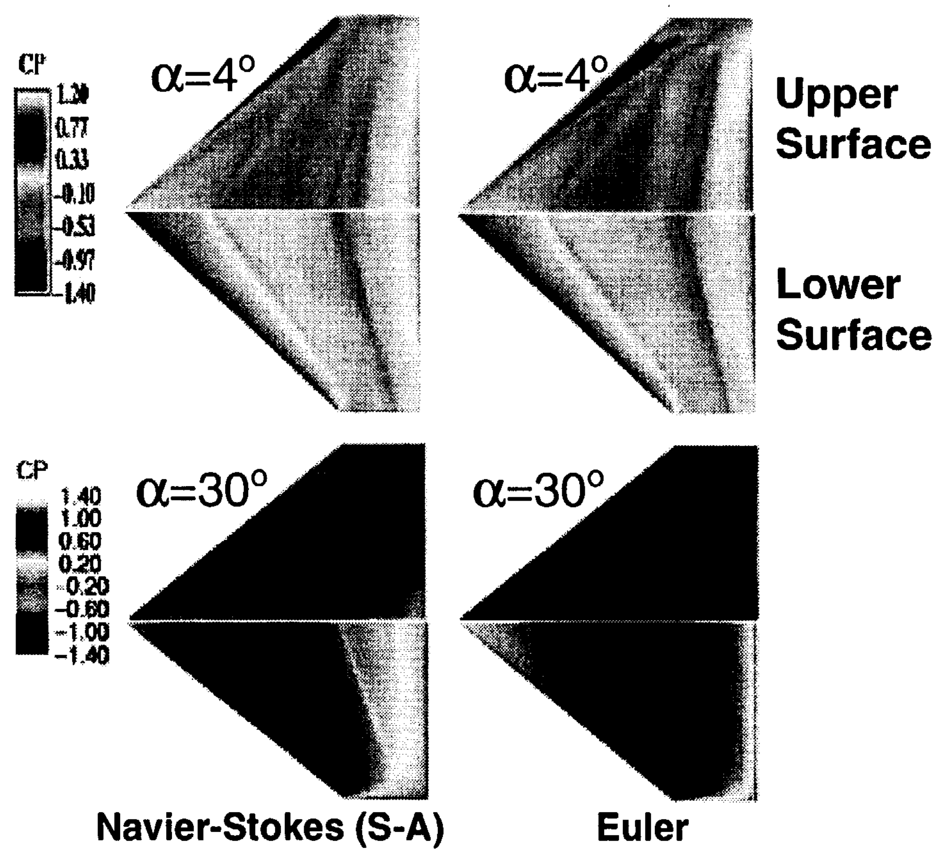

Text for Surface Streamlines on Canard 2

The surface streamlines on the "Canard 2" planform show the formation of the leading edge vortex at low angle of attack (AoA = 4 deg), but the vortex has largely broken down at the 30 deg. AoA condition. Both the Navier-Stokes and Euler solutions show evidence of major separation, though the Euler solution predicts a more organized flow.

Off-Surface Streamlines for Isolated Canard-2 Planform

M=0.9, α=4 and 30°, Re=10E6
OVERFLOW Code
(upper surface shown)

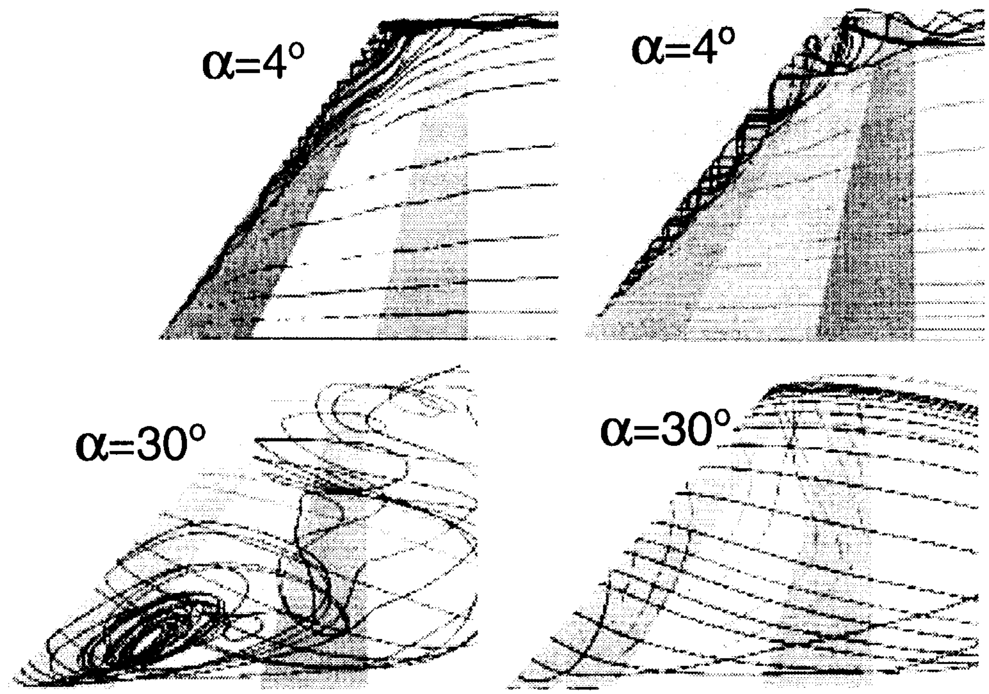

Navier-Stokes (S-A) **Euler**

Text for Results--Effects of Viscosity/Turbulence Model and Planform on Lift

The basic lift curves for the two planforms are shown here, as predicted by three methods: Euler, Navier-Stokes (N-S) with the Spalart-Allmaras (S-A) turbulence model, and N-S with the Baldwin-Barth (B-B) turbulence model. The lift predicted using the S-A turbulence model is significantly higher than with the B-B model. This is particularly noticeable on the Baseline planform, where the S-A results are nearly as high as the Euler levels.

Initial predictions were performed with the S-A model, but convergence was poor at high AoA, especially for conditions with deflected elevators. The B-B model was utilized because of its more robust convergence characteristics; the large variation in CLmax was unexpected by the authors. At low AoA (4 deg. and less) the N-S predictions converged with the Euler predictions for both turbulence models.

Estimates from DATCOM are also included on this figure. The DATCOM results are shown as a band because there are two sets of design curves for different thickness distributions, and the current planforms fell near the dividing line. The DATCOM results fall on top of the B-B curve for Canard-2, but closer to the S-A curve for the Baseline, so the DATCOM estimates cannot be taken to consistently support either set of results.

Effect of Viscosity/Turbulence Model and Planform

M=0.9

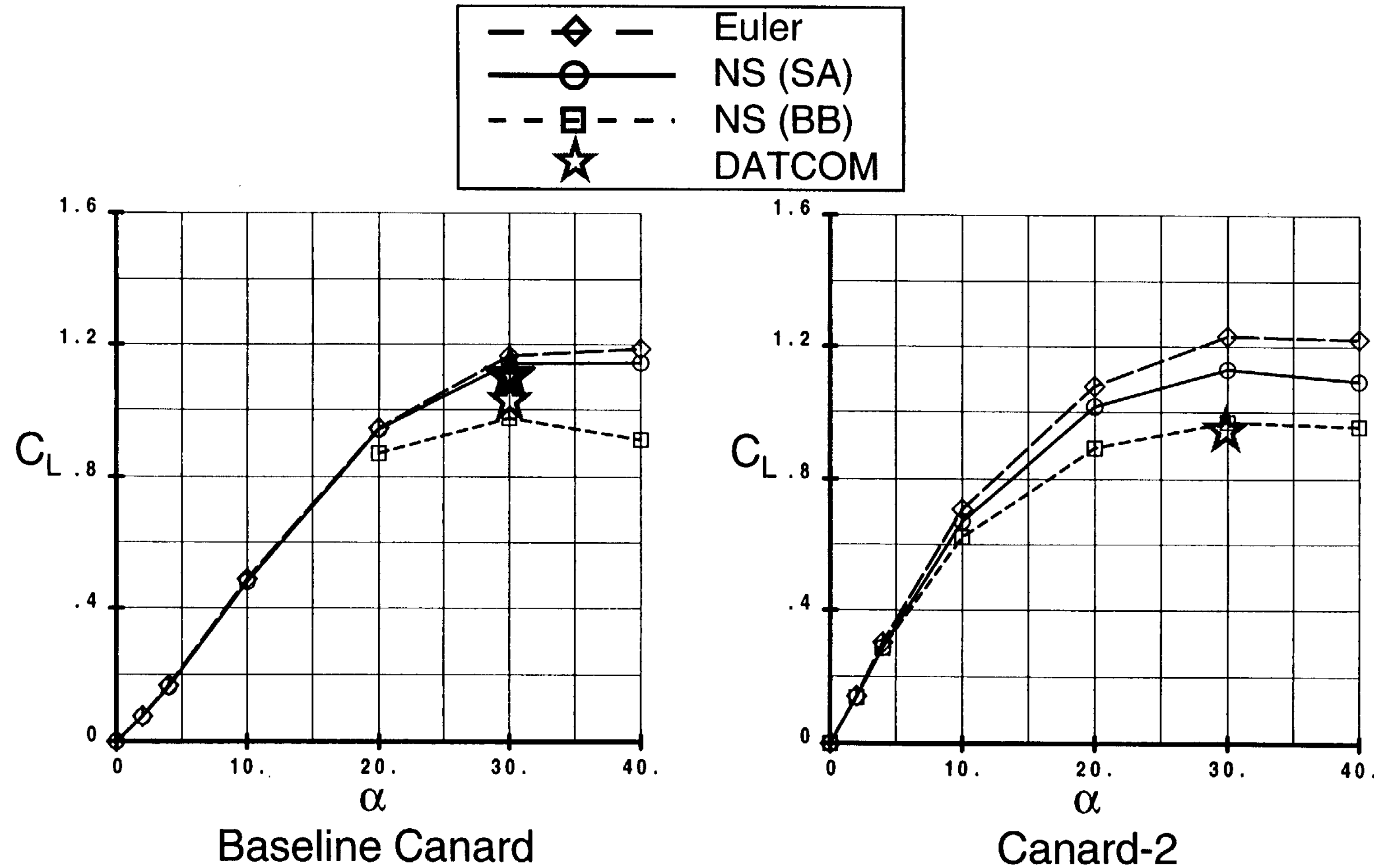

Text for Results--Effects of Viscosity/Turbulence Model and Planform on Pitching Moment

Pitching moment for the two planforms are shown here plotted against lift, as predicted by three methods: Euler, Navier-Stokes (N-S) with the Spalart-Allmaras (S-A) turbulence model, and N-S with the Baldwin-Barth (B-B) turbulence model. The specific stability levels predicted for these control surface planforms are not critical, since the canard pivot point can be selected to minimize hinge moments; however, they are a good indication of the differences in the solutions because small changes in pressure distribution near the leading or trailing edge will show up in pitching moment more clearly than in lift.

The moment reference point is at 50% MAC, so the airfoil is unstable about this point. The sharp break in the curve near CLmax indicates that the vortex lift near the leading edge has saturated, so the center of lift moves aft with increasing AoA. The Euler predictions are seen to be more stable (actually, less unstable) than the viscous predictions except at low lift levels. The two N-S solutions predict similar characteristics except for the lift level at which the pitching moment curve breaks. The B-B model predicts an earlier vortex burst than does S-A.

Effect of Viscosity/Turbulence Model and Planform

M=0.9

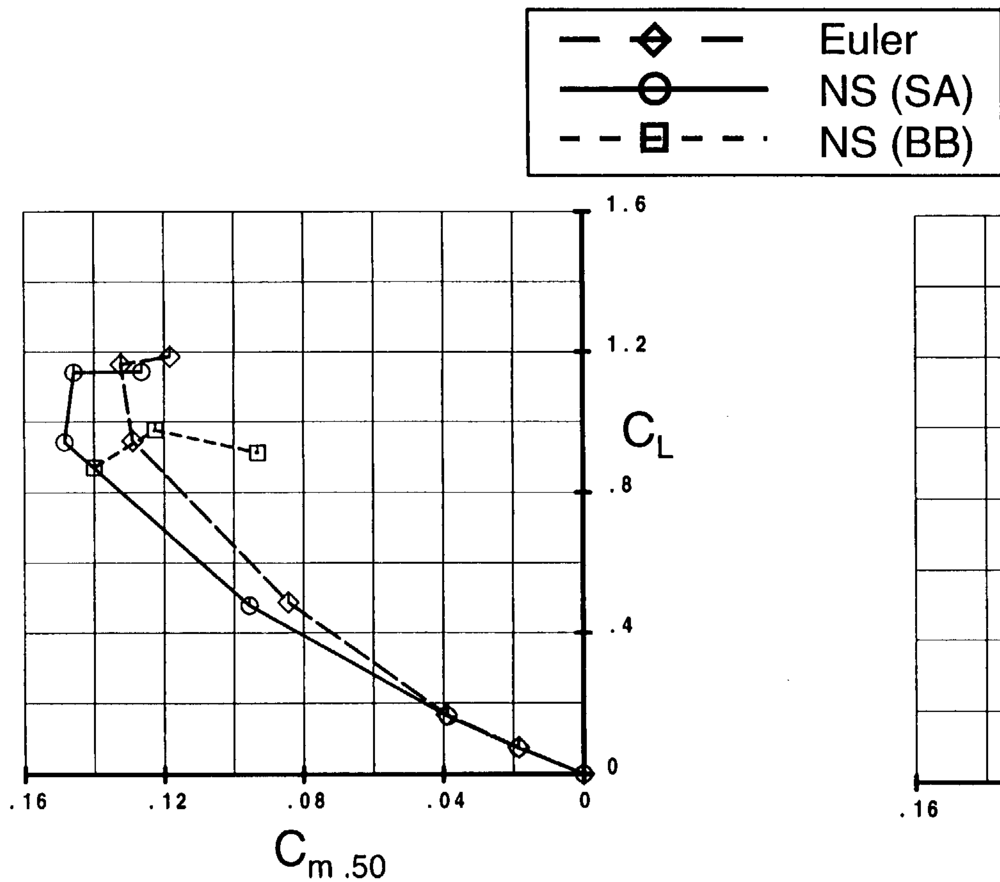

Baseline Canard

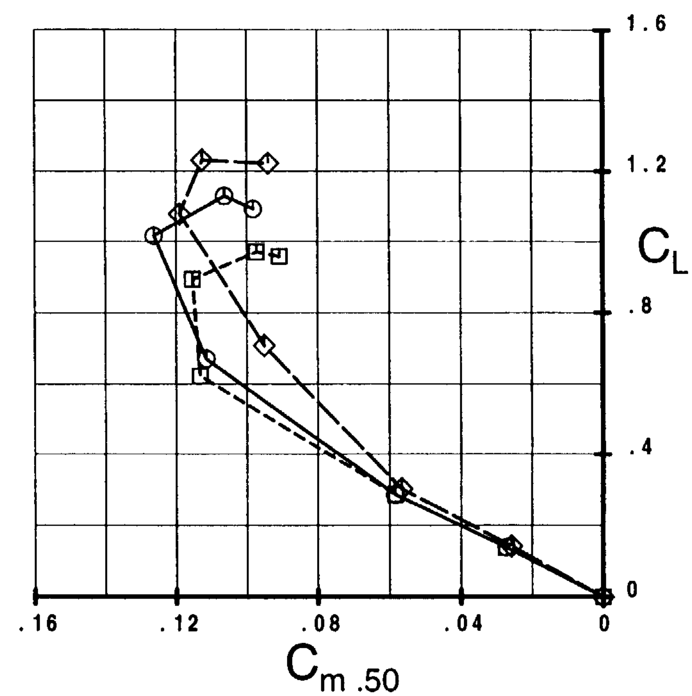

Canard-2

Text for Results--Effects of Reynolds Number

The effect of Reynolds number was explored for the Baseline planform. Two Reynolds numbers were studied: 10E6, and 1.76E6 (based on MAC). These numbers were chosen primarily for computational practicality; 10E6 was the highest Reynolds number which could practically be run on the SGI workstation with good grid characteristics, while the 1.76E6 level provided the same chord Reynolds number (for the canard) as in the associated wing-body-canard studies (the Reynolds number in wing-body-canard analyses was also chosen to fit on the SGI, with a resulting Re of 6E6 based on wing MAC). In practice, the 1.76E6 number is representative of the canard conditions which would be encountered in typical wind tunnel tests.

Varying Reynolds number caused a neglible change in results with the B-B turbulence model, and only a small difference in the results with the S-A model.

Effect of Reynolds Number

M=0.9

Baseline Canard

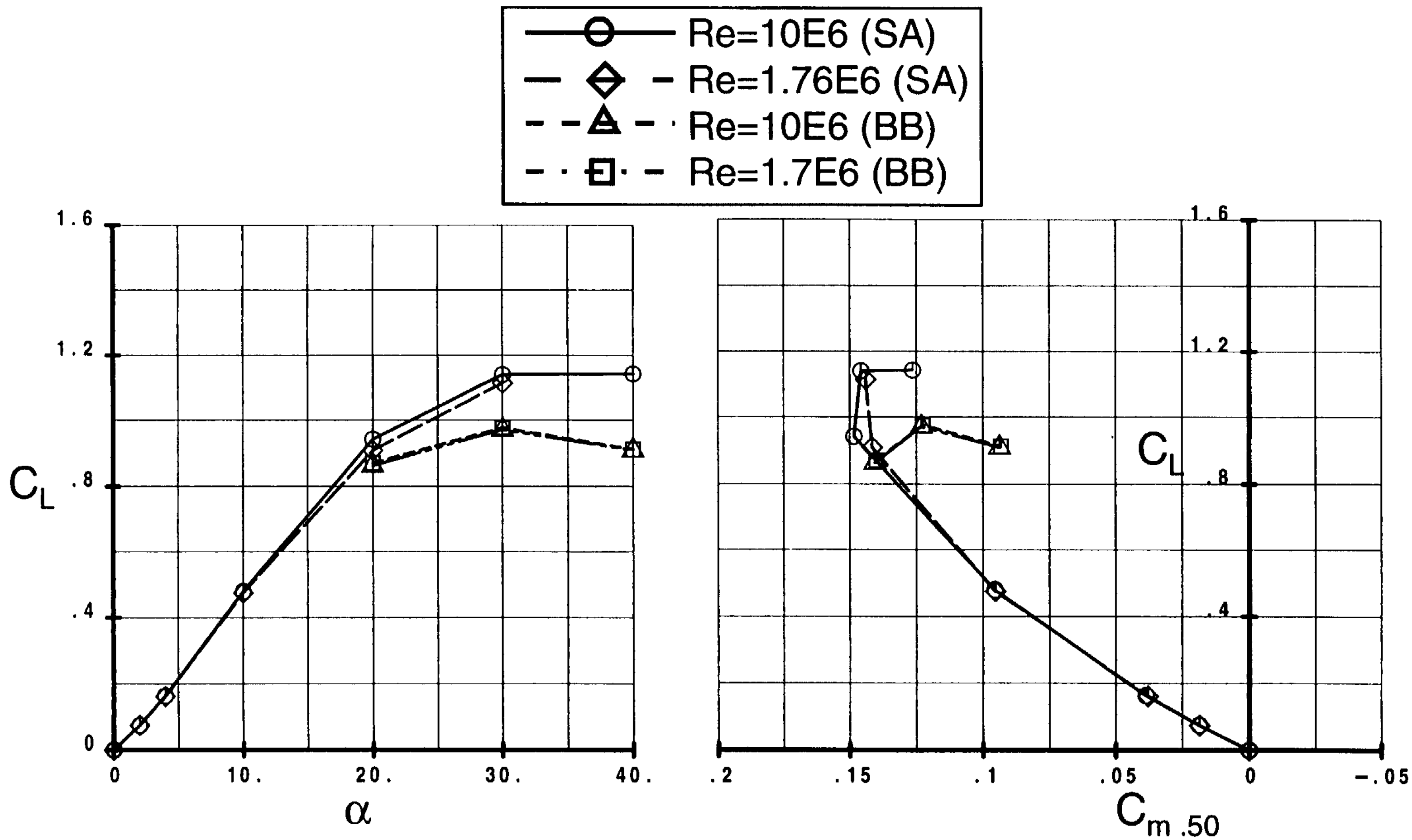

Text for Results--Effects of Planform and Mach

Solutions were generated at Mach 0.9 and 0.24 with the Baldwin-Barth turbulence model. An interesting observation is that CLmax for the Baseline planform is essentially the same at the two Mach numbers, while CLmax for Canard 2 is reduced substantially at the lower Mach number. The significance of this prediction is that the controls are typically sized by low-speed conditions such as takeoff rotation or high-alpha recovery, so the lower CLmax of the Canard 2 configuration would require it to be larger than the Baseline.

DATCOM levels are shown on this figure as well. DATCOM also predicts that the Baseline is more effective at low Mach than Canard-2, although the DATCOM levels at low Mach are substantially higher than CFD predictions.

Effect of Planform and Mach

Baldwin-Barth Turbulence Model, Re=10E6

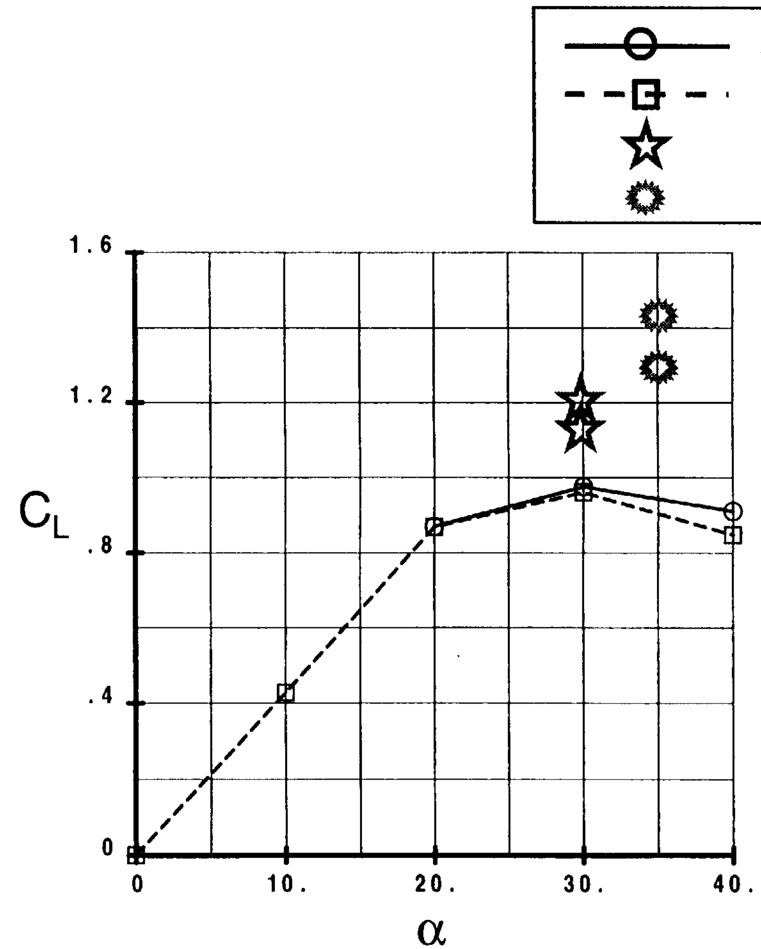

Baseline Canard

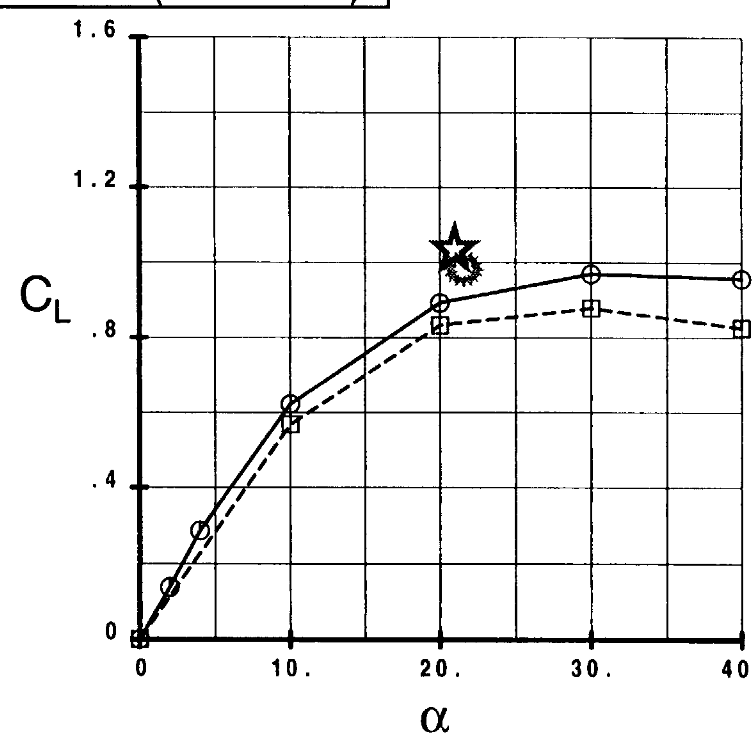

Canard-2

Text for Results--DATCOM predictions of CLmax

On several of the preceding charts, estimated values of CLmax from DATCOM (reference below) are presented. Some insight can be gained by looking at the curves from DATCOM for low-aspect wings. The Baseline planform falls in a region which permits a fairly wide variation in CLmax, depending on the thickness gradient over the front 6% of the wing and on the point of maximum thickness, in addition to the more familiar quantities of leading edge sweep, aspect ratio, and taper ratio. These quantities all affect the stability of vortex flow, and relatively small changes can change the estimated CLmax significantly. By contrast, the Canard 2 planform falls in a region which is less sensitive to changes in these quantities.

It might be expected that the differences between turbulence models, which affect vortex stability, would also show greater variation for the Baseline planform than for Canard 2. This result was observed.

Reference: "USAF Stability and Control DATCOM (Data Compendium)," McDonnell Douglas Corporation, Douglas Aircraft Division, Revised April 1978, USAF Contract F33615-76-C-3061

DATCOM Results

Notes: Symmetric Airfoils
Re = 1 X 10^6 to 10 X 10^6
Δy = Thickness growth over forward .06c
Δy for airfoil at MAC
A = Aspect ratio
β = f(M)
C_1 = f(Taper ratio)
Additional correction required for Mach 0.9

Baseline M=0.2
Baseline M=0.6
Canard-2 M=0.2
Canard-2 M=0.6

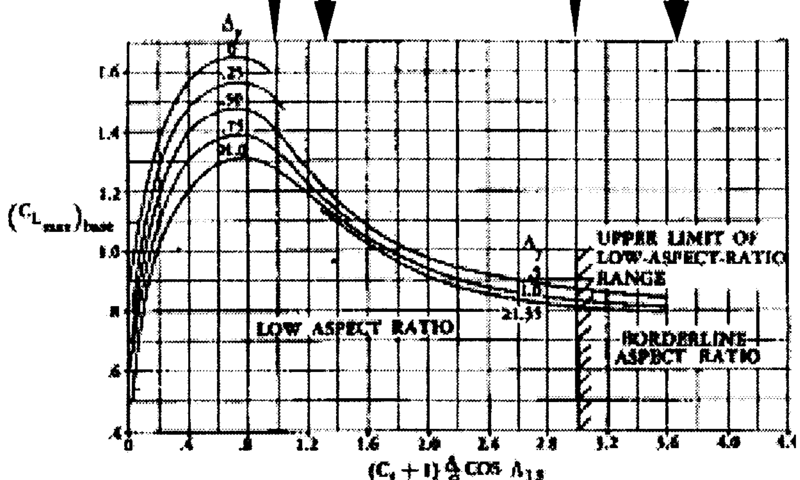

MAXIMUM LIFT OF WINGS WITH MAXIMUM THICKNESS AT OR FORWARD OF .35c

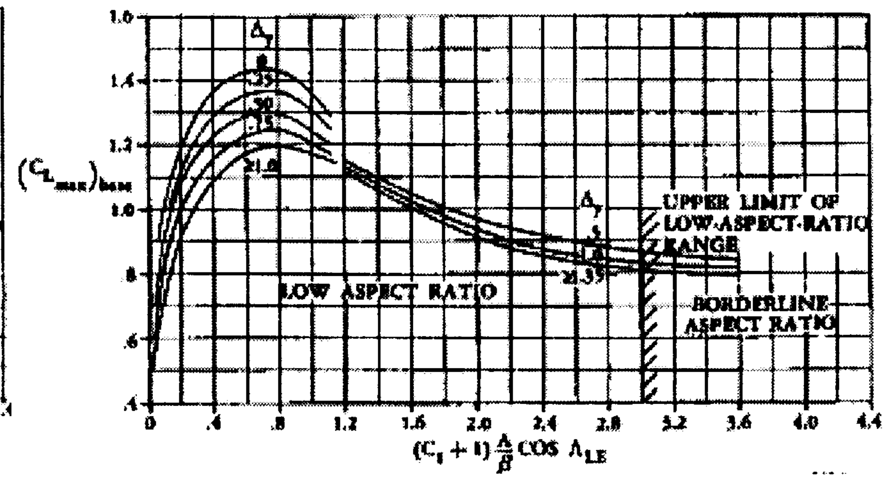

MAXIMUM LIFT OF WINGS WITH MAXIMUM THICKNESS BETWEEN .35c AND .50c

Text for Results--Effect of Planform on Drag (Isolated Canard)

The following curves compare the effect of planform on drag of the isolated canard. It can be seen that Canard 2, as expected, displays a lower drag at low-to-moderate lift levels than the Baseline. The Baldwin-Barth results were not generated at low angles of attack for the Baseline planform, so Spalart-Allmaras results are shown as well.

Although not shown, it was found that the Euler predictions for drag agreed well with the Navier-Stokes pressure drag results at low angles of attack.

Effect of Planform on Drag

M=0.9, Re=10E6

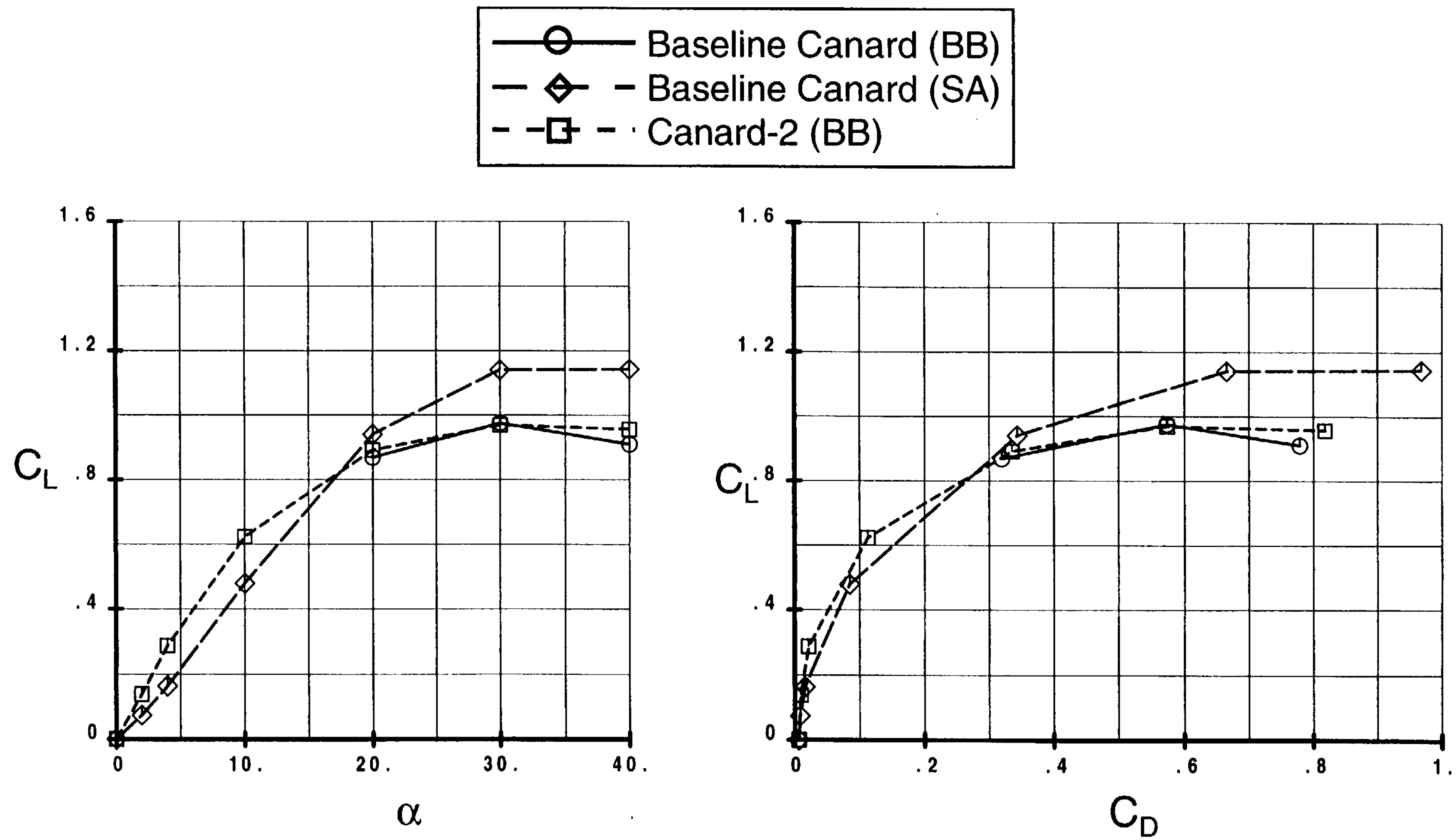

Text for Results--Effect of Planform on Elevator Effectiveness (Isolated Canard)

The isolated planforms were also analyzed with the elevator deflected 5 deg. and 20 deg. The 5 deg. analyses were intended to provide data to support structural mode control analyses, and were analyzed with an Euler code at Mach 0.9 only.

Looking at the results for a 5 deg. elevator deflection shown in the following figure, it is apparent that the "Canard 2" elevator provides much more lift for a small deflection than the Baseline elevator (0.10/deg. vs. 0.066/deg., based on Euler analyses).

Effect of Planform on Elevator Effectiveness

M=0.9

Euler Solutions

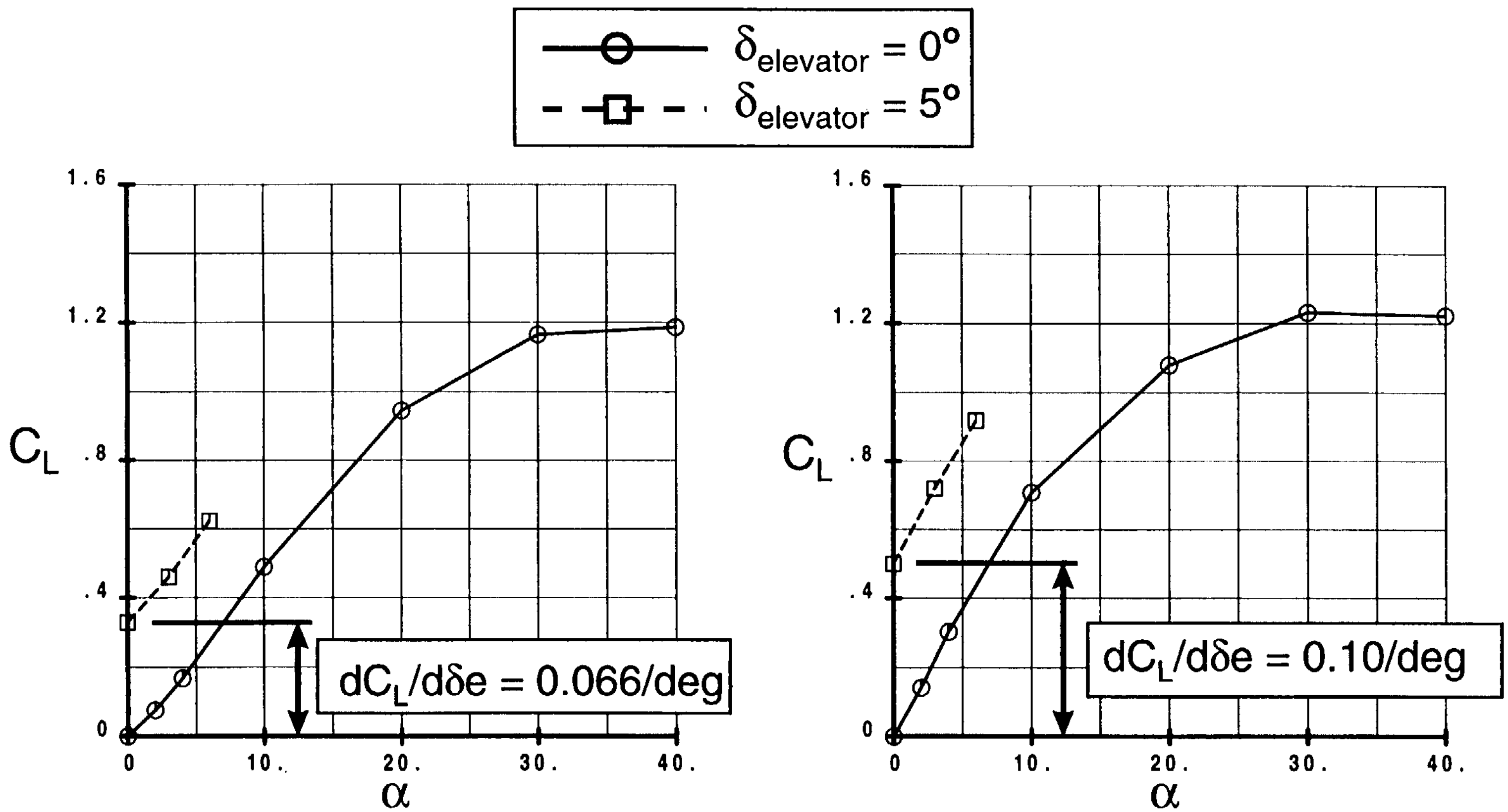

Baseline Canard

Canard-2

Text for Results--Effect of Planform on CLmax with Deflected Elevator

The 20 deg. results addressed CLmax with deflected elevator, and were analyzed with the N-S code using the Baldwin-Barth turbulence model at Mach 0.9 and Mach 0.24.

At Mach 0.9, the CLmax achieved with deflected elevator appeared slightly greater for the Baseline planform than Canard 2. This result isn't very conclusive due to the sparsity of data points.

BOEING

HSCT Aerodynamics

Effect of Planform on CLmax with Deflected Elevator

M=0.9

Baldwin-Barth Turbulence Model, Re=10E6

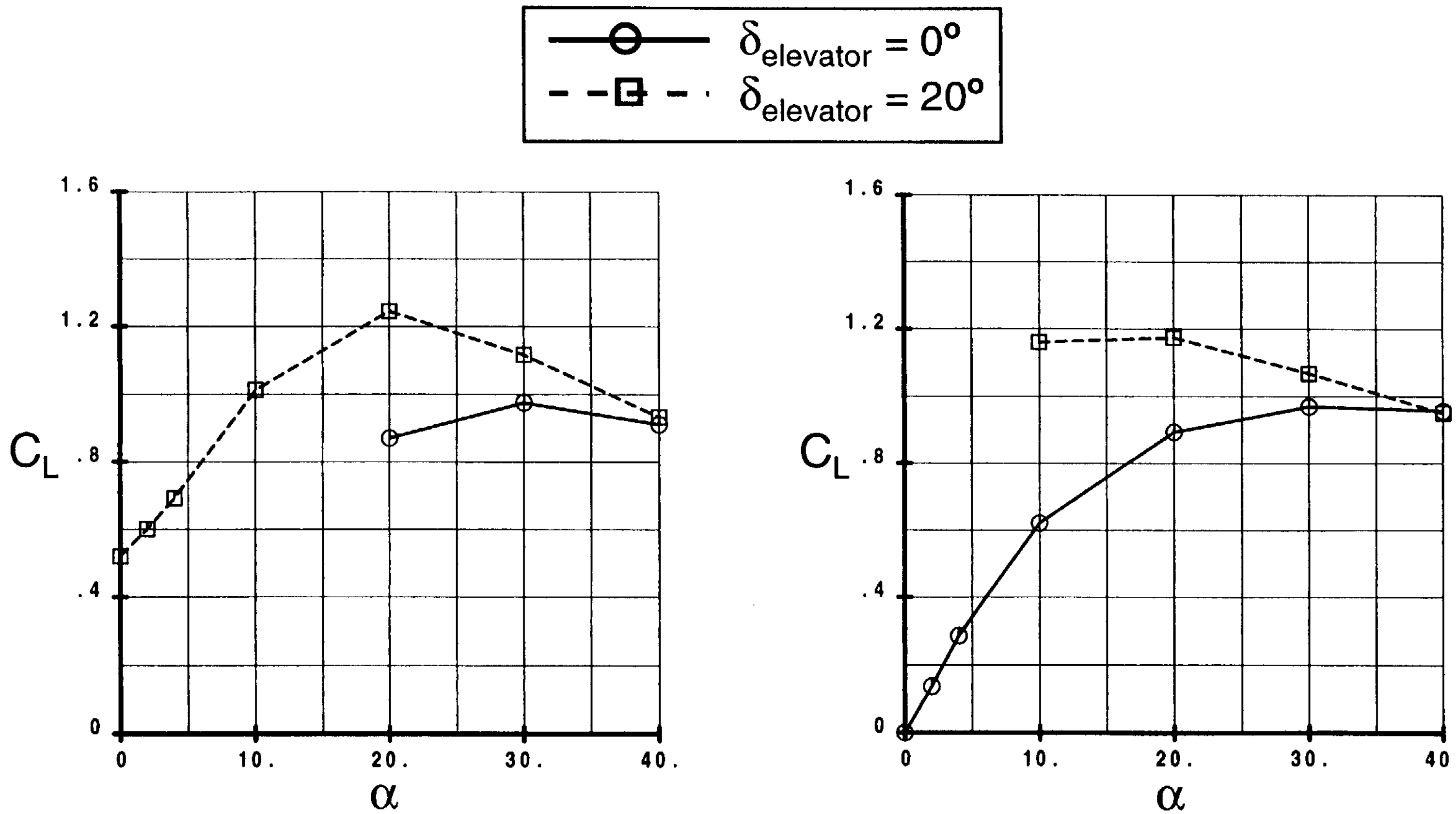

Baseline Canard

Canard-2

Text for Results--Effect of Planform on CLmax with Deflected Elevator (Cont.)

The CLmax achieved at Mach 0.24 with deflected elevator was significantly greater for the Baseline planform than Canard 2. A maximum CL of 1.44 was achieved. This result supports the historical choice of this relatively low-aspect ratio planform for HSCT pitch controls, which have typically been sized by available CL at low-speed conditions.

It might be noted that the level achieved here is well below the CL = 1.66 (based on exposed horizontal tail area) used to size the aft tail of the TCA. The tail-sizing value was derived from available low-speed experimental data, and suggests that the N-S solutions presented here may be underpredicting CLmax.

Effect of Planform on CLmax with Deflected Elevator

M=0.24

Baldwin-Barth Turbulence Model, Re=10E6

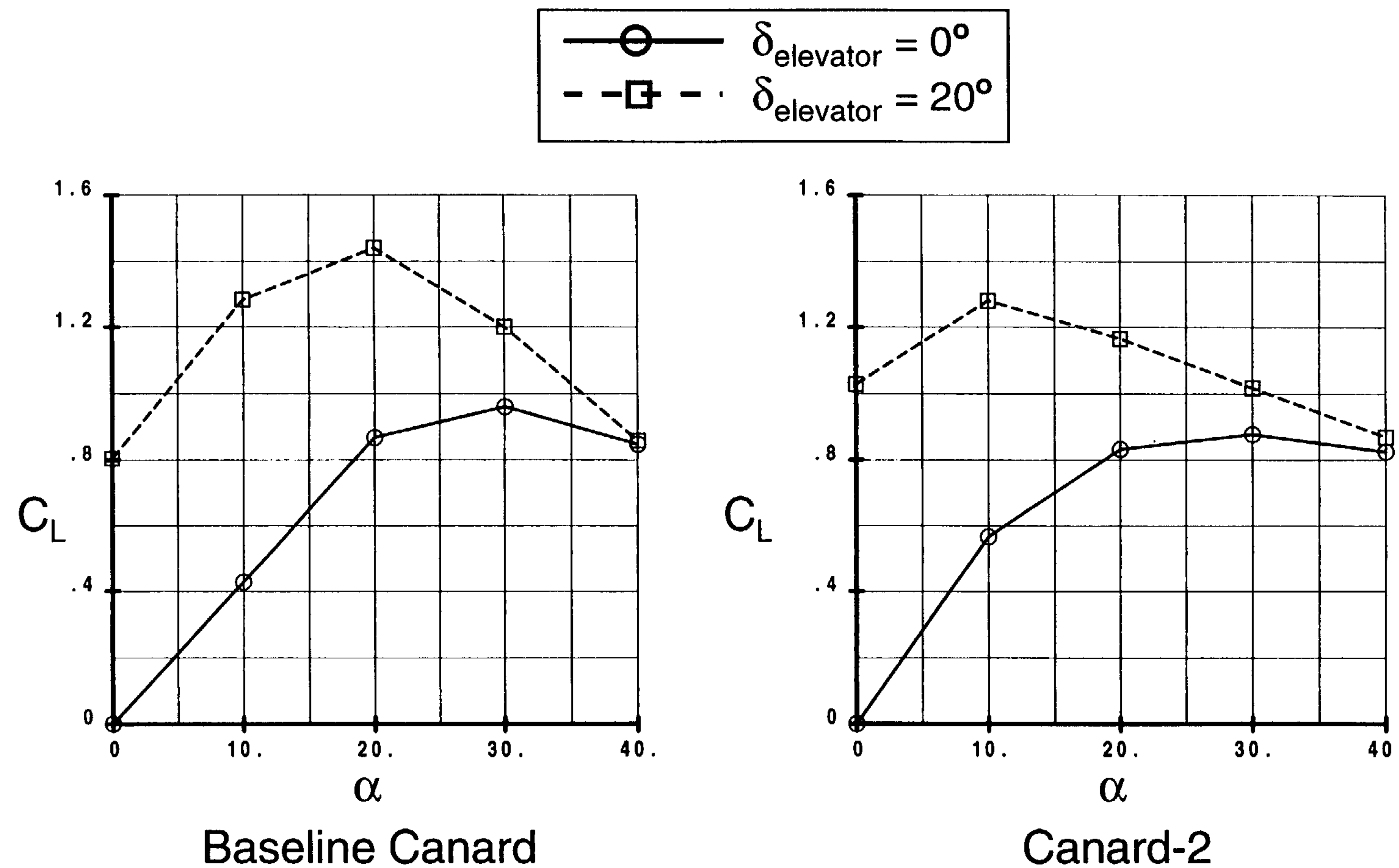

Text for Results--Effect of Planform on Installed Canard Control Effectiveness

The following figure shows installed control effectiveness for the two canard planforms at Mach 0.9, 3.7 deg. AoA. The results presented are integrated over the entire wing/body/canard, and reduced with TCA wing parameters. For small canard deflections (-4 deg. to +4 deg.), the canard surface was projected into the body surface to simulate a perfect side-of-body seal. The side of body was not recontoured to provide a wiping surface. For larger deflections (10 deg. and up), the canard planform was modified to leave a 4 in. gap (airplane scale) between the canard and body at zero deflection; the modified canard was then deflected to the desired position. This gap was large enough to be gridded succesfully, but felt to be small enough to not greatly affect the answer. The exposed area was reduced somewhat by this trimming, so the reduced area was used as the area reference for those data using the trimmed geometry. It might be noted that this 4 in. gap would be equivalent to a 0.067 in. (1/16 in.) gap on 1.675% model.

The result at zero deflection for Canard 2 is anomalous. This solution was examined in detail, but no explanation for the behavior was found. Canard 2 provides greater pitch trim effectiveness, and adds a small net lift for a positive deflection, whereas the Baseline planform contributes little to airplane lift.

Effect of Planform on Installed Control Effectiveness

M=0.9, α = 3.7°

Baldwin-Barth Turbulence Model, Re=10E6

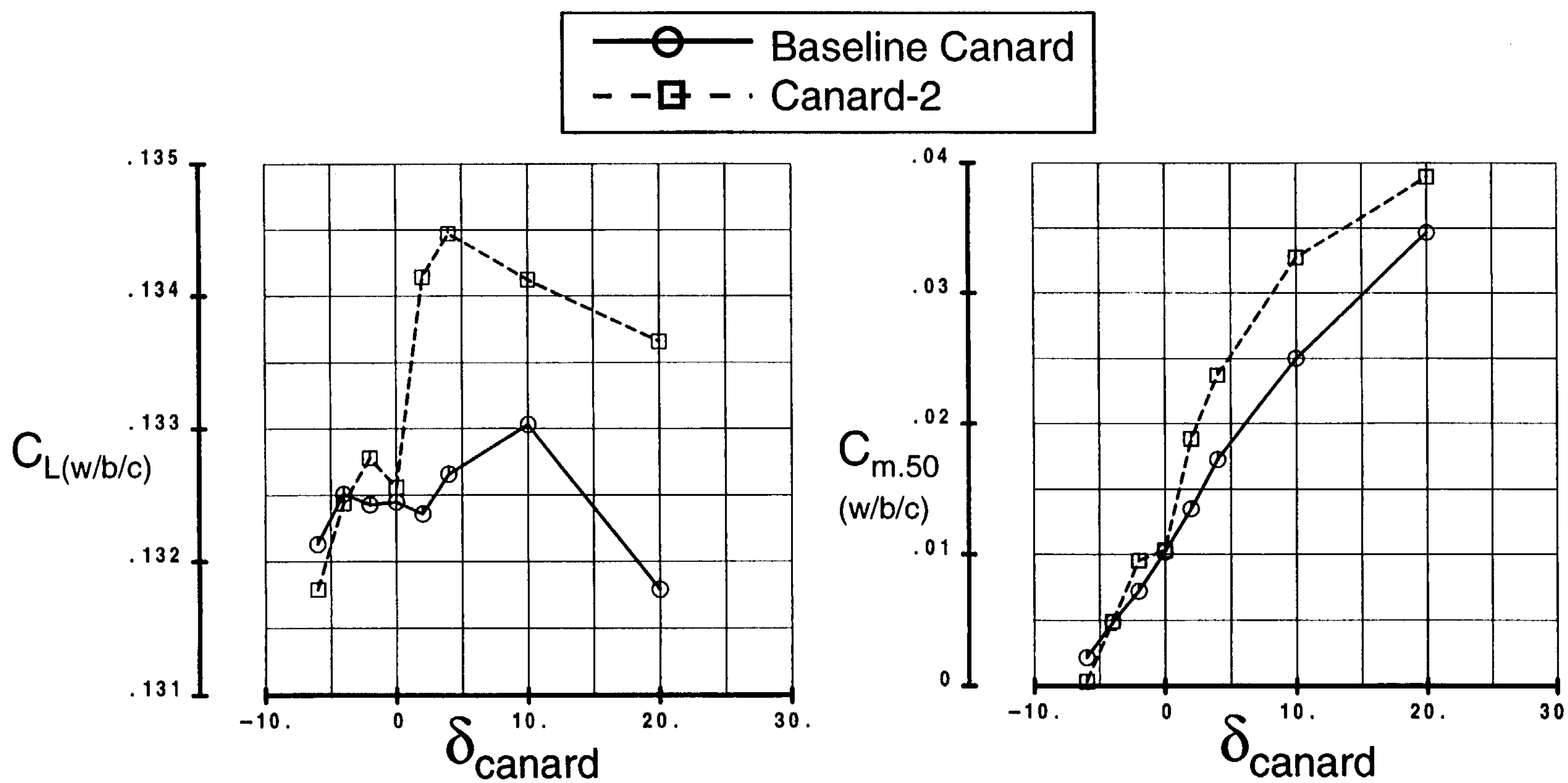

Text for Results--Effect of Planform on Installed Canard Trim Drag

The following figure shows trim drag for the two canard planforms at Mach 0.9, 3.7 deg. AoA. Both lift and pitching moment vs. drag are shown, for varying canard deflections at constant AoA. Drag values are integrated over the entire wing/body/canard, reduced with TCA wing parameters.

The anomalous behavior at zero deflection for Canard 2 can again be seen, and make it non-productive to compare the curves at low canard deflections. From the higher deflections it can be seen that Canard 2 creates less drag to trim a given pitching moment at constant AoA.

Effect of Planform on Installed Trim Drag

M=0.9, α = 3.7°

Baldwin-Barth Turbulence Model, Re=10E6

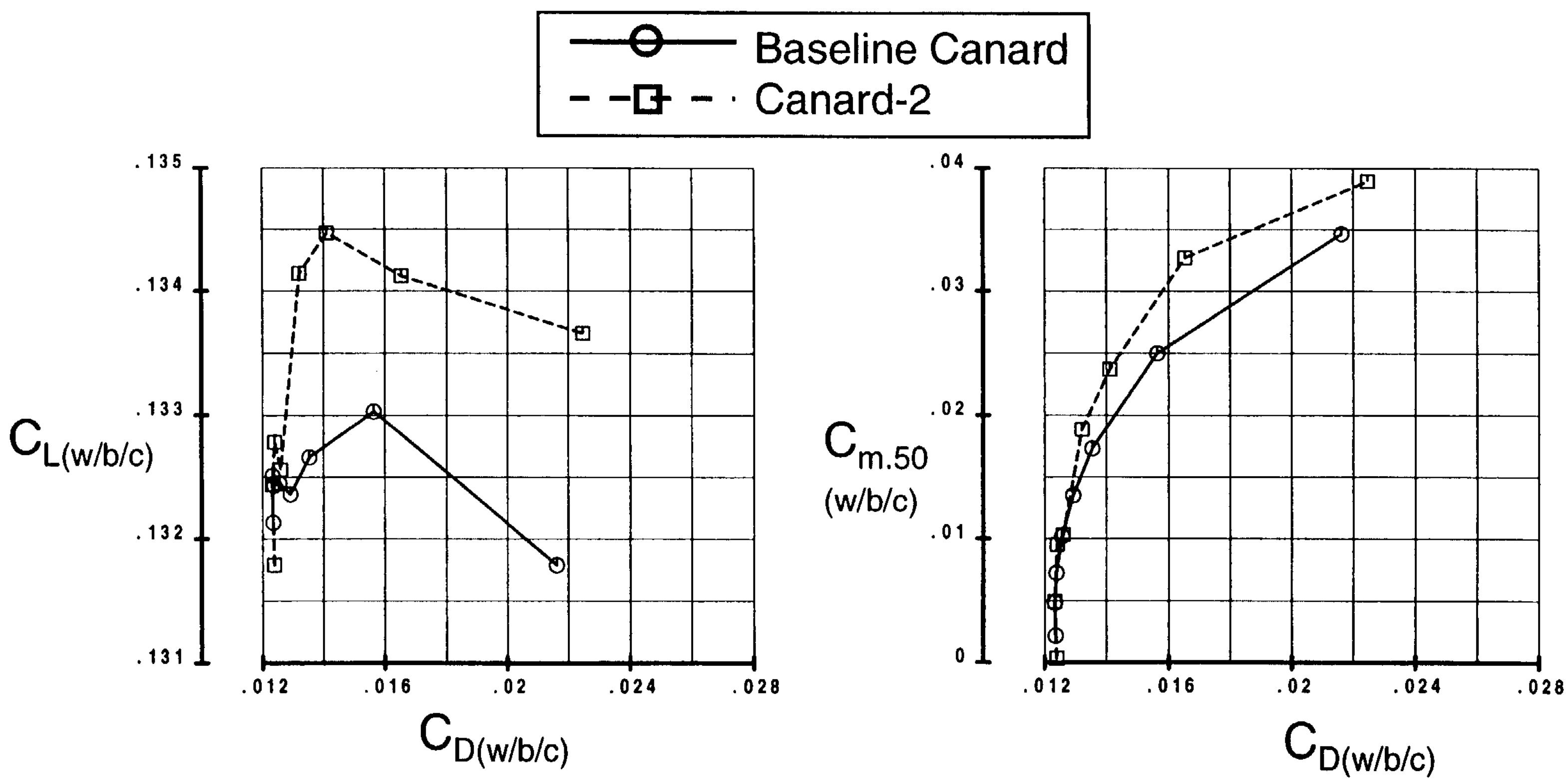

Text for Results--Canard-Wing Interference Effects

The following figure illustrates the effect of canard-wing interference. This comparison is only shown for the Baseline canard because the anomalous behavior seen with Canard-2 at zero deflection made it difficult to interpret the results.

The first plot shows incremental lift due to canard deflection. One curve shows lift integrated over the exposed canard surface only, while the other is integrated over the entire wing/body/canard. It can be seen that the incremental wing/body/canard lift is nearly zero, implying that the canard lift is canceled by induced effects on the wing.

The second plot shows incremental moment about the wing 50% MAC reference point due to canard deflection. Again, one curve represents moment integrated over the exposed canard only, while the other is integrated over the wing/body/canard. The interference effects are much smaller for moment than for lift, especially for small deflections. At the largest deflections, the w/b/c pitching moment is reduced by approximately 25% compared to what would have been predicted from the exposed canard alone. It should be noted that these solutions do not include the effect of canard downwash acting on the horizontal tail, which would generally increase canard control effectiveness.

Canard - Wing Interference Effects

Baseline Canard

M=0.9, α = 3.7°

Baldwin-Barth Turbulence Model, Re=10E6

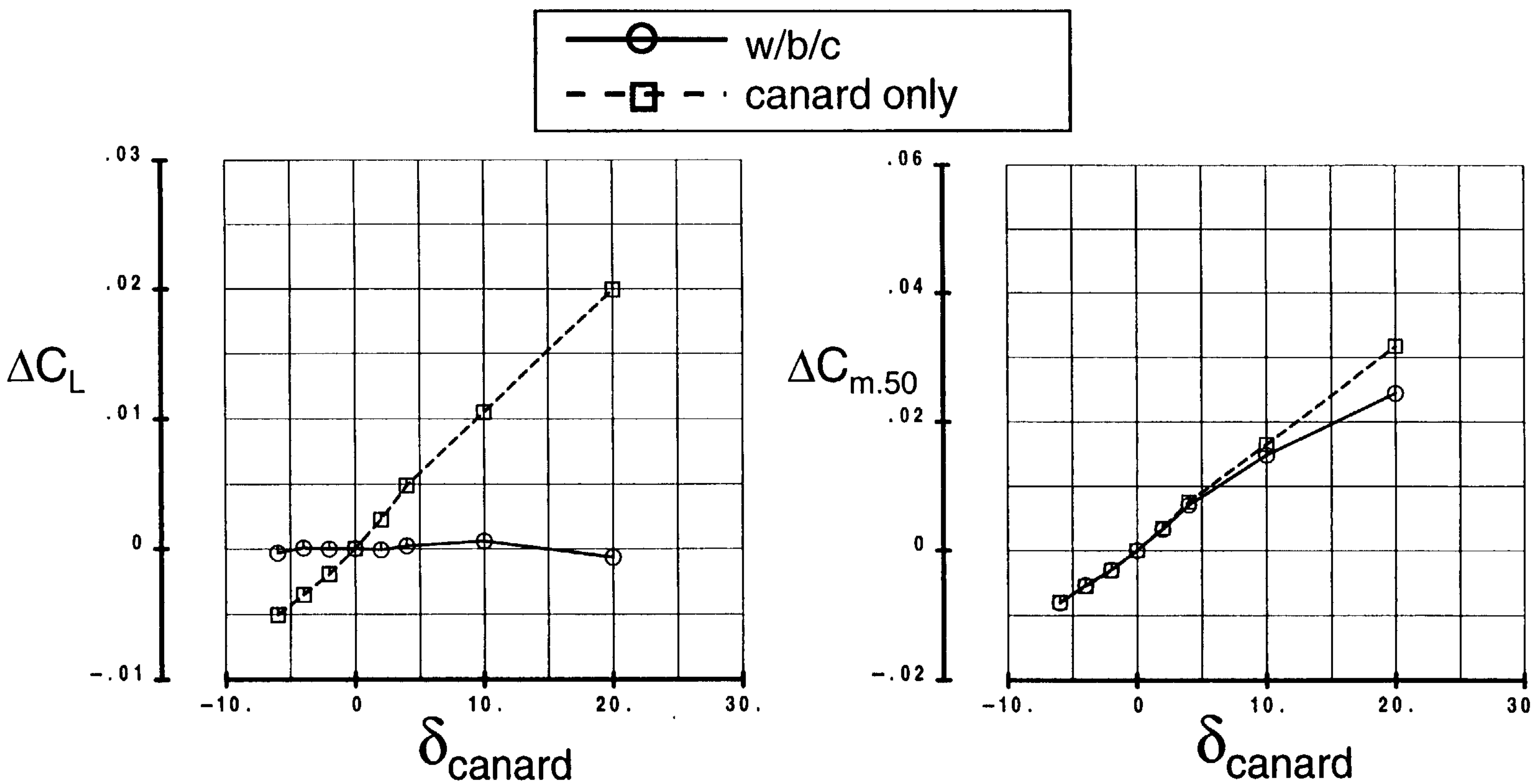

Text for Results--Installed vs. Isolated Canard Lift

The lift behavior of the isolated canard planform was compared to the lift on the exposed surface of the installed canard to determine how well isolated results would predict installed behavior. For the installed cases, canard lift is calculated by integrating over the exposed canard area and coefficients are referenced to those areas. Recall that for the large canard deflections (10 deg. and greater) the canard geometry was trimmed to clear the side of body, so a smaller reference area was used for those points. The installed curve, which was derived by deflecting the canard, was shifted so that zero "local α_c" corresponded to zero lift.

For the Baseline planform, the installed lift levels are ~10% lower than the isolated predictions, while for Canard 2 the curves are intertwined. The dip in the Canard 2 data at AoA of ~ 5 deg. corresponds to the anomalous result at zero canard deflection mentioned earlier.

The lift of the installed Baseline canard was somewhat lower than the isolated planform. This may be due to the unintentional difference in geometry mentioned earlier, which led to a higher-aspect ratio on the isolated canards. The difference is much more significant on the Baseline than Canard 2. Also, it might be expected that lift on the exposed canard might be reduced at large deflections due to the large side of body gap at those deflections, again more significant on the Baseline.

Lift on Installed Canard vs. Isolated Surface

M=0.9, Re = 1.76E6 (based on canard chord)

Notes:
1. B-B turb. model except S-A used for isolated Baseline at low α_{canard}
2. α_{canard} includes upflow corrections for installed case

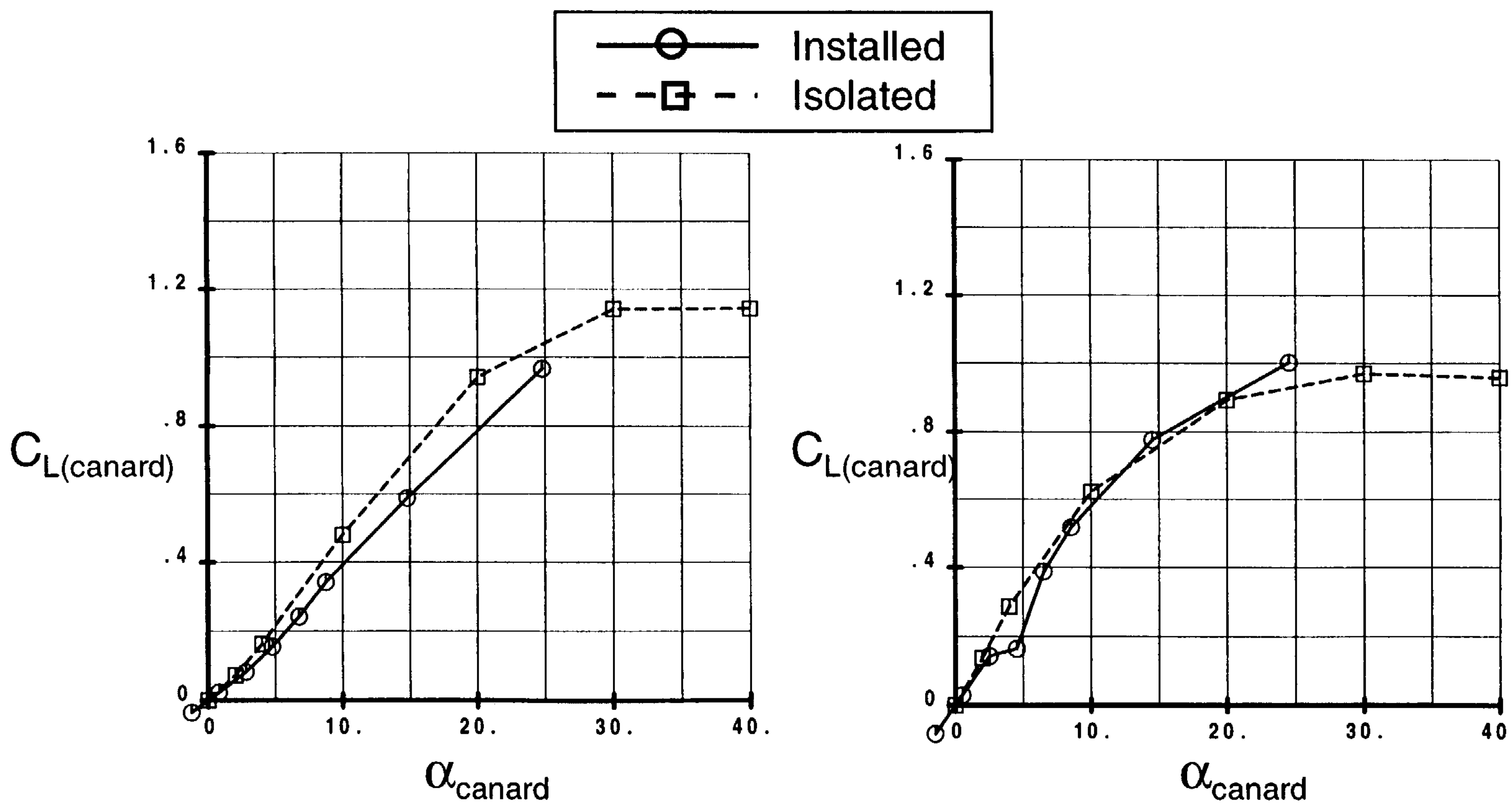

Baseline Canard   Canard-2

Text for Results--Streamlines from Deflected Canard at Subsonic Cruise

Streamlines were traced from the canard for various deflections. For It was found that the tip vortex passed above the wing, but the canard-body junction vortex turned down sharply behind the canard and passed under the wing. The flow through the gap between the canard and body can be seen in these streamlines.

This solution was run at an airplane AoA of 3.7 deg. with a canard deflection of 10 deg. Similar results were observed at higher and lower canard deflections.

It is not known whether this canard-body junction vortex would interfere with the nacelle inlet flow, or whether the vortex is strong enough to be of concern for inlet performance.

TCA Wing/Body/Canard Off-Surface Streamlines

$M=0.9$, $\alpha=3.7°$, $\delta(\text{canard})=10°$, $Re=6.04E6$
OVERFLOW (Navier-Stokes/Baldwin-Barth)

Baseline Canard

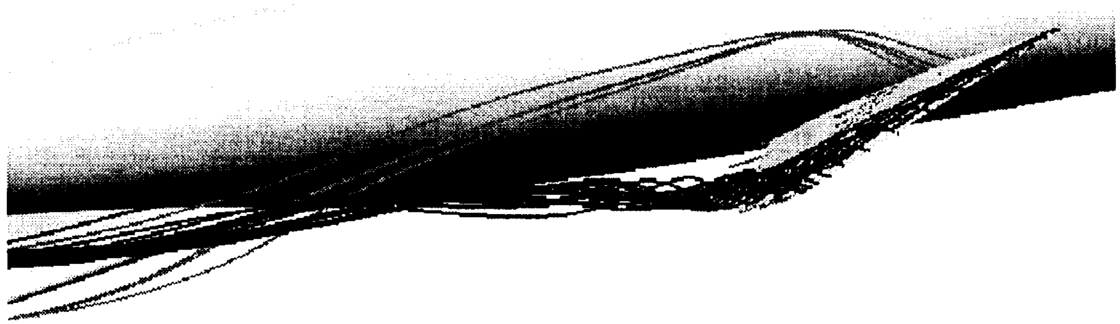

Canard-2

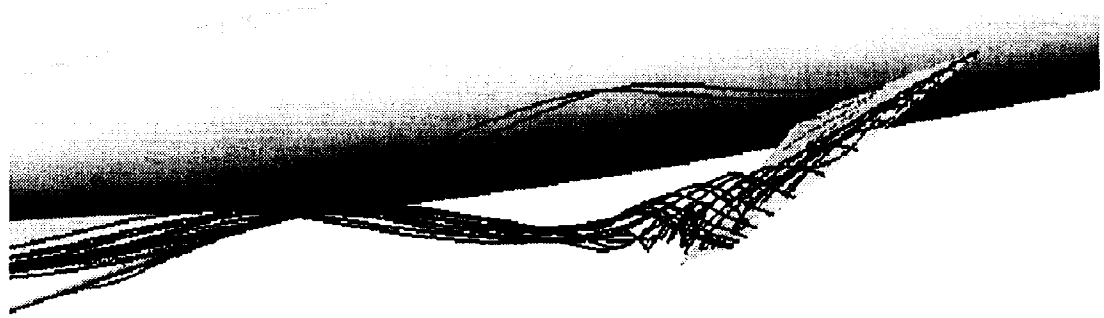

Text for Conclusions

Conclusions are summarized on the following slide. Perhaps the most notable conclusion is that CLmax predictions are sensitive to turbulence models even for these thin airfoils with sharp, highly-swept leading edges, and that this variation and lack of specific experimental validation makes CFD-based conclusions tentative.

In general, the analyses supported the conclusions that the Baseline planform is better for CLmax at low Mach, especially with deflected elevator, while the Canard-2 planform provides a higher CLalpha, greater $\delta CL/\delta elevator$, and lower drag at moderate lift levels. These trends are consistent with estimates from DATCOM, but the CFD levels were generally lower.

It was also concluded that lift on the exposed surface of the installed canard followed the trends observed on the isolated planform. The w/b/c pitching moment due to canard deflection was 0 - 25% lower than would be predicted from lift on the exposed canard surface, but the canard lift was esentially cancelled by the effect of canard downwash acting on the wing/body.

Conclusions:

- Predicted CLmax is sensitive to turbulence model, even for these sharp, highly-swept leading edges.
- Variation in CFD results makes conclusions tentative.
- Planform trends are generally consistent with DATCOM.
- CLmax at low Mach is greater for Baseline than Canard 2.
- Elevator effectiveness ($dCL/d\delta e$) is greater for Canard 2.
- Installed pitch control behavior can be estimated from isolated characteristics.

Text for Lessons Learned

The major lesson learned was that to use CFD with confidence in this regime, additional attention must be paid to validation of predictions against relevant experimental results.

Another lesson is that extra care must be taken to ensure that the geometries are as intended for the purposes of the study before significant data are generated. This lesson is especially applicable when numerous individuals are involved in planning and executing the study.

Lessons Learned:

- Turbulence model must be validated for comparable geometry at relevant flow conditions.
- Care must be taken to ensure desired geometry, especially when there are numerous participants.

Canard Integration Wind-Tunnel Tests and Computational Results

Todd E. Magee, Paul Kubiatko, Suk C. Kim
The Boeing Company, Phantom Works
Long Beach, California 90807

Hamid Jafroudi
Alpha STAR Corporation
Long Beach, California 90807

Abstract

This paper presents experimental and CFD investigations into the effect of canard integration on the TCA (Technology Concept Aircraft) aerodynamic performance and Stability & Control. Specifically, results from the Supersonic Canard Integration Wind Tunnel Test (Test 1705) at the NASA Langley UPWT (Unitary Plan Wind Tunnel) and the Transonic Canard Integration Wind Tunnel Test (Test 508) at the NASA Langley 16-foot Transonic Wind Tunnel are presented. Comparisons of this test data with extensive CFL3D computational fluid dynamic (CFD) solutions are shown, as well as the results of a CFL3D directional stability & control study for the full TCA configuration (wing/body/canard/empennage). CFL3D shows good correlation with the test data for all configurations tested, except the ACC (alternate controls concept) canard configuration at a canard incidence angle of 4°. Navier-Stokes results for both the Baldwin-Lomax and Menter's κ–ω SST models are also shown. The CFL3D directional stability study indicates that the interaction of the PTC (Preliminary Technology Concept) canard tip vortices with the tail of the aircraft have a significant effect on directional stability. This tip vortex interaction is similar to low speed results which indicate a strong correlation between canard tip height and the angle-of-attack at which representative HSCT configurations become directionally unstable. Conditions for the studies presented in this paper range from M_∞=0.6, 0.9, and 1.1 for the transonic studies to M_∞=2.4 for the supersonic studies. Reynolds numbers for all studies were approximately 4 million/ft.

Canard Integration Wind-Tunnel Tests and Computational Results

Todd E. Magee
Paul Kubiatko
Suk C. Kim
The Boeing Company, Phantom Works - Long Beach

Hamid Jafroudi
Alpha STAR Corporation

High Speed Research Airframe Review
Anaheim, California
February 8-11, 1999

BOEING

Outline

The topics listed in this chart outline the extensive canard integration work that has been completed by the Boeing Phantom Works organization for the High Speed Research (HSR) program in 1998. The objective is to determine the effect of canard integration on aircraft performance and stability & control through experimental (wind tunnel) and computational (CFD) investigations. We will take an incremental approach by focusing on specific canard issues in each of the four topics listed on the following page. By the end of the paper it will be apparent what data and investigations will be required to understand the performance and stability & control of the complete configuration.

The paper will begin with a presentation of the results from the Supersonic Canard Integration Wind Tunnel Test (Test 1705) that was conducted at the NASA Langley Unitary Plan Wind Tunnel (UPWT) in April 1998. Once the supersonic wind-tunnel results have been presented, comparisons will be shown with CFL3D Navier-Stokes and Euler results for both overset and patched grid topologies, as well as comparisons with Baldwin-Lomax and Menter's $\kappa-\omega$ SST turbulence models. The third topic for this presentation will discuss the Transonic Canard Integration Wind-Tunnel Test conducted at the NASA Langley 16-foot Transonic Tunnel in September/October 1998. Finally, the last topic will discuss the effect of canard integration on the directional stability characteristics of the full configuration (wing/body/canard/empennage) through Euler computations with CFL3D. At the end of the paper, the remaining canard integration work will be outlined from now until the end of the HSR program in September 1999.

Outline

- The Supersonic Canard Integration Wind Tunnel (UPWT Test 1705)
- CFL3D Performance Results for Overset and Patched Grid Topologies
- The Transonic Canard Integration Wind Tunnel Test (16TT Test 508)
- CFL3D Canard-On Directional Stability Characteristics
- Future Work (Now until September 1999)

BOEING

The Supersonic Canard Integration Wind Tunnel Test (UPWT Test 1705)

BOEING

Supersonic Canard Integration Test Information

The Supersonic Canard Integration Test was conducted at the NASA Langley Unitary Plan Wind Tunnel, Test Section #2, from April 8, 1998 to May 4, 1998. This amounted to 19 single-shift days. Two models were used during this experimental investigation, Model 2b and Model 52. Model 2b is a 1.675% representation of the Baseline Technology Concept Aircraft (TCA) with a truncated aftbody and four one-piece nacelle/diverters. Model 52 is comprised of the Model 2b with two new forebodies that were fabricated to integrate several canard configurations. The test was conducted at a Mach number of 2.4, angles-of-attack from -4° to 12°and sideslip angles from -6°to 6°. The Reynolds number used at the UPWT was 4 million/ft.

Supersonic Canard Integration Test Information

High Speed Aerodynamics, Long Beach

- Test facility: LaRC UPWT Test Section 2
- Test date: 4/8/98 - 5/4/98
- Test duration: 19 single shift days
- Models
  - Model 2b - 1.675% Baseline TCA with truncated aftbody and one-piece nacelle/div
  - Model 52 - Model 2b with two new forebodies to accommodate several canard configurations
- Test conditions:
  - $M_\infty = 2.4$, $\alpha = -4°$ to $12°$, $\beta = -6°$ to $+6°$
  - Re = 4 million/ft

BOEING

Supersonic Canard Integration Test Objectives

The objectives of the Supersonic Canard Integration Test are outlined in the following chart. Essentially, the purpose of the test was to obtain a data base for CFD code validation for canard integration at the supersonic cruise condition. Both wing/body/canard and wing/body/canard/nacelle/diverter data were obtained in this experimental study. The effect of the canard on the tail could not be analyzed in this investigation, since the 1.675% model is too large to integrate a tail for the 4-ft test section of the UPWT. Any aftbody would have been shock reflected in the UPWT at a Mach number of 2.4. The second objective was to determine the influence of the canard wake and tip vortex on wing and nacelle flowfields through extensive flow visualization. It was hypothesized that the tip vortex could be ingested by the inboard nacelles at certain angles-of-attack and canard incidence angles. The effect of these flow structures could also result in performance penalties and stability & control problems. The last two objectives from the test were to determine the effect of canard location on performance and determine the influence of canard location on the S&C characteristics of the configuration.

Supersonic Canard Integration Test Objectives

- Acquire experimental database for CFD code validation on W/B/C and W/B/C/N/D
- Acquire flow visualization data for the canard wake to see how it influences the wing and nacelle flowfields
- Assess the effects of canard location on performance
- Acquire limited S&C characteristics (high alpha, multiple canard deflection angles, and sideslip angles)

BOEING

The NASA Langley Unitary Plan Wind Tunnel

The wind-tunnel facility utilized for this experimental investigation was the NASA Langley UPWT. The UPWT is a closed-circuit (continuos flow) pressure tunnel with two test sections that are 4-ft square by 7-ft long. This test utilized test section #2, which has a Mach number range of 2.3 to 4.63. The Mach number variation is obtained through an asymmetric sliding block which allows the throat-to-test-section area ratio to change. The tunnel circuit can operate for pressures from near-vacuum to 10 atm. The major elements of the UPWT facility are 74.6 MW drive system, a dry air supply system, an evacuating system, a cooling system, and extensive ducting to connect both tunnel test sections. The average free-stream conditions for test section #2, during this test entry, were M_∞=2.4, Re=4×10^6 /ft, Po=3039 psfa, To=125 °F, and q=838 psfa. For additional information on the UPWT please refer to Reference 1.

The NASA Langley Unitary Plan Wind Tunnel

High Speed Aerodynamics, Long Beach

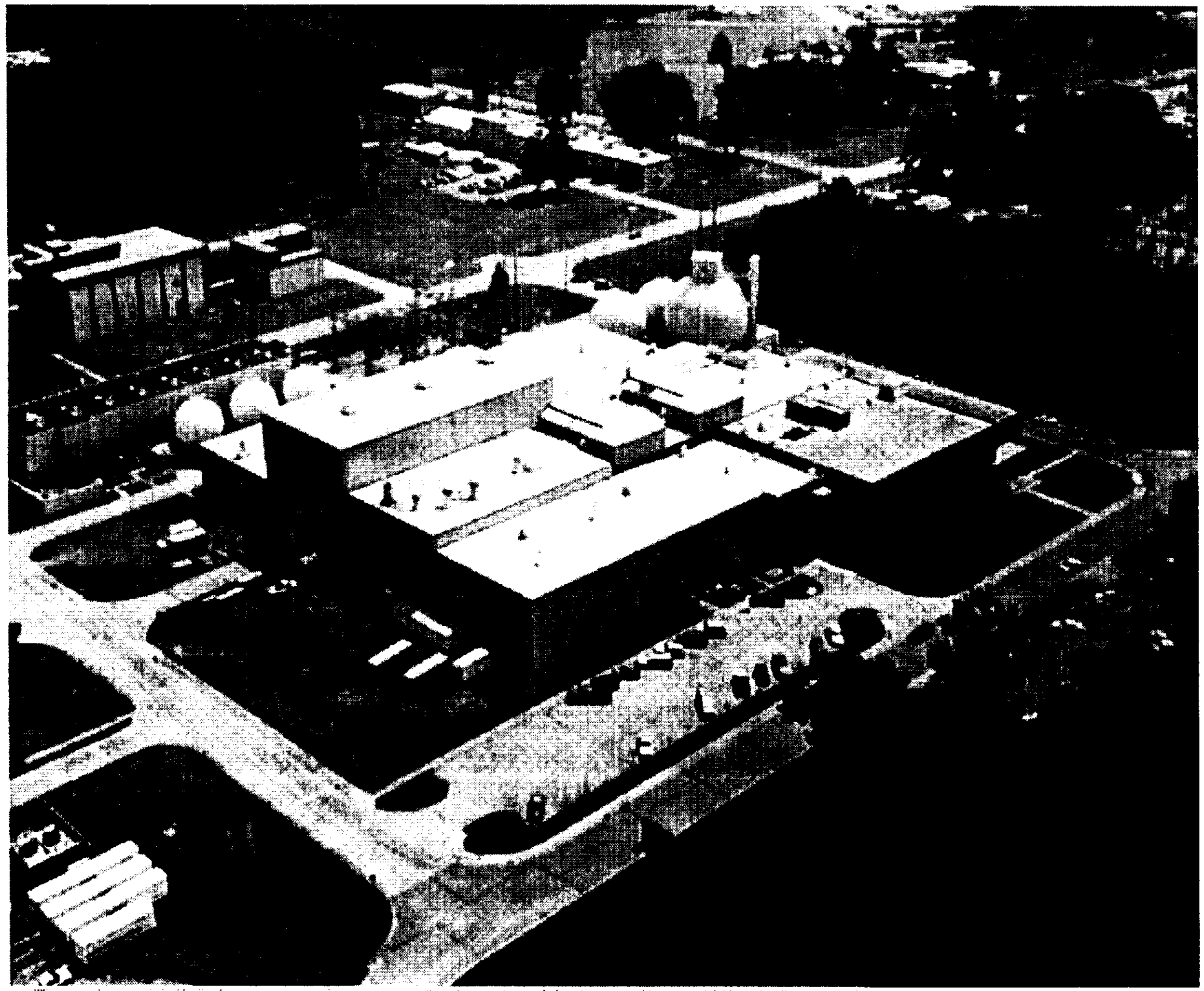

The NASA Langley Research Center Unitary Plan Wind Tunnel
NASA Langley Research Center 7/10/1992 Image # EL-1996-00048

BOEING

1.675% Baseline TCA Model 2b and Model 52 Hardware

This chart shows the model hardware utilized for Test 1705. The existing Baseline TCA Model 2b is shown in the center of the photograph. Two new forebodies and canard planforms comprise Model 52. They were fabricated for this test entry. In the lower left is forebody #1 which was fabricated to integrate the PTC (Preliminary Technology Concept) canard. This forebody has a ±4° wiping surface, so that the canard will have no gap between the canard and the side-of-body for ±4° range of canard deflections. The metal blocks located near forebody #1 are used to attach the canards to the forebody for the desired deflections in this test. Only the mid-mounted PTC canard can be attached to forebody #1. In the upper left corner of the photograph is forebody #2. This forebody allows integration of the PTC canard at low(-20° dihedral) and high(15° dihedral) mounting locations and the integration of a larger ACC (alternate controls concept) canard at a low(-15° dihedral) mounting location. The ACC canard is also located closer to the wing. Forebody #2 does not have sealed deflection capability. Instead, there are different size gaps between the canard and the side-of-body depending upon which canard you have and what the canard deflection angle is. During the test this gap was filled and unfilled with body filler material to determine the affect of the gap on the results. Next to forebody #2 is as forebody adapter that mates both forebody #1 and #2 to the Model 2b wing strongback.

1.675% Baseline TCA Model 2b and Model 52 Hardware

High Speed Aerodynamics, Long Beach

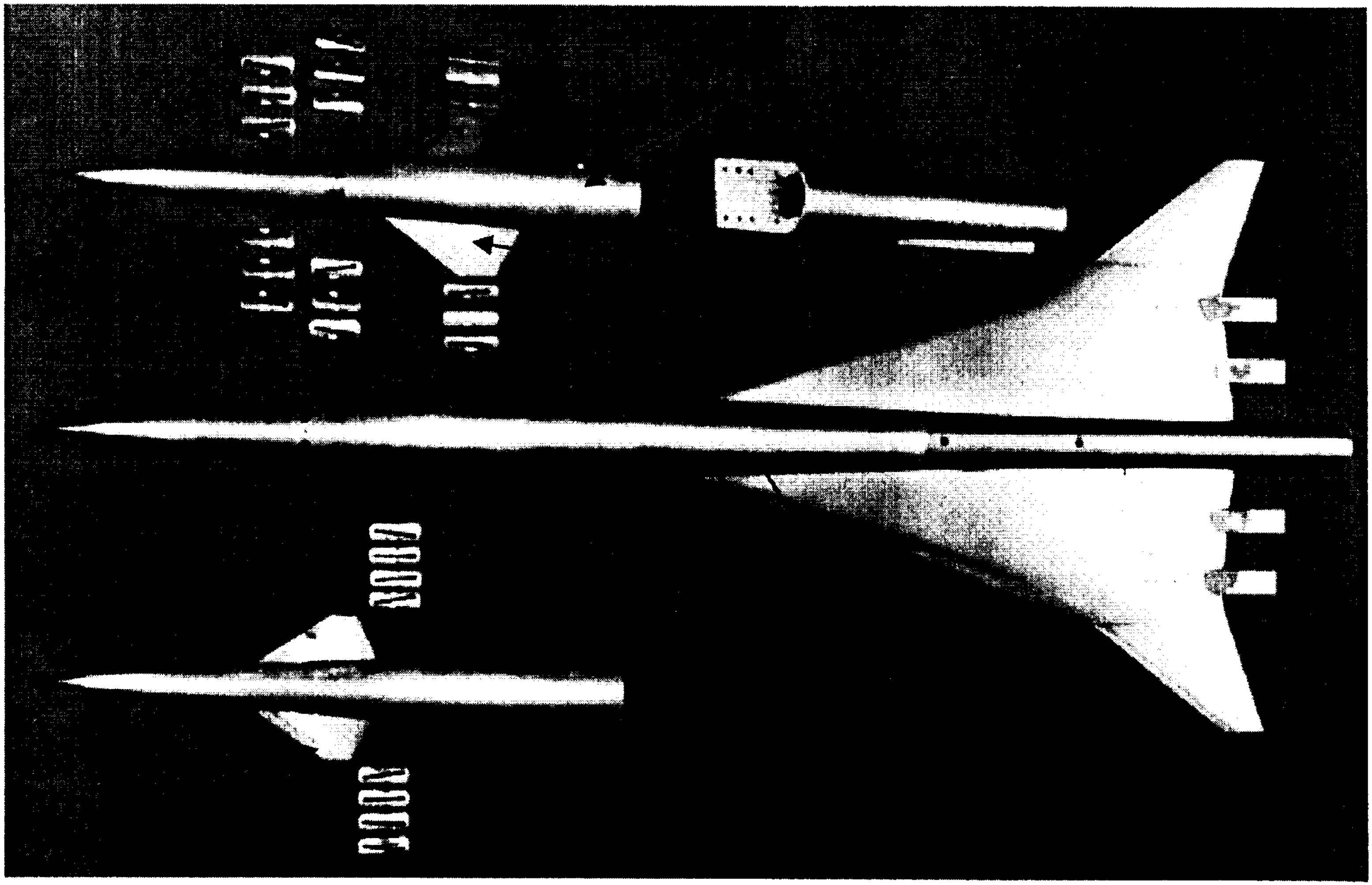

BOEING

Close-up of the Mid-Mounted PTC Canard

This photograph shows a close-up view of the mid-mounted canard attached to forebody #1. The ±4° wiping surface can be seen in the photograph. For ±10°, the mid-mounted PTC canard was un-ported (gap between the canard and the side-of-body).

Close-up of Mid-Mounted PTC Canard

High Speed Aerodynamics, Long Beach

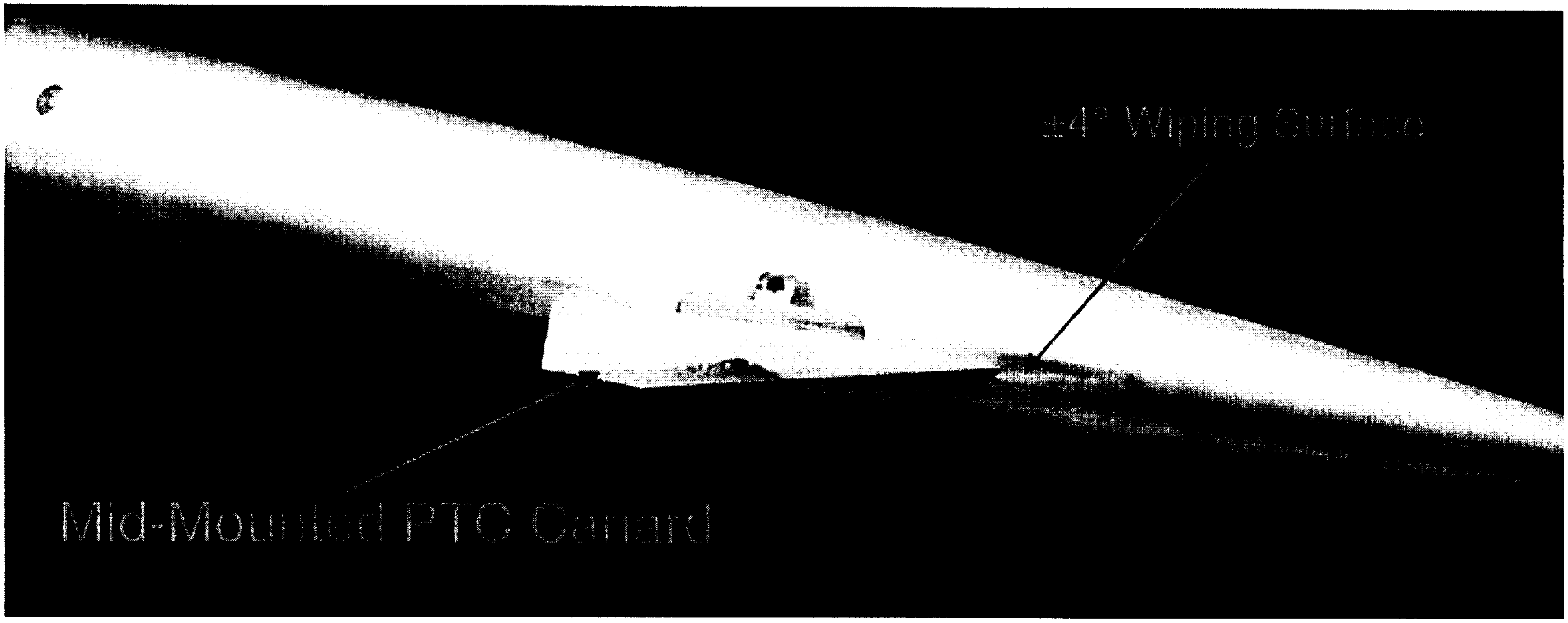

BOEING

1.675% Model 52 with Mid-Mounted PTC Canard

This chart shows the mid-mounted PTC canard configuration with nacelles installed in the UPWT test section #2 with the wings oriented vertically.

1.675% Model 52 with Mid-Mounted PTC Canard

High Speed Aerodynamics, Long Beach

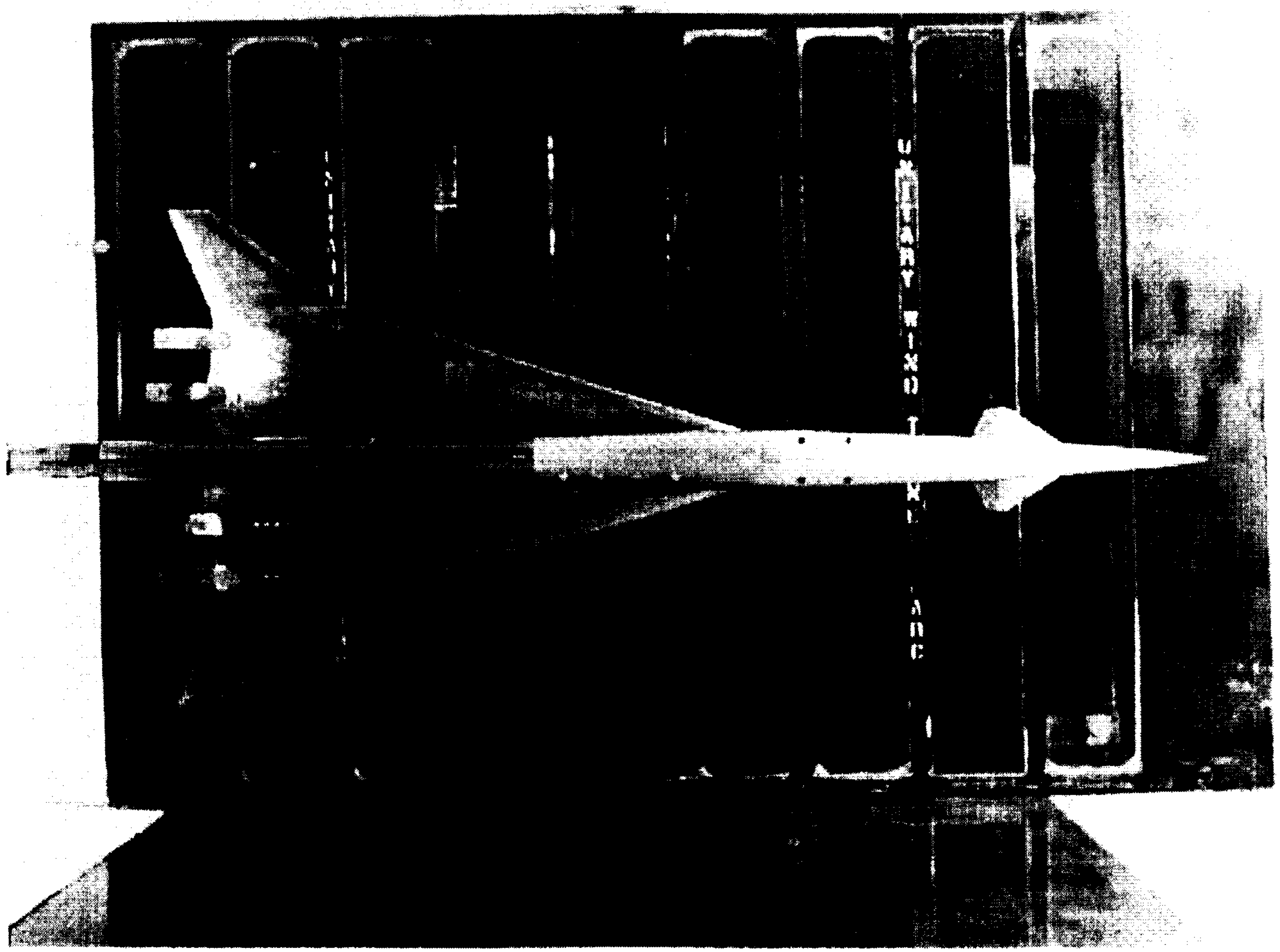

BOEING

1.675% Model 52 with Low-Mounted ACC Canard

The following photograph shows the low-mounted canard configuration with nacelles, installed in the UPWT test section #2.

1.675% Model 52 with Low-Mounted ACC Canard

High Speed Aerodynamics, Long Beach

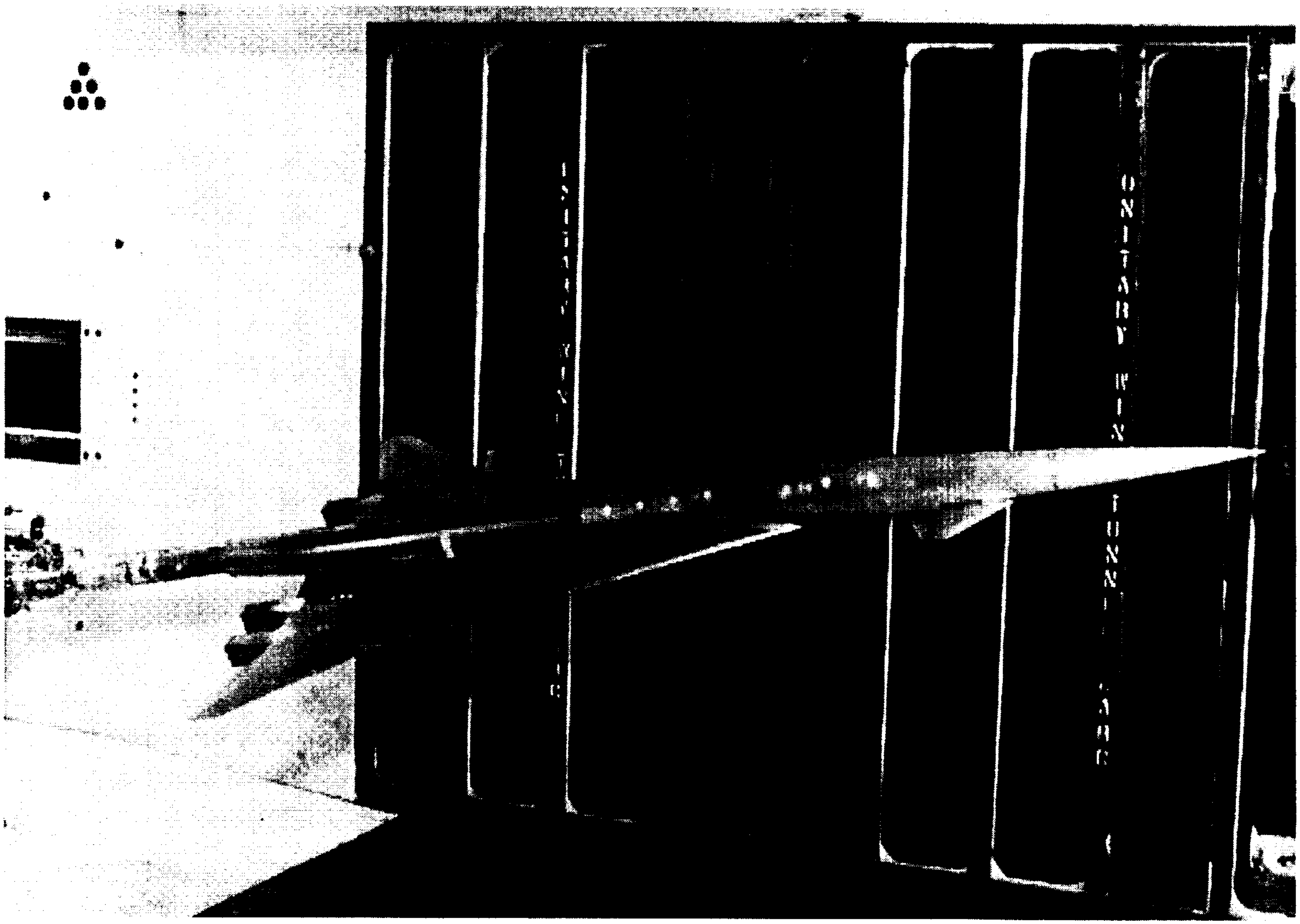

BOEING

Close-up of the Low-Mounted ACC Canard

This view shows a close-up of the ACC canard installed on Forebody #2. The ACC canard has 15° anhedral and the gap between the canard and the side-of-body is clearly shown. Testing with the gap filled and unfilled with body filler material found that the gap adds an additional count of drag to the configuration.

Close-up of Low-Mounted ACC Canard

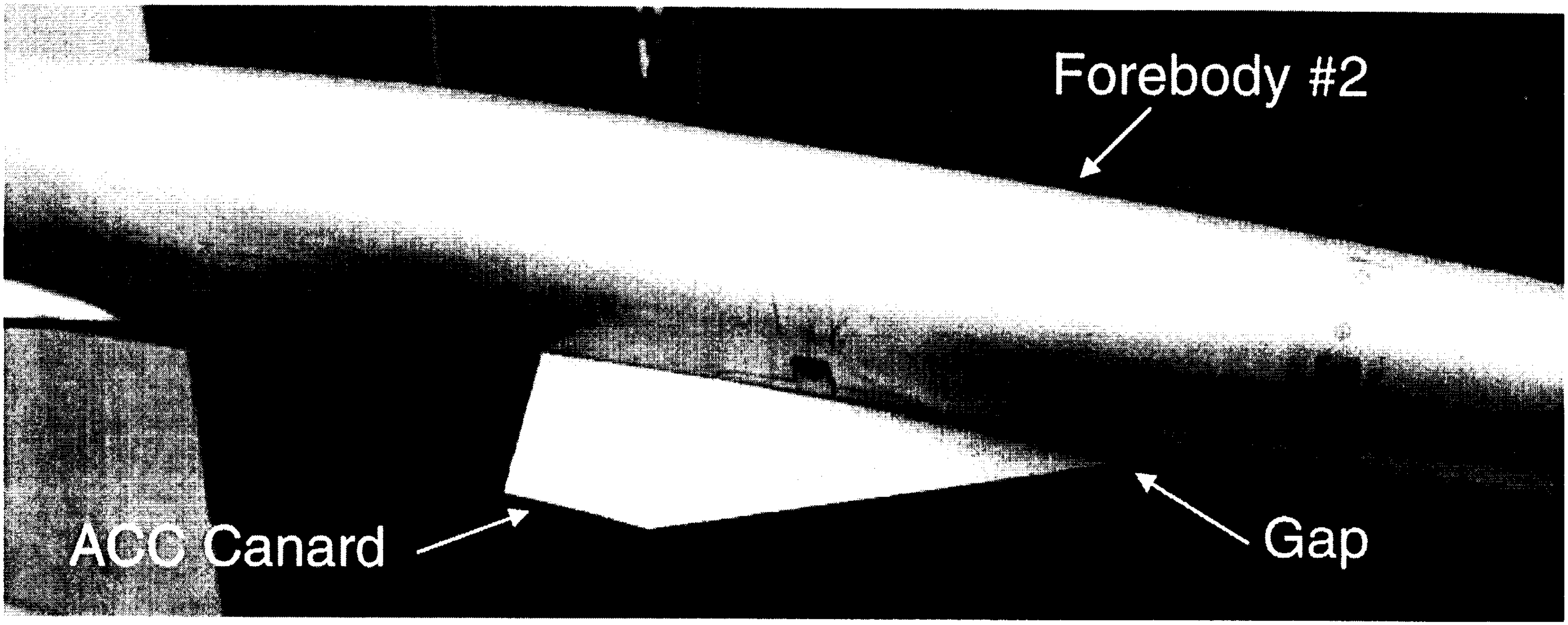

Test Techniques Utilized During UPWT 1705

The following test techniques were used during Test 1705 to satisfy the test objectives.

Test Techniques Utilized During UPWT 1705

- Force & Moment (6-component)
  - To validate CFD, obtain performance data and S&C data
- Laser Vapor Screen (LVS)
  - To determine the influence of canard tip vortex and wake on the wing and nacelle flowfields
- Ultra-Violet Oil Flow
  - To determine the influence of the canard on the wing surface flow topology and for CFD validation
- Sublimation
  - To assess the state of the boundary layer on the wing and canard
- Schlieren Photographs
  - To assess the influence of canard induced shock systems

BOEING

Instrumentation for UPWT 1705

The following instrumentation was utilized during test 1705. A NASA Langley sting (350-19A) and balance (UT-65A) was utilized during this test entry. During the test the dynamic limit on normal force and pitching moment was exceeded at about 11° angle-of-attack with the PTC canard at ±10° incidence angle. In addition, the balance was installed during test 1703 (NCV flow diagnostic test) to save time. Since the balance was installed during Test 1703, repeatability comparisons with this test shall be considered medium-term repeatability. Pressure instrumentation was utilized to make body cavity corrections, as well as nacelle base pressure corrections. The UT-65A balance had three thermocouples installed (front, middle and back) to monitor temperature gradients along the balance. Angle-of-attack was measured with an accelerometer on the strut and then corrected for flow angularity and sting bending.

Instrumentation for UPWT 1705

- Sting: Langley 350-19A
- Balance: UT-65A (Installed during UPWT Test 1703)

Balance Limits (Last Calibration - 5/8/97)

Normal Force	±800 lbs
Axial Force	60 lbs
Pitching Moment	±2000 in-lbs
Rolling Moment	±820 in-lbs
Yawing Moment	±1000 in-lbs
Side Force	±400 lbs

- Pressure Instrumentation
  - 4 - 5psid Druck transducers (body chamber pressure)
  - 2 - 5 psid Druck transducers (nacelle base pressures)
- Temperature Instrumentation
  - 3 prt on UT-65A
- Angle-of-Attack Measurement
  - accelerometer on strut plus corrections for flow angularity and sting/bal bending

BOEING

Transition Trip Dot Locations on Model 2b and Model 52

To ensure turbulent flow over the majority of the model, artificial transition elements were employed. The chart on the following page shows the location of these transition elements on the configuration. The sublimation technique was utilized to ensure the effectiveness of these transition elements. The location and size of the artificial transition elements are tabulated on the chart.

NASA Langley Research Center
Unitary Plan Wind Tunnel
Test 1705 - HSR Carnard Integration
Trip dot locations for TCA-2B model

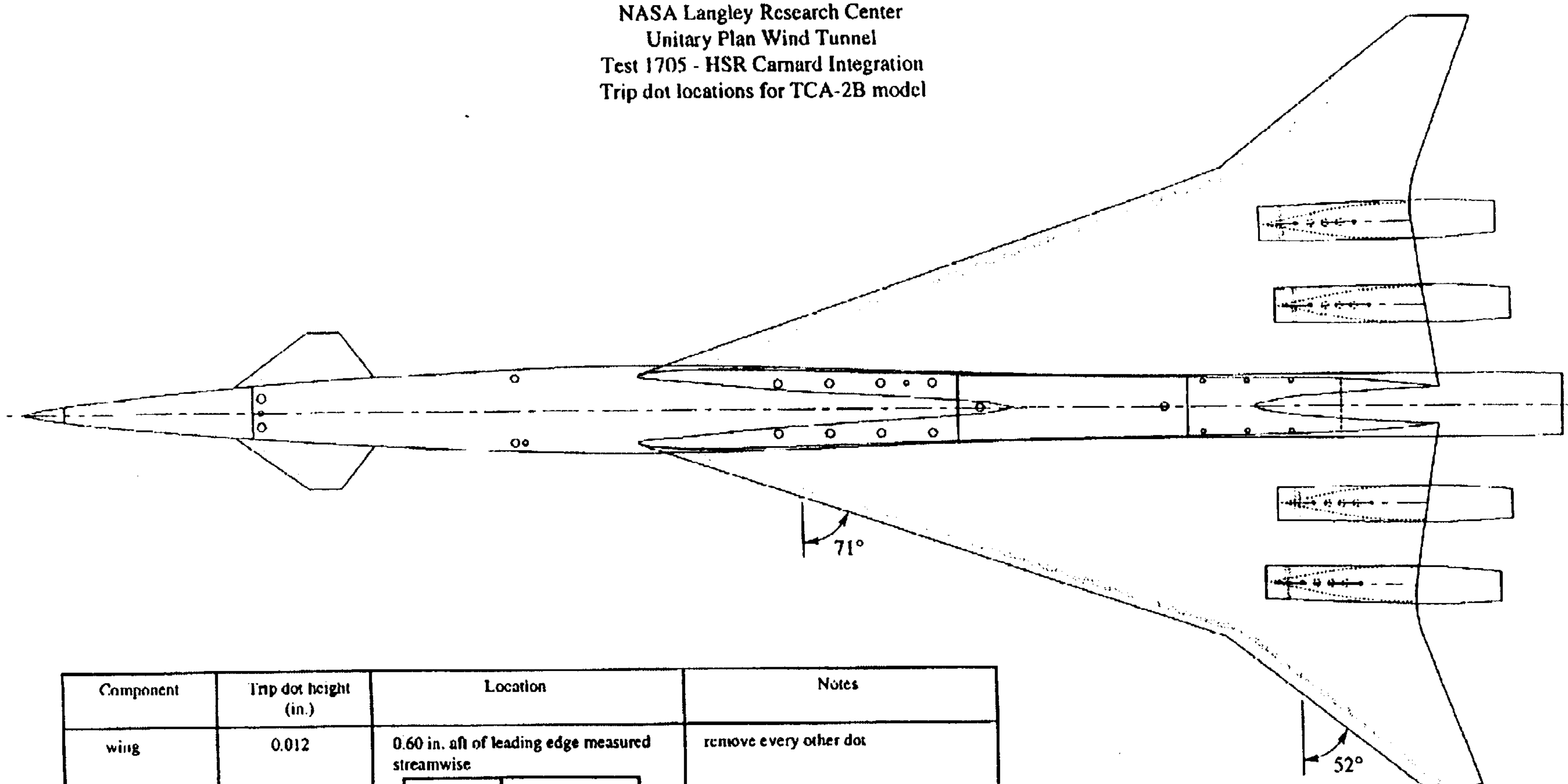

<table>
<tr><th>Component</th><th>Trip dot height (in.)</th><th>Location</th><th>Notes</th></tr>
<tr><td>wing</td><td>0.012</td><td>0.60 in. aft of leading edge measured streamwise<table><tr><th>sweep angle, Λ</th><th>distance perpendicular to leading edge</th></tr><tr><td>71°
52°</td><td>0.20 in.
0.37 in.</td></tr></table></td><td>remove every other dot</td></tr>
<tr><td>nose</td><td>0.012</td><td>1.0 in. from nose measured along model surface</td><td></td></tr>
<tr><td>nacelle</td><td>0.012</td><td>0.60 in. aft of leading edge measured streamwise</td><td>inside and outside nacelle surfaces</td></tr>
<tr><td>canards</td><td>0.012</td><td>0.60 in. aft of leading edge measured streamwise<table><tr><th>sweep angle, Λ</th><th>distance perpendicular to leading edge</th></tr><tr><td>54.2°</td><td>0.35 in.</td></tr></table></td><td>remove every other dot</td></tr>
</table>

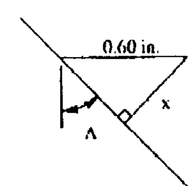

$\cos \Lambda = x/0.60$
$x = 0.60 \cos \Lambda$

Sublimation Results

Sublimation was employed during this test entry to determine the effectiveness of the trip dots. The HSR program has achieved the state-of-the-art with this test technique. The sublimation paint consists of a solution of 25g of Fluorene ($C_{13}H_{10}$) in 1 quart of Genesolv 2004. The mid-mounted PTC canard configuration (wing/body/canard) at a -4° incidence angle was run at Mach 2.4, 3.5° angle-of-attack, and a Re=4 million/ft to assess the state of the boundary layer. This was Run 13 of Test 1705. A trip height of 0.012 inches was used during this run with 2 dots on either side of an isolated dot removed on the inboard and outboard wing, as well as in the middle of the canard to show the full extent of laminar flow. A multitude of camera equipment was mounted to the window on both sides of the test section to take both still and video images during the run. The model was mounted in the tunnel with the wings mounted vertically. The run lasted approximately 25 to 30 minutes taking hasselblad pictures every 30 seconds and video for the whole 30 minutes.

Sublimation Results

- Experimental Set-up and Conditions
  - A Solution of Fluorene ($C_{13}H_{10}$) and Genesolv 2004
  - Run 13, $M_\infty = 2.4$, $\alpha = 3.5°$, Mid-Mounted Canard, i_c=-4°
  - Re = 4 million/ft
  - k = 0.012 inches, with some isolated trip dots on wing and canard
  - 4 hasselblad cameras, 2 video cameras, 1 digital camera, 2 continuos mercury vapor lights, 2 strobe lights

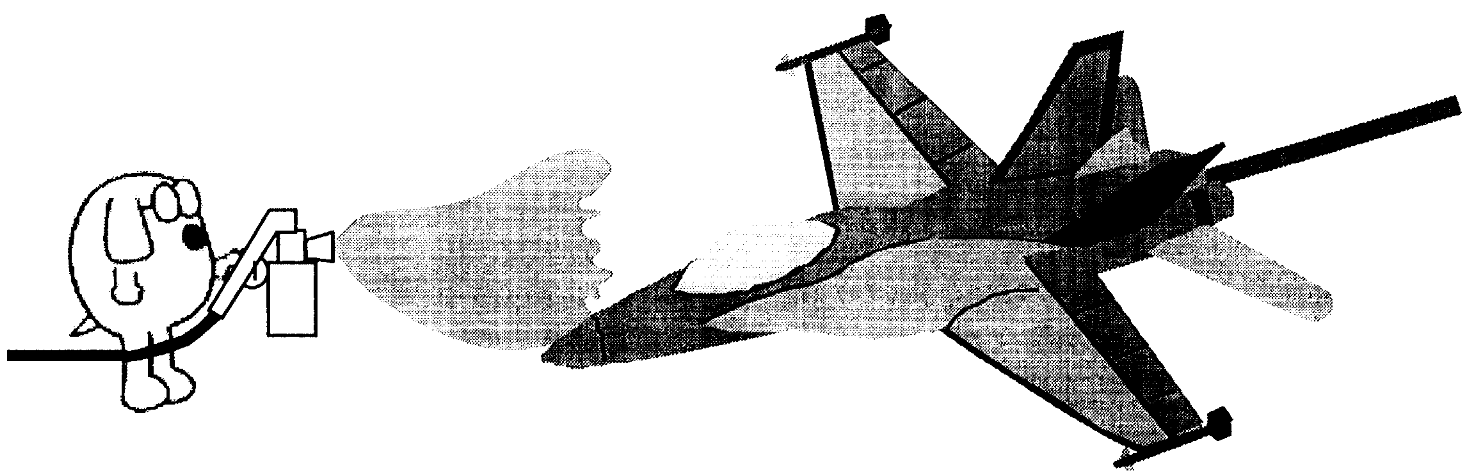

BOEING

Sublimation Results (Continued)

The results of the sublimation run indicate that the flow on the canard transitions promptly at the trip dots. The transition characteristics for the upper and lower wing are almost exactly the same as that for the wing/body from previous test entries. There was concern that the canard may influence the transition characteristics of the inboard upper and lower wing, but for the conditions tested with sublimation there appeared to be very little influence of the canard on the inner wing.

Sublimation Results (Continued)

- Results
  - Flow transitions at trip dots on the upper and lower canard surface
  - Some paint remained on the upper surface of the canard (near the tip) until the film ran out
  - Wing transitioned similar to previous test results

BOEING

Sublimation of Model 52 with Mid-Mounted PTC Canard (Continued)

The chart on the following page shows a sublimation image on the upper surface of the wing. This image matches those taken during previous tests without the canard present.

Sublimation of Model 52 with Mid-Mounted PTC Canard (Continued)

High Speed Aerodynamics, Long Beach

UPWT 1705, M = 2.4, $\alpha = 3.5°$, $i_c = -4°$, Run 13, Pt 843

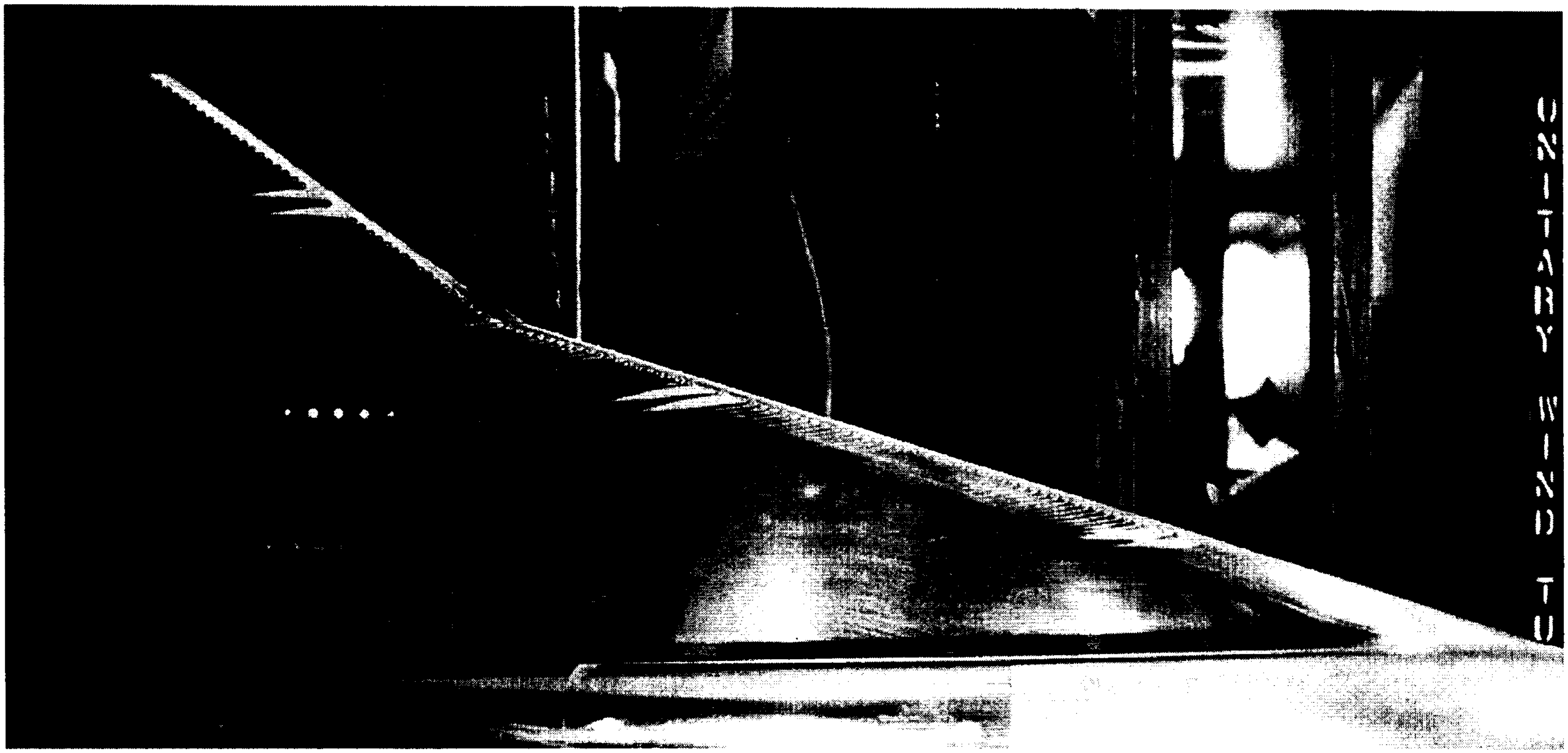

Upper Surface of Wing

BOEING

Sublimation of Model 52 with Mid-Mounted PTC Canard (Cont.)

This photograph shows the sublimation for the upper surface of the PTC canard. The turbulent wedge originating from the isolated trip dot spreads immediately indicating prompt transition.

Sublimation of Model 52 with Mid-Mounted PTC Canard (Continued)

High Speed Aerodynamics, Long Beach

UPWT 1705, M = 2.4, $\alpha = 3.5°$, $i_c = -4°$, Run 13, Pt 843

Upper Surface of Canard

BOEING

Short-Term Repeatability

The short-term repeatability for Test 1705 was approximately ±0.5 drag counts over most of the lift coefficient range considered. Toward the higher lift coefficients, there are a few outliers and near C_{D_o} the repeatability is around ±0.1 counts. The short-term repeatability indicates the level of precision of the force and moment measurements. The results indicate that we are within our specified tolerance of ±0.5 drag counts.

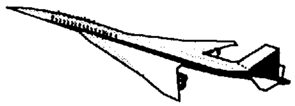

Short Term Repeatability

High Speed Aerodynamics, Long Beach

1.675% TCA Model 52 (forebody #1), W/B1
UPWT Test 1705, M_∞=2.4, Re=4.0 x 10^6 /ft

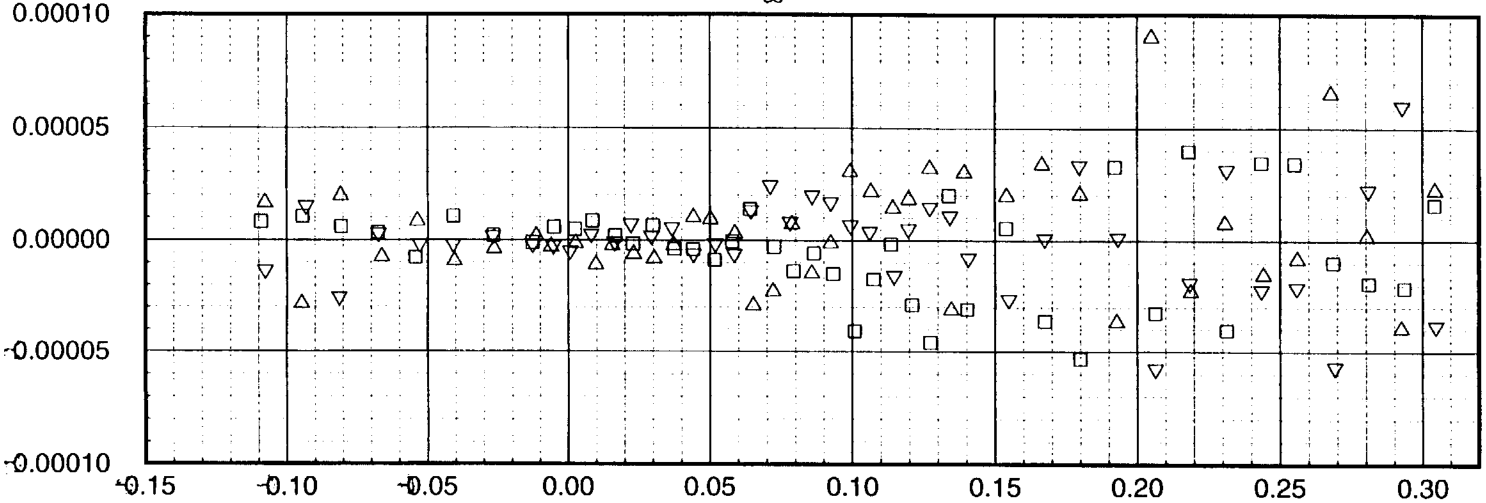

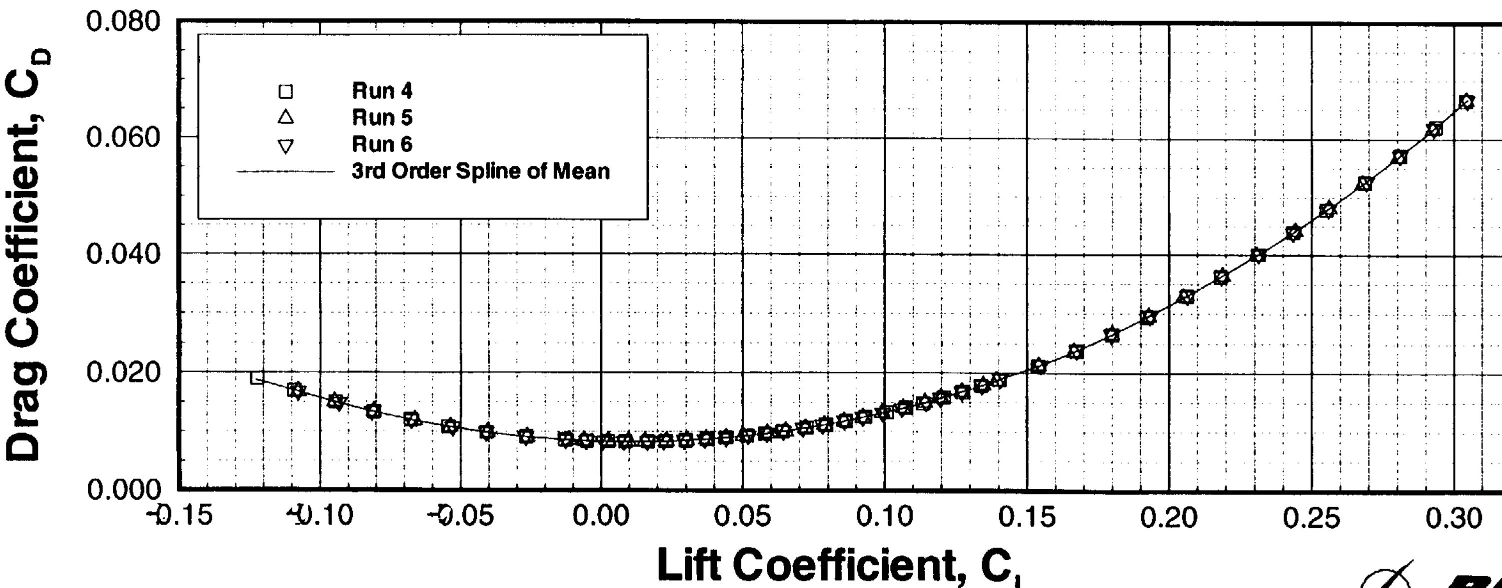

BOEING

Medium Term Repeatability

The following plot shows the level of medium-term repeatability for Test 1705. As mentioned earlier, since the same balance installation was used in Test 1703 and 1705, comparisons between these two tests are considered medium-term repeatability. Again, these types of comparisons give an indication of the quality of the data. The plot shows the drag residual of individual data points from a 3rd-order cubic spline representation of the two sets of data. The data generally shows a ±0.5 drag count medium-term repeatability with some outliers as you go above the cruise lift coefficient of C_L=0.1.

Medium Term Repeatability

High Speed Aerodynamics, Long Beach

1.675% TCA Model 2b, W/B

UPWT Test 1703 and 1705, M_∞=2.4, Re=4.0 x 10^6 /ft

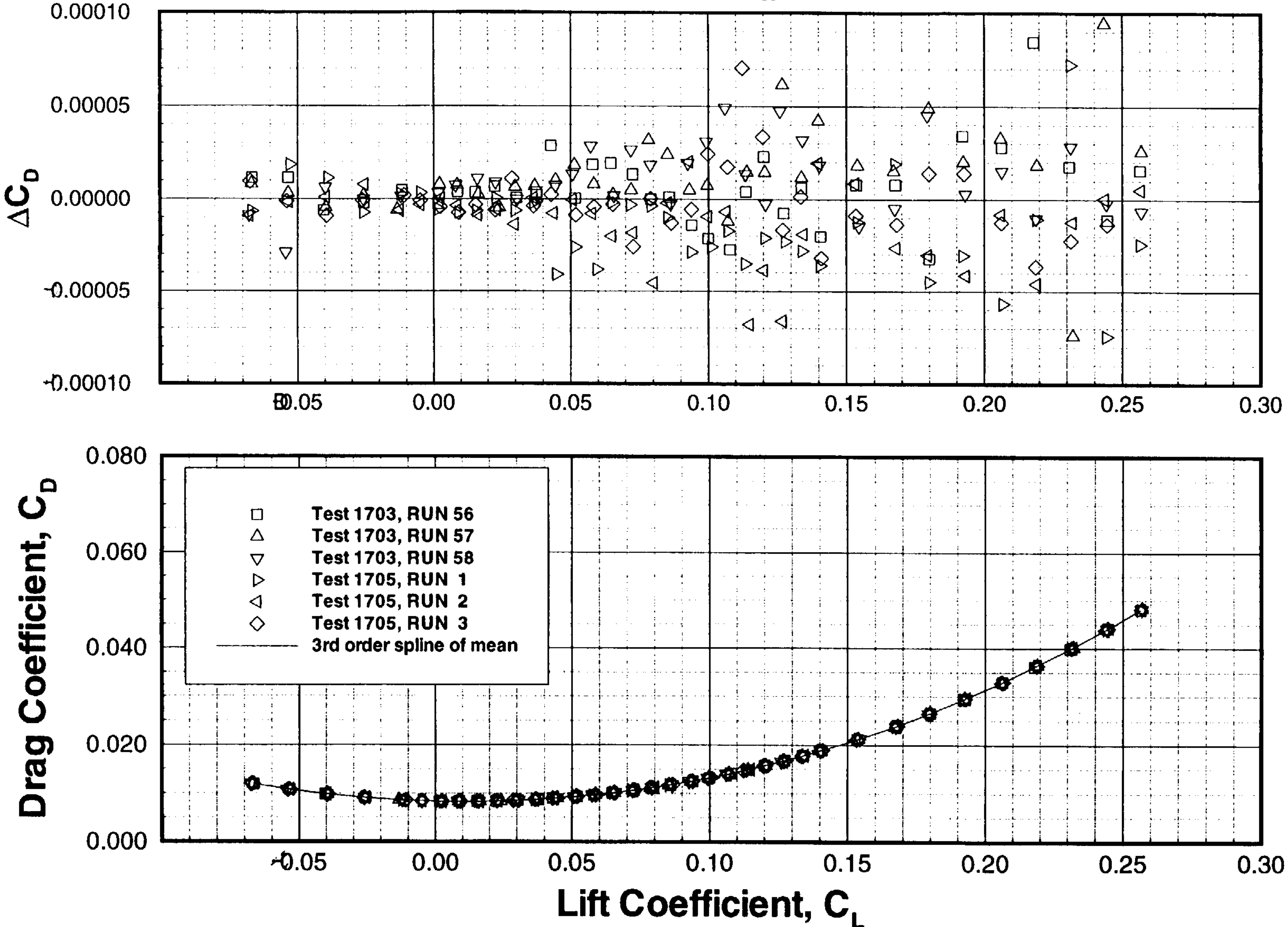

BOEING

Test-to-Test Drag Comparison (UPWT Tests 1705, 1687, and 1679)

This chart shows a drag polar comparison for wing/body/nacelle/diverter for several test entries of the Model 2b with two different forebodies. The current test is using Forebody #1 and test 1687 and 1679 are using the Model 2b forebody. Test 1705 and Test 1687 agree very well with each other indicating that the wiping surface in Forebody #1 has very little or no impact on the performance of the configuration tested. The test 1679 data does not agree as well with the others, but it is still within the tolerance of our measurements (±0.5 drag counts). The test-to-test comparison shown indicates that the current test data is of high quality and consistent with previous test entries.

Test-to-Test Drag Comparison (UPWT Tests 1705, 1687, and 1679)

High Speed Aerodynamics, Long Beach

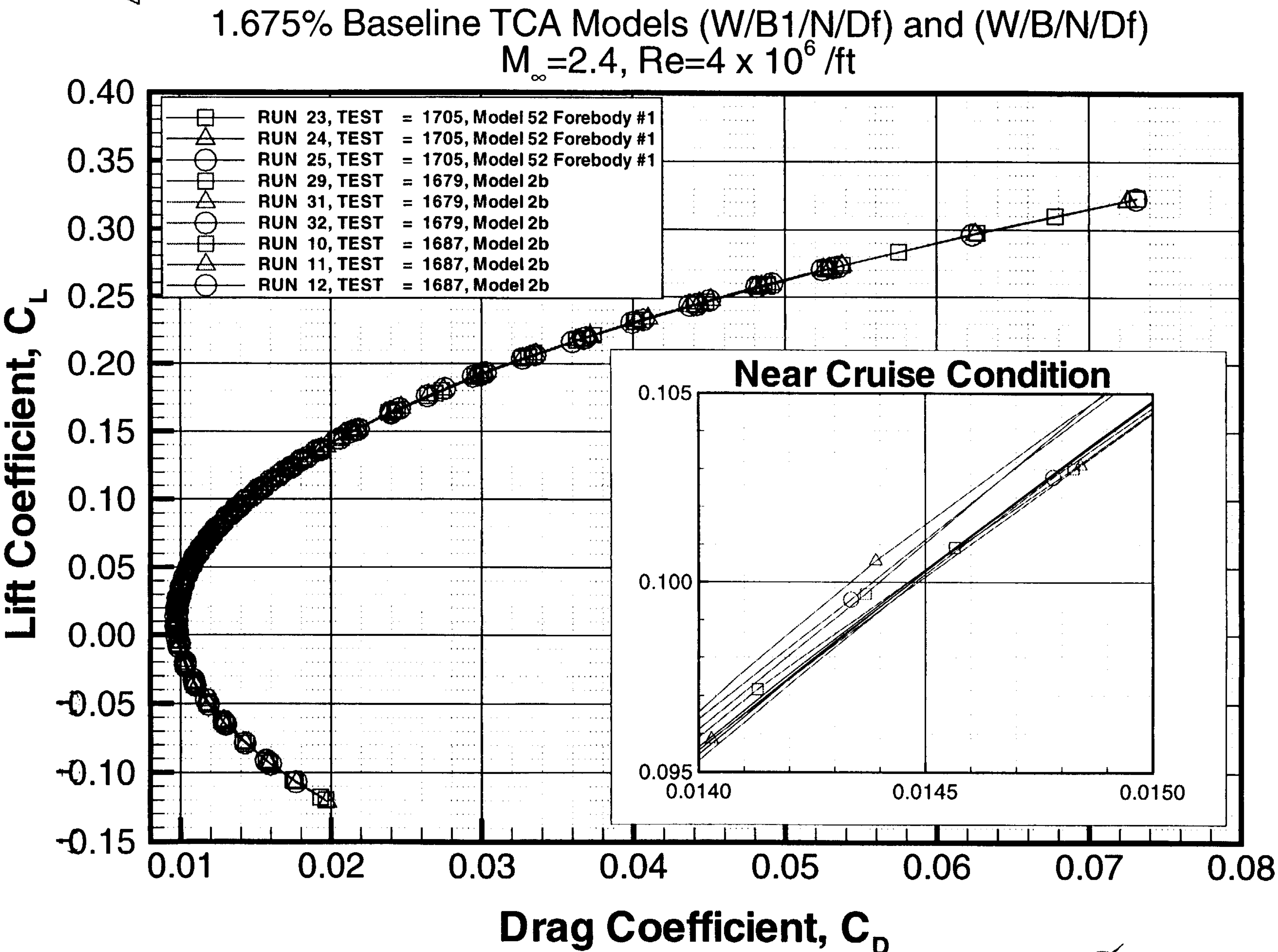

BOEING

Drag Polar Comparison (Model 2b vs. Model 52)

A comparison of the Model 2b and Model 52 Forebody #1 is shown on the following page from Test 1705 data for the wing/body. A mean line is fit through both series of data. The difference between the two mean lines is well within the tolerance of the data. This indicates that the wiping surface in Forebody #1 has no effect on the performance.

Drag Polar Comparison (Model 2b vs. Model 52)

High Speed Aerodynamics, Long Beach

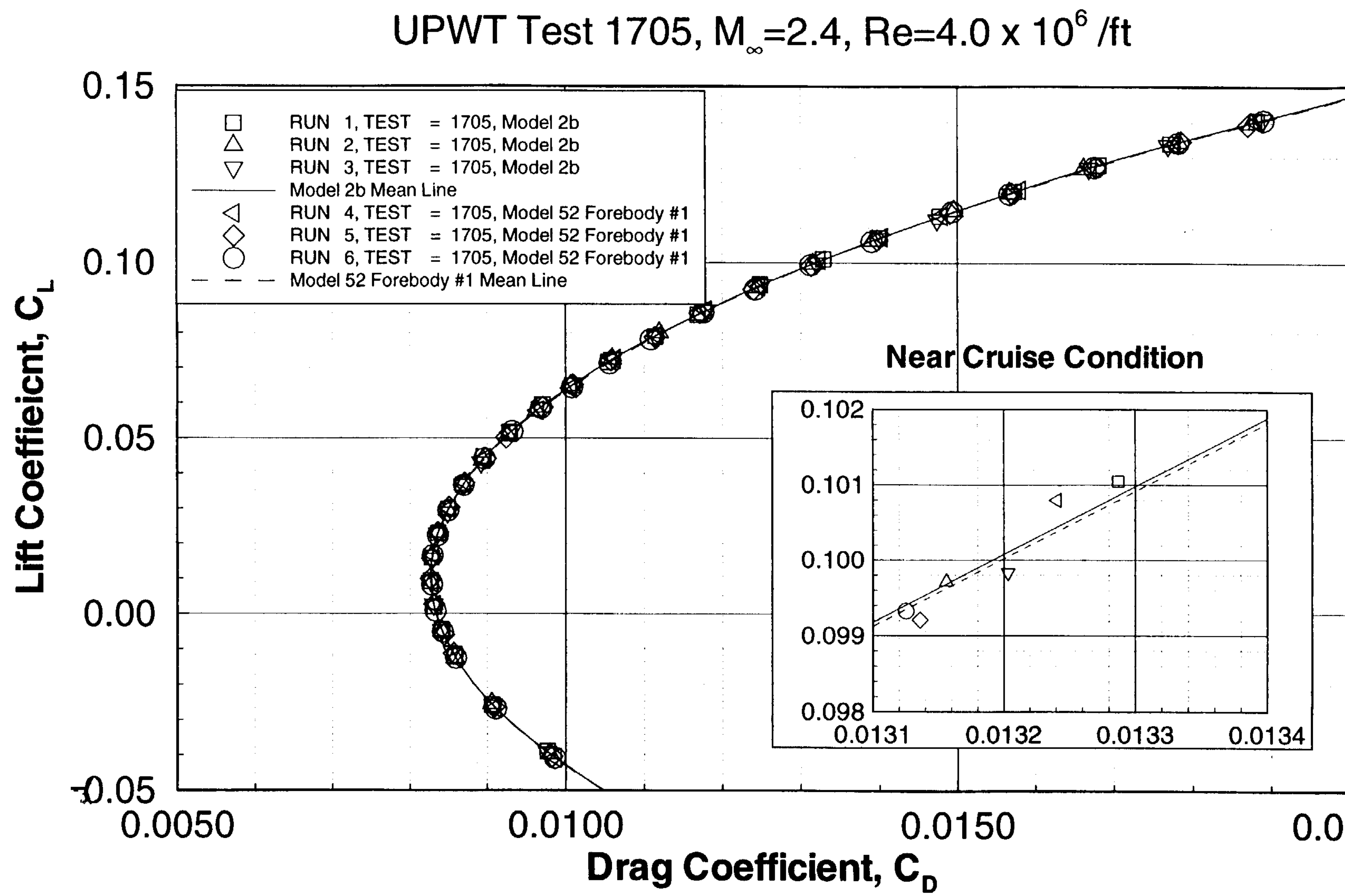

Stability & Control Characteristics for Test 1705

The longitudinal stability and control characteristics for the PTC and ACC canard configurations (wing/body/nacelle/diverter) are shown in the following plot of pitching moment coefficient vs. angle-of-attack. While the slope of the curves are essentially the same (the same longitudinal stability) the ACC canard configuration shows a $-C_{mo}$ shift and a greater pitch-up at higher angles-of-attack than the PTC canard configuration. This is believed to be the result of a larger canard planform and more closely coupled nature of the ACC canard with the wing. Control effectiveness (incremental pitching moment per degree of canard deflection) appears to be the same for both the ACC and the PTC canard. Additionally, control effectiveness appears to be the same between positive and negative canard deflection angles.

Stability & Control Characteristics for Test 1705

High Speed Aerodynamics, Long Beach

Mid-mount PTC vs. Low-mount ACC Canard Configuration
W/B/N/Df, $M_\infty = 2.4$, $Re = 4.0 \times 10^6$ / ft

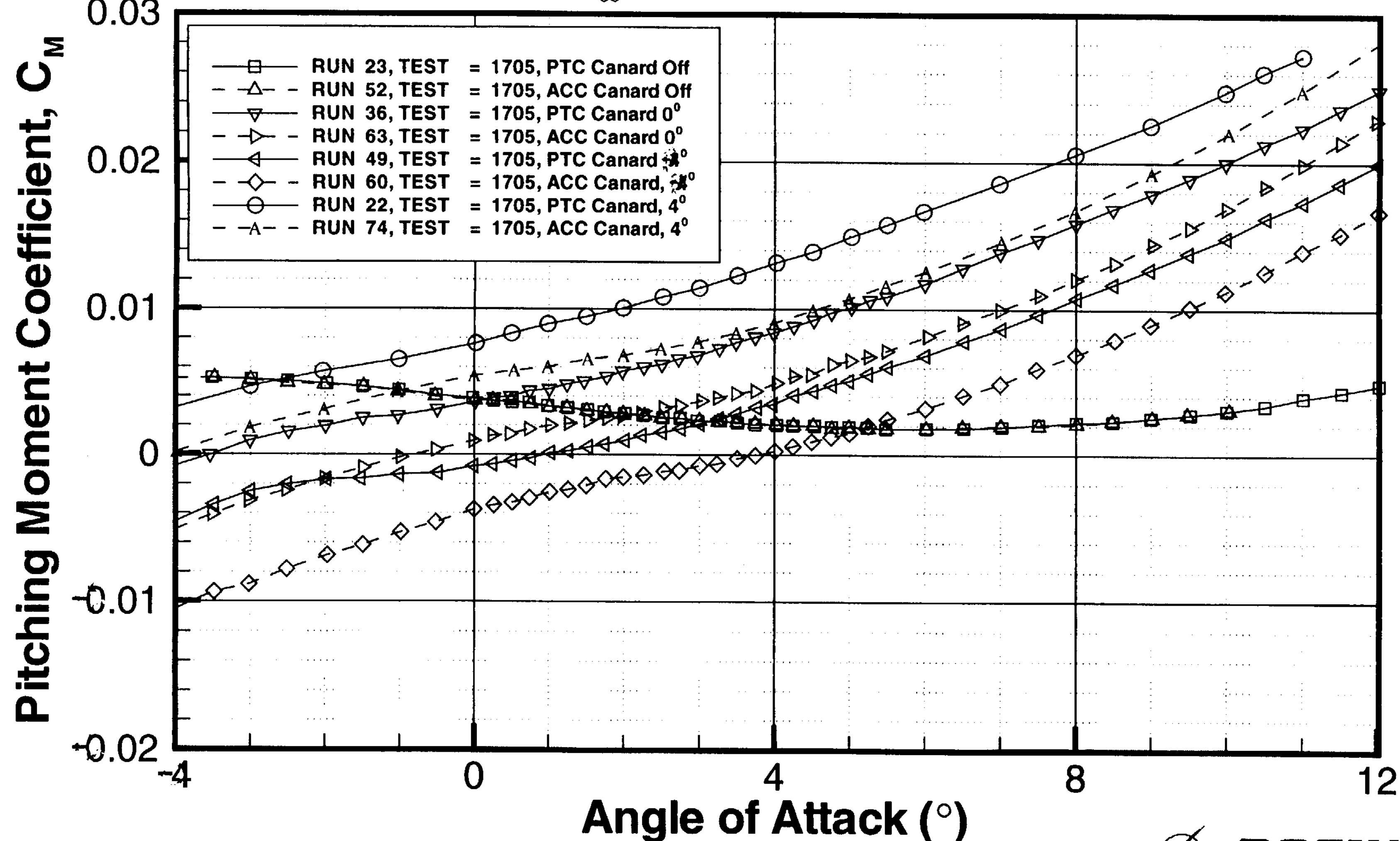

BOEING

Stability & Control Characteristics for Test 1705 (Cont.)

This chart shows a comparison of the directional stability for the PTC and ACC canard configurations (wing/body/nacelle/diverter) with respect to the canard-off configuration. Yawing moment coefficient is plotted vs. sideslip angle for a representative angle-of-attack of 4°. While all configurations are directionally unstable (typical of vertical tail-off data), the ACC canard configuration shows a further decrease in directional stability with respect to the canard-off configuration. The PTC canard configuration shows a small increase in directional stability with respect to the canard-off configuration.

Stability & Control Characteristics for Test 1705 (Cont.)

High Speed Aerodynamics, Long Beach

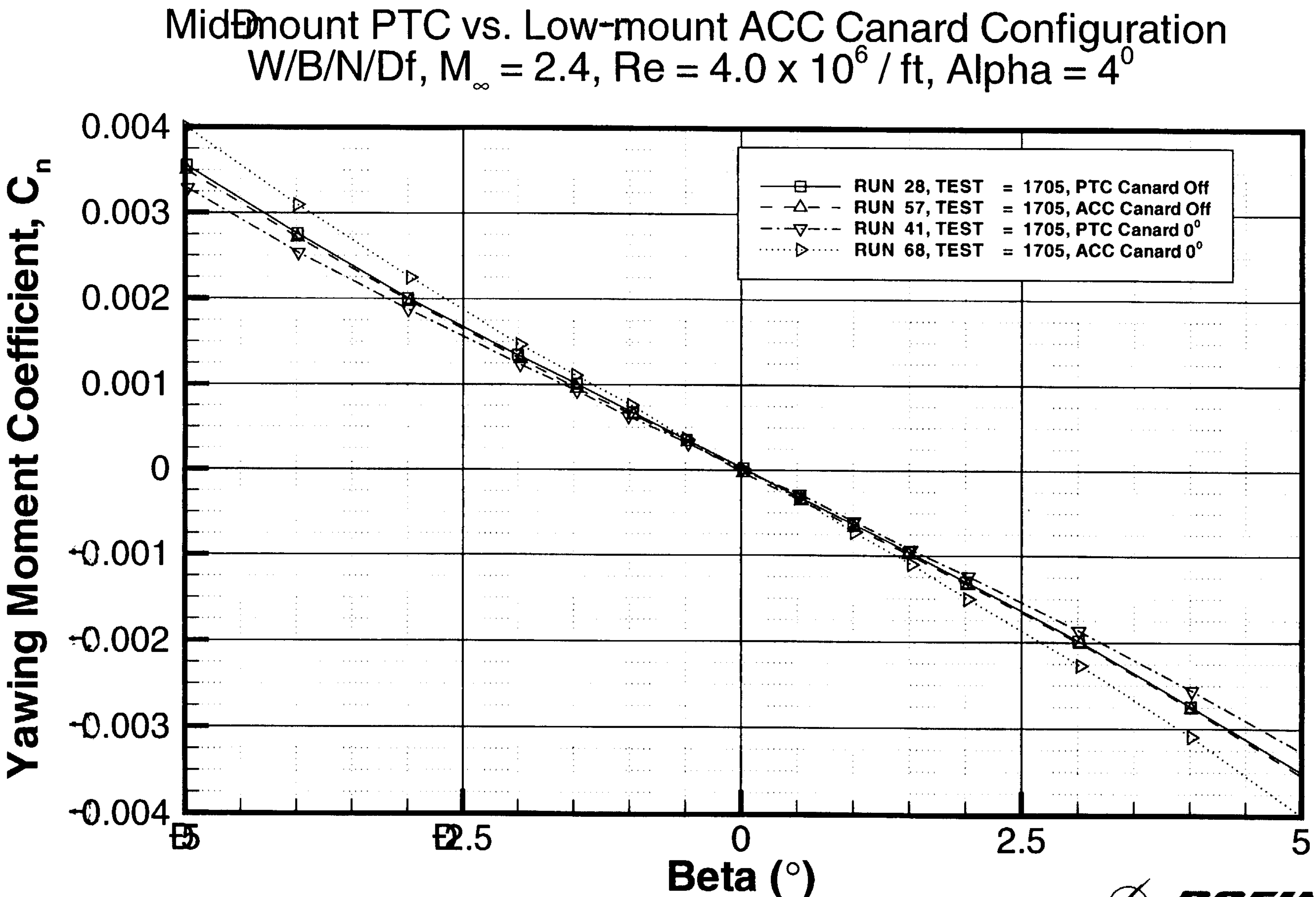

BOEING

Laser Vapor Screen Set-up for Test 1705

The set-up for Laser Vapor Screen flow visualization is simple. First, vapor is introduced into the tunnel by injecting water just downstream of the test section. Next, a laser sheet is produced from an Argon laser and an optics package that illuminates a given cross-section of the wind-tunnel test section The model is than translated through this laser light sheet and photographs are taken, from a 80 mm hasselblad camera mounted on the ceiling, at specific longitudinal stations (designated by reflective targets) on the model. The chart on the facing page shows the location of the reflective targets on the model at which still photographs were taken. The location of the ACC and PTC canards are shown, with the PTC canard located closer to the nose-tip. There are 20 longitudinal stations for which photographic data was obtained. Throughout the flow visualization, continuos video is taken from a video camera that is mounted on the strut. The video camera has a more axial view, while the camera has an oblique view of the illuminated cross-section.

NASA Langley Research Center
Unitary Plan Wind Tunnel
Test 1705 - HSR Carnard Integration
Location of dots used to position model durnig vapor screen tests

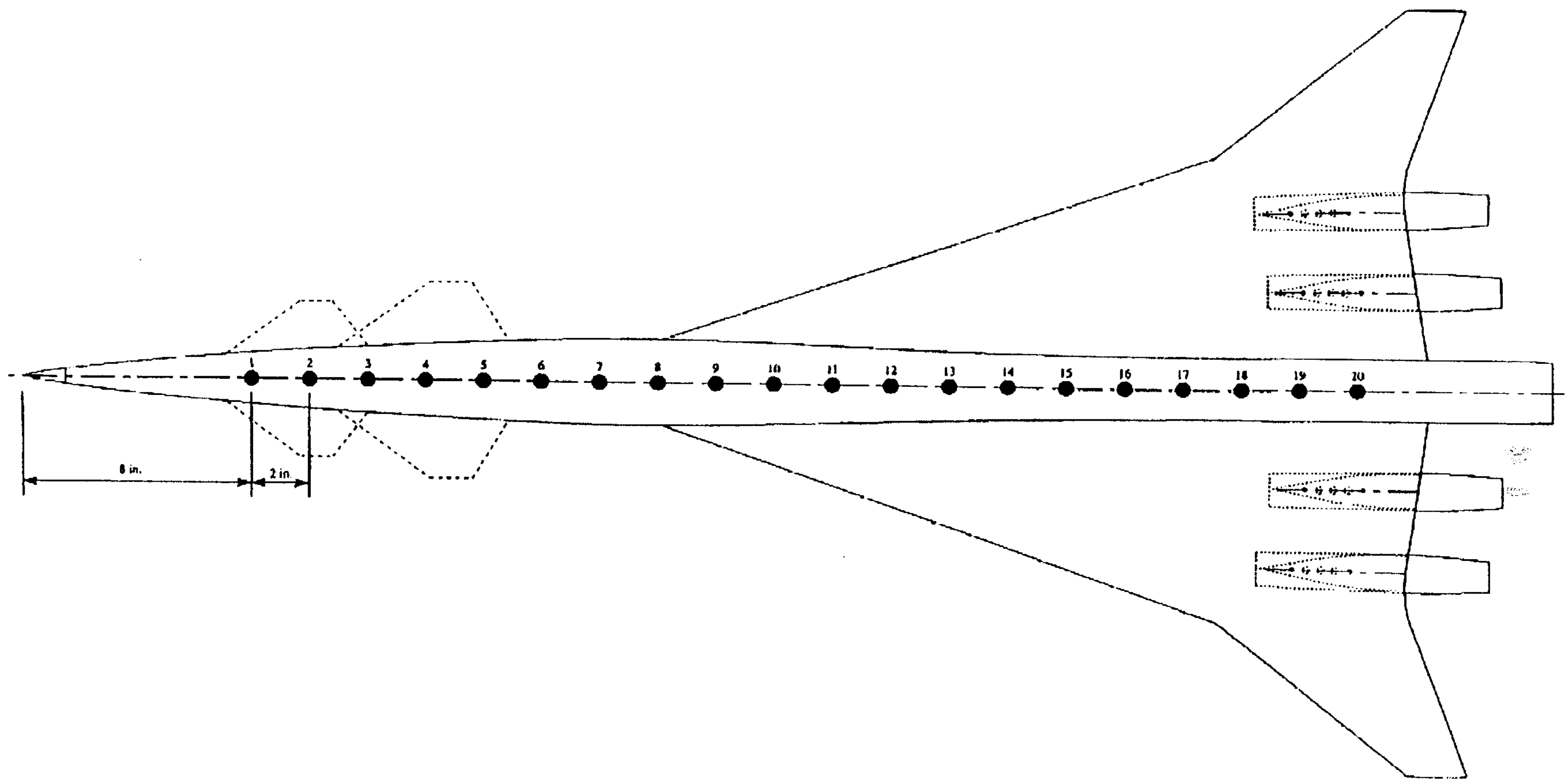

Laser Vapor Screen Shows Canard Tip Vortex Trajectory

High Speed Aerodynamics, Long Beach

PTC Mid-Mounted Canard, i_c=10°, Γ_c=0°, M_∞=2.4, Re=4x10^6/ft, α=8°, β=3°

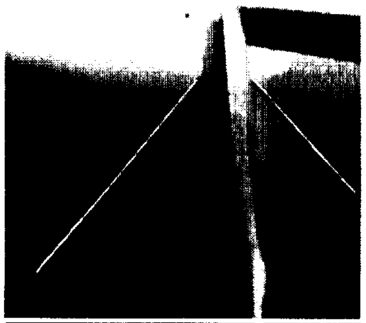

pt 4611 / dot 4

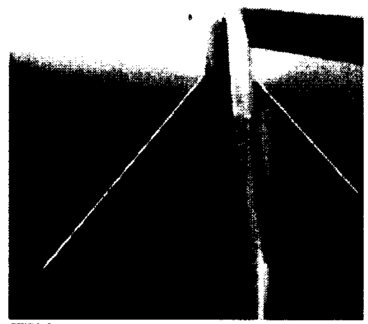

pt 4613 / dot 6

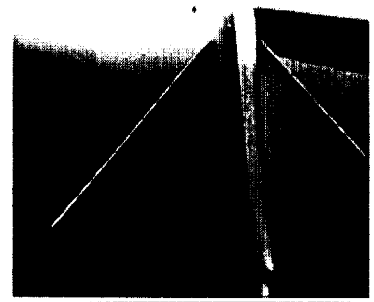

pt 4615 / dot 8

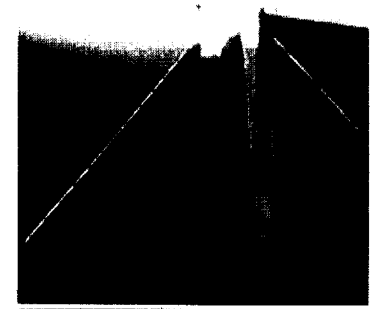

pt 4617 / dot 10

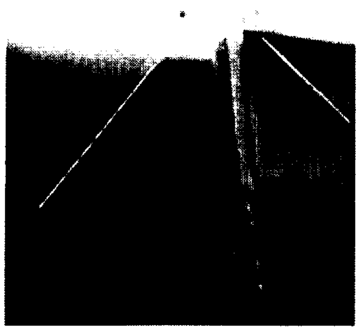

pt 4619 / dot 12

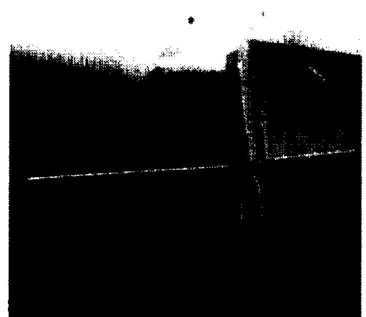

pt 4621 / dot 14

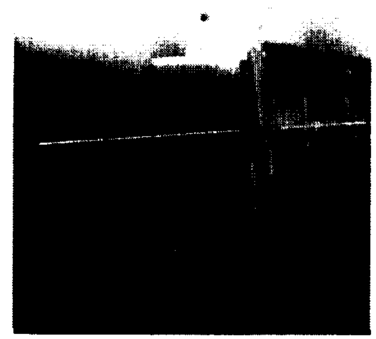

pt 4623 / dot 16

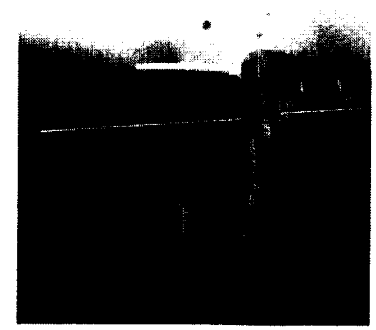

pt 4625 / dot 18

BOEING

Laser Vapor Screen Results

This chart summarizes the laser vapor screen flow visualization for Test 1705.

Laser Vapor Screen Results

- Canard tip vortex trajectory clearly visible in photographs and video tape
- Mid-mounted PTC canard tip vortex passes above wing for all i_c's tested and for 3.5° & 8° angle-of-attack
- The ACC canard tip vortex passes below the wing at 3.5° angle-of-attack for i_c=0° and -4°
- At high i_c two canard tip vortices are formed, one from the leading edge tip and one from the trailing edge tip

BOEING

Laser Vapor Screen Results (Cont.)

This chart also summarizes the laser vapor screen flow visualization for Test 1705.

Laser Vapor Screen Results (Cont.)

- For β=3°and α=8.0° the two canard tip vortices on the leeward side of the aircraft coalesce, while the windward side tip vortices spread and are located directly over the fuselage at the last LVS station
- For β=3°and α=3.5° the two canard tip vortices do not pass over the fuselage, but are barely visible at the last LVS station

BOEING

The Influence of the ACC Canard Tip Vortex on the Wing Lower Surface

In this chart an ultra-violet oil flow comparison is made between the ACC canard configuration (wing/body/nacelle/diverter) and the same configuration without the canard. The left photograph shows the lower wing surface for the configuration without the canard and the right photograph shows the lower wing surface for the configuration with the ACC canard. For the ACC canard configuration the canard is deflected 4° and the canard has 15° anhedral. Both images are for a freestream Mach number of 2.4, angle-of-attack of 3.5°, and a Reynolds number of 4 million/ft (essentially, the cruise condition). In the right photograph the interaction of the ACC canard tip vortex can be seen on the inboard lower surface of the wing near the leading edge. This interaction is shown by the red arrow in the photograph. At these conditions, based on the right photograph, it is quite possible that the ACC canard tip vortex travels into the inboard nacelle. Nevertheless, the closely coupled nature of the ACC canard with the wing is clearly evident in this comparison.

The Influence of the ACC Canard Tip Vortex on the Wing Lower Surface

High Speed Aerodynamics, Long Beach

UPWT Test 1705, $M_{\infty}=2.4$, $\alpha=3.5°$, $\beta=0°$, $Re=4.0\times10^{6}/ft$

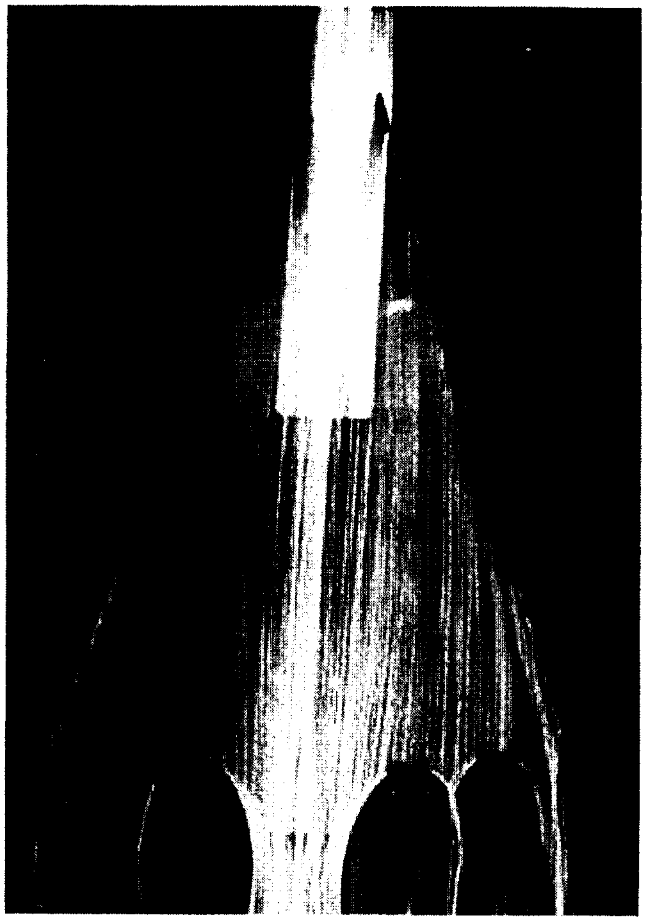

Run 115, Pt 5100, no canard

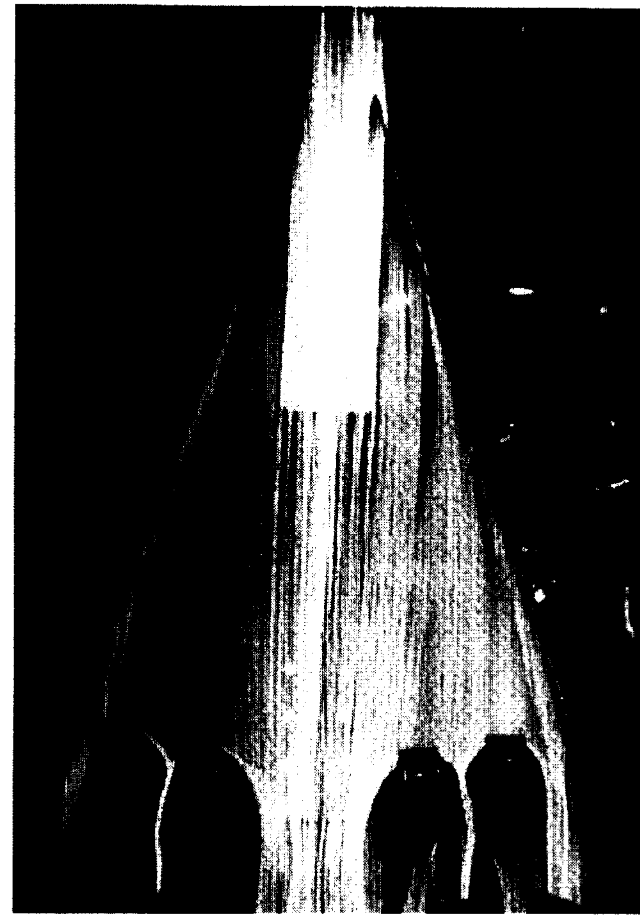

Run 114, Pt 5070, $\Gamma_c=-15°$, $i_c=4°$

uence of
vortex

BOEING

ACC Canard-Induced Shock Systems

Here a comparison of shock systems on the configuration with and without the ACC canard is made through close examination of Schlieren photographs. The configuration (wing/body/nacelle/diverter) without a canard is shown in the left photograph and the configuration with an ACC canard at an incidence angle of 4° is shown in the right photograph. The condition for these photographs were a freestream Mach number of 2.4, angle-of-attack of 3.5°, and a Reynolds number of 4 million/ft (essentially the cruise condition). The configuration with the ACC canard shows a leading and trailing-edge shock off of the canard below the configuration, but only a trailing-edge shock off of the canard above the configuration. This trailing-edge shock off of the canard above the configuration also seems to interact with the wing. This is evident by the dark line above the configuration very near where the wing is located. In the view without the canard there is no such dark line evident near the wing. This may explain the noticeable increase in drag for the ACC canard at 4° incidence angle. This will be seen in the next section. Thus, the closely coupled nature of the ACC canard with the wing is evident due to the trailing-edge shock interaction shown in this comparison.

ACC Canard Induced Shock Systems

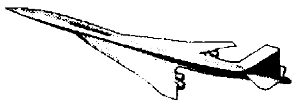

High Speed Aerodynamics, Long Beach

UPWT Test 1705, M_∞=2.4, α=3.5°, β=0°, Re=4.0x10^6/ft

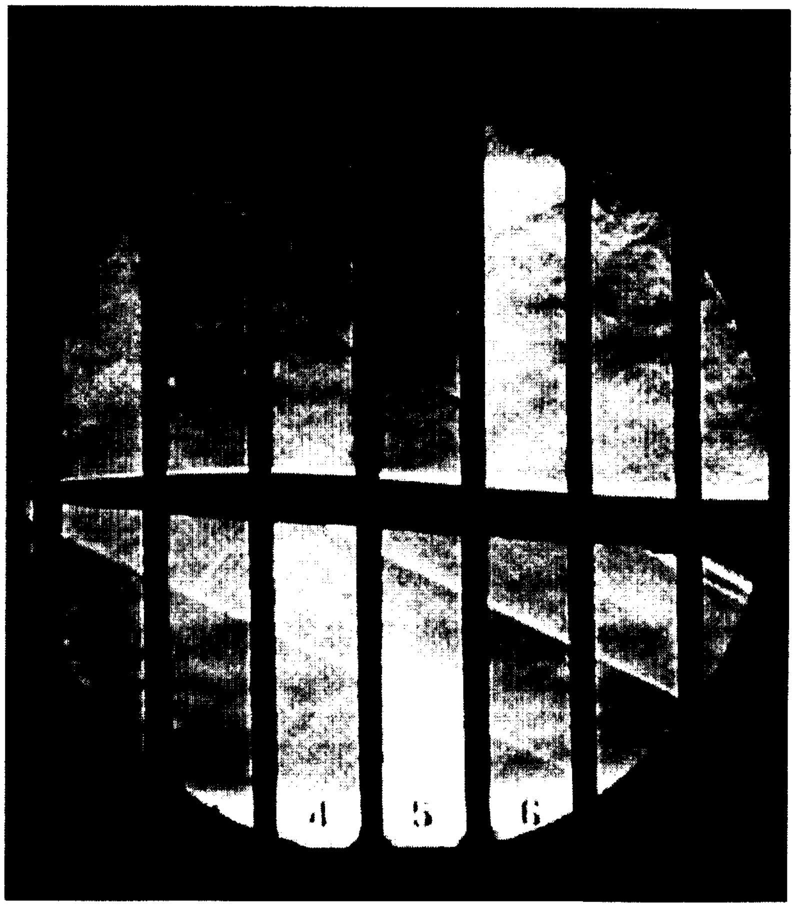

W/B2/N/Df, Run 52, Pt 2459

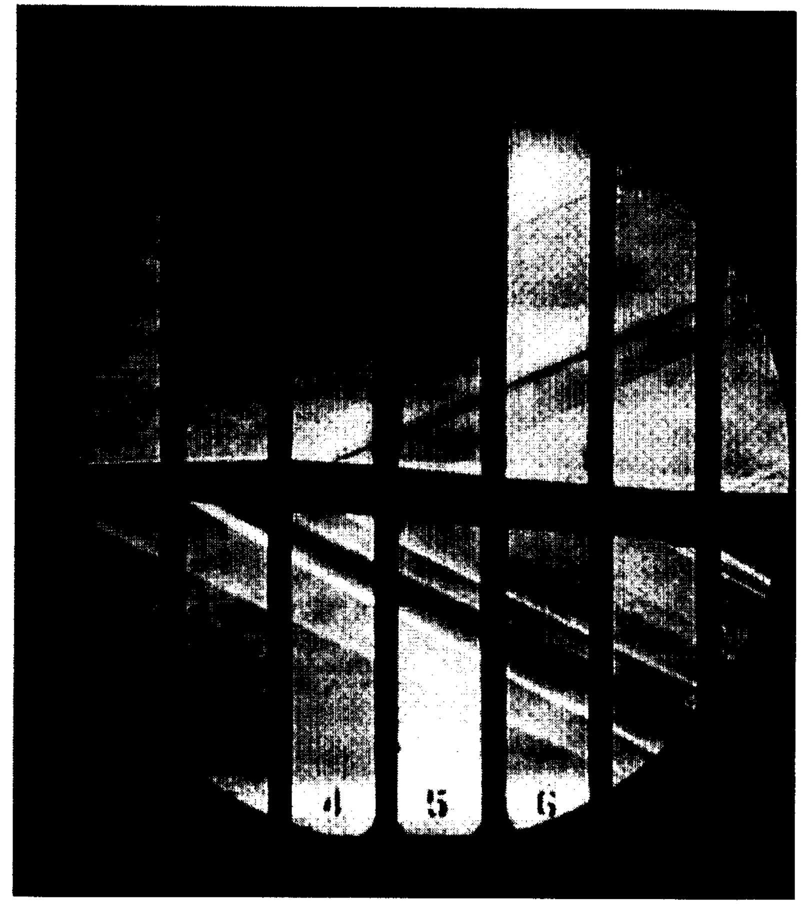

W/B2/C2/N/Df, Run 73, Pt3302

Γ_c=-15°, i_c=4°

Supersonic Canard Integration Test Conclusions

The next two charts outline some of the major conclusions from the Supersonic Canard Integration Wind Tunnel Test 1705. The conclusions from the performance part of the test will be included in the next section after the comparisons with CFD results have been made. The test showed that the wiping surface forebody (forebody #1) had a minimal impact on the performance of the configuration. The canard configurations were tested with and without the gap between the canard and the side-of-body and it was determined that the drag of the gap was worth about 1 count. Data quality was excellent throughout the entire test. The flow visualization techniques clearly showed the trajectory of the canard tip vortices, and there interaction with the wing and the nacelles for the ACC canard. This entry also showed the superior qualities of the UV-oil technique in obtaining surface streamlines at 3 angles-of-attack for a single application of the paint. In general, the ACC and PTC canard configurations have approximately the same effect on longitudinal stability, although the ACC canard has more pitch-up at higher angles-of-attack and a $-C_{mo}$ shift. The directional stability of the PTC canard configuration was found to be slightly better than the ACC canard configuration, partly due to the closely coupled ACC canard with the wing.

The test was a success due to the exceptional efforts of the Test Engineer, Floyd Wilcox, and the entire LARC UPWT staff.

Supersonic Canard Integration Test Conclusions

- Wiping surface (forebody #1) has small impact on performance
  - Change is less than 0.5 counts with respect to Model 2b
- Data quality is good and consistent with previous tests
  - Short term repeatability ≤ 0.5 drag counts
  - Medium term repeatability ≤ 0.5 drag counts (some outliers)
  - Long term repeatability (agreement superb between Test 1705 and 1687)
- Gap between canard and side-of-body is worth 1 drag count
- UV-oil technique provides very good results for 3 different angles-of-attack with just one application of the paint.
- LVS results were good, the canard tip vortex trajectory can clearly be seen in the photographs and video tape.

Canard Integration Test Conclusions (Cont.)

High Speed Aerodynamics, Long Beach

- ACC and PTC canard have approximately the same effect on the longitudinal stability
  - ACC has more pitch-up at higher angles of attack
  - ACC canard has a $-C_{mo}$ shift equal to 2° of i_c
- The closely coupled ACC canard reduces the directional stability while the mid-mounted PTC canard improves directional stability
- Test was a success because of the exceptional efforts of Floyd Wilcox and the entire LARC UPWT staff

CFL3D Performance Results for Overset and Patched Grid Topologies

The main objective of the Supersonic Wind Tunnel Test 1705 was to acquire canard integration data for CFD code validation. This section of the paper addresses CFD comparisons with the performance data of Test 1705. At the end of this section the performance conclusions of the test will be presented. Initially (before the test), overset Euler + Van Driest flat plate skin-friction solutions were generated for comparisons with the test data. After the test, overset Navier-Stokes solutions were to be generated for refined comparisons with the data. The overset approach was undertaken because they would provide rapid turnaround on the great number of canard configurations that needed to be generated. The CFL3D overset Navier-Stokes solutions initially did not work, so we decided to use patched Navier-Stokes solutions, while we figured out the difficulty with the overset solutions. During this time we developed a patched grid perturbation procedure to rapidly obtain patched solutions for the great number of canard configurations that needed to be obtained. Recently, the problem with the overset Navier-Stokes solutions using CFL3D was solved and now both techniques are available.

CFL3D Performance Results for Overset and Patched Grid Topologies

BOEING

Overset Grid Generation Allows Rapid Analysis

This chart summarizes the initial approach taken by the Boeing company to analyze the PTC and ACC canard configuration using an overset grid topology. An overset grid topology was employed to simplify the grid generation and to allow integration of existing grids for additional aircraft components (i.e., nacelles, flaps, and empennage) as will be shown in the last section of the paper. A C-O grid topology was used for the wing/body and an H-O grid topology was used for the canard. A total of 1.4 million grid points were used to define the wing, body, and canard. The grid indices are shown for each grid. For the wing/body grid, l is in the spanwise direction, j is in the streamwise direction, and k is in the normal direction. For the canard grid, l is in the streamwise direction, j is in the normal direction, and k is in the roll direction.

An automated canard grid generation has been developed by David Yeh of the Boeing Long Beach High-Lift group based on the HYPGEN grid generation code. It will integrate a canard at any given mounting location (i.e., high, mid, or low) and axial station, and will rotate and deflect the canard to any dihedral and incidence angles. Once the canard is placed in the appropriate location, an H-O grid is generated by the code. The grid generation on a C-90 takes less than 10 minutes of wall clock time.

The CFL3D version 4.1 flow solver was used in the Euler mode to obtain the CFD solutions. Van Driest II flat plate skin friction results were added to the Euler results for comparisons with the test data. All solutions were generated on a Cray C-90 computer. The FOMOCO (Force and Moment Computation) code was used to get accurate inviscid force and moments by generating a zipper grid between the overset grids. These are the same routines utilized by the OVERFLOW code to integrate forces and moments.

Overset Grid Generation Allows Rapid Analysis

❍ Grid generation

- Overset grid topology

Wing / body:	C-O, (i, j, k):	(93, 241, 41)
Canard:	H-O, (i, j, k):	(109, 33, 137)

- The Long Beach automated grid generation code
  - Variable canard mounting positions (i.e., high, mid, or low)
  - Variable canard dihedral and incidence angles
  - Takes less than 10 minutes (wall clock) on C-90

❍ Flow Solver

- CFL3D v4.1, Euler + Van Driest II flat plate skin friction
- Solutions obtained on C-90 (vn)

❍ FOMOCO used to integrate forces/moments

BOEING

Baseline TCA Wing/Body/Canard Overset Grid

This chart shows a typical wing/body/canard overset grid utilized by Boeing for comparisons with the Test 1705 data. The red region shows the canard grid and the black region shows the wing/body grid. Note that only every other point in the grid is shown in this chart.

Baseline TCA Wing/Body/Canard Overset Grid

High Speed Aerodynamics, Long Beach

Preliminary Technology Concept Canard Geometry, Every Other Point Shown

Global View

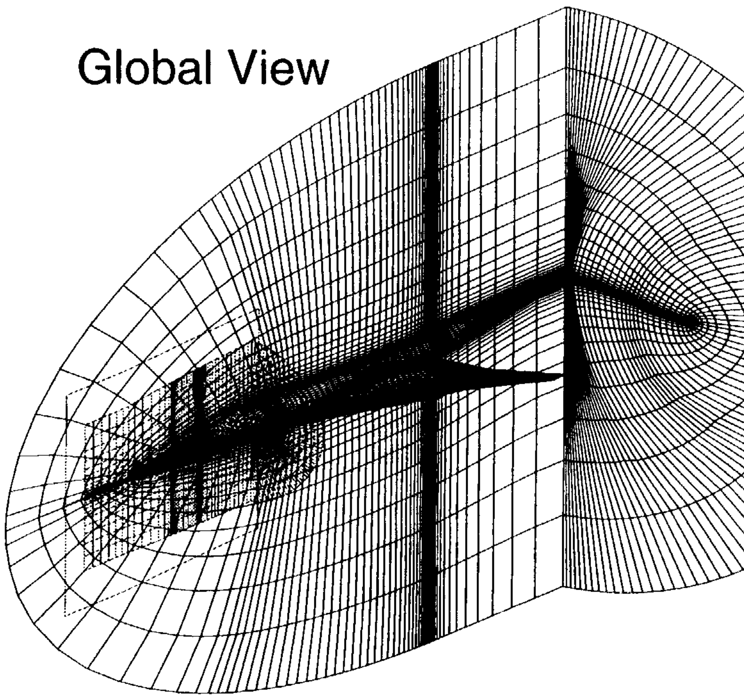

Forebody Region

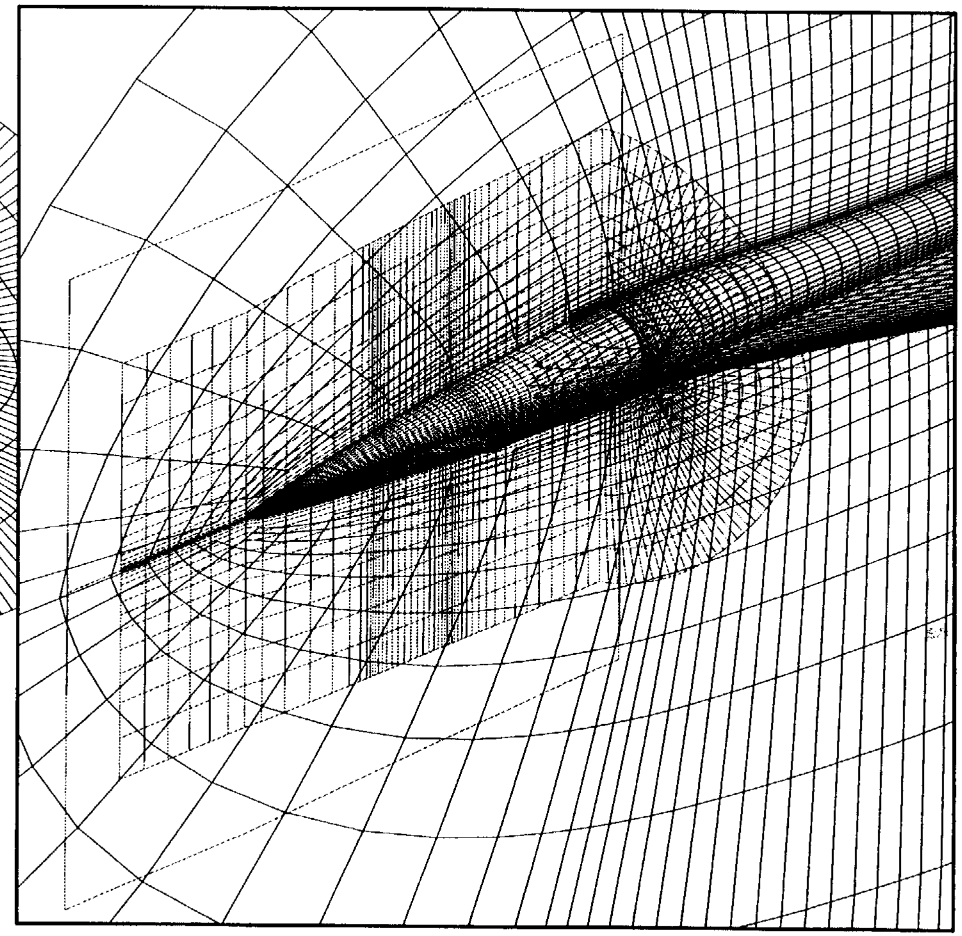

Drag Polar Comparison (Experiment vs. CFD)

This chart shows a comparison between experimental drag polars and CFD overset Euler results + Van Driest II skin friction for the baseline TCA model with and without the PTC canard at M_∞=2.4 and Re=4 million/ft. Trip drag has not been removed from the experimental results, so only incremental comparisons can be made. The region around the cruise point has been enlarged in the plot in the lower right corner of the chart. The results show that the increments predicted by the overset Euler +Van Driest II skin friction agree very well with the increments measured in the wind tunnel for the mid-mounted PTC canard. In the upper right corner of the chart the actual incremental values (canard-on – canard-off) for the experiment and the CFD results are tabulated. The greatest difference between the CFD and experimental incremental results is 0.4 drag counts at a C_L=0.09, which is within the uncertainty of the data. It should be noted that the series of 3 wind-tunnel data runs for each canard incidence angle shown in the chart have been represented by their mean values.

Drag Polar Comparison (Experiment vs. CFD)

High Speed Aerodynamics, Long Beach

1.675% Baseline TCA Model w/without PTC Canard
UPWT Test 1705, $M_\infty = 2.4$, $Re = 4 \times 10^6$ / ft, W/B1

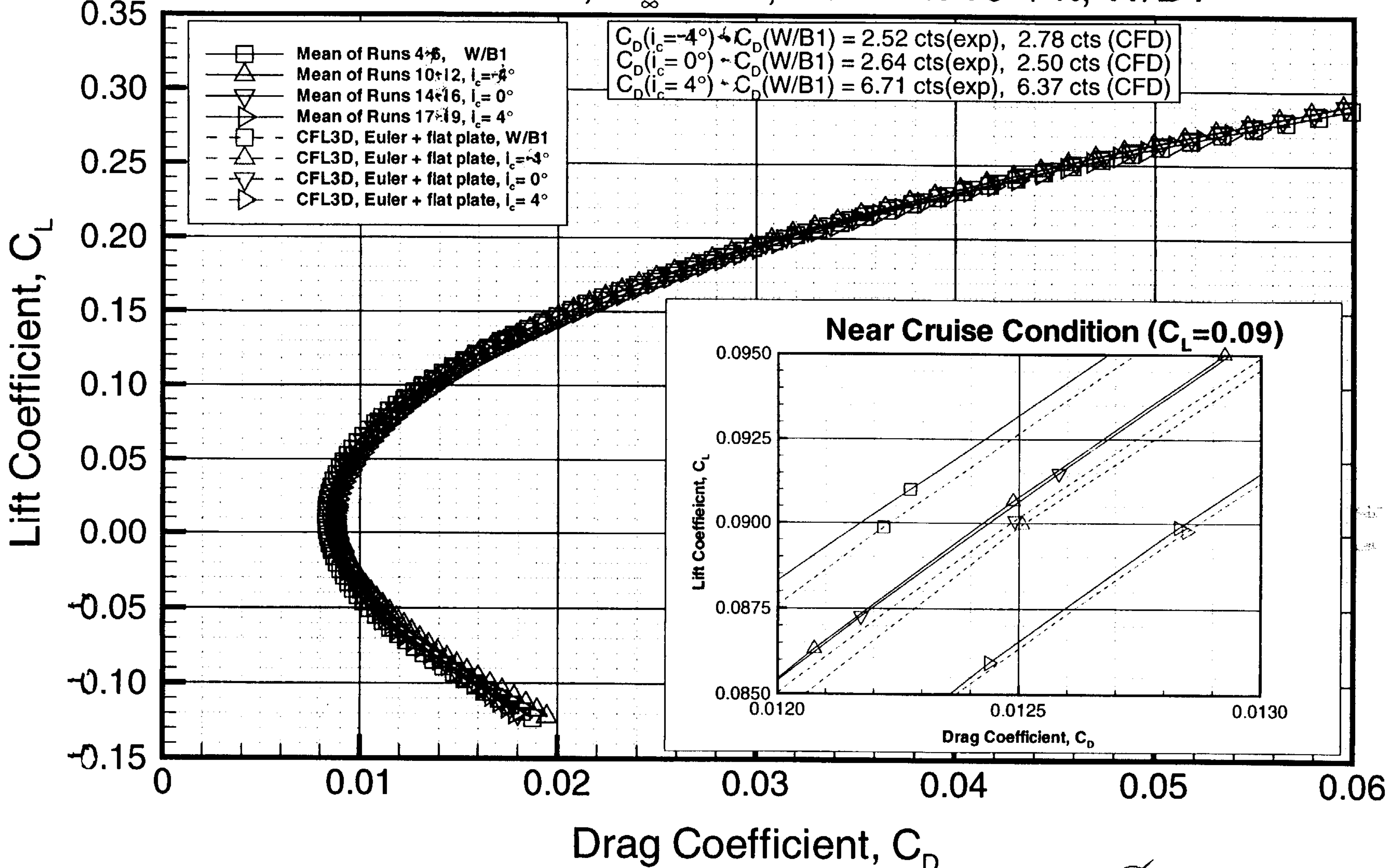

BOEING

Drag Comparison: ACC vs. PTC Canard

This chart shows a comparison between experimental drag polars and CFD overset Euler results + Van Driest II skin friction for the baseline TCA model with and without the PTC and ACC canard at M_∞=2.4, Re=4 million/ft and an i_c=4°. Trip drag was not removed from the experimental data in this chart, so only incremental comparisons can be made. Incremental agreement is good between CFD and experiment for the PTC canard, but the incremental agreement between CFD (Euler + Van Driest II flat plate skin friction) and experiment for the ACC canard at an incidence angle of 4° is poor. In fact, the wind-tunnel data for the ACC and PTC canard configuration (wing/body/canard) at 4° incidence angle shows the same value of drag at a C_L=0.09. This was unexpected since the ACC canard planform is significantly larger than the PTC planform. It was theorized that the Euler + flat plate skin friction results were not accurately modeling the viscous nature of the canard wake and tip vortices. Therefore, this type of computation was not suitable for predicting the favorable interaction of the ACC canard wake and tip vortices with the wing. To investigate this theory, patched Navier-Stokes solutions were undertaken using Baldwin-Lomax and Menter's $\kappa-\omega$ SST turbulence models for both the PTC and ACC canard configurations.

Drag Comparison: ACC vs. PTC Canard

High Speed Aerodynamics, Long Beach

1.675% TCA W/B and W/B/C, UPWT Test 1705, M_∞=2.4, Re=4 x 10^6 /ft, i_c=4°

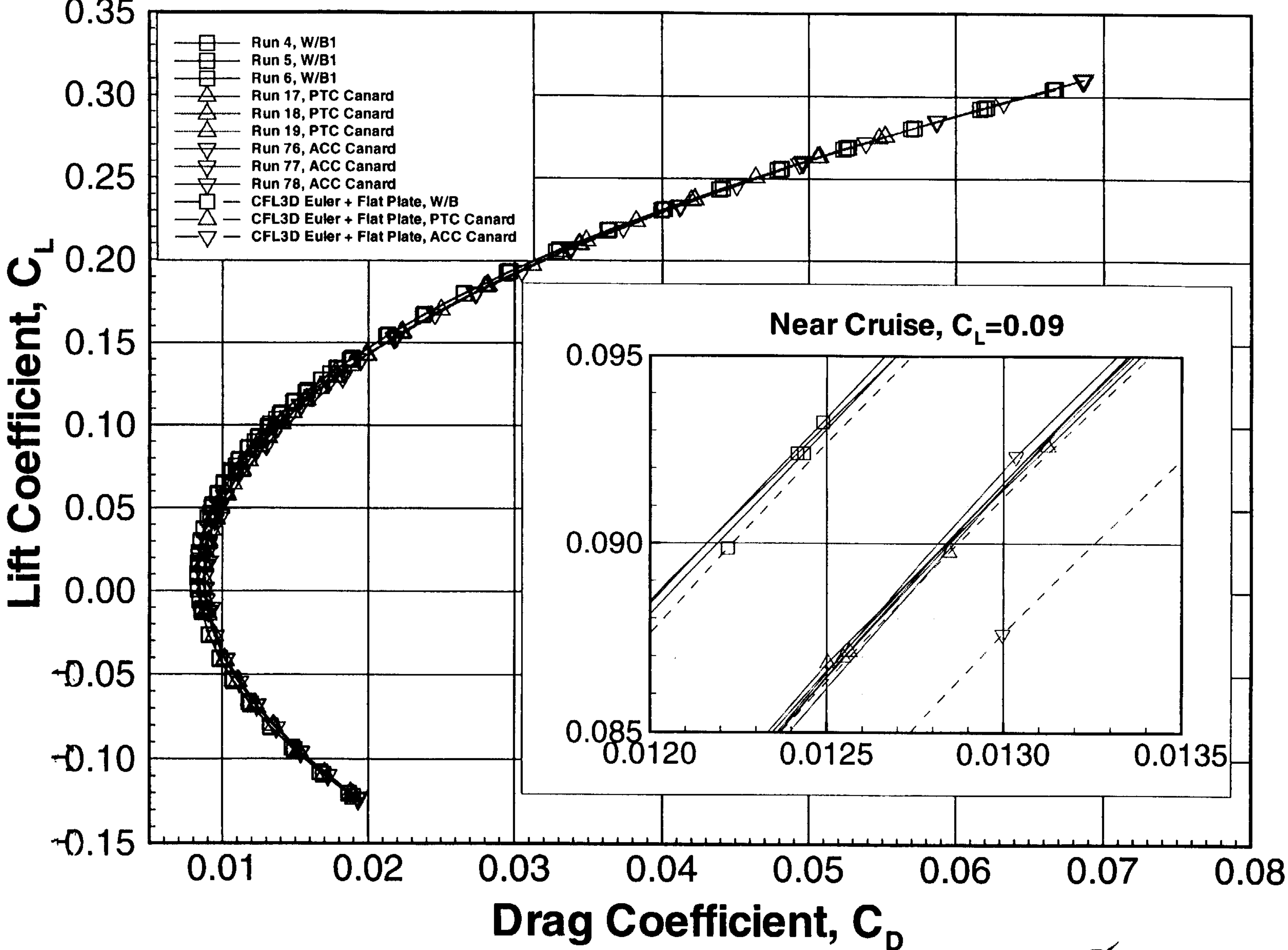

BOEING

Patched Grid Solutions

Initially, we avoided patched Navier-Stokes solutions due to the lengthy grid generation process required for the large number of configurations we wanted to analyze. This problem was significantly alleviated when Eric Unger of the High Speed Aerodynamics group at long Beach developed a procedure to rapidly generate patched grids for different canard deflections, once an initial patched grid was constructed. Using Boeing proprietary grid generation software the initial patched wing/body/canard grid takes approximately 2 days to construct from an existing wing/body grid. The patched grids for the alternate canard deflections are then constructed in a manner of minutes using CSCMDO to perturb the surface geometry and volume grid.

The flow solver used for the patched grid Navier-Stokes solutions was CFL3D version 4.1. In this study two turbulence models were utilized; the Baldwin-Lomax algebraic model and the Menter's $\kappa-\omega$ SST two equation model. All computations were generated on a Cray C-90. The objectives for the patched Navier-Stokes solutions were to determine the cause of the anomalous results obtained for the ACC canard at 4° incidence angle and to determine which turbulence model agrees best with the supersonic canard integration wind-tunnel data.

Patched Grid Solutions

Patched Grid Generation

- Initial patched grid generated from single block wing/body grid (COWF2 / MACGS)
  - Takes ~ 2 days to generate
- Alternate canard deflections obtained by perturbation of grid using CSCMDO
  - Takes a couple of minutes to generate

Flow Solver

- CFL3D v4.1, Navier-Stokes
- Turbulence Models: Baldwin-Lomax & k-ω
- Computations conducted on Cray C-90 (vn)

BOEING

ACC Canard Configuration Patched Grid Topology

This chart shows a typical patched wing/body/canard grid for the ACC canard configuration utilized for the current study. The grid consists of 11 blocks with a total of 3.5 million grid points. The grid for the symmetry plane and the block boundaries for the blocks in the field are shown. Each color represents a different block. The PTC canard grids utilized in this study were slightly different. They consisted of 7 blocks with a total of 2.4 million points for the PTC wing/body/canard configuration and 24 blocks with a total of 7.9 million points for the PTC wing/body/canard/nacelle/diverter.

ACC Canard Configuration Patched Grid Topology

High Speed Aerodynamics, Long Beach

11 Blocks
3.5 million points

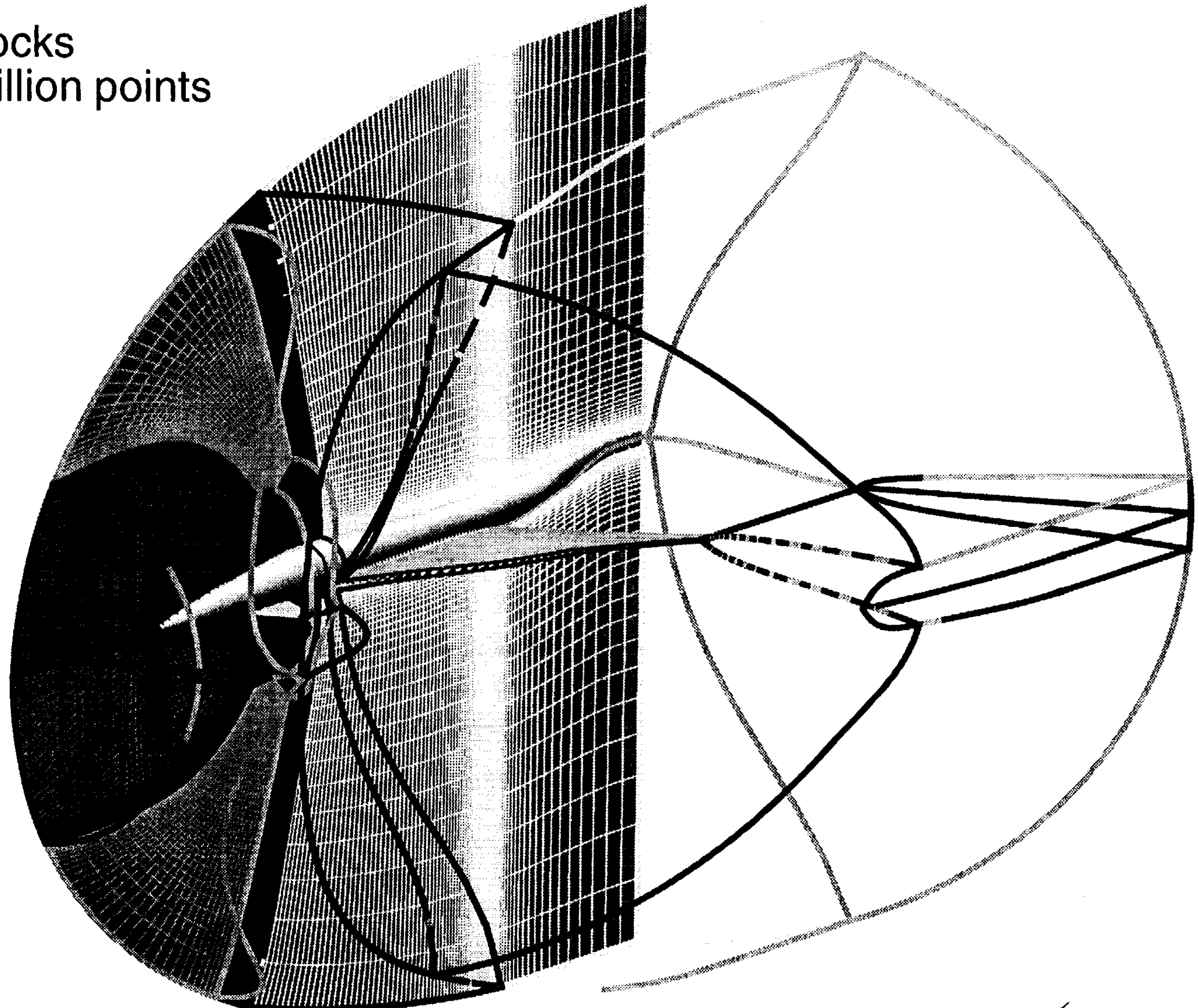

Trip Drag & Laminar Run Corrections

To make accurate absolute comparisons between the patched Navier-Stokes computations and the experimental results, the data has to be corrected for trip drag and laminar run. The table on the following page list the trip drag and laminar run corrections for each element (i.e., wing/body, nacelles, and canards). The value of the trip drag and laminar run for the wing/body was obtained from BCAG. The trip drag and laminar run corrections for all other components were computed. For trip drag these component values are determined based on the number of trip dots on the component compared with the number of trip dots on the wing/body. For example,

PTC Canard Trip Drag = (Number of Dots on the Canard / Number of Dots on the wing-body)*(trip drag on the wing-body)

The laminar run for each component was determined in a similar manner except laminar run area was used instead of the number of trip dots. The table shows that for wing/body/canard/nacelle/diverter data 4 counts will be removed from the data, while for wing/body/canard configurations approximately 2.5 counts will be removed from the data. It should be noted that results obtained from NASA Ames using similar trip drag methodology show, that for the 0.012 inch trip dots used on these models, the trip drag and laminar run corrections offset each other resulting in essentially a net zero correction for the wing/body configuration. Therefore, when looking at the following charts the corrected and uncorrected data reflect the BCAG and NASA Ames trip drag results, respectively.

Trip Drag & Laminar Run Corrections

High Speed Aerodynamics, Long Beach

Configuration	Number of Trip Dots	Trip Drag (Counts)	Laminar Run (Counts)	Trip Drag - Laminar Run (Counts)
Wing / Body *	580	3.60	1.20	2.40
4 Nacelles *	282	1.75	0.25	1.50
PTC Canard	64	0.40	0.30	0.10
ACC Canard	72	0.45	0.30	0.15
Wing / Body / Nacelle / PTC Canard	926	5.75	1.75	4.00
Wing / Body / Nacelle / ACC Canard	934	5.80	1.75	4.05
Wing / Body / PTC Canard	644	4.00	1.50	2.50
Wing / Body / ACC Canard	652	4.05	1.50	2.55

* Values Obtained from Kevin Mejia (BCAG)

BOEING

Drag Polars for the PTC Canard on TCA W/B/N/D Configuration

This chart compares the corrected (trip drag & laminar run) drag polar wind tunnel data with Navier-Stokes solutions using Baldwin-Lomax and Menter's $\kappa-\omega$ SST turbulence models for the PTC canard configuration (wing/body/canard/nacelle/diverter) at $M_\infty=2.4$, $Re_c=6.36\times10^6$(4 million/ft), and $i_c=0°$. From the expanded view about the cruise condition ($C_L=0.1$) the Menter's k-w SST model agrees very well with the corrected data, while the Baldwin-Lomax turbulence model is closer to the uncorrected data (~2.0 drag counts high).

Drag Polars for the PTC Canard on TCA W/B/N/D Configuration

High Speed Aerodynamics, Long Beach

CFL3D (Navier-Stokes with B-L & SST Turbulence Models), UPWT Test 1705

$M_\infty=2.40$, $Re_c = 6.36\times10^6$, $i_c=0^\circ$, $\Gamma_c=0^\circ$

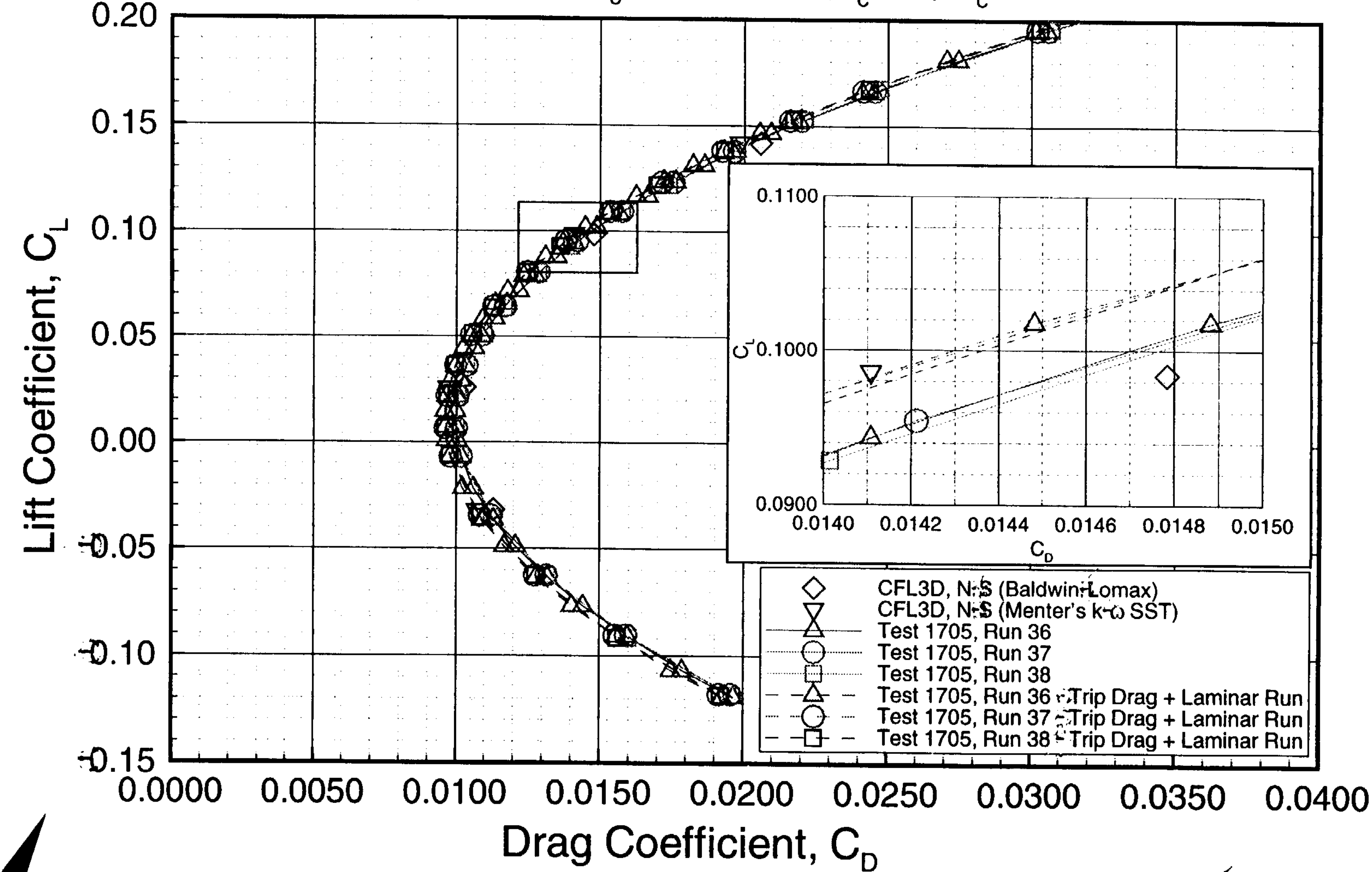

Alpha STAR CORPORATION

BOEING

Drag Polars for the PTC Canard on TCA W/B/N/D Configuration (Cont.)

This chart compares the corrected (trip drag & laminar run) drag polar wind-tunnel data with Navier-Stokes solutions using Baldwin-Lomax and Menter's $\kappa-\omega$ SST turbulence models for the PTC canard configuration (wing/body/canard/nacelle/diverter) at $M_\infty=2.4$, $Re_c=6.36x10^6$(4 million/ft), and $i_c=4°$. From the expanded view about the cruise condition ($C_L=0.1$) the Menter's $\kappa-\omega$ SST model does not agree as well with the corrected data (~2.5 drag counts low), while the Baldwin-Lomax turbulence model agrees very well with the uncorrected data.

Drag Polars for the PTC Canard on TCA W/B/N/D Configuration

High Speed Aerodynamics, Long Beach

CFL3D (Navier-Stokes with B-L & SST Turbulence Models), UPWT Test 1705

$M_\infty=2.40$, $Re_c = 6.36 \times 10^6$, $i_c=4°$, $\Gamma_c=0°$

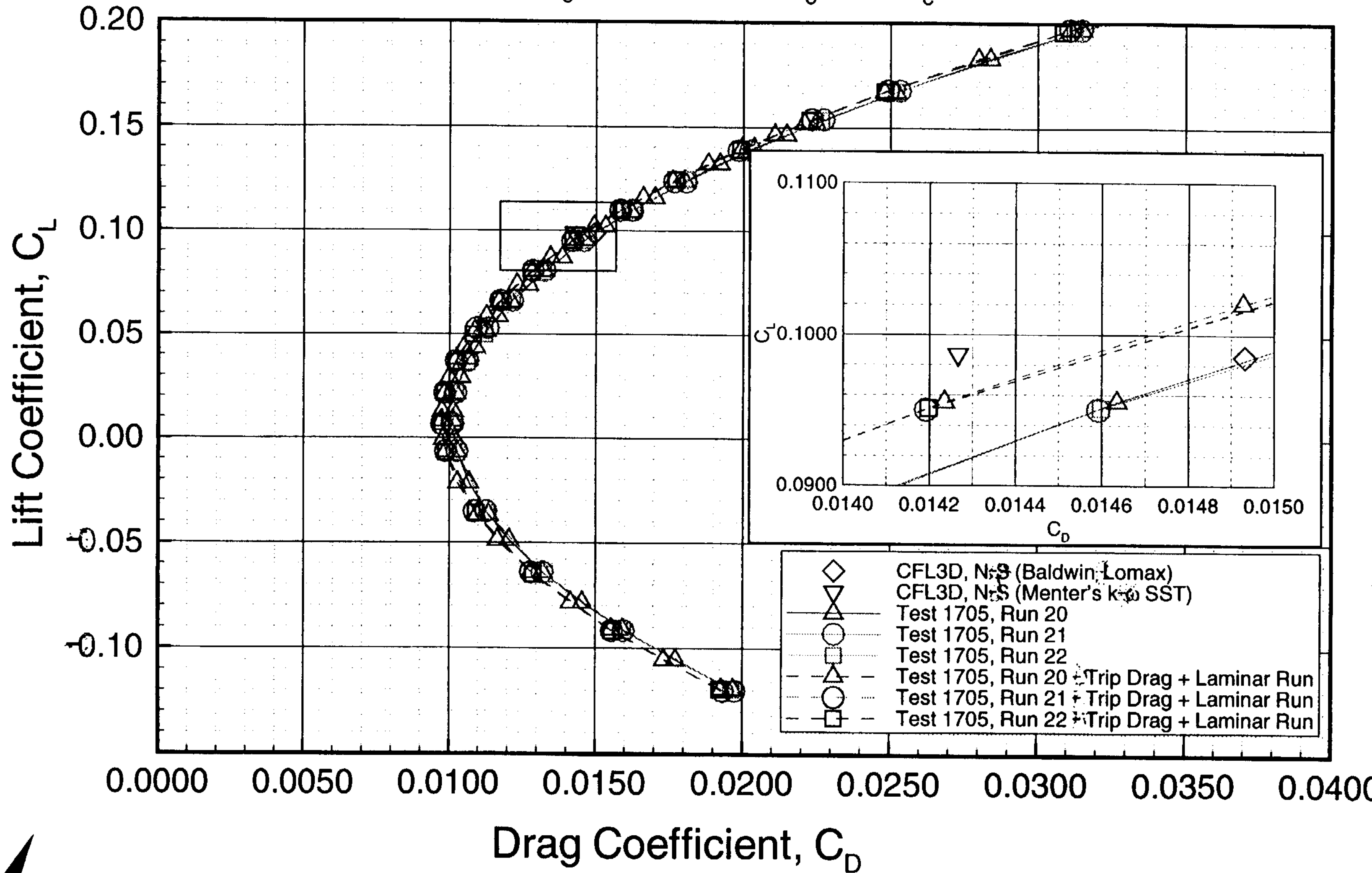

Alpha STAR CORPORATION

BOEING

Drag Polars for the ACC Canard on TCA W/B Configuration

This chart compares the corrected (trip drag & laminar run) drag polar wind-tunnel data with Navier-Stokes solutions using Baldwin-Lomax and Menter's $\kappa-\omega$ SST turbulence models for the ACC canard configuration (wing/body/canard) at M_∞=2.4, Re_c=6.36x10^6(4 million/ft), and i_c=0°. From the expanded view about the cruise condition (C_L=0.1), the Menter's $\kappa-\omega$ SST model is 1.5 drag counts lower than the corrected data, while the Baldwin-Lomax turbulence model agrees very well with the uncorrected data.

Drag Polars for the ACC Canard on TCA W/B Configuration

High Speed Aerodynamics, Long Beach

CFL3D (Navier-Stokes with B-L & SST Turbulence Models) , UPWT Test 1705

$M_\infty = 2.40$, $Re_c = 6.36 \times 10^6$, $i_c = 0°$, $\Gamma_c = -15°$

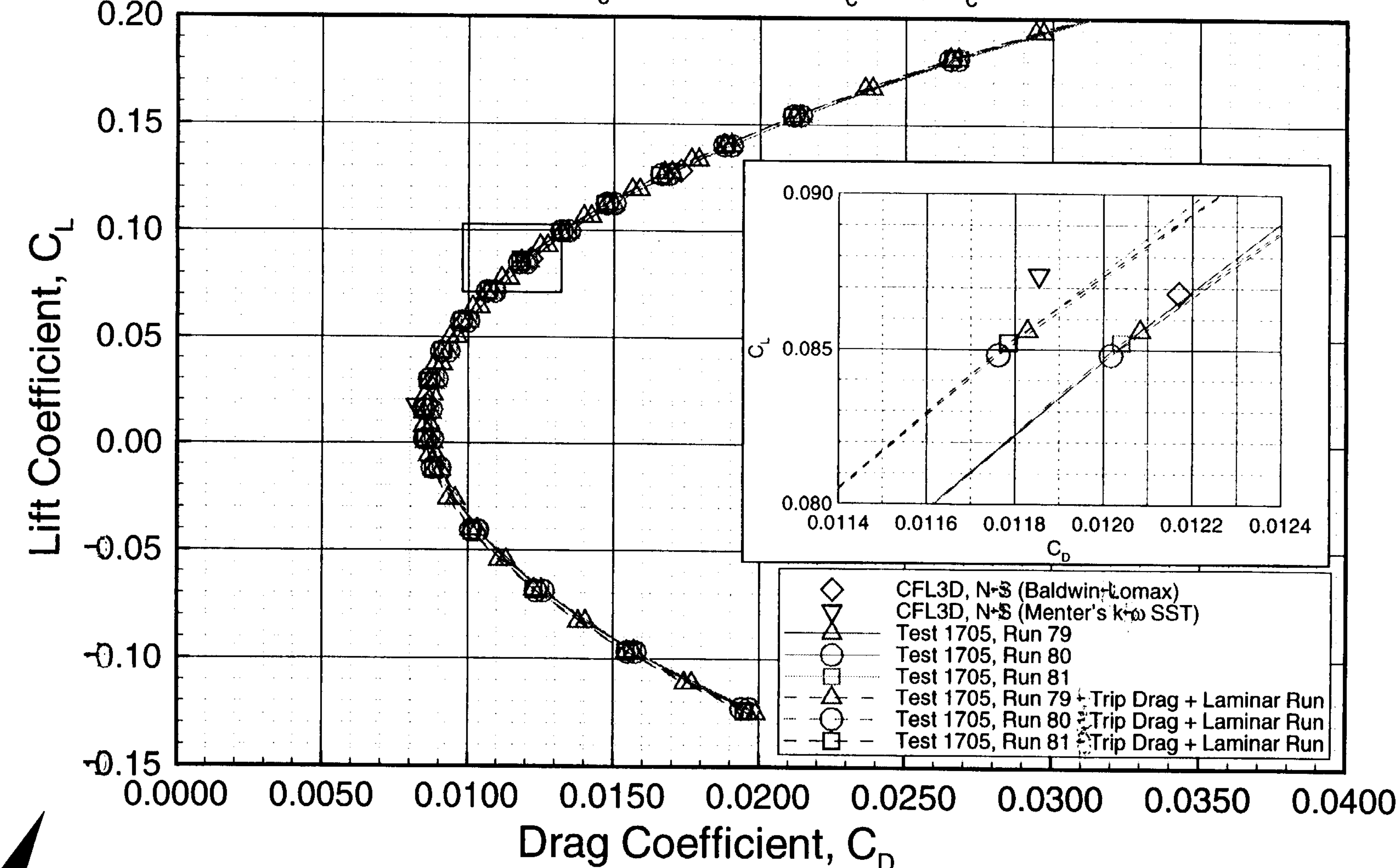

Alpha STAR CORPORATION

BOEING

Drag for the PTC Canard on TCA W/B Configuration

This chart shows the inviscid and viscous components of the drag coefficient versus angle-of-attack for the Baldwin-Lomax and Menter's $\kappa-\omega$ SST turbulence models for the PTC canard configuration (wing/body/canard) at M_∞=2.4, Re_c=6.36x10^6(4 million/ft), and i_c=0°. The difference in drag between the turbulence models is solely due to the viscous drag coefficient, while the pressure for each is exactly the same. This is a typical result that is seen in the computations shown in this section.

Drag for the PTC Canard on TCA W/B Configuration

High Speed Aerodynamics, Long Beach

CFL3D, Navier-Stokes, Seven-Zone Patched Grid, 2.4 Million Points

$M_\infty=2.40$, $Re_c = 6.36\times10^6$, $i_c=0°$, $\Gamma_c=0°$

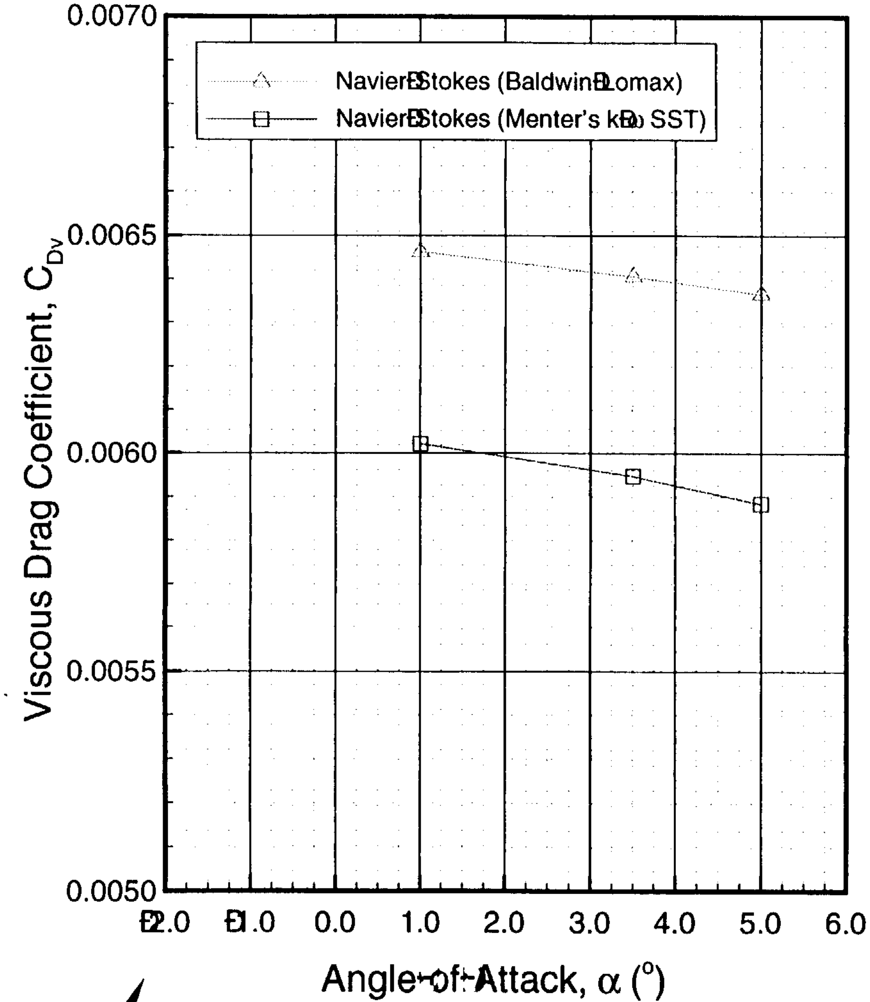

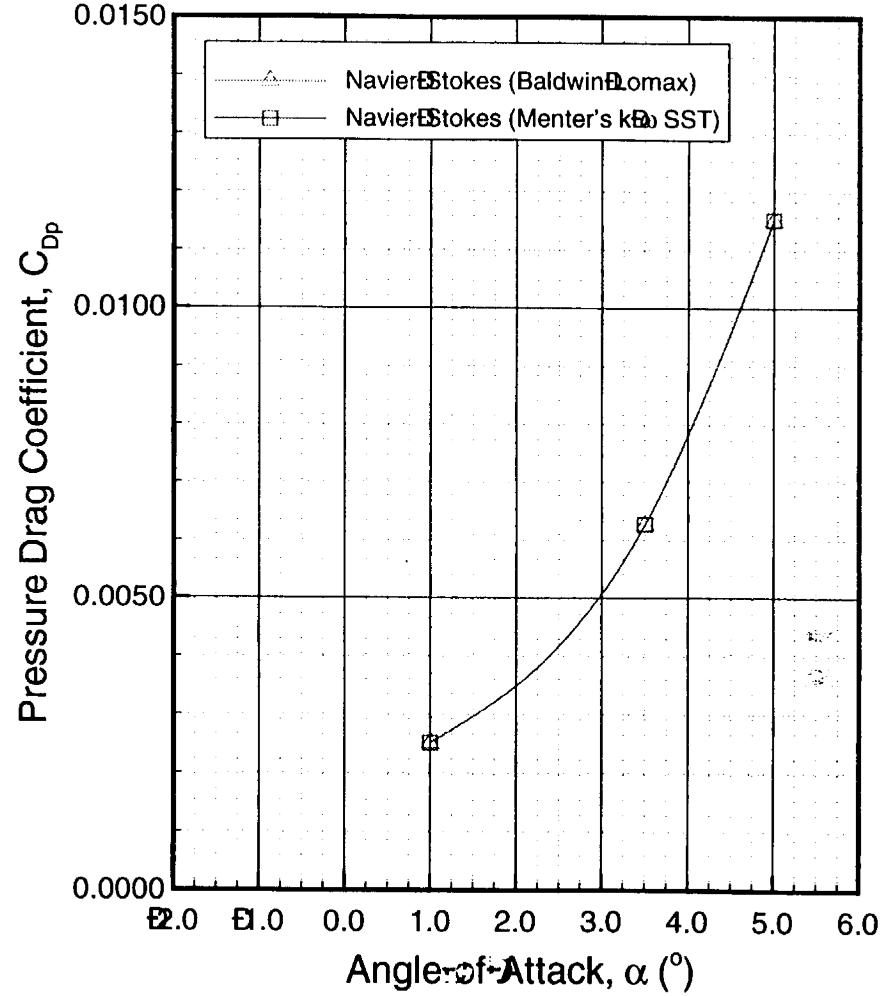

Alpha STAR CORPORATION

BOEING

Summary of CFL3D Performance Results

The conclusions of the performance data from Test 1705 and the computational results show that for the cruise condition (C_L=0.1) the Menter's $\kappa-\omega$ SST turbulence model generally agrees well with the corrected canard configuration data at canard i_c=0°, but significantly under-predicts the drag (~2.5 drag counts low) for PTC canard i_c=4°. The Baldwin-Lomax turbulence model generally agrees with the uncorrected data for most canard incidence angles except the PTC canard at 0° incidence angle where it over predicts the drag by approximately 2 counts.

Canard drag increments predicted using overset grids in CFL3D + Van Driest II flat plat skin friction agree fairly well with all of the test data except for the ACC canard configuration at an i_c=4°. This study has been inconclusive as to what is causing the poor agreement for the ACC canard configuration at an i_c=4°, but it is believed to be due to the viscous nature of the canard wake and tip vortices, which are not captured by an Euler method coupled with a flat plate skin friction method. Instead, Navier-Stokes solutions are required for the ACC canard configuration at an i_c=4°. This condition has yet to be run using patched Navier-Stokes grid topologies for either the Baldwin-Lomax or the Menter's $\kappa-\omega$ SST turbulence models. Hopefully, these solutions will indicate the reason why the PTC and ACC canard at an i_c=4° provide the same drag.

From the computational analyses undertaken in this section, it has been determined that both the overset and patched grid methodologies allow rapid solutions through a range of canard incidence angles.

Summary of CFL3D Performance Results

- At the cruise condition (α=3.5°), Wind Tunnel data - Trip Drag + Laminar Run agrees best with k–ω model for i_c=0°
- Agreement not as good at i_c=4° (~2.5 counts)
- Canard drag increments predicted using overset grids in CFL3D + flat plate skin friction agree fairly well with test data except for the ACC canard at an i_c=4°
- The ACC canard at i_c=4° is the only case that remains to be run with the patched NS grid
- Both overset and patched grid methodologies allow rapid solutions through a range of i_c's

BOEING

The Transonic Canard Integration Wind Tunnel Test (16TT Test 508)

After the supersonic canard integration data was obtained, the same kind of data was obtained for transonic Mach numbers. Here the effect of selected optimized transonic flap settings was added to determine the effect of canard integration on transonic performance for realistic transonic configurations. Here again data was not obtained with the tail on, since the model used did not have one.

The Transonic Canard Integration Wind Tunnel Test (16TT Test 508)

Transonic Canard Integration Test Information

The Transonic Canard Integration Wind-Tunnel Test (Test 508) was conducted from 9/13/98 thru 10/2/98 at the NASA Langley 16-foot Transonic Tunnel. It was a two-shift operation (15 days) and a 145 runs were completed. Two models were used during Test 508 similar to the Supersonic Canard Integration Test (Test 1705) except Model 5 was used instead of Model 2b. The Baseline TCA Model 5 was used because it had various transonic flaps (baseline and the Mach 0.9 optimum) that could be tested with the canards from Model 52. The Model 5 is a 1.675% representation of the baseline TCA configuration. The test conditions for this entry were; M_∞=0.6, 0.9, & 1.1, angles-of-attack from –4° to 12°, sideslip angles from –6° to 6°, and Reynolds number of approximately 4 million/ft.

Transonic Canard Integration Test Information

- **Test facility: LaRC 16-foot Transonic Tunnel**
- **Test date: 9/13/98 - 10/2/98**
- **Test duration: 15 two-shift days**
- **Models**
  - Model 5 - 1.675% Baseline TCA with truncated aftbody and one-piece nacelle/div
  - Model 52 - Model 5 with two new forebodies to accomodate several canard configurations
- **Test conditions:**
  - M_∞ = 0.6, 0.9, 1.1, α = -4° to 12°, β = -6° to +6°
  - Re = 4 million/ft

BOEING

Transonic Canard Integration Test Objectives

The objectives of Test 508 were the same as Test 1705 except now certain transonic flap settings would be utilized in addition to all of the PTC and ACC canard settings tested in Test 1705.

Transonic Canard Integration Test Objectives

High Speed Aerodynamics, Long Beach

- Acquire experimental database for CFD code validation on W/B/C and W/B/C/N/D with and without selected transonic flaps settings
- Acquire flow visualization data for the canard wake to see how it influences the wing and nacelle flowfields
- Assess the effects of canard location on performance
- Acquire limited S&C characteristics (high alpha, multiple canard deflection angles, and sideslip angles)

BOEING

The NASA Langley 16-foot Transonic Wind Tunnel

This photograph shows an aerial view of the NASA Langley 16-foot Transonic Wind Tunnel (16 TT). The NASA Langley 16-foot Transonic Tunnel is a closed-circuit single-return atmospheric wind tunnel that has a slotted transonic test section with a Mach number range from 0.1 to 1.3. For a detailed description of the 16 TT, please refer to Reference 2.

The NASA Langley 16 ft Transonic Wind Tunnel

High Speed Aerodynamics, Long Beach

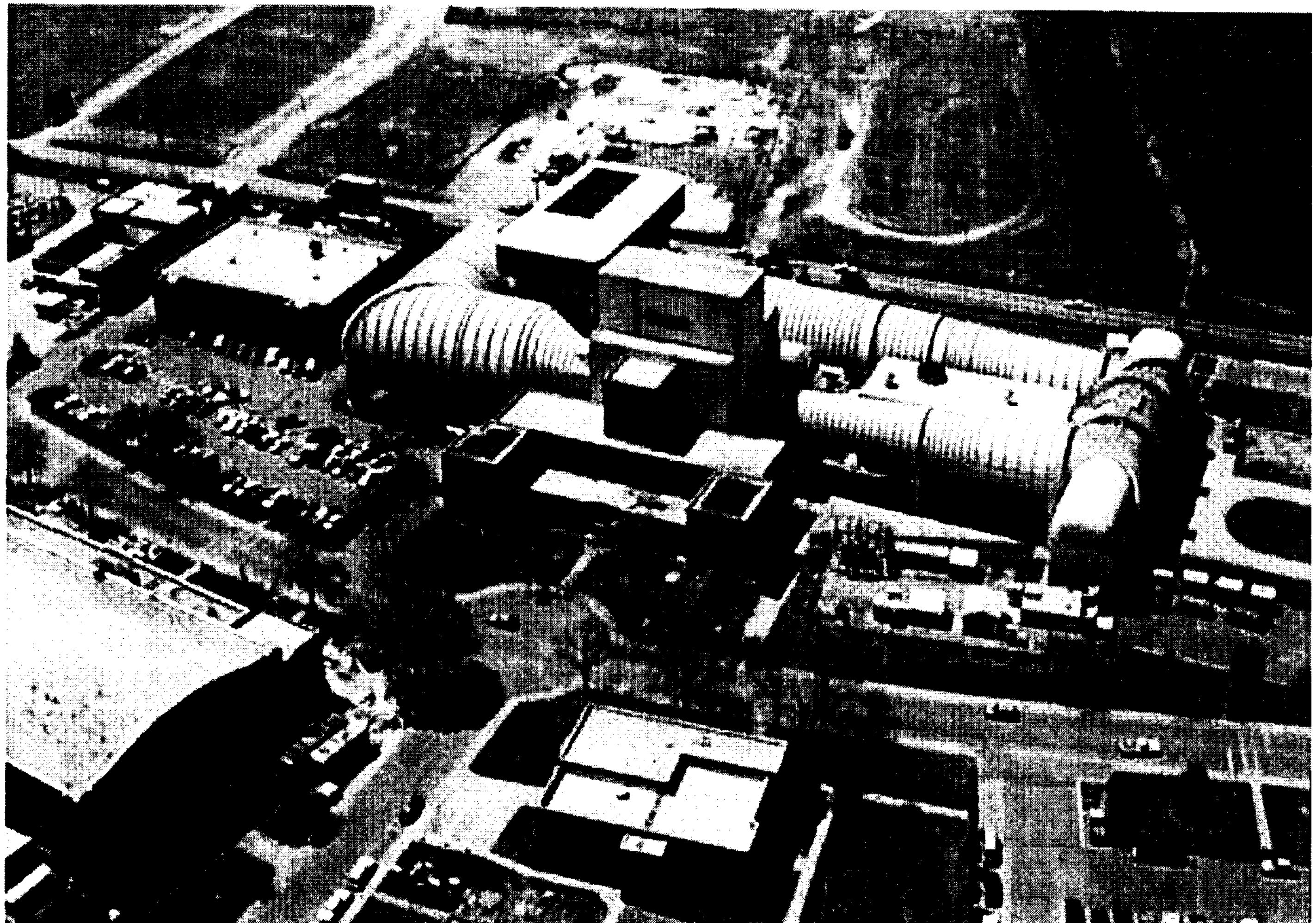

Aerial: The 16 foot Transonic Tunnel
NASA Langley Research Center 4/25/1986 Image # EL-1996-00039

BOEING

1.675% Model 5 with PTC Mid-mounted Canard Installed at 16TT

The photograph on the facing page shows the mid-mounted PTC canard configuration installed in the 16-foot Transonic Wind Tunnel.

1.675% Model 5 with PTC Mid-mounted Canard Installed at 16TT

High Speed Aerodynamics, Long Beach

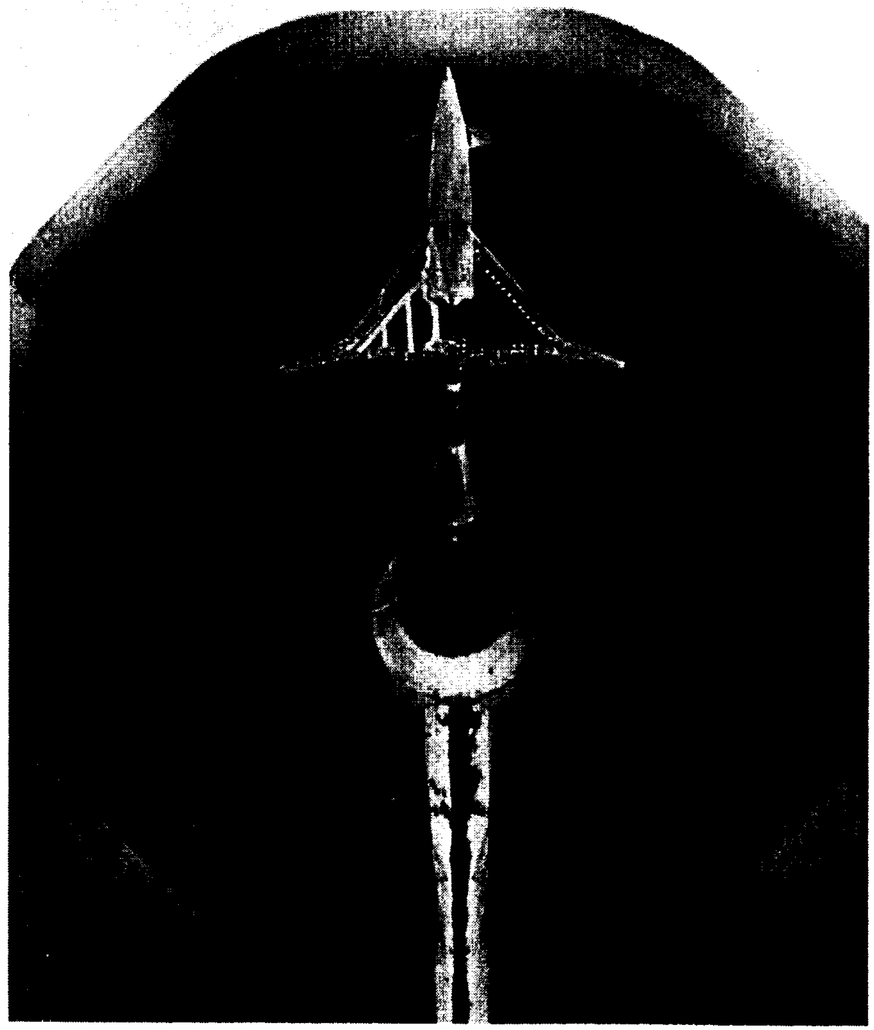

BOEING

Additional PTC Canard Parts were Fabricated for Test 508

The next two charts show the additional model parts that were fabricated for Test 508. In the first chart, the mid PTC canard was existing from Test 1705, but the high and low PTC canards were fabricated due to fitting problems discovered during Test 1705 when using the mid PTC canard in the high and low positions. The second chart shows the mounting hardware for the high and low PTC canard that was fabricated for Test 508.

Additional PTC Canard Parts were Fabricated for Test 508

High Speed Aerodynamics, Long Beach

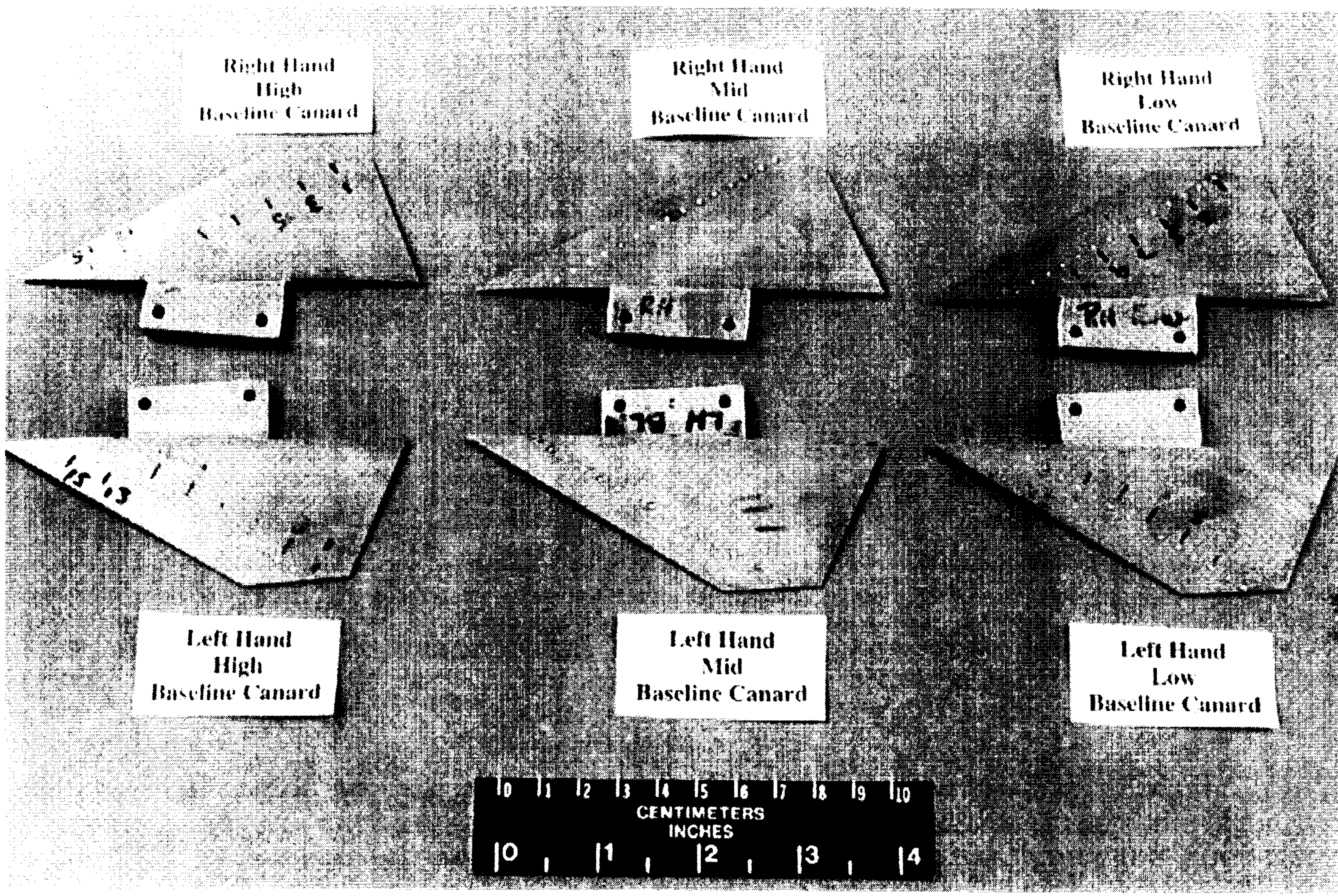

BOEING

Additional PTC Canard Parts were Fabricated for Test 508

High Speed Aerodynamics, Long Beach

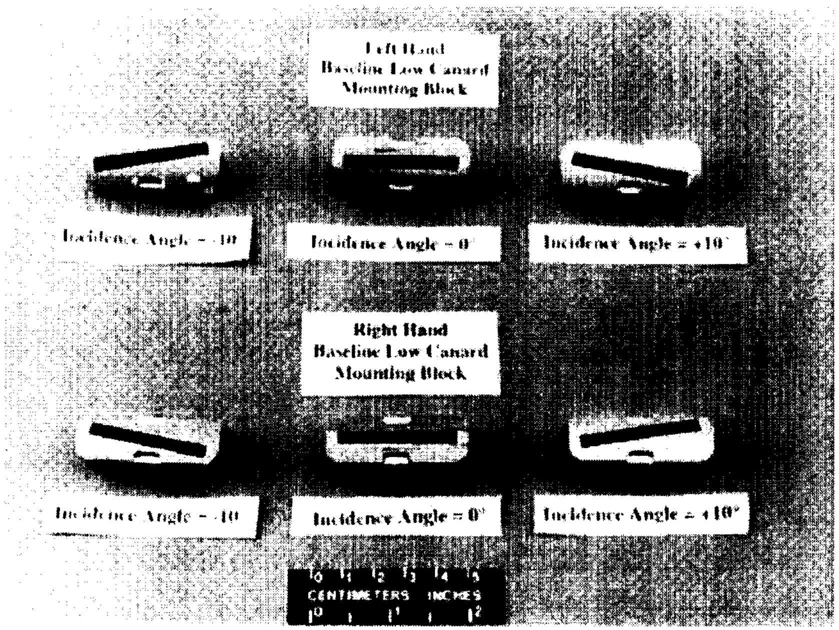

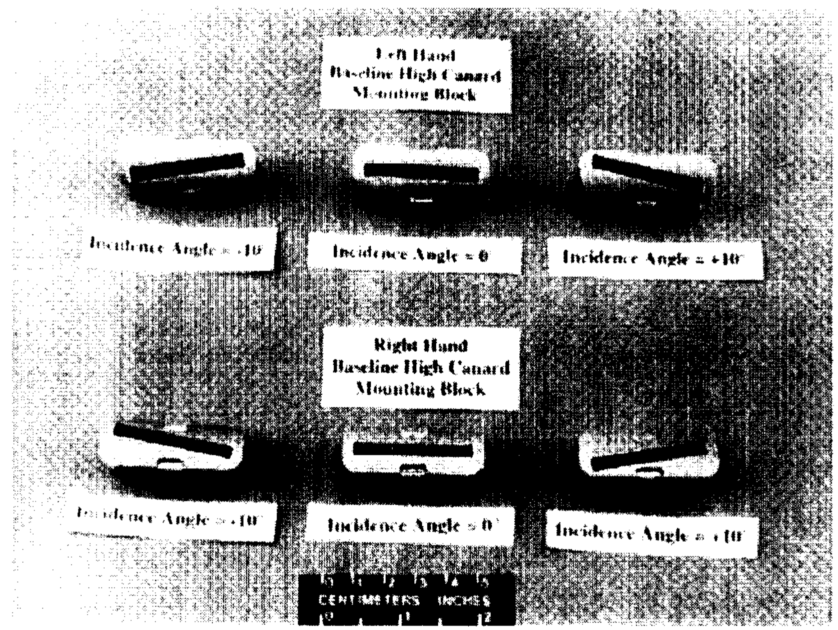

BOEING

Test Techniques Utilized During 16TT Test 508

The test techniques utilized for Test 508 are described in the following chart. The Ultra-Violet oil flow technique was not used due to time limitations during the test. The Shadow Graph technique was used during Test 508, but the results were not suitable for determining the shock structures at Mach 0.9 and 1.1 at the 16 TT.

Test Techniques Utilized During 16TT Test 508

High Speed Aerodynamics, Long Beach

- Force & Moment (6-component)
  - To validate CFD, obtain performance data and S&C data
- Ultra-Violet Oil Flow*
  - To determine the influence of the canard on the wing surface flow topology and for CFD validation
- Sublimation
  - To assess the state of the boundary layer on the wing and canard
- Shadow Graph Photographs
  - To assess the influence of canard induced shock systems

* Time limitations prevented obtaining this data

Instrumentation for 16TT Test 508

The instrumentation utilized for Test 508 is listed on the facing page. It is very similar to the instrumentation used for the Supersonic Canard Integration Test (Test 1705) at the UPWT.

Instrumentation for 16 TT Test 508

- Sting: UPWT 350-19C2 (max normal force ±1000 lbs)
- Balance: UT-52B

Balance Limits (Last Calibration - 8/3/98)

Normal Force	±1200 lbs
Axial Force	120 lbs
Pitching Moment	±2400 in-lbs
Rolling Moment	±800 in-lbs
Yawing Moment	±1200 in-lbs
Side Force	±600 lbs

- Pressure Instrumentation
  - 4 - 5psid Druck transducers (body chamber pressure)
  - 2 - 5 psid Druck transducers (nacelle base pressures)
- Temperature Instrumentation
  - 3 prt on UT-52B
- Angle-of-Attack Measurement
  - accelerometer on strut plus corrections for flow angularity and sting/bal bending

BOEING

Sublimation for Canard Upper Surface

The photograph on the facing page shows the sublimation image for the upper surface of the PTC canard at a Mach number of 0.9 and an angle-of-attack of 3.5°. There are some questions as to the validity of the method, since it took as long to get on point as it did for the length of time spent on condition. The time spent on condition was approximately a couple of minutes. From the image on the facing page, the flow appears to be fully turbulent after the trip dots. This can be seen by the characteristic turbulent wedge seen originating from the isolated trip dot.

Sublimation for the Canard Upper Surface

High Speed Aerodynamics, Long Beach

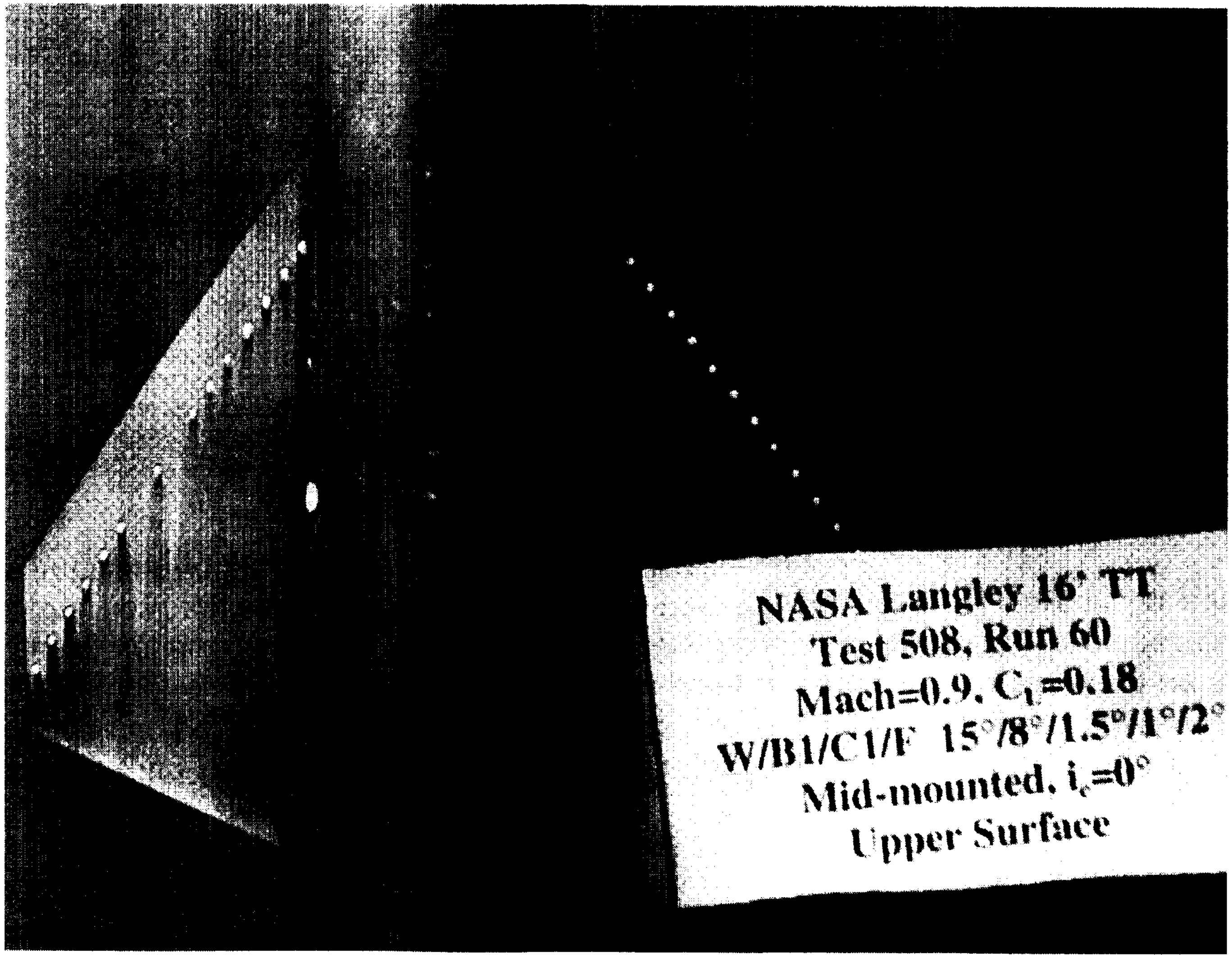

BOEING

16TT Test 508 Post-Test Analysis and Status

The next two charts list the status of the Test 508 post-test analysis and some initial conclusions. The final data has not been delivered as of the date of this presentation, because of a problem with the model leveling and up-flow angularity during the test. The data engineer was out sick with Meningitis during Test 508, resulting in the upflow corrections not being made during the test. The 16TT staff is currently working on putting these corrections into the data. The sublimation from the test indicates that the 0.006 inch trip dots were effective, but many questions remain as to the validity of the sublimation technique at the 16TT for Mach 0.9. The Shadowgraph system did not appear to work very well for determining the shock structures at Mach 0.9 and 1.1 at the 16TT. Finally, the test was plagued with trip dot problems during the test. Specifically, the inboard trip dots on the wing were constantly wearing down and needed to be replaced during this test entry. It is not known whether this was a result of the flow environment or the model changes during the test.

16TT Test 508 Post-Test Analysis and Status

High Speed Aerodynamics, Long Beach

- Final data not delivered yet because of problems with model leveling and upflow angularity during the test
- Sublimation results indicate 0.006" trip dots are effective, but many questions remain as to the validity of the sublimation test technique at the 16TT and transonic trip and transition in general
- Post-test analysis will begin after the workshop and shall be complete in two months
- Shadow graph not suitable for determining shock structures at Mach 0.9 and 1.1 at 16TT

BOEING

16TT Test 508 Post-Test Analysis and Status (Cont.)

- Majority of test conducted without a data engineer to make corrections to data
- Inboard trip dots on the wing consistently had to be replaced (similar problem noted in Test 496)

CFL3D Canard-On Directional Stability Characteristics

This final section will present a CFD study focused on the full configuration (wing/body/canard/empennage) directional stability characteristics. Currently, there is no high speed data available for the affect of canard integration on the directional stability characteristics of the full configuration. This CFD study was undertaken in hopes of a better understanding of the directional S&C of the full configuration.

CFL3D Canard-On Directional Stability Characteristics

BOEING

Objectives

The objectives of this study were to use the CFL3D Euler solver to determine if there are any adverse directional characteristics at transonic speeds when the forward mounted canard (Preliminary Technology Concept size and longitudinal position) is located in either the high or low radial position.

This study was a small subset of the originally planned study which intended to use the CFL3D Euler solver to map out the canard design space, with respect to the impact on lateral-directional stability characteristics, by varying the canard planform, canard location (both longitudinal and radial), canard dihedral/anhedral, canard deflection, angle-of-attack, sideslip angle, and Mach number. This larger study was envisioned to be complementary to the concurrent Boeing-Seattle study which was focused on using CFD to obtain isolated canard aerodynamic characteristics and the investigation of historical HSCT canard wind-tunnel data. By combining the results of both the Long Beach and Seattle studies, it was hoped that the aerodynamic characteristics of canards and their influence on the rest of the airplane configuration could be better understood and the results provided to TI to help define the Technology Configuration.

OBJECTIVES

- Using CFL3D (Euler), investigate the effect of canard placement on the high-speed directional stability characteristics of a HSCT full configuration (W/B/E).

- Combine results with Boeing-Seattle (Dynacs) canard study, and previous canard experimental database (Reference H modular controls model, TCA canard integration model) to understand canard influence on the overall aircraft characteristics to support the Technology Configuration airplane downselect.

TCA: Directional Stability Derivative Variation with Angle-of-Attack

This figure shows the variation of the directional stability derivative (yawing moment due to sideslip) with angle-of-attack for the Technology Configuration Airplane (TCA) with both the vertical tail-on and vertical tail-off at Mach=0.90. This figure shows that the tail-on directional stability is stable and fairly constant with angle-of-attack up to approximately 7 degrees alpha, beyond which the directional stability begins to diminish rapidly. When a canard is added to the configuration, it will have some effect on the directional stability variation with angle-of-attack as illustrated in the next figure.

TCA: Directional Stability Derivative Variation with Angle-of-Attack

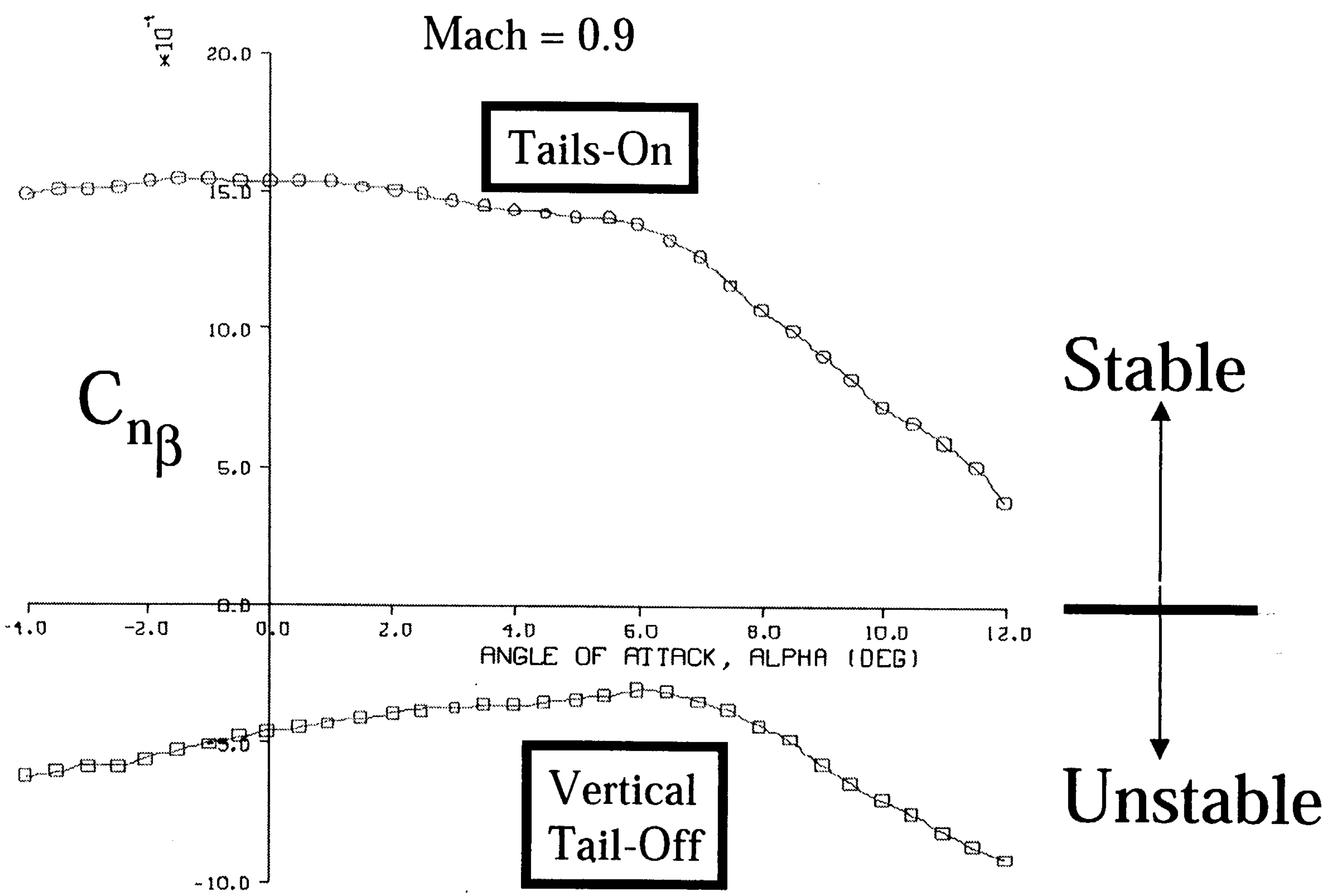

Background-1

This figure illustrates the effect of canard tip waterline location on the angle-of-attack at which tail-on directional stability becomes negative (unstable) for a representative HSCT configuration at low speeds. The figure demonstrates the adverse impact on directional stability when the canard waterline is moved from a low-mount configuration (waterline 180) to a high-mount configuration (waterline 300). Although the experimental data shown is at low speeds, a similar trend is expected at transonic and supersonic speeds. The focus of the study, discussed in this paper, is on verifying whether this trend is present at transonic speeds. If the trend is observed, then the contributing factors causing the trend will be investigated.

BACKGROUND-1

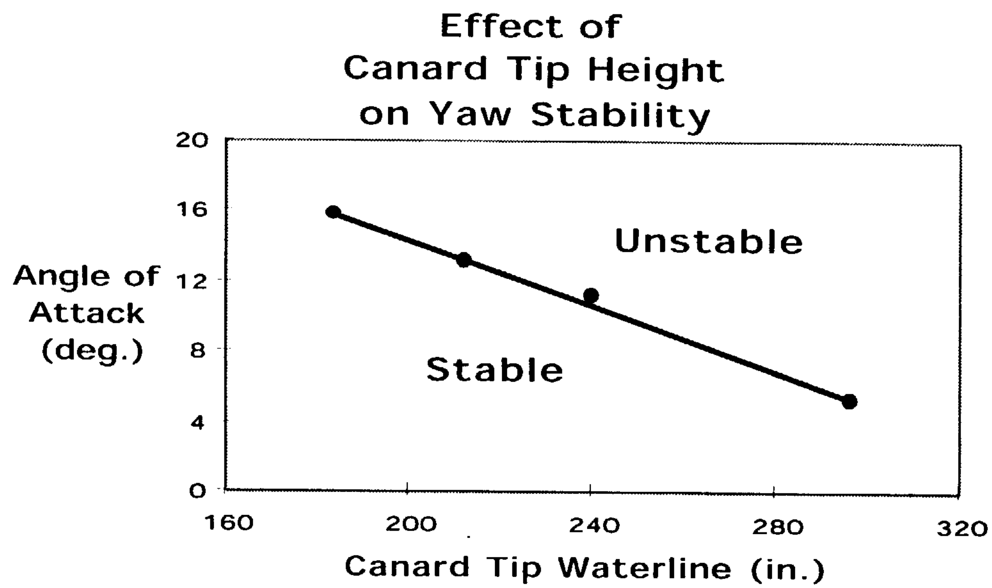

Low-speed wind tunnel data indicates a strong correlation between canard tip height and the angle-of-attack at which a representative HSCT configuration becomes directionally unstable

Approach-1

The next two slides outline the approach taken for this study. Using the overset grid topology method to model the canard and forebody, grids could be generated rapidly for various canard locations and deflections. The CFL3D Euler flow solver was selected for this study because of it's recent success in rapidly evaluating canard placement aerodynamic effects for the canard integration wind-tunnel test.

The originally proposed study focusing on canard vertical location, canard deflection, angle-of-attack, sideslip angle, and Mach number would take over 360 CFD runs. Because this was not feasible, a much smaller subset which focused on a high-mount and low-mount PTC sized canard and longitudinal location was selected. The high-mount canard was configured with 15 degrees of dihedral while the low mount canard was configured with 20 degrees of anhedral. The amount of canard deflection at either radial location was limited by the CFL3D constraint that the canard grid cannot go beyond the crown line of the fuselage grid. For the hig- mount configuration the maximum deflection was +4 degrees; and for the low-mount configuration, the maximum deflection was -8 degrees. A +4 degrees deflected low-mount canard was also modeled in order to have a similar deflection with the high-mount canard. Additionally, a canard-off configuration was modeled in order to determine the incremental canard effects. These canard deflected and canard-off configurations were run at Mach=0.9 and angles-of-attack of 1, 3.5, and 5 degrees. In order to determine the directional stability effects of the canard, solutions at a sideslip angle of 3 degrees were also run at the aforementioned angles-of-attack. This combination of configurations, angles-of-attack, and sideslip angles resulted in 16 CFD solutions.

APPROACH-1

- Use overset grid topology for rapid canard grid generation and CFL3D (Euler) for rapid solution turnaround to compute the directional stability of the TCA full configuration (W/B/E)
- Obtain solutions at various combinations of canard locations, canard deflection angles, angles-of-attack, sideslip angles and Mach numbers.

APPROACH-2

- Proposed CFL3D study: (>360 runs)

$$\begin{Bmatrix} High \\ Med \\ Low \end{Bmatrix}_{canard\_vert\_position} \begin{Bmatrix} +10 \\ 0 \\ -10 \end{Bmatrix}_{\delta canard} \begin{Bmatrix} Canard-off \\ Tail-on\_\delta=0 \\ Tail-off \end{Bmatrix} \begin{Bmatrix} -4 \\ 0 \\ 4 \\ 8 \\ 12 \end{Bmatrix}_{\alpha} \begin{Bmatrix} 0 \\ +3 \end{Bmatrix}_{\beta} \begin{Bmatrix} 0.9 \\ 2.4 \end{Bmatrix}_{Mach}$$

- CFL3D study completed: (16 runs)

$$\begin{Bmatrix} High \\ \\ Low \end{Bmatrix}_{canard\_vert\_position} \begin{Bmatrix} +4 \\ \\ +4,-8 \end{Bmatrix}^{*}_{\delta canard} \begin{Bmatrix} Canard-off \\ Tail-on\_\delta=0 \\ \end{Bmatrix} \begin{Bmatrix} +1 \\ +3.5 \\ +5 \end{Bmatrix}_{\alpha} \begin{Bmatrix} 0 \\ +3 \end{Bmatrix}_{\beta} \begin{Bmatrix} 0.9 \end{Bmatrix}_{Mach}$$

* Maximum canard deflection was limited by overset grid limitations

CFL3D (Euler) Results

This slide provides an outline of the CFL3D results that will be shown in the remainder of this paper. The yawing moment coefficient variation with angle-of-attack will be presented for the canard-off, high-mount canard (deflected +4 degrees), and the low-mount canard (deflected +4 and -8 degrees) configurations. Side-by-side comparisons will be presented showing the particle trace trajectories, at an angle-of-attack of 3.5 degrees, for the high-mount vs. the low-mount canard canards deflected +4 degrees and the low-mount canard deflected +4 degrees vs. the low-mount canard deflected -8 degrees. Additionally, side-by-side pressure contours showing the the incremental pressure between the aforementioned canard deflected configurations and a canard-off configuration at an angle-of-attack of 3.5 degrees will be shown.

CFL3D (EULER) RESULTS

- Computed Force and Moment Data
  - Yawing Moment Coefficient vs. α
    - Canard-off
    - High-mount canard-on ($\delta_c = +4^o$)
    - Low-mount canard-on ($\delta_c = +4^o, -8^o$)
- Particle Trace Visualization at $\alpha = 3.5^o$
  - High-mount ($\delta_c = +4^o$) vs. low-mount ($\delta_c = +4^o$)
  - Low-mount ($\delta_c = +4^o$) vs. low-mount ($\delta_c = -8^o$)
- Pressure Contours at $\alpha = 3.5^o$
  - ΔCp = (Canard-on) - (Canard-off)

Yawing Moment Coefficient vs. Angle-of-Attack

This slide shows the CFL3D (Euler) predicted variation of yawing moment coefficient with angle-of-attack for the canard-off, high-mount canard (deflected +4 degrees), and low-mount canard (deflected +4 and -8 degrees) configurations at an angle-of-sideslip of +3 degrees and Mach =0.90. All canard-on and canard-off configurations were modeled with the vertical tail-on and the nacelles-off. The nacelles were removed from the configuration in order to reduce the number of solution iterations required for convergence. Directional stability is determined by dividing the yawing moment coefficient at any angle-of-attack by the sideslip angle of 3 degrees.

The data show that the variation of directional stability with angle-of-attack is affected by both canard vertical location and deflection. For the low-mount canard at either deflection, directional stability is shown to increase with increasing angle-of-attack. For the high-mount canard, directional stability is shown to decrease with increasing angle-of-attack. While the variation of directional stability with angle-of-attack does not appear to be affected by canard deflection, the overall level of directional stability appears to be significantly affected. The canard-off directional stability variation with angle-of-attack is relatively constant with a small bias towards increasing with increased angle-of-attack.

Yawing Moment Coefficient vs. Angle of Attack

High Speed Aerodynamics, Long Beach

TCA W/B/C/E Configuration with PTC Canard, $\beta = 3°$

CFL3D Euler, M_∞=0.9

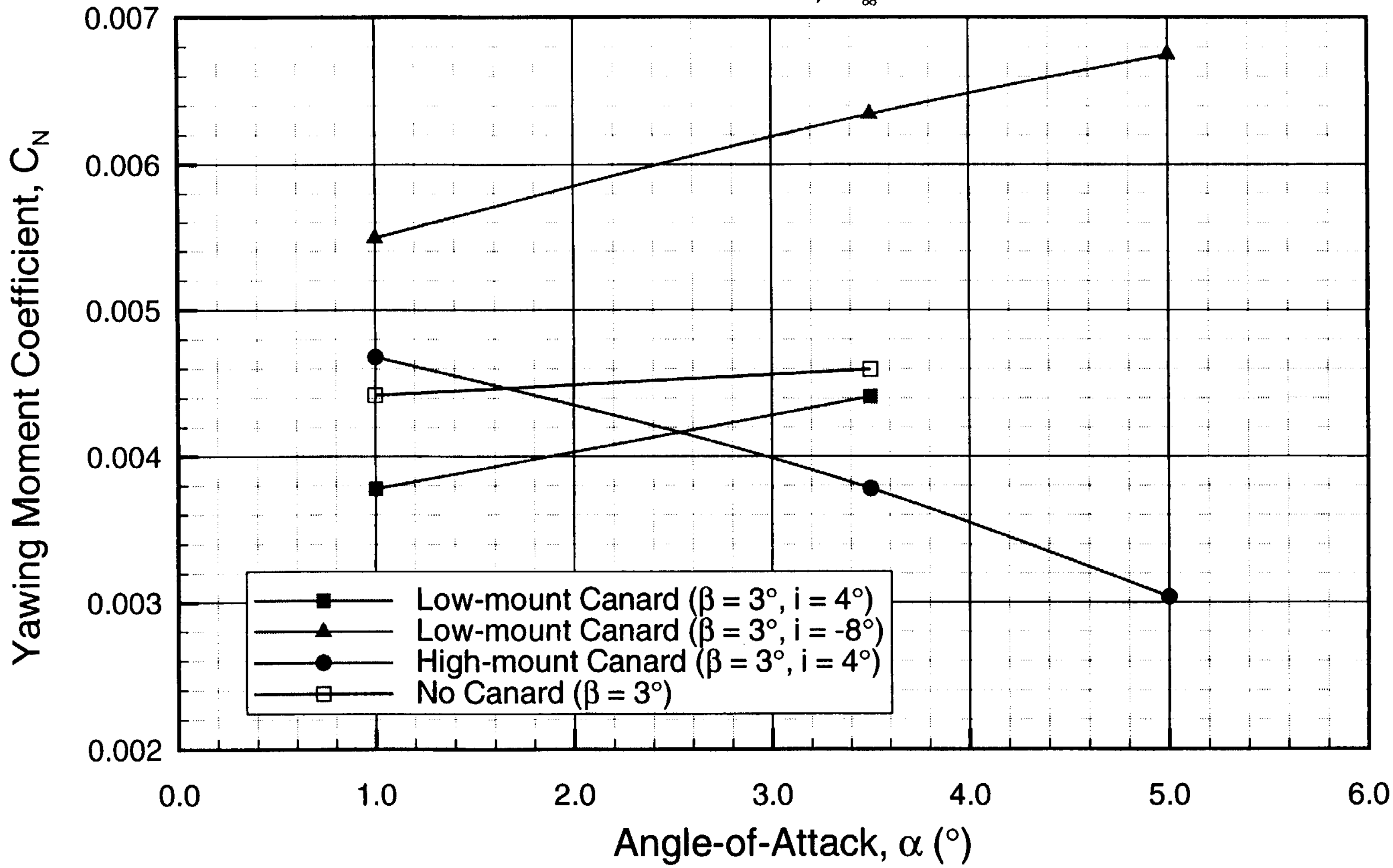

BOEING

Reference H: Directional Stability Derivative Variation with Angle-of-Attack

This slide shows the variation of the directional stability derivative with angle-of-attack for the Reference H configuration with two different undeflected mid-mount canard (dihedral =0 degrees) and canard-off configurations at Mach 0.90. The data was obtained for the Reference H configuration at the 16'TT wind-tunnel using the alternate controls model and is the only full-configuration, canard-on experimental data available. The CFL3D results shown on the previous slide show similar trends as the experimental data in this figure. Specifically, the variation of directional stability with angle-of-attack for the canard-off configuration is relatively constant over the range of angles-of-attack evaluated using CFL3D, and the affect of the canard is a significant change to the variation of directional stability with angle-of-attack. Although the canards tested were mid-mount with 0 degrees of dihedral, their affect on directional stability is similar to the low-mount canard results observed in the previous slide.

Reference H: Directional Stability Derivative Variation with Angle-of-Attack

Mach = 0.9

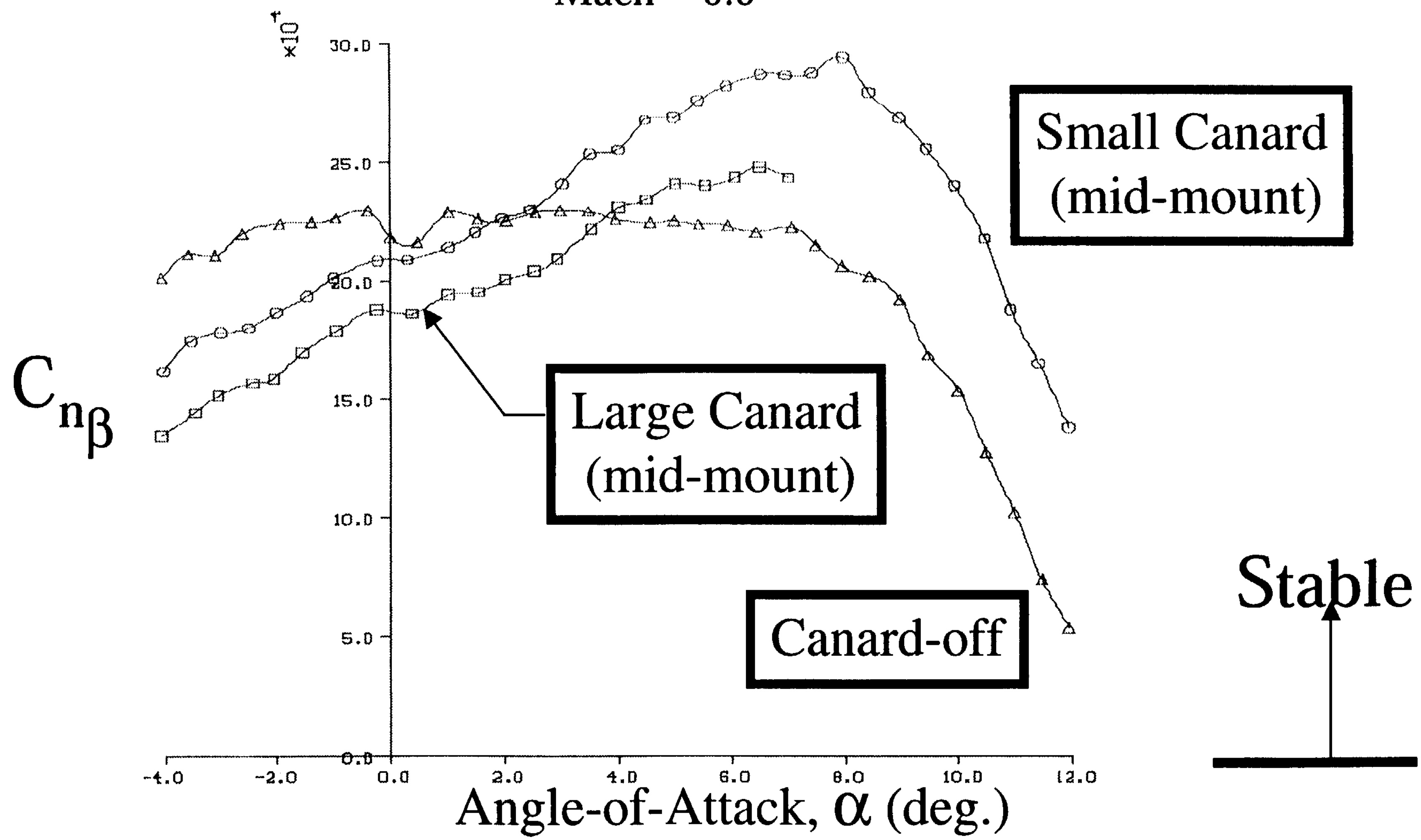

Particle Traces over the TCA W/B/E with PTC Canard (Top View)

The following three slides show the top, front, and side view comparisons of the canard wing-tip vortex trajectories between the high-mount canard with +4 degrees of deflection and the low-mount canard with +4 degrees of deflection at an angle-of attack of +3.5 degrees and sideslip angle of +3 degrees.

The windward (right-hand) canard-tip vortex for both the high and low-mount canard is shown to remain on the windward side of the aircraft downstream to the empenage. However, for the low mount-canard, the canard-tip vortex interacts with the leading-edge of the wing and remains relatively low on the fuselage passing near the horizontal tail . For the high-mount canard, the windward canard-tip vortex is shown to remain high enough to not interfere with either the wing or the fuselage until it approaches near the empenage, at which point it has significant interaction with the fuselage and vertical tail. The effect of this canard-tip vortex interaction on yawing moment will be discussed in the next set of slides.

The leeward (left-hand) canard-tip vortex for both the high and low-mount canard is shown to move outboard and does not have much interaction with the fuselage or empenage; although the low-mount canard-tip vortex has significant interaction with the wing leading-edge.

Particle Traces over the TCA W/B/E with PTC Canard

High Speed Aerodynamics, Long Beach

CFL3D Euler, $M_{\infty} = 0.9$, $\alpha = 3.5°$, $\beta = 3.0°$

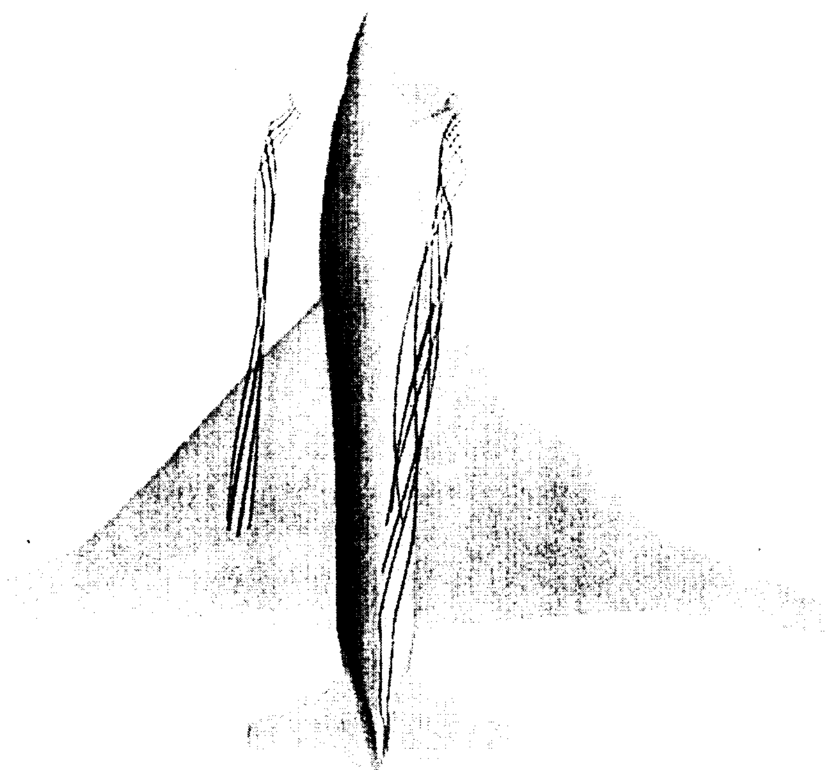

high–mount canard (i = 4°)

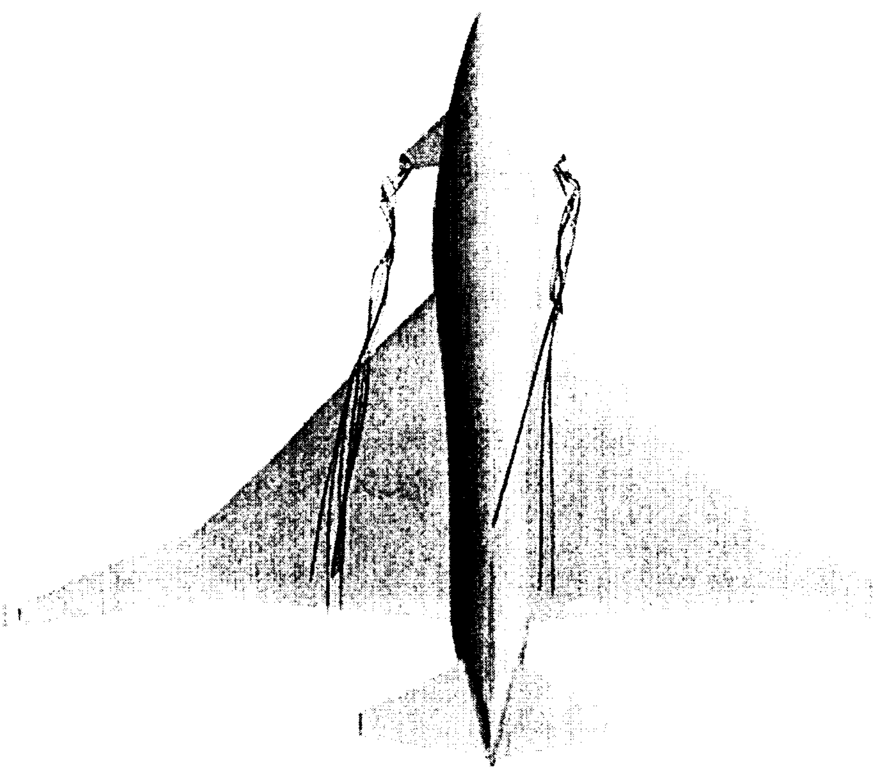

low–mount canard (i = 4°)

BOEING

Particle Traces over the TCA W/B/E with PTC Canard

High Speed Aerodynamics, Long Beach

CFL3D Euler, $M_\infty = 0.9$, $\alpha = 3.5^\circ$, $\beta = 3.0^\circ$

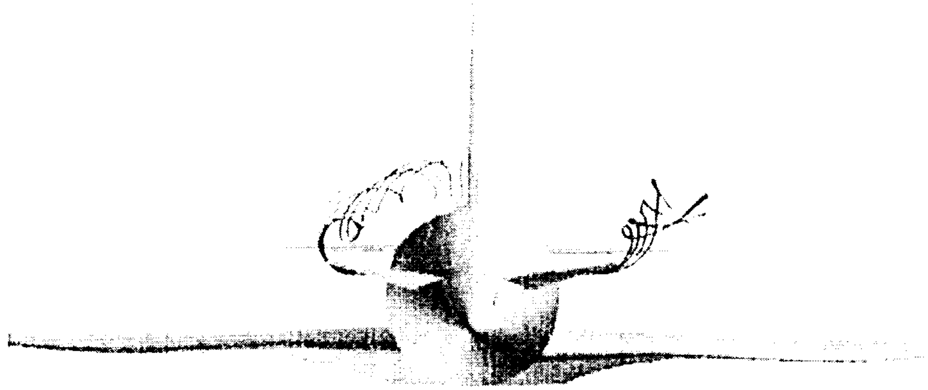

high–mount canard ($i = 4^\circ$)

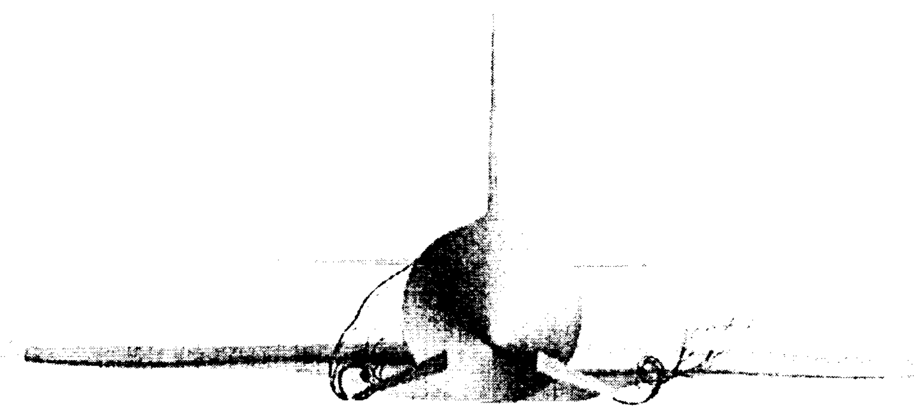

low–mount canard ($i = 4^\circ$)

BOEING

Particle Traces over the TCA W/B/E with PTC Canard (Side View)

High Speed Aerodynamics, Long Beach

CFL3D Euler, $M_\infty = 0.9$, $\alpha = 3.5°$, $\beta = 3.0°$

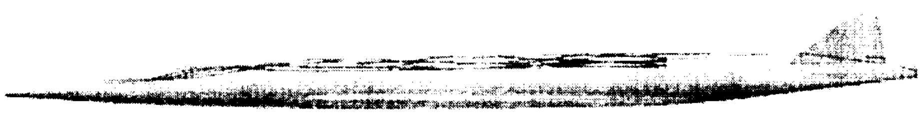

high–mount canard (i = 4°)

low–mount canard (i = 4°)

ΔC_p on the TCA W/B/E with PTC Canard

The following three slides show incremental pressure data as contours, solid surface (positive pressures), and solid surface (negative pressures), respectively, for the high-mount canard with +4 degrees of deflection and the low-mount canard with +4 degrees of deflection at an angle-of attack of +3.5 degrees and sideslip angle of +3 degrees. The incremental pressure data was obtained by subtracting the canard-off solution from the canard-on solutions. The solid surface incremental pressure plots were separated into positive and negative pressure ranges to help identify the magnitude of the subtle incremental pressures observed.

It is clear from the incremental pressure data that the windward high-mount canard-tip vortex has a significant effect on the aft fuselage and vertical tail while the windward and leeward low mount canard-tip vortices have a significant effect on the wing leading-edge. The result of the interaction of the windward high-mount canard-tip vortex is a reduction in the pressure (increased suction) on the right-hand side of the airplane and an increase in the pressure (reduced suction) on the left-hand side of the airplane. Both of these effects cause a reduction in the total yawing moment of the configuration. As angle-of-attack increases, the high-mount canard-tip vortex effects a larger section of the vertical tail and therefore reduces the overall yawing moment even further. This would explain the reduction in directional stability with angle-of-attack observed for the high-mount canard.

The interaction of the low-mount canard-tip vortices with the wing leading-edges does not appear to cause a significant change in the total yawing moment level at this angle-of-attack as the yawing moment of the canard-off and canard-on configurations are almost the same.

ΔC_p on the TCA W/B/E with PTC Canard

CFL3D Euler, $M_\infty = 0.9$, $\alpha = 3.5°$, $\beta = 3.0°$

$\Delta C_p = C_{p\ \text{canard on}} - C_{p\ \text{canard off}}$

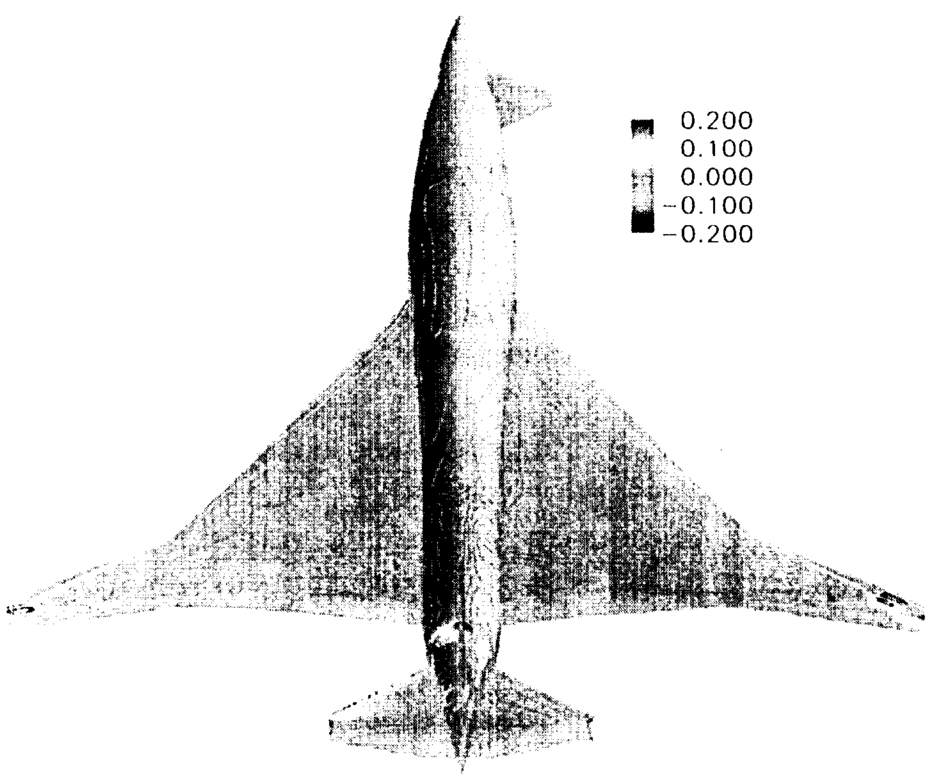

high–mount canard (i = 4°)

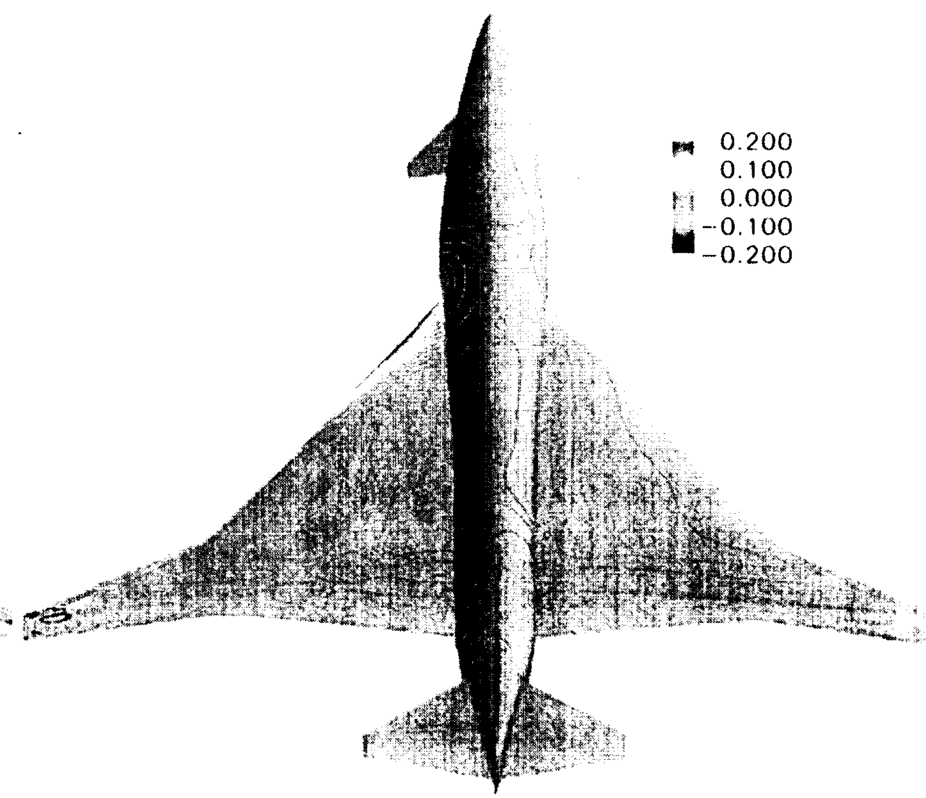

low–mount canard (i = 4°)

BOEING

ΔC_p on the TCA W/B/E with PTC Canard (positive values)

High Speed Aerodynamics, Long Beach

CFL3D Euler, $M_\infty = 0.9$, $\alpha = 3.5°$, $\beta = 3.0°$

$\Delta C_p = C_{p\ \text{canard on}} - C_{p\ \text{canard off}}$

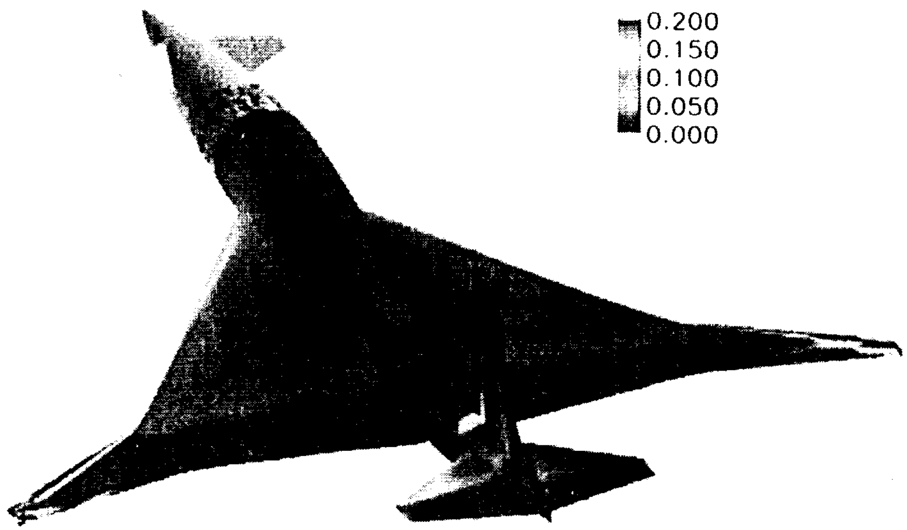

high–mount canard (i = 4°)

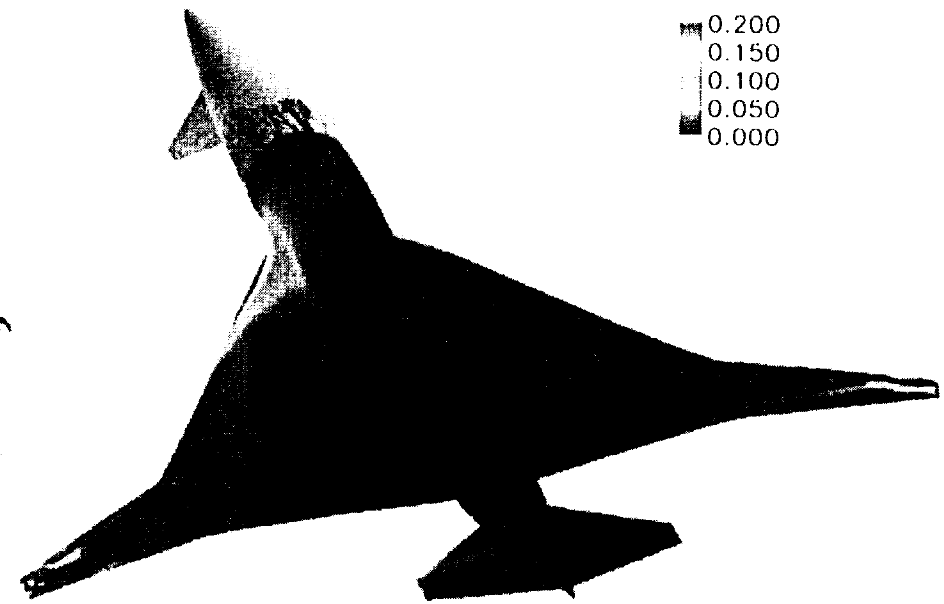

low–mount canard (i = 4°)

BOEING

ΔC_p on the TCA W/B/E with PTC Canard (negative values)

High Speed Aerodynamics, Long Beach

CFL3D Euler, $M_\infty = 0.9$, $\alpha = 3.5°$, $\beta = 3.0°$

$$\Delta C_p = C_{p\ \text{canard on}} - C_{p\ \text{canard off}}$$

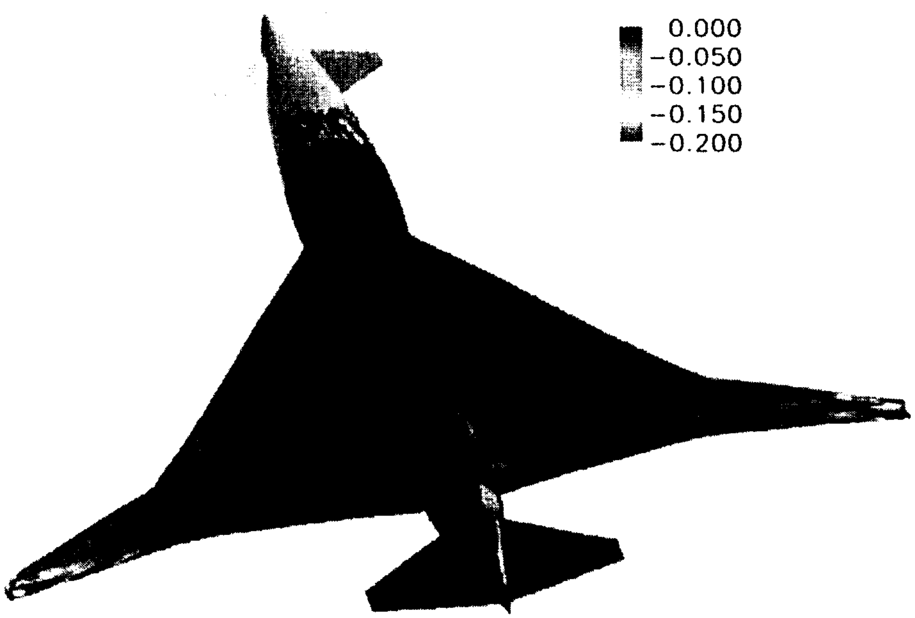

high–mount canard (i = 4°)

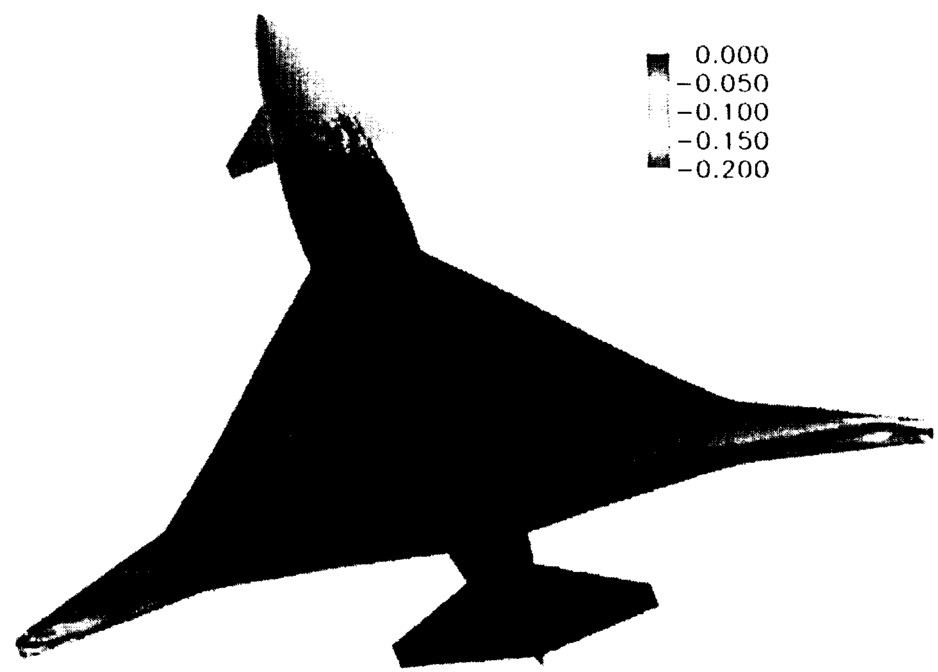

low–mount canard (i = 4°)

BOEING

Particle Traces over the TCA W/B/E with PTC Canard (Top View)

The following three slides show the top, front, and side view comparisons of the canard wing-tip vortex trajectories between the low-mount canard with +4 degrees of deflection and the low-mount canard with -8 degrees of deflection at an angle-of attack of +3.5 degrees and sideslip angle of +3 degrees.

These figures indicate that for the low-mount canard deflected -8 degrees, the canard-tip vortex from the windward canard (right-hand) wraps around the fuselage and passes on the left-hand side of the fuselage below the vertical tail, while the vortex from the leeward canard-tip (left-hand) gets entrained by the wing circulation and is forced to go straight back to affect the outboard tip of the horizontal tail. As discussed previously for the low-mount canard deflected +4 degrees, the canard-tip vortices from both the windward and leeward canards appear to have a significant interaction with the wing leading edge and little interaction with either the aft fuselage or empennage.

Particle Traces over the TCA W/B/E with PTC Canard

High Speed Aerodynamics, Long Beach

CFL3D Euler, $M_{\infty} = 0.9$, $\alpha = 3.5°$, $\beta = 3.0°$

low–mount canard (i = 4°)

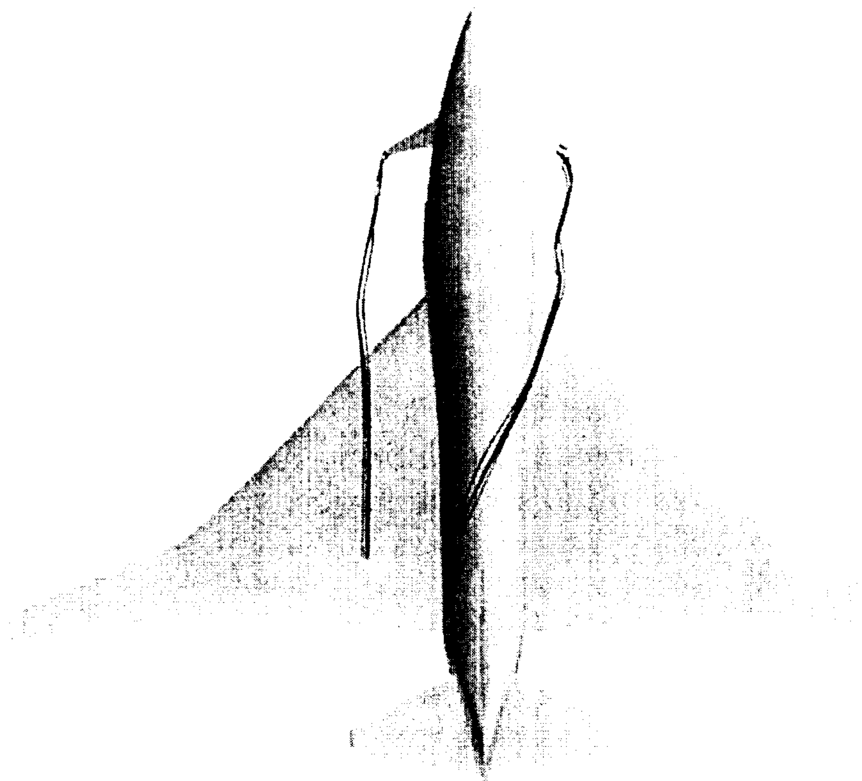

low–mount canard (i = –8°)

BOEING

Particle Traces over the TCA W/B/E with PTC Canard

High Speed Aerodynamics, Long Beach

CFL3D Euler, $M_{\infty} = 0.9$, $\alpha = 3.5°$, $\beta = 3.0°$

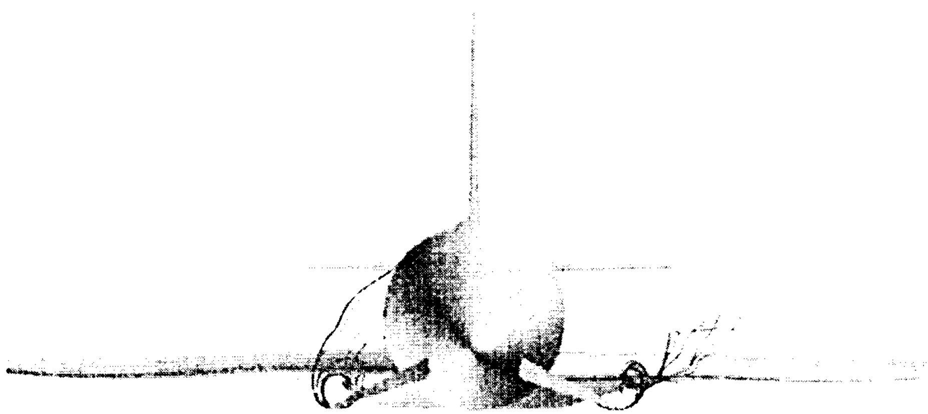

low–mount canard (i = 4°)

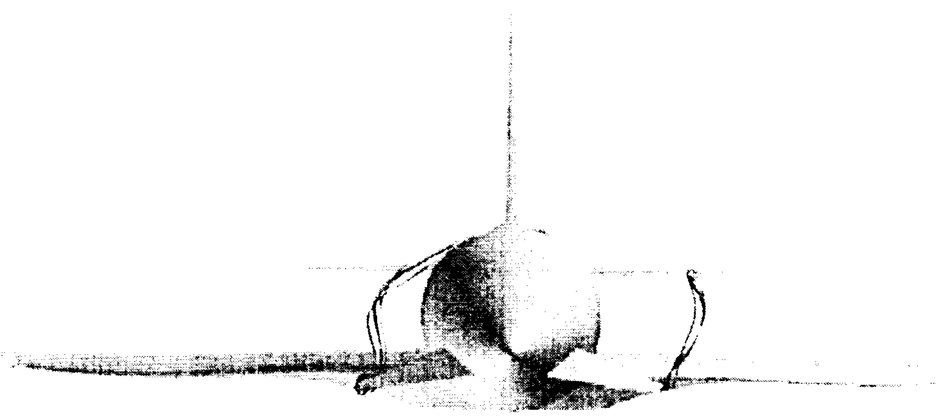

low–mount canard (i = –8°)

BOEING

Particle Traces over the TCA W/B/E with PTC Canard (Side View)

High Speed Aerodynamics, Long Beach

CFL3D Euler, $M_\infty = 0.9$, $\alpha = 3.5°$, $\beta = 3.0°$

low–mount canard (i = 4°)

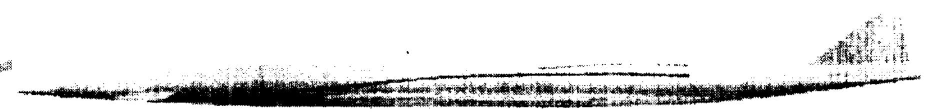

low–mount canard (i = –8°)

BOEING

ΔC_p on the TCA W/B/E with PTC Canard

The following three slides show incremental pressure data as contours, solid surface (positive pressures), and solid surface (negative pressures), respectively, for the low-mount canard with +4 degrees of deflection and the low-mount canard with -8 degrees of deflection at an angle-of attack of +3.5 degrees and sideslip angle of +3 degrees. The incremental pressure data was obtained by subtracting the canard-off solution from the canard-on solutions. The solid surface incremental pressure plots were separated into positive and negative pressure ranges to help identify the magnitude of the subtle incremental pressures observed.

The incremental pressure data shows that the windward canard-tip vortex, for the -8 degree deflection case, results in a reduction of the pressure (increased suction) over that part of the fuselage that it wraps around. Because the reduced pressure appears to be over the aft, left-hand side of the airplane, an increase in the total yawing moment of the configuration is expected. This was shown to be the case earlier in the yawing moment variation with angle-of-attack figure.

The interaction of the canard-tip vortices with the wing leading-edges for the +4 degrees deflected canard configuration does not appear to cause a significant change in the total yawing moment level at this angle-of-attack as the yawing moment of the canard-off and canard-on configurations are almost the same.

ΔC_p on the TCA W/B/E with PTC Canard

High Speed Aerodynamics, Long Beach

CFL3D Euler, $M_\infty = 0.9$, $\alpha = 3.5°$, $\beta = 3.0°$

$\Delta C_p = C_{p\ \text{canard on}} - C_{p\ \text{canard off}}$

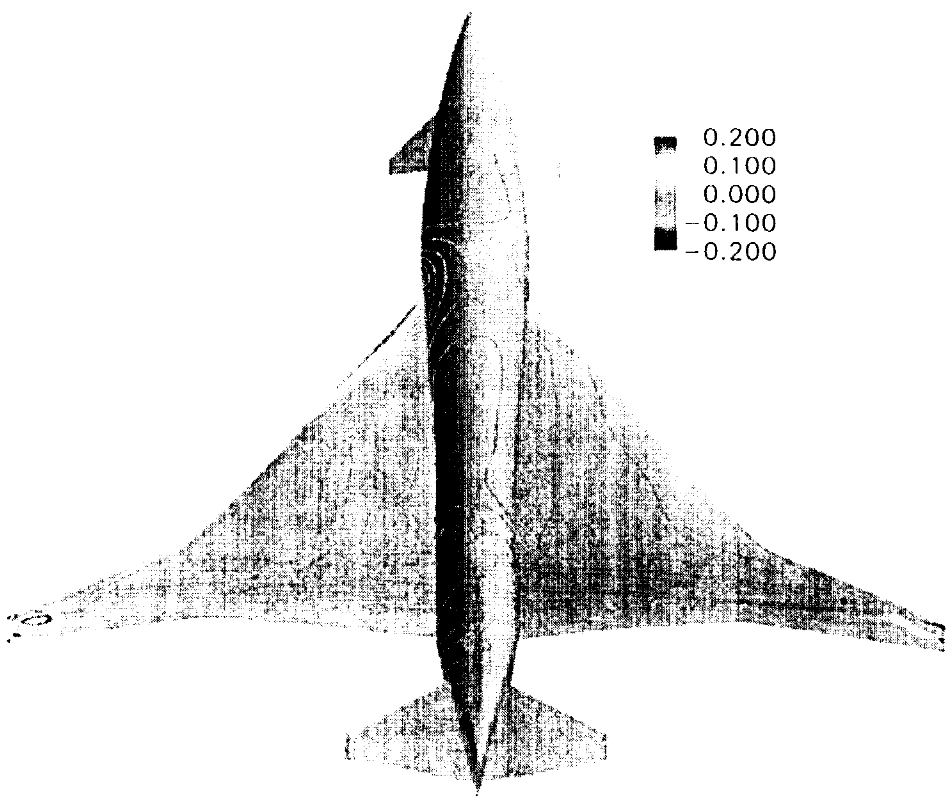

low–mount canard (i = 4°)

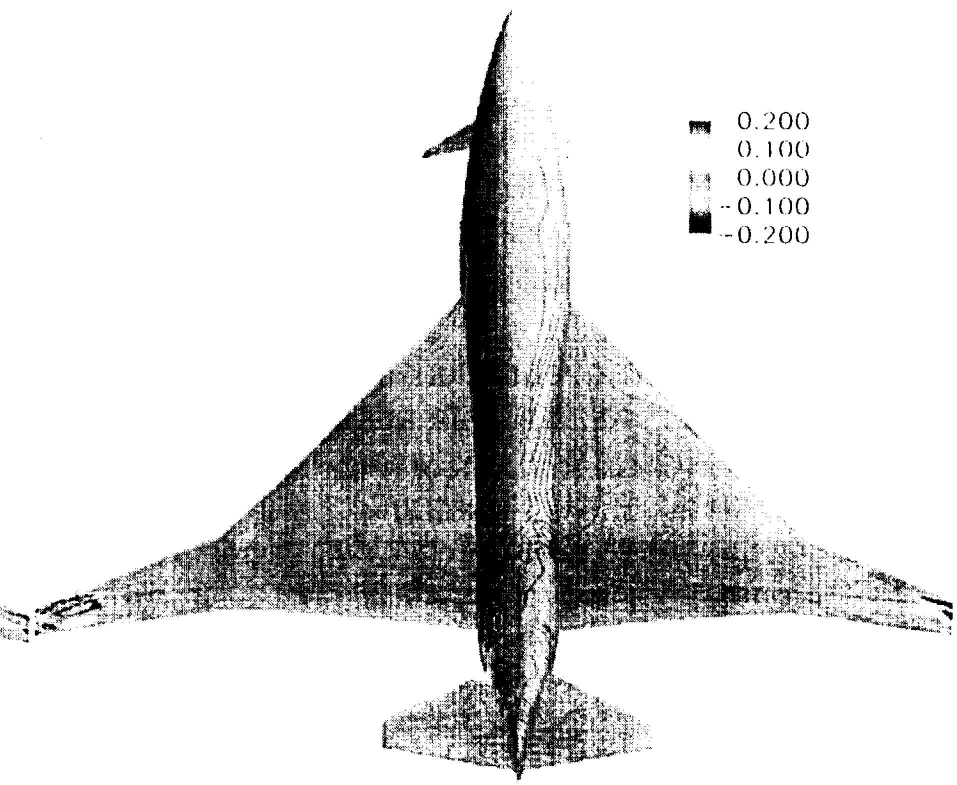

low–mount canard (i = −8°)

BOEING

ΔC_p on the TCA W/B/E with PTC Canard (positive values)

High Speed Aerodynamics, Long Beach

CFL3D Euler, $M_\infty = 0.9$, $\alpha = 3.5°$, $\beta = 3.0°$

$\Delta C_p = C_{p\ \text{canard on}} - C_{p\ \text{canard off}}$

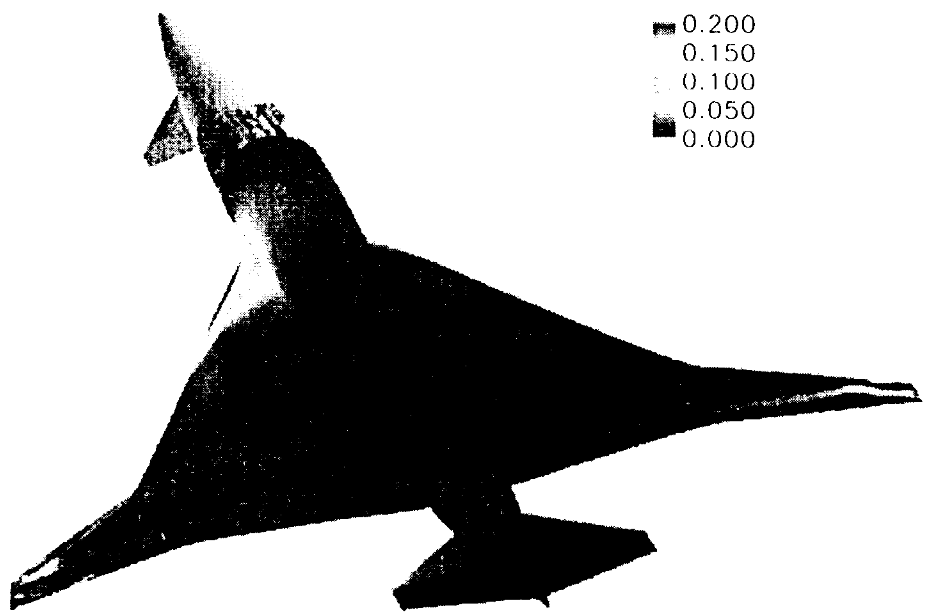

low–mount canard (i = 4°)

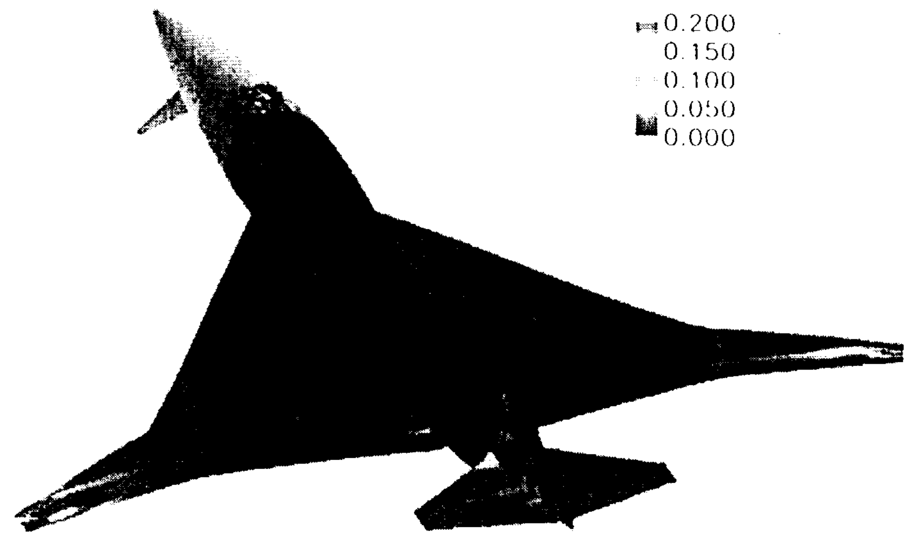

low–mount canard (i = –8°)

BOEING

ΔC_p on the TCA W/B/E with PTC Canard (negative values)

High Speed Aerodynamics, Long Beach

CFL3D Euler, $M_\infty = 0.9$, $\alpha = 3.5°$, $\beta = 3.0°$

$\Delta C_p = C_{p\ \text{canard on}} - C_{p\ \text{canard off}}$

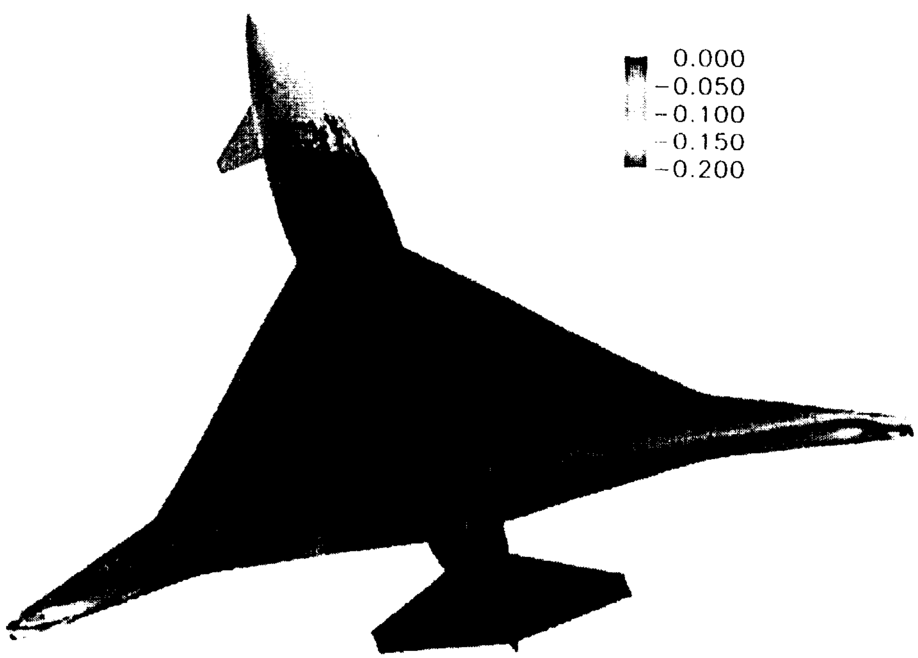

low–mount canard (i = 4°)

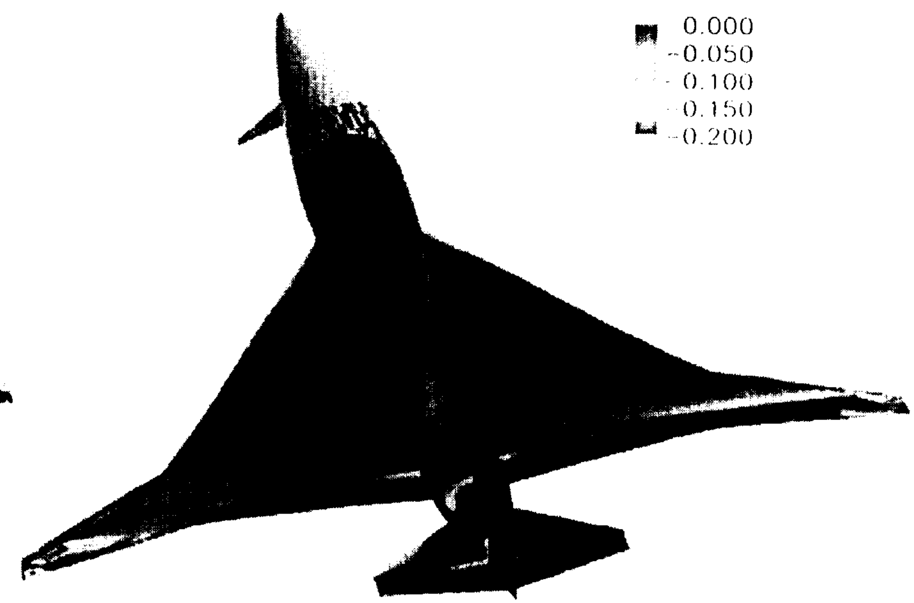

low–mount canard (i = –8°)

BOEING

Summary of CFL3D Study Results

In summary, directional stability was shown to be affected by both canard radial location and canard deflection. The high-mount canard was shown to adversely affect the variation of directional stability with angle-of-attack, reducing the total yawing moment at a +3 degree sideslip angle. Conversely, the low-mount canard was shown to favorably affect the variation of directional stability with angle-of-attack, increasing the total yawing moment at a +3 degree sideslip angle. Canard deflection, for the low mount configuration, was shown to have a significant effect on the level of directional stability, but not the variation with angle-of-attack. The interaction of the windward canard-tip vortex with the aft fuselage and empenage was shown to be the main cause of the different effects observed.

SUMMARY of CFL3D STUDY RESULTS

- Canard vertical position affects the directional stability variation with α
  - High-mount: decreasing directional stability
  - Low-mount: increasing directional stability
- Canard deflection affects the directional stability level but not the variation with α
- Canard-on directional stability characteristics are significantly influenced by the interaction of the canard vortex with the aft fuselage/empennage

Future Work (Now until September 1999)

There are three tasks remaining for the canard integration work under HSR. First, the Supersonic Canard Integration Wind Tunnel test post-test report needs to be completed. Second, the Transonic Canard Integration Wind Tunnel test data needs to be delivered and the post-test report needs to be written. Finally, patched Navier-Stokes solutions are required for the ACC canard configuration at an $i_c=4°$ so that this anomalous high speed data at $M_\infty=2.4$ can be investigated.

Future Work (Now until Sept. 1999)

- Finish UPWT Test 1705 Post-test Report
- Begin and Complete 16 TT Test 508 Post-test Report
- Run CFL3D for the ACC canard configuration at an i_c=4°

References

1. Jackson, Charlie M.; Corlett, William A.; Monta, William J.: "Description and Calibration of the Langley Unitary Plan Wind Tunnel," NASA TP-1905, 1981.

2. Capone, Francis J.; Bangert, Linda S.; Asbury, Scott C.; Mills, Charles T. L.; Bare, E. Ann; "The NASA Langley 16-foot Transonic Tunnel - Historical Overview, Facility Description, Calibration, Flow Characteristics, and Test Capabilities," NASA TP-3521, September 1995.

Unstructured Navier-Stokes Analysis of Wind-Tunnel Aeroelastic Effects on TCA Model 2

Neal T. Frink and Dennis O. Allison
NASA Langley Research Center

Paresh C. Parikh
Paragon Research, Inc.

Aerodynamic Performance Workshop
HS R Annual Airframe Review
Anaheim, CA
February 8-11, 1999

Unstructured Navier-Stokes Analysis of Wind-Tunnel Aeroelastic Effects on TCA Model 2

A method is presented which accounts for aeroelastic effects in Navier-Stokes computations of low aspect-ratio wind-tunnel models. It is applied and validated in this presentation on the TCA Model 2 configuration.

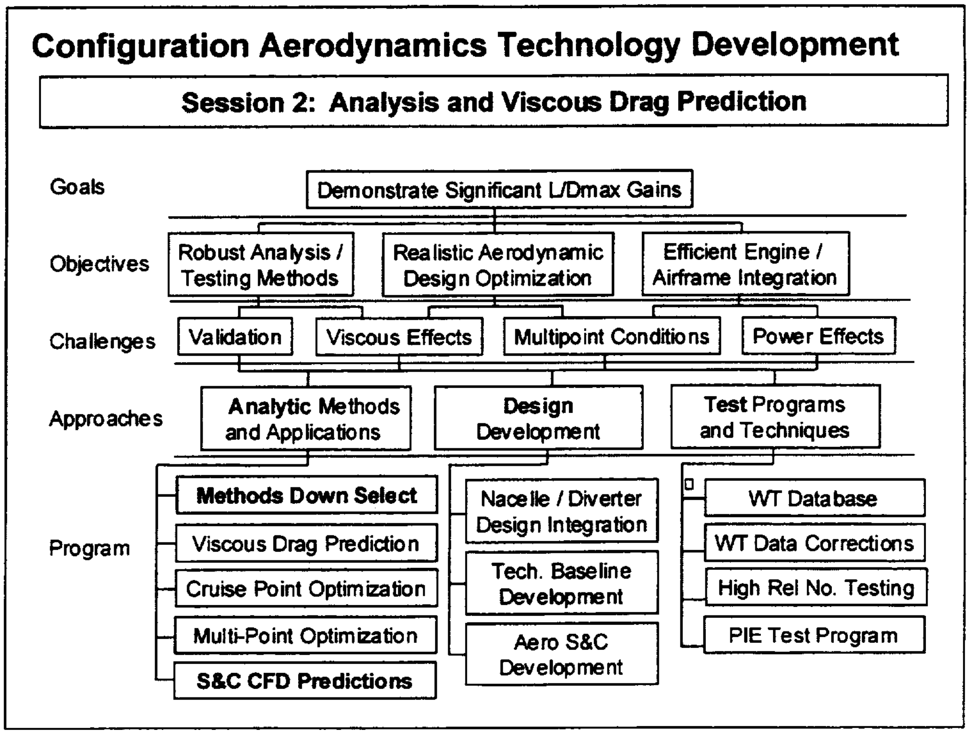
Configuration Aerodynamics Technology Development
Session 2: Analysis and Viscous Drag Prediction
Goals
Demonstrate Significant L/Dmax Gains
Objectives
Robust Analysis / Testing Methods
Realistic Aerodynamic Design Optimization
Efficient Engine / Airframe Integration
Challenges
Validation
Viscous Effects
Multipoint Conditions
Power Effects
Approaches
Analytic Methods and Applications
Design Development
Test Programs and Techniques
Program
Methods Down Select
Viscous Drag Prediction
Cruise Point Optimization
Multi-Point Optimization
S&C CFD Predictions
Nacelle / Diverter Design Integration
Tech. Baseline Development
Aero S&C Development
WT Database
WT Data Corrections
High Rel No. Testing
PIE Test Program

Outline

- The Problem
- Objective
- Approach
- Methodology & Procedures
- Results
- Summary

Problem - WT Aeroelastic Effects

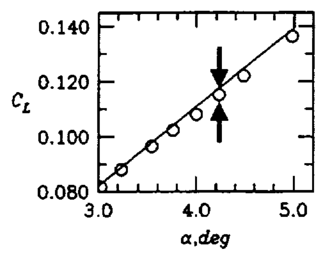

For rigid low AR HSR planforms, CFD predicts:
- Lift slightly high
- PM significantly low

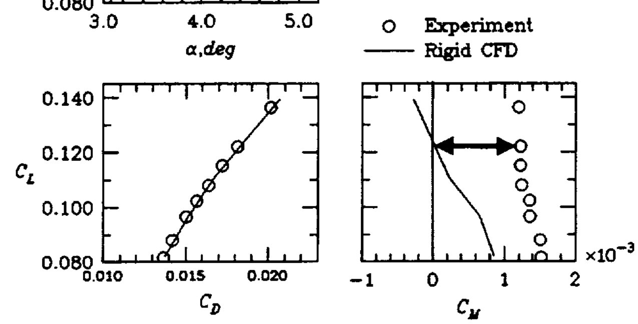

The Problem: Wind-Tunnel Aeroelastic Effects

The issue to be addressed is how to account for the effects of wind-tunnel model deformation in numerical computations of low-aspect ratio planforms without relying on measured model deformation data.

During wind-tunnel tests of the low aspect ratio planforms characteristic of HSR configurations, the load induced displacement and twist of the thin outer wing panels tends to unload those panels. This results in a decrease in lift and increase in pitching moment. The variation of drag with lift is not adversely affected. Thus, it is important to include the model deformation within numerical computations to remove the noted aeroelastic-induced inconsistencies.

Objective

- To improve CFD correlations with TCA Model 2 UPWT data by coupling a simple calibrated structural model* into Navier-Stokes computations of wind-tunnel configuration
- Validate over a range of experimental test points using a single point calibration of structural model

** This approach has been successfully applied to high aspect-ratio Advanced Subsonic Transport configurations*

Objective

The aim of this work is to demonstrate a simple technique which accounts for aeroelastic deformations experienced by HSR wind-tunnel models within CFD computations. With improved correlations, CFD can become a more effective tool for augmenting the post-test understanding of experimental data.

The present technique involves the loose coupling of a low-level structural representation within the ELAPS code, to an unstructured Navier-Stokes flow solver, USM3Dns. The ELAPS model is initially calibrated against bending characteristics of the wind-tunnel model.

The strength of this method is that, with a single point calibration of a simple structural representation, the static aeroelastic effects can be accounted for in CFD calculations across a range of test conditions. No prior knowledge of the model deformation during the wind-on test is required.

This approach has been successfully applied to the high aspect-ratio planforms of subsonic transports. The current challenge is to adapt the procedure to low aspect-ratio planforms typical of HSR configurations.

Approach

- Set up 6-plate ELAPS structural model of TCA Model 2
  - Input geometric and material characteristics to ELAPS
  - Perform pre-test bending calibration of wind-tunnel model
- Compute USM3Dns/ELAPS coupled N-S solution of TCA
  - W/B/N/D/E at Mach 2.4, α=3.5°, Re_c=6.4M
  - Manually move viscous grid with POSTGRID and restart sol'n
  - Integrate F&M for W/B/N/D
- Compare α=3.5° solution with Pitching Moment data
  - Scale calibrated wing deformation until PM data is matched
- Run additional AOA's with final calibration and validate with other test point data
  - F&M and wing deflection/twist measurements

Approach

This slide outlines the overall approach. Additional details will be described in the remaining slides.

The approach is to construct a 6-plate structural representation of the TCA Model 2 with the Equivalent Laminated Plate Solution (ELAPS) code. The ELAPS model requires some geometric and material characteristics to be prescribed as input. This model is calibrated by a pre-test model bending procedure.

A coupled USM3Dns/ELAPS Navier-Stokes solution will be generated on the full W/B/N/D/E configuration at the cruise point, Mach 2.4 and angle of attack 3.5 degrees. Force and moments will be integrated only over the W/B/N/D portion for comparison with the Model 2 data. Grid movement will be performed manually using the POSTGRID code, which is part of the VGRIDns unstructured grid generation system.

The α=3.5° solution will be compared with the experimental pitching moment data in order to fine tune the ELAPS calibration. Once the calibration is complete, the method will be tested at other angles of attack to validate the generality of the procedure. Correlations will be made against experimental force/moment and wing deflection/twist data.

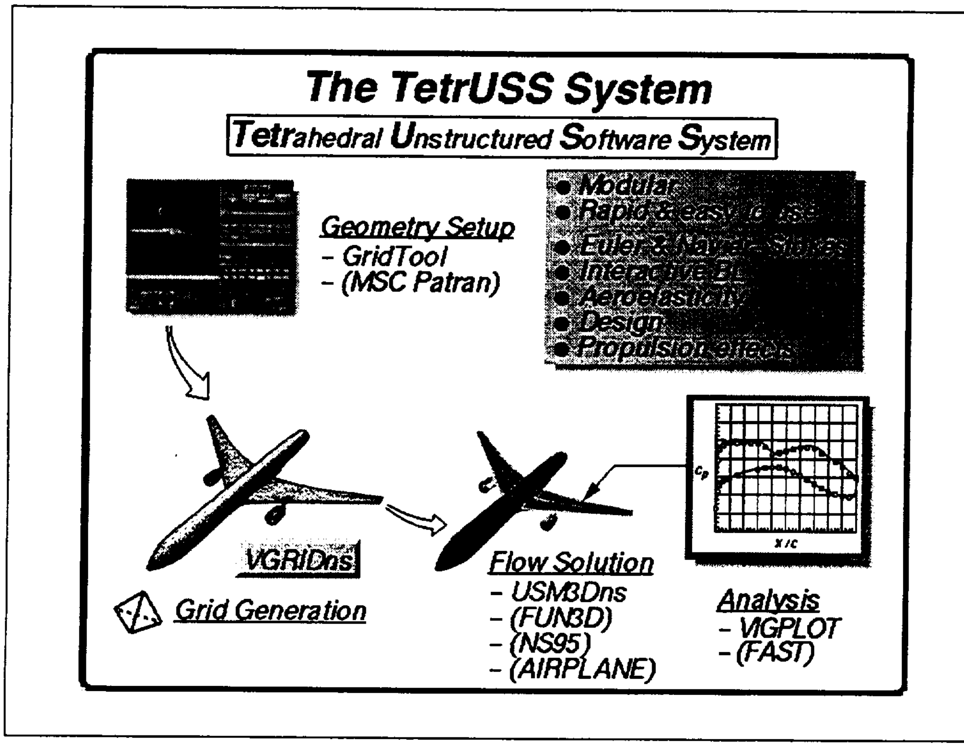

The TetrUSS System

The flow computations are performed using the Tetrahedral Unstructured Software System (TetrUSS). This is a modular set of codes for solving Euler and Navier-Stokes problems on complex configurations. The system is based on tetrahedral volume elements which are extremely flexible for modeling the most complex of configurations.

TetrUSS consists of a geometry setup tool, GridTool, tetrahedral grid generator, VGRIDns/POSTGRID, flow solver, USM3Dns, and graphical analysis tool, VIGPLOT. These tools been relatively easy to use by a broad range of users. Because of it's loose coupling, other codes have have also been utilized within the framework by various users as denoted by parenthesis.

The TetrUSS system supports additional engineering capabilities such as interacting boundary layer (Euler/IBL), aeroelasticity, iterative design, and propulsion effects. These capabilities will be described in more detail in the next slide.

Modular TetrUSS Capabilities

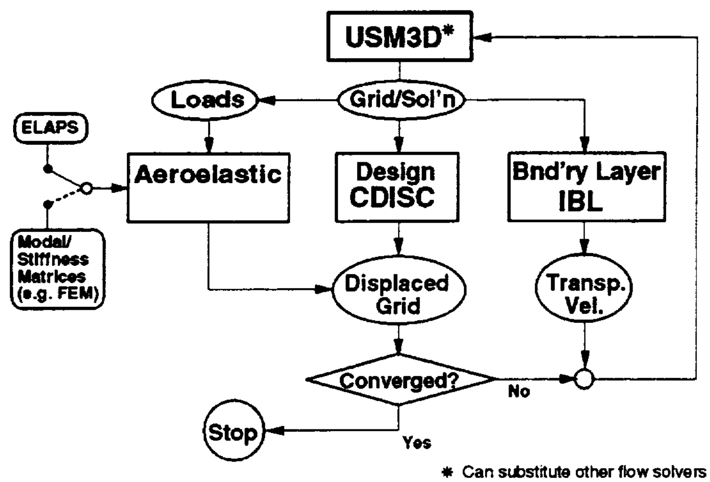

Modular TetrUSS Capabilities

TetrUSS includes a modular capability for computing aeroelastic effects, iterative design, and/or interactive boundary layer. Each component is maintained independently and is coupled to the system by pre- and post-processing utilities. The capabilities can all be used simultaneously, or in any combination.

During the script-driven update cycle, a solution file is written by the flow solver and is used by the sub-modules. Both the aeroelastic and design features involve grid movement, whereas the IBL feature generates transpiration boundary condition velocities.

The aeroelastic component converts the loads from the flow file into input for the structural code. The present options for structural modeling include a coupling with the ENSAERO system and the ELAPS code. Higher-level Finite Element Model (FEM) structural representations can be input through ENSAERO via modal or stiffness matrices.

While higher-order structural modeling is an option of this system, the present work is focused on utilizing a low-order structural representation through a simple plate model in the ELAPS code.

USM3Dns - Salient Features

- Tetrahedral cell-centered, finite volume
- Euler and Navier-Stokes
  - Spalart-Allmaras turbulence model with wall function
- Time Integration - Implicit GS and Explicit RK
- Roe's upwind FDS with flux limiting
- Platforms
  - Cray vector machines with multitasking
  - Massively parallel computers or loosely coupled workstations
- Coming capabilities
  - Advanced 2-eqn turbulence models (in testing)
  - Low-Mach preconditioning (in testing)
  - Time-accurate moving grid (planned)

USM3Dns - Salient Features

USM3Dns is a tetrahedral cell-centered, finite volume Euler and Navier-Stokes flow solver. Turbulence is modeled by the Spalart-Allmaras one-equation model. The sublayer region of the boundary layer can also be modeled analytically by a wall function in order to reduce near-wall grid density.

Solutions are advanced in time by either an implicit Gauss-Seidel scheme or the Jameson Runge-Kutta explicit time-stepping. Cell flux is computed with the Roe's Flux Difference Splitting (FDS), which can be limited by either a MinMod or SuperBee limiters.

USM3Dns will run on Cray vector processors with multitasking efficiencies of 6 out of 10 processors. Another Message Passing Interface (MPI) version of the code will run on massively parallel computers or loosely coupled workstations. Superlinear performance has been demonstrated on an Origin 2000 with 150 processors.

Additional capabilities such as 2-equation k-epsilon and Reynolds stress turbulence models, and low-Mach preconditioning have been implemented and are currently being tested in a non-release version of USM3Dns. The current plan is to a add time-accurate moving grid capability.

ELAPS Structural Code

- ELAPS - Equivalent Laminated Plate Solution
  - Computationally efficient method based on plate model
  - Employs Rayleigh-Ritz method with a global displacement polynomial function
- Less cumbersome to use than FEM
  - Suitable for preliminary aeroelastic effects
- Easily coupled with USM3D
  - Deformed surface points displaced vertically
  - Volume grid moved manually* (at this time) via. POSTGRID

* *Can be easily automated in the future*

ELAPS Structural Code

The ELAPS code, developed by Dr. Gary Giles at NASA LaRC, is based on an equivalent laminated plate technology. For the present work, it can be applied to set up a computationally efficient polynomial plate representation of the wing planform. The Rayleigh-Ritz method is used to generate a polynomial function of vertical displacement over the wing planform.

While one could utilize a more complex finite-element model in the TetrUSS system, the advantage of the present approach is in its simplicity and rapid set up time.

Grid movement involves moving both the thin-layered 'viscous' tetrahedra as well as the outer 'inviscid' cells. This function is performed manually with the POSTGRID code at this time, but could be easily automated in the future.

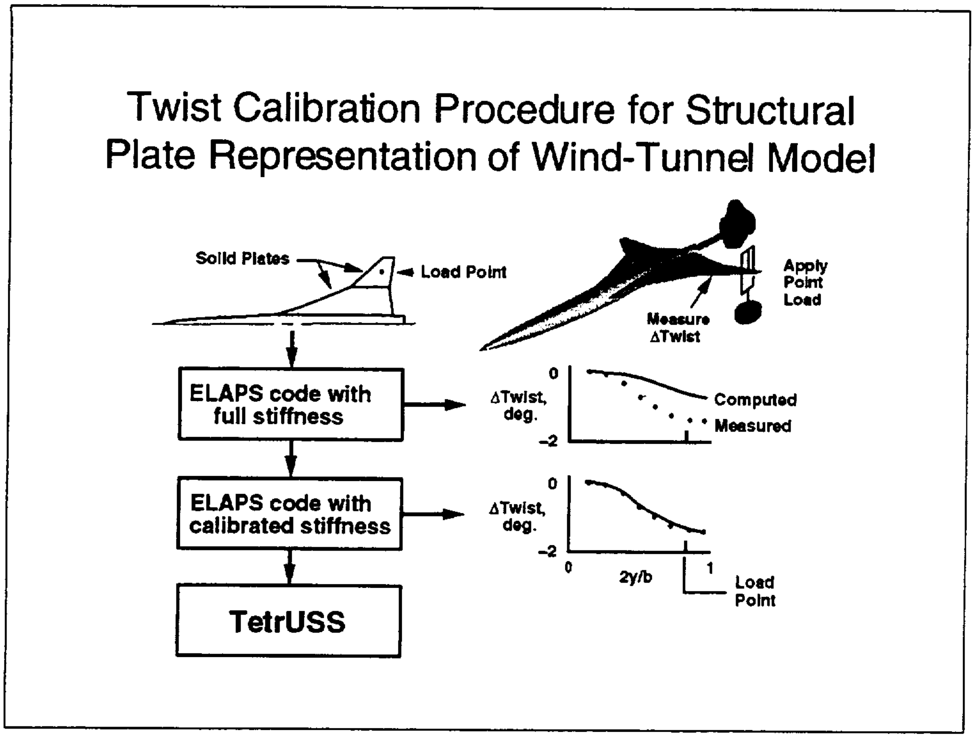

Twist Calibration Procedure

This slide describes a simple pre-test calibration procedure of the ELAPS structural representation. Weights are hung a selected points on the outer wing panel of the wind-tunnel model. Measurements of model deformation are recorded at several locations on the configuration.

A simple solid plate representation is constructed of the model structure within the ELAPS code. Preliminary estimates of material properties are also prescribed. Simulated point loads are applied to the ELAPS model which produce an initial "computed" twist distribution which is compared to the measured values. The material properties are adjusted within ELAPS until there is reasonable agreement between the twist deformations from the computed and measured data.

Once this calibration is achieved, the coupled ELAPS model is then included in the Navier-Stokes computations across the test polar.

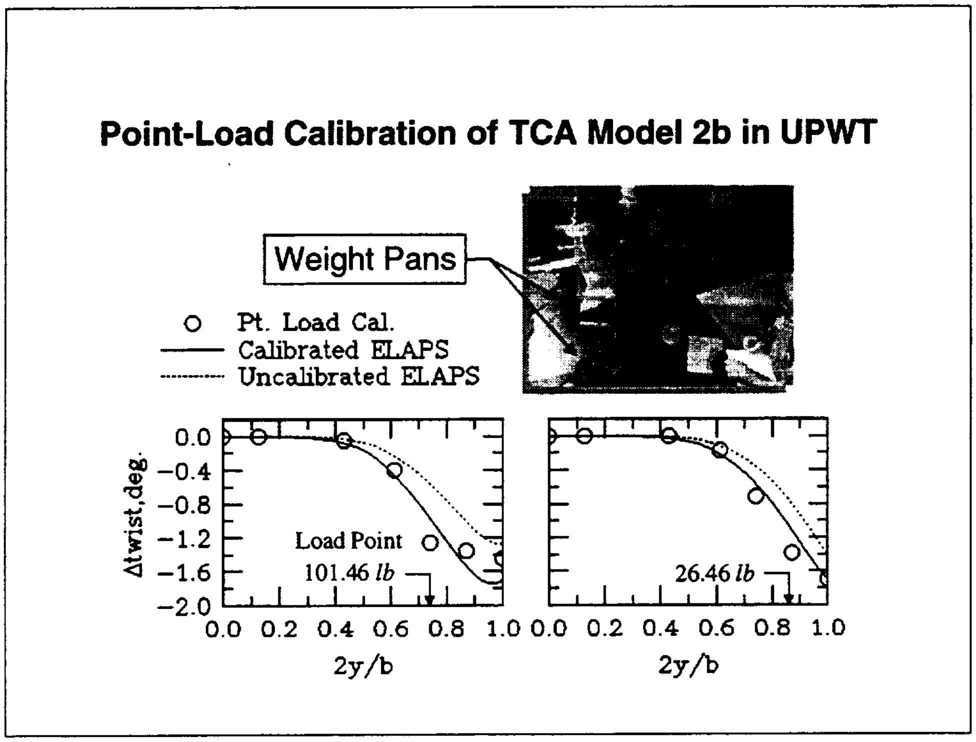

Point-Load Calibration of TCA Model 2b in UPWT

This slide illustrates how the weights are applied to the inverted TCA Model 2b in the Unitary Plan Wind Tunnel. The inset photo depicts the recording of a measurement of tip deflection.

The plots contain the measured twist distribution induced by point loads applied at the 72-percent and 87-percent span stations. The dashed line is the raw "uncalibrated" ELAPS twist distribution based on the prescribed geometric and material properties of the model. The solid "calibrated" line was derived by adjusting the material properties in the 6-plate ELAPS model until a reasonable approximation of the measured data was obtained. As can be observed in the plots, some discrepancies do remain particularly at the tip with the inboard load point.

Changes to ELAPS Calibration Strategy

- Initial N-S calculations with standard pre-test calibration procedure achieved about a 40-percent improvement in pitching moment correlation at α=3.5°
- Adjusted calibration of 6-plate ELAPS model by *doubling* its surface displacements
  - achieved close match with pitching moment data at α=3.5°
- Found last minute oversight in calibration
  - Bending calibration done on Model 2b from T1846 (solid wing)
  - Correlations made with Model 2a from T1671 (has flap cutouts)
  - T1671 measured deformations twice that of T1846

Changes to the ELAPS Calibration Strategy

After the initial Navier-Stokes calculation using the calibrated ELAPS model, the correlation with the experimental pitching moment had improved only 40-percent. It was initially assumed that the robustness of the 6-plate ELAPS model was not adequate to yield a straight forward calibration for low-aspect ratio planforms. A further adjustment was then made by doubling the surface displacements produced by the ELAPS model. This yielded a close match with the experimental pitching moment data at α=3.5°.

The source of this shortcoming was later determined to be an oversight on which Model 2 was calibrated. The bending calibration was performed on the Model 2b from T1846 which had a solid wing structure, whereas the experimental data was taken from Model 2a of T1671 which was considerably more flexible due to leading- and trailing-edge flap cutouts. After a last minute check of optically measured model deformation data from the two tests, it was determined that twist measurements differed normally by a factor of two. Additional calculations will be made after the workshop to resolve this inconsistency.

Solution Characteristics

- Thin-Layer Tetrahedral Grid
  - 1,428,427 cells (897,078 in 'viscous' layer)
  - Average y^+ of 1st node is 20.1, and cell centroid is 4.5
  - Approx. 18 tetrahedra across mid-chord BL
- Flow conditions
  - M=2.4, α=3, 3.5, 4, & 5 deg, $Re_c=6.4\text{x}10^6$
- Flow model
  - Full Reynolds-averaged Navier-Stokes
  - Spalart-Allmaras turbulence model
  - Wall function below first node (y^+ approx. 20)

Solution Characteristics

A tetrahedral grid of 1.4 million cells was generated with VGRIDns. The average y^+ obtained by averaging the values at the first node above the surface on all viscous surfaces was 20.1. Noting that the distance of the centroid of a first layer tetrahedral viscous cell above the surface is 1/4 that of the first node, the average y^+ at the cell centroids was 4.5.

The flow conditions are Mach 2.4, α=3, 3.5, 4, & 5 degrees, Re_c=6.4 million. The computations incorporate the full Reynolds averaged Navier-Stokes equations above the first layer of tetrahedral cells using the Spalart-Allmaras turbulence model, and model the flow within the first layer (below y^+ approx. 20) using a wall function.

HSR Technology Concept Airplane

Tetrahedral Viscous Grid (1,428,427 cells)

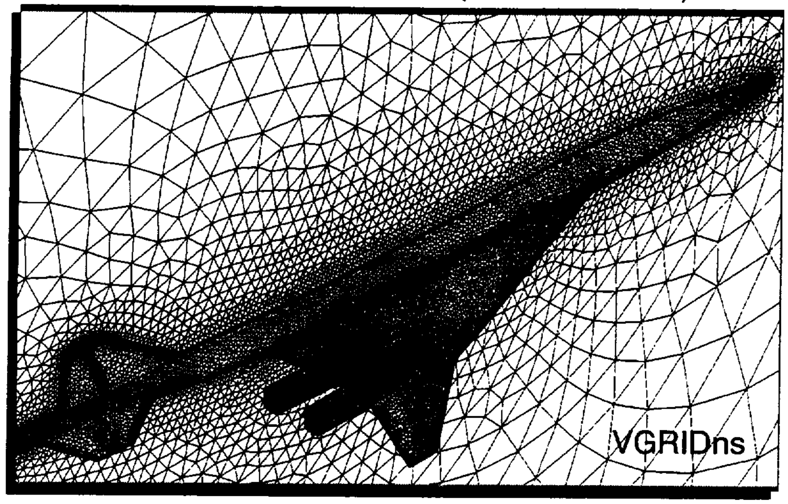

HSR Technology Concept Airplane

This slide depicts the surface and symmetry plane grid used in the computation. Note the clustering of the 'viscous' cells along the fuselage/symmetry plane boundary. All solutions were computed on the full W/B/N/D/E configuration, but forces and moments were integrated only over the truncated W/B/N/D geometry for comparison with supersonic wind-tunnel data.

Regarding movement of the nacelle/diverters under aeroelastic deformation, no special treatment was applied. TetrUSS has a capability for slaving the movement of components. But this could not utilized for TCA due to the tight integration of nacelle/diverter with the wing. Fortunately, the required nacelle movement was very small.

Solution Strategy

- Run 700 cycles on initial "rigid" grid
  - Run additional 500 cycles to generate "rigid" reference sol'n
- Move grid using preceding flow solution
  - Move surface grid front with PREELAPS utility
  - Move volume grid with POSTGRID
- Restart USM3Dns from rigid solution for another 100 to 150 cycles with USM3Dns
  - repeat process 3 times to converge aeroelastic solution
- Resource requirements
  - Memory: 250MW
  - CPU time: 12.5 C90 hours per AOA for initial 700 cycles; 7 hours to converge aeroelastic solution

Solution Strategy

The aeroelastic solutions were generated through a series of restart runs beginning with a partially converged 'rigid' solution, and continuing after each movement of the grid. The grid was moved manually with POSTGRID. A total of three movements/restarts were required to converge the aeroelastic deformation at each angle of attack. Each case required 250 megawords of memory and 20 hours of Cray C-90 time.

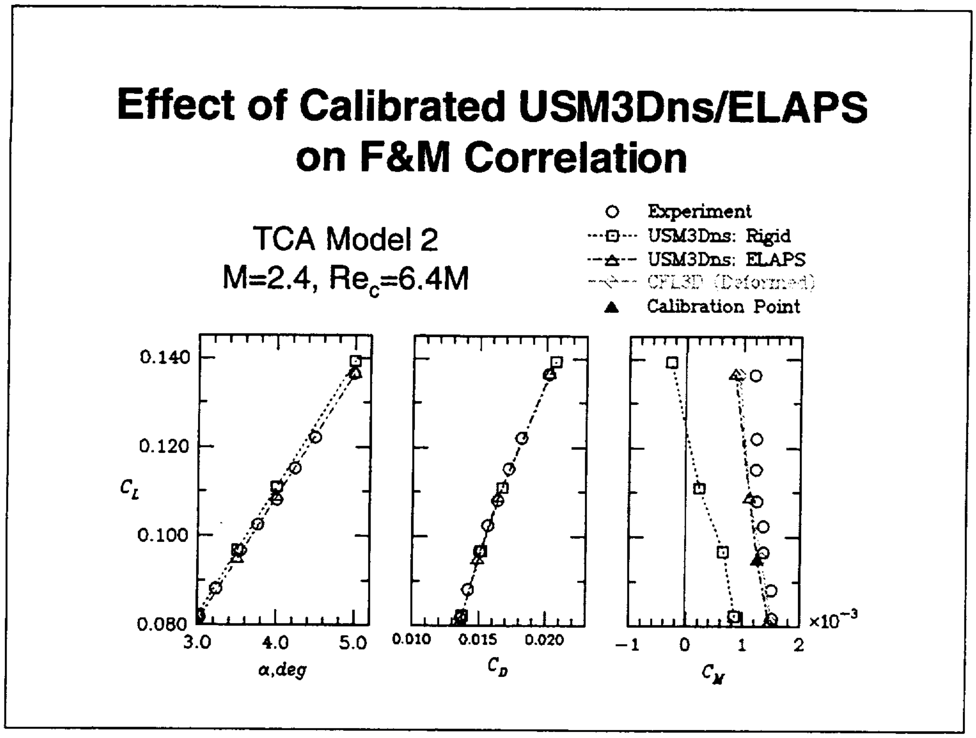

Effect of Calibrated USM3Dns/ELAPS on F&M Correlation

This slide presents the CFD correlations with force and moment data from UPWT T1671. Note that the 'rigid' USM3Dns result over-predicts lift and significantly under-predicts pitching moment. The drag coefficient is in good agreement and includes corrections for nacelle base pressure and for trip drag by the k^2 method.

The ELAPS calibration point is denoted by the *solid* triangle on the pitching-moment curve. The remaining *open* triangles were computed with USM3Dns using the calibrated ELAPS model. Note the good agreement of both the lift curve and the pitching moment with experimental data. Note further the excellent agreement with the CFL3D computation presented by Kuruvila, et al. The CFL3D result was computed on a deformed structured grid which matched the optically measured shape of the wind tunnel model.

Thus, the present approach offers a simplified technique for addressing aerodynamic deformation effects of low-aspect ratio wind-tunnel models in CFD computations without prior knowledge of those deformations.

References

Kuruvila, G., Hartwich, P. M., Baker, M. L.: "Effect of Aeroelasticity on the Aerodynamic Performance of the TCA", 1998 NASA High-Speed Research Program Aerodynamic Performance Workshop, NASA CDCP-1006, Volume 1, Part 2, pp. 1589-1648

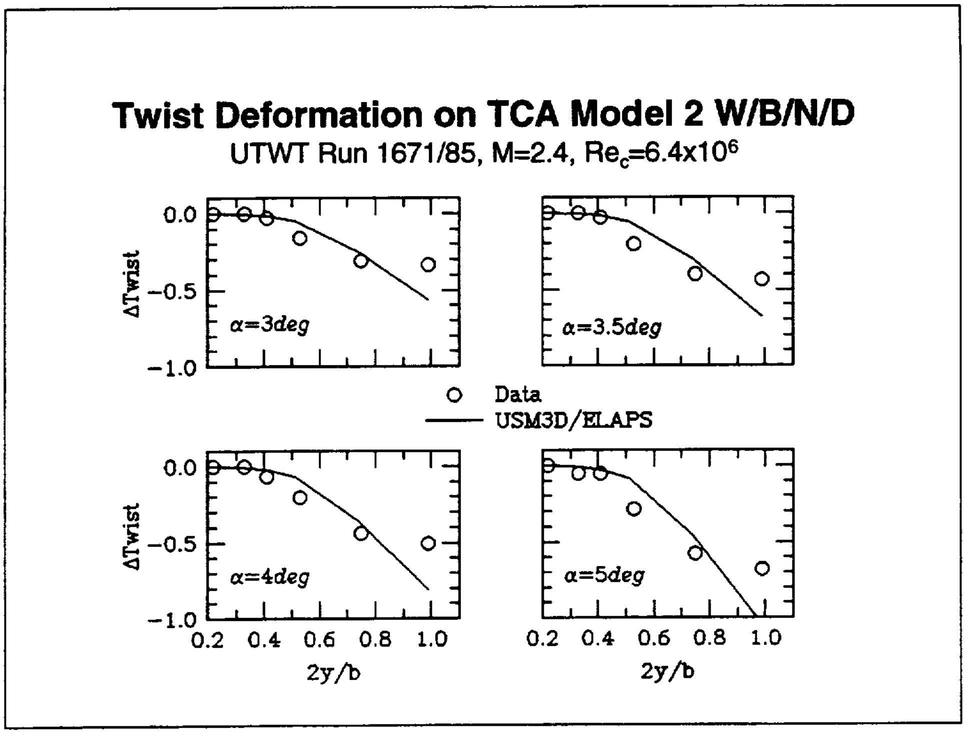

Twist Deformation on TCA Model 2 W/B/N/D

This slide conveys the correlation of computed and experimentally measured changes to spanwise distribution of wing twist at the four angles of attack. The general agreement is good, but the computed curves do not reflect the inflection present in the experimental curves. In particular, the changes in twist are under-predicted in the mid-span region and over-predicted near the tip.

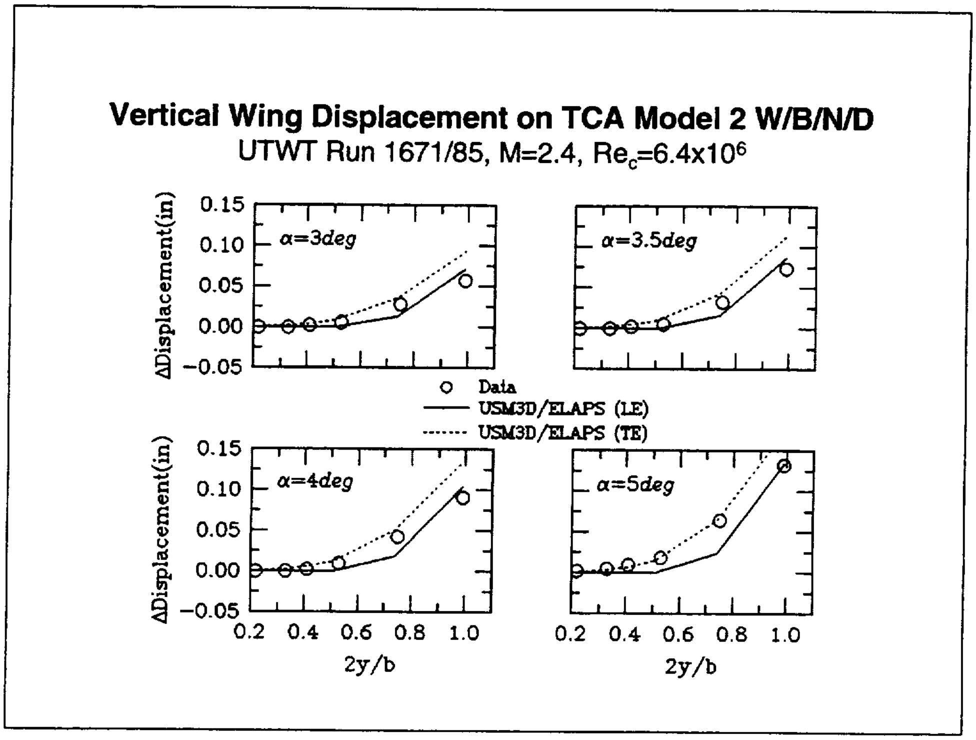

Vertical Wing Displacement on TCA Model 2 W/B/N/D

A comparison of the experimentally measured and computed spanwise distribution of vertical displacements are presented here for the four angles of attack. The experimental displacements were measured optically at several spanwise locations on the wing surface. Time did not permit us to extract the computed displacements at the same locations, thus, the leading- and trailing-edge values are included on this figure. Note that the computed displacement curves tend to bracket the experimental ones, with the exception that the tip is over predicted.

The results on this and the prior two slides suggest that while the simple 6-plate structural representation does not resolve all of the details of the aeroelastic phenomenon, it does result in a good estimate of the aggregate aerodynamic performance loads on the configuration.

A better detailed modeling might be achieved either by gaining more experience with the ELAPS model, or by applying a similar calibration procedure to a higher-order structural model.

Summary

- Applied simple point-calibrated structural model to include WT aeroelastic effects in N-S computations of low aspect-ratio HSR planform
- Demonstrated coupled system of unstructured N-S flow solver (USM3Dns) and low-level structural code (ELAPS) with movement of 'viscous' grid
- Improved N-S correlations with TCA Model 2 over range of test points
  - Force and moment test data
  - CFL3D solution with measured deformations
- Reasonable agreement of twist and displacement with data

Summary

The objective of this work was to demonstrate a simple technique which accounts for aeroelastic deformations experienced by HSR wind-tunnel models within CFD computations with a view toward improving the effectiveness of CFD as tool for augmenting the post-test understanding of experimental data.

Such a method has been validated herein using an unstructured Navier-Stokes flow solver, USM3Dns, and a low-level polynomial plate rendition of the structure through the ELAPS code. Technical challenges such as modular coupling of codes and movement of 'viscous' grids on a complex geometries have been overcome. The supporting results demonstrate that the aggregate aerodynamic performance loads are well predicted. While there is some deficiency in distributed quantities, the agreement of computed twist and displacement of the wing are in reasonable agreement with the data.

In summary, the present approach offers a simplified technique for addressing aerodynamic deformation effects of low-aspect ratio wind-tunnel models in CFD computations without prior knowledge of those deformations.

Automated Euler/Navier-Stokes Grid Generation/Grid Perturbation for Wing/Body Configurations

David Saunders (Raytheon)
James Reuther (MCAT)
Stephen Edwards (U.C. Davis)

NASA Ames Research Center

February, 1999

Configuration Aerodynamics Technology Development

Program Selects Best Analysis / Design Optimization Methods

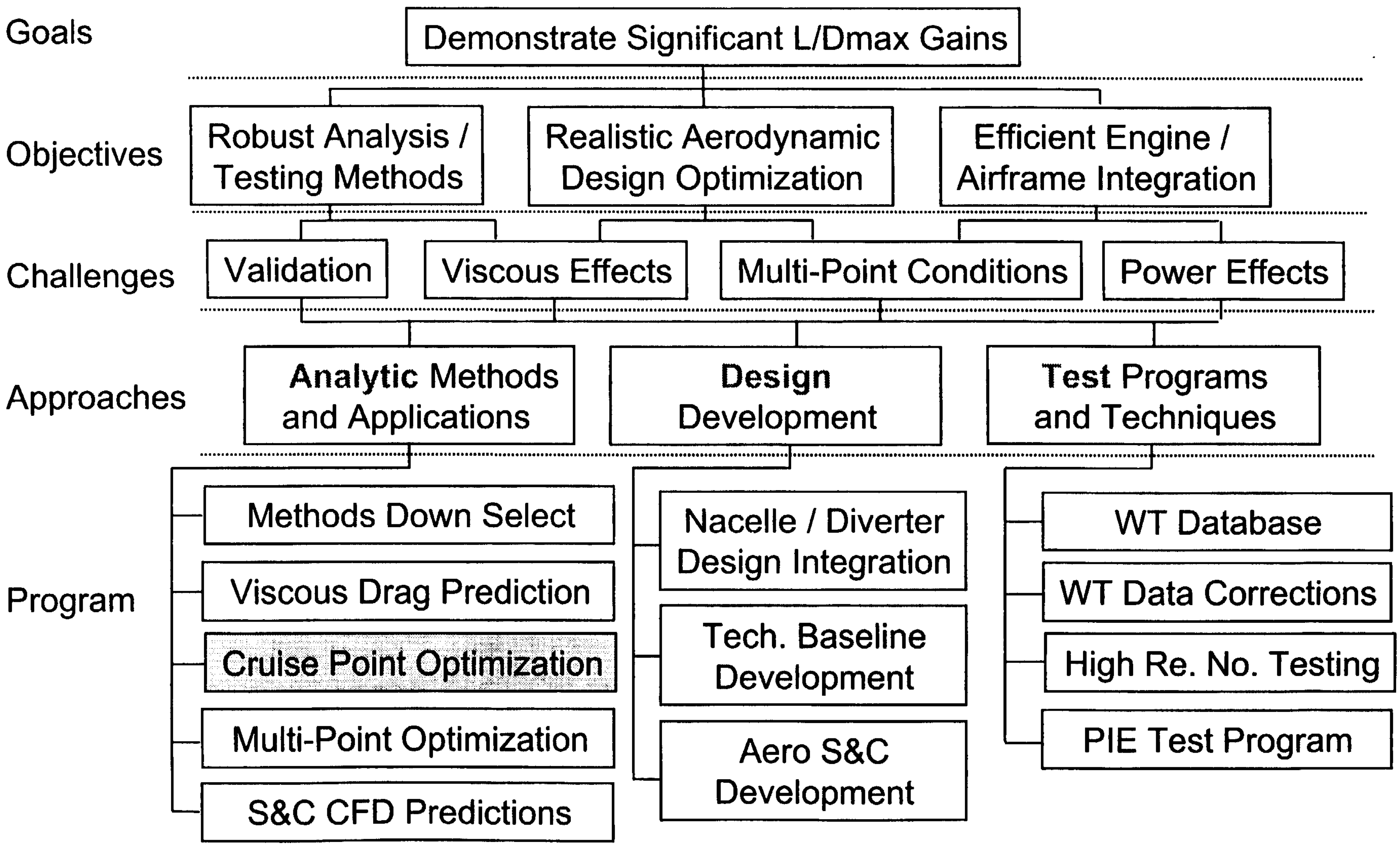

Automated Euler/Navier-Stokes Grid Generation/Grid Perturbation for Wing/Body Configurations

Introduction

This document describes the **single-block wing/body** grid generation package developed at NASA Ames Research Center during 1994-1998 as part of the design-by-optimization activities supporting the High Speed Research Program. Application of the gridding to optimization requires **complete automation** for the initial full grid generated from scratch at the beginning of a design run, combined with an **efficient means of perturbing** that initial grid many times during the run. Use of a single-block flow solver by the design code has forced the use of a **C-H topology**. (The bulk of a **C-O-type tip treatment** has also been incorporated, but this option remains incomplete following experience with a preliminary implementation which traded other disadvantages for the better tip resolution.)

It is well known that a **C-H topology** is adequate for plain wings, but less well-suited to wing/bodies. The present implementation has been refined enough that it probably represents the best that can be done for wing/bodies given the single-block restriction and the automation requirement. In combination with the single-block design code's **pseudo-nacelle** option for supersonic applications, this grid generator played a key role in the successful creation of the January 1997 **Ames 01-03** refinement of the TCA-6 High Speed Civil Transport. Nearly two years later, initial efforts to optimize the full Ames 01-03 wing/body/nacelle/diverter configuration with the SYN107-MB multiblock design code suggest that the **great bulk of the possible improvement** over the baseline TCA-6 was indeed found by SYN87-SB with its pseudo-nacelle approximation.

Recent incorporation of a **Navier-Stokes capability** was prompted by the potential for application to the optimization of HSCT wing flap/slat settings. The gridding is ready, but **viscous flow calculations** are **still not an option** in SYN87-SB at the time of writing. Indeed, it is not clear that such a capability is practical in view of the large memory requirements and limited potential for distributed processing (limited to autotasking on CRAY C90-class supercomputers). Nonetheless, automated Navier-Stokes gridding for any likely wing/body configuration represents a potentially valuable capability which, at least, can be used in conjunction with the FLO107-MB multiblock solver. This solver has produced the only calculations on these grids so far. Proper validation of the calculations remains a loose end, but flow solver convergence provides a certain measure of grid quality, and no surprises were encountered in these initial viscous solutions.

OUTLINE

- Nomenclature & History
- Capabilities, Performance, & Limitations
- Basic Design: C-H Topology, 8 Sub-blocks
- Body Surface Grid Strategy
- Indirect Navier-Stokes Strategy
- Rapid Grid Perturbation
- Reusable Software Utilities
- Illustrations

Representative Example

The preliminary illustration below shows the upper surfaces of a 193 x 49 x 65 **Euler grid** for the **TCA-6 wing/body** configuration. Such grids, in combination with the pseudo-nacelle scheme of the single-block design code SYN87-SB, led to the January 1997 Ames 01-03 optimization of TCA-6 which has yet to be significantly improved upon.

Representative Single-Block 193 x 49 x 65 Euler Grid (TCA-6 Wing/Body)

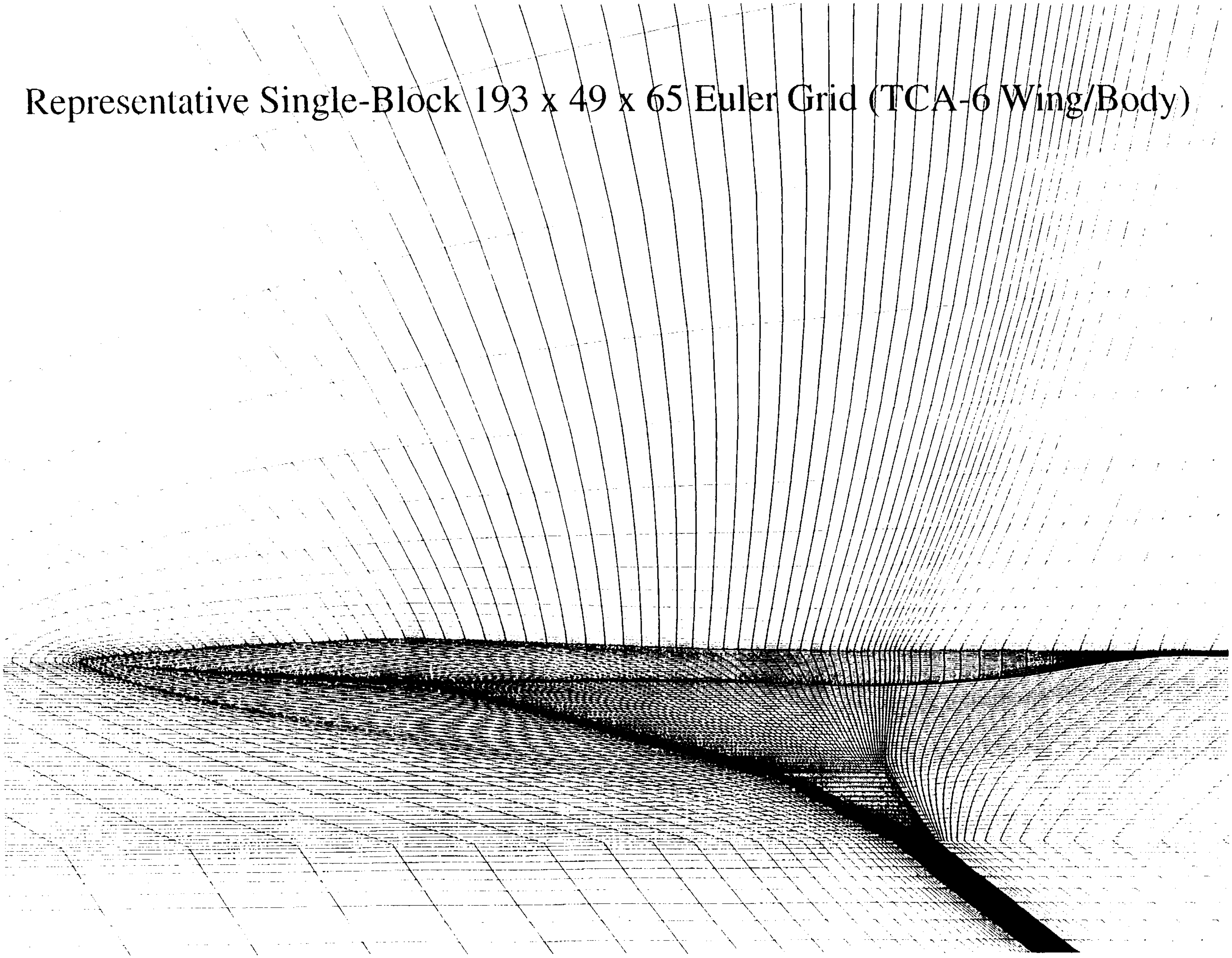

Nomenclature and History

The basic package is now known as (subroutine) **GRIDWB**, which is employed without change by two programs: **SYN87-SB** and **CH_GRID**.

The adjoint-based wing/body design code, **SYN87-SB**, is an outgrowth of the OPT67 finite-difference wing/body design code which employed an adaptation of the **WBGRID** package from Lockheed (Burris and Raj?) linked to a wing/body adaptation of the single-block flow solver, FLO67. Several years of grid generation development on behalf of SYN87-SB have produced a complete rewrite of WBGRID, with the symmetry plane's outer boundary shape—a reversed D—literally the only recognizable fragment remaining.

Early in 1997, the gridding portion of SYN87-SB was extracted as a stand-alone wing/body grid generator, **CH_GRID**. This simplified further development by eliminating the encumbrance of the flow and adjoint solvers, the ghost nacelle scheme, and the grid perturbation option. However, in mid-1998, translation to **Fortran 90** with a view to making the software independent of grid size via **dynamic allocation** of workspace led to resurrection of the grid perturbation capability in CH_GRID in order to ease maintenance of the two programs.

Initial efforts to produce **Navier-Stokes**-type grids focused on adapting the **elliptic smoothing** portions of the basic Euler method to cope with drastically tighter spacing and correspondingly more extreme stretching. In essence, this meant an alternative to the **index-based** "foreground" control of **orthogonality** at the boundaries and "background" control of **spacing**. An option for **arc-length-based** decay of orthogonality control was incorporated in the ELLIP2D utility and variations were tested at great length via the CGRID airfoil grid generator. Actually, the eventual scheme used a **hybrid arc-length/index-based formulation** to decay the orthogonality terms away from the boundaries, among other refinements. However, results remained marginal at best, with instabilities very likely in boundary layer regions and very limited spreading of the orthogonality into the grid interior. No satisfactory method was found to decay the orthogonality control terms smoothly in a way which influenced the full thickness of the boundary layer region without also affecting opposite boundaries adversely. While the final scheme remains an option in ELLIP2D, it did not appear worthwhile to incorporate comparable capability in either ELLIPQ3D (for smoothing 3-space grid planes) or ELLIP3D (for grid volumes, where the analogous scheme would have been unacceptably expensive in terms of storage and computation).

Instead of a direct approach to Navier-Stokes grid stretching, an **indirect approach** has been implemented with far greater success. All the quality (in terms of orthogonality at the wing surface) of the underlying Euler grid is retained in the redistributed Navier-Stokes grid. In fact the indirect option, which is very cheap computationally, can also overcome the main visual weakness of the direct Euler results (namely a tendency to pull the C lines too much towards the wing surface in the quadrants above and below the wing), although the effect on Euler solutions is minimal. Further details of the direct and indirect approaches follow.

NOMENCLATURE & HISTORY

- **WBGRID Origins (Lockheed) Have Vanished**
- **GRIDWB Pkg. Common to SYN87-SB & CH_GRID**

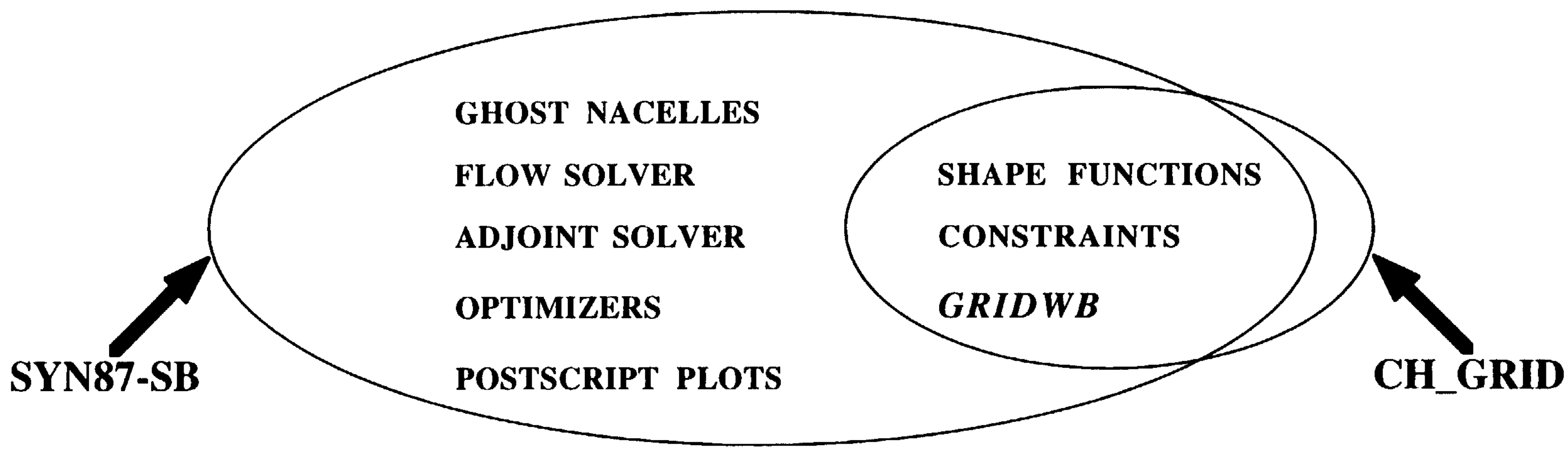

- **Direct Navier-Stokes Grid Has Poor Orthogonality**
- **Indirect Euler —> Navier-Stokes is Much Better**

Current Capabilities

The single-block gridding within SYN87-SB and CH_GRID handles either a **plain wing** on a wall, or a **wing/body** configuration. The left wing and left half fuselage are treated; zero yaw is assumed. **Geometry inputs** consist of planar streamwise cuts for the wing, and planar body cross sections (**point definitions** not related to the surface grid dimensions). Input wing sections may be normalized or not. Output wing sections (possibly perturbed) may be normalized/unpitched, normalized/pitched, or full-scale/pitched. Here, pitch (about the leading edge) means the local angle of attack—sometimes referred to improperly as local twist.

Wing/body **intersection calculations** are **protected** by an option to **fudge the body** sections if the wing drops below the fuselage. The intersection consists of many line/surface intersection points, each calculated rapidly and robustly via a **safeguarded Newton** iteration on t, u, and v using piecewise linear wing lines and bilinear or bicubic parametric body surface interpolation with derivatives.

Planform cranks or other desirable wing surface grid stations may be specified as inputs. These are blended smoothly into the nominal wing grid stations, which are controlled with sine/cosine inputs to allow clustering towards the root and/or tip.

In anticipation of significant **leading and trailing edge deflections**, the mean-line slopes of each wing surface grid section are carefully **extrapolated into the sheets fore and aft of the wing**. Spanwise irregularities observed along the leading edge as a result of discrete choice of leading edge points have been eliminated by continuous calculation of the true leading for each (rounded) wing station.

Arbitrary flap/slat hinge lines are handled at the "PERTURB" level above GRIDWB, but no attempt is made to resolve the streamwise edges of flaps or slats—the surface grid just **smears** these regions. A related class of "**variable center**" shape functions allows perturbing "bumps" to be imposed **along lines parallel to such features as shocks** off nacelle/diverter leading edges. (This capability was implemented too late for the TCA-6 optimization which led to the Ames 01-03 design of January 1997, but the need for getting away from spanwise perturbations along constant x/c lines was frequently expressed at the time.)

Performance

Performance-wise, using 100 **volume grid smoothing** iterations, a typical **193 x 49 x 65** Euler grid takes about **150** CPU seconds from scratch on a CRAY C90. For a **305 x 97 x 65** viscous grid, the initial Euler-spacing grid (which must be the **same** dimensions) takes about **800** seconds on a 225 MHz SGI R10000 processor, or 900+ seconds on a 195 MHz Origin2000, using 200 smoothing iterations. The **conversion** from Euler spacing **to Navier-Stokes spacing** takes less than 6 seconds on any of these systems. Note that essentially none of the full grid generation vectorizes, while DO-loop-level parallelization via autotasking on a C90 is not appropriate.

Warping the initial full grid, on the other hand, does vectorize. A **single pass** through each sub-block volume interpolates corner, edge, and face perturbations into the interior in less than 3 seconds (Euler, C90) or less than 9 seconds (Navier-Stokes, R10000).

CAPABILITIES & PERFORMANCE

- Wing On Wall or Wing + Body (No Yaw)
- Wing May Drop Below Body (Body is Fudged)
- Wing Surface Grid Captures Specified Cranks
- Wing Flap & Slat Angles Carry Into Flow Field
- Wing Shape Functions Need Not Follow Fixed *x/c*

- 193 x 49 x 65 Euler Grid Takes ~150 CPU sec. (C90)
- 305 x 97 x 65 Euler ~800 sec. (225 MHz R10000)
- 305 x 97 x 65 Euler—> Navier-Stokes Takes < 6 sec.
- Warp: < 3 sec. (Euler, C90); < 9 sec. (N-S, R10000)

Current Limitations

As indicated above, the **left wing** and left half **fuselage** are treated; **zero yaw** is assumed. **Geometry inputs** consist of **planar cuts** for the wing and body—that is, **point definitions**. The long-desirable capabilty of gridding directly from **CAD surface definitions** remains as far from reality as ever. The design application complicates the CAD/CFD interface greatly, because the communication needs to be two-way. The control points of the NURBS curve/surface representations should become the design variables to avoid introducing approximations in the transfer of design results back to CAD/CAM systems. However, preliminary experience at Ames with 2D airfoil design via NURBS curve control points as design points has not been particularly encouraging. (Hicks-Henne-type shape functions, while capable of introducing spanwise waviness, are much more benign in the chordwise direction, whereas working with B-spline control points is not unlike working directly with section grid points as design variables in their tendency to introduce high-frequency irregularities.) Treating wing surfaces similarly at Ames has been limited to an oblique all-wing transport application where a handful of defining sections were represented as NURBS curves, with carefully optimized blending of thickness and chord in the spanwise direction. All section curves used the same knots to allow the lofting of (x,y)s to be performed via lofting of control points. There are no plans to pursue such approaches for the single-block methodology.

While wing flaps and slats may have arbitrary hinge-lines, no attempt is made in the gridding to resolve the streamwise **edges of the control surfaces**—the surface grid just **smears** these regions.

Wing tip resolution is poor in the C-H topology. A C-H/C-O gridding option to improve the tip handling was implemented in 1995 and has been carried along since, but is presently somewhat incomplete. It would require a boundary condition change in the single-block flow solver, and there has been little incentive to pursue the option, although that remains a possibility.

Fuselage resolution is inevitably the weakest aspect of the single-block approach. Cell skewing is unavoidable on the **nose**, and especially below the **root leading edge** of low-mounted wings. The 3D elliptic smoothing normally overcomes all **negative cell volumes** in the flow field, even though the 3D transfinite interpolation used to initialize the volume grid always produces odd skewing when a body is present, and particularly in the presence of cranked wing planforms, but positive cell volumes everywhere is the only explicit measure of grid quality. The **aft body** is also normally poorly resolved in deference to more-or-less steady growth of grid spacing between the root trailing edge and the far downstream boundary. The aft-most body station is captured precisely, however.

The wing/body grid generation is **not parallelized**. In principle, the 8-sub-block topology could be taken advantage of once all the block face boundaries are established for the initial full grid, by distributing smoothing of the sub-blocks among processors. For pure grid generation (perhaps to be handed on to a parallelized flow solver), the typical times of 150 seconds and 800 seconds for Euler and Navier-Stokes grids make such a possibility of parallelism an unnecessary complication. For the design application, the initial full grid represents a small fraction of the total run time. Use of a very rapid grid perturbation scheme and the absence of parallelized flow and adjoint solvers again makes parallelizing the initial volume grid smoothing a pointless complication. On the other hand, the typical Euler grid of 600,000+ points requires 50+ Mwords on a CRAY C90, so the far larger memory requirements of a single-block/single-processor scheme with a (yet to be incorporated) Navier-Stokes solver on a ~2 million-point grid may well make single-block viscous design by optimization effectively impractical for quite some time.

LIMITATIONS

- Left Wing + Left Body Only (No Yaw)
- Geometry I/O is Planar Cuts—not CAD Surfaces
- Edges of Wing Flaps & Slats are not Resolved
- Wing Tip and Body Extremes are Weakly Resolved
- Cell Skewing is Inevitable On & Near the Fuselage
- Parallelization is Not Practical
- Vast Memory Requirements May Make Viscous Single-Block Design by Optimization Impractical

Basic Design: C-H Topology & 8 Sub-Blocks

The **single-block C-H topology** is an obvious choice for a **wing on a wall**, although the C-H/C-O variation mentioned above makes better use of the same number of grid points to resolve the tip, at the expense of a different boundary condition for the FLO87 flow solver which has not been implemented in SYN87-SB for lack of demand on HSCT applications. This is increasingly unlikely in view of the advances made with multiblock techniques.

Inclusion of a **fuselage** capability pushes the single-block topology to its limits. Retention of that topology has the advantage of enabling fully automated grid generation and avoiding the use of a far more complex multiblock flow solver. Through a series of refinements starting with a much-improved body surface grid strategy (more on which below), the topology limitations have been overcome probably as well as is likely to be done anywhere given the automation requirements.

Reliable **elimination of** all **negative-volume cells** in the flow-field grid, along with **precise control of grid increments** at key boundary locations, have been achieved mainly through the introduction of **additional sub-block boundaries** and **enhanced elliptic smoothing utilities** featuring orthogonality control. For instance, a boundary sheet forward of the wing leading edge, properly smoothed, enabled overcoming grid lines which crossed the forward part of the fuselage nose. This sheet later became essential for capturing the **slopes of deflected** wing leading edge **slats**. The present **8 sub-block scheme** is the natural result of the need for precise control of initial radial increments at the wing leading edge, wing trailing edge, and far downstream wake boundary, for each of the wing root, the wing tip, and the beyond-the-tip outer boundary. These initial increments are specified as fractions of local chord. In the spanwise direction, they are varied linearly from root to tip and from tip to outer boundary. In the wrap-around streamwise direction, the variation is mostly linear, but the 2-D smoothing utility permits nonlinear variation of the initial increment where appropriate, such as in the C grid at the wing tip.

The following illustration shows the 8-sub-block C-H topology of the single-block grid applied to the TCA wing/body. The grid dimensions are 193 x 49 x 65 as recommended for Euler solutions. The outer boundary radius has been set to half the vertical range, although it could be smaller. The interior edges orthogonal to the wing tip at the trailing edge are constructed with 5-point splines. Other radial edge boundaries are similar, with slopes of leading and trailing edge deflections captured in the sheets forward and aft of the wing. (No flap or slat deflections are present in this figure.) A "fan" is barely visible in the symmetry plane aft of the fuselage; it completes the C lines wrapping around the wing on the fuselage. In the plan view, the upstream and downstream boundaries reflect the average wing sweep by default, although this can be controlled otherwise.

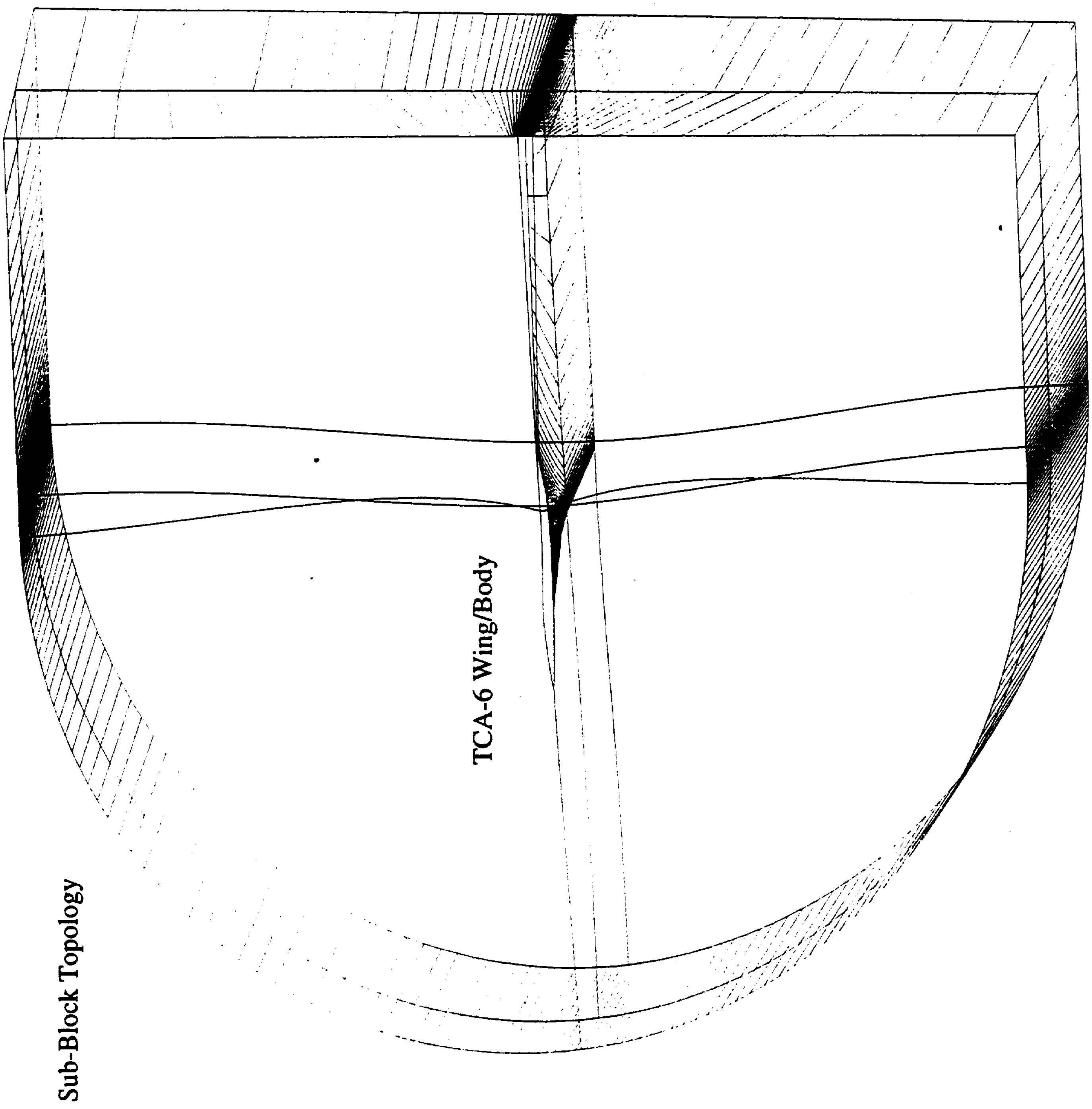
8 Sub-Block Topology
TCA-6 Wing/Body

Basic Design: C-H Topology & 8 Sub-Blocks, Continued

In addition to the more powerful elliptic smoothing, the **starting guesses** for the **sub-block interiors** have also been improved with the implementation of a **3D TFI** (transfinite interpolation) utility using Soni-type optimal blending functions. Even so, these starting guesses can be surprisingly skewed by the body, particularly in the presence of wing planform cranks, so an extra boundary plane has been introduced for TFI3D purposes at the end of the fuselage, normal to the wake sheet, as a partial fix.

The **price paid** for additional sub-block boundaries is the potential loss of smoothness in the grid lines across boundaries. Specifying orthogonality at these boundaries helps in some regions but is not appropriate at others. (For instance, the sheet in front of a swept wing should not force the initial lines away from/parallel to the wing leading edge to be normal to the fuselage or the boundary edge forward of the tip—parallel to the leading edge is more appropriate.) Fortunately, Euler solvers tend to be insensitive to such sub-block boundary discontinuities. As a check, the current radial-redistribution option has been applied using Euler rather than Navier-Stokes spacings as a way of smoothing some of these discontinuities, but the effect on the computed force/moment coefficients was negligible. In the N-S case, the radial redistribution has the effect of smoothing the grid lines across some of these boundaries. Converged N-S solutions have been obtained so far only via the multiblock solver, FLO107-MB, since an N-S option has yet to be installed in SYN87-SB, so N-S experience is limited at this time.

Further grid illustrations appear at the end of this document.

C-H TOPOLOGY & 8 SUB-BLOCKS

- C-H is Natural for Wing Alone; Retained for W/B
- Single Block Has Evolved to 4, 6, Now 8 Sub-blocks
- 8 Sub-blocks Allow Precise Control of Initial Radial Spacing at 9 Corners/Smooth Variation in Between
- Interior Boundary Sheets are Needed Also for Capturing Wing Flap/Slat Deflection Slopes
- 3D TFI Utility Helps the Volume Grid Smoothing via Improved Starting Guesses
- Enhanced Elliptic Smoothing Utilities Allow Control of Orthogonality at Specified Boundaries

Body Surface Grid Strategy

The **crude body surface** gridding in **WBGRID** (basically a non-parametric scheme **projecting points** from the symmetry plane on to the body) was the first main portion to be **replaced**. **Parametric techniques** (x, y, z as functions of u and v) were highly desirable, yet problematic near the singularity at the nose point. No amount of elliptic smoothing of (u,v) grid lines imposed on the traditional normalized (u,v) representation of the fuselage sections could overcome that nose singularity, where u had to jump from 0 to 1 over an infinitesimal edge length. Instead, working with **true arc lengths**, or something close to them, appeared crucial. The strategy adopted was to **shear** the ***un*normalized** geometry arc lengths in the vertical direction by half the total length at each axial station, then to clean up the edge corresponding to the last body section by **regularizing** the lengths of **the axial lines** in the v direction.

Boundaries in this (u,v) space are established for four sub-blocks wrapping around the line corresponding to the wing/body intersection and wake line. This is nontrivial along the intersection, requiring a Newton iteration at each (x,y,z) which actually produces the desired (u,v) as a by-product of determining the z corresponding to the given x and y. (Here, the nomenclature is that of Antony Jameson, with z being spanwise.) Since u and v are essentially arc lengths, the 2D elliptic (u,v) smoothing can utilize root-chord-related initial and final increments. Nevertheless, following bilinear or bicubic interpolation of (x,y,z) at each grid (u,v), a final step redistributes the radial lines on the body to impose precise radial arc-length increments at points along the wing root, the aft body wake line, and the crown and keel.

BODY SURFACE GRID STRATEGY

- **Parametric Body Surface Gridding is Innovative in its Use of <u>Un</u>normalized Approximate Arc Lengths**

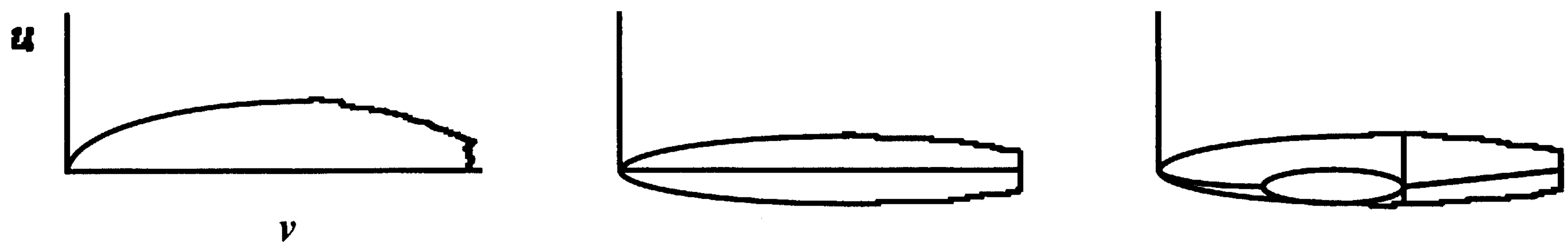

Pure Body Arc Lengths **Sheared/Regularized** **4-Patch Redistribution**

- **4-Sub-block Scheme in Arc-Length-Like (u,v) Space Uses 2D TFI and 2D Elliptic Smoothing of (u,v) Pts.**
- **Final Step, Radial Redistribution, Imposes Precise Initial and Final Increments on the Body Grid Lines**

Indirect Navier-Stokes Grid Strategy

As indicated in the history above, the **indirect** approach to achieving Navier-Stokes-type spacing was resorted to following **unsatisfactory** results with attempts to achieve **direct arc-based control** (as an alternative to index-based control) of spacing and orthogonality in the elliptic smoothing. Convergence in the boundary layer region was unreliable, even with extreme under-relaxation, and the orthogonality barely extended beyond the boundary layer at best.

The elliptic smoothing with Euler-type spacing works so well that retaining it held great appeal. **Growing the grid dimensions** following the initial Euler gridding was also considered, but soon **abandoned** as too complex. **Starting with the correct N-S dimensions** means nominally that redistribution is required in only **one direction**. However, simply redistributing each radial line independently is ***not*** sufficient. (The extreme skewing that can result is perhaps best seen by considering a spanwise vertical plane along the wing trailing edge, where the azimuthal distribution along the body section must surely be taken into account by the radial lines near the body.) More careful blending is required, as will be explained.

With an initial full grid in hand, the radial redistribution **starts** by copying the **second set of input controls** to the working variables and **regridding** all of the **radial edges** of all sub-blocks. A **hybrid geometric/Vinokur** scheme is used for precise control before and after redistribution: typically, the first 20 points in the (nominal) N-S boundary layer have geometric spacing with growth factor 1.1, while an overlapping Vinokur distribution (controlled by the first and last increments) is imposed beyond the boundary layer region. The same scheme for Euler grids typically uses just 4 points geometrically spaced at the surface and a similar growth factor of 1.1 (all variable inputs, of course).

Experience showed that **blending** sub-block face distributions **across planform cranks** is a **bad** idea, producing skewed cells and negative volumes in the case of TCA-6. Therefore, **any** or all of the **crank** stations specified as inputs may be flagged as **additional** redistribution **boundaries**.

The **second** main **step** is to **blend pairs** of radial **edges** of each sub-block face via **arc-length**-based **weighting** to produce **new faces**.

The **final step** is to **blend** the new radial distributions of the **sub-block faces** into the **sub-block interiors**. Consider the sub-block volume above the wing, with face boundaries forward of the leading edge, above the trailing edge, at the wing tip and wing root, plus the wing surface and its opposite at the far outer boundary. A new interior radial distribution emanates from a point, say $(i,1,k)$, on the interior of the wing surface. This relative distribution (beyond the boundary layer region, that is) is formed as a **2D transfinite interpolation**-type combination of the relative radial distributions emanating from points $(ile,1,k)$, $(itu,1,k)$, $(i,1,1)$, and $(i,1,ktip)$, where the nomenclature should be obvious.

As already indicated, this blending strategy appears to work well enough to produce no cells with negative volume as long as an additional blending face is introduced at the k plane of any crank in the wing planform.

INDIRECT N-S STRATEGY

- Start With an Euler Grid of N-S Grid Dimensions
- Input Both Euler and N-S Radial Controls
- Precise Geometric Growth in the Boundary Layer: e.g., NBL & RBL = 4 & 1.1 (Euler), 20 & 1.1 (N-S)
- Regrid Radial Edges of Sub-block Faces + Edges of Specified Planform Crank Stations
- Regrid Faces by 1D Blending of Relative Radial Distributions of New Edges
- Regrid Volumes by 2D TFI Blending of Relative Radial Distributions of New Faces

Rapid Grid Perturbation

Even with a fully-automated grid generator and adjoint-based gradients for the aerodynamic objective function, the possibility of hundreds of design variables makes **full grid generation for every change** of a variable **out of the question**. (The geometric derivatives required for each adjoint-based derivative of the objective function are actually computed by **finite differencing** in the design code.) Therefore, it is essential to have an accurate and efficient means of **perturbing/warping/morphing** the initial grid.

Such a warping capability is an integral part of GRIDWB. The wing/body intersection and surface gridding are sufficiently rapid that, in combination with 2D or quasi-3D warping of other sub-block boundaries, all of the sub-block faces can be computed in "warp" mode very efficiently. The face perturbations are then interpolated into the sub-block interiors, and this too is very efficient. For instance, the **typical Euler case** (193 x 49 x 65) takes just **2.83 seconds** of CRAY C90 CPU time to perturb the grid.

Grid warping uses the initial **relative interior arc lengths** in order to interpolate boundary perturbations into the interior. For the **1D** case, a **single pass** through the interior points adjusts them for given new end points. The **2D** and quasi-3D cases perturb the interior in **two stages**, by first calculating 1D-type edge perturbations from just the corner perturbations, then calculating a second set of edge perturbations that move the interim edges to the desired edges. These two sets of edge perturbations are interpolated into the face interior via independent arc-length-based combinations of the contributions from the two pairs of opposite edges corresponding to the index directions. The two stages can be combined in a single vectorizable pass through the interior grid points. Analogously, the **3D** warping case is performed in **three stages**:

(1) Determine face perturbations corresponding to **corner** perturbations (only).
(2) Determine further face perturbations corresponding to perturbing the interim edges to the final **edges**.
(3) Determine further face perturbations corresponding to perturbing the interim faces from stage 2 to the final **faces**.

The perturbations from each stage can be interpolated into the volume interior via appropriate arc-length-weighted combinations of three pairs of perturbations—a different weighting for each stage, because only in the final stage are the contributions from the the three index directions independent. These three stages can also be combined in a **single vectorizable pass through the interior** grid points.

In the stand-alone case (CH_GRID), a "**check warp**" option is incorporated to exercise the grid perturbation scheme. In this case, following completion of the full grid, the first variable[1] is perturbed by the input "*h*" and the grid is immediately regenerated in "warp" mode. If the scale factor associated with the first variable is also input as zero, then the perturbation is actually zero, and the resulting grid should be identical to the initial grid. Any difference, no matter how slight, would introduce spurious effects during a gradient calculation in the design code. Perfecting the warping option for the new indirect mode required considerable care setting up all the sub-block boundaries. Edge distributions actually have to pass through the Euler stage before N-S redistribution to get the exact match reqd.

[1] CH_GRID also retains the design variable and constraint inputs of the design code, as it may be used to perturb geometry and/or check constraints without doing any grid generation.

RAPID GRID PERTURBATION

- Grid Warping is Included so that the GRIDWB Module is Common to CH_GRID and SYN87-SB
- Wing & Body are Regridded from Scratch; Most Other Sub-block Faces can be Warped
- Sub-block Volumes are Warped in 3 Stages:
  - (1) Corner Motion (Only) Produces Interim Faces
  - (2) Edge Motion Produces Further Interim Faces
  - (3) Face Motion Produces Desired Faces
- Face Deviations from Each Stage are Arc-length Blended into the Interior in 1 Pass which Vectorizes

Reusable Software Utilities

The **GRIDWB** single-block grid generation package that is common to CH_GRID and SYN87-SB represents a good example of reusable software in action. While GRIDWB contains 7,367 lines of **application-specific** source code of which 4,169 are Fortran 90, the remaining components—**about two-thirds of the bulk**—are **general-purpose**, **argument-driven utilities**: more than 50 Fortran 77 and Fortran 90 numerical subroutines (16,264/7,850 lines of source/code) are suitable for other applications.

Three sets of 2D, quasi-3D, and 3D gridding utilities are of interest to grid generators:

(1) The **transfinite interpolation** routines **TFI2D**, **TFIQ3D**, & **TFI3D** serve for cheap algebraic filling of grid interiors given the boundaries. For the plane and surface cases, the Soni-type blending functions at point (i,j) are derived from the intersection of the straight lines connecting opposite normalized-arc-length edge points i and j. In the 3D case, Soni-type blending functions[2] are calculated with a Jacobi iteration, starting with the average of two estimates at each volume point from application of the 2D blending formula to planes through the point. Application of the converged blending functions is a three-stage process[3] which can be performed in a single vectorizable pass through the volume points.

(2) The **elliptic smoothing** routines **ELLIP2D**, **ELLIPQ3D**, & **ELLIP3D** have evolved substantially from the TTM2D and -3D routines that were part of WBGRID, mainly in their addition of **Sorenson**-type "foreground" **orthogonality** control to the **Thomas-Middlecoff**-type "background" **spacing** control. The automatic array feature of Fortran 90 has enabled all three to be fully argument-driven without the need for reuse of available workspace via common blocks that made the Fortran 77 versions less portable. The option in ELLIP2D to moderate relative arc lengths can help background control if the curvature at one boundary greatly exceeds the curvature at the opposite boundary (as is the case for an airfoil leading edge vs. the trailing edge). ELLIPQ3D is really suited only to interior faces—not geometry surfaces. It is necessarily index-based, which is a weakness if the spacing is far from uniform. Parts of GRIDWB are using ELLIP2D on just two of three coordinates where a more effective ELLIPQ3D is really appropriate. ELLIP3D, while expensive, tends to perform well if the boundary faces are in good shape. All 3 utilities perform SLOR iterations which do not vectorize because of the tridiagonal systems solved for every i line. See the book of Thompson, et al. (below) and Sorenson's GRAPE/3DGRAPE for more.

(3) The grid perturbations routines **WARP2D**, **WARPQ3D**, & **WARP3D** are detailed above, and are very efficient.

Many other **1D & 2D spline** utilities, **search** routines, **intersection** routines, **1D distribution** utilities, etc., are among these reusable numerical utilities. Surface intersections are calculated as multiple line/surface intersections using a safeguarded Newton iteration for each line. Heavy use is made of "**local**" **spline** techniques where the spline coefficients are calculated on the fly as needed from 4-point formulas. This is perfectly adequate for smooth, well-resolved data. Among the 1D distribution utilities is perhaps the most thorough of **Vinokur**-type implementations, carefully iterated to produce precise end increments. The 1D **zero-finding**, **minimization**, & **quadrature** utilities have been reworked, using **reverse communication** to simplify use on arbitrary functions.

---

[2] "Two- and Three-Dimensional Grid Generation for Internal Flow Applications of CFD", AIAA 85-1526.

[3] Best described in the "projectors" section of "Numerical Grid Generation" by Thompson, Warsi, and Mastin (1985), pp. 315-326

REUSABLE SOFTWARE UTILITIES

- 50+ GRIDWB Components are General Purpose Fortran 77 & Fortran 90 Numerical Utilities
- TFI2D, -3D, & -Q3D are Fully Argument-driven
- ELLIP2D, -3D, & -Q3D are Fully Argument-driven
- WARP2D, -3D, & -Q3D are Fully Argument-driven
- Many 1D & 2D Spline Utilities, Search Routines, Intersection Routines, 1D Distribution Utilities, etc.
- 16,264 Lines of Source Code/7,850 Lines of Fortran are General Purpose Utilities

Further Illustrations (1)

The $k = 1$ plane containing the body surface is shown in the nose region for the 193 x 49 x 65 **TCA-6 Euler grid**, along with part of the wing surface ($j = 1$). Of the 49 points in the radial direction, *jcrown* = 25 are on the body. The fuselage C lines are inevitably a stretch for such an elongated nose, with substantial skewing of cells. Radial spacing is input-controlled at the crown/keel (between *jcrown* and *jcrown* ± 1) and along the wing/body intersection. Axial spacing is controlled at the nose and at the end of the aft body.

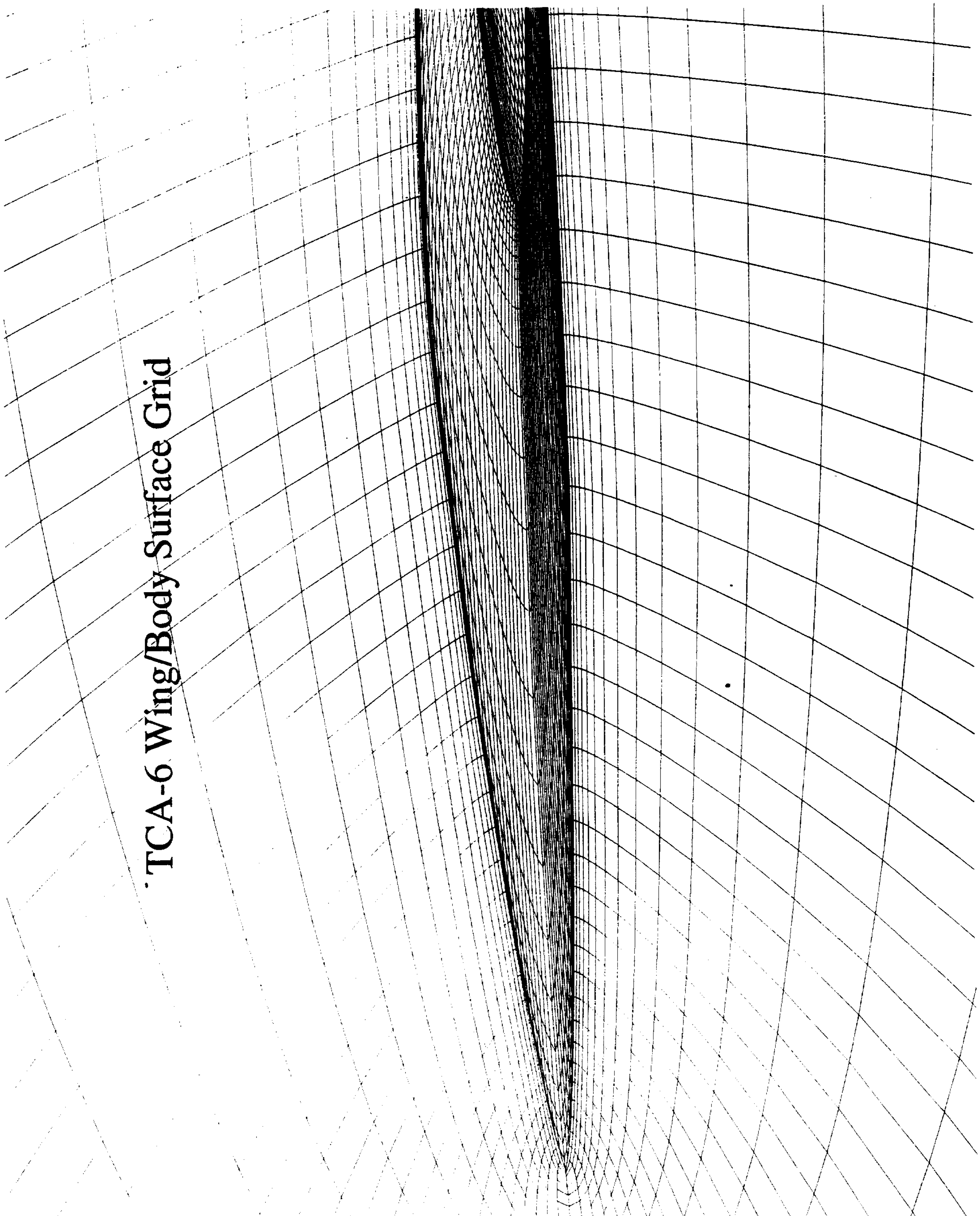

TCA-6 Wing/Body Surface Grid

Further Illustrations (2)

The upper surfaces of the **TCA-6** wing and body are shown for the same 193 x 49 x 65 **Euler** grid along with the wake sheet, the $i = ile$ sheet forward of the leading edge, and the corresponding sheet beyond the wing tip.

The wing surface grid has captured the **planform crank** at the z = 480.416" station as well as an **artificial crank** at z = 125" beyond which wing grid section lines are essentially planar and virtually unaffected by possible fuselage diameter perturbations. This prevents unintended spanwise motion of pseudo-nacelle effects during HSCT optimization.

Once-troublesome crossing of grid lines at the nose (worst for shorter, rounder noses) is eliminated by a combination of 2D and quasi-3D elliptic smoothing of the sheet forward of the leading edge. Note that specifying orthogonality at the "water-line" edge along the side of the nose is not appropriate for swept-wing cases because of the consequences very near the root, where following the leading edge sweep is more critical. The same is true along the edges fore and aft of the wing tip.

TCA-6 Wing/Body Upper Surface

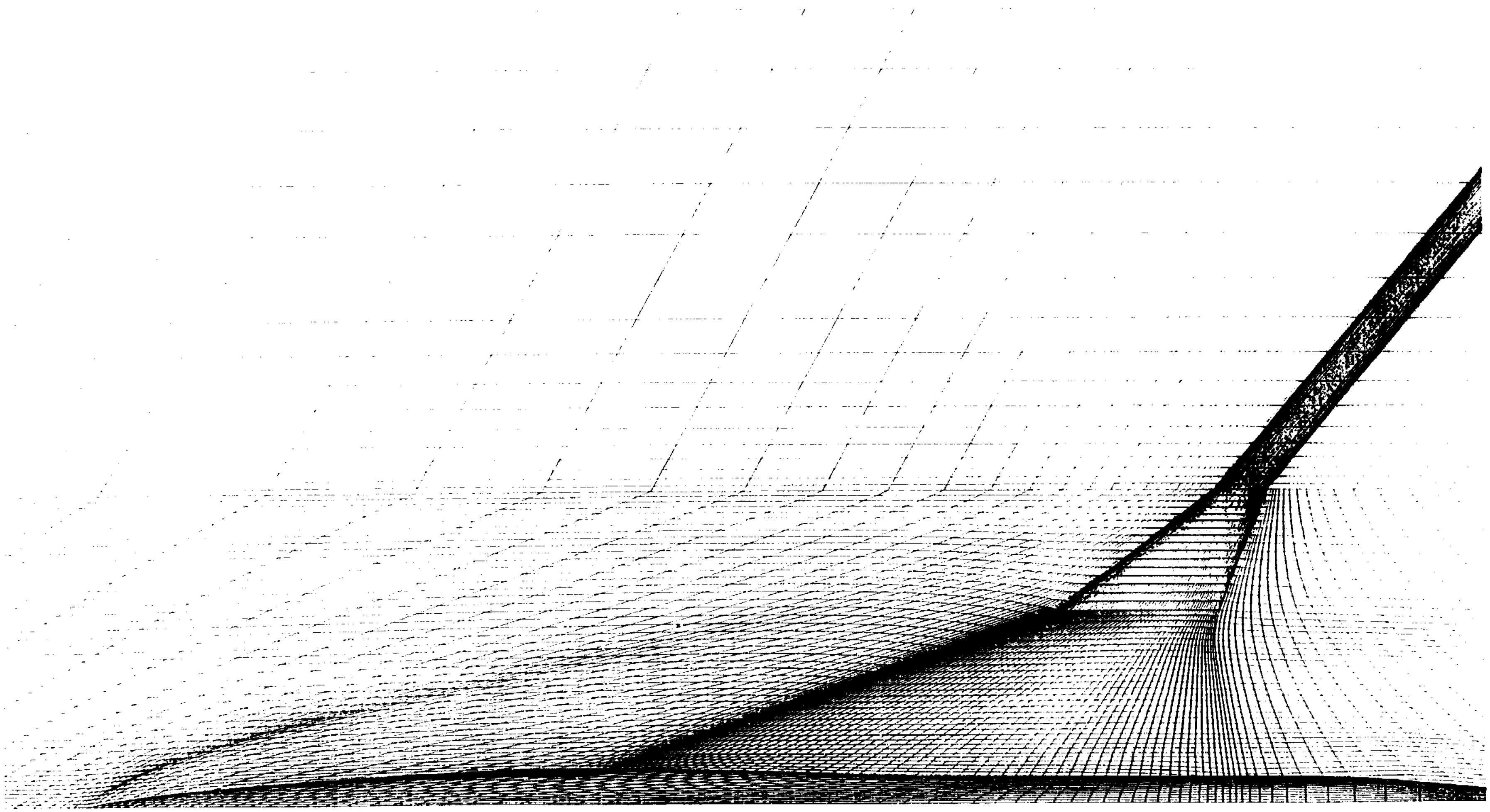

Further Illustrations (3)

The remaining illustrations are shown in **groups of three** in order to compare a standard 193 x 49 x 65 Euler grid with Navier-Stokes-sized grids before and after redistribution of the interim large Euler-type grid. Clearly, the radial redistribution of the interim Euler-type grid lines that is required to capture the wing boundary layer has deleterious effects elsewhere. The preliminary grid has more than enough points for Euler-type spacing, so any before/after comparison is bound to be unfavorable. Comparison beyond the boundary layer of the N-S grid with the typical 193 x 49 x 65 Euler grid is therefore more meaningful, and is for the most part quite favorable.

The **interim Euler grid** must have the **same dimensions** as the final Navier-Stokes-type grid. The dimensions here are 297 x 97 x 65, with *jcrown* = 65. Other key N-S inputs are *nblayer* = 20 and *rblayer* = 1.1, vs. *nblayer* = 4 and *rblayer* = 1.1 for the smaller Euler grid. (The first *nblayer* points off the $j = 1$ surface for every radial grid line are **spaced geometrically** using the growth factor *rblayer*. The spacing is **Vinokur-type** beyond that.) The initial increments vary here from 0.003 to 0.005 of local chord in the Euler cases. They are 0.00001 of local chord for the N-S case in this example.

The case shown is a small business jet rather than an HSCT, to help illustrate the **flexibility** of the grid package. Growing a bulge on the aft body via optimization to match an experimental wing pressure distribution, then freezing the bulge during further optimization, is a proven technique for improving the effectiveness of the single-block methodology on such configurations with aft-body-mounted nacelles.

The first set of bizjet illustrations shows most of the body surface grid. Note that the N-S grid spacing, with more streamwise points as well as more radial points beyond the boundary layer region, compares favorably with the standard Euler grid spacing.

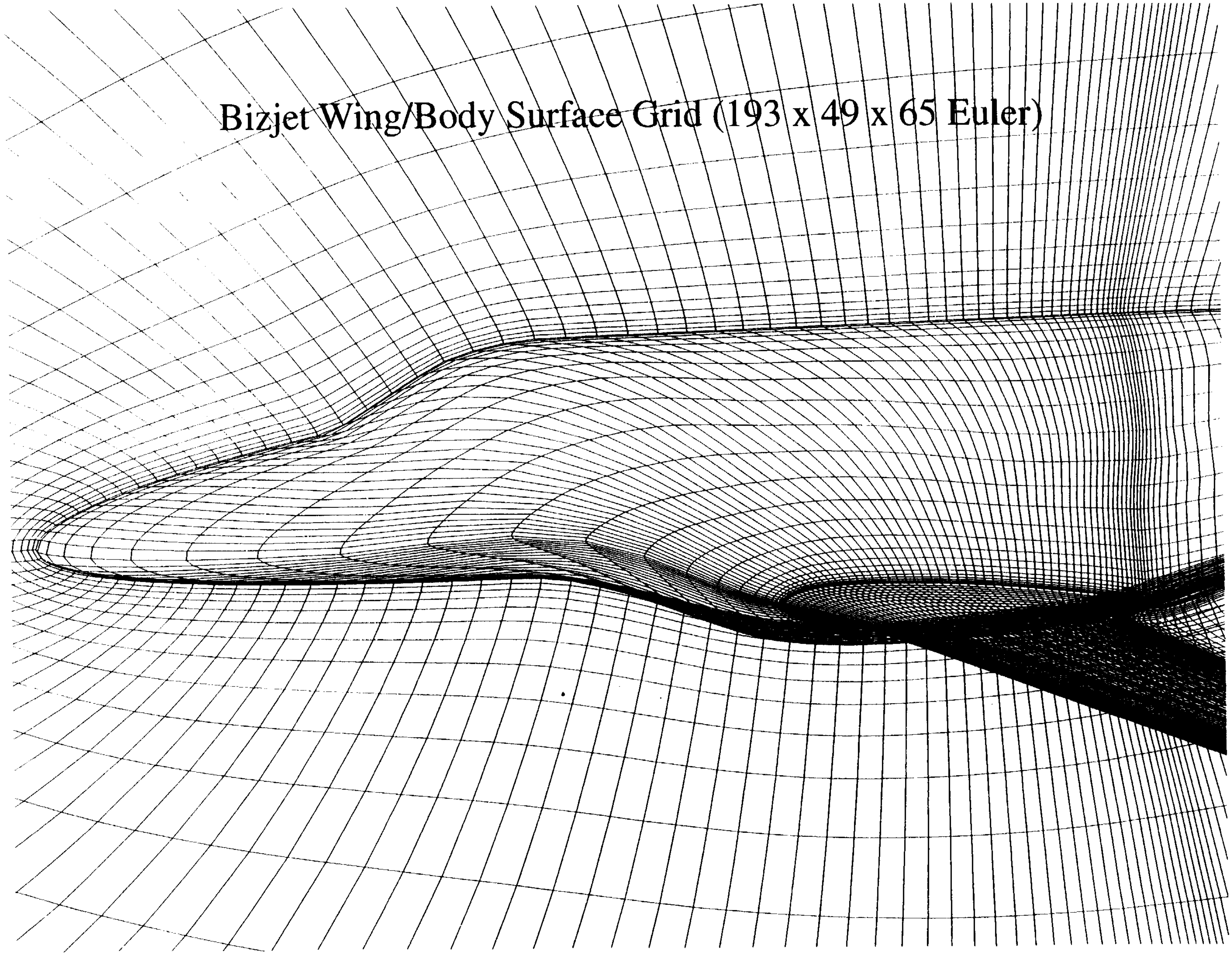
Bizjet Wing/Body Surface Grid (193 x 49 x 65 Euler)

Bizjet Wing/Body Surface Grid (297 x 97 x 65 Euler)

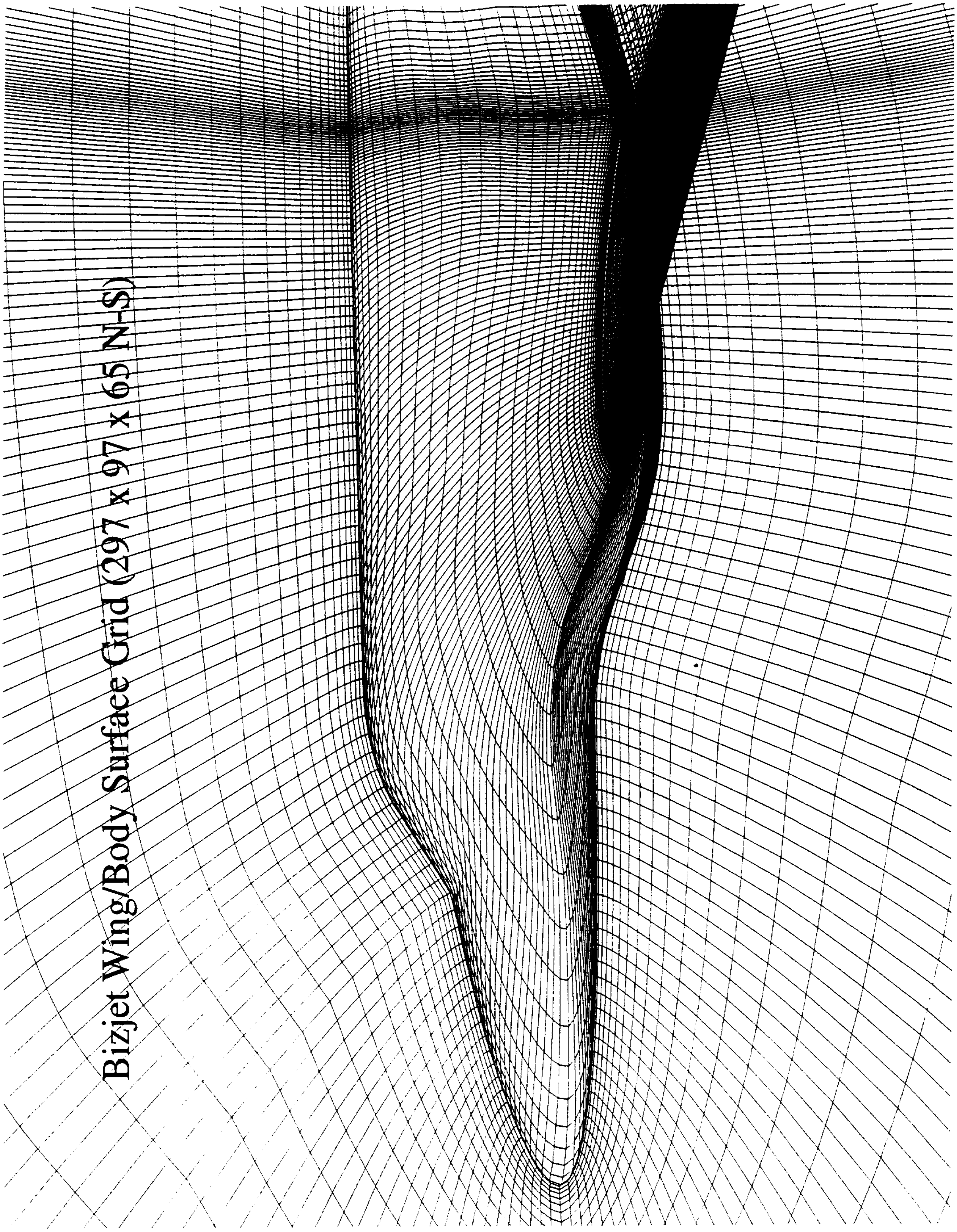

Bizjet Wing/Body Surface Grid (297 x 97 x 65 N-S)

Further Illustrations (4)

The **cross-stream** plots show i grid planes at approximately 80% wing x/c. The traditional spanwise resolution prevents the C-H topology from bunching k planes at the body surface, where the flow calculations are therefore strictly inviscid and rather crude at best. The two Euler-type grids achieve fair **orthogonality at the body surface** and symmetry plane ($k = 1$), but much of this is lost in the Navier-Stokes form as a result of pulling the radial points towards the wing. This is unlikely to have a significant effect, but quantitative results are not available.

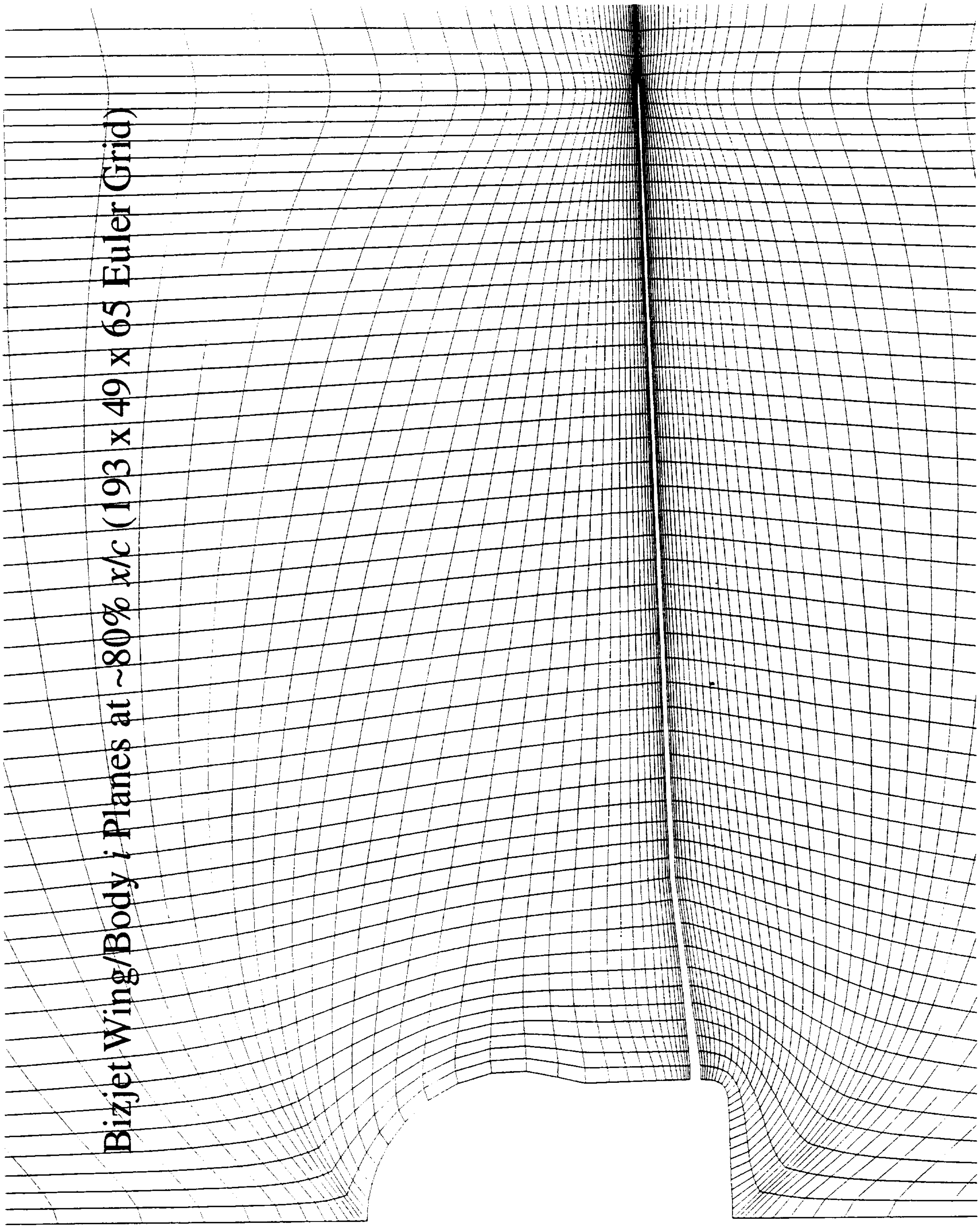

Bizjet Wing/Body i Planes at ~80% x/c (193 x 49 x 65 Euler Grid)

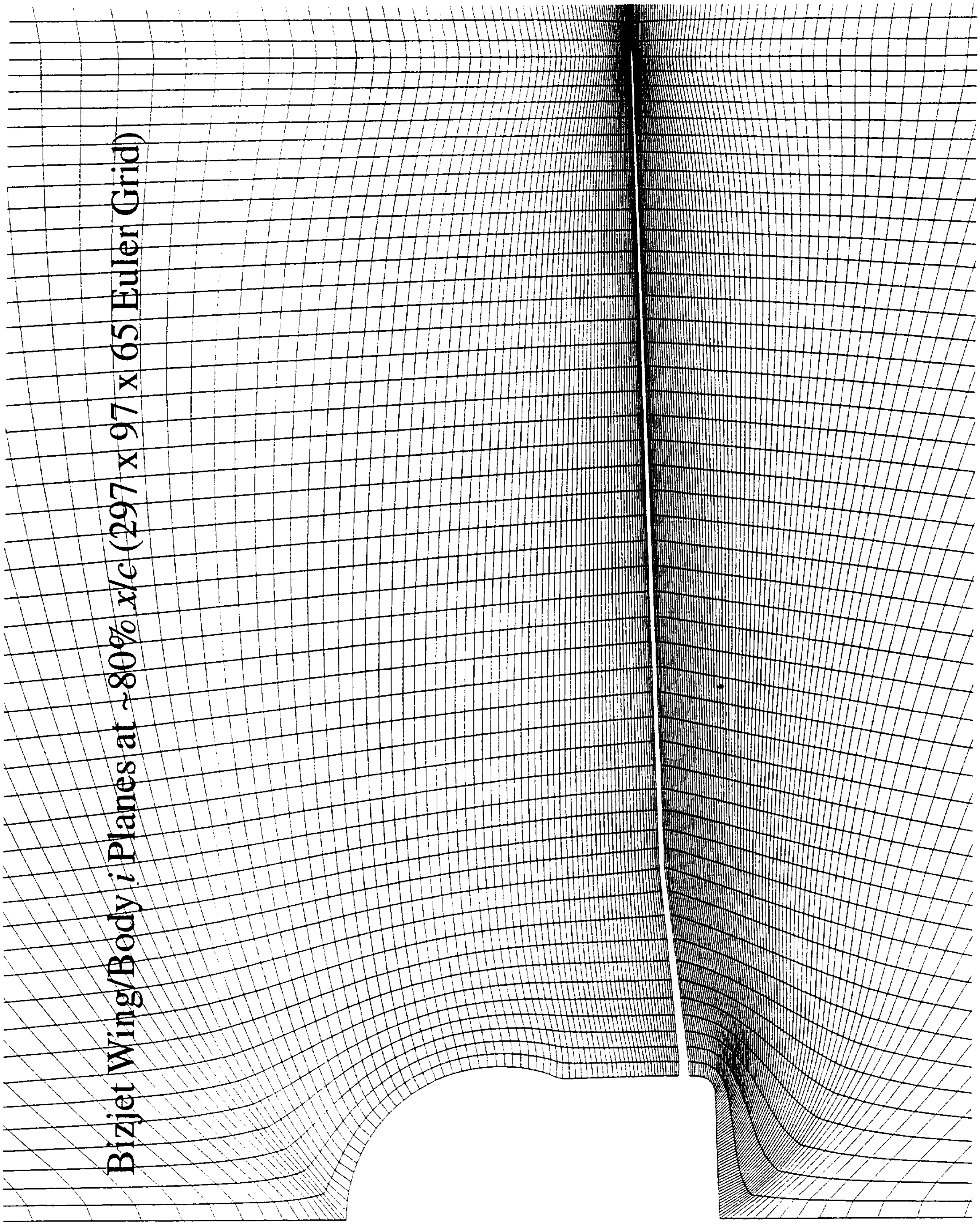

Bizjet Wing/Body i Planes at ~80% x/c (297 x 97 x 65 Euler Grid)

Bizjet Wing/Body i Planes at ~80% x/c (297 x 97 x 65 N-S Grid)

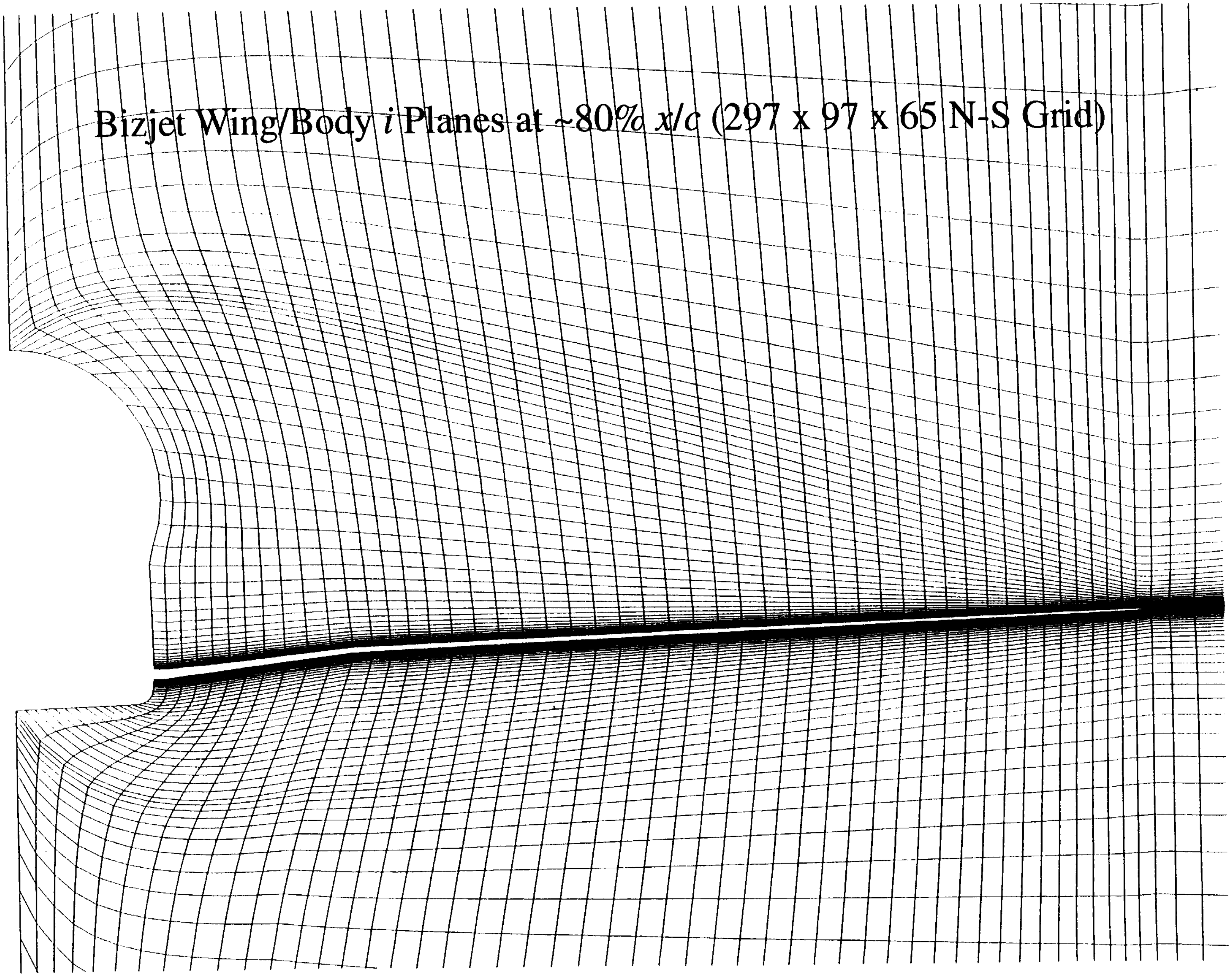

Further Illustrations (5)

Two sets of three wing-section plots show the **mid-span** k = 25 grid planes, where *ktip* = 49. In the first set, the influence of the fuselage is still apparent. The **excellent orthogonality** of the radial Euler grid lines at the **wing surface** attained by the 3D elliptic smoothing is fully preserved in the N-S grid. **Smoothness across** the three **interior** sub-block **faces** (above and below the trailing edge, and forward of the leading edge) is also respectable in all three cases.

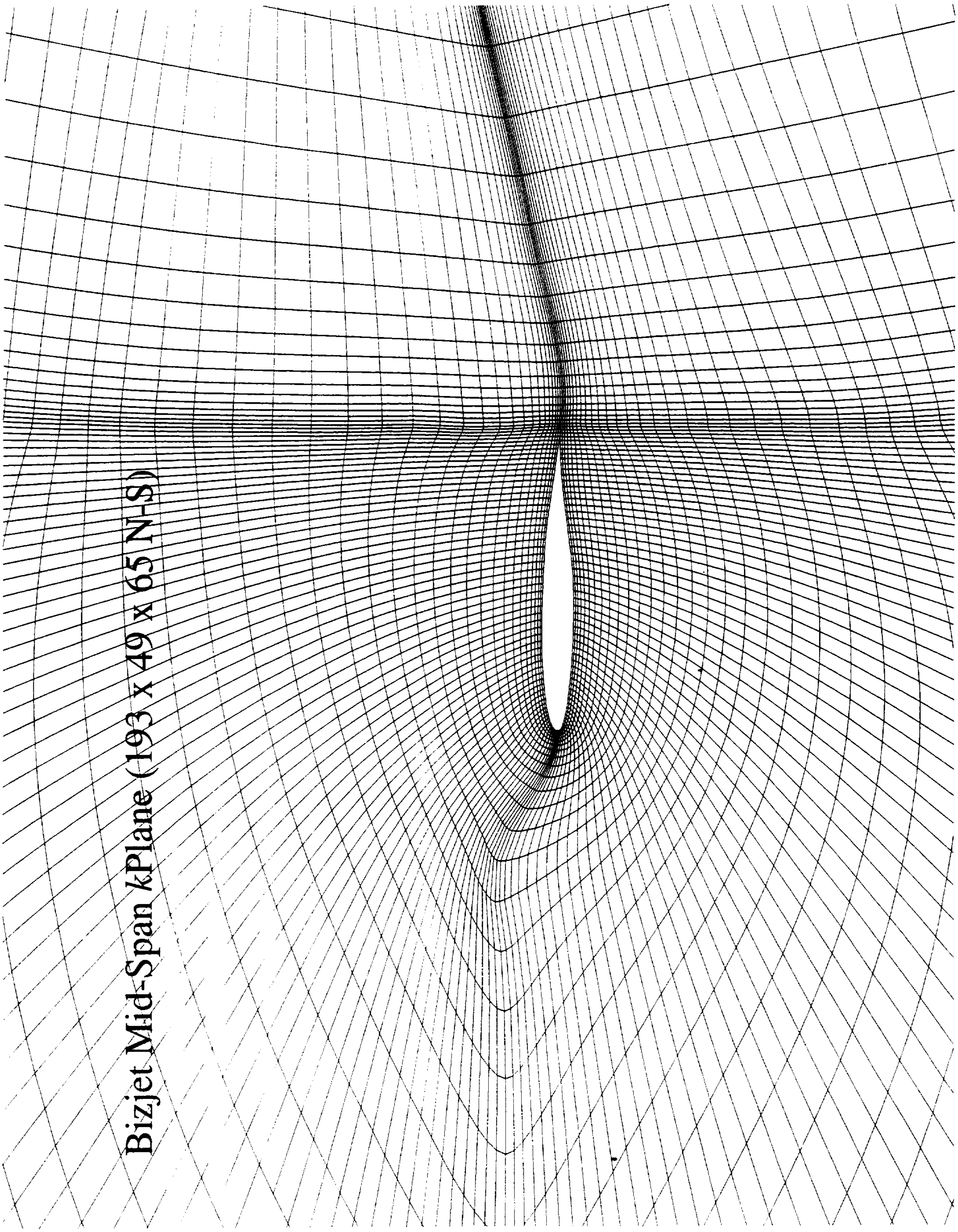

Bizjet Mid-Span *k*Plane (193 x 49 x 65 N-S)

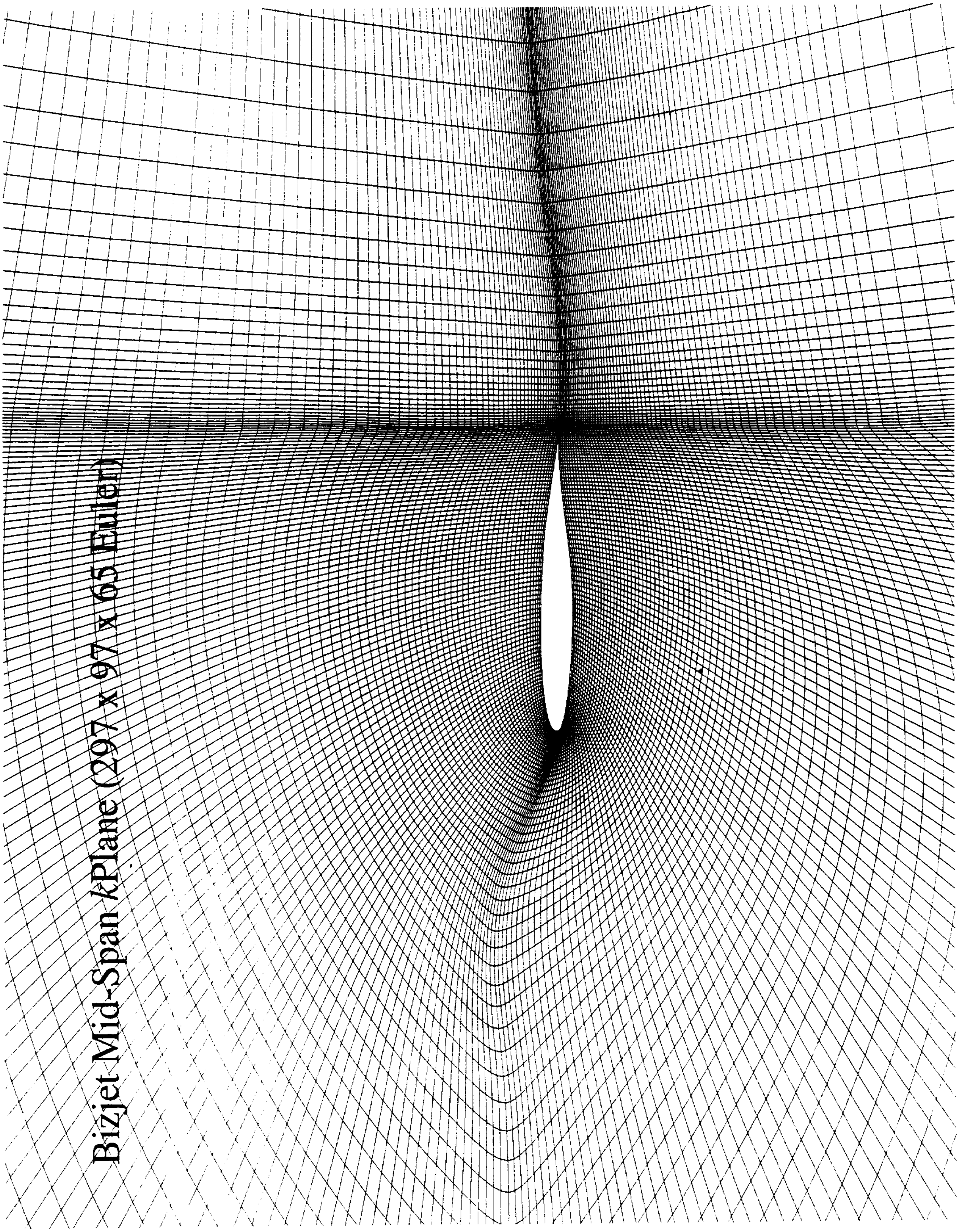

Bizjet Mid-Span *k*Plane (297 x 97 x 65 Euler)

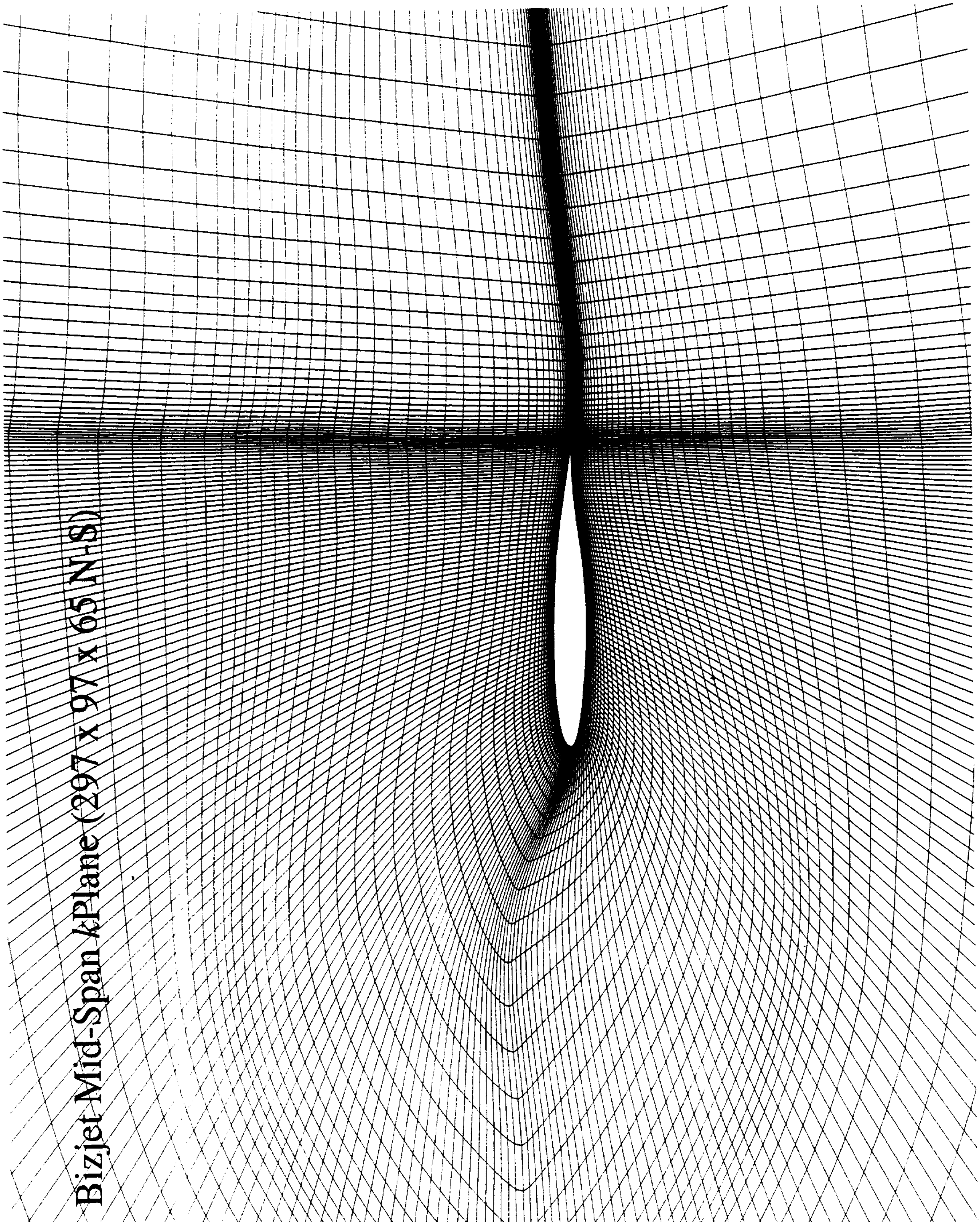

Bizjet Mid-Span *k*-Plane (297 x 97 x 65 N-S)

Further Illustrations (6)

This final set of three wing-section plots shows the **same mid-span** $k = 25$ grid planes, zoomed to show more of the boundary layer regions, with their excellent orthogonality.

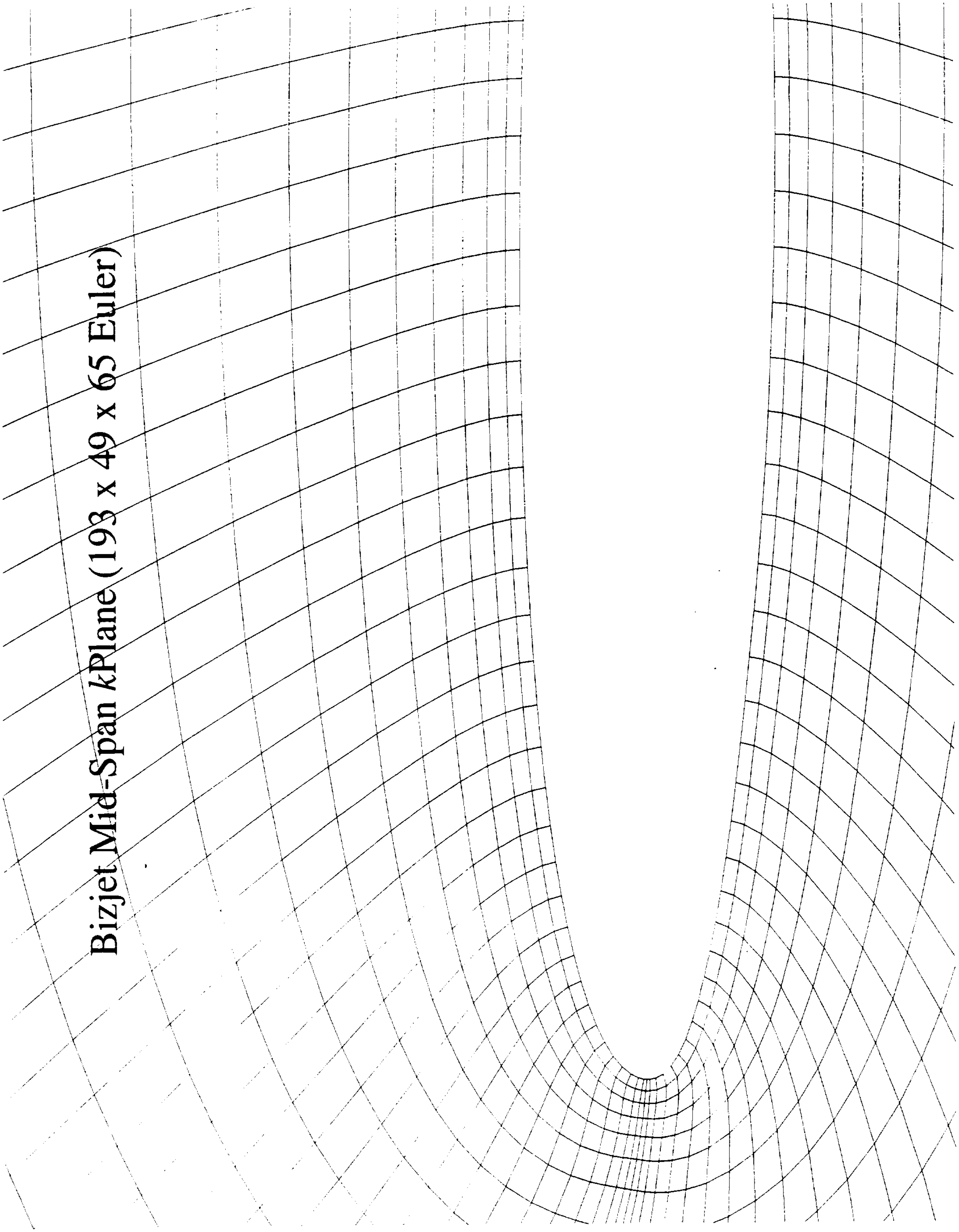

Bizjet Mid-Span *k*Plane (193 x 49 x 65 Euler)

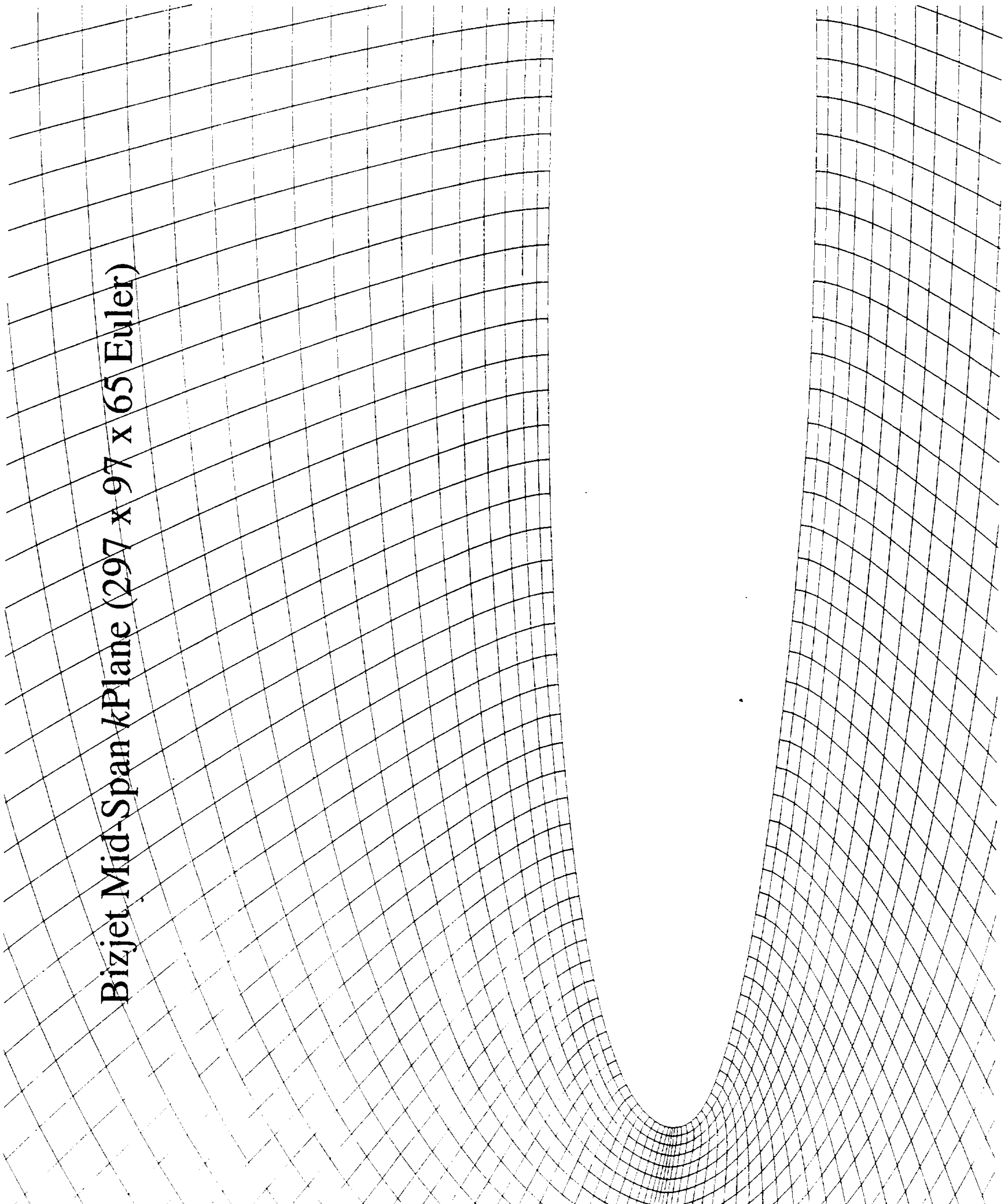
Bizjet Mid-Span *k* Plane (297 x 97 x 65 Euler)

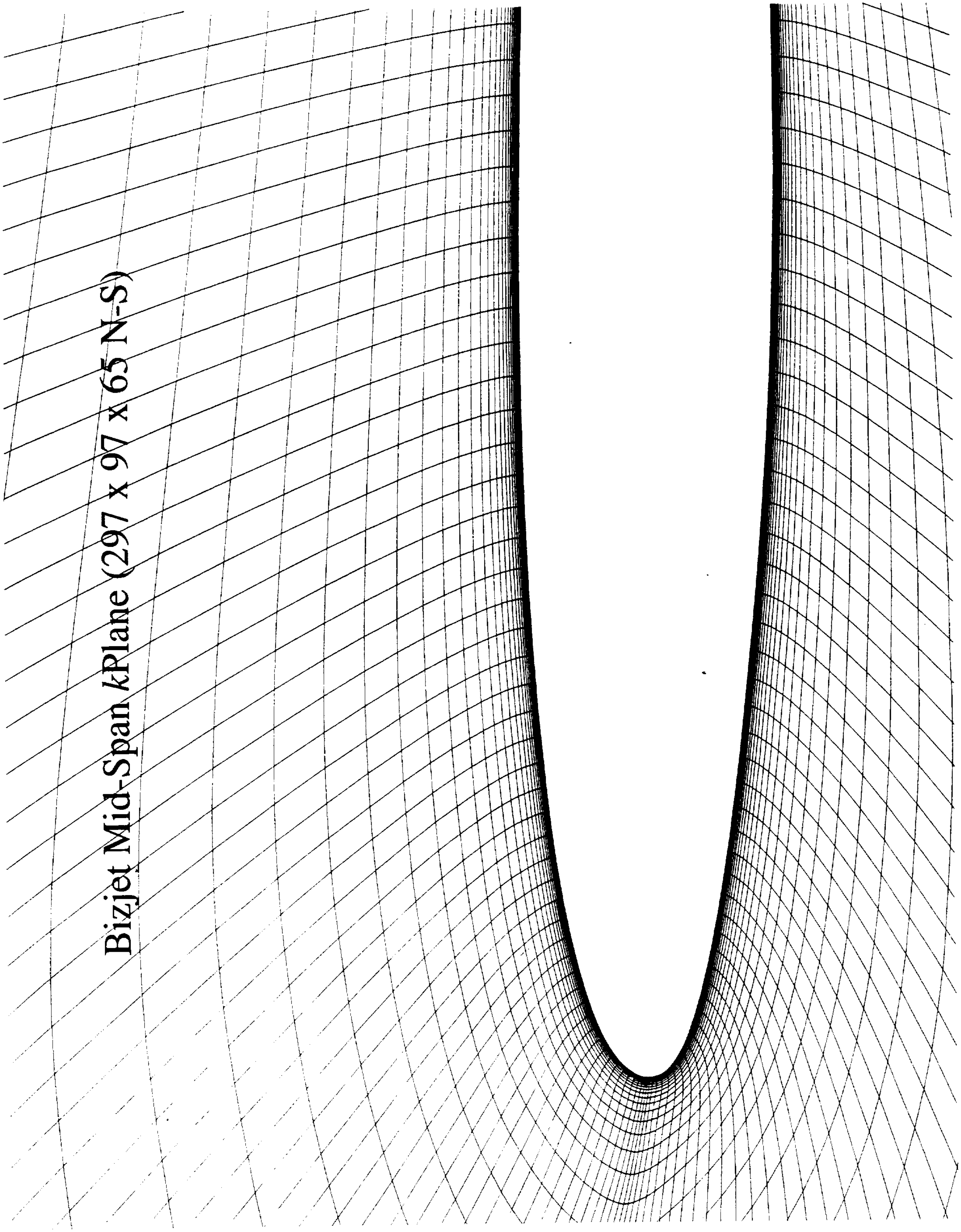
Bizjet Mid-Span *k*Plane (297 x 97 x 65 N-S)

Nacelle/Diverter Integration into the Design Optimization Process Using Pseudo, Warped, and Real Nacelles

HSR Airframe Technical Review

Anaheim, California February 8-12, 1999

Susan E. Cliff, NASA Ames Research Center
James J. Reuther, MCAT
David A. Saunders, Raytheon
Mark J. Rimlinger, Raytheon

Chart 2

CFD Performance Improvements Over TCA

The computational results of the optimized complete configurations, including nacelles and diverters, are presented in terms of drag count improvement compared with the TCA baseline configuration at Mach 2.4, $C_L = 0.1$, in chart 2. The three candidate designs are designated by the organization from which they were derived. ARC represents the Ames Research Center 1-03 design, BCAG represents the Boeing Commercial Aircraft Group's design from Seattle, and BLB represents the design from Boeing Long Beach. All CFD methods are in unanimous agreement that the Ames 1-03 configuration has the largest performance improvement, followed closely by the BCAG configuration, with a much smaller improvement attained by Boeing Long Beach.

The Ames design was obtained using the single-block wing/body code SYN87-SB with its "pseudo" nacelle option—an elaborate technique for incorporating nacelle/diverter effects into the design optimization process. This technique uses AIRPLANE surface pressure coefficient data with and without the nacelles/diverters. Further details of this method are described in subsequent charts.

It is reasonable to expect that further improvements could be achieved by including the "real" nacelles directly into the optimization process by use of the newly-developed multiblock optimization code, SYN107-MB, which can handle full configurations.

CFD Performance Improvements over TCA

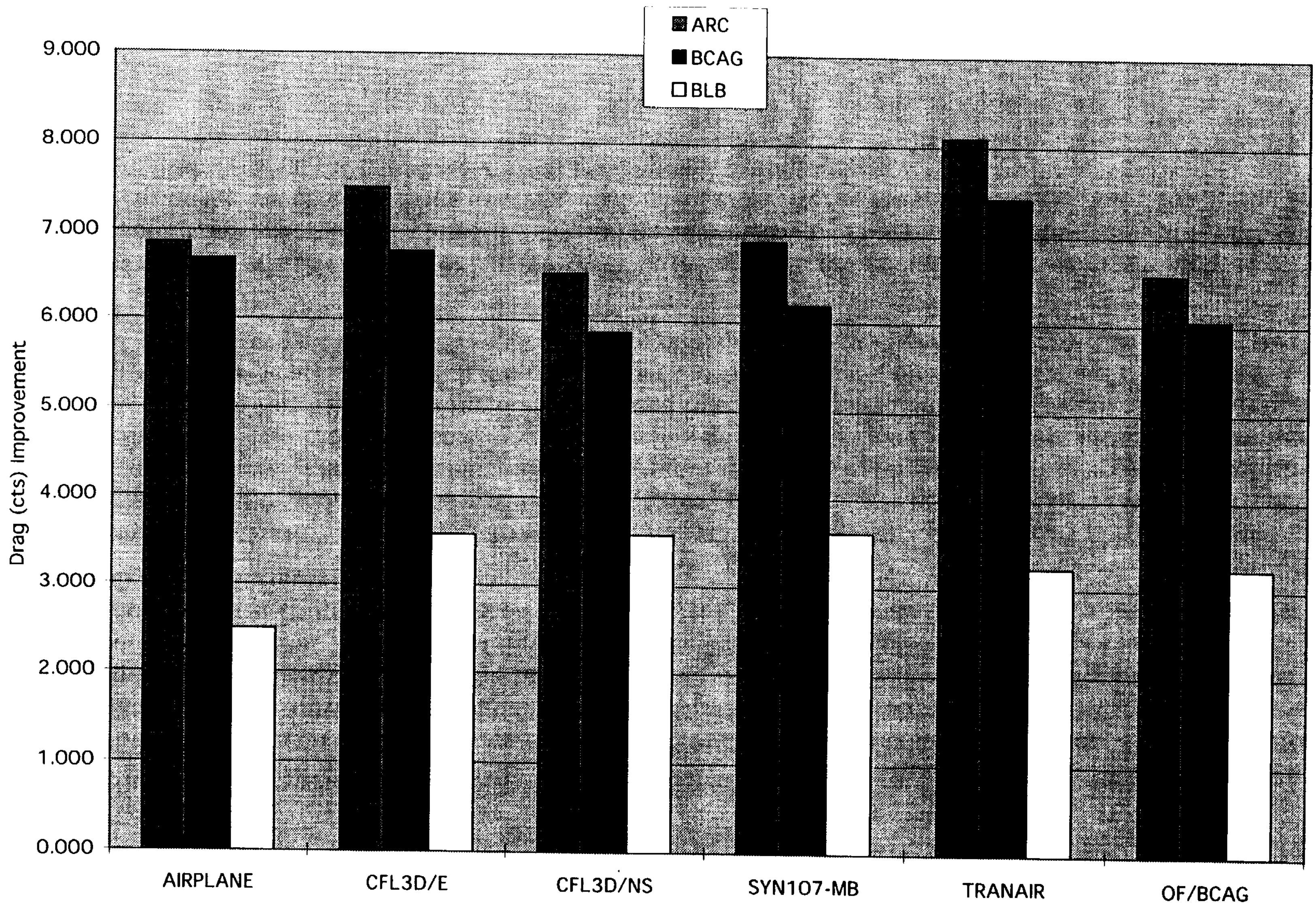

Methods of Incorporating Nacelle/Diverter Effects into the Design Process

Three methods have been used to incorporate the nacelle/diverter effects into the optimization procedures. The first method, which has been used extensively on several HSR configurations for the past several years, is called the "pseudo" nacelle method. This term means there are no nacelles or diverters actually present in the optimization process, but the effects of having nacelles and diverters present are incorporated by using information obtained from the differences between AIRPLANE solutions for wing/body and wing/body/nacelle/diverter configurations.

The second method utilized the original version of the multiblock optimization code, SYN107-MB, to incorporate the real nacelles into the optimization process by using a multiple-block mesh which includes the nacelles and diverters. During optimization of the wing, whereby design variables are applied to deform the wing surfaces, the grid blocks representing the nacelles may be deformed when the volume grid is perturbed to follow the shape of the wing. This method is referred to as the "warped" nacelle method, and was thought to be suitable for mature designs for which the majority of the wing shaping in the nacelle and diverter region of the wing had been performed with the "pseudo" nacelle method and only minor warping of the nacelles would be expected.

The third method, which required extensive work to incorporate the nacelle and diverter geometries properly into the optimization process, is called the "rigid" nacelle method. This more recent version of SYN107-MB ensures that as the lower wing shape evolves, each nacelle/diverter is moved as a rigid body during the process of maintaining the original diverter height at its leading and trailing edges.

Methods of Incorporating Nacelle/ Diverter Effects into the Design Process

- "**Pseudo**" - Nacelle/diverter effects derived from AIRPLANE W/B and W/B/N/D solutions incorporated into SYN87-SB W/B design
- "**Warped**" - Nacelle/diverter blocks present in SYN107-MB CFD grid, but may warp (shear) as wing shape changes
- "**Rigid**" - Real nacelle/diverter geometries included during wing design with SYN107-MB, with nacelle shapes and diverter heights at inlets maintained

Method Advantages and Disadvantages

A few advantages and disadvantages for each of the methods are given. The "pseudo" nacelle method has the advantage that each (single-block C-H) grid is generated automatically from sectional wing and body planar cuts within the optimization code. The need for AIRPLANE nacelles-on and -off solutions, which should be updated periodically to maintain the accuracy of the nacelle/diverter approximation, is a drawback. However, the AIRPLANE solution about a complete configuration is easier to obtain than a structured grid solution since the user only needs to generate an unstructured surface grid. After an initial surface triangulation is generated, the volume grid is generated automatically, and all subsequent surface meshes for intermediate designs can be morphed to the new geometry.

The "warped" nacelle method has the disadvantage of warping the nacelles during wing design. (The nacelle geometries are not actually present—they are merely represented in the initial multiblock mesh, and the corresponding grid blocks can become distorted as the lower wing shape changes.) This method was thought to be adequate for small perturbations in the nacelle and diverter regions, and was applied to the Ames 1-03 design which already had significant surface contouring in the nacelle and diverter regions. The method was used only during the period when SYN107-MB was being modified to maintain precise nacelle and diverter shapes during optimization.

The "real" nacelle method, which should be the most effective and robust method, has the advantage that the nacelles and diverters are modeled accurately within the optimization code, and their positions relative to the wing are maintained throughout the design process. This required extensive alterations to the AEROSURF geometry paneling package within SYN107-MB in order to find new diverter/wing and diverter/nacelle intersections as the nacelle/diverter positions are adjusted to follow lower wing shape changes, and to panel the wing surface around the diverter cutouts.

Method Advantages and Disadvantages

"Pseudo"

(+) Single-block C-H wing/body grids generated automatically

(-) AIRPLANE baseline & intermediate design solutions required, but volume grids generated automatically, and surface grid morphs to intermediate designs

"Warped"

(+) Multiblock method parallelizes and handles complex geometries

(+) Possible to get design improvement for small nacelle perturbations, but no advantage over "rigid" nacelle method

(-) Nacelle/diverter distortions coupled to wing & volume grid deformations

"Rigid"

(+) Nacelle/diverter geometry accurately modeled and maintained

(+) "Buoyancy" and "nacelle effects on the wing" are inherent in flow solutions

(-) Structured multiblock surface & volume grids of WBND required (4+ wks)

Procedure for Incorporating Pseudo Nacelle/Diverter Effects into SYN87-SB

The procedure for incorporating the pseudo nacelle/diverter effects into SYN87-SB requires several steps in order to model both the "nacelle on wing" and "wing on nacelle" effects properly. The first step is to obtain an AIRPLANE solution for the complete configuration with nacelles and diverters at the design angle of attack. This angle of attack is the angle which provides the design lift coefficient for the complete configuration. After arriving at the design alpha, α_d, AIRPLANE is run without nacelles and diverters at this same angle of attack. These two solutions are used to provide the third step whereby the "wing on nacelle" effects, also referred to as the "buoyancy effects", are incorporated into SYN87-SB. The external surface geometry files and surface pressure coefficients obtained for the nacelle and diverter are input into SYN87-SB. The geometric surfaces are used to interpolate the effects of the wing changes onto the nacelles. As the flow field changes below the wing in the vicinity of the nacelles during optimization, the changes in the pressures are measured by interpolating the flow solution onto the AIRPLANE surface nacelle and diverter geometries to establish a change in forces on the nacelles which captures the "wing on nacelle" effects. The two AIRPLANE solutions are also used to capture the "nacelle on wing" effects, whereby the differences in the pressure distributions on the lower surface of the wing with and without nacelles and diverters are interpolated onto the SYN87-SB structured wing/body grid. The accuracy of both types of effects deteriorates as the wing shape evolves, so periodic updates are required for the data input from AIRPLANE. The next step is to optimize using D/L as the objective function, but prior to this a mini-polar which includes the design lift coefficient for a single-point design must be obtained to find a minimum C_D so that $(L/D)_{max}$ occurs at α_d. This minimum C_D is included in the drag çoefficient computations so that true improvements to L/D can be attained. Without this shift in the drag coefficient value, the optimization code can "exploit the design" by modifying the lift coefficient to find the $(L/D)_{max}$. The final step is to update the nacelle/diverter information periodically by evaluating intermediate designs, with and without nacelles and diverters, using AIRPLANE. The frequency with which the nacelle/diverter effects should be updated is not known. However, since these effects will vary as the configuration shape is modified, they should be updated as often as practical.

Procedure for Incorporating Pseudo Nacelle/ Diverter Effects into SYN87-SB

- Compute AIRPLANE W/B/N/D solutions to obtain α_d (design alpha) for cruise C_L
- Obtain AIRPLANE W/B solution at α_d
- Transfer AIRPLANE information to SYN87-SB

⇨ "wing on nacelle" or "buoyancy" effects

  a) nacelle/diverter external surface geometry files

  b) nacelle/diverter surface Cps

⇨ "nacelle on wing" effects

  a) ΔC_ps of wing lower surface ($C_{p_{W/B/N/D}}$ - $C_{p_{W/B}}$) at α_d

- Optimize at α_d or $(L/D)_{max}$ (after adjusting $C_{D_{min}}$)
- Update nacelle/diverter information with W/B & W/B/N/D AIRPLANE solutions for intermediate designs

Chart 6

AIRPLANE Nacelle/Diverter Grids and Solutions Used for the "Pseudo" Nacelle Method

This figure illustrates the actual nacelle and diverter grids that were extracted from the AIRPLANE wing/body/nacelle/diverter solutions. The nacelles have a very dense distribution of grid points over the entire surface, particularly on the upper surfaces of the nacelles. This very refined grid was necessary to obtain accurate surface triangulations using the former AIRPLANE mesh generation code, MESHPLANE. The diverters were somewhat coarsely gridded since adding additional points to the diverter also caused triangulation difficulties in MESHPLANE. The current version of the AIRPLANE mesh generator, MESH3D, does not have these limitations. The surface pressure distributions were integrated during optimization to obtain force and moment corrections to the wing/body coefficients computed by SYN87-SB.

AIRPLANE Nacelle/Diverter Grids and Solutions Used for "Pseudo" Nacelle Method

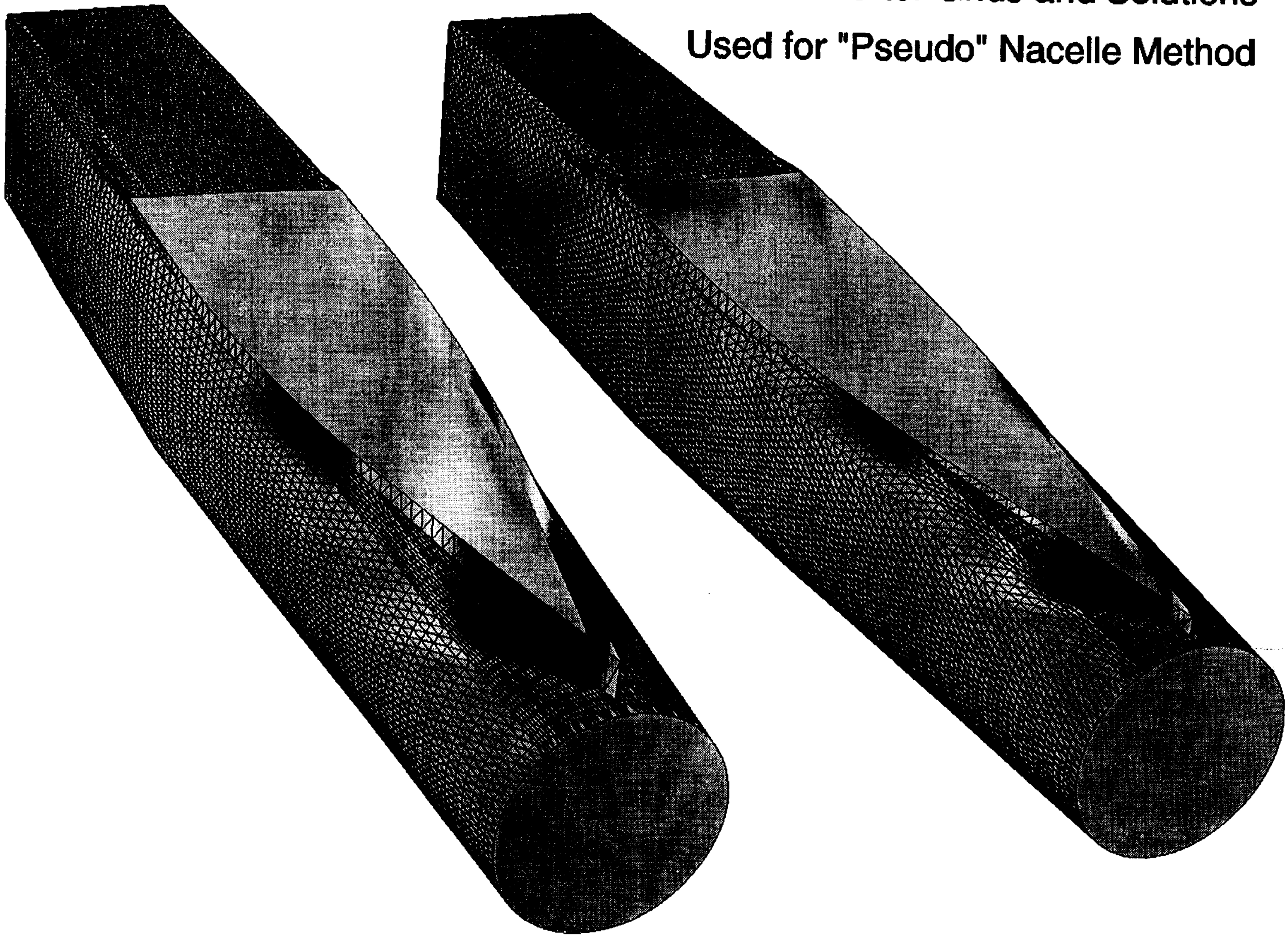

Chart 7

Incorporation of "Nacelle on Wing" Effects Into SYN87-SB, Mach 2.4, alpha 3.756

This figure compares a lower wing surface solution from SYN87-SB (including the nacelle/diverter correction) with the corresponding wing/body/nacelle/diverter AIRPLANE unstructured grid and solution. The AIRPLANE solution (lower half of the picture) has the nacelles and diverters removed in order not to obscure the grid on the wing in the vicinity of the nacelles. The AIRPLANE grid is very dense on the lower surface, producing the crisp nacelle shocks shown. The shocks in the SYN87-SB solution (upper half of picture) are not as crisp because of the coarser grid used. A denser grid would capture the nacelle effects more accurately, but may also produce a more aggressive shaping of the lower wing surface that may be less likely to hold up in a viscous flow-field.

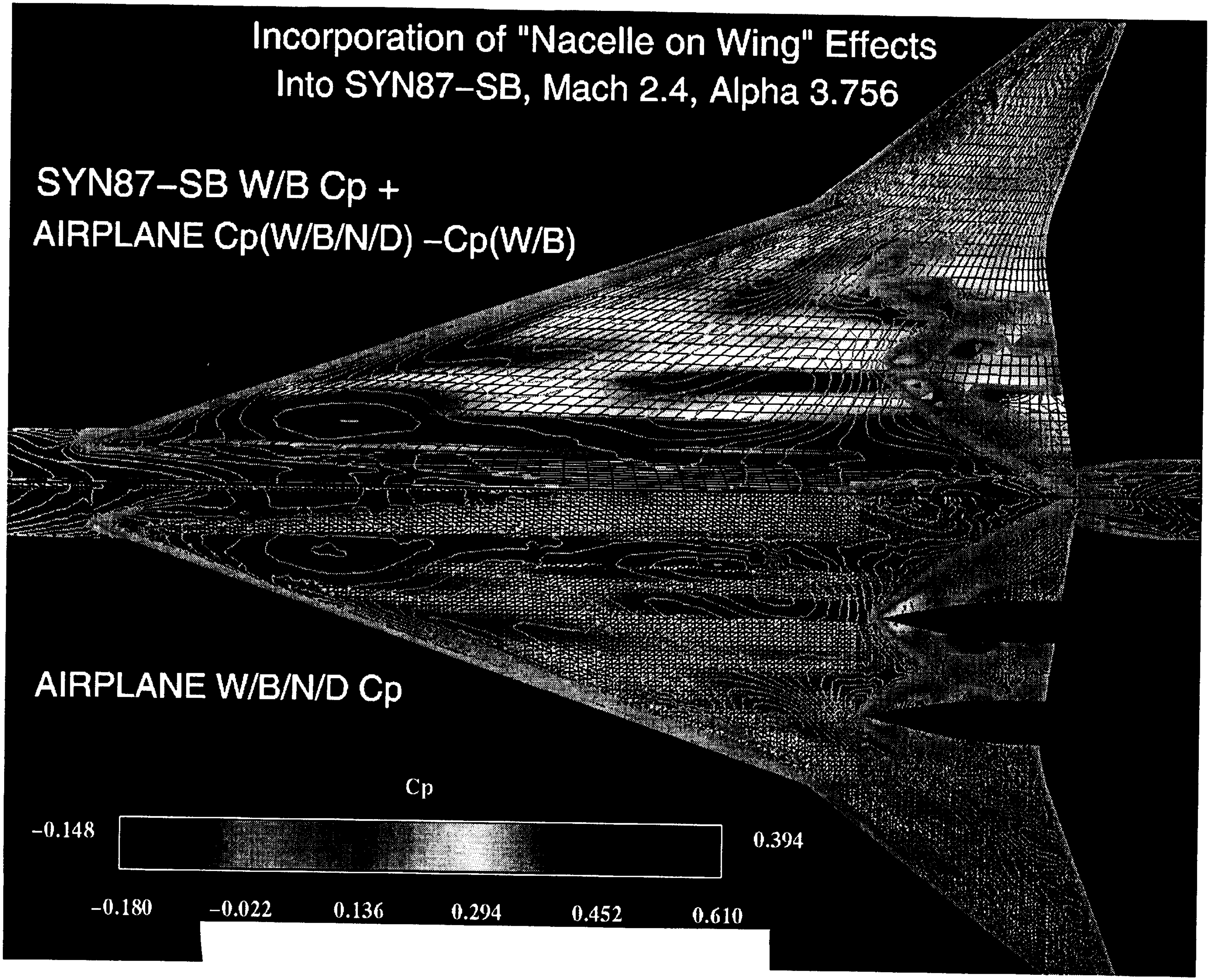

Incorporation of "Nacelle on Wing" Effects
Into SYN87–SB, Mach 2.4, Alpha 3.756
SYN87–SB W/B Cp +
AIRPLANE Cp(W/B/N/D) –Cp(W/B)
AIRPLANE W/B/N/D Cp
Cp
–0.148
0.394
–0.180
–0.022
0.136
0.294
0.452
0.610

Intermediate Design Cps: AIRPLANE Mach 2.4, alpha 3.756

The AIRPLANE lower surface pressure coefficients are shown for the intermediate designs computed during the design of the Ames 1-03 configuration. This chart illustrates the importance of updating the nacelles-on/-off pressure data used by SYN87-SB. The nacelle shocks are weakened during the course of the design process, and the changes between designs should eventually become negligible. Note that both the shocks which emanate from the nacelles and the shocks reflected by the adjacent nacelle continue to be weakened during optimization.

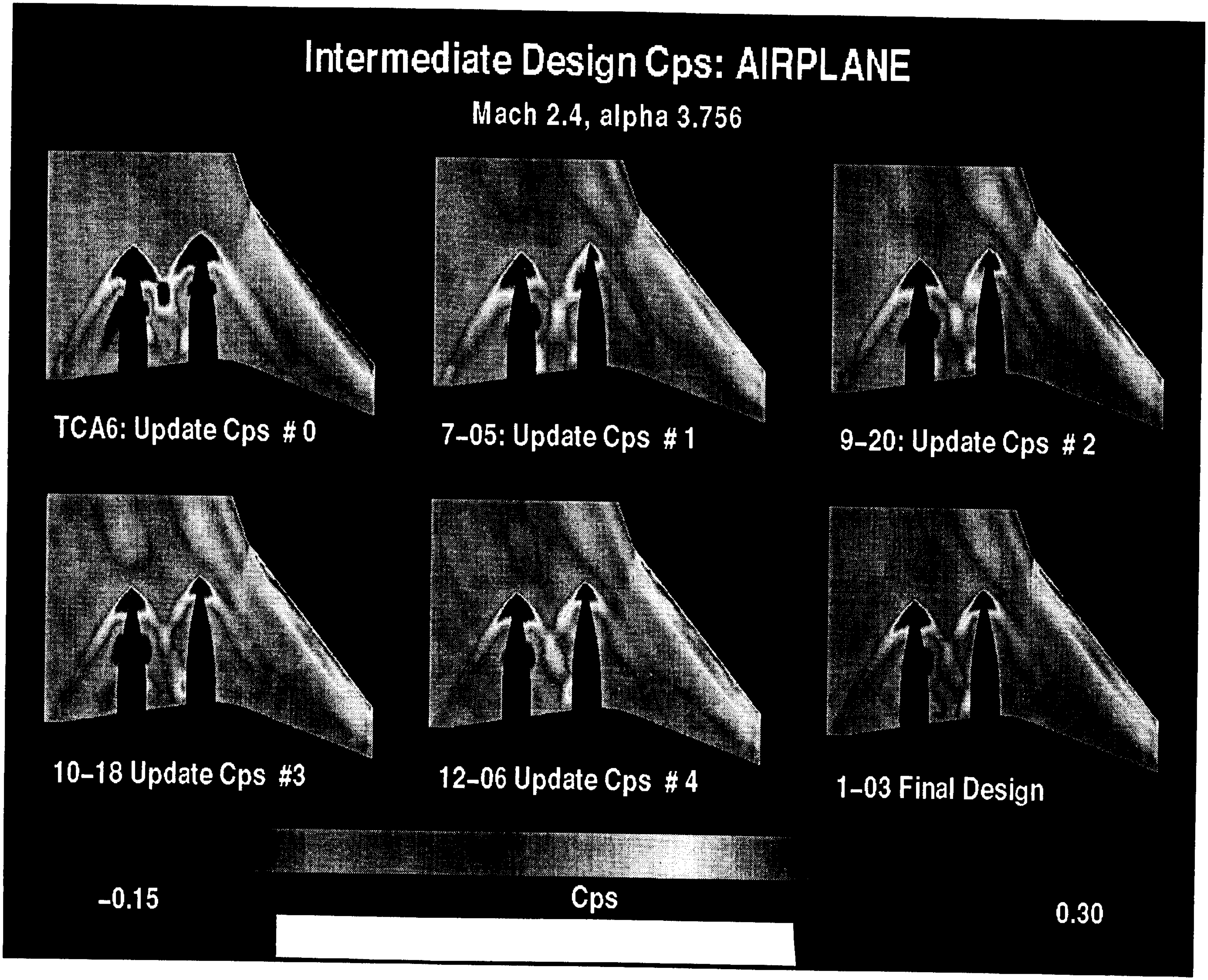
Intermediate Design Cps: AIRPLANE
Mach 2.4, alpha 3.756
TCA6: Update Cps # 0
7–05: Update Cps # 1
9–20: Update Cps # 2
10–18 Update Cps #3
12–06 Update Cps # 4
1–03 Final Design
–0.15
Cps
0.30

Chart 9

Baseline TCA: AIRPLANE Solution Mach 2.4, alpha 3.6

The baseline TCA AIRPLANE solution in the vicinity of the nacelles is shown. Strong shocks are evident on the nacelles and lower surface of the wing. Compare these pressures with the following figure of the Ames 1-03 configuration at the same lift coefficient.

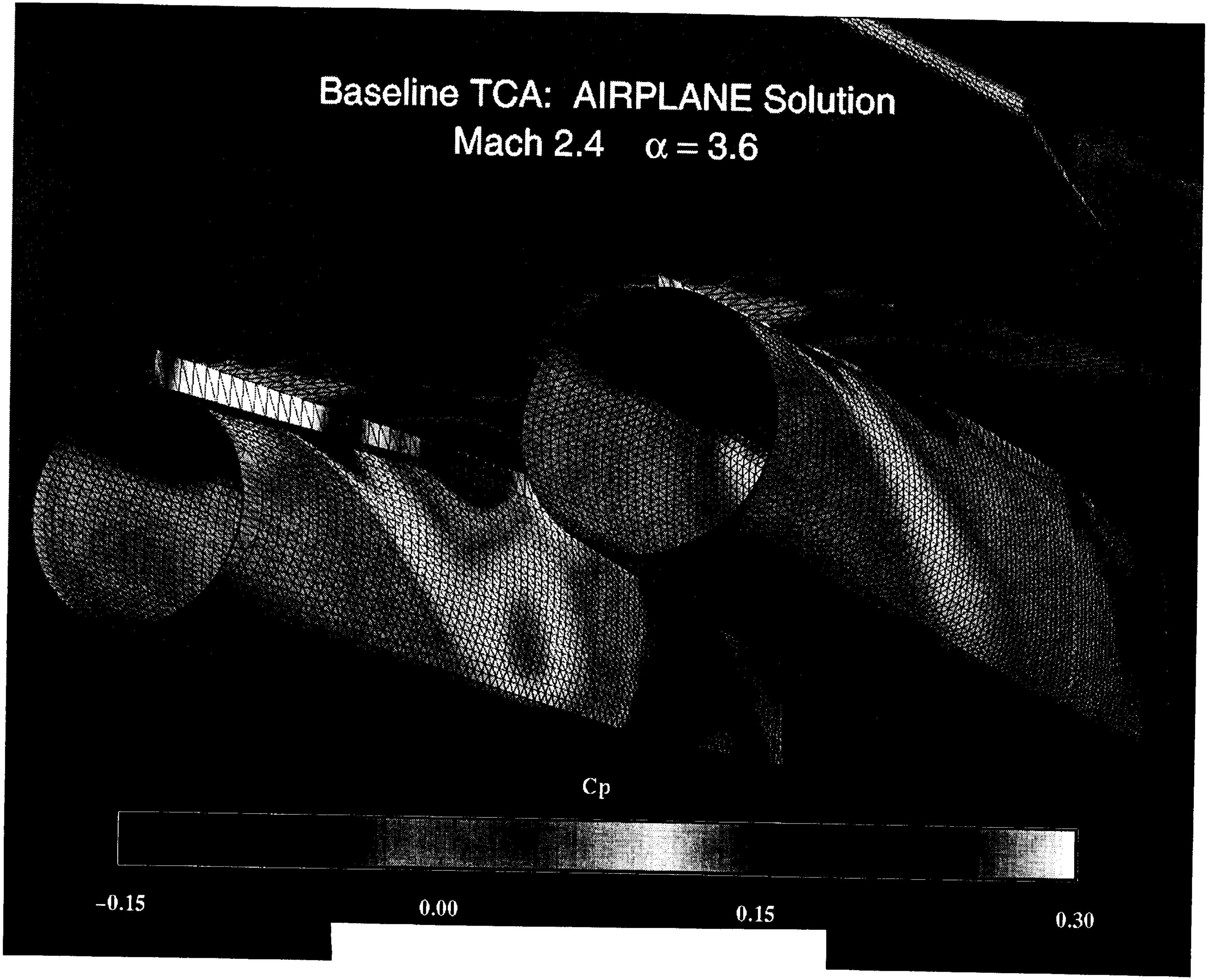
Baseline TCA: AIRPLANE Solution
Mach 2.4   α = 3.6
Cp
−0.15
0.00
0.15
0.30

Chart 10

Ames 1-03: AIRPLANE Solution Mach 2.4, alpha 3.756

This figure shows significant reductions in the nacelle shock strengths on the lower surface of the wing and on the sides of the nacelles. This reduction in shock strength is a result of extensive shaping of the wing in this region. This chart should be compared with the previous chart of the baseline TCA configuration. This chart and the previous chart show the effectiveness of the pseudo nacelle method in reducing the shocks on the wing lower surface and the nacelles.

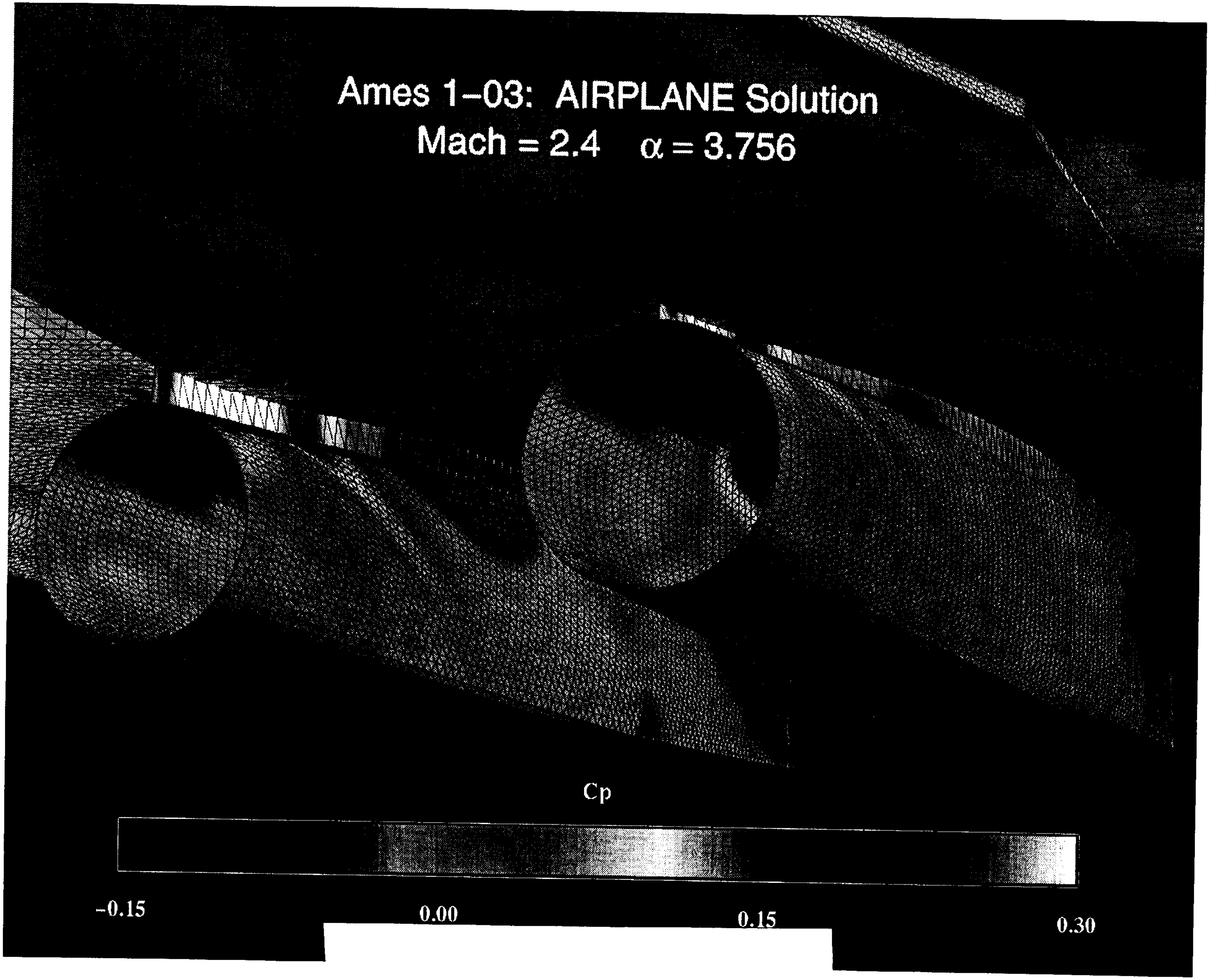
Ames 1–03: AIRPLANE Solution
Mach = 2.4 α = 3.756
Cp
-0.15
0.00
0.15
0.30

Chart 11

Warped Nacelle Method

The Ames 1-03 design was further optimized using an interim version of the newly developed SYN107-MB. Multiple-block grids about the Ames 1-03 complete with nacelles and diverters were generated. The multiblock code was being enhanced to maintain the contours of the original nacelle shape, but this required extensive modification to the code and several months of code development. The code could be used during this interim period of time, but the nacelle shape could be distorted as a result of following the shape changes applied to the wing. This was thought to be acceptable for the mature design of the Ames 1-03 since the wing was already extensively modified, and only a limited warping of the nacelles was expected.

Warped Nacelle Method

- Used during interim while multiblock code extended to maintain shape of nacelle/diverter geometries
- Applicable to mature designs where the majority of wing shaping is complete and limited nacelle warping is expected
- Initial multiblock CFD grid includes nacelles/diverters as for rigid method, but perturbed grids can distort nacelle blocks

Chart 12

SYN107-MB W/B/N/D Surface Grid and Solution Used with "Warped" and "Rigid" Nacelle Methods

The figure shows the multiblock surface grid and solution from SYN107-MB. This grid was used for the warped and rigid nacelle methods. Note that the grid on the nacelles is much coarser than in the AIRPLANE computations.

SYN107-MB W/B/N/D Surface Grid and Solution Used with "Warped" and "Rigid" Nacelle Methods

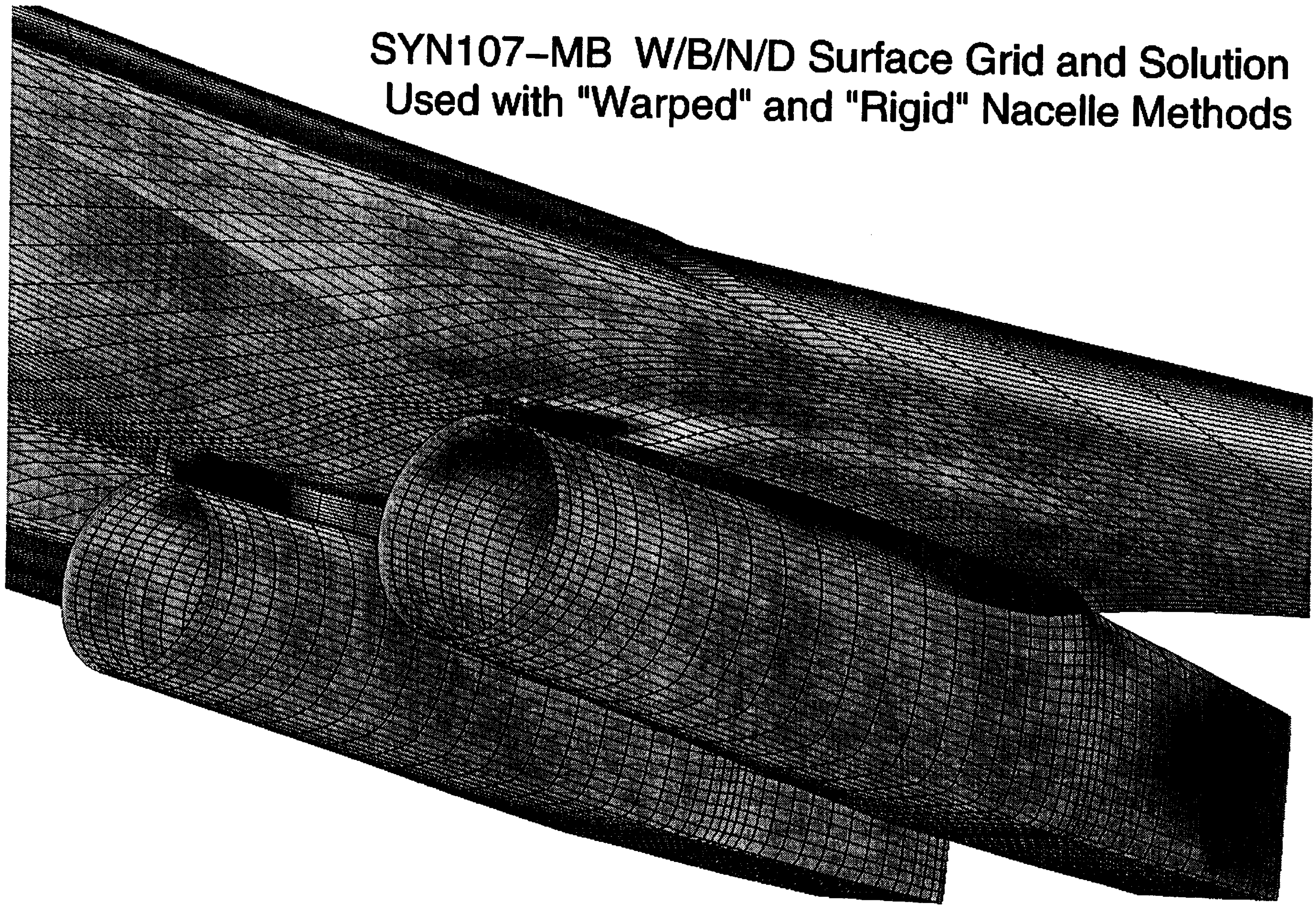

Chart 13

SYN107-MB Lower Surface Grid and Solution Used with "Warped" and "Rigid" Nacelle

The multiblock grid shown in the previous chart is shown in this chart with the nacelles and diverters removed in order to compare it with the single-block and AIRPLANE grids shown in chart 7. The SYN107-MB grid shown here is denser than the SYN87-SB grid but still much coarser than the AIRPLANE grid. The increased density of the grid relative to the SYN87-SB grid will cause a more aggressive shaping of the lower wing in the nacelle/diverter region.

SYN107–MB Lower Surface Grid and Solution Used with "Warped" and "Rigid" Nacelle Methods

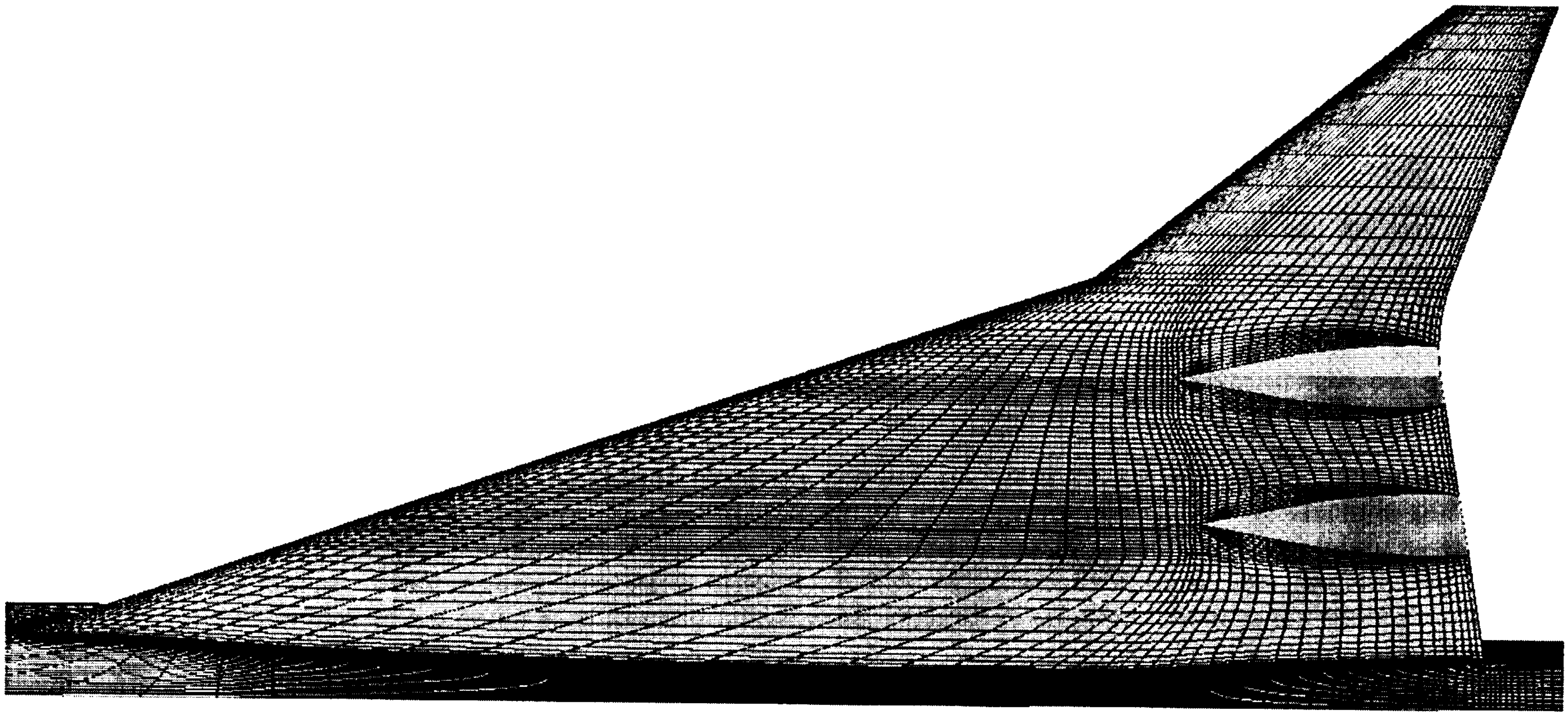

Pressure Drag Comparisons, Wing/Body/Nacelle/Diverter

This chart shows a drag reduction of approximately 1.3 counts was predicted by the warped nacelle method. This improvement was obtained after additional thickness and camber optimization was performed on the Ames 1-03 configuration. The baseline TCA computation is shown using Jameson's scalar dissipation scheme. The Ames 1-03 results are shown for both the scalar and CUSP (Convective Upwind and Split Pressure) dissipation schemes. The approximate 0.5 count shift in the drag between schemes is expected because the shocks are more crisply captured and the losses in total pressure at the leading edge of the wing are reduced with the CUSP dissipation scheme. The CUSP dissipation results are more accurate, but require more time to obtain a converged solution. The computation for the 6-08 design shown in the figure and all the optimization runs leading to this design used the CUSP dissipation method. The improvement for the 6-08 design is therefore measured against the Ames 1-03 CUSP solution.

SYN107-MB Warped Nacelle Design Comparison, Wing/Body/Nacelle/Diverter
M=2.4, no internal or base nacelle forces, entire fuselage

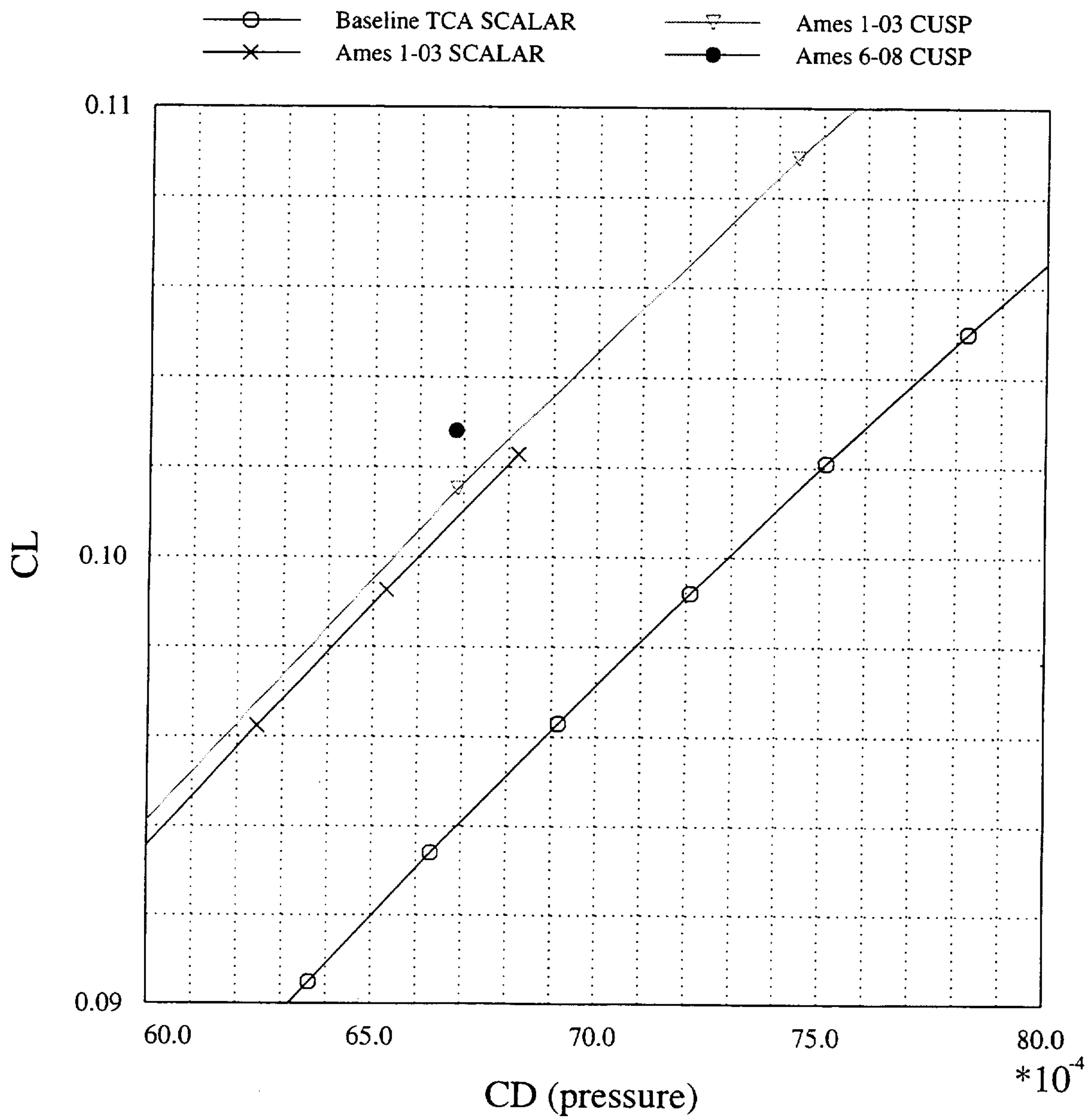

Chart 15

Wing/Body Pressure Drag Comparisons (Ames 6-08 vs. Ames 1-03)

The wing/body component forces for the Ames 1-03 and the 6-08 (warped nacelle) designs were taken from the output files and plotted to show that a drag reduction of only about 0.25 counts improvement is attributable to the changes in pressures on the wing.

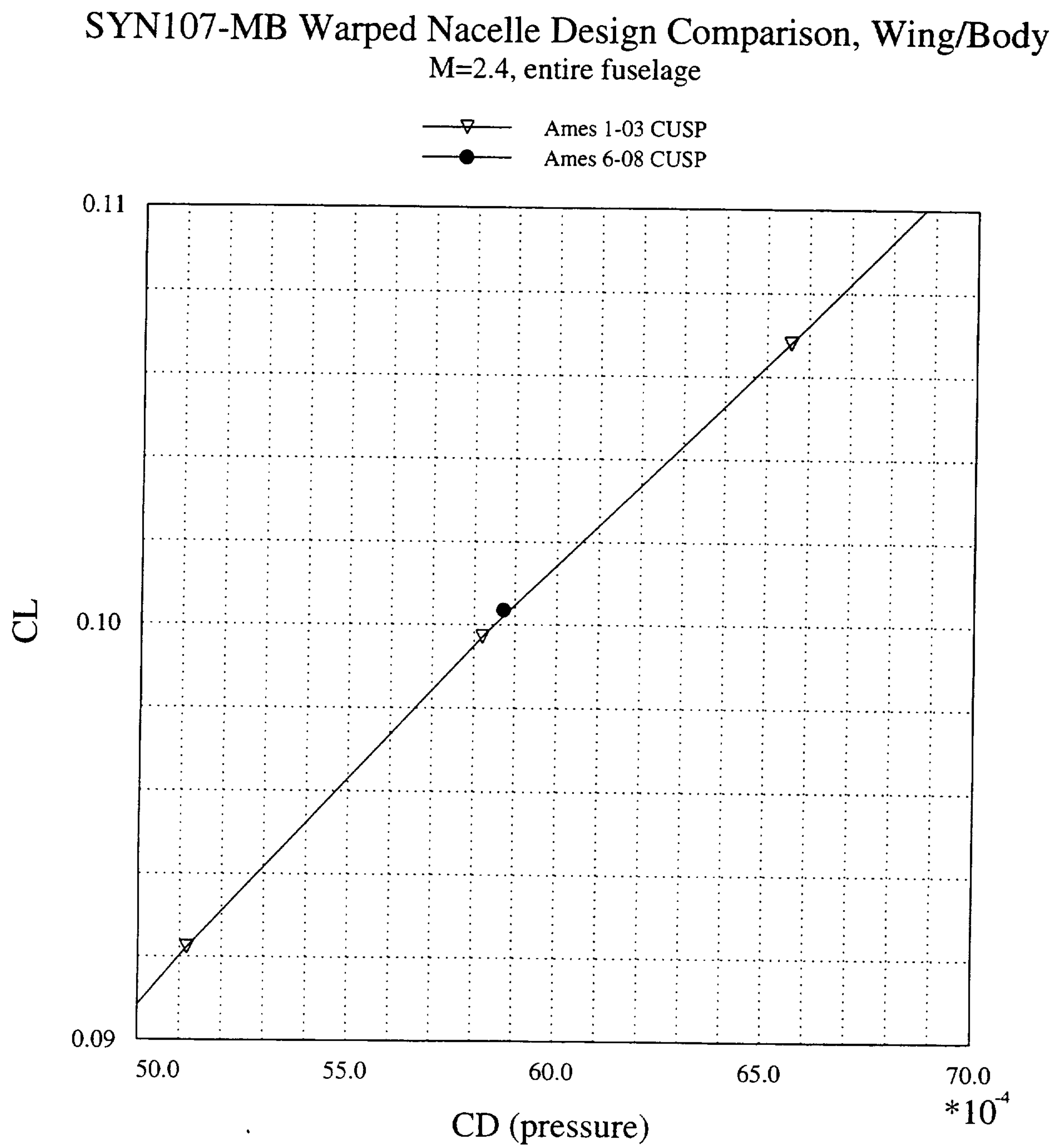
SYN107-MB Warped Nacelle Design Comparison, Wing/Body
M=2.4, entire fuselage
Ames 1-03 CUSP
Ames 6-08 CUSP
0.11
0.10
0.09
CL
50.0
55.0
60.0
65.0
70.0
*10^-4
CD (pressure)

Chart 16

Nacelle/Diverter Pressure Drag Comparisons (Ames 6-08 vs. Ames 1-03)

The nacelle and diverter component forces are plotted similarly for the Ames 1-03 and 6-08 warped nacelle design. Note that more than a count of drag improvement is attributable to the nacelles and diverters. This unfortunately indicates that the wing was being shaped to warp the nacelles in a beneficial way. However, the nacelles must be constrained to maintain their original shape and thus the majority of this improvement cannot be realized.

SYN107-MB Warped Nacelle Design Comparison, Nacelle/Diverter

M=2.4

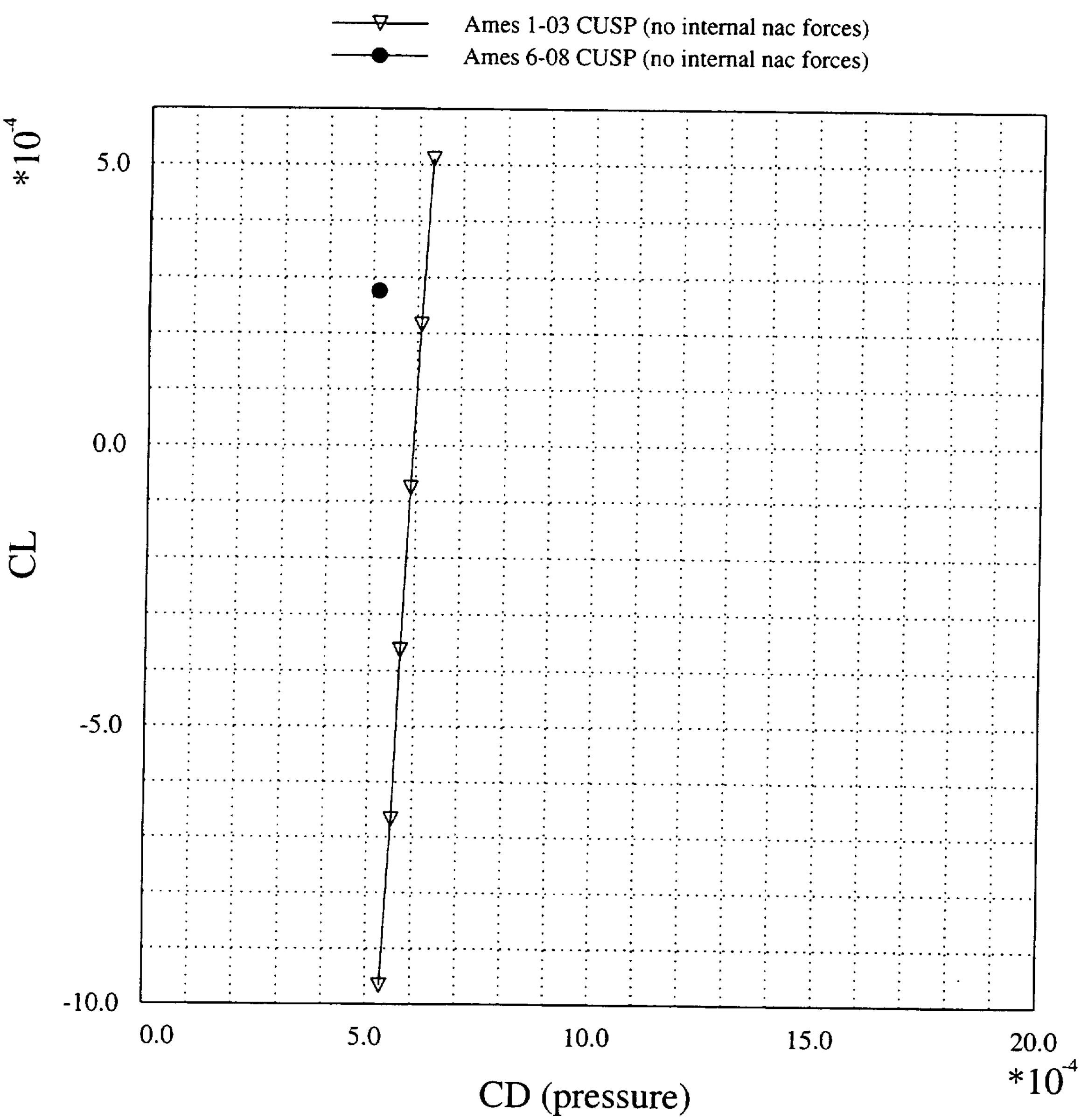

Chart 17

Geometry and Pressure Distribution Comparisons (Ames 980608 vs. Ames 1-03, X=2500 and X=2600)

Comparisons of the Ames 1-03 and 6-08 (980608) warped nacelle design geometries and pressure distributions at X=2500 and X=2600 are shown in this figure. The pressure distributions are displayed for just the wing/body, whereas the complete geometry including the nacelles and diverters are depicted in the figure. The wing exhibits aggresssive shaping in this region.

Geometry and Pressure Distribution Comparisons
Ames 980608 vs. Ames 1-03, X=2500 and X=2600

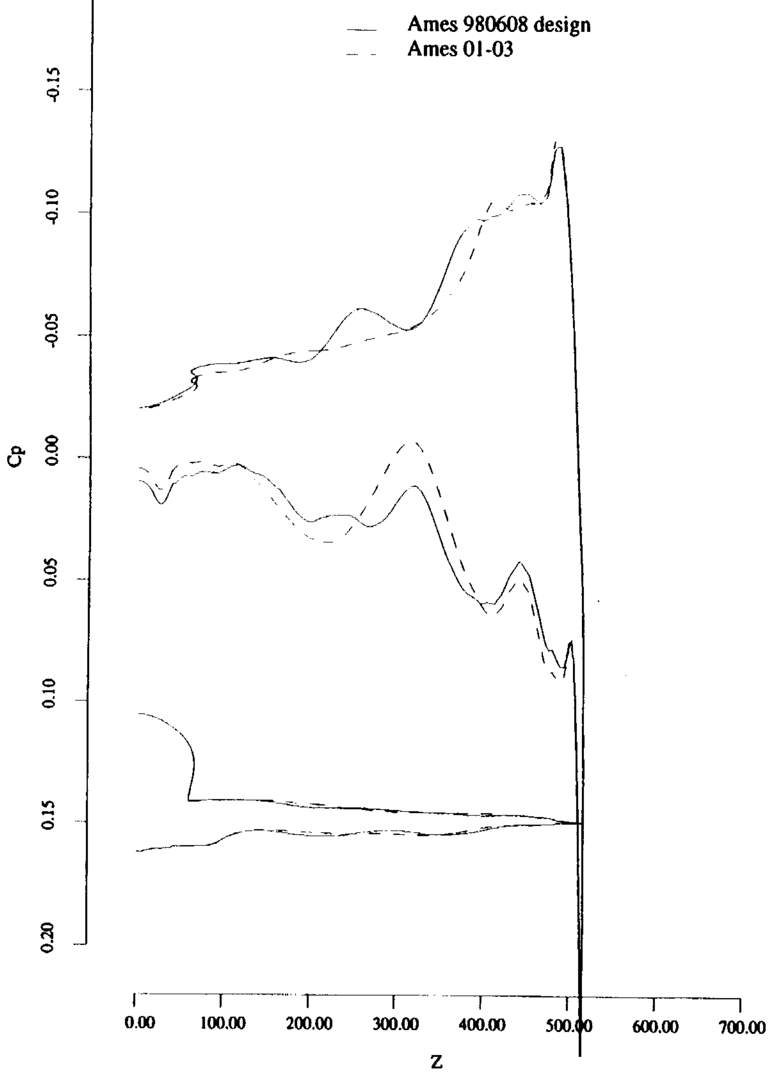

Ames 980608 vs. Ames 01-03

Mach	Alpha	Re	CL	CD	X
2.400	3.756	0.00E+00	0.10407	0.00561	2500.000
2.400	3.756	0.00E+00	0.10327	0.00549	2500.000

Geometry and Pressure Distribution Comparisons
Ames 980608 vs. Ames 1-03, X=2500 and X=2600

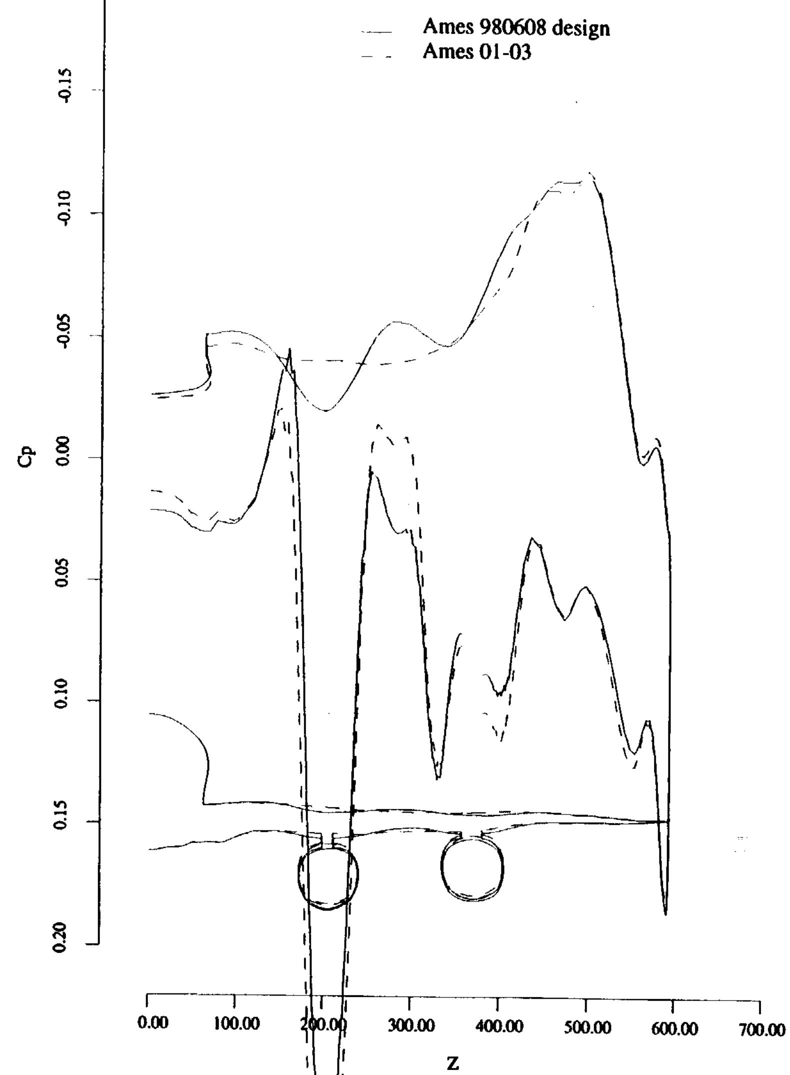

Ames 980608 vs. Ames 01-03

Mach	Alpha	Re	CL	CD	X
2.400	3.756	0.00E+00	0.10407	0.00561	2600.000
2.400	3.756	0.00E+00	0.10327	0.00549	2600.000

Chart 18

Geometry and Pressure Distribution Comparisons (Ames 980608 vs. Ames 1-03, X=2700 and X=2800)

Pressures and geometry comparisons near the trailing edge of the wing are shown. The extensive camber changes result in a wavy upper surface pressure distribution and relatively small changes are seen in the lower surface pressures.

Geometry and Pressure Distribution Comparisons
Ames 980608 vs. Ames 1-03, X=2700 and X=2800

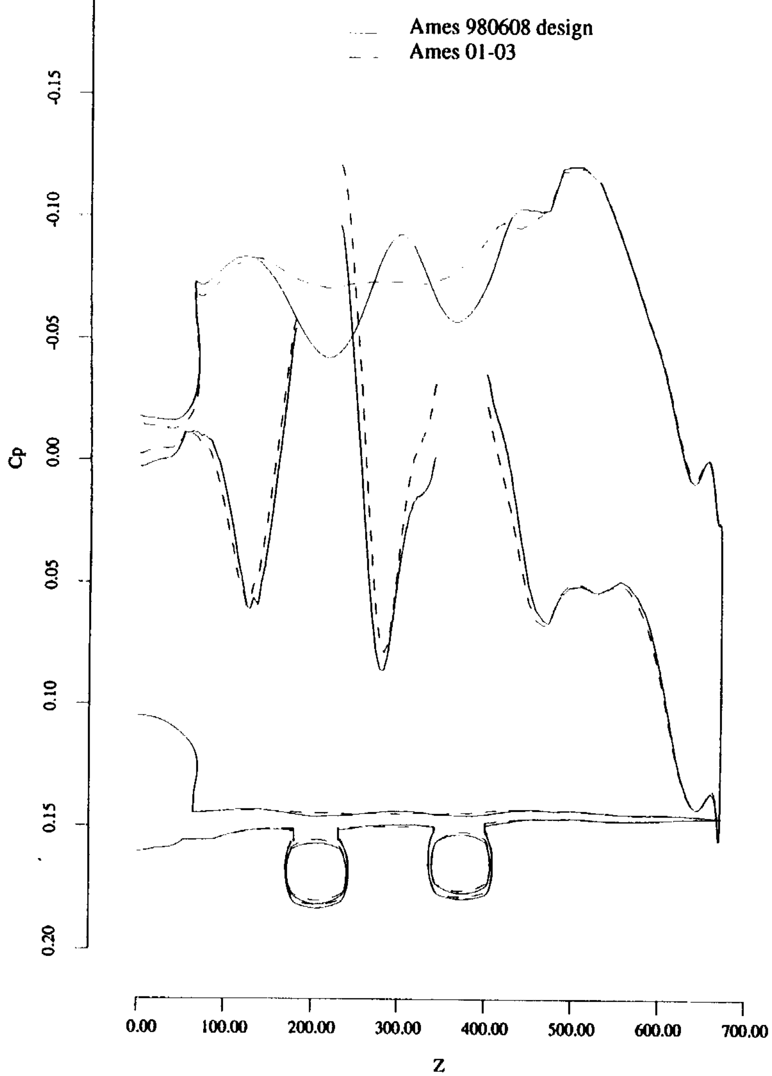

Ames 980608 vs. Ames 01-03

Mach	Alpha	Re	CL	CD	X
2.400	3.756	0.00E+00	0.10407	0.00561	2700.000
2.400	3.756	0.00E+00	0.10327	0.00549	2700.000

Geometry and Pressure Distribution Comparisons
Ames 980608 vs. Ames 1-03, X=2700 and X=2800

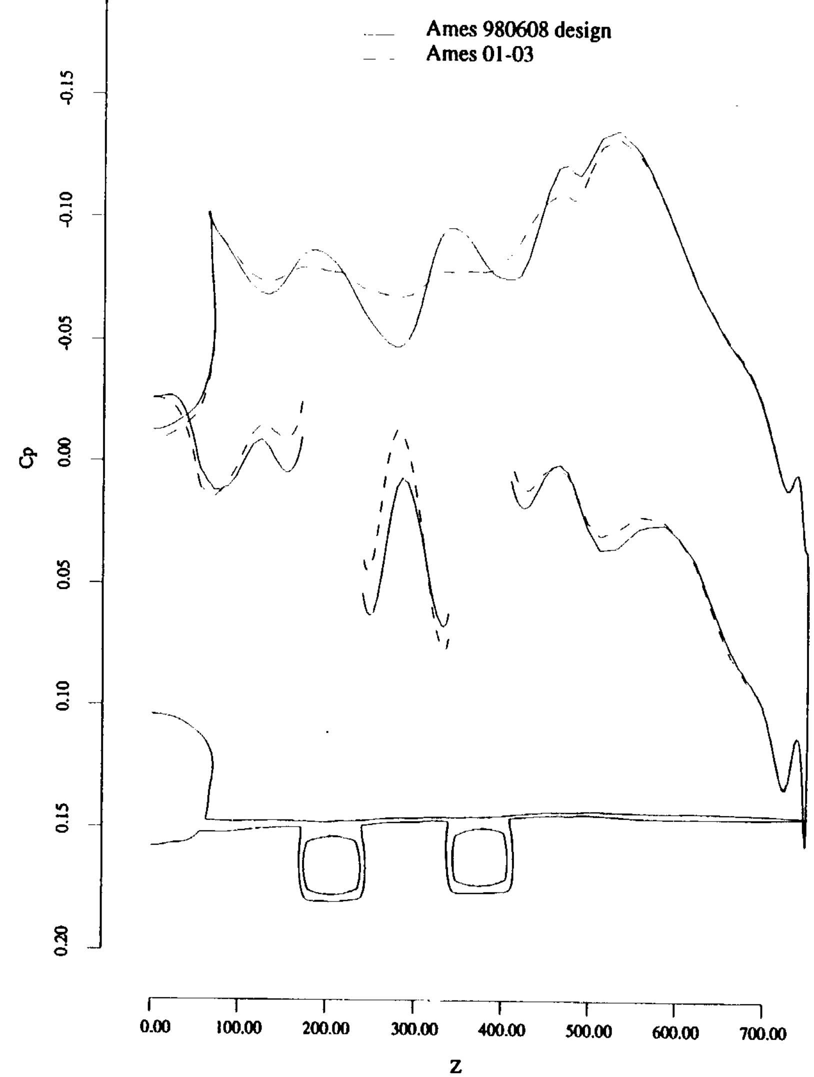

Ames 980608 vs. Ames 01-03

Mach	Alpha	Re	CL	CD	X
2.400	3.756	0.00E+00	0.10407	0.00561	2800.000
2.400	3.756	0.00E+00	0.10327	0.00549	2800.000

Geometry and Pressure Distribution Comparisons (Ames 980608 vs. Ames 1-03, Z=210 and Z=288)

Constant spanwise cuts are shown, where Z=210 cuts through the inboard nacelle and Z=288 is a station between the inboard and outboard nacelles. The inboard nacelle appears warped slightly. The nacelle shocks on the wing between the nacelles differ upstream of the nacelle shocks but are of the same approximate magnitude at 80-95% chord.

Geometry and Pressure Distribution Comparisons
Ames 980608 vs. Ames 1-03, Z=210 and Z=288

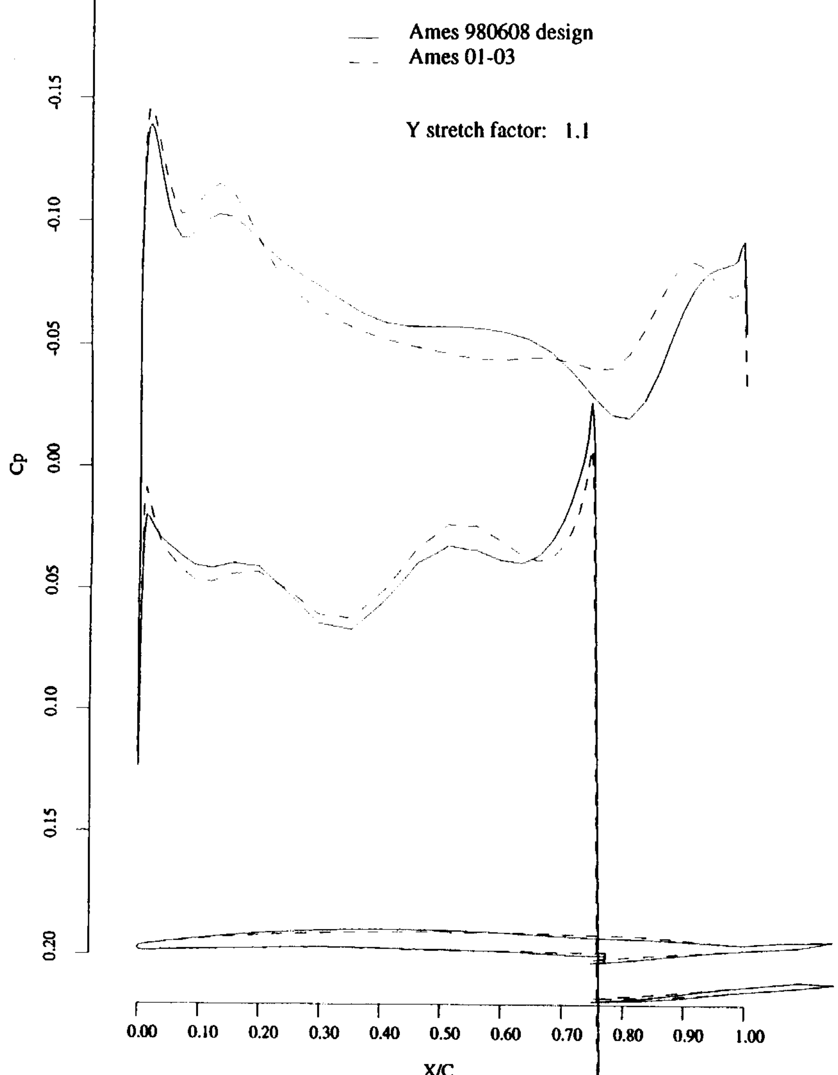

Ames 980608 vs. Ames 01-03

Mach	Alpha	Re	CL	CD	Z	Cl	Cd	Cm	Load
2.400	3.756	0.00E+00	0.10407	0.00561	210.000	0.10101	0.00593	0.04199	0.10622
2.400	3.756	0.00E+00	0.10327	0.00549	210.000	0.10292	0.00607	0.04398	0.10823

Geometry and Pressure Distribution Comparisons
Ames 980608 vs. Ames 1-03, Z=210 and Z=288

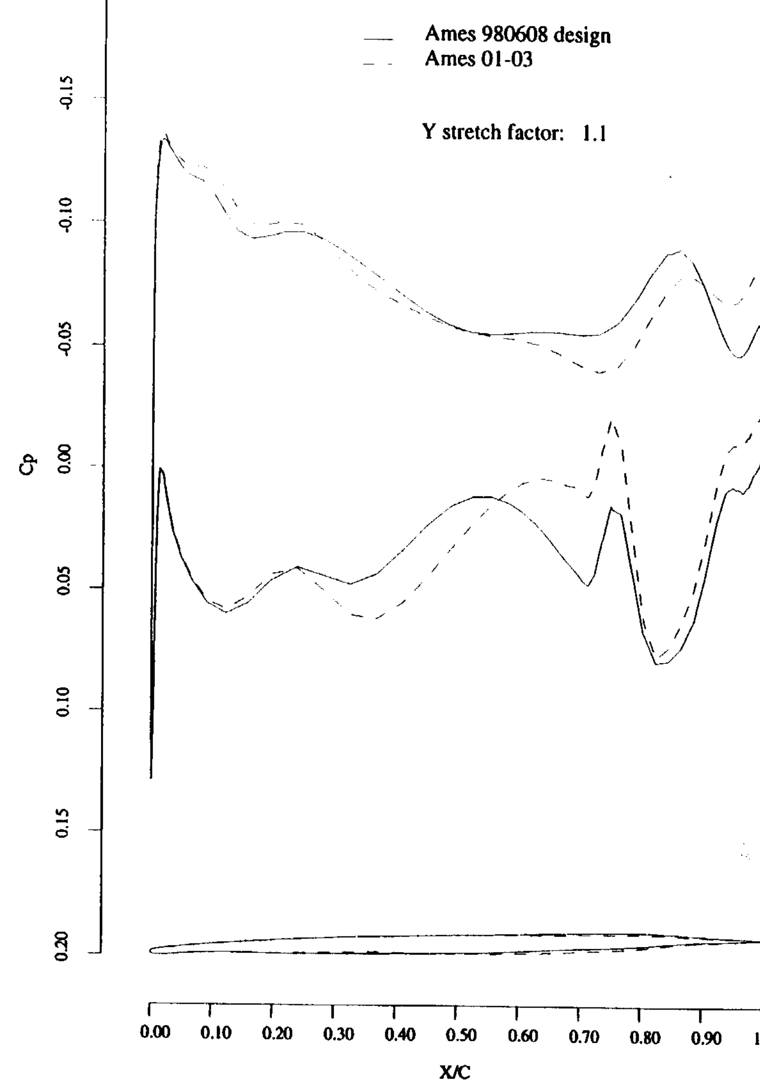

Ames 980608 vs. Ames 01-03

Mach	Alpha	Re	CL	CD	Z	Cl	Cd	Cm	Load
2.400	3.756	0.00E+00	0.10407	0.00561	288.000	0.11364	0.00479	0.05107	0.09573
2.400	3.756	0.00E+00	0.10327	0.00549	288.000	0.10822	0.00457	0.04542	0.09116

Chart 20

Geometry and Pressure Distribution Comparisons (Ames 980608 vs. Ames 1-03, Z=365 and Z=442)

The cut at Z=365 cuts through the outboard nacelle. The pressure distributions are not significantly different. The strength of the nacelle shocks cannot be compared since they are outside the plot range. The Z=442 station is located outboard of the outboard nacelle. Here the nacelle shock is reduced slightly for the 6-08 design.

Geometry and Pressure Distribution Comparisons
Ames 980608 vs. Ames 1-03, Z=365 and Z=442

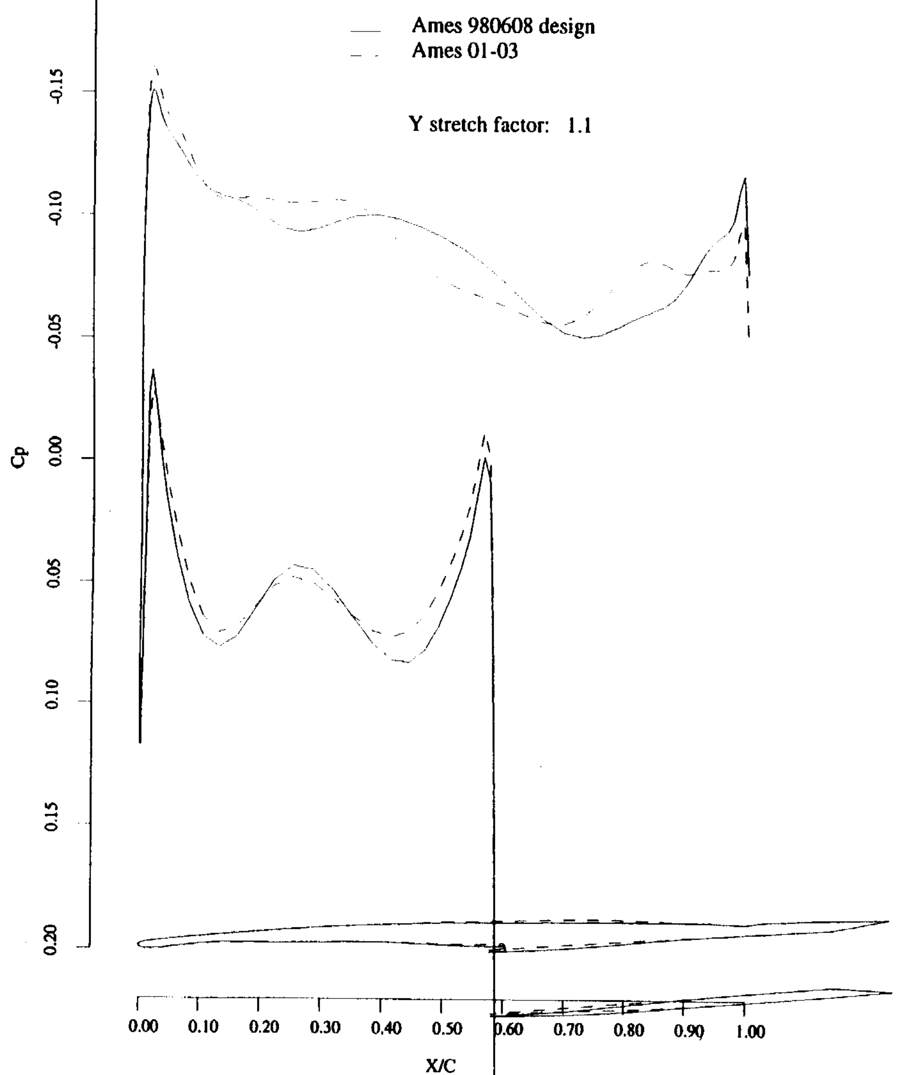

Ames 980608 vs. Ames 01-03

Mach	Alpha	Re	CL	CD	Z	Cl	Cd	Cm	Load
2.400	3.756	0.00E+00	0.10407	0.00561	365.000	0.12561	0.00514	0.05257	0.07984
2.400	3.756	0.00E+00	0.10327	0.00549	365.000	0.12333	0.00459	0.05134	0.07840

Geometry and Pressure Distribution Comparisons
Ames 980608 vs. Ames 1-03, Z=365 and Z=442

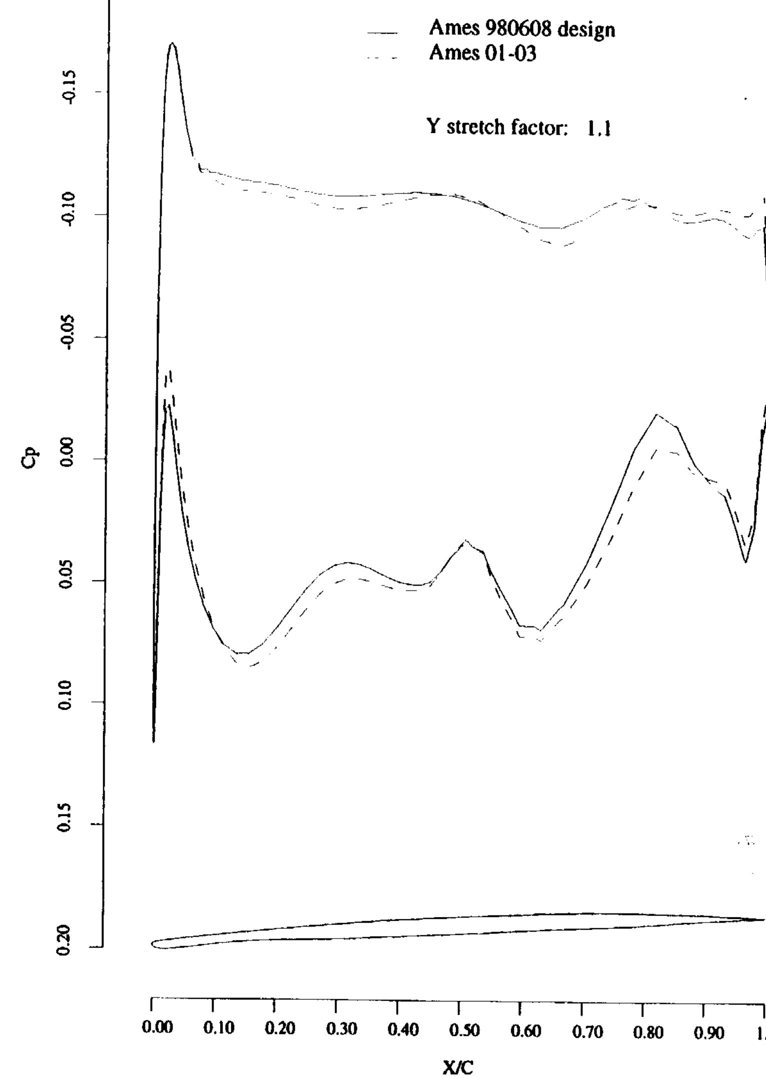

Ames 980608 vs. Ames 01-03

Mach	Alpha	Re	CL	CD	Z	Cl	Cd	Cm	Load
2.400	3.756	0.00E+00	0.10407	0.00561	442.000	0.14573	0.00351	0.06601	0.06404
2.400	3.756	0.00E+00	0.10327	0.00549	442.000	0.14767	0.00361	0.06793	0.06489

Chart 21

Comparison of the 6-08 configuration with Deformed and Original Nacelles

The original undistorted nacelle and diverter geometries were installed on the wing/body of the 6-08 design. The drag reduction relative to Ames 1-03 with unaltered nacelles is approximately 0.3 counts, whereas the deformed nacelle configuration of the 6-08 design indicated 1.3 counts. The warping of the nacelles rather than the wing design changes dominated the performance gain with 77% of the gain from warping. This clearly indicates that any method which permits the nacelles to be warped is not suitable for designs which require the nacelles and diverters to remain of fixed geometry. Hence, this design process was abandoned until the rigid nacelle design capability was available.

Comparison of the 6-08 Configuration with Deformed and Original Nacelles

M=2.4, no internal or base nacelle forces, entire fuselage

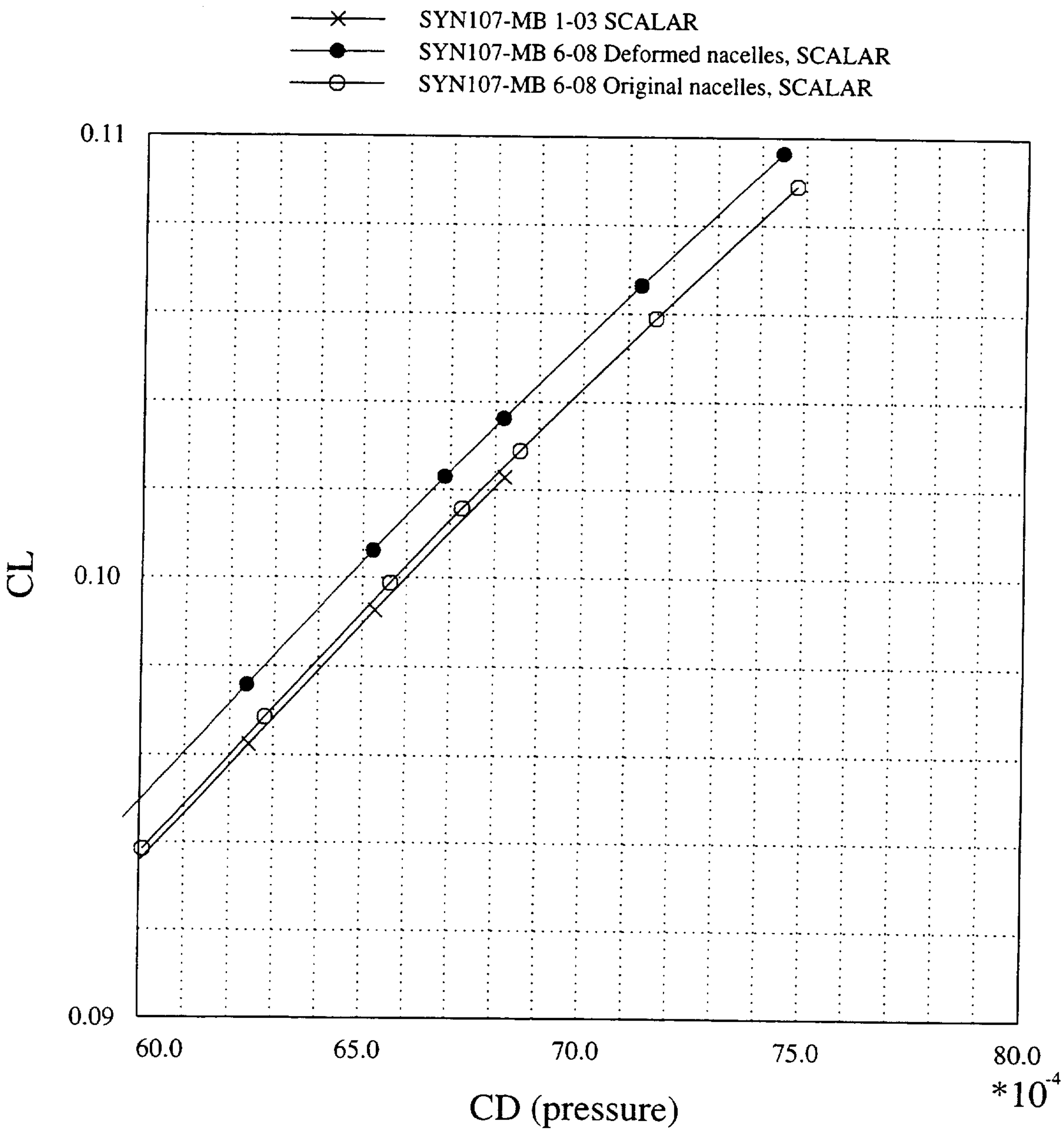

Rigid Nacelle Method

By late October 1998, SYN107-MB had been modified to permit optimization of the wing while maintaining the original shapes of the nacelles and diverters. This method, like the warped nacelle method, requires a complete surface and volume grid in a multiblock format with one-to-one grid abutments between adjoining blocks, and each block must be dimensioned with $2^n + 1$ points so that multigrid flow and adjoint solutions can be obtained. The rigid nacelle method requires additional inputs to the AEROSURF surface paneling subsystem that pertain to the nacelles and diverter geometry. Radial nacelle cuts and sets of diverter cuts are required for the rigid method that are not required for the warped method, in addition to the planar wing and body cuts needed for all methods. These cuts of the nacelles and diverters are necessary for AEROSURF to obtain proper component intersections and a fully-paneled representation of the complete configuration for use by the grid perturbation scheme, whereas the warped nacelle method used a previous version of AEROSURF which paneled only the wing/body components.

This latest method maintains the essential shape of the nacelles, and repositions each nacelle such that the diverter height is maintained at the leading edge during optimization. The diverters are forced to zero height at the trailing edge by minor warping towards the nacelle centerlines. The nacelles maintain the original roll angle with the upper aft nacelle surfaces adjusted to match the wing trailing edge angle. The wing surface paneling around the diverters is also much more involved, and is done in stages starting with the paneling of the plain wing. The entire process of intersecting and paneling all components of the TCA three-surface configuration nevertheless takes just 1 CPU second on an SGI Origin2000-class processor. Some of the resulting 54 surface patches are shown in the following figure.

Rigid Nacelle Method

- AEROSURF paneling includes nacelle/diverter geometries—requires many more surface patches
- Same W/B/N/D multiblock CFD grid as before
- Nacelle shapes maintained during optimization
- Diverter heights at nacelle inlet maintained during optimization
- Wing/diverter & nacelle/diverter intersections computed automatically during wing optimization
- Nacelles maintain roll angle—upper aft nacelles adjusted to match wing trailing edge changes

AEROSURF Paneling Used With Rigid Nacelle Method

This figure shows the AEROSURF parametric patches in the vicinity of the nacelles and diverters. The parametric patches are created after design variables are applied to the basic geometric components (such as wings, bodies, and nacelles) and these components are intersected. The parametric patches form a closed geometry definition that serves as a template to move the surface CFD mesh points such that they will conform to the exact geometry representation. The mapping between the parametric patches and the CFD mesh is calculated as a preprocessing step (program UV_MAP) using the baseline configuration.

AEROSURF Paneling Used With Rigid Nacelle Method

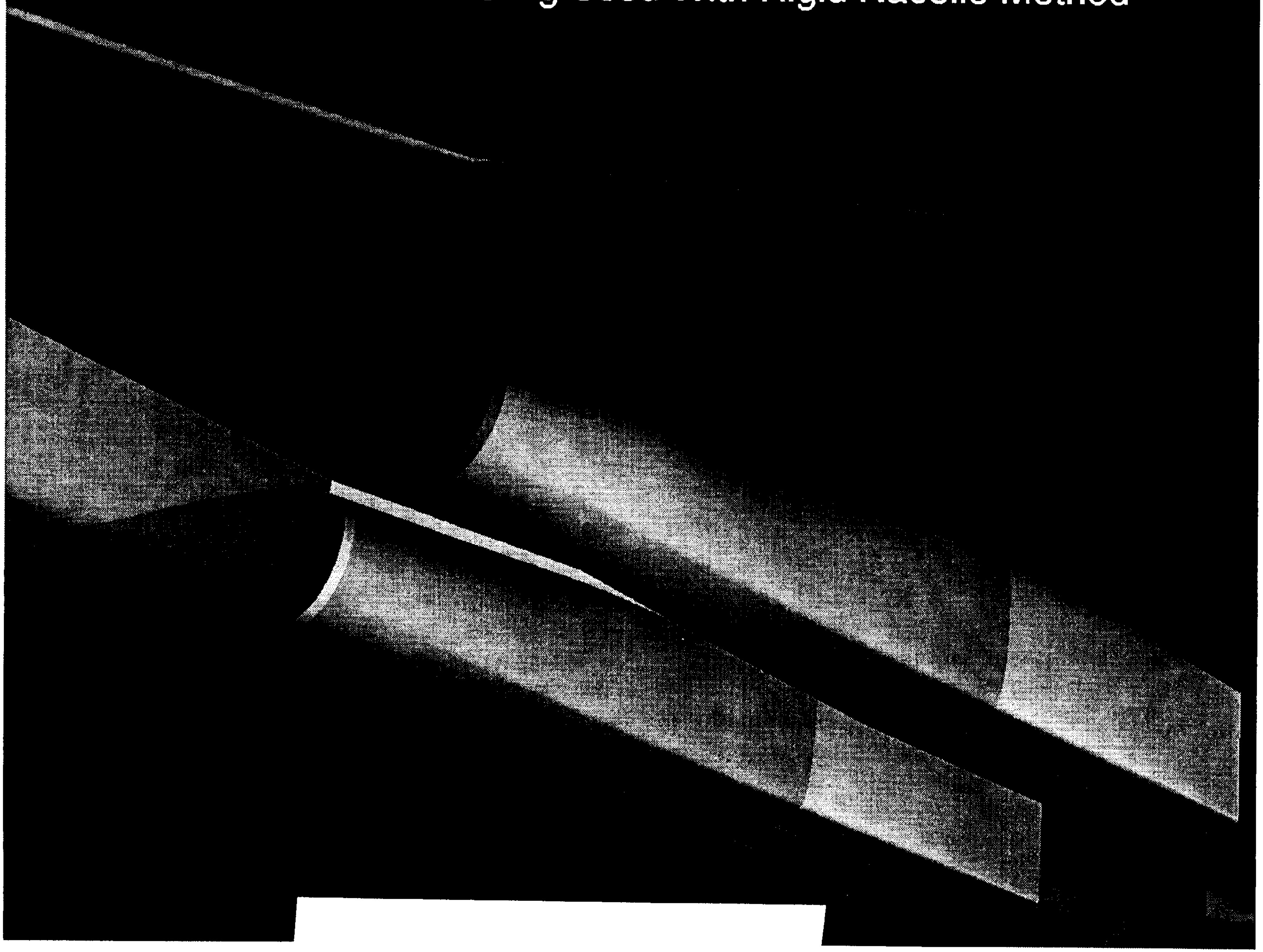

Chart 24

SYN107-MB Rigid Nacelle Design Drag Comparison, Wing/Body/Nacelle/Diverter

The Ames 1-03 was optimized using the rigid nacelle method with the same set of design variables (wing thickness and camber) as were applied with the warped nacelle method which produced the 6-08 design. The result of this rigid nacelle design is the 12-10 design, with approximately 0.6 count drag reduction over the Ames 1-03 configuration.

SYN107-MB Rigid Nacelle Design Comparison, Wing/Body/Nacelle/Diverter

M=2.4, no internal or base nacelle forces, entire fuselage

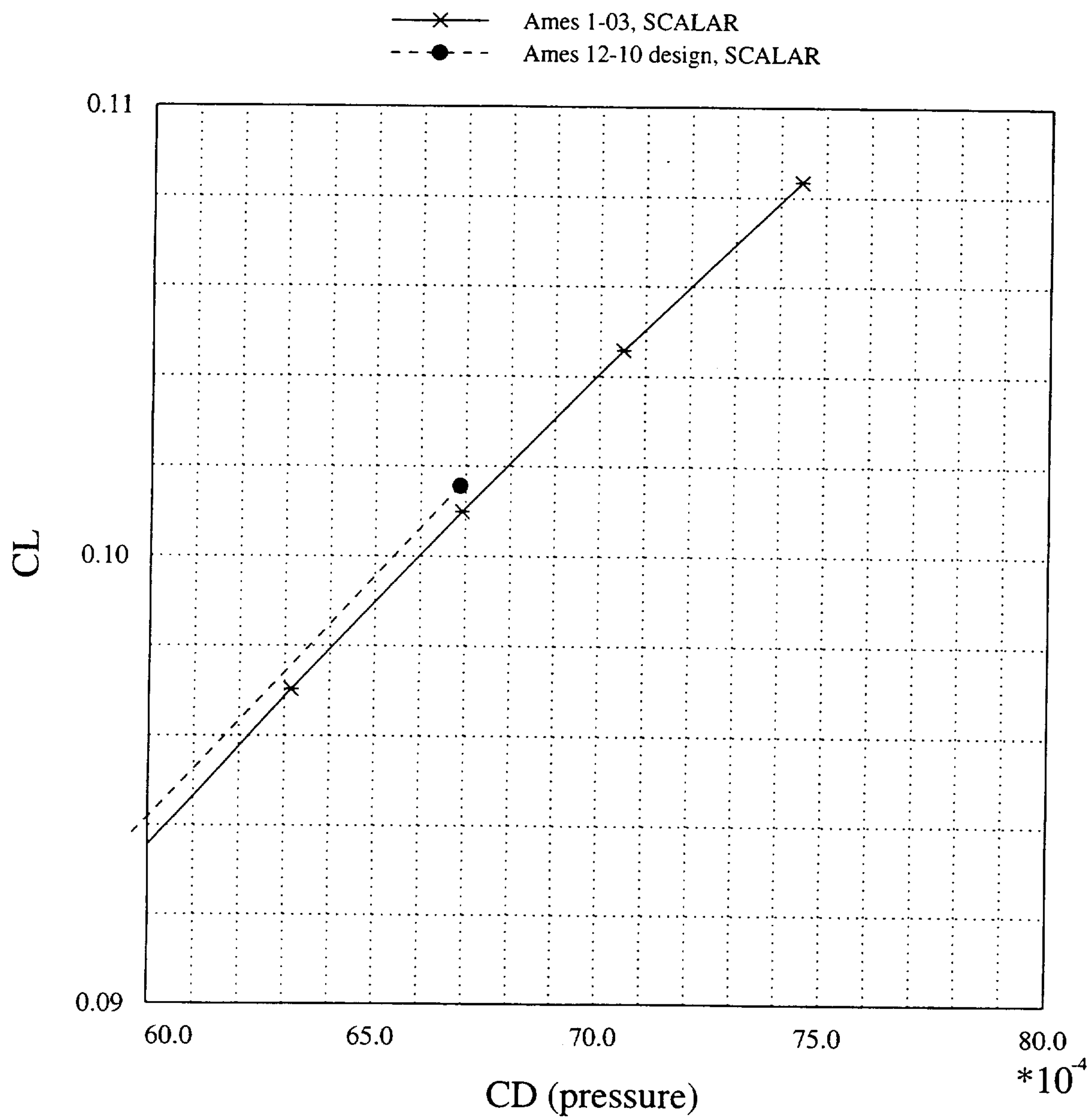

Chart 25

SYN107-MB Rigid Nacelle Design, Wing/Body Drag Comparison

The wing/body component forces for the Ames 1-03 and the 12-10 (rigid nacelle design) have been extracted from the output files and plotted to show a performance decrement of approximately 0.25 counts for the 12-10 wing/body components compared with the Ames 1-03 design.

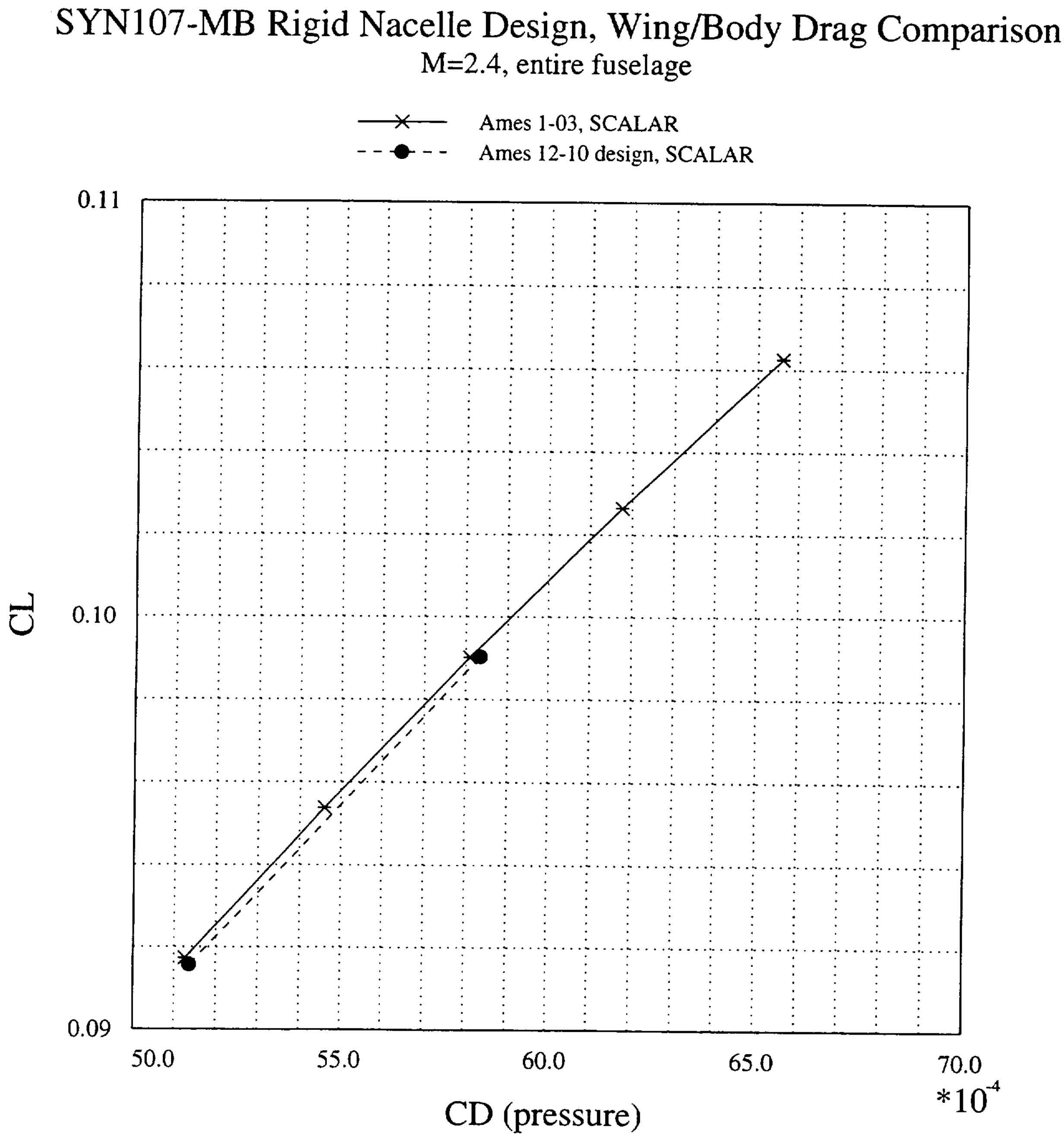
SYN107-MB Rigid Nacelle Design, Wing/Body Drag Comparison
M=2.4, entire fuselage
Ames 1-03, SCALAR
Ames 12-10 design, SCALAR
0.11
0.10
0.09
CL
50.0
55.0
60.0
65.0
70.0
*10^-4
CD (pressure)

Chart 26

SYN107-MB Rigid Nacelle Design, Nacelle/Diverter Drag Comparison

The nacelle and diverter component forces without the internal drag for the Ames 1-03 and the 12-10 (rigid nacelle design) have been plotted to show that a large increase in lift on the nacelles and diverters is achieved along with a drag improvement. The large shift in lift coefficient without incurring any drag penalty is responsible for producing the majority of the improvement for the complete configuration (see chart 24). The data from this chart combined with that of the previous chart indicate that the performance gain for this design is evidently from improved "wing on nacelle" effects.

SYN107-MB Rigid Nacelle Design, Nacelle/Diverter Drag Comparison

M=2.4, no internal nacelle forces

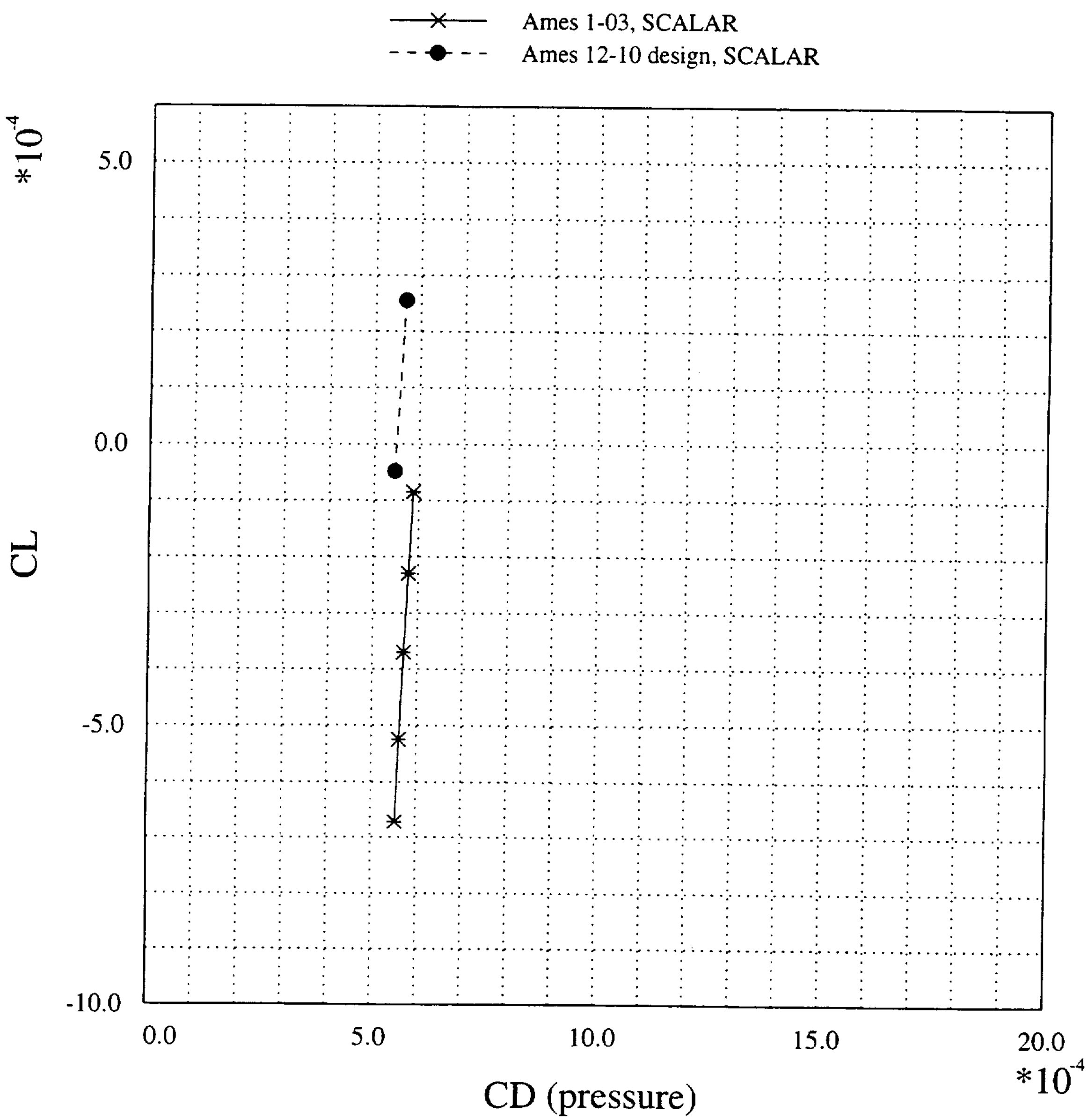

Geometry and Pressure Distribution Comparisons (Ames 12-10 vs. Ames 1-03, X=2500 and X=2600)

The pressure distributions and geometry cuts at constant axial locations of X=2500 and X=2600 are shown for the Ames 12-10 and 1-03 configurations. The changes for the 12-10 design appear to be similar to but less aggressive than those seen for the 6-08 design (compare with chart 18). Some of the cambering effects generated to modify the flow in the nacelle and diverter region have caused a more wavy pressure distribution on the upper surface of the wing. The pressure distributions between the nacelles at X=2600 show an increase in pressure, which may account for the 0.25 count drag increase observed for the wing/body components.

Geometry and Pressure Distribution Comparisons
Ames 981210 vs. Ames 1-03, X=2500 and X=2600

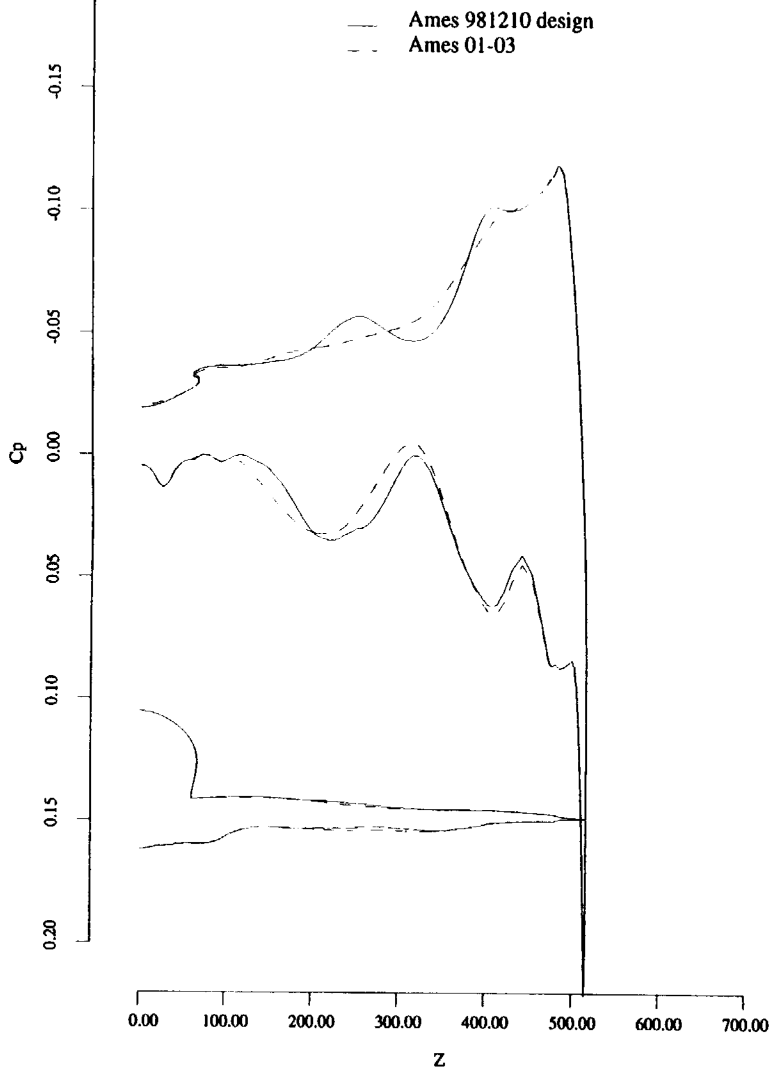

Ames 981210 vs. Ames 01-03

Mach	Alpha	Re	CL	CD	X
2.400	3.756	0.00E+00	0.10211	0.00548	2500.000
2.400	3.756	0.00E+00	0.10278	0.00550	2500.000

Geometry and Pressure Distribution Comparisons
Ames 981210 vs. Ames 1-03, X=2500 and X=2600

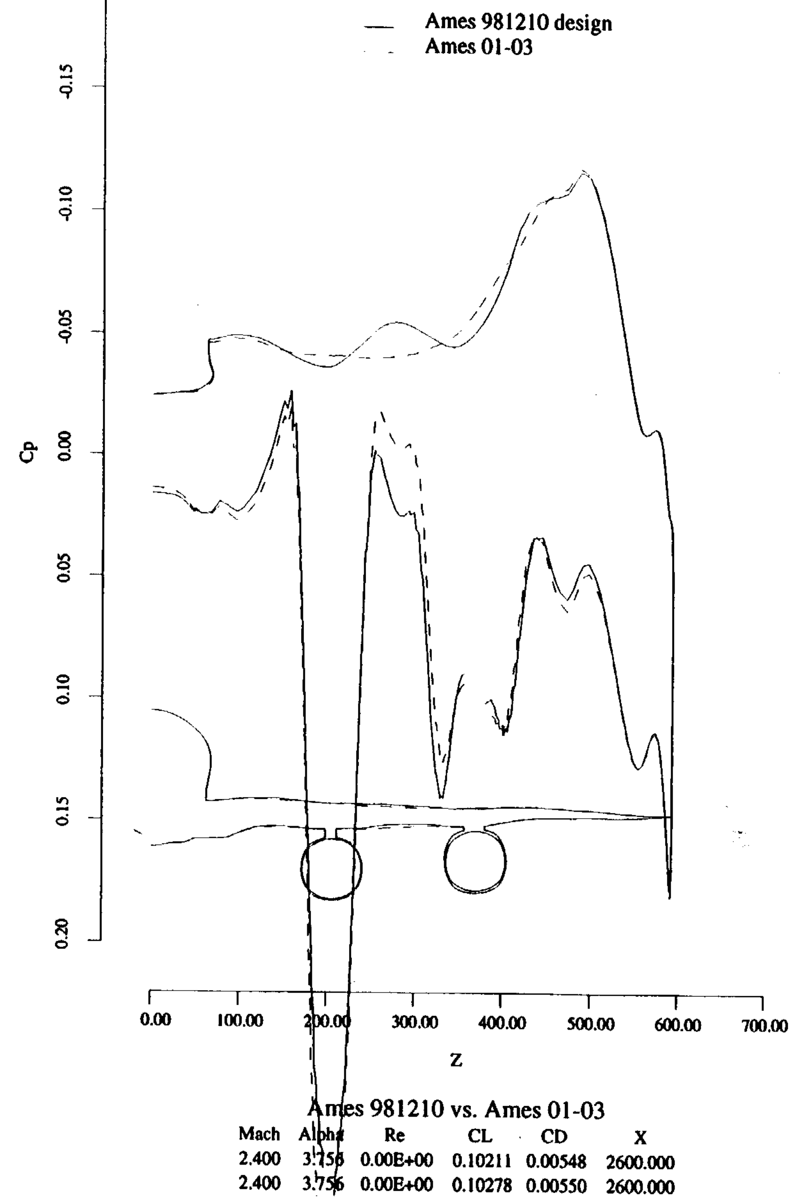

Ames 981210 vs. Ames 01-03

Mach	Alpha	Re	CL	CD	X
2.400	3.756	0.00E+00	0.10211	0.00548	2600.000
2.400	3.756	0.00E+00	0.10278	0.00550	2600.000

Geometry and Pressure Distribution Comparisons (Ames 12-10 vs. Ames 1-03, X=2700 and X=2800)

The pressure distributions here show changes similar to those shown in the previous chart. The upper surface pressures are more wavy, and the lower surfaces show an increase in pressure from the nacelle shocks. The geometry differences are much smaller at these axial locations than at the previous locations, with little or no changes at X=2800. The trailing edge was not modified.

Geometry and Pressure Distribution Comparisons
Ames 981210 vs. Ames 1-03, X=2700 and X=2800

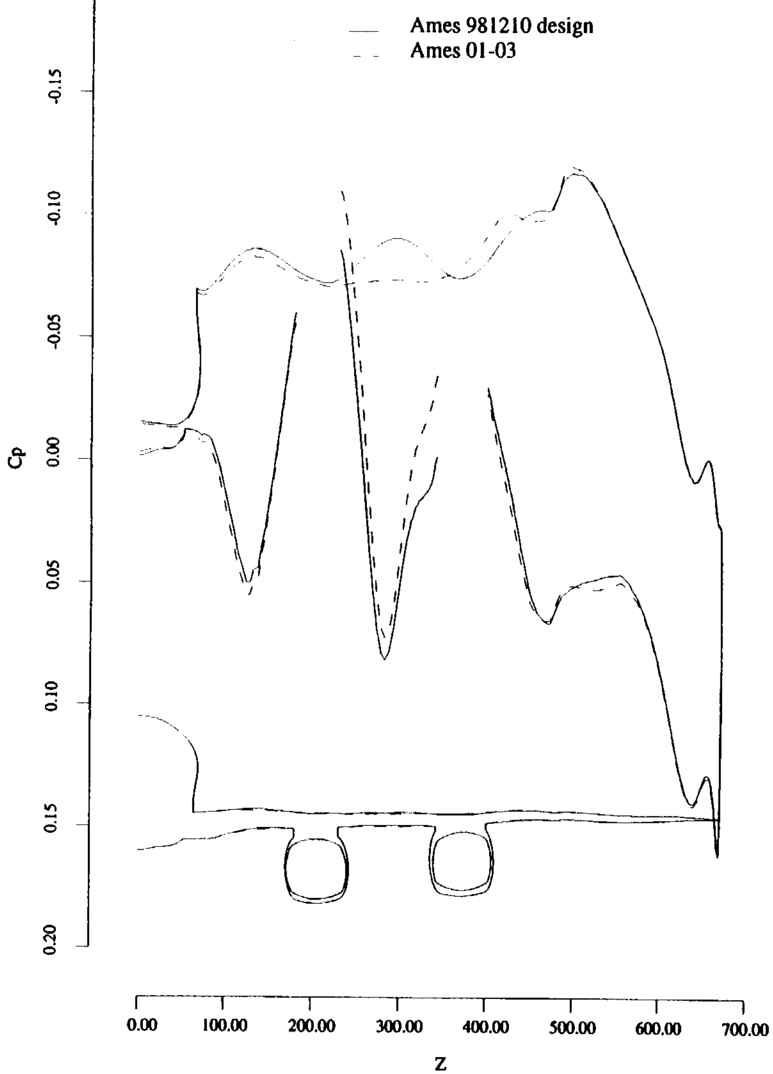

Ames 981210 vs. Ames 01-03

Mach	Alpha	Re	CL	CD	X
2.400	3.756	0.00E+00	0.10211	0.00548	2700.000
2.400	3.756	0.00E+00	0.10278	0.00550	2700.000

Geometry and Pressure Distribution Comparisons
Ames 981210 vs. Ames 1-03, X=2700 and X=2800

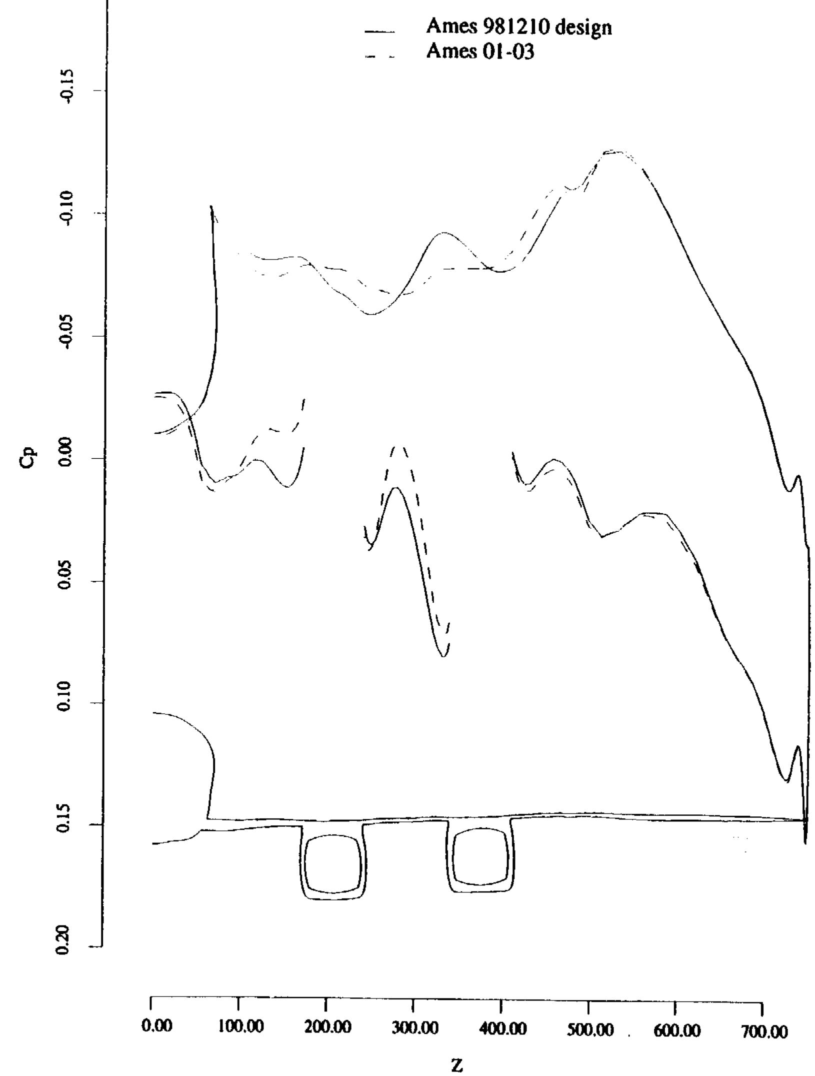

Ames 981210 vs. Ames 01-03

Mach	Alpha	Re	CL	CD	X
2.400	3.756	0.00E+00	0.10211	0.00548	2800.000
2.400	3.756	0.00E+00	0.10278	0.00550	2800.000

Chart 29

Geometry and Pressure Distribution Comparisons (Ames 12-10 vs. Ames 1-03, Z=210 and Z=288)

The geometry and pressures are shown for span stations 210 and 288, representing cuts through the inboard nacelle and between the inboard and outboard nacelle. The geometry changes appear to consist of positive changes in camber upstream of the inboard nacelle. A definite thinning of the wing is seen for the station between the nacelles. The 12-10 design nacelle shocks also appear stronger compared with the Ames 1-03 in this view as seen before in the cross-stream cut views.

Geometry and Pressure Distribution Comparisons
Ames 981210 vs. Ames 1-03, Z=210 and Z=288

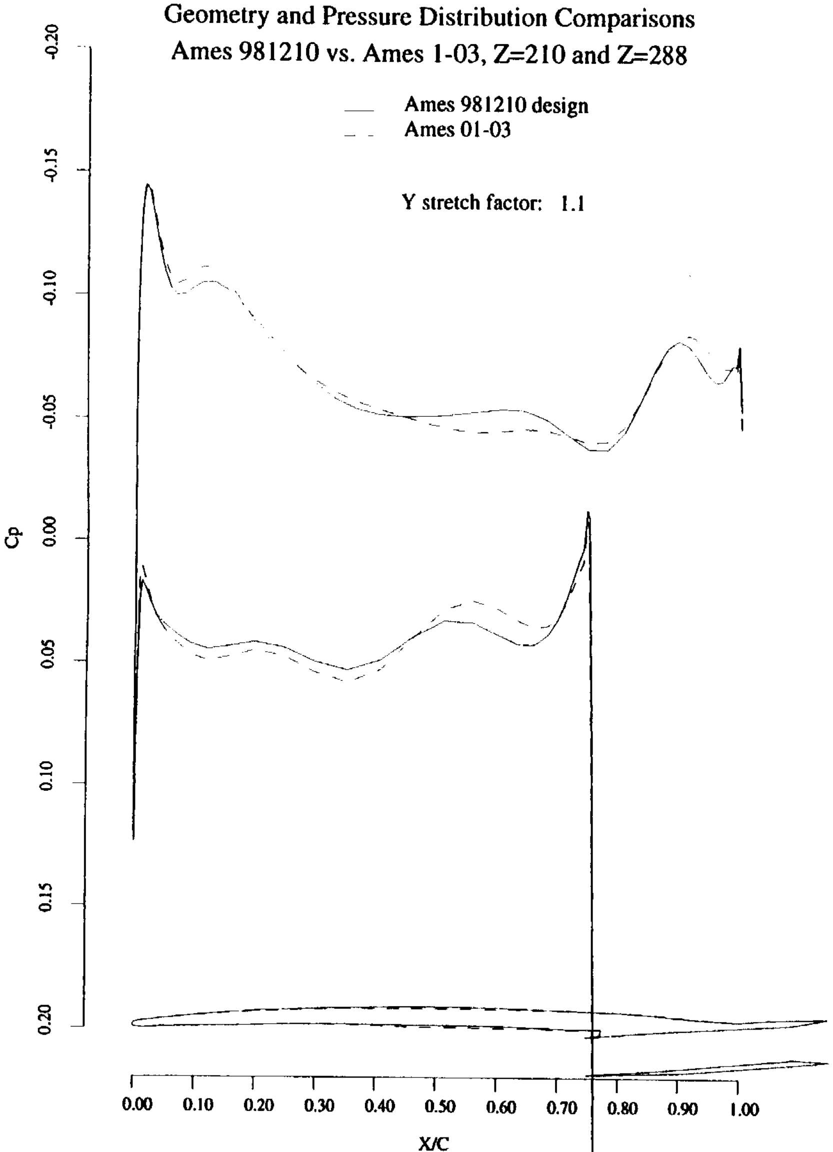

Ames 981210 vs. Ames 01-03

Mach	Alpha	Re	CL	CD	Z	Cl	Cd	Cm	Load
2.400	3.756	0.00E+00	0.10211	0.00548	210.000	0.10182	0.00600	0.04396	0.10708
2.400	3.756	0.00E+00	0.10278	0.00550	210.000	0.10229	0.00606	0.04368	0.10758

Geometry and Pressure Distribution Comparisons
Ames 981210 vs. Ames 1-03, Z=210 and Z=288

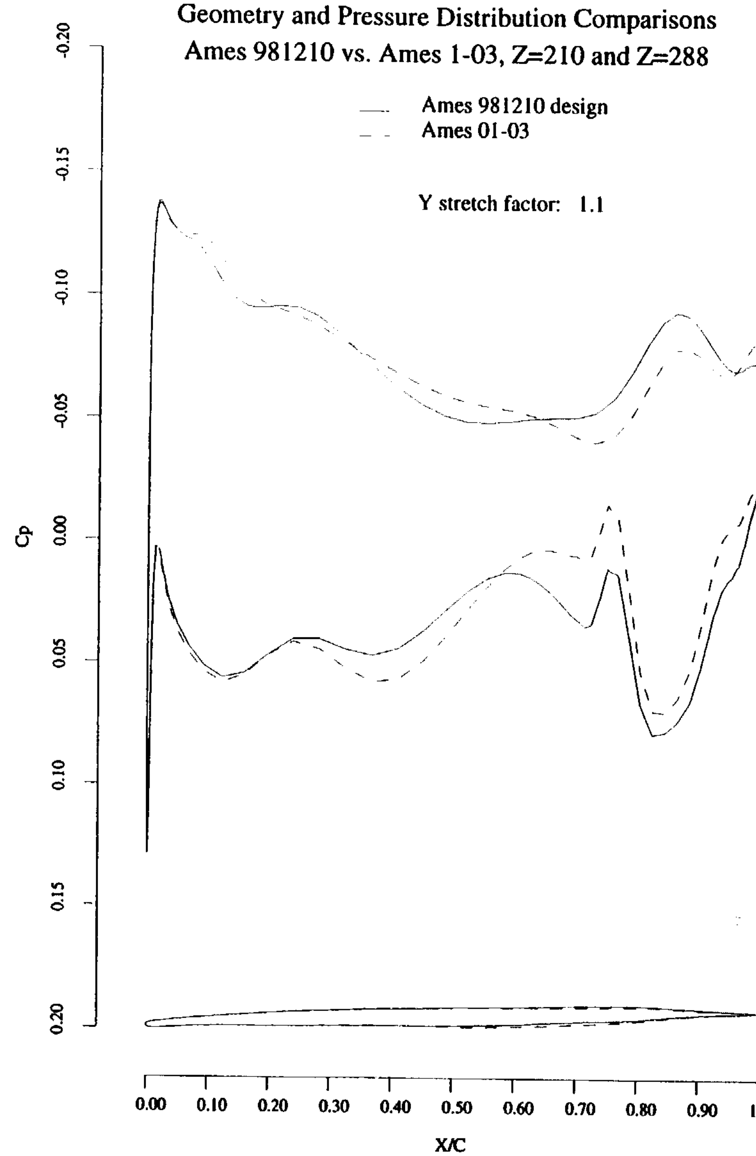

Ames 981210 vs. Ames 01-03

Mach	Alpha	Re	CL	CD	Z	Cl	Cd	Cm	Load
2.400	3.756	0.00E+00	0.10211	0.00548	288.000	0.11295	0.00488	0.05146	0.09515
2.400	3.756	0.00E+00	0.10278	0.00550	288.000	0.10810	0.00463	0.04553	0.09106

Chart 30

Geometry and Pressure Distribution Comparisons (Ames 12-10 vs. Ames 1-03, Z=365 and Z=442)

The changes to the geometry and the pressure distributions at these span stations (through the outer nacelle and outboard of it) appear small.

Geometry and Pressure Distribution Comparisons
Ames 981210 vs. Ames 1-03, Z=365 and Z=442

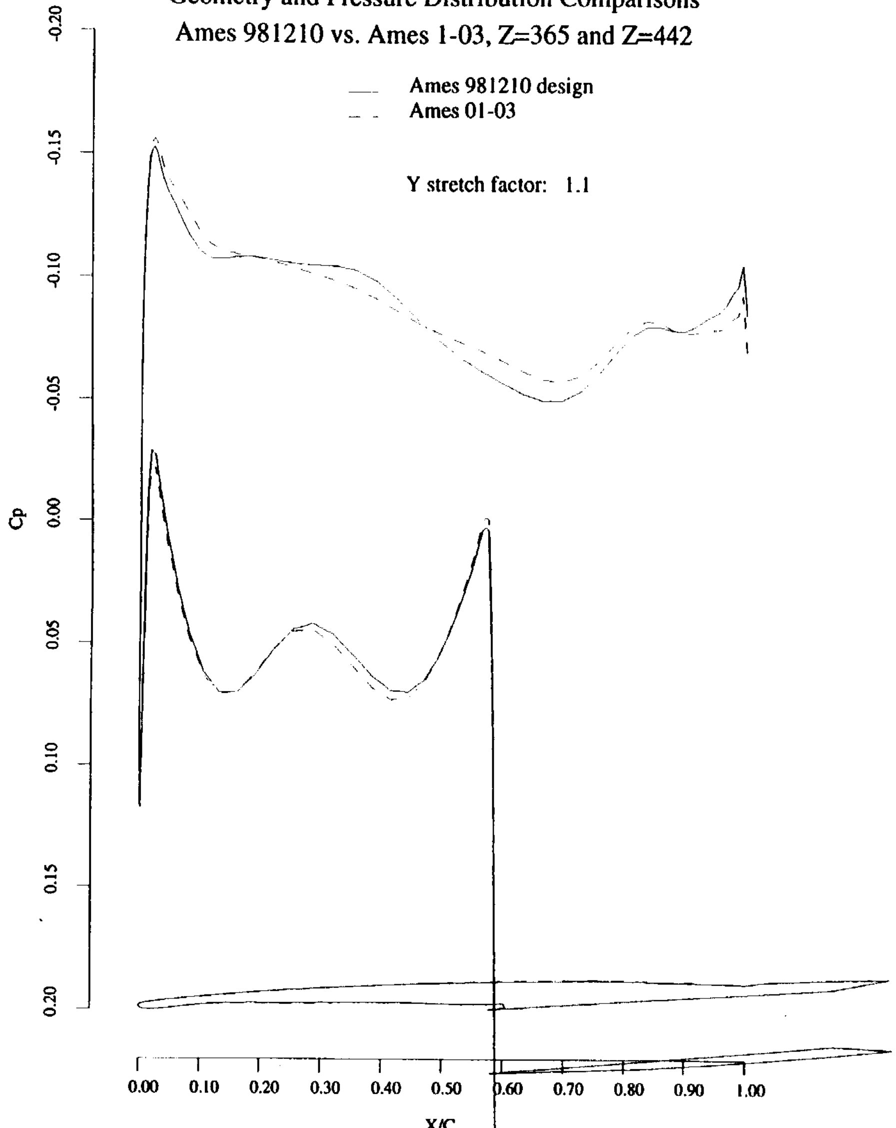

Ames 981210 vs. Ames 01-03

Mach	Alpha	Re	CL	CD	Z	Cl	Cd	Cm	Load
2.400	3.756	0.00E+00	0.10211	0.00548	365.000	0.12019	0.00457	0.05043	0.07640
2.400	3.756	0.00E+00	0.10278	0.00550	365.000	0.12231	0.00462	0.05104	0.07775

Geometry and Pressure Distribution Comparisons
Ames 981210 vs. Ames 1-03, Z=365 and Z=442

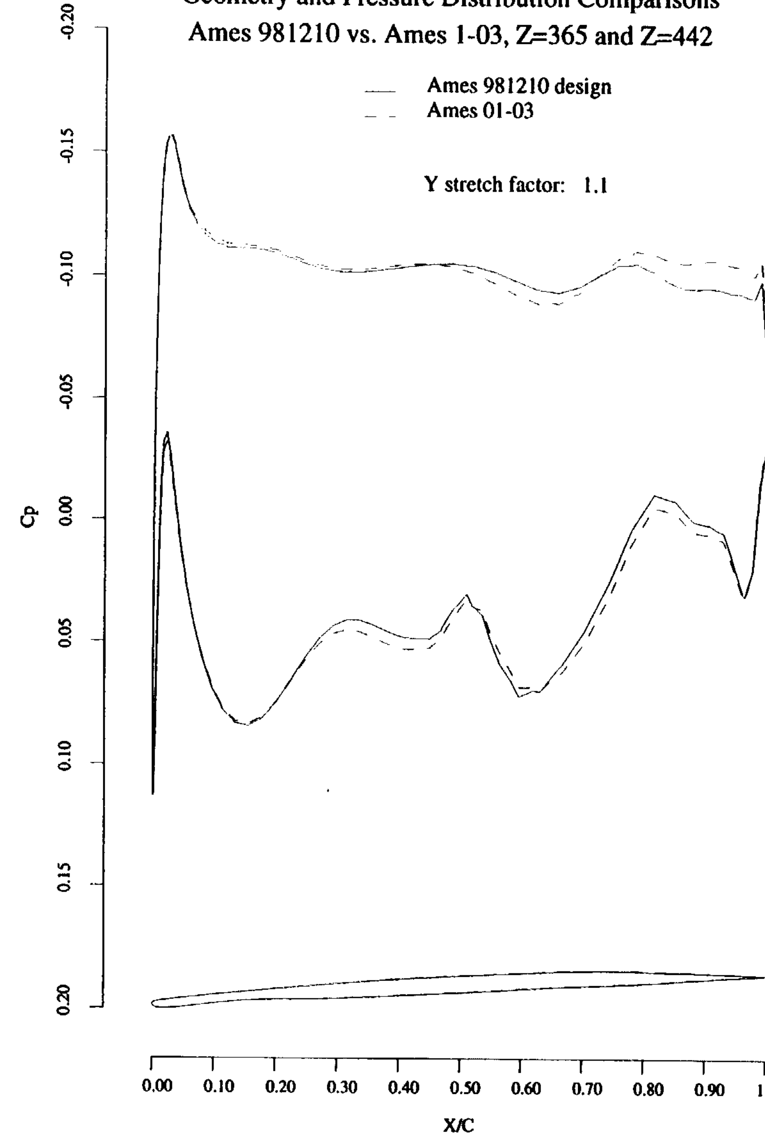

Ames 981210 vs. Ames 01-03

Mach	Alpha	Re	CL	CD	Z	Cl	Cd	Cm	Load
2.400	3.756	0.00E+00	0.10211	0.00548	442.000	0.14261	0.00348	0.06496	0.06267
2.400	3.756	0.00E+00	0.10278	0.00550	442.000	0.14652	0.00367	0.06776	0.06439

Chart 31

Summary

The majority of improvements achieved over the TCA design were found using the pseudo nacelle method with SYN87-SB and AIRPLANE nacelle/diverter effects. This method after several years of development to account for the both the "wing on nacelle" and "nacelle on wing" effects has proven to do a very good job of incorporating these effects into the optimization procedure.

The warped nacelle method was largely ineffective, and is now superseded by the rigid nacelle method.

The rigid nacelle method led to a more aggressive wing shaping in the nacelle/diverter region than the pseudo nacelle method, but this may be attributed to the larger number of grid points used on the lower surface of the wing for the rigid nacelle method than was used for the pseudo nacelle method.

The configuration resulting from the rigid nacelle design method showed a negative improvement in the wing body performance, with all of the improvements on the nacelles and diverters. This implies that the performance gain is attributable to improved "wing on nacelle" effects.

Coarser grids similar to those used with the pseudo nacelle method could result in more realistic designs since the nacelle shocks are more dispersed and may be more similar in location and strength to viscous nacelle shocks.

Summary

- Majority of TCA improvements found using pseudo nacelle method
- Warped nacelle method ineffective—superseded by rigid nacelle design capability
- Rigid nacelle design led to more aggressive wing shaping than pseudo nacelle method
- Rigid nacelle design performance gain due to improved "wing on nacelle" effects
- Differences in designs may be due to grid density differences rather than method differences
- Coarse grids may produce more realistic designs—dispersed nacelle shocks may be more similar to viscous shocks in strength/location

A PTC Optimization and Control Surface Interference Study

HSR Airframe Technical Review

Anaheim, California February 8-12, 1999

Raymond Hicks
Susan Cliff
Mark Rimlinger
Scott Murman
James Reuther

This report considers the effect of canard and horizontal tail vertical position on the aerodynamic characteristics of the PTC configuration without nacelles and diverters. This analysis is followed by three optimization studies using canard and tail incidence as design variables in the first problem followed by an optimization run with canard and tail incidence and wing camber design variables and finally an optimization run with canard incidence and wing camber. The first problem was run at fixed lift while the other two problems were run at fixed angle of attack. The final investigation reported here will show data from a component buildup study using the PTC configuration. This final study will show the aerodynamic interference between the canard, wing and horizontal tail.

Outline

- Effect of canard and horizontal tail vertical position
- Trim opt. with canard and tail incidence
- Trim plus performance opt. with canard and tail incidence and wing camber
- Component buildup

This figure shows the effect of the vertical position of the horizontal tail on the wing drag of the PTC configuration without nacelles and diverters and with the canard fixed at the baseline position. The analysis was conducted at a constant lift coefficient of 0.0995 and Mach 2.40 using the Euler design code SYN107MB. Note that the wing lift increases nearly linearly with increasing tail position. The increase in wing lift is primarily due to an increasing angle of attack needed to maintain configuration lift. The tail lift decreases with increasing vertical position as shown in a subsequent figure. There is a small break in slope at the baseline position indicated by 0.00 on the abscissa. This break is thought to be related to the grid warping technique used to create grids for each new tail position. The total change in drag from the lowest position of -10.0 inches to the highest position of 20.0 inches is approximately 1.8 drag counts; a significant quantity.

rmh - 2

PTC Tail Position Effect on Wing Drag, Canard at Original Position

SYN107-MB Analysis, M = 2.40, fixed lift

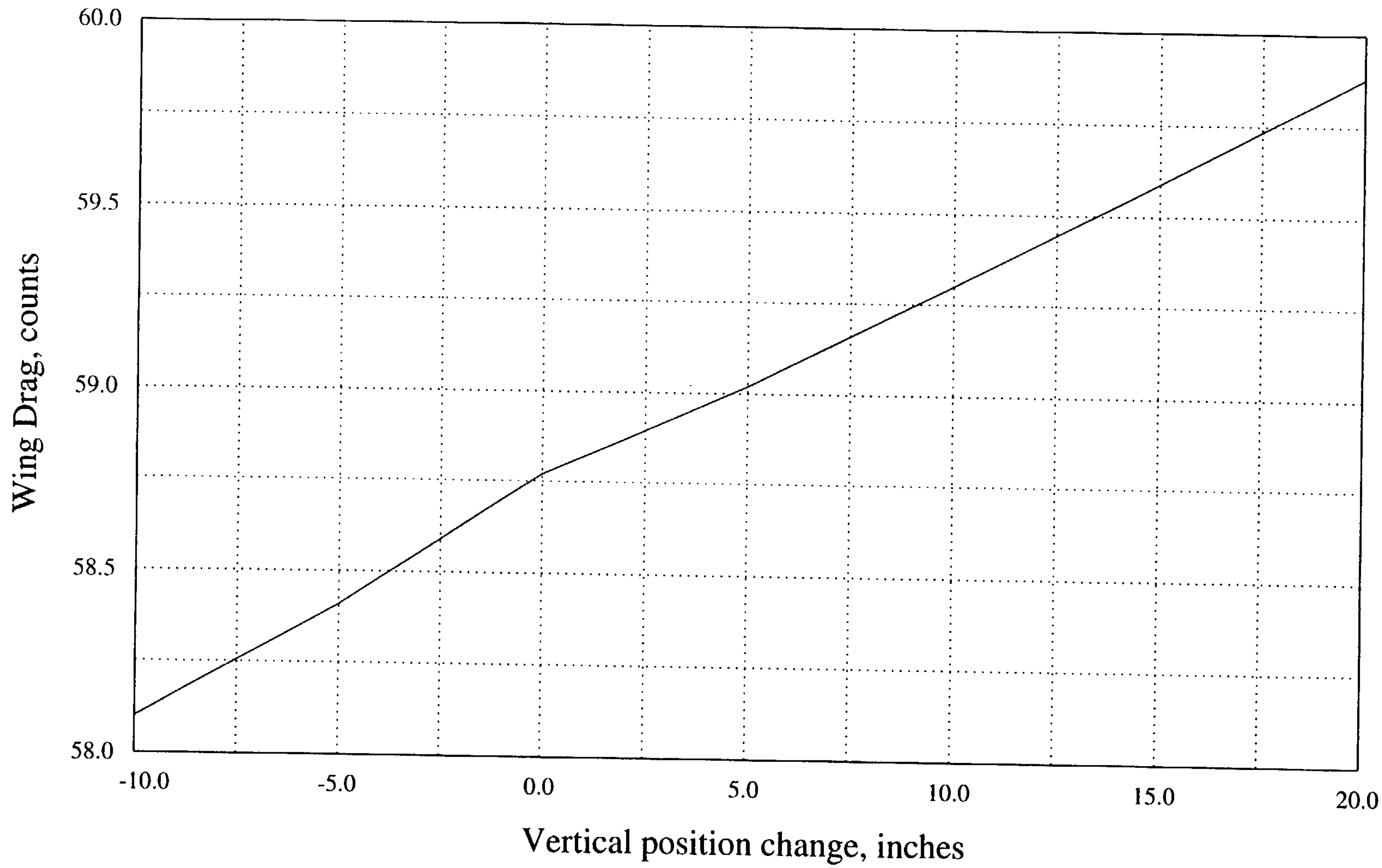

This figures shows the variation of the drag of the horizontal tail as a function of vertical position of that control surface. Note the opposite trend from that shown in the previous figure where wing drag was shown to increase with increasing tail vertical position. However, the drag change is much smaller that that shown for the wing due to the smaller size of the tail and the fact that the configuration reference area was used to calculate these data. Note that the break in slope noted for the wing at the baseline vertical position is not evident here. There does seem to be a small slope change at the 5.0 inch position.

rmh - 3

PTC Tail Position Effect on Tail Drag, Canard at Original Position
SYN107-MB Analysis, M = 2.40, fixed lift

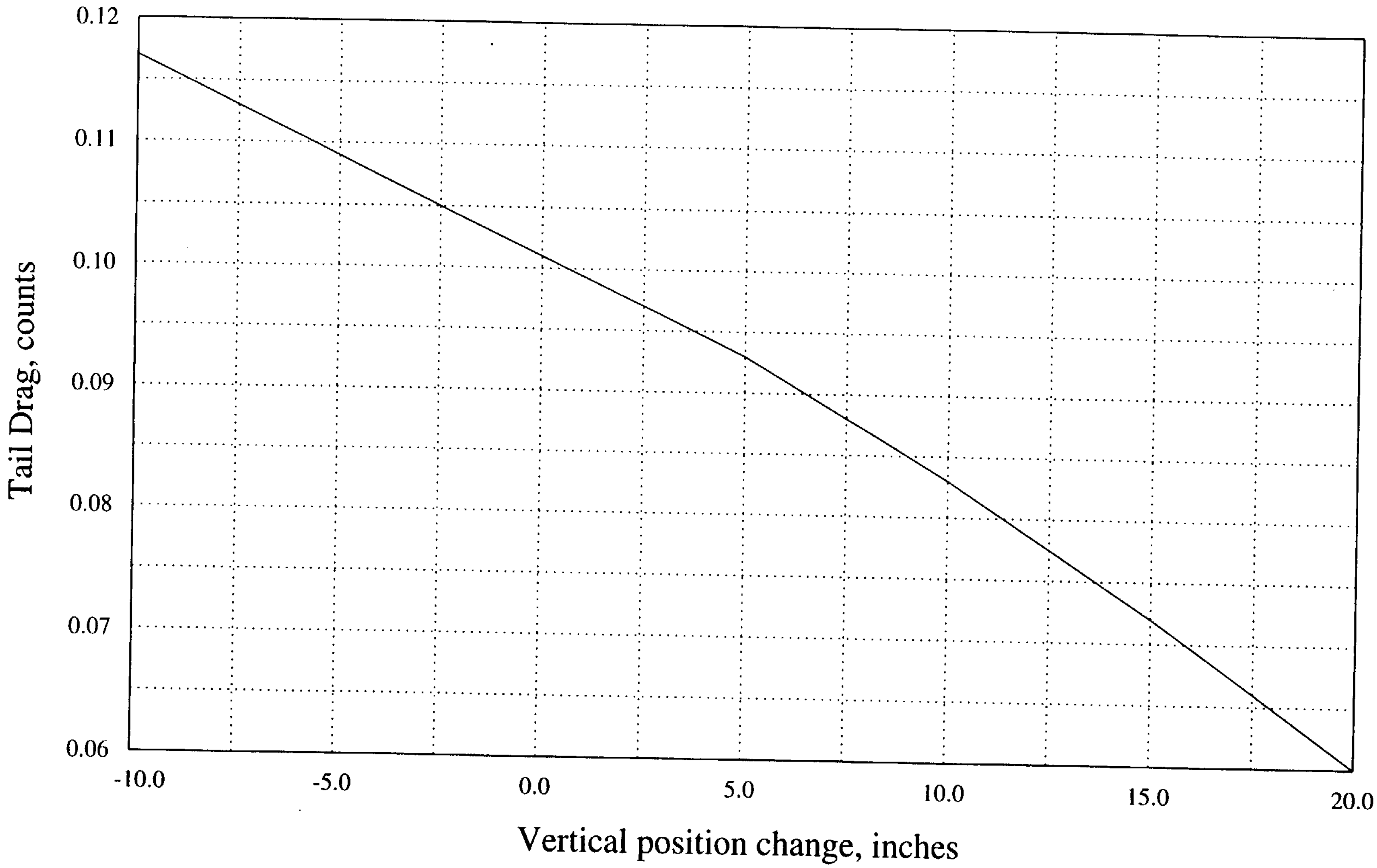

The total drag data shown in this figure exhibits a similar trend to the wing drag data shown in a previous figure. The drag change from the lowest to the highest position is approximately 1.7 counts which is consistent with the 1.8 count increase for the wing and the 0.1 count decrease for the tail. Note that the break in slope and the baseline tail position observed for the wing is clearly evident here. The total drag and wing drag increases are due primarily to an increase in angle of attack needed to compensate for the decreasing tail lift and the requirement to maintain total lift. This will become more evident in subsequent figures.

rmh - 4

Tail Position Effect, PTC, Canard at Original Position
SYN107-MB Analysis, M = 2.40, fixed lift

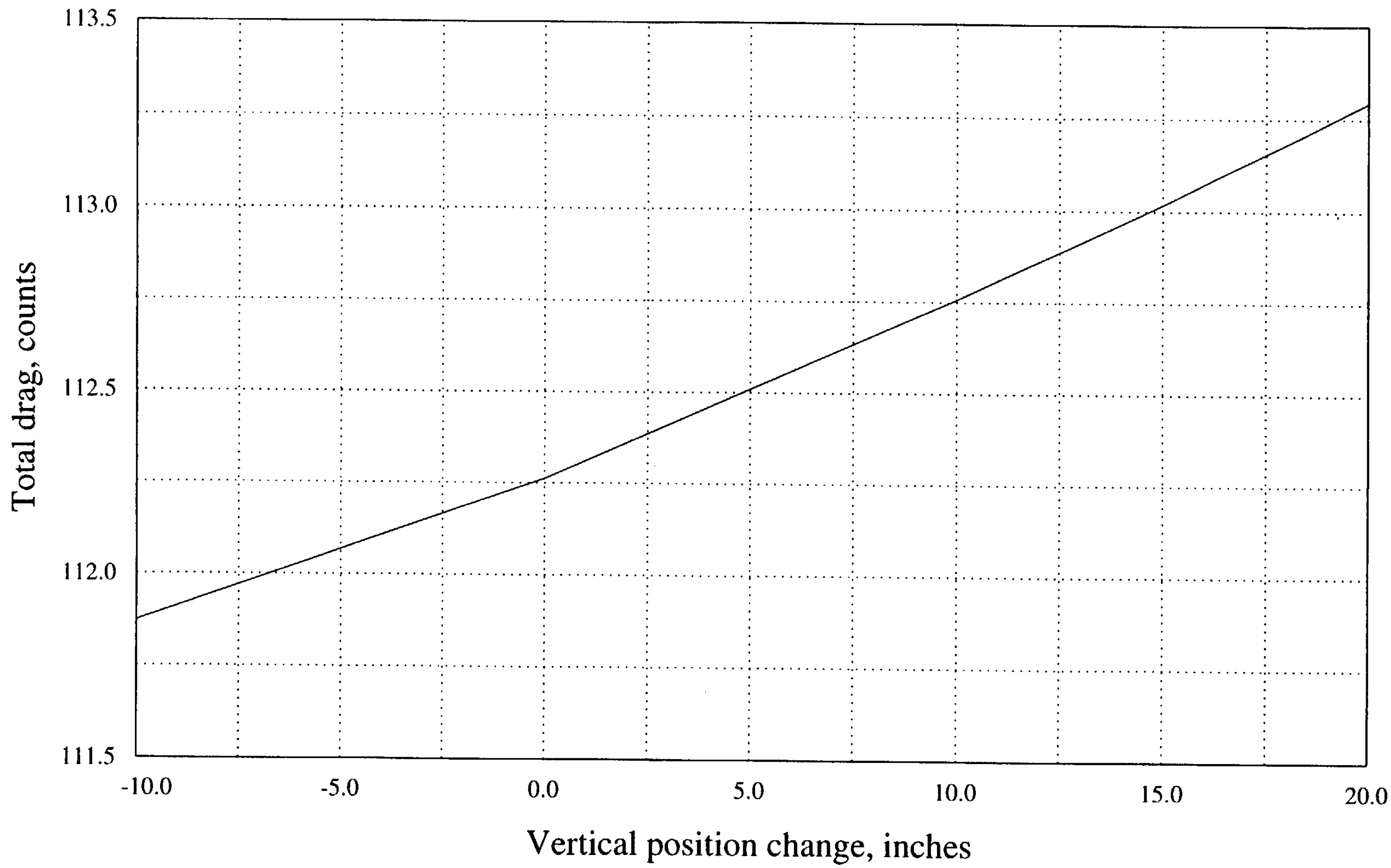

The wing lift coefficient data shown here reflect the increasing angle of attack needed to maintain total lift in response to the decreasing tail load with increasing vertical position. Note the break in the slope at the baseline position. This break is consistent with that shown in previous figures.

rmh - 5

PTC Tail Position Effect on Wing Lift, Canard at Original Position

SYN107-MB Analysis, M = 2.40, fixed lift

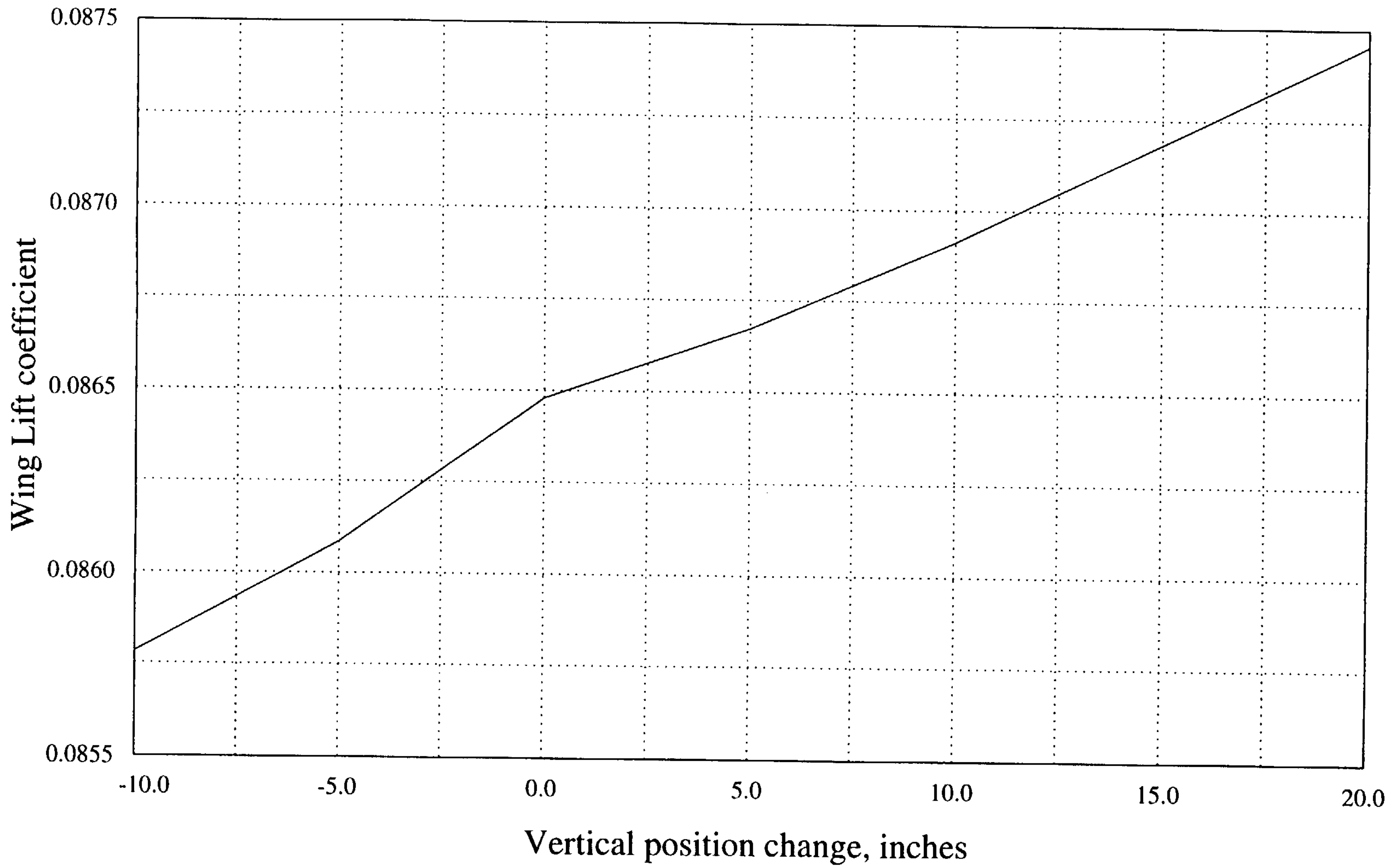

The tail lift coefficient data shown here exhibit a constant slope over the entire range of vertical positions. This is interesting because the grid warping is associated with the moving tail not a moving wing. The slope breaks shown previously were thought to be related to the grid warping but this data seems to contradict that assumption. The tail lift coefficient decreases by approximately 0.0015 when the tail is moved from -10.0 inches to 20.0 inches which is about the increase observed in the wing lift coefficient in the previous figure. This shows that the increase in angle of attack needed to maintain total lift is almost totally responsible for the increasing wing lift. The changes in body and canard lift are negligible. The tail lift coefficients shown in this figure are based on the configuration reference area. Note that the coefficient values shown on the ordinate have been multiplied by a factor of 100.

rmh - 6

PTC Tail Position Effect on Tail Lift, Canard at Original Position
SYN107-MB Analysis, M = 2.40, fixed lift

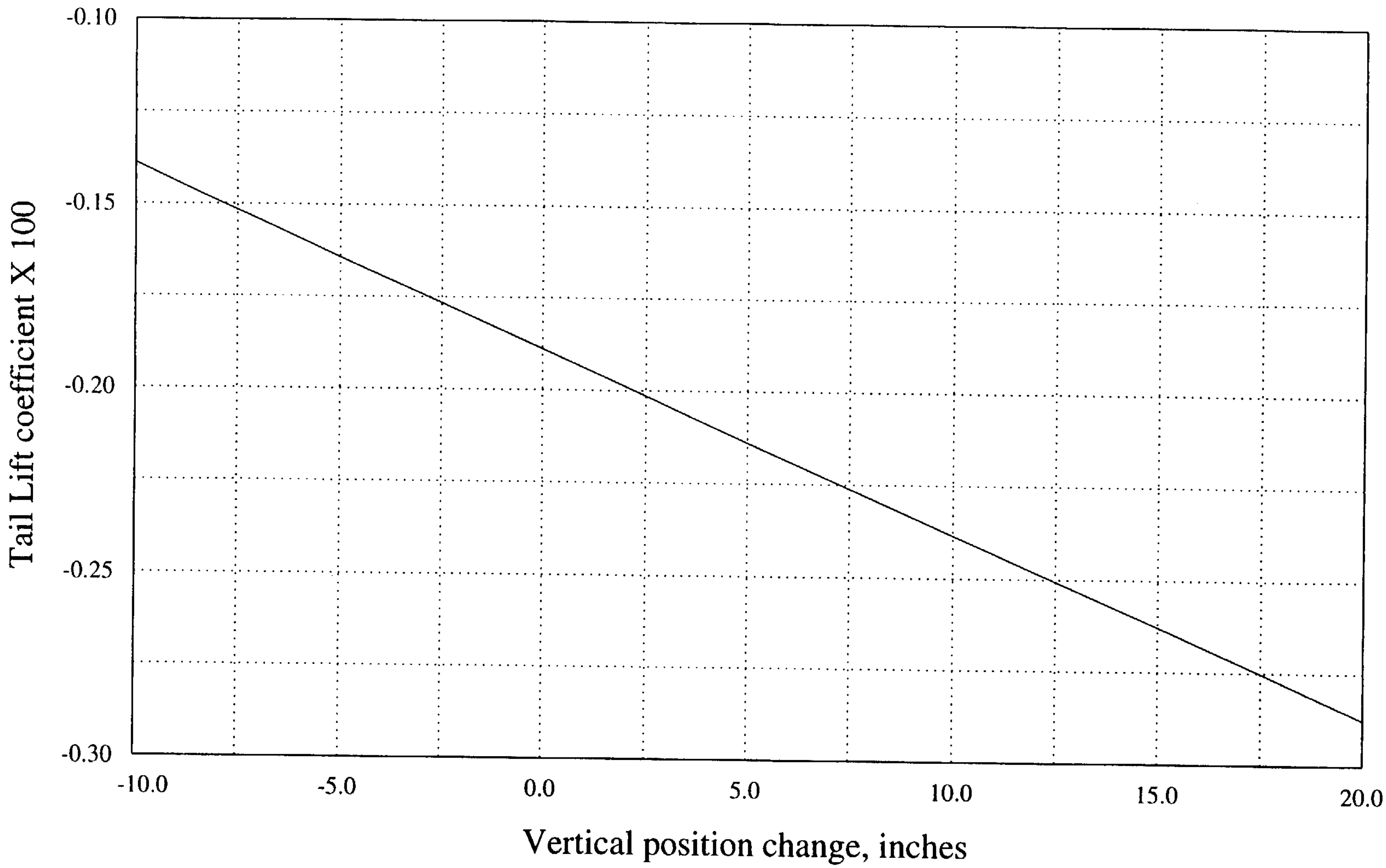

Total configuration drag is plotted against canard vertical position in this figure. The horizontal tail was fixed at the baseline position for these calculations. The two most obvious differences between these data and those shown for the horizontal tail position changes are the smaller drag changes associated with moving the canard compared with moving the tail and the more significant break in slope. In fact, the slope changes sign at the baseline position for canard movement. If the drag changes were larger it might be worth spending a little time to try to understand the sign change. The range of vertical movement for the canard is smaller than for the tail due to less body height at the canard location available to move the canard compared with that for the tail.

rmh - 7

Canard Position Effect, PTC, Tail at Original Position
SYN107-MB Analysis, M = 2.40, fixed lift

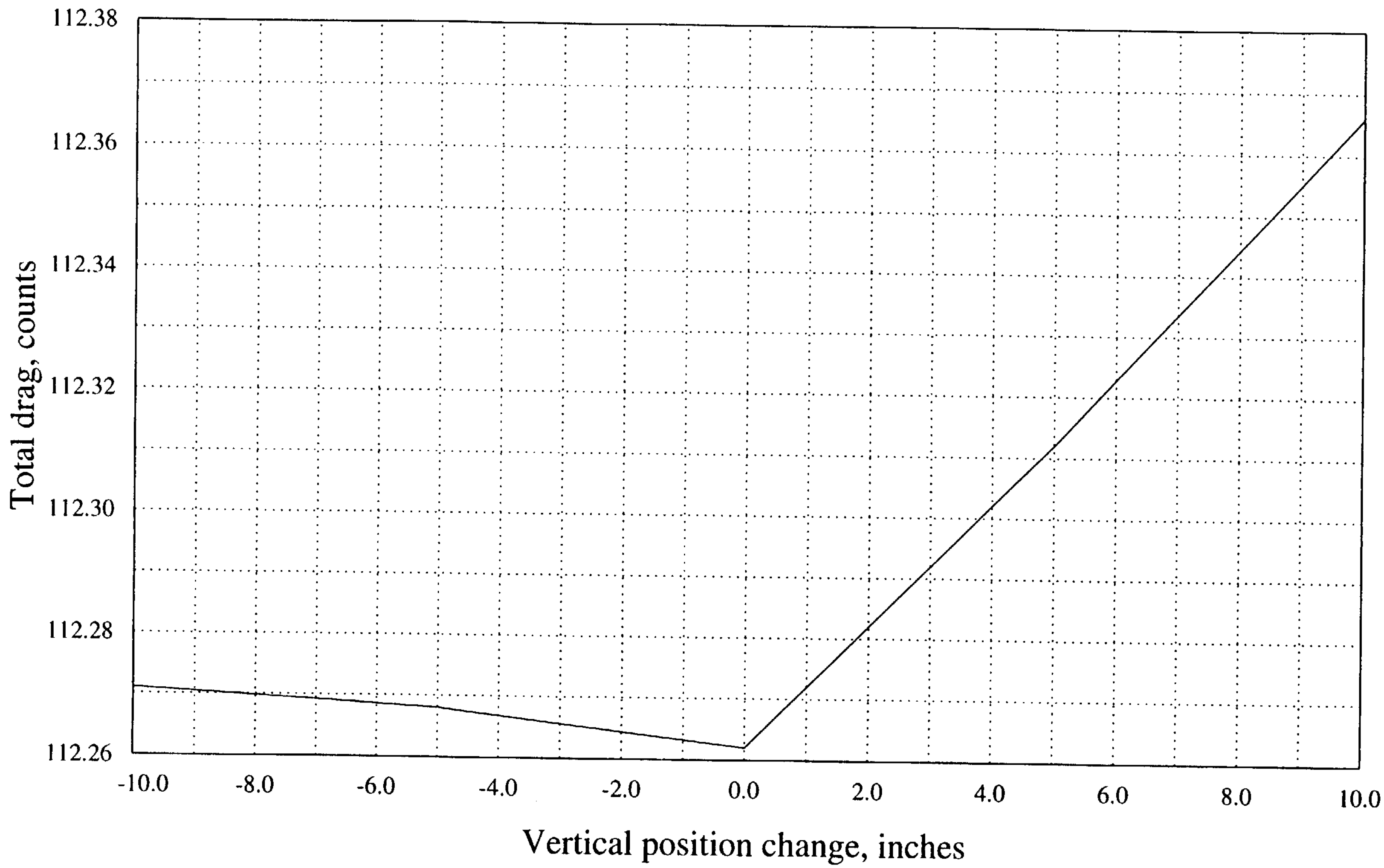

This figure shows the variation of total configuration drag as a function of optimization search step. Search steps are used on the abscissa rather than optimization iteration because the false steps (increasing objective function) can be seen. When optimization iteration is used only the final search step is observed and the data tend to look smoother. This type of plot shows that the optimization algorithm takes several steps in the search direction which do not result in an improvement in the objective function. The objective function is defined in the figure and the design variables were canard and tail incidence angle. The rotation axis for the canard and tail was 70% of the root chord which is approximately 50% of the tip chord of each surface. Note that there were three steps with increasing drag and several steps with no drag decrease before reaching the final value. The objective function for this case is composed of two terms representing an effort to trim the aircraft while minimizing drag. The weighting factor multiplying the moment term is an order of magnitude greater than the drag weighting factor but the moment coefficient is squared so the drag term is actually larger than the moment term. This optimization problem was conducted at constant cruise lift so the angle of attack changed during optimization. This optimization run resulted in a drag decrease of nearly 3.0 counts while reducing the pitching moment to near trim. The moment data will be shown in the next figure. The center of gravity was located quite far aft at 2304.71 inches from the nose. This center of gravity position produced a decrease in canard incidence and an increase in tail incidence for trim. Both drag and pitching moment move in the desired direction for this aft c.g. position when the canard load is decreased and the tail load is increased.

rmh - 8

PTC Trim Study, Tail and canard at Original Positions
SYN107−MB, M = 2.40, fixed lift, OBJ = $500(C_D) + 5000(C_M)^2$

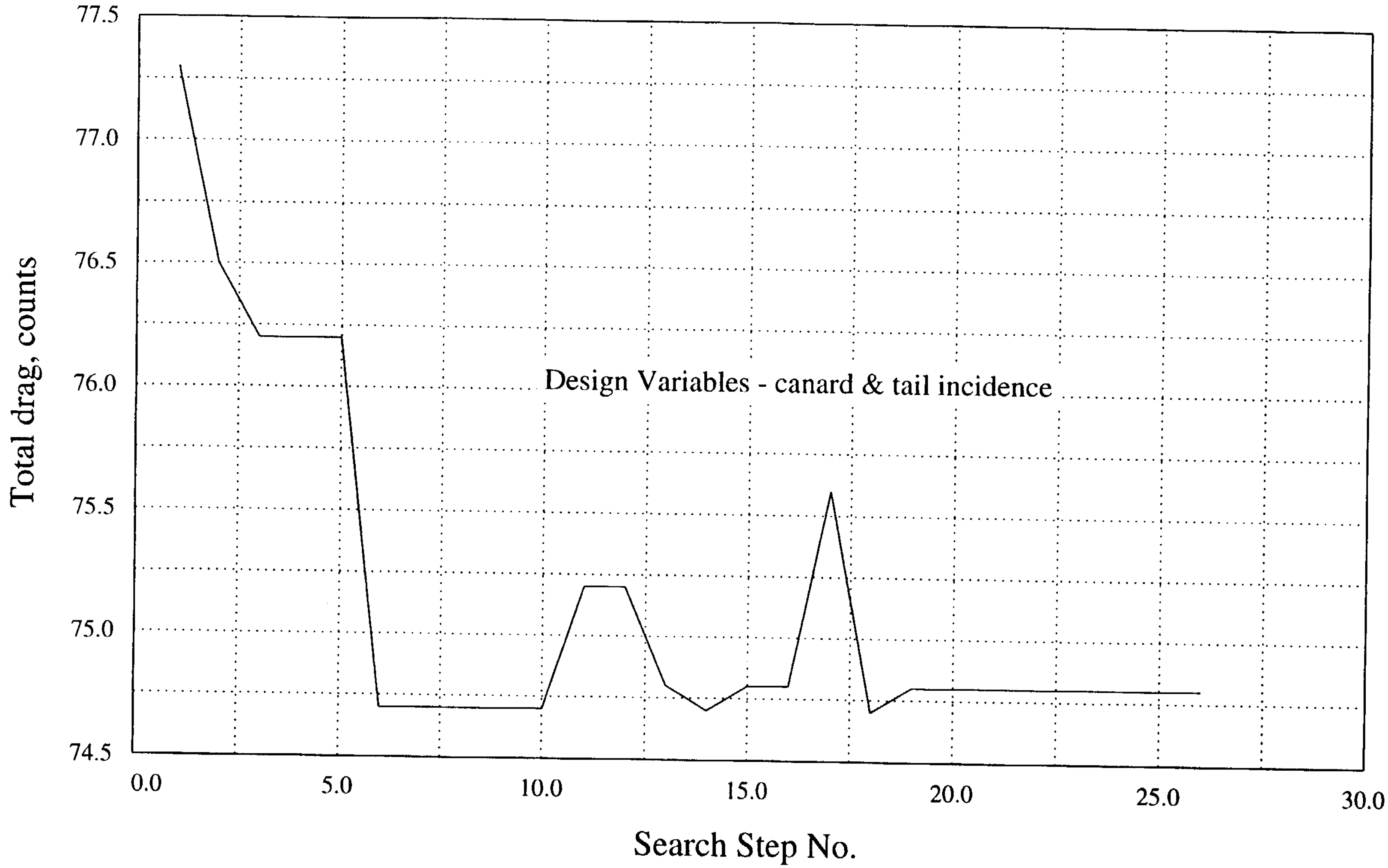

The pitching moment history shown in this figure has approximately the same trend as the drag data shown in the previous figure with similar false steps and the number of steps required to reach a final level of pitching moment. Note that the pitching moment did not reach a precise value of 0.0 showing one of the weaknesses in the penalty function method of conducting numerical optimization studies. The pitching moment could have been forced to a smaller value by increasing the weighting factor on the moment term in the objective function definition or decreasing the magnitude of the drag term weighting factor or both but the result would have produced less drag reduction. A better method of controlling pitching moment while reducing drag would be to impose a hard constraint on pitching moment with a drag objective function. This capability was not available in the design code at the time of this investigation.

rmh - 9

PTC Trim Study, Tail and canard at Original Positions

SYN107–MB, M = 2.40, fixed lift, OBJ = $500(C_D) + 5000(C_M)^2$

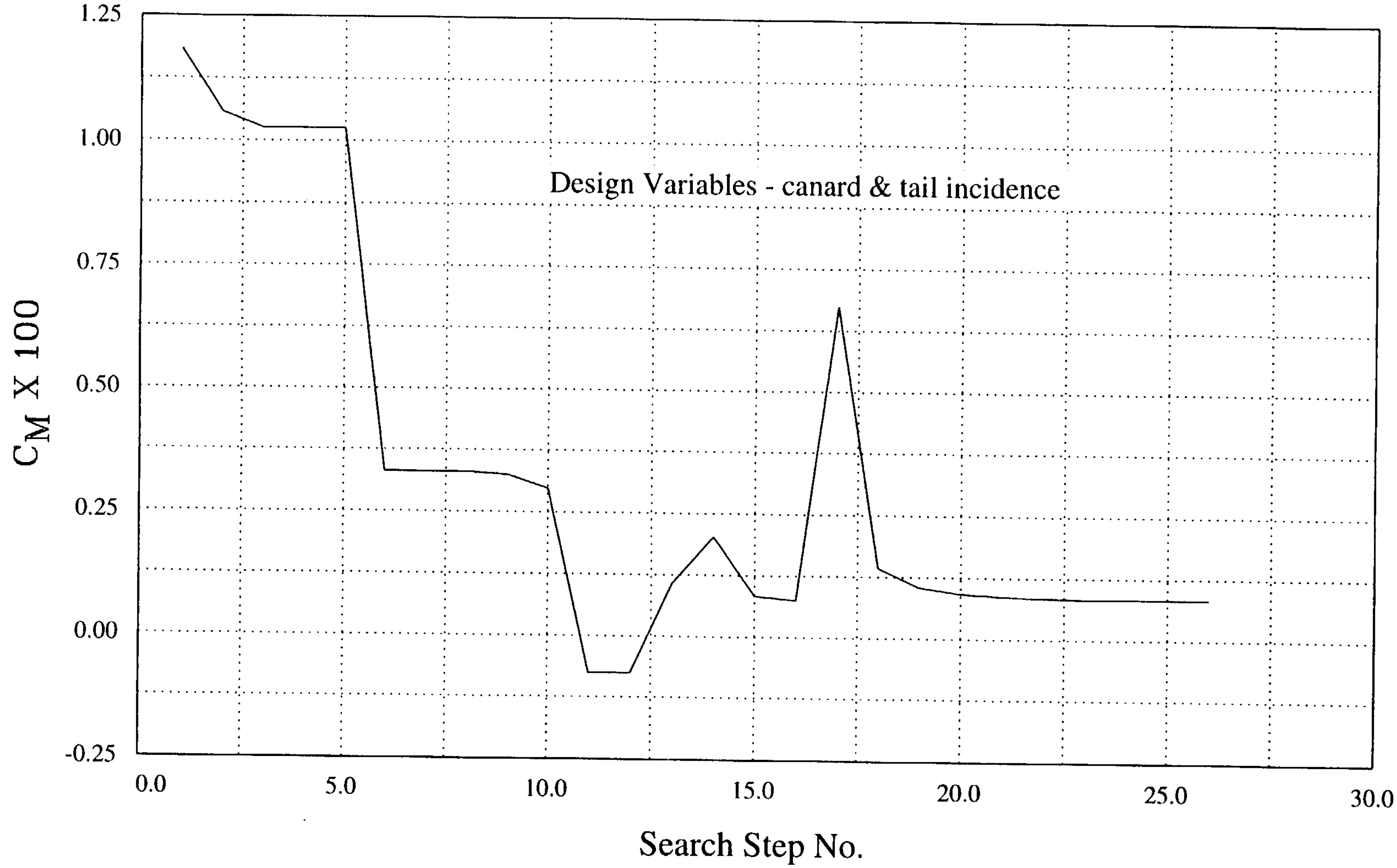

The angle of attack data shows a nearly monotonic decrease during the optimization process resulting primarily from an increasing tail load and the requirement to maintain total lift during design. As stated earlier the canard load decreased during optimization but the canard is smaller than the horizontal tail by nearly a factor of 2 so the increasing load on the tail more than offset the decreasing load on the canard. The same false steps noted earlier for the drag and pitching moment are visible here but are smaller. The angle of attack decreased by approximately 0.20 degrees to maintain the cruise lift coefficient of 0.0995. If this problem had been conducted at constant angle of attack the configuration lift would have increased in response to the increasing tail load during optimization.

rmh - 10

PTC Trim Study, Tail and canard at Original Positions

SYN107–MB, M = 2.40, fixed lift, OBJ = $500(C_D) + 5000(C_M)^2$

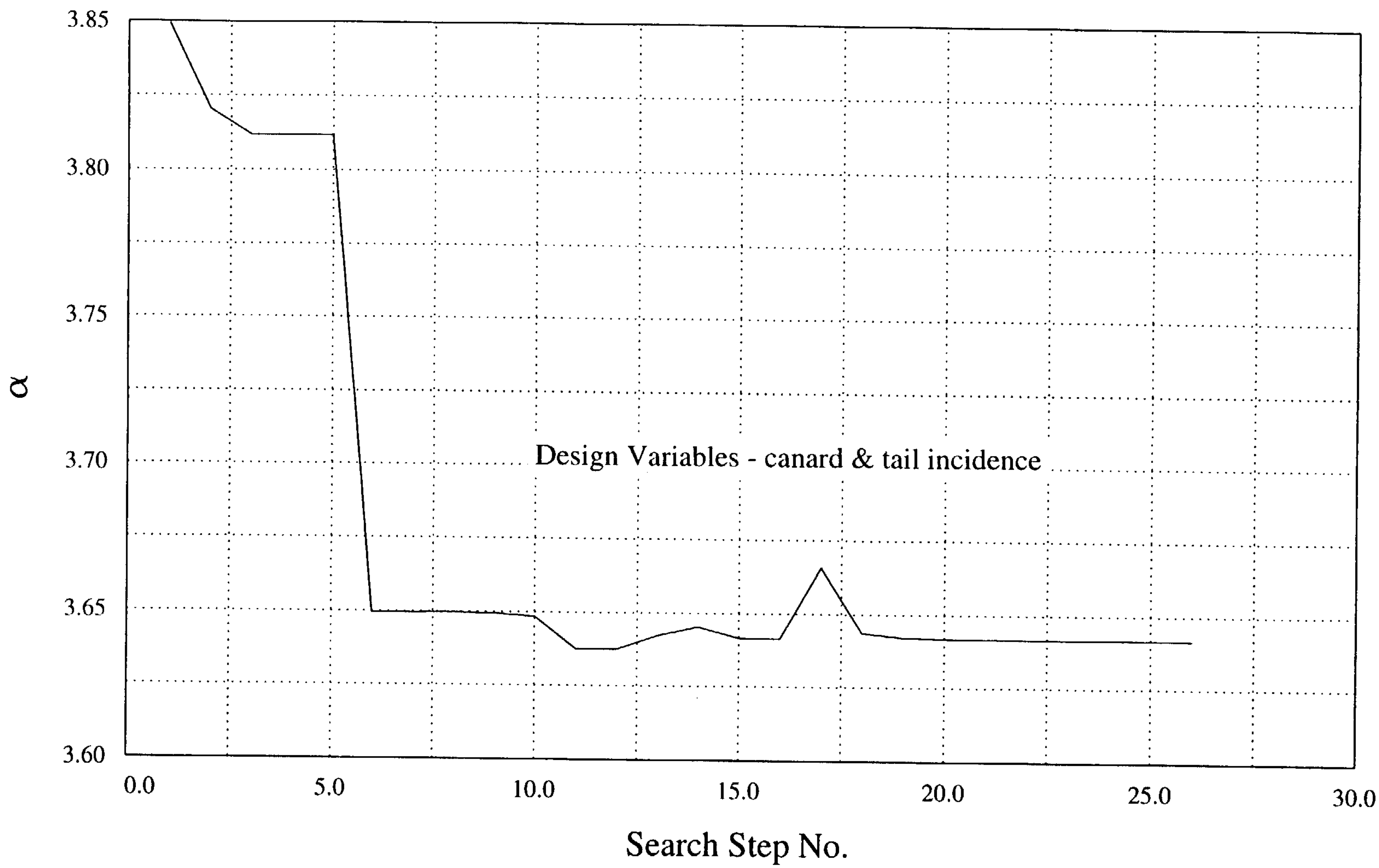

A lift-drag ratio history is shown in this figure. The data shows that the lift-drag ratio increased from 12.85 to 13.28 during the optimization process. This is a fairly substantial increase from the use of only two design variables and would not be possible if the drag and pitching moment did not require the same direction of movement of the canard and tail. As discussed previously, this increase is only realizable when the center of gravity is located in an aft position. When a forward location is used the horizontal tail load decreases while the canard load increases resulting in a decrease in the lift-drag ratio. This decrease occurs for two reasons. First, when the canard load increases a down-load is produced on the tail by the canard flow field and second, a reduced tail load makes it necessary for the wing to carry more load resulting in more induced drag for the wing. It has been shown previously that it is desirable to increase the tail load to reduce the total drag.

rmh - 11

PTC Trim Study, Tail and canard at Original Positions
SYN107–MB, $M = 2.40$, fixed lift, $OBJ = 500(C_D) + 5000(C_M)^2$

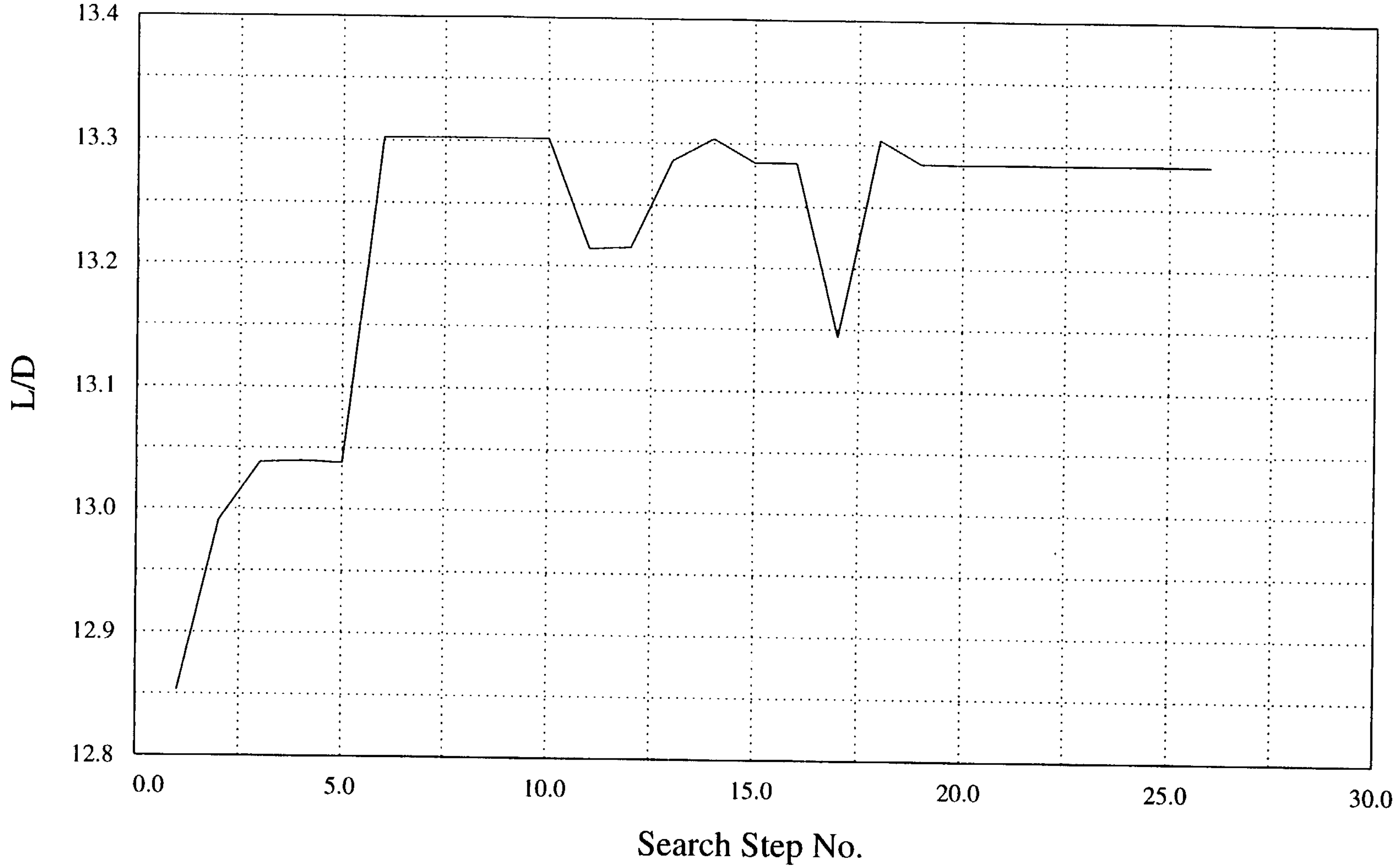

When wing camber is added to the set of design variables and the problem is conducted at fixed angle of attack the optimization results shown here and in the next few figures is obtained. Wing camber was represented by a uniformly distributed set of sine functions beginning at the third wing defining station and ending at the tip. Nine functions were located at each wing defining station beginning at 10% chord and ending at 90% chord. The objective function consisted of two terms as before but the first term contained the lift-drag ratio instead of the drag coefficient. The center of gravity was located at the same aft position as for the last problem. The most significant differences between this problem and the problem shown in the last set of figures is that the angle of attack was held constant at 3.85 degrees and the lift-drag ratio was used during optimization with a resulting increase in configuration lift and drag. Note that the drag increased by approximately 1.50 counts during optimization while a drag reduction was obtained when lift was held constant. The abscissa is optimization iteration instead of search step for this set of figures resulting in a smoother trend for the data. Note that the drag increases and then decreases before settling to a fairly constant value.

rmh - 12

PTC Optimization, Design Variables - Wing Camber, Canard & Tail Incidence
SYN107, M = 2.40, Xref = 2304 inches, Obj = $10(D/L) + 5000(C_M)^2$

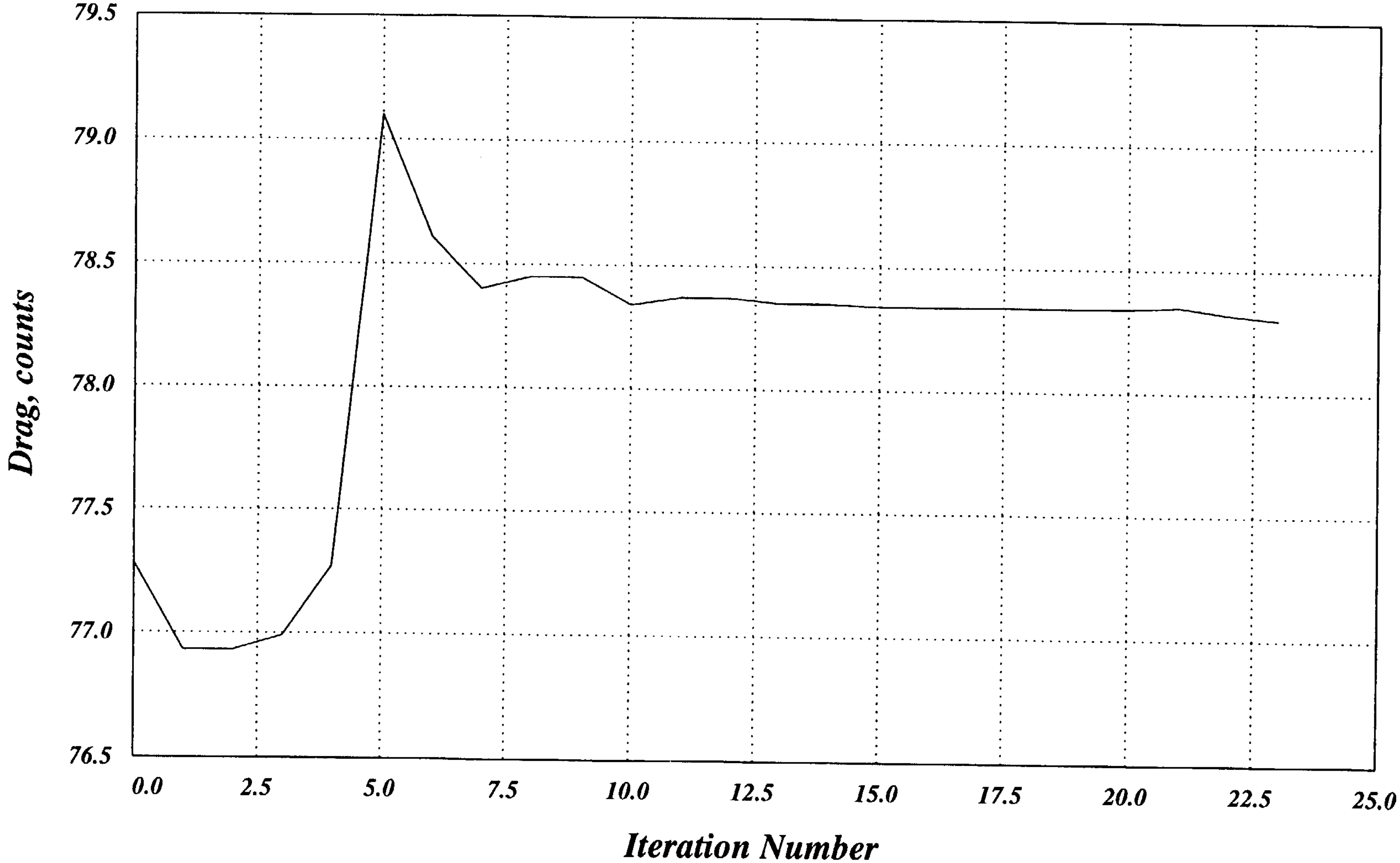

The pitching moment data shown here exhibit a nearly monotonic decrease toward trim reaching a value near zero after only five optimization iterations. As noted previously, the final value of pitching moment is not precisely zero because of the use of a penalty function to achieve trim.

rmh - 13

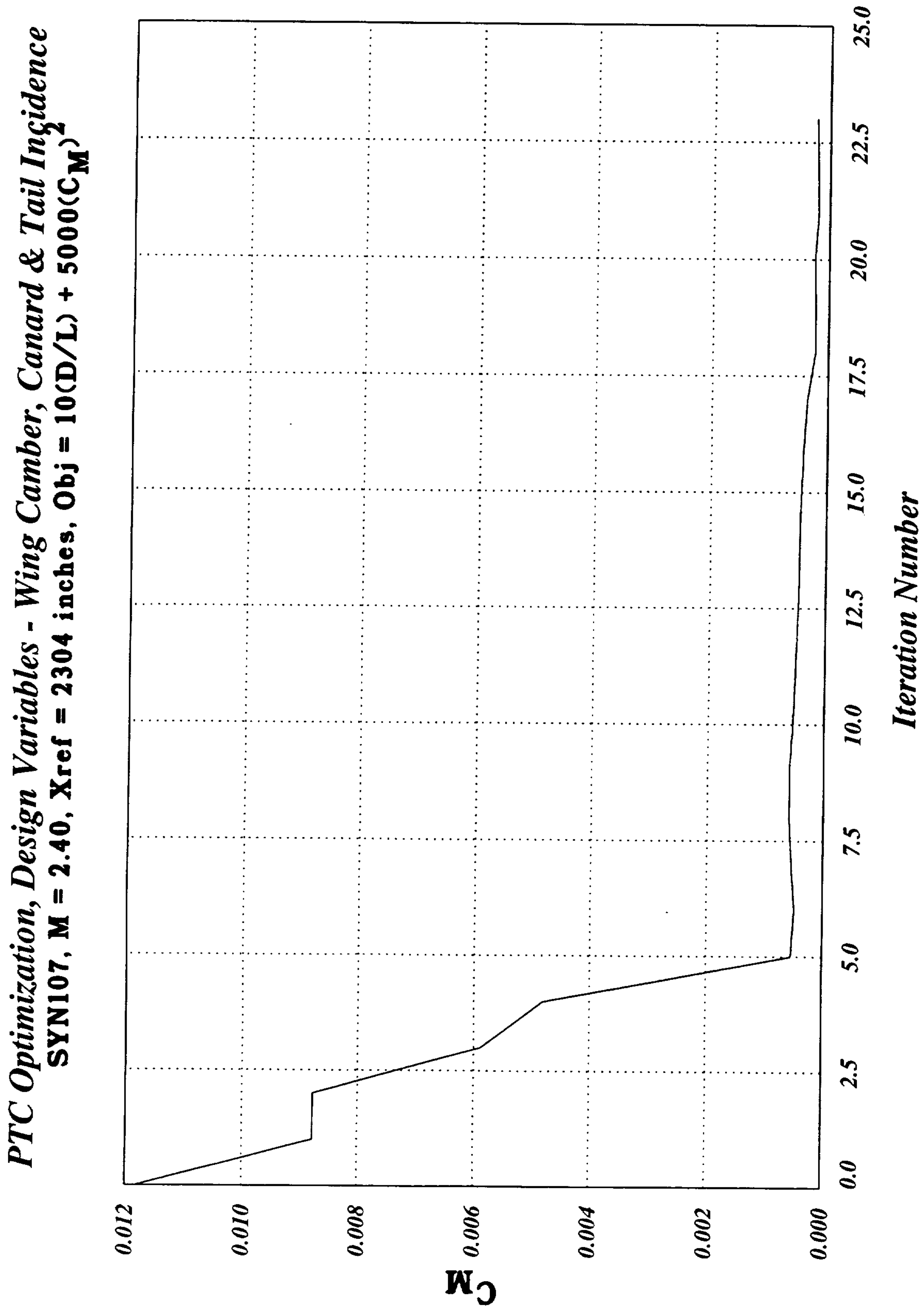
PTC Optimization, Design Variables - Wing Camber, Canard & Tail Incidence
SYN107, M = 2.40, Xref = 2304 inches, Obj = 10(D/L) + 5000(C_M)^2
C_M
0.012
0.010
0.008
0.006
0.004
0.002
0.000
0.0
2.5
5.0
7.5
10.0
12.5
15.0
17.5
20.0
22.5
25.0
Iteration Number

The lift coefficient history shown here exhibits a nearly monotonic increase during the optimization process similar to that observed for the pitching moment. Again a nearly constant value is achieved after only five optimization iterations. The lift coefficient increases faster than the drag coefficient giving an increase in the lift-drag ratio and a decrease in the objective function as shown in the next two figures. The increasing lift coefficient is due to the increasing tail load required to achieve trim.

rmh - 14

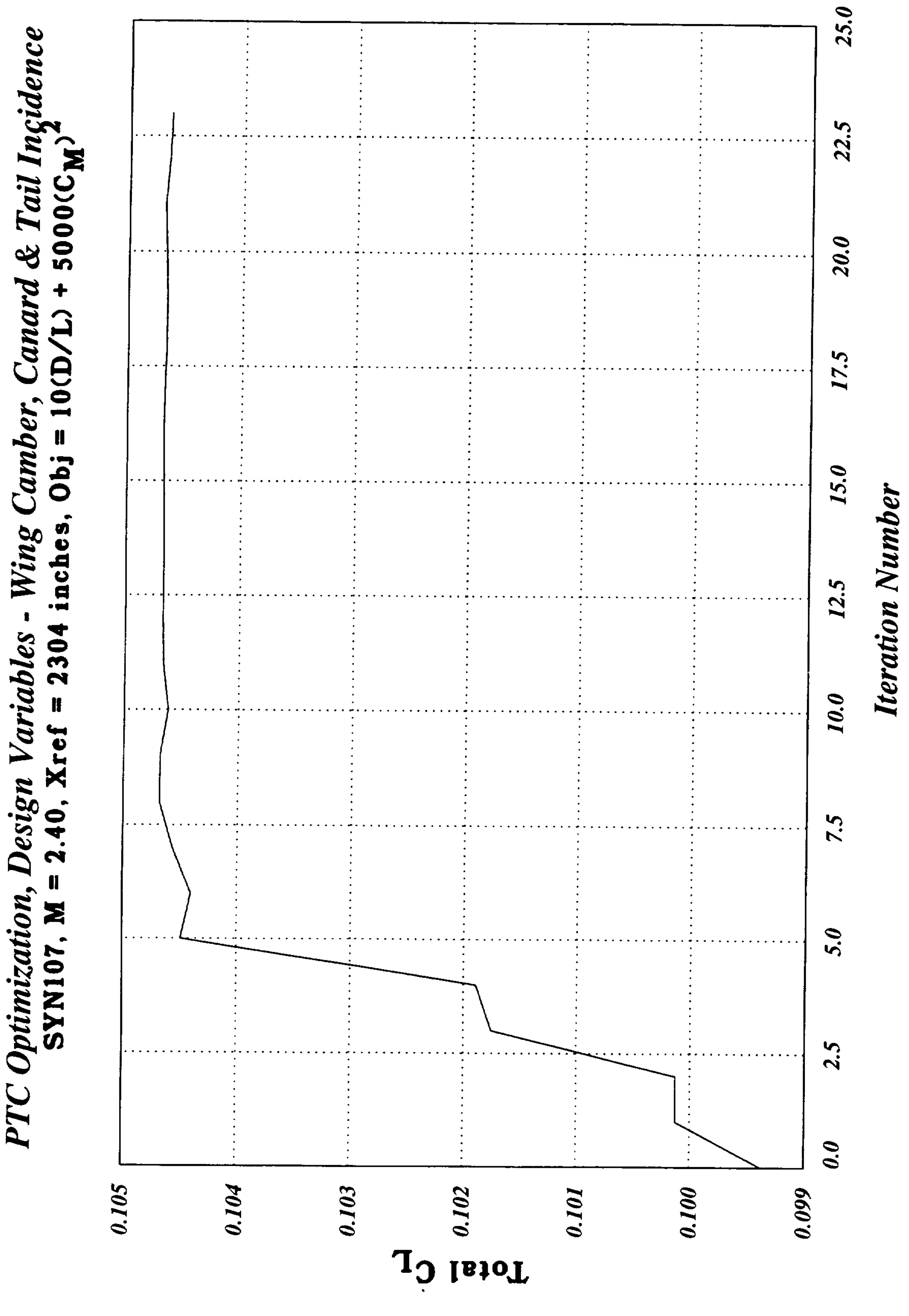
PTC Optimization, Design Variables - Wing Camber, Canard & Tail Incidence
SYN107, M = 2.40, Xref = 2304 inches, Obj = 10(D/L) + 5000(C_M)^2
Total C_L
Iteration Number
0.105
0.104
0.103
0.102
0.101
0.100
0.099
0.0
2.5
5.0
7.5
10.0
12.5
15.0
17.5
20.0
22.5
25.0

The lift-drag ratio history is shown here. Note that the lift-drag ratio increased from 12.85 to approximately 13.38, a larger increase than that observed for the constant lift problem discussed previously. The optimization code had the ability to change the wing camber during design unlike the previous problem where only canard and tail incidence were used as design variables so the greater increase noted here is really not significant given the larger design space for the present problem.

rmh - 15

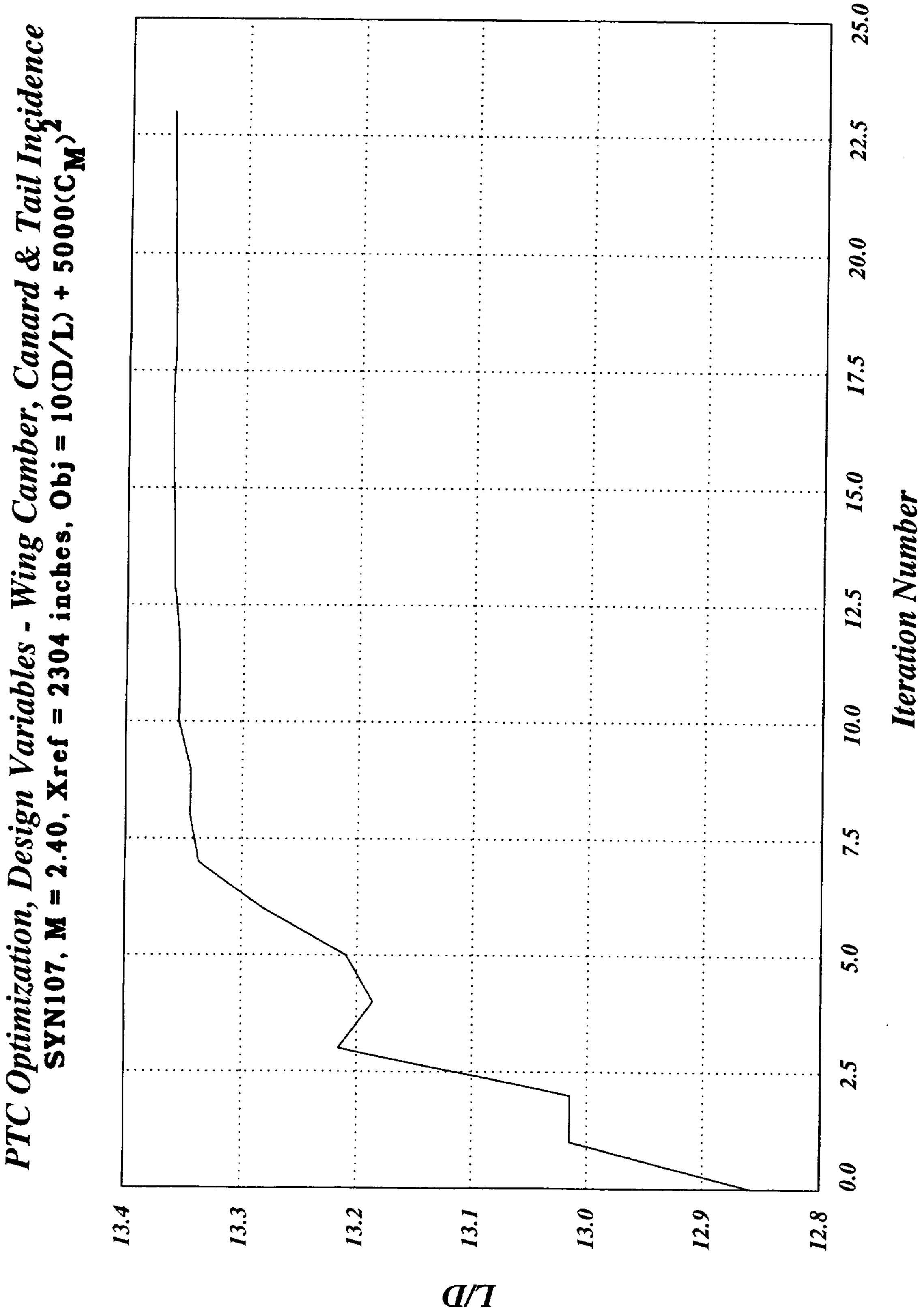

PTC Optimization, Design Variables - Wing Camber, Canard & Tail Incidence
SYN107, M = 2.40, Xref = 2304 inches, Obj = 10(D/L) + 5000(CM)2
L/D
13.4
13.3
13.2
13.1
13.0
12.9
12.8
0.0
2.5
5.0
7.5
10.0
12.5
15.0
17.5
20.0
22.5
25.0
Iteration Number

The variation of the objective function during optimization is shown here. Again a nearly monotonic decrease is observed with the final value achieved after only five iterations. It is interesting that the optimization algorithm runs out of ability to achieve gain after only five iterations given the large set of sine functions describing the wing camber. The gain here is not greatly different than that observed when only canard and tail incidence were used as design variables.

rmh - 16

PTC Optimization, Design Variables - Wing Camber, Canard & Tail Incidence
SYN107, M = 2.40, Xref = 2304 inches, Obj = $10(D/L) + 5000(C_M)^2$

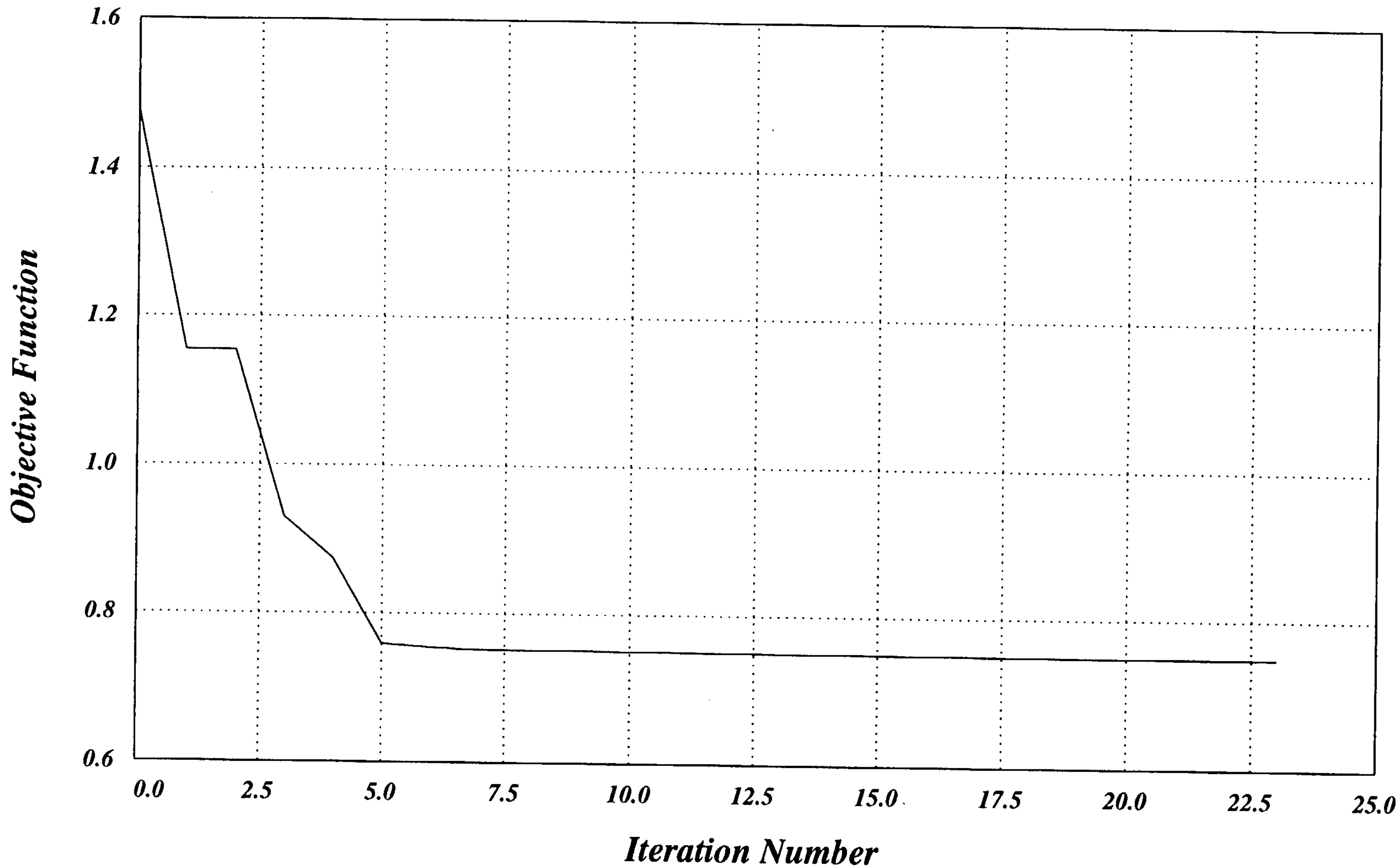

A brief optimization study was conducted using the incidence of the canard and wing camber and thickness as design variables. The changes to the wing were primarily camber changes since the wing thickness was constrained at 252 uniformly distributed locations from wing station 101 to the tip and from near the leading edge to near the trailing edge at eleven wing stations. Wing camber and thickness changes were accomplished by use of SIN2 functions located at 11 spanwise stations on the upper and lower surfaces with the functions uniformly distributed along each of the 11 chord stations beginning at 10-percent chord and ending at 90-percent chord with intervals of 10-percent chord. Design changes were confined to the wing between station 101 and the tip. The objective function was 10(D/L) for this problem. The changes in the lift-drag ratio for 12 optimization iterations are shown in this figure. Note that a large change in the lift drag-ratio occurs during the first optimization iteration after which a more modest increase is achieved for the next 6 or 7 iterations. Another fairly rapid increase begins near the eighth iteration. This second increased rate of change in the lift-drag ratio correlates with an increased rate of decrease in the incidence angle of the canard as shown in the next figure. The increase in the lift-drag ratio is approximately 0.3 compared with approximately 0.5 when the tail incidence is included in the design variable set. This again shows the importance of carrying a positive load on the tail.

rmh - 17

PTC Canard Incidence and Wing Camber Optimization
SYN107 – M = 2.40 – α = 3.85 deg.

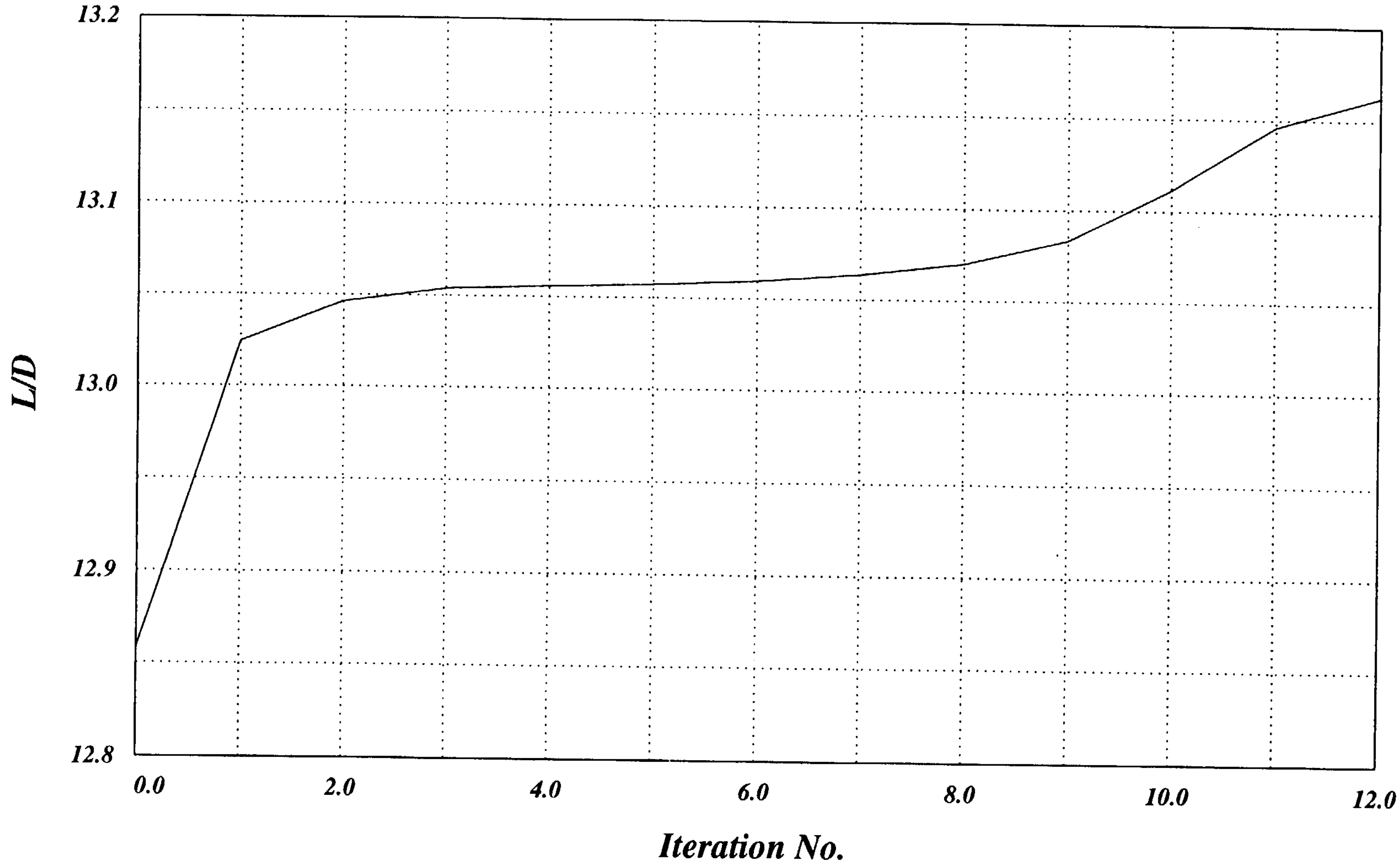

The canard incidence angle as a function of optimization iteration is shown here. Note that the angle decreases monotonically from the baseline value of 0.0 degrees to -2.0 degrees during design. The canard load was still positive with an incidence of -2.0 degrees. The canard load did not become negative for any of the optimization problems considered during these studies a finding that is consistent with intuition since it is fairly obvious that if a lifting surface is carried on the aircraft it should probably carry part of the load if possible.

rmh - 18

PTC Canard Incidence and Wing Camber Optimization
SYN107 - M = 2.40 - α = 3.85 deg.

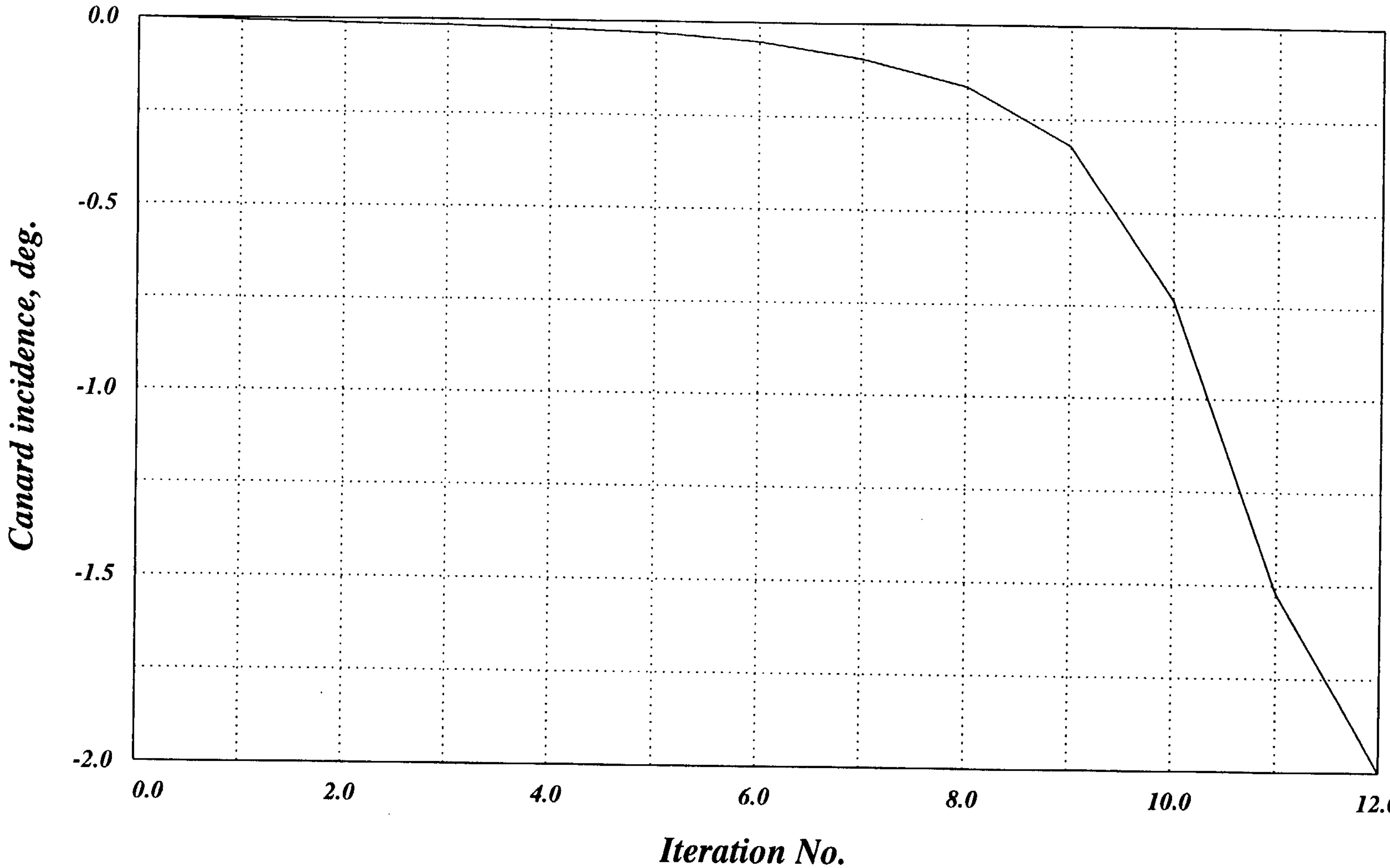

This figure contains data that was part of a study of the effect of center of gravity position on optimization results. Three different center of gravity positions were investigated. The first cg position studied is the baseline position of 2304.71 inches. Optimization runs were conducted at constant lift so any changes in drag are directly related to changes in configuration lift-drag ratio. The optimization code was run until a local minimum was found as indicated by a termination message from NPSOL. The objective function was $500(C_D) + 5000(C_M)^2$ and the design variables were the canard and tail incidence angles. When the cg position is such that the initial pitching moment is nose up the changes in canard and tail incidence angle give a decrease in drag and pitching moment simultaneously. When the cg is moved forward to a position where trim occurs for the baseline configuration the canard and tail incidence changes during optimization are in the same direction as when the cg position is aft so the drag decreases by nearly the same magnitude for both cg positions. Moving the cg to 2000.0 inches gives a nose down pitching moment for the baseline configuration and the opposite direction of change for both the canard and tail incidence angles during optimization as might be expected; the canard incidence increases while the tail incidence angle decreases. These changes produce an increase in configuration angle of attack of approximately 0.20 degrees. The configuration drag increases by 12.0 counts as the optimization code moves the configuration toward trim. The changes that occurred during optimization to the pitching moment and drag coefficients and the terms in the objective function equation were a little surprising as shown here. These are the initial and final values resulting from an optimization study carried out until the changes in the objective function became negligible with further iterations. Despite the smaller initial value for the pitching moment term the optimization code worked pitching moment much harder than drag as indicated by the increase in the drag term and drag coefficient and the decrease in the pitching moment term and pitching moment coefficient. Changes in the weighting factors would give different results but little information would be gained by conducting a weighting factor study. Penalty function methods are fairly well understood by the engineering community so this study was concluded at this point.

rmh - 19

PTC Configuration without nacelles, $M = 2.40$, c.g. = 2000 inches

	initial	**final**
moment term	1.098	0.102
drag term	3.863	4.468
$\mathbf{C_D}$	0.0077	0.0089
$\mathbf{C_M}$	-0.0148	-0.0045

This data shows results from a component-build-up study using the PTC configuration without nacelles and boundary layer diverters. The analysis code FLO107MB was used during this study. Initially, configuration components were "turned off" by imposing flow-through boundary conditions on selected components without eliminating thickness to avoid generating a new grid for each configuration. However, the components are thin so the grid displacement around each flow-through component was not considered to be a serious impediment to reliable flow solutions. Some of the results shown here are a little surprising and corroborative analyses from the Euler code AIRPLANE was conducted for verification. Drag polars for 5 different combinations of configuration components are shown here. The wing/body has the lowest drag, as expected. Addition of the vertical tail causes a drag increase of less than 1.0 count. Adding the horizontal tail to the wing/body/vertical-tail configuration produces an additional drag increase of approximately 2.0 counts as shown in the figure. When the canard is added to the wing/body/vertical-tail configuration without the horizontal tail the drag increase is negligible. The drag and lift of the canard increase in the right proportions to maintain lift-drag ratio over the small range of angles of attack shown in this figure. This will become more apparent when the lift curves are presented in the next figure. Adding the canard to the wing/body/vertical-tail/horizontal-tail gives a drag increase of approximately 1.0 count showing that the interaction between the canard and the horizontal tail is greater than that of the canard with the other components. The canard produces a download on the horizontal tail causing a reduction in lift at a given angle of attack resulting in a polar shift in the direction of higher drag. It is interesting that the canard seems to produce a greater download on the horizontal tail than on the wing given the greater distance between the canard and horizontal tail. A final check on the validity of these results was conducted by creating new grids for the PTC configuration with selected components removed. These results verified the results shown here and in subsequent figures.

rmh - 20

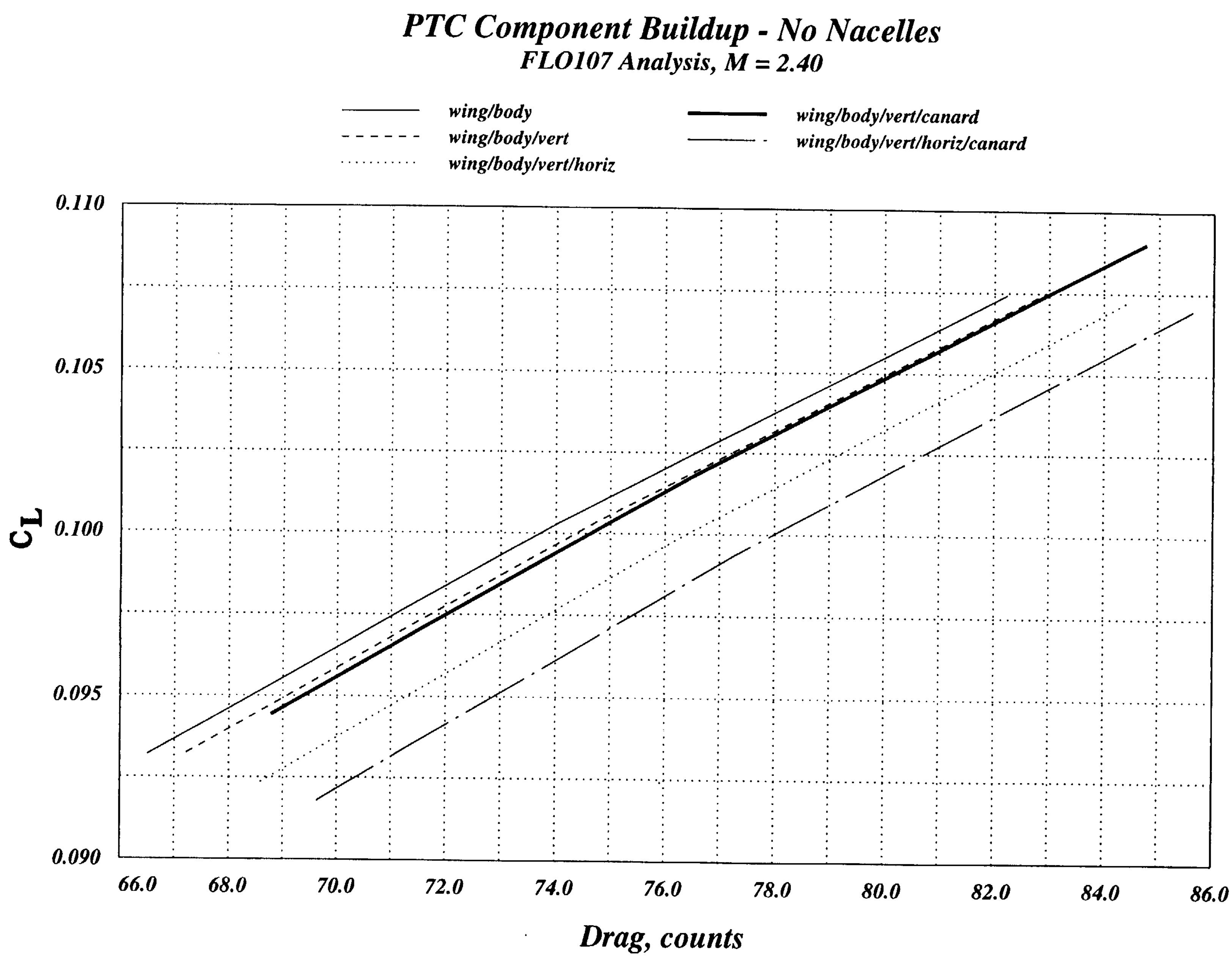
PTC Component Buildup - No Nacelles
FLO107 Analysis, M = 2.40
wing/body
wing/body/vert
wing/body/vert/horiz
wing/body/vert/canard
wing/body/vert/horiz/canard
C_L
0.110
0.105
0.100
0.095
0.090
66.0
68.0
70.0
72.0
74.0
76.0
78.0
80.0
82.0
84.0
86.0
Drag, counts

This figure compares AIRPLANE and FLO107MB calculation for all configurations shown in the previous figure except the wing/body. These data are shown for a lift coefficient of 0.10 at the supersonic cruise Mach number. Note that AIRPLANE and FLO107MB give similar results regarding the drag increments between the various configurations but AIRPLANE consistently shows higher drag for all component combinations. This figure shows very clearly that an interference drag increment between the canard and horizontal tail exists and has a magnitude of approximately 1.5 drag counts.

rmh - 21

Component Build-Up M=2.4, CL =0.1

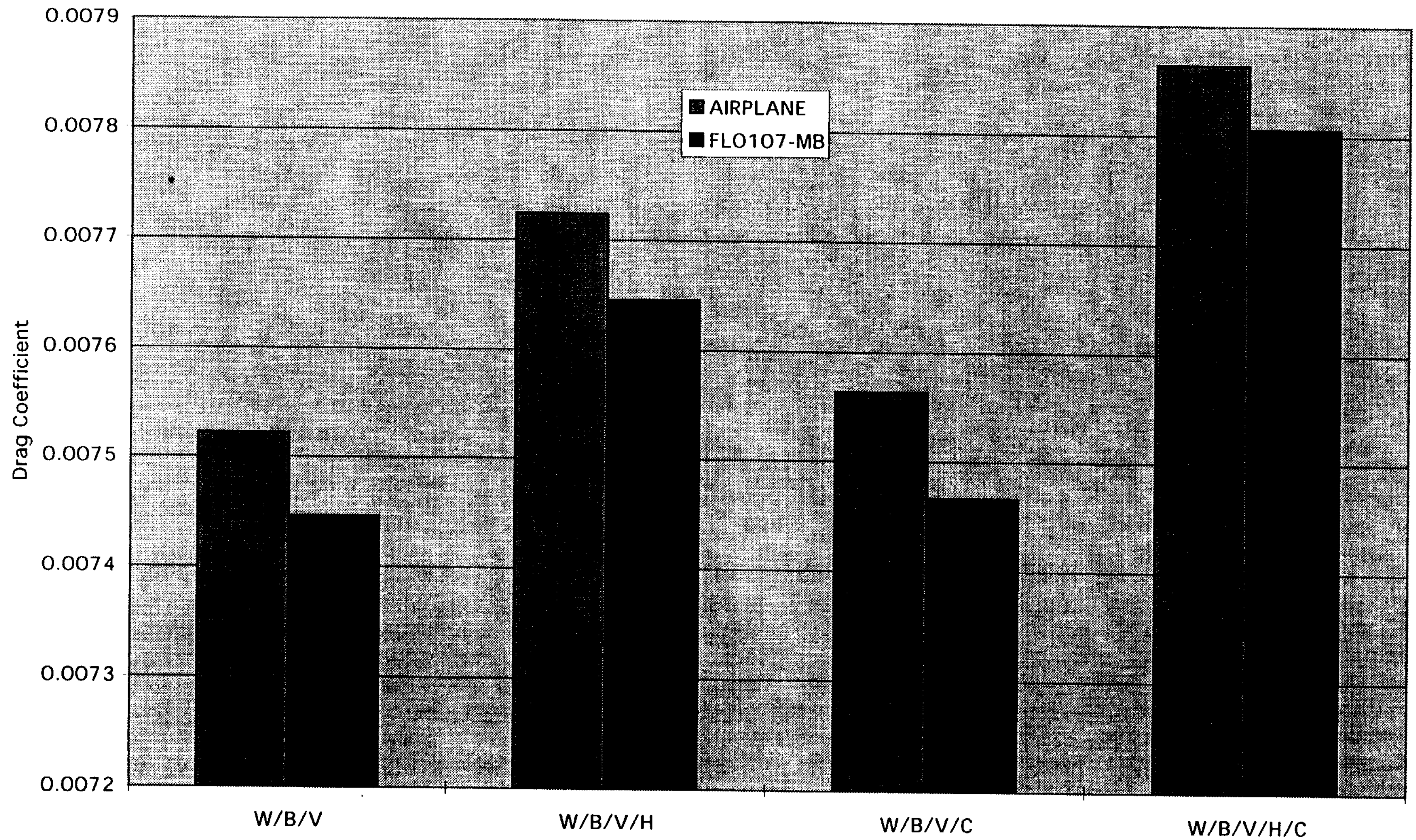

Lift curves for the 5 component combinations discussed above are shown in this figure. Note that the lift-curve slopes for all configurations are nearly parallel with the main difference between configurations being the effective camber of each component combination. The wing/body/vertical-tail/canard has the greatest effective camber while the wing/body/vertical-tail/horizontal-tail/canard has the least effective camber. This again shows that the canard produces a download on the horizontal tail for these incidence angles and angles of attack. The canard and horizontal tail have geometric incidence angles of 0.0 and -2.0 degrees respectively. The lift curves for the wing/body and wing/body/vertical-tail configurations are nearly identical, as expected. Adding the horizontal tail to the wing/body/vertical-tail causes an effective camber reduction due to the 2.0 degree negative incidence of the horizontal tail. Adding the canard to the wing/body/vertical-tail/horizontal-tail configuration causes an additional camber reduction due to an unfavorable interaction between the 2 horizontal surfaces despite the positive camber produced by the canard as shown in the figure. This interaction could be made more favorable by appropriate changes in the incidence and/or camber and the vertical position of the canard and horizontal tail.

rmh - 22

PTC Component Buildup - No Nacelles

FLO107 Analysis, M = 2.40

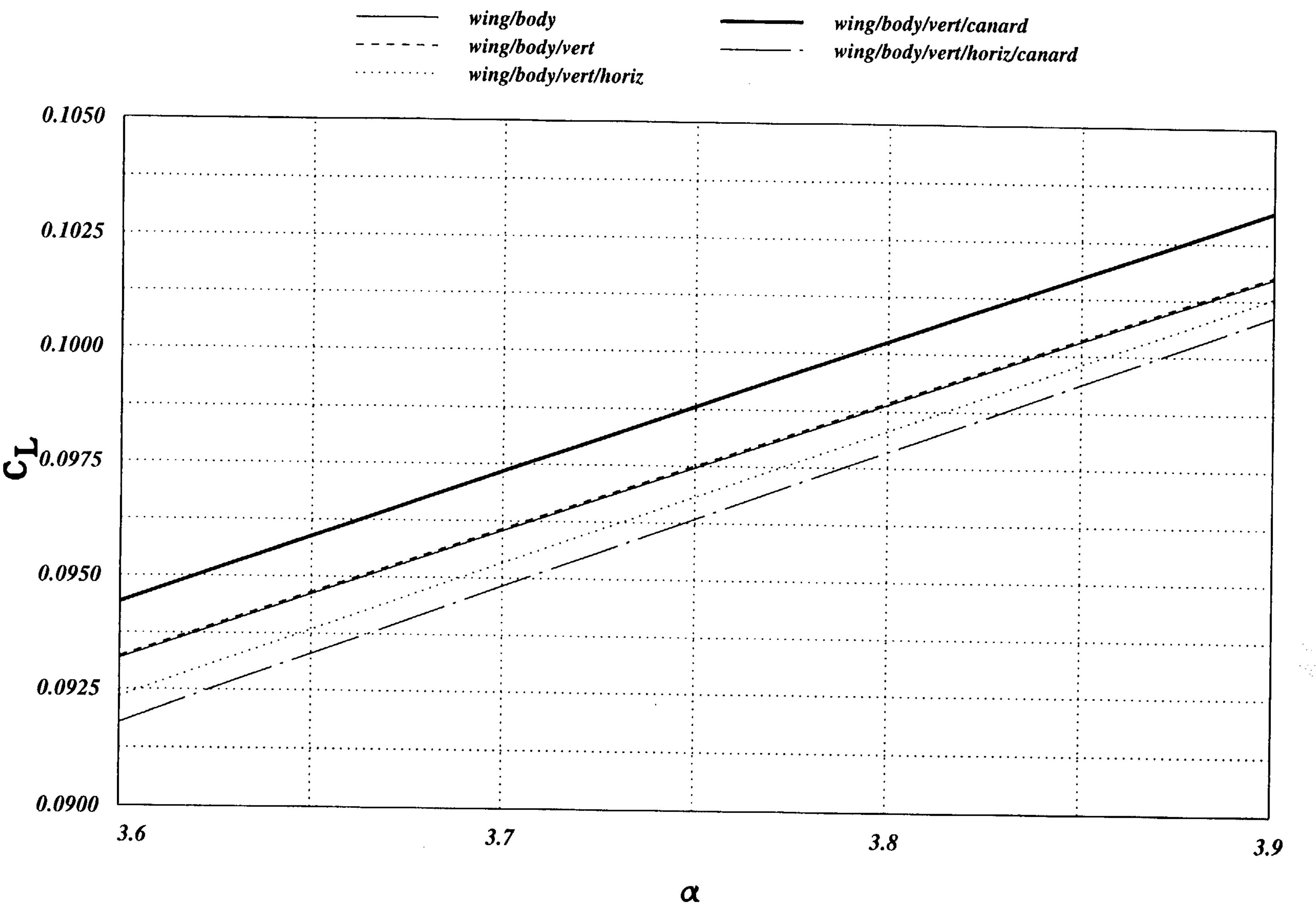

Selected component lift and drag coefficient data are shown in the following table. The component aerodynamic coefficients are based on component areas for these data. The following effects are noted from the data in this table.

1) Adding the vertical tail has little effect on the wing and body

2) Adding the horizontal tail to the wing/body/vertical-tail has no effect on the wing, decreases lift and increases drag on the body.

3) Adding the canard to the wing/body/vertical-tail/horizontal-tail increases lift and drag on the body and decreases lift and drag on the wing.

4) The canard increases the download on the horizontal tail by more than a factor of 4 and decreases the drag on the horizontal tail.

rmh - 23

Component buildup for PTC configuration - no nacelles
FLO107-MB, M = 2.40, Alpha = 3.85 deg.

wing/body

	CL	CD
Body	0.01101	0.00132
Wing	0.08931	0.00608

wing/body/vertical

	CL	CD
Body	0.01101	0.00132
Wing	0.08931	0.00608
Vertical Tail	0.00005	0.00007

wing/body/horizontal/vertical

	CL	CD
Body	0.01091	0.00133
Wing	0.08931	0.00608
Horizontal Tail	-0.00540	0.00180

wing/body/horizontal/vertical/canard

	CL	CD
Body	0.01214	0.00136
Wing	0.08639	0.00587
Horizontal Tail	-0.02268	0.00120
Canard	0.05985	0.00408

This figure shows the effect of component buildup for the PTC configuration on the drag coefficients at Mach 0.90. These data were generated for the original grid with small flux leaks and the non-zero thickness for the canard and tails discussed above. The trends in the lift and drag coefficients shown above for Mach 2.40 are similar to those shown here for Mach 0.90. The increased download on the horizontal tail generated by the canard is still present and the interference drag due to the canard and tail is similar to that observed at Mach 2.40. Note the sum of the drag increments due to adding the canard and vertical tail separately to the configuration is smaller than that generated by adding the canard and horizontal tail together . It is this fact that leads to the belief that the placement of the trimming surfaces should be considered during design of the final configuration. It might be interesting to study locating the horizontal tail on the vertical tail. A T-tail configuration might be undesirable for structural reasons but a mid-mounted horizontal tail on the vertical tail might be acceptable and the interference drag between the canard and tail of approximately 1.1 counts might be eliminated or substantially reduced. Also the horizontal tail effectiveness might be improved by moving it out of the wakes from the canard and wing.

rmh - 24

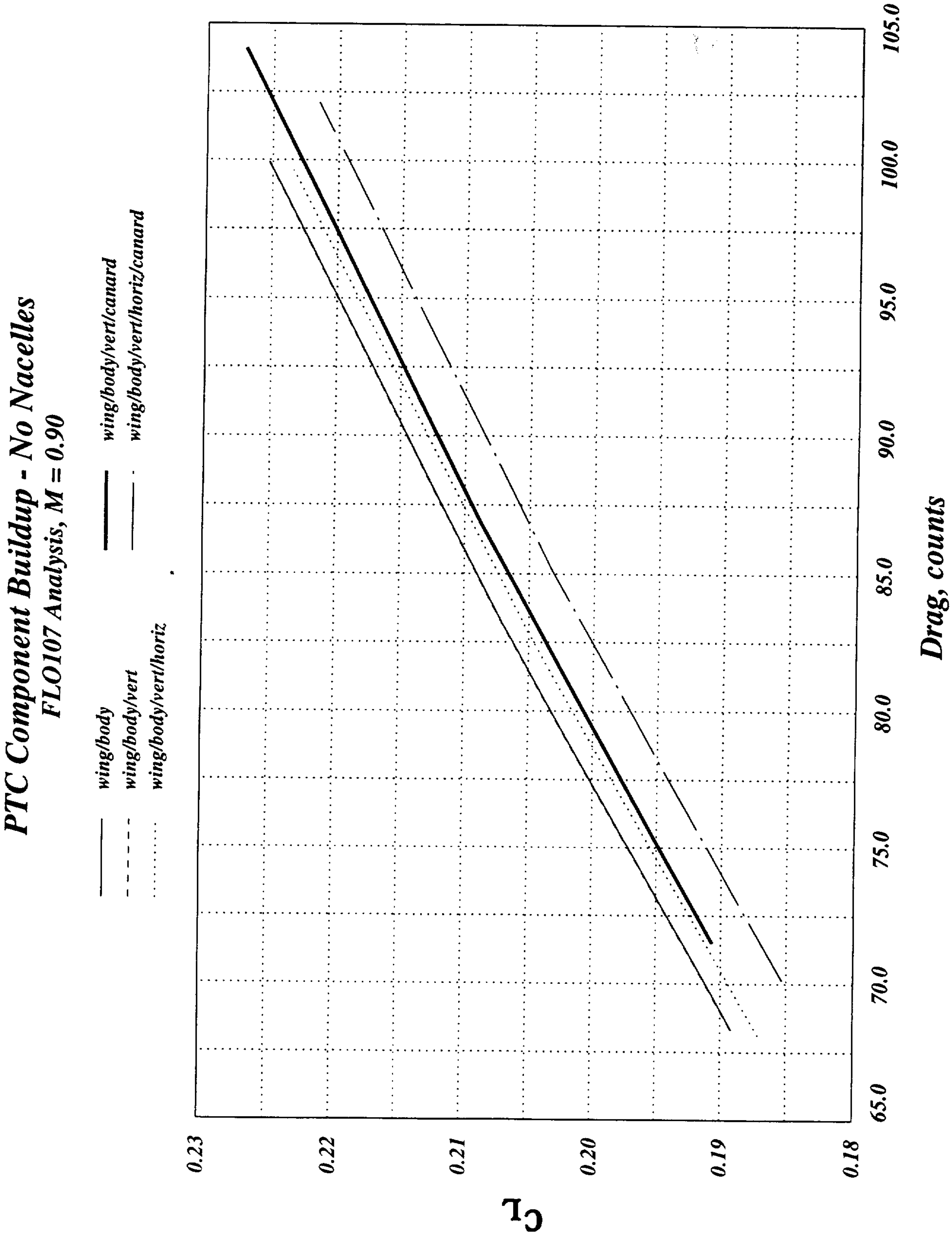
PTC Component Buildup - No Nacelles
FLO107 Analysis, M = 0.90
wing/body
wing/body/vert
wing/body/vert/horiz
wing/body/vert/canard
wing/body/vert/horiz/canard
C_L
0.23
0.22
0.21
0.20
0.19
0.18
65.0
70.0
75.0
80.0
85.0
90.0
95.0
100.0
105.0
Drag, counts

The lift-curve data shown here are similar to that shown for Mach 2.40 with the wing/body and wing/body/vertical-tail having nearly identical lift curves and the canard adding camber to the configuration due to it's positive load. The horizontal tail decambers the configuration due to it's download without the canard and even more substantial decambering occurs when the canard is present due to the induced download on the tail by the canard.

rmh - 25

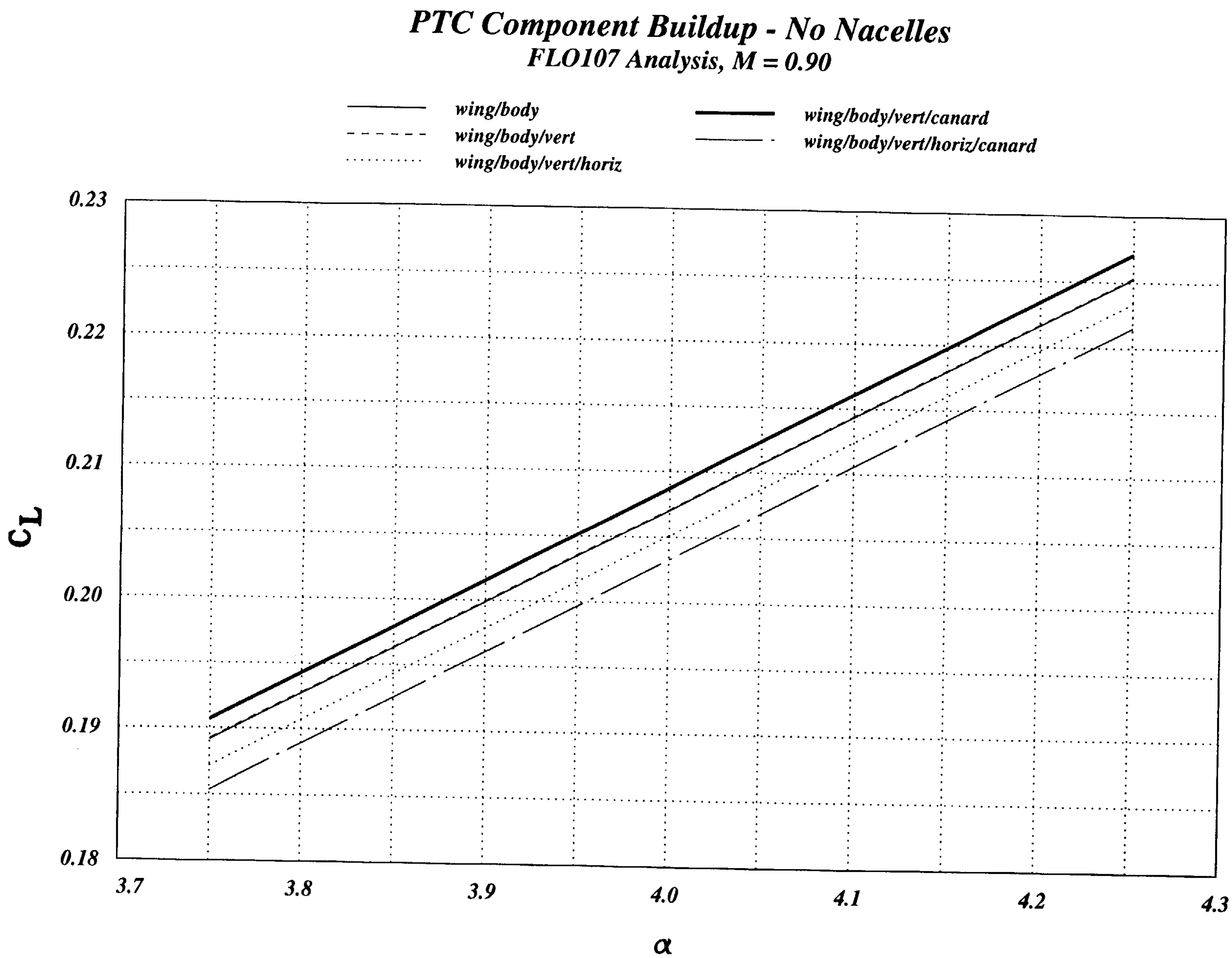

PTC Component Buildup - No Nacelles
FLO107 Analysis, M = 0.90
wing/body
wing/body/vert
wing/body/vert/horiz
wing/body/vert/canard
wing/body/vert/horiz/canard
0.23
0.22
0.21
0.20
0.19
0.18
C_L
3.7
3.8
3.9
4.0
4.1
4.2
4.3
α

This brief study using the PTC 3-surface configuration without nacelles and diverters has revealed some interesting results. The calculations were performed by use of the Euler codes SYN107MB and FLO107MB. The canard was found to reduce the lift on the horizontal tail by a factor of more than 4 at the cruise flight conditions. The total drag of the configuration decreases with decreasing vertical position of the canard and horizontal tail. These results have been verified by use of the Euler code AIRPLANE and the Navier-Stokes code OVERFLOW. The center of gravity position was found to have a large effect on the canard and tail incidence angles for trim.

rmh - 26

Conclusions

- 30 inch decrease in tail vertical position reduces drag 1.8 counts
- Canard vertical position has negligible effect on drag
- AIRPLANE, SYN107 and Overflow predict similar results
- Canard imposes large download on horizontal tail
- Trim and drag reduction need similar canard and tail angles at aft c.g.
- Trim and drag reduction need opposite canard and tail angles at forward c.g.
- Penalty function optimization is not precise

Multi–Configuration and Aeroelastic Shape Design

James Reuther, *MCAT*

Juan J. Alonso, *Stanford University*

Steve Smith, *NASA Ames*

HSR Airframe Technical Review
Anaheim, CA
February 8–12, 1999

Multi-Configuration and Aeroelastic Shape Design

This presentation describes the advances being made with the Aerodynamic Shape Optimization (ASO) and high-fidelity Multidisciplinary Optimization (MDO) software used in the High Speed Research Program at NASA Ames Research Center. The main authors for this work are James Reuther (MCAT, Inc./NASA Ames), Juan Alonso (Stanford University), and Steve Smith (NASA Ames), all of whom played crucial roles in the development of the Aeroelastic Shape Optimization (AESO) capability. James also integrated the new capabilities presented herein for HSR applications.

The description starts with the motivation for continued ASO/MDO development. Objectives of the current work are then presented. A list of ingredients deemed necessary for a flexible design environment is discussed, and the HSR requirement for different geometries at different design points is explained. Multiple design disciplines within a high-fidelity design environment are demonstrated. Finally, progress so far is summarized and planned future work is outlined.

Outline

- Motivation
- Objectives
- Flexible Design Environment Ingredients
- Multiple Geometry and Grid Capability
- Multiple Disciplinary Capability
- Conclusions and Future Work

Motivation

The motivation for on-going development of ASO and MDO methods comes from several realizations. First, high-fidelity ASO implementations are inherently complex if they are applied to realistic aircraft design problems. Not only do these methods bring all the difficulties associated with applying CFD to complex geometries such a mesh generation, parameter setting, convergence criteria, boundary conditions, and turbulence models in the case of Navier-Stokes-based methods—they also deal with a host of other challenges. Among these new complexities are mesh motion, aerodynamic and manufacturing constraints, multiple design points, propulsion effects, off-design considerations, sensitivity analysis, optimization algorithms, design problem specification, and design space parameterization. As any CFD expert can testify, even analysis of complex configurations is no small task. The added complexity of performing CFD-based design for complex geometries leads to software that is among the most elaborate in the field of high performance computing. Such algorithms which require many years to develop cannot justify the expense of their development if they are not flexible enough to apply to many different problems.

Recent advances in the ASO field have been both expensive and difficult, requiring the maturation of sensitivity analysis in particular. All indications are that these difficulties and expenses will only continue to be amplified as the field advances. Yet despite the need to support development costs, programs that can leverage advantages from these technologies tend not to be long-lived. Thus the ASO and MDO technologies must be developed within a flexible architecture such that they can continue to be developed in the face of changing goals and applications.

Motivation

- Aerodynamic Shape Optimization (ASO) Software is Becoming Increasingly Complex
- Development of ASO Software is Expensive and Difficult
- Research Programs Have Limited Lifetimes
- Given these Conditions New ASO Software Must be Flexible/Recyclable

Objectives

The present work addresses several issues that either apply to HSR directly or allow ASO and MDO technologies to be more flexible in their applicability. The leading objectives are to develop a flexible design environment, allow multiple geometries, grids and design variables for multiple design points, allow multiple high-fidelity disciplines such as aerodynamics and structures, and develop a multidisciplinary sensitivity analysis framework.

Objectives

- Develop a Flexible Design Environment
- Employ High Fidelity Modeling
- Allow Multiple Geometries, Multiple Grids and/or Multiple Design Points
- Allow Multiple Disciplines with Accurate Coupling
- Develop Multi–Disciplinary Sensitivity Analysis

Flexible Design Environment Ingredients

A flexible design environment requires modular software components with well-defined application programming interfaces (APIs). The APIs make it possible to plug in various components and substitute alternatives as needed with little or no new coding. In particular, the different disciplines communicate via a common interface or database, which in the case of the ASO and CSM (structures) disciplines is a geometry interface based on the outer mold lines (OML) of the configuration. At present, the OML common interface is defined as a set of parametric patches constructed on the external surfaces of the intersected basic geometry components.

Adoption of the MPI message passing interface standard provides flexibility in terms of computing platforms—normally multiprocessor systems performing intensive computations which have been parallelized where possible. In addition, all the present ASO modules are flexible in terms of problem size through their use of dynamic memory such that no recompilation is needed to deal with larger problems.

Flexible Design Environment Ingredients

- **All Software Modularized**
- **All Software Modules Use Dynamic Memory**
- **Most Software Elements Accessed Through an API**
  - CFD Solver
  - CFD Adjoint
  - CSM Solver
- **Common Geometry Interface Based on Outer Mold Lines (OML) of Vehicle**

Structural API

An example of an API is shown in the chart. In this case, a list of standard calls has been defined to transfer information to and from the structural solver. The various calls cover everything necessary to start and run any general purpose structures solver. Such an API promotes interchangeability of solvers without sacrificing computational efficiency.

Structural API

- Provides Flexibility in Using Different Structural Solvers
- States Exact Form of Functions and Arguments

– `CSM_Init (...)`	memory allocation
– `CSM_Solve (...)`	structural deflections
– `CSM_Stress (...)`	element stresses
– `CSM_GetPoint (...)`	surface information

OML Geometry Interface

The OML geometry interface or database that is common to the CFD algorithm and the CSM solver is shown in the figure for a high speed transport application. The patches on the external surfaces of the intersected airframe components are created by the AEROSURF geometry engine within the ASO module. On the CFD side, these parametric OML patches enable rapid surface grid perturbation (and hence volume grid perturbation) during optimization by enabling the CFD surface mesh points to be mapped to each newly paneled surface as the configuration shape changes. For the introduction of aeroelastic effects, the patches similarly allow surface pressure loads to be mapped to the CSM solver surface nodes. In turn, geometry deflections calculated by the CSM solver can be mapped from the solver nodes to the OML and hence to the CFD grid.

For more than one reason, schemes which simply transfer information directly between solver surface grids without underlying geometry components (which can be reintersected as their shapes change to change the outer mold lines) may be limited in applicability, or flawed, or both. The common geometry interface ensures that the different disciplines are treating identical geometries, with exact agreement when the design process is complete. The common OML also facilitates force- and work-equivalent transfer of loads and displacements, the importance of which is discussed below. Ultimately, a CAD-based geometry engine should become the common interface, but for now the AEROSURF approach provides adequate accuracy with efficiency that will be hard to match: it takes less than 1 CPU second to generate 139,500 points as 54 surface patches on the three-surface TCA configuration, using a single 225MHz SGI R10000 processor.

OML Geometry Interface

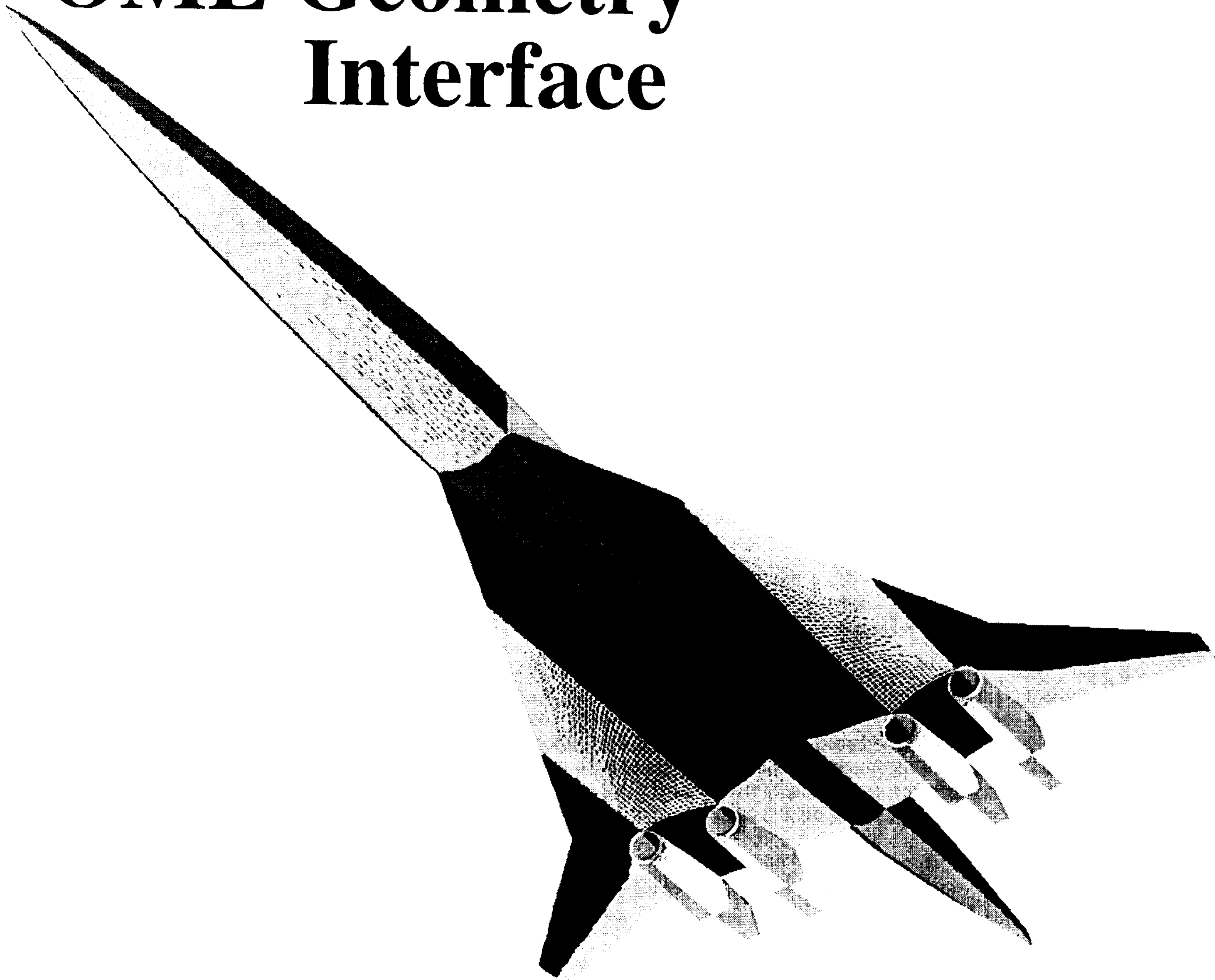

Multiple Geometries

The need for multiple geometries at multiple design points is illustrated by the HSCT, which must be modeled with deflected wing flaps and slats at transonic speeds. The upper level routines of the ASO software have been modified to treat multiple geometries and multiple CFD grids, and to activate the design variables according to the design point. As each design point is treated, the appropriate geometry and mesh are loaded into working memory. The design variables that are appropriate are then applied. The sequence of running the geometry engine, perturbing the CFD surface and volume mesh points, and running the CFD solver as needed is applied only to the working data. After the sequence is completed, the next design point is processed similiarly. Each design point contributes to the composite objective function in some weighted fashion.

In addition to allowing, say, flaps to be deflected at some design point(s) while remaining undeflected at the cruise point, the new capability allows a given geometry component to be designed in the presence of different configurations. An example would be a wing being designed in the presence of different nacelles or different fuselages such that it represented the best compromise design.

Multiple Geometries

- **Multiple Geometries Maintained During Design**
- **Multiple Grids Maintained During Design**
- **Permits Design Variables to be Active/Inactive for Each Design Point**
  - Flap schedule optimization
- **Permits Component Design in the Presence of Different Configurations**
  - Wing design in the presence of different engines

Multiple Geometries Flow Chart

This chart illustrates how multiple design points with different geometries are handled by the optimization method. Everything from calling the geometry engine (AEROSURF) through morphing the CFD grid and calculating the flow and adjoint solutions is repeated for each design point in series. This ensures full geometric, mesh, and design variable flexibility at each design point. The chart also indicates communication between the flow and adjoint solvers via the OML interface, along with one-way communication from the flow solver to the adjoint solver (the flow state variables being required for the adjoint calculation).

Multiple Geometries Flow Chart

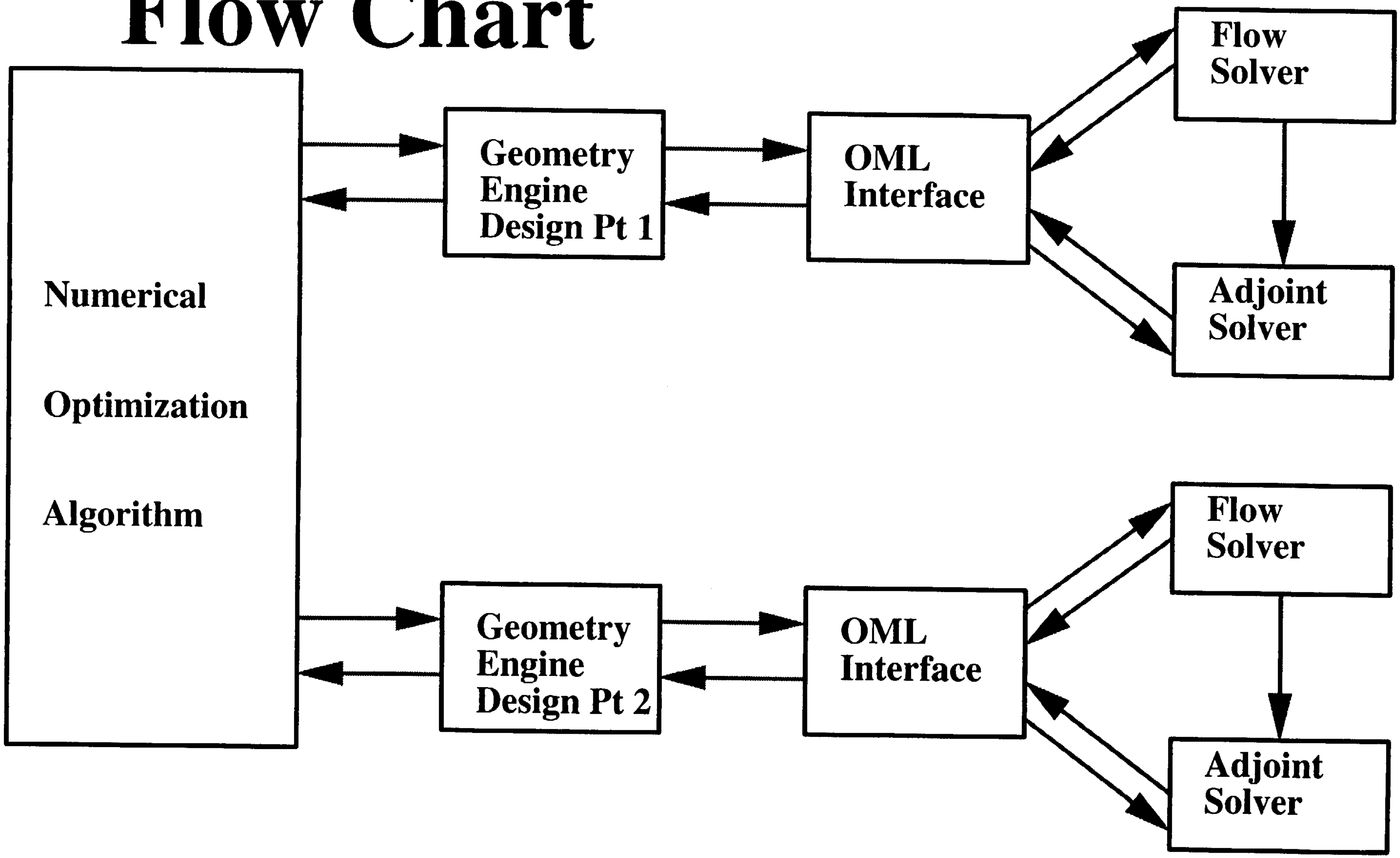

Multiple Geometries: TCA Flap Scheduling

This figure shows two flow calculations on the three-surface TCA configuration, one supersonic with no flap deflections, the other transonic with flaps deflected. The two calculations are from snapshots taken during a multipoint design run.

Multiple Geometries TCA Flap Scheduling

Supersonic:
No Flap Deflections

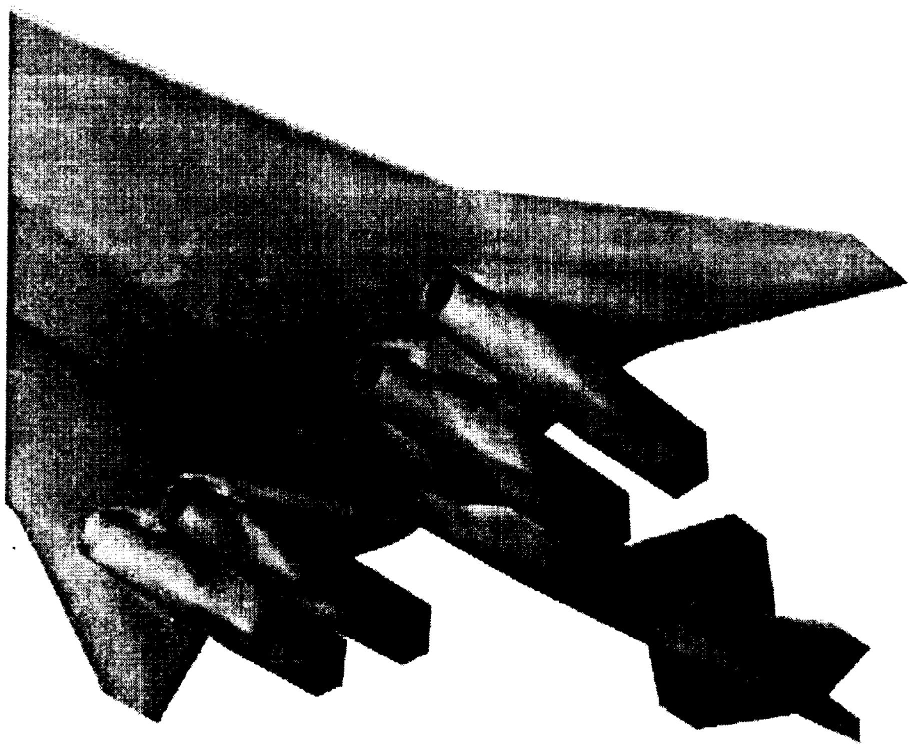

Transonic:
With Flap Deflections

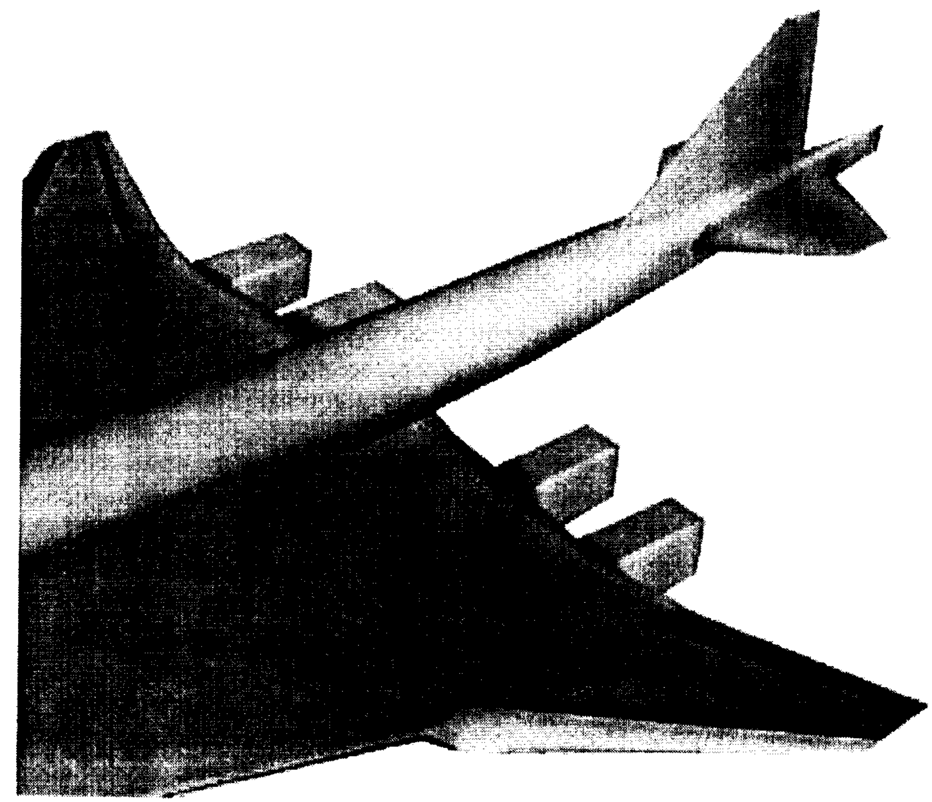

Multiple Disciplines

In order to allow for multiple high-fidelity disciplines to be treated in a coupled design process, some of the basic capabilities have now been developed. Aeroelastic shape optimization (AESO) has served as a proof-of-concept problem, but many other MDO problems may be considered (such as treatment of radar cross-section issues via a computational electromagnetics module). The focus of our implementation is to use high fidelity for each of the disciplines involved throughout the design process, because anything less can too easily lead to "optimal" solutions that are not trustworthy.

Considerable research has already been conducted on the multidisciplinary optimization (MDO) of flight vehicles. The paper by Sobieszczanski-Sobieski and Haftka (Multidisciplinary Aerospace Design Optimization: Survey of Recent Developments) provides a comprehensive discussion of much of the work completed to date. These efforts have ranged from the development of techniques for discipline coupling to actual demonstrations on real-world design problems. In most cases, these research efforts have shown the importance of inter-disciplinary coupling, as well as the inability of sequential disciplinary optimization to achieve the true global optimum of a coupled system. Unfortunately, the fidelity in the modeling of the various component disciplines in these preliminary design tools has remained at a relatively low level. Therefore, while useful at the conceptual design stage, these tools cannot accurately represent a variety of nonlinear phenomena, such as wave drag, which can play a key role during the detailed design phase.

On the other hand, the ASO techniques used in the HSR program to date have had their own share of problems. In the case of aerodynamic wing design, planform and thickness constraints have often been artificially imposed so that structural weight, fuel volume, and takeoff/landing requirements would not be adversely affected by the changes in the wing shape. These constraints were typically guided by the result of low-fidelity multidisciplinary models and individual decisions made by experts from selected disciplines. By neglecting the coupling between various disciplines, design constraints have often been too restrictive to permit significant performance improvements, or not restrictive enough, thus allowing ASO to produce infeasible designs. In addition, improvements in aerodynamic performance resulting from span load changes cannot be accurately quantified in view of their unknown impact on the structural weight.

The goal of the current research is to establish a new framework for high-fidelity MDO. The important contributions presented to support such a framework are:

- The use of high-fidelity modeling of two disciplines (Reynolds-Averaged Navier-Stokes aerodynamics and linear FEM structures).
- An OML geometry database which serves as both an interface to the optimization algorithm and an interface for communication between disciplines.
- Sophisticated coupling algorithms that link each discipline to the OML such that information transfer between the disciplines is consistent and conservative.
- A framework for the computation of coupled sensitivities.

Multiple Disciplines

- **Aeroelastic Design as Proof of Concept**
- **High Fidelity Modeling of Multiple Disciplines**
  - Euler or Navier–Stokes CFD Solver
  - Linear Finite Element CSM Solver
- **Discipline Coupling**
  - OML Used as Common Interface
  - Bi–directional Transfer of Loads and Displacements:
    - Consistent (Force and Moment Equivalent)
    - Conservative (Work Equivalent)
- **Sensitivity Analysis**
  - Coupled Adjoint is Possible
  - Current Implementation Uses:
    - Adjoint Aerodynamic Sensitivities
    - Finite Difference Structural Sensitivities

Multiple Disciplines Flow Chart

This chart summarizes the high-fidelity MDO algorithm proposed in this research. Note that the common OML interface or database is used to transfer all information between the multiple disciplines (two in this case). Coupling between the CSM adjoint and the CFD adjoint has not been implemented yet, but the other components are in place.

Multiple Disciplines Flow Chart

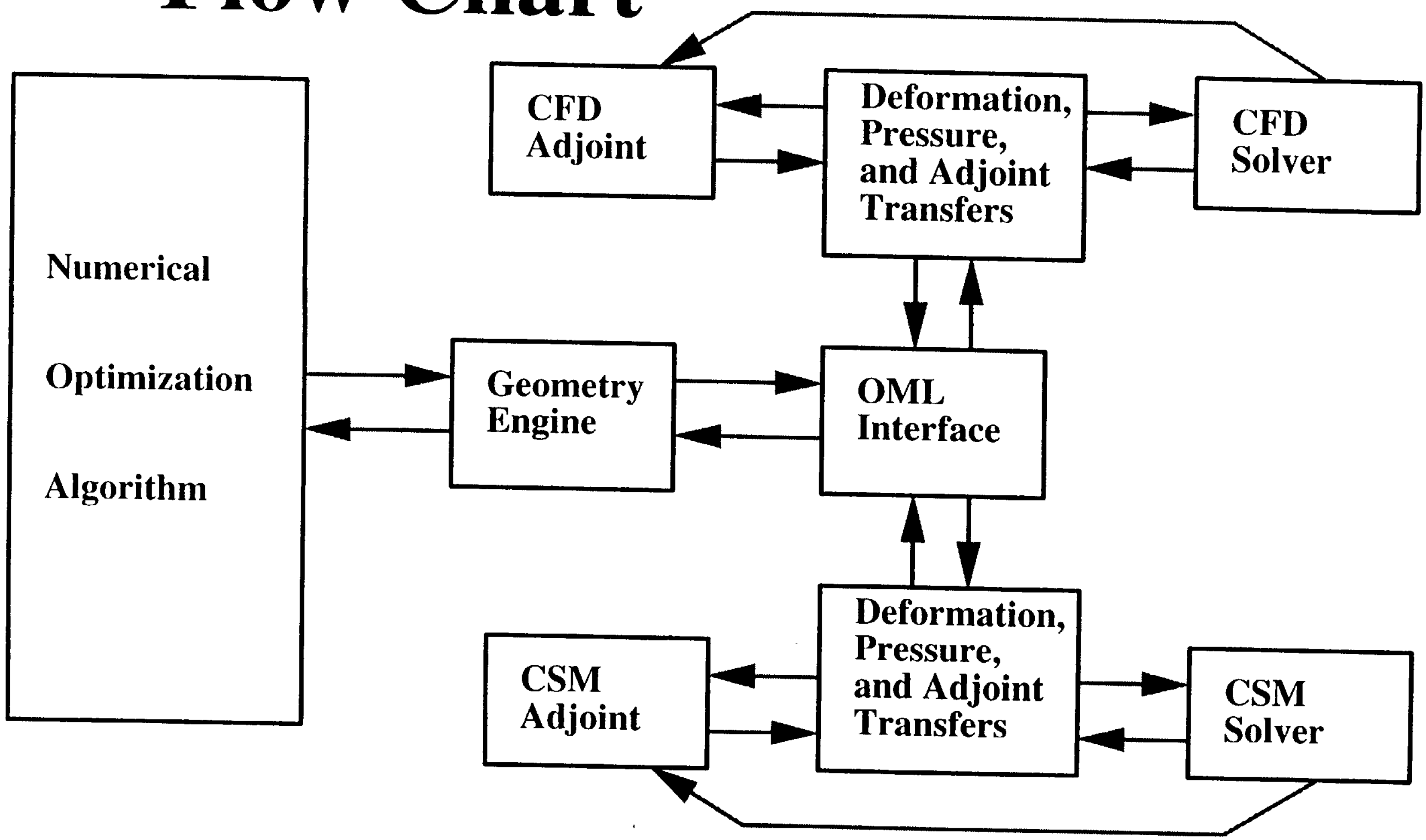

High-Fidelity CFD

In order to obtain the necessary level of accuracy, high-fidelity modeling is being used from the start for both the aerodynamic and structural subsystems. Euler and Reynolds Averaged Navier-Stokes (RANS) flow solvers are used to model the aerodynamics. The details of the multiblock solver, FLO107-MB, can be found in AIAA Paper 96-0094 (Aerodynamic Shape Optimization of Complex Aircraft Configurations via an Adjoint Formulation, by Reuther et al.), and its parallel implementation on a variety of computing platforms has been described in AIAA Papers 96-0409 (Jameson & Alonso) and 97-0101 (Reuther, et al.). Flow solver characteristics are summarized in the chart.

High–Fidelity CFD

- FLO107–MB: Parallel Multiblock RANS Flow Solver
- Scalar or CUSP Dissipation Schemes
- 5–Stage Runge–Kutta Algorithm
- Multigrid
- Residual Smoothing
- MPI Parallel Implementation

Sample Business Jet Navier-Stokes Solution

The sample business jet depicted illustrates the complex geometry Navier-Stokes flow solution capability of FLO107-MB. The solution is seamless across block boundaries. This analysis on 240 blocks with 5.8 million mesh points at Mach 0.82 took 1.3 hours using 48 processors of an SGI Origin2000.

Sample Business Jet

Transonic Business Jet
FLO107-MB Solution
Baldwin-Lomax Turbulence Model
Mach = .82   240 Blocks   5.8 Million Mesh Points

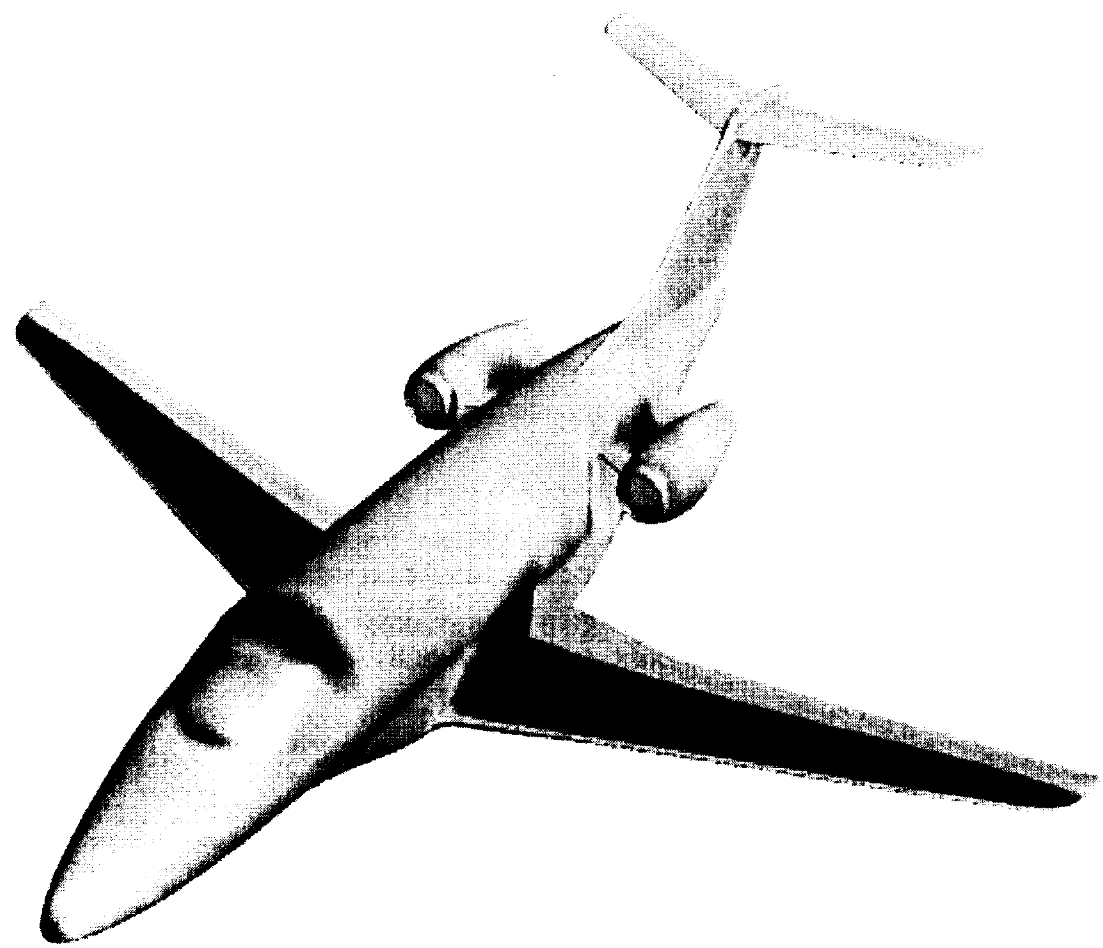

Sample Supersonic Transport Euler Solution

This figure shows the complex nacelle and empennage geometry components treated by FLO107-MB for the three-surface TCA configuration at cruise Mach 2.4 and angle of attack 3.75°. The number of grid cells in this Euler calculation is about 2 million.

Supersonic Aircraft

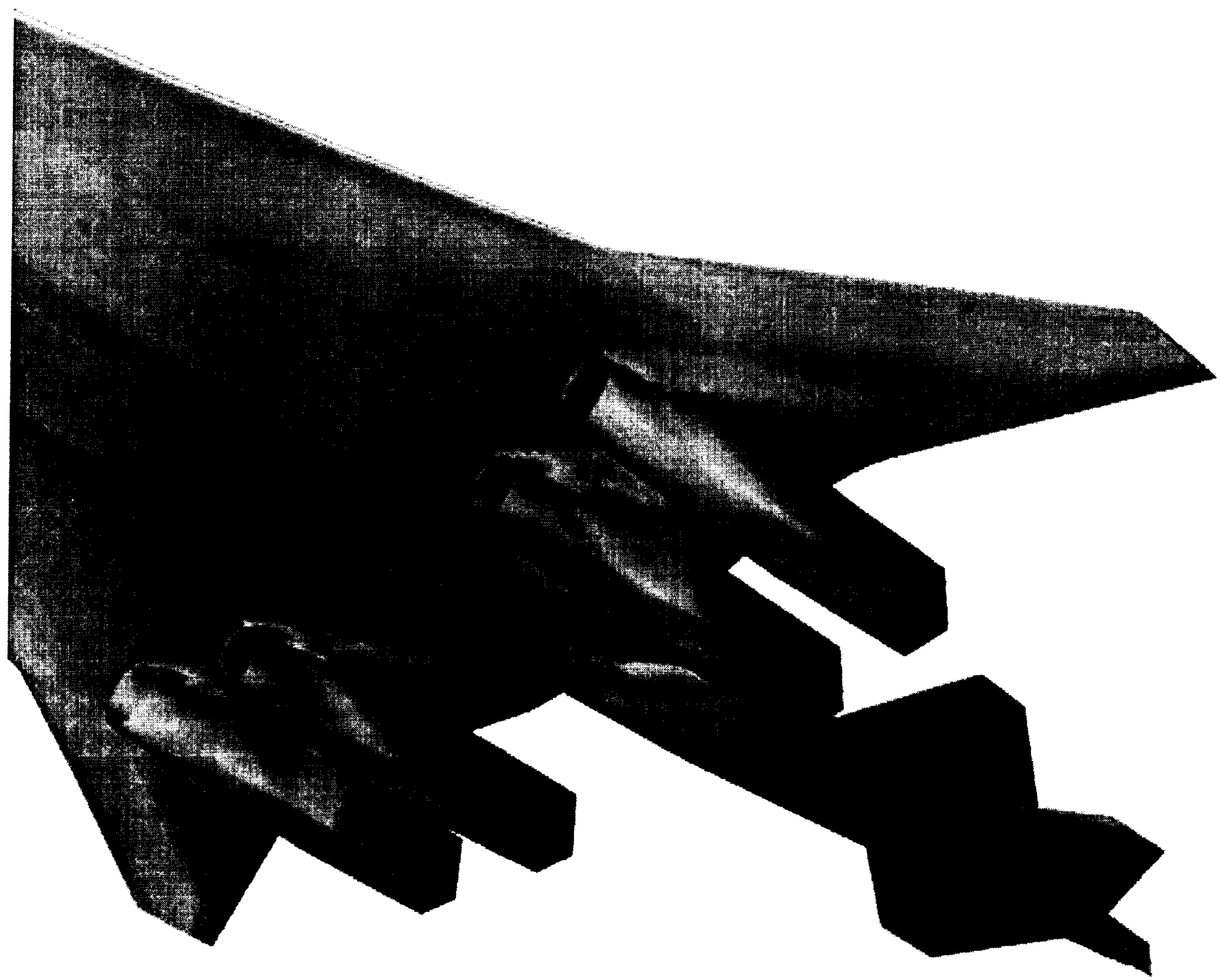

Structural Models

Two different finite element methods (FEM) have been used for the description of the behavior of structures. The first is a linear FEM model that uses brick elements which are appropriate for solid wind tunnel configurations. The second is a linear FEM that uses truss and triangular plate elements to model the structural components of aircraft configurations. Given these choices of the physical models for the disciplines involved, it will be possible to capture many of the key trade-offs present in the aero-structural design problem.

The figure shows the wing structural model for the business jet illustrated above. The upper and lower wing skins have been removed on one side to reveal the underlying structure. The colors represent levels of stress (red being high magnitude and blue low). The individual triangular elements can also be seen in the figure. This calculation was performed with our second FEM solver, suited to realistic aircraft structures rather than wind tunnel models. In the future, a commercial CSM package such as NASTRAN will be tried instead of our simpler demonstration code.

Structural Model

- Triangular Plate and Truss Elements
- Skins Modeled with Plates
- Spars and Ribs Modeled with Plates and Trusses
- Simplified but Realistic and Accurate

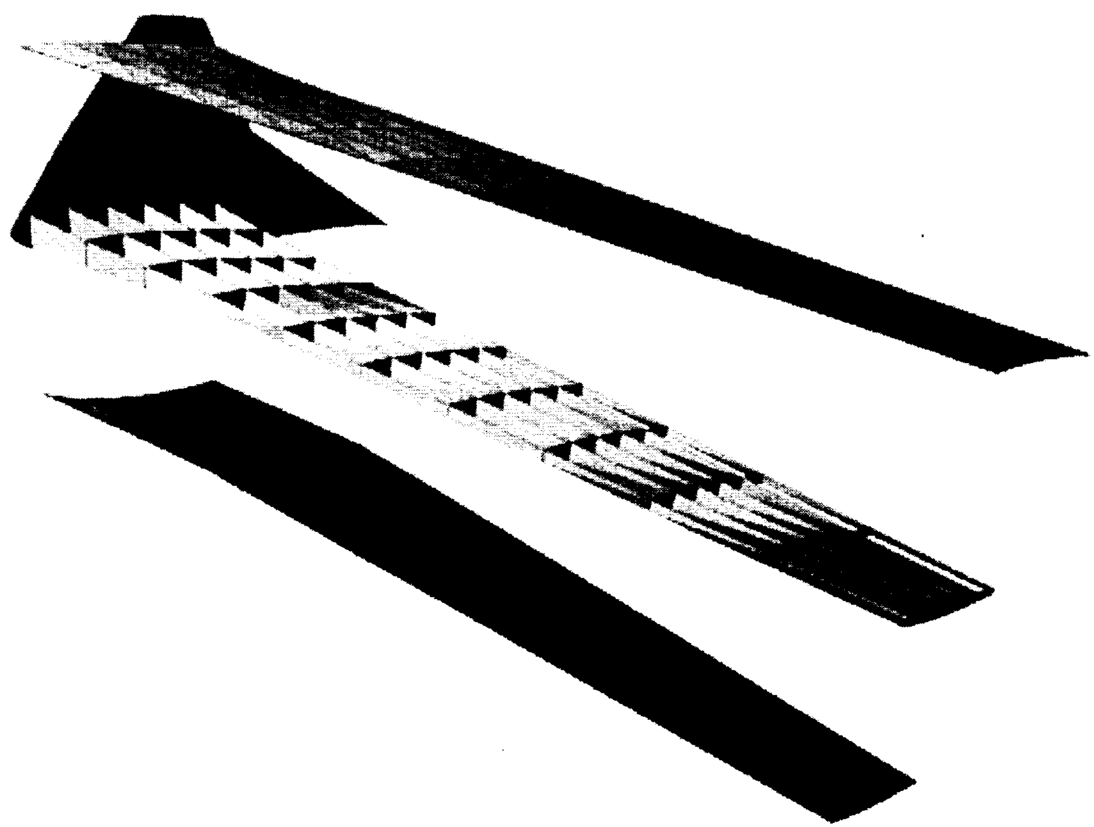

Transfer Equations

Within the framework described previously, the optimization of aero-structural systems requires, at a minimum, the solution of the coupled aeroelastic analysis problem. The interaction between these two disciplines, aerodynamics and structures, is quite strong since the former provides the necessary loads to the latter in order to determine the displacement field of the structure. In return, the structure provides surface deflections that change the aerodynamic properties of the initial configuration.

Two issues in this transfer of information between disciplines are of utmost importance to the success of an automatic design technique: first, the level of fidelity in the coupling of both disciplines has to be carefully considered in order to guarantee that the accuracy of the individual disciplines is not jeopardized, and second, the evolving disciplinary designs must have exact geometric agreement by the end of the design process.

In order to tackle the fidelity of the coupling, we have chosen to ensure that the transfer of the distributed pressure forces and moments from the CFD calculation to the CSM nodal load vector is both consistent and conservative as defined in the approach developed by Brown (Displacement Extrapolation for CFD + CSM Aeroelastic Design, AIAA Paper 97-1090). The property of consistency implies that the resultant forces and moments imparted by the distributed pressure field, p, must be equal to the sum of the nodal forces and moments in the CSM load vector, $\mathbf{f}$. Conservation addresses the important issue that the virtual work performed by the load vector, $\mathbf{f}$, undergoing a virtual displacement of the structural model (represented by $\delta\mathbf{q}$) must be equal to the associated work performed by the distributed pressure field, p, undergoing the associated displacement of the CFD mesh surface, $\delta\mathbf{r}$. Thus, a procedure is devised that describes the motion of every surface point in the CFD mesh as a function of the nodal displacements of the structural model,

$$\delta\mathbf{r} = [\eta]^T \delta\mathbf{q}$$

where $[\eta]$ is a matrix of linear weights on the displacement vector that is a combination of interpolations within the CSM mesh and extrapolations to the OML as described by Brown. The virtual work in the CSM model can be represented as

$$\delta W_{CSM} = \mathbf{f}^T \delta\mathbf{q},$$

while the virtual work performed by the fluid acting on the surface of the CFD mesh is given by

$$\delta W_{CFD} = \int_{\partial\Omega} p\, \mathbf{n}^T \delta\mathbf{r}\, dS + \int_{\Omega} \Omega \mathbf{b}^T \delta\mathbf{r}\, dV$$

Here, $\mathbf{b}$ represents a distributed body force per unit mass, if it exists, and $\partial\Omega$ is the CFD mesh surface that describes the interface between the fluid and the structure. For a conservative scheme, $\delta W_{CFD} = \delta W_{CSM}$, and the consistent and conservative load vector is given by:

$$\mathbf{F}^T = \int_{\partial\Omega} p\, \mathbf{n}^T [\eta]^T dS + \int_{\Omega} \mathbf{b}^T [\eta]^T dV$$

Transfer Equations

- **Transfer of CSM Nodal Displacements to OML Database**

$$\delta \mathbf{r} = [\eta]^T \cdot \delta \mathbf{q},$$

$$\mathbf{F}^T = \int_{\partial\Omega} p\, \mathbf{n}^T \cdot [\eta]^T \, dS + \int_{\Omega} \mathbf{b}^T \cdot [\eta]^T \, dV.$$

Pressure and Displacement Transfer

In order to enable communication between the aerodynamic and structural solvers, a standardized OML surface representation of the configuration of interest is required. Solutions from each of the disciplines (aerodynamics and structures) are interpolated onto this OML database so that they may be accessed as needed by the other disciplines.

Each AEROSURF point is associated with a point on the surface of the CSM model in a preprocessing step. During optimization, the displacements for each AEROSURF point are calculated by first using the CSM basis functions to interpolate the CSM nodal displacements at the projected AEROSURF point. Then extrapolation functions are used to carry the displacements from the CSM mesh to the OML. When the CSM solver dictates a new position for the structure, the locations in three-dimensional space of all the AEROSURF points are updated by adding the deflections to the jig-shape points. This update process effectively constructs new parametric patches to represent the surface of the perturbed configuration. In a similar fashion, during a preprocessing step, every point on the surface of the CFD mesh is associated with an AEROSURF patch and a parametric location within that patch. The CFD points are assumed to be "tied" to these parametric locations, and, when the AEROSURF database is altered, the location of the CFD surface mesh points can be obtained by straightforward evaluation of their parametric locations on the corresponding AEROSURF patches. As can be seen, AEROSURF plays a central role in the transfer of displacements from CSM to CFD.

<Continued on the next page.>

Pressure Transfer

- Pressure Distributions from CFD Cell Centers Interpolated to OML Database
- Pressures Integrated on the OML to Obtain OML Point Loads
- OML Loads Transferred to the CSM Node Points Using the $[\eta]$ Matrix

Pressure and Displacement Transfer (Continued)

Furthermore, the AEROSURF database also plays a similar role in the transfer of pressure information from the CFD calculation to the structural load vector. The transfer of surface pressure information to the AEROSURF database is achieved by identifying the "donor" cells from the CFD mesh that contain the desired information. The pressure integrations in the last equation above are then performed with the same accuracy as can be achieved if the integration were to occur directly on the surface of the CFD mesh. The underlying assumption is that the mesh resolution of the AEROSURF database is comparable to, if not better than, that of the CFD surface mesh. This has always been the case in our design efforts. The coupling between aerodynamic and structural solvers in order to obtain an aeroelastic solution is achieved in an explicit, sequential, iterative fashion by exchanging information at regular intervals during the convergence process. This coupling is greatly simplified by the fact that only static aeroelastic solutions are considered in this work, and the issue of time accuracy is inconsequential.

Displacement Transfer

- Using CSM Nodal Displacements and the [η] Matrix, New Locations for the OML Points are Found
- Displacements of the OML Points are Transferred to the CFD Mesh
- WARP–MB is Used to Perturb the CFD Volume Mesh

Coupled Sensitivities

The proposed high-fidelity MDO framework also needs a strategy to perform design changes in a way that minimizes the need for expensive function evaluations. Detailed shape optimization of aerodynamic surfaces for transonic wing design problems requires a parameter space of $O(100)$ or larger. (See, for instance, Wing Design by Numerical Optimization, by Hicks and Henne (Journal of Aircraft, 15:407-412, 1978), and Improved Method for Transonic Airfoil Design-by-Optimization, by Kennelly (AIAA Paper 83-1864).) This requirement combined with the enormous cost of each function evaluation renders the use of zeroth-order methods, such as random searches and genetic algorithms, inefficient for this problem. The alternative of using a response surface whereby a polynomial fit of the design space is constructed prior to optimization is also plagued with intractable computational costs since the number of function evaluations required is proportional to the square of the number of design variables.

If we assume that the basic topology of the structure (i.e., the number of spars, the number of ribs, the choice of materials, etc.) is not altered during the design, the design space should be smooth. Although many alternative global optimization strategies exist, for the aero-structural problem of interest, a gradient-based procedure holds the most promise. Gradient-based optimization algorithms can be shown to converge only to a local optimum. If the cost function of the aero-structural problem is sufficiently multi-modal, these algorithms can fail to achieve the global optimum. Nevertheless, when used in conjunction with lower-fidelity MDO tools that provide a reasonable starting point for the optimization, they can yield significant and credible improvements in the design.

When compared with zeroth-order methods, gradient-based algorithms shift the computational burden from evaluating the cost function to calculating values of its gradient. The most direct way to estimate gradients is the finite-difference approach in which a separate function evaluation is required for each design variable in the problem. By using gradient information, the total number of function evaluations is greatly reduced. However, given the large computational cost involved in each function evaluation, the finite-difference method has proven to be unaffordable for the aerodynamic design of complete configurations. This limitation of the finite-difference method has provided the motivation to develop new methods of obtaining sensitivity information for aerodynamic design problems. In particular, the adjoint technique has proven extremely valuable in making these kinds of calculations possible.

The computation of sensitivities for the aero-structural problem has components of both ASO and structural optimization techniques. However, if the true sensitivities of the design problem are needed, the coupling terms cannot be neglected. For example, the sensitivity of the stress in a given element of the CSM model to an aerodynamic twist variable has a component that depends on the change to the geometry of the structural model and a second component that depends on the changing load vector applied to the structure. Both of these contributions are significant and must be accounted for. Although in the results presented here a simplified penalty function is used to obtain a first cut at the aero-structural design problem, we feel it is important to place the mathematical framework for coupled sensitivities on a more solid footing. It will inevitably turn out that the choice of the use of an adjoint approach will depend upon the problem at hand. Since we seek a flexible design environment, the possibility of using a coupled adjoint must be admitted. The following explication is adapted from AIAA Paper 99-0187, A Coupled Aero-Structural Optimization Method for Complete Aircraft Configurations, by Reuther, Alonso, Martins, and Smith.

Coupled Sensitivities

$$R_{as} = \begin{pmatrix} R(\mathbf{w}, \mathbf{q}, \mathcal{F}, \mathcal{P}) \\ S(\mathbf{w}, \mathbf{q}, \mathcal{F}, \mathcal{P}) \end{pmatrix} = 0$$

$$\delta I = \frac{\partial I^T}{\partial \mathbf{w}} \delta \mathbf{w} + \frac{\partial I^T}{\partial \mathbf{q}} \delta \mathbf{q} + \frac{\partial I^T}{\partial \mathcal{F}} \delta \mathcal{F} + \frac{\partial I^T}{\partial \mathcal{P}} \delta \mathcal{P}$$

$$\begin{aligned} \delta R_{as} &= \left[\frac{\partial R_{as}}{\partial \mathbf{w}}\right] \delta \mathbf{w} + \left[\frac{\partial R_{as}}{\partial \mathbf{q}}\right] \delta \mathbf{q} + \left[\frac{\partial R_{as}}{\partial \mathcal{F}}\right] \delta \mathcal{F} + \left[\frac{\partial R_{as}}{\partial \mathcal{P}}\right] \delta \mathcal{P} \\ &= 0 \end{aligned}$$

$$\psi_{as} = \begin{pmatrix} \psi_a \\ \psi_s \end{pmatrix}$$

Coupled Sensitivities (Continued)

Consider, for example, a cost function where both aircraft weight and drag are included. Then, if $\mathbf{q}$ and P denote respectively the structural displacement field and structural parameters of the structural model, $\mathbf{w}$ denotes the flow solution, and F represents the design parameters of the undeformed aircraft shape, the aeroelastic objective function whose sensitivity we seek becomes $I\,(\mathrm{w}, \mathbf{q}, F, P)$. The variations in I are subject to the constraint $R_{as}\,(\mathbf{w}, \mathbf{q}, F, P) = 0$, where R_{as} designates the set of aero-structural equations and can be partitioned as shown in the preceding chart. Here, R denotes the set of fluid equations and S the set of structural equations. The variation δI can be expressed as shown. In order to eliminate $\delta\,\mathbf{w}$ and $\delta\,\mathbf{q}$ from the above equation, the constraint $\delta R_{as} = 0$ can be introduced, where δR_{as} is defined in the chart. This calls for the partitioned Lagrange Multiplier Ψ_{as} where Ψ_a is the portion of the adjoint associated with the fluid, and Ψ_s is the portion of the adjoint associated with the structure. It follows that the first expression of δI can be replaced by the expressions shown in the next chart.

Coupled Sensitivities

$$\delta I = \frac{\partial I^T}{\partial \mathbf{w}}\delta \mathbf{w} + \frac{\partial I^T}{\partial \mathbf{q}}\delta \mathbf{q} + \frac{\partial I^T}{\partial \mathcal{F}}\delta \mathcal{F} + \frac{\partial I^T}{\partial \mathcal{P}}\delta \mathcal{P}$$
$$-\psi_{as}^T \left(\left[\frac{\partial R_{as}}{\partial \mathbf{w}}\right] \delta \mathbf{w} + \left[\frac{\partial R_{as}}{\partial \mathbf{q}}\right] \delta \mathbf{q} + \left[\frac{\partial R_{as}}{\partial \mathcal{F}}\right] \delta \mathcal{F} + \left[\frac{\partial R_{as}}{\partial \mathcal{P}}\right] \delta \mathcal{P} \right)$$

$$\delta I = \left\{ \frac{\partial I^T}{\partial \mathbf{w}} - \psi_{as}^T \left[\frac{\partial R_{as}}{\partial \mathbf{w}}\right] \right\} \delta \mathbf{w} + \left\{ \frac{\partial I^T}{\partial \mathbf{q}} - \psi_{as}^T \left[\frac{\partial R_{as}}{\partial \mathbf{q}}\right] \right\} \delta \mathbf{q}$$

$$+ \left\{ \frac{\partial I^T}{\partial \mathcal{F}} - \psi_{as}^T \left[\frac{\partial R_{as}}{\partial \mathcal{F}}\right] \right\} \delta \mathcal{F} + \left\{ \frac{\partial I^T}{\partial \mathcal{P}} - \psi_{as}^T \left[\frac{\partial R_{as}}{\partial \mathcal{P}}\right] \right\} \delta \mathcal{P}$$

$$\begin{pmatrix} \left(\frac{\partial R_{as}}{\partial \mathbf{w}}\right)^T \\ \left(\frac{\partial R_{as}}{\partial \mathbf{q}}\right)^T \end{pmatrix} \begin{pmatrix} \psi_a \\ \psi_s \end{pmatrix} = \begin{pmatrix} \frac{\partial I}{\partial \mathbf{w}} \\ \frac{\partial I}{\partial \mathbf{q}} \end{pmatrix}$$

Coupled Sensitivities (Continued)

Now, if Ψ is chosen as the solution of the aero-structural adjoint equation shown, the expression for δI simplifies to $\delta I = G_F \delta F + G_P \delta P$ where G_F and G_P are defined as shown. Hence, the sought-after objective, which is the elimination of $\delta \mathbf{w}$ and $\delta \mathbf{q}$ from the from the expression for δI, is attainable but requires the solution of the adjoint *coupled aero-structural* problem shown for Ψ_a and Ψ_s.

Now, since the creation of a completely coupled aero-structural adjoint would compromise our objective of developing a flexible MDO framework, we can rewrite a lagged form of the equations as shown, where $\tilde{\Psi}_s$ and $\tilde{\Psi}_a$ are updated via outer iterations. This implies that existing adjoint solvers for both the aerodynamics and structures can be used subject to convergence of the iteration. The additional right-hand-side forcing terms can then be updated in the same way as has been presented earlier for the state equations. Thus, the OML geometry can serve to couple both the state and co-state equations.

Beyond employing a coupled adjoint, the alternative of using a coupled direct approach also exists. The development follows the one above very closely in terms of the coupling. However, since prefactoring of the CFD Jacobian matrix is problematic, the approach will not be much cheaper than using finite differencing. An alternative to either the adjoint or the direct approaches is the use of a decomposed optimization strategy such as multi-level optimization (see A Practical Approach to MDO and its Application to an HSCT Aircraft, by Baker and Giesing, AIAA Paper 95-3885) or collaborative optimization (see Decomposition and Collaborative Optimization for Large-Scale Aerospace Design, by Kroo, in Multidisciplinary Design Optimization: State of the Art, SIAM, 1996). Exploring all of these various possibilities will form the basis of our future work.

For the purposes of the present work where a coupled adjoint has yet to be implemented, the sensitivities are obtained without coupling. The aerodynamic adjoint is used to obtain aerodynamic sensitivities and finite differences are used to obtain the structural sensitivities. This approximation inherently implies that gradient information for a combined aerodynamic plus structural objective function will not be completely accurate. The earlier example of exploring how wing twist affects structural stress levels highlights our current limitation. Without the coupling, we will capture only the portions of the sensitivities that result from structural changes. The loading will act as if it were frozen. Future works will address this limitation by implementing the coupled adjoint as outlined above. Finally, for a detailed treatment of the overall design process, refer to the two-part article in the January 1999 special issue of the Journal of Aircraft on MDO, Constrained Multipoint Aerodynamic Shape Optimization Using an Adjoint Formulation and Parallel Computers, by Reuther, et al.

Coupled Sensitivities

$$\delta I = \mathcal{G}_{\mathcal{F}} \delta \mathcal{F} + \mathcal{G}_{\mathcal{P}} \delta \mathcal{P}$$

$$\mathcal{G}_{\mathcal{F}} = \frac{\partial I^T}{\partial \mathcal{F}} - \psi_{as}^T \left[\frac{\partial R_{as}}{\partial \mathcal{F}} \right], \qquad \mathcal{G}_{\mathcal{P}} = \frac{\partial I^T}{\partial \mathcal{P}} - \psi_{as}^T \left[\frac{\partial R_{as}}{\partial \mathcal{P}} \right]$$

$$\begin{pmatrix} \left(\frac{\partial R}{\partial \mathbf{w}}\right)^T & \left(\frac{\partial S}{\partial \mathbf{w}}\right)^T \\ \left(\frac{\partial R}{\partial \mathbf{q}}\right)^T & \left(\frac{\partial S}{\partial \mathbf{q}}\right)^T \end{pmatrix} \begin{pmatrix} \psi_a \\ \psi_s \end{pmatrix} = \begin{pmatrix} \frac{\partial I}{\partial \mathbf{w}} \\ \frac{\partial I}{\partial \mathbf{q}} \end{pmatrix}$$

$$\left(\frac{\partial R}{\partial \mathbf{w}}\right)^T \psi_a = \frac{\partial I}{\partial \mathbf{w}} - \left(\frac{\partial S}{\partial \mathbf{w}}\right)^T \tilde{\psi}_s$$

$$\left(\frac{\partial S}{\partial \mathbf{q}}\right)^T \psi_s = \frac{\partial I}{\partial \mathbf{q}} - \left(\frac{\partial R}{\partial \mathbf{q}}\right)^T \tilde{\psi}_a$$

Demonstration Problem (1): Wind Tunnel Business Jet Model, Low Sweep

Results of the application of our initial aero-structural design methodology are presented for two existing wind tunnel business jet models, and for representative aeroelastic design at flight configurations. These cases use the two different structural models outlined above. In addition, some of the results used the Euler equations, while others used the Reynolds Averaged Navier-Stokes equations to model the fluid flow.

First, results of the rigid and aeroelastic analysis of two different wind tunnel models representing typical complete configuration business jets are presented and compared with the available experimental data. The CFD meshes used for each of the two models contain the wing, body, pylon, nacelle, and empennage components. The mesh for the first model (model A) uses 240 blocks with a total of 5.8 million cells while the second mesh (model B) contains 360 blocks and a total of 9 million cells. The large mesh sizes are required for adequate resolution of all the geometric features for each of the configurations and the high Reynolds number boundary layers on their wings. It should be mentioned that viscous and structural effects are resolved only on the wing surface; all other surfaces in the model are assumed to be inviscid and rigid. All calculations were run using 48 processors of an SGI Origin2000 parallel computer. A total of 1.3 hours (model A) and 2.0 hours (model B) of wall clock time were required for the rigid-geometry solutions, while 1.4 hours and 2.1 hours were required for the aeroelastic calculations. The structural model is the linear FEM model with brick elements which more closely approximates the behavior of the wind tunnel model structure. Experimental wind tunnel data are available for the two models at flight conditions as follows: Model A, M = 0.80, Re = 2.5 million and cruise C_L, and Model B, M = 0.80, Re = 2.4 million and cruise C_L. Aeroelastic updates were performed every 10 multigrid iterations of the flow solver. A total of 400 iterations were used to ensure an aeroelastically converged solution. All solutions were calculated at a fixed C_L by incrementally adjusting the angle of attack.

Demonstration Problem

- Aeroelastic Wing Design
- Interaction Between Aerodynamics and Structures
- Induced Drag vs. Structural Performance
- Compressibility Drag vs. Structural Performance

Demonstration Problem (1) (Continued): Wind Tunnel Business Jet Model, Low Sweep

The accompanying figure shows a comparison of the pressure distributions for the rigid wing, the aeroelastic wing, and the wind tunnel data for model A. The sectional cut is near mid-span where wind tunnel measurements were available. The figure shows that for this case the aeroelastic deformation of the wing is so small that virtually no difference between the two computed results exists. In fact, the maximum tip deflection of the model was calculated to be only 0.3% of the wing span. Agreement with the sparse wind tunnel data indicates that the CFD is capturing the right trends present in the tested configuration. The fact that the differences between the computed rigid and elastic wings are so small leads to the conclusion that the wind tunnel data from this test probably need not be corrected for aeroelastic deflections. In retrospect, it can be noted that the model A configuration has low sweep so there is very little twist due to bending. Thus, since the outboard wing tip is not twisting much, large differences in the pressure distribution do not appear. If these calculations had been performed before test entry, the confidence level on the tunnel data could have been increased.

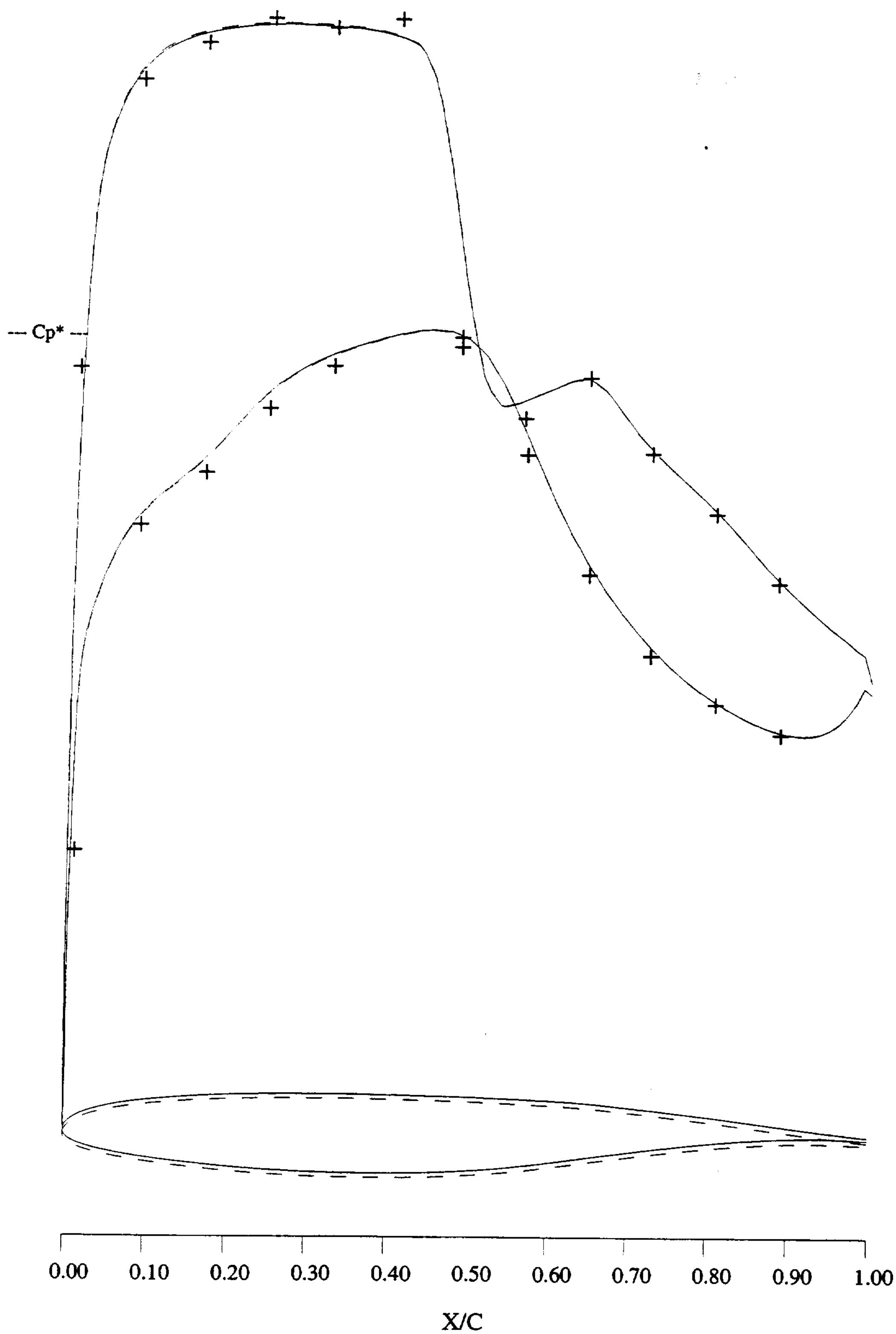

Figure 5: C_p distribution at near wing tip station. Navier-Stokes calculations, $M = 0.80$, $Re = 2.5$ million
———, Aeroelastic solution
– – –, Solid geometry solution
+ + +, Wind tunnel data

Demonstration Problem (2):
Wind Tunnel Business Jet Model, Higher Sweep

The next figure shows a similar comparison of pressure distributions for rigid, aeroelastic, and wind tunnel data from model B. It is immediately clear that the deflections predicted by the aeroelastic calculation have a much larger impact on the pressure distributions than in the case of model A. The changes in the pressure distributions show all the typical signs of aeroelastic relief in swept-back wings: a decrease in the twist of the outboard sections of the wing with the consequent forward motion of the shock location and alterations in the spanload distribution.

Although the aeroelastic solution does not agree fully with the experimental data for model B, it is clear that the aeroelastic effects change the solution in the correct direction to improve the agreement. Additional discrepancies are believed to be caused by inaccuracies in the Baldwin-Lomax turbulence model. It is also evident that this wind tunnel model is flexible enough that significant aeroelastic effects are present in the wind tunnel data. In view of the small increase in cost of the aeroelastic solutions, it is clear that this type of analysis is preferable for the comparison between experimental and wind tunnel data in order to eliminate some of the uncertainties causing the differences.

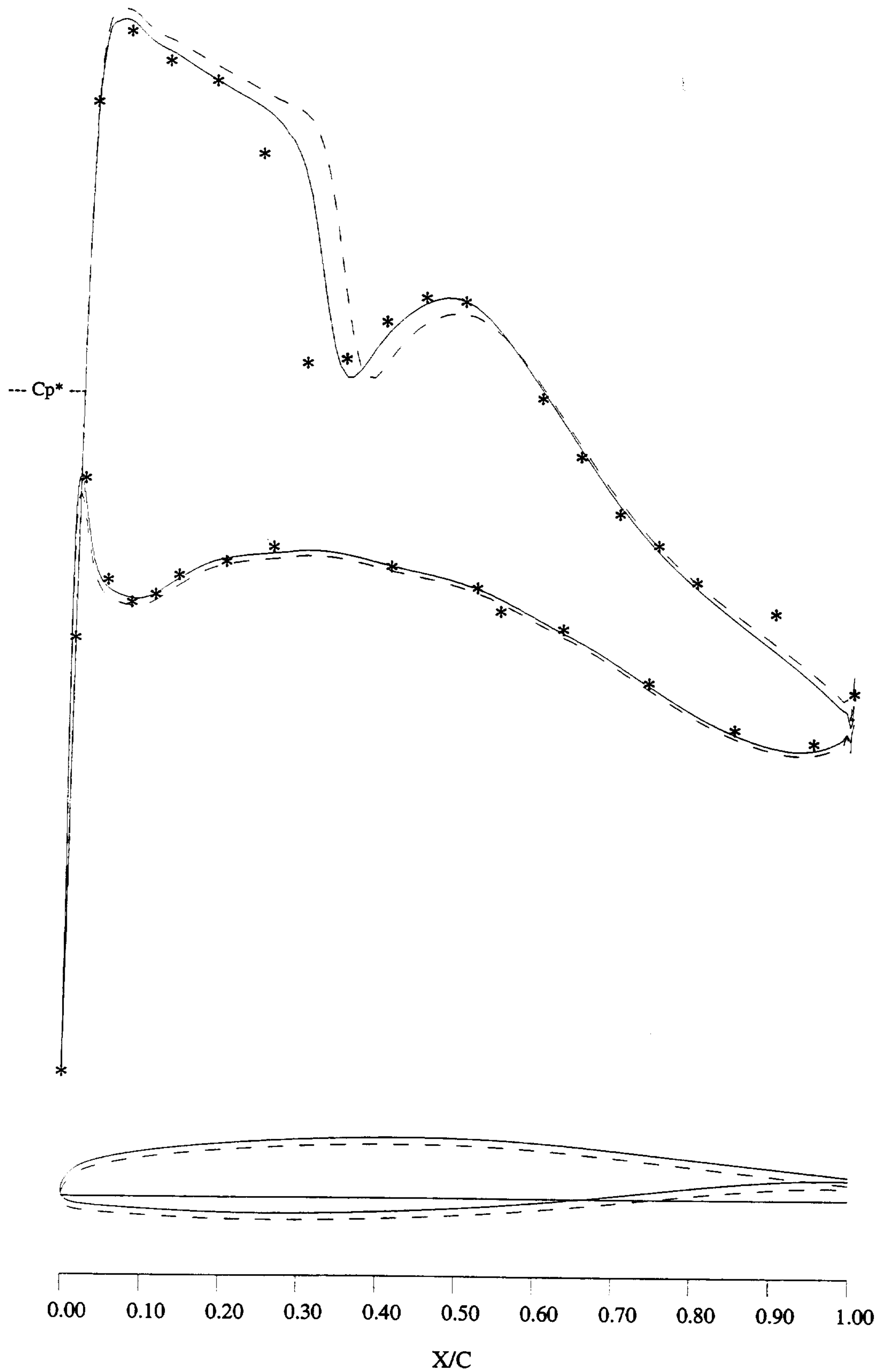

Figure 7: C_p distribution at near wing tip station. Navier-Stokes calculations, $M = 0.80$, $Re = 2.4$ million
———, Aeroelastic solution
– – –, Solid geometry solution
+ + +, Wind tunnel data

Demonstration Problem (3): Aerodynamic Shape Optimization of a Flight Wing-Alone Geometry (Rigid)

Before presenting aeroelastic results using the second structures model, the aerodynamic shape optimization of a rigid geometry is shown as a baseline representative of our earlier works. The structural model is completely inactive.

The geometry to be optimized is the wing of a typical business jet having the smaller wing sweep of model A above. The flow field is computed using the Euler equations. A multiblock mesh following a C-H topology is constructed around the configuration with a total of 32 blocks and 750,000 cells. A total of 133 design variables are used to parametrize the surface of the wing. Hicks-Henne perturbation functions combined with exponential functions at the wing trailing edges were distributed across the entire span of the wing to provide full geometric flexibility. Thickness constraints typical of our previous works are imposed in order to maintain the structural soundness of the final outcome of the design process. These constraints include spar depth constraints at 10% and 80% chord, a leading edge radius constraint ahead of the 2% location, a trailing edge included angle constraint behind the 95% chord location, and an additional thickness constraint to maintain maximum thickness and fuel volume at 40% chord. It should be noted that these thickness constraints are the results of low-fidelity analyses and are derived from years of accumulated experience by aerodynamic and structural designers. The objective function is the wing C_D at a fixed cruise C_L of 0.35 and a fixed M_∞ of 0.82. Note that these flight conditions represent a significant increase in both Mach number and lift coefficient over those for which the original baseline wing was designed. It is therefore expected that improved aerodynamic designs should be attainable with the use of optimization. All wing-alone design calculations presented hereafter were carried out on an SGI Origin2000 parallel computer using 16 processors.

The results of this single-point shape optimization process can be seen in the accompanying figure which shows the initial and final pressure distributions for several span stations along the wing. Similar results have been presented in AIAA Paper 95-0123, Aerodynamic Shape Optimization of Wing and Wing-Body Configurations Using Control Theory, by Reuther and Jameson. Notable features are the decrease in induced drag due to the shifting of the spanload towards the tip and the decrease of wave drag that results from the weakening or disappearance of the shock waves on the upper and lower surfaces. Note that at the location of the front spar (10% chord) where the thickness constraint is active, the lower surface pressure distribution at some of the stations exhibits an oscillation and a loss of lift due to the requirement of maintaining thickness. The changes in airfoil shape are rather small, but the overall effect on the C_D of the configuration is drastic: after 20 design iterations, the total value of C_D is reduced by 31%, or from 95.6 counts to 65.6 counts.

<Continued on the next page.>

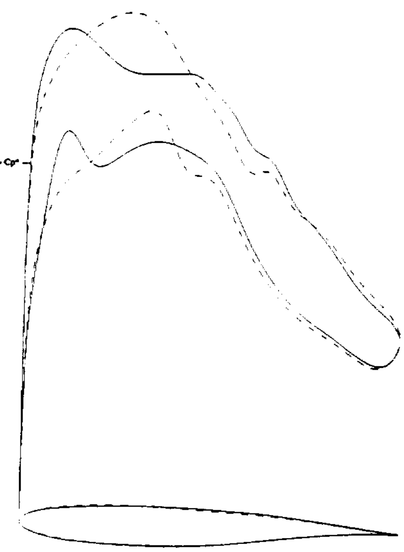

8a: span station $z = 0.194$

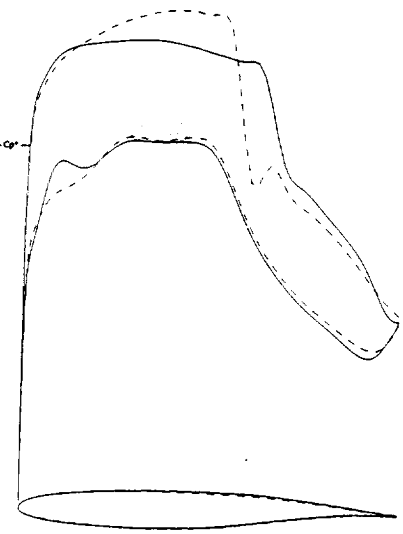

8b: span station $z = 0.387$

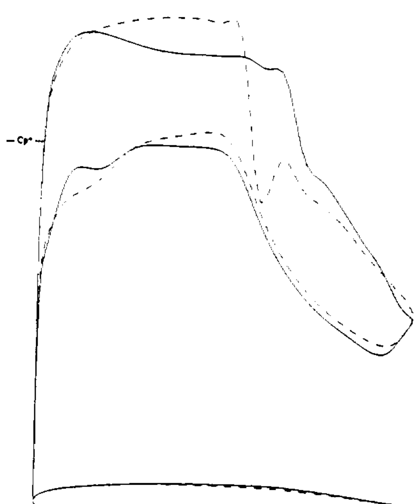

8c: span station $z = 0.581$

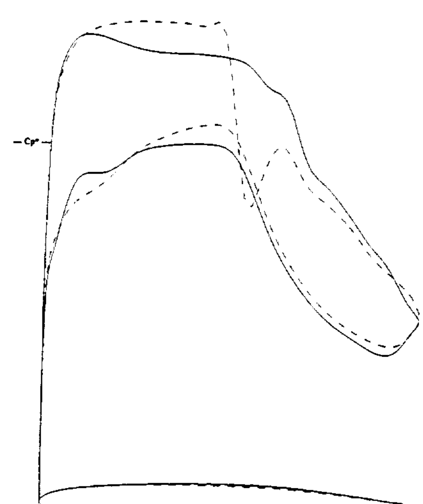

8d: span station $z = 0.775$

Figure 8: Typical Business Jet Configuration. Drag Minimization at Fixed C_L.
Rigid Design, $M = 0.82$, $C_L = 0.35$, 133 Hicks-Henne variables. Spar Constraints Active.
Rigid Analysis at Fixed C_L.
– – –, Initial Pressures
———, Pressures After 20 Design Cycles.

Demonstration Problem (3): Aerodynamic Shape Optimization of a Flight Wing-Alone Geometry (Rigid) (Continued)

As shown in the next figure, a comparison of aeroelastic analyses of the baseline and resulting designs reveals that the maximum stress levels for the rear spar have increased substantially in the inboard wing region, especially near the crank point.

<Continued on the next page.>

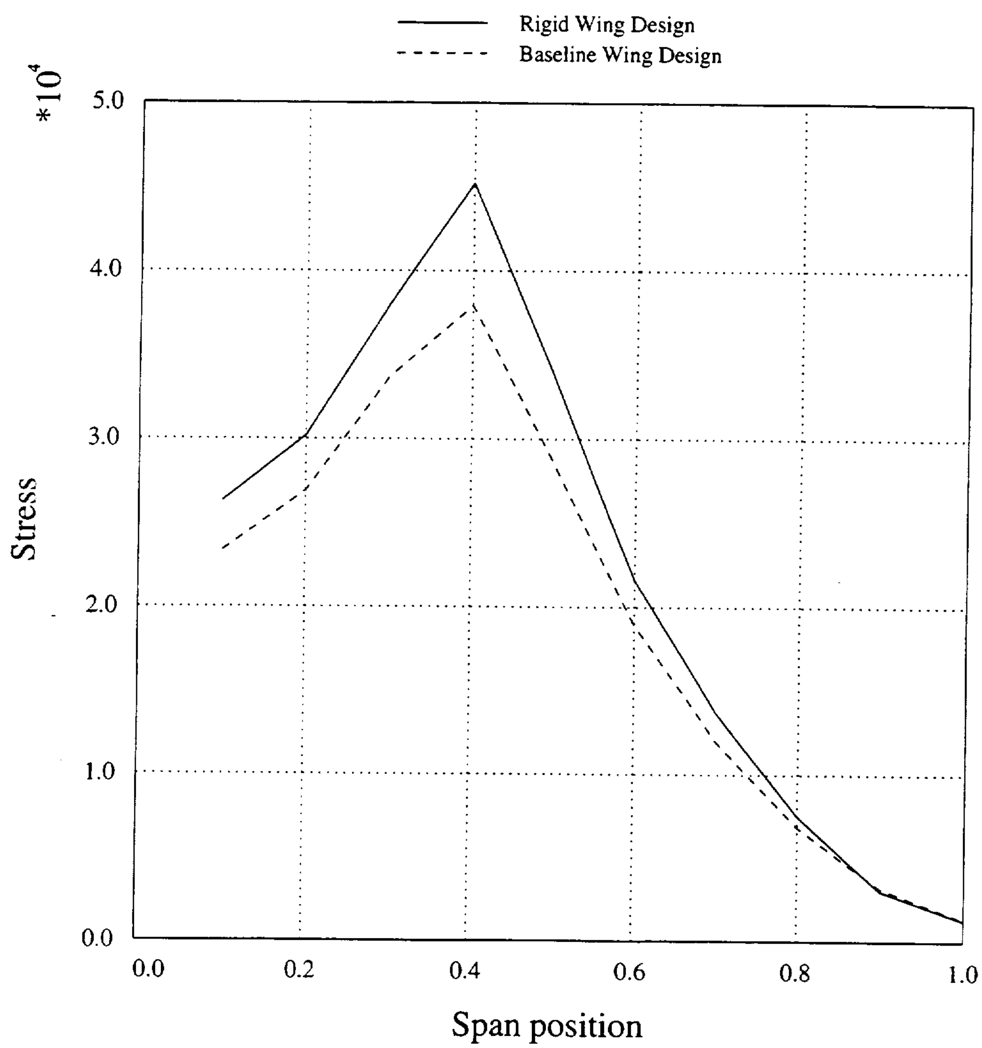

Figure 10: Spanwise Stress Distribution for the Rear Spar.
Comparison of the Rigid Design and the Baseline Design.
Wing Alone Configuration.
Rigid Design. Drag Minimization at Fixed C_L.
Aeroelastic Analysis at Fixed C_L.

Demonstration Problem (3): Aerodynamic Shape Optimization of a Flight Wing-Alone Geometry (Rigid) (Continued)

The following figure shows that the reason for the increase in stress in the rear spar is that the span loading has been shifted outboard substantially for this rigid-wing design in an effort to reduce the induced drag. Since the optimization algorithm cannot see a structural penalty in this outboard shift of the spanload, it simply maintains the required thickness constraints and redistributes the load as it sees fit.

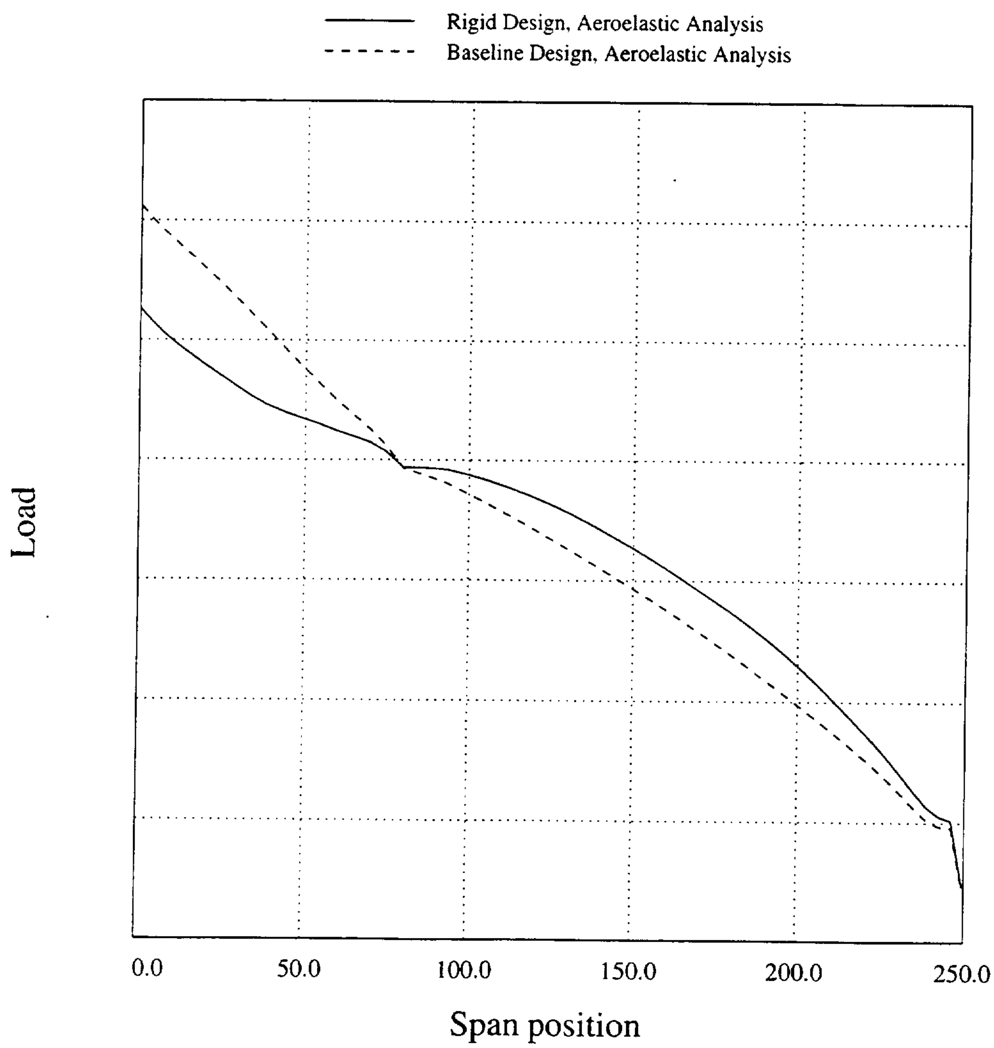

Figure 9: Spanwise Load Distribution.
Comparison of the Rigid Design and the Baseline Design.
Wing Alone Configuration.
Rigid Design, Drag Minimization at Fixed C_L.
Aeroelastic Analysis at Fixed C_L.

Demonstration Problem (4): Aero-Structural Shape Optimization of a Flight Wing-Alone Geometry

The idea in this wing-alone design case is to incorporate some basic elements of the aero-structural interaction present in the existing design methodology. Despite the fact that development of the complete coupled sensitivity analysis is not yet implemented, several results of interest can be shown which establish the soundness of the procedure. In this particular case, we utilize the geometry of the previous example, the same CFD mesh, and the same set of aerodynamic shape variables, but include the second structural model and a composite objective function. The artificial thickness constraints are removed, leaving only the leading edge radius and included trailing edge angle constraints. The design is now set up with both the coefficient of drag and the L^2 norm of the stress in the structure as a combined cost function. This combined penalty function method can be thought of as a first cut approach to minimizing total drag in the presence of structural constraints. The ASO adjoint system is used to calculate the gradient of the aerodynamic cost function C_D and finite differencing is used to calculate the gradient contribution from the structural changes. While these sensitivities are not fully accurate because of the lack of coupling, they provide our first approximation for solving the AESO (AeroElastic Shape Optimization) problem. The weights between the two components of the objective function were arbitrarily chosen such that the stress penalty was equal to about 40% of the drag penalty. This choice resulted in an optimized design where the L^2 norm of the stress in the structure remained largely unchanged.

The next figure depicts the pressure distributions before and after the design process. Once more, the resulting pressure distributions and changes to the sections look similar to those from the previous case. However, there are some noteworthy differences. The oscillation in the lower surface pressure distribution seen in the earlier solution near the 10% span chord location is not present. Since we are no longer imposing artificial thickness constraints, the resulting design was able to thin this region with some benefit to the aerodynamics and without a significant increase in the structural stress distributions. The more clearly observable difference between this solution and the previous one is the dramatic thickening of the airfoil section near the crank point. This is the location where the highest stress level is recorded in the rear spar.

<Continued on the next page.>

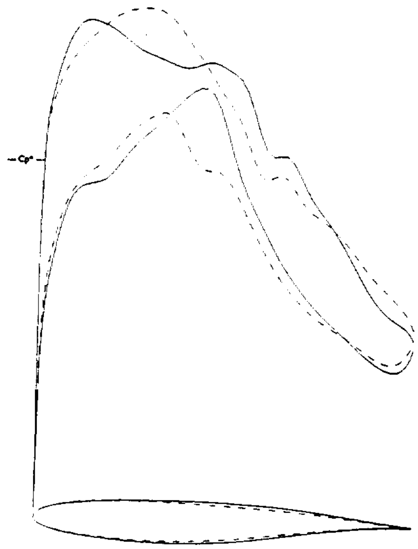

14a: span station $z = 0.194$

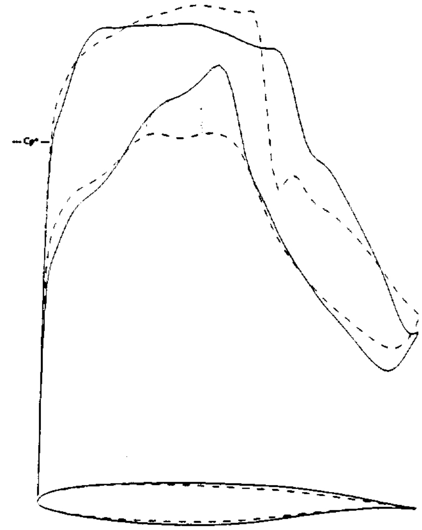

14b: span station $z = 0.387$

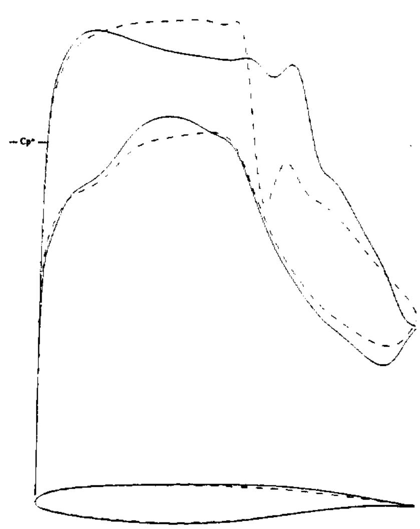

14c: span station $z = 0.581$

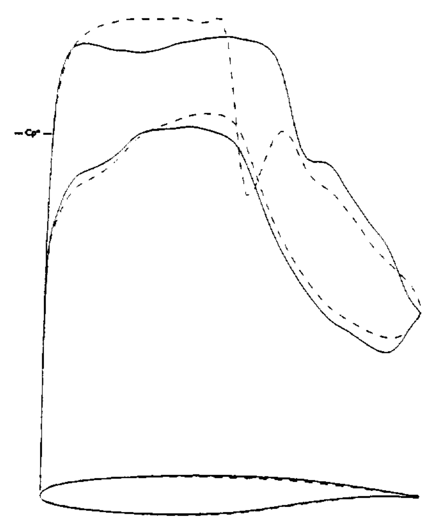

14d: span station $z = 0.775$

Figure 14: Typical Business Jet Wing Configuration. Drag + Stress Minimization at Fixed C_L.
Aeroelastic Design with Stress Penalty Function. $M = 0.82$, $C_L = 0.35$
133 Hicks-Henne variables. Spar Constraints Inactive.
Aeroelastic Analysis at Fixed C_L.
– – –, Initial Pressures
———, Pressures After 13 Design Cycles.

Demonstration Problem (4): Aero-Structural Shape Optimization of a Flight Wing-Alone Geometry (Continued)

The following figure shows that the design has dramatically changed the loading distribution by moving part of the load outboard. This has a corresponding tendency to increase the load at the critical crank point rear spar location. The design algorithm has chosen to increase the airfoil thickness at this station to compensate for the shift in load outboard. It is worth remembering that changes to the wing thickness can have an effect on wave drag. Indeed a re-examination of the previous figure reveals that the shock strength on the lower surface has been increased from the original design. However, since the final design in this case is less than one count higher in drag than that achieved in the previous case, this weak lower surface shock must not be incurring a significant drag penalty.

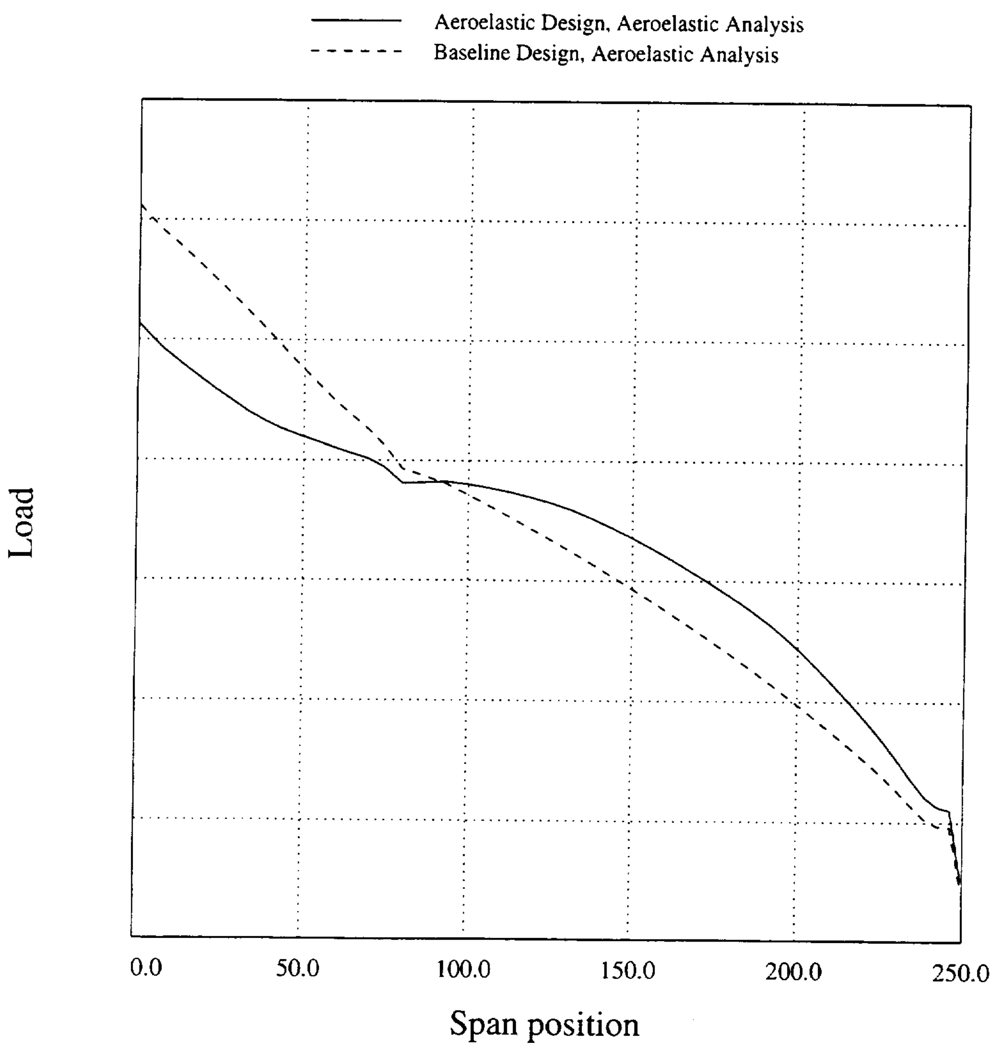

Figure 15: Spanwise Load Distribution.
Comparison of the Aeroelastic Design and the Rigid Design.
Wing Alone Configuration.
Aeroelstic Design, Drag + Stress Minimization at Fixed C_L.
Aeroelastic Analysis at Fixed C_L.

Demonstration Problem (4): Aero-Structural Shape Optimization of a Flight Wing-Alone Geometry (Continued)

The final figure illustrates the benefit of adding the stress penalty function to the design problem. The spanwise stress on the rear spar at the planform break has been reduced slightly in the optimized configuration. Assuming that no other constraints were placed on the problem, it would then be possible to shift the load on the wing outboard, while thickening the inboard sections so as to keep the wing weight approximately constant. With a more accurate description of the cost functions and constraints in the problem, these kinds of trade studies will allow the designer to make better-informed choices about the development of the configuration.

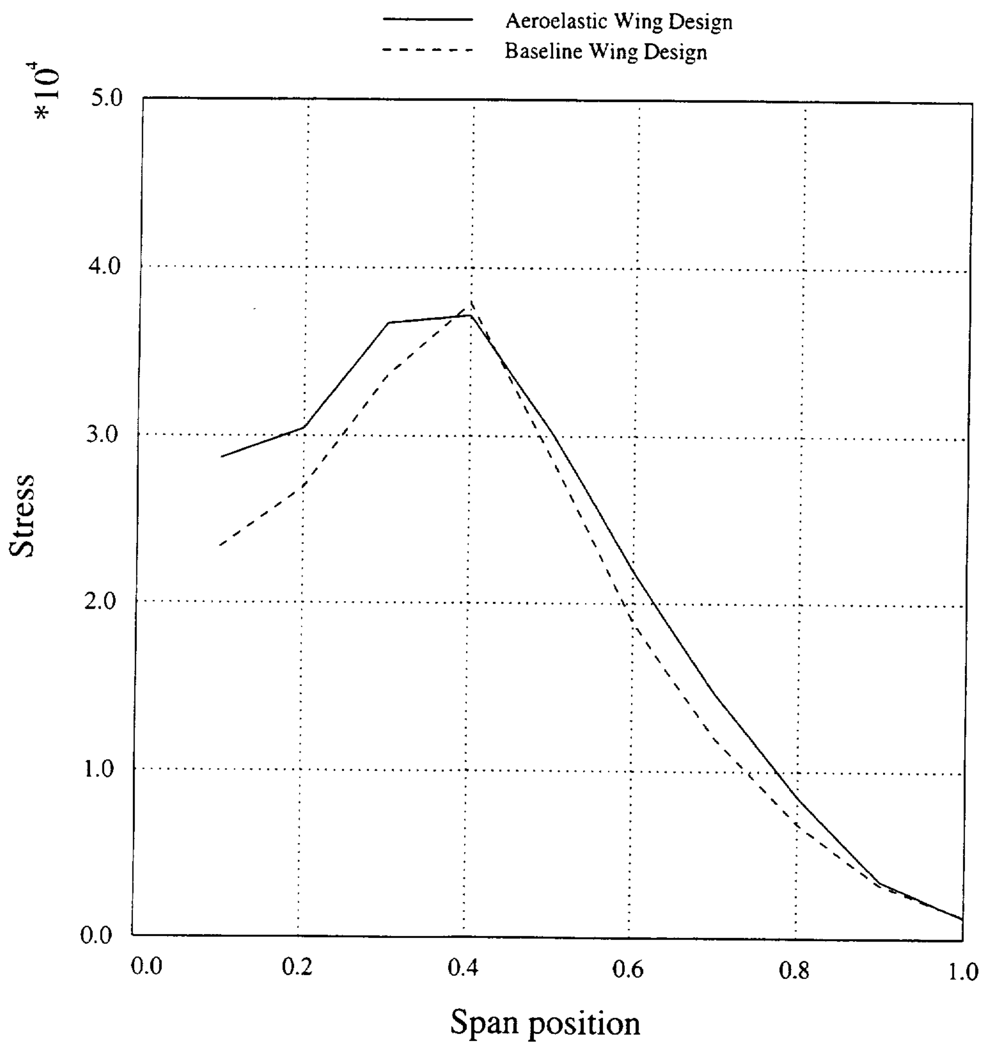

Figure 16: Spanwise Stress Distribution for the Rear Spar.
Comparison of the Aeroelastic Design and the Rigid Design.
Wing Alone Configuration.
Aeroelstic Design, Drag + Stress Minimization at Fixed C_L.
Aeroelastic Analysis at Fixed C_L.

Conclusions

The work presented here represents our first step towards the establishment of a high-fidelity multidisciplinary environment for the design of aerospace vehicles. The environment is in its infancy and should continue to evolve during the coming years. At its core, it consists of the following key elements:

- High-fidelity modeling of the participating disciplines (RANS flow models for the aerodynamics and linear finite element model for the structure).
- An OML geometry database which serves as the interface between disciplines. This database contains information regarding the current shape of the configuration and the physical solutions from the participating disciplines.
- A force- and work-equivalent coupling algorithm designed to preserve a high level of accuracy in the transfer of loads and displacements between aerodynamics and structures.
- A framework for the computation of coupled sensitivities of the aero-structural design problem.

This design environment has been used to perform RANS aeroelastic analysis of complete configuration flight and wind-tunnel models with an additional cost which is less than 10% of the cost of a traditional rigid-geometry CFD solution. These solutions can be used to determine *a priori* whether significant aeroelastic corrections will or will not be needed for the resulting wind tunnel data.

In addition, simplified design cases have been presented that include the effect of aeroelastic deformations in the design process. These cases have shown that our design methodology is able to predict the correct trades between aerodynamic performance and structural properties present in these types of wing design problems. A structural stress penalty function added to the wing coefficient of drag allowed elimination of the artificial thickness constraints that are typically imposed in aerodynamic shape optimization methods. This rudimentary coupling of aerodynamics and structures in the design not only eliminates the necessity to impose artificial constraints, but also produces designs where aerodynamic performance is balanced with a measure of wing structural weight.

Conclusions

- **Steps Toward a Flexible Design Environment have been Completed**
  - All Software Modularized
  - APIs Used to Link Modules
  - Common OML Geometry Interface Defined
- **A Multiple Geometry Capability has been Developed**
- **A Multiple Discipline Capability has been Developed**
  - Consistent and Conservative Coupling Using OML
  - Aeroelastic Design Problem Used as Demonstration

Future Work

Further work will focus on the continued development and application of the MDO framework outlined here. Topics requiring significant research include sensitivity analysis, optimization strategy, Navier-Stokes-based design, use of commercially available CSM codes, multipoint design, and CAD integration. The multiple-geometry capability is indispensable for treating the multipoint "core" problem that represents the final major Configuration Aerodynamics activity of the HSR program before it winds down at the end of FY99. (Performances at Mach 2.4, Mach 1.1, and Mach 0.9 are to be optimized both sequentially and simultaneously.) The aeroelastic capability may also be applied as part of the Ames "extended" variation of this multipoint problem.

Future Work

- Testing and Application of Multiple Geometry Design Capability for HSR Multipoint Core Problem
- Testing of Aeroelastic Shape Optimization for HSR Multipoint Extended Problem
- More Work to Extend the Flexibility of the Software

REPORT DOCUMENTATION PAGE

Form Approved
OMB No. 07704-0188

1. AGENCY USE ONLY *(Leave blank)*	2. REPORT DATE	3. REPORT TYPE AND DATES COVERED
	December 1999	Conference Publication

4. TITLE AND SUBTITLE
1999 NASA High-Speed Research Program Aerodynamic Performance Workshop
Volume I—Configuration Aerodynamics

5. FUNDING NUMBERS
537-07-51-10

6. AUTHOR(S)
Edited by David E. Hahne

7. PERFORMING ORGANIZATION NAME(S) AND ADDRESS(ES)
NASA Langley Research Center
Hampton, VA 23681-2199

8. PERFORMING ORGANIZATION REPORT NUMBER
L-17911A

9. SPONSORING/MONITORING AGENCY NAME(S) AND ADDRESS(ES)
National Aeronautics and Space Administration
Washington, DC 20546-0001

10. SPONSORING/MONITORING AGENCY REPORT NUMBER
NASA/CP-1999-209704/
VOL1/PT1

11. SUPPLEMENTARY NOTES

12a. DISTRIBUTION/AVAILABILITY STATEMENT
Unclassified–Unlimited
Subject Category 02 Distribution: Nonstandard
Availability: NASA CASI (301) 621-0390

12b. DISTRIBUTION CODE

13. ABSTRACT ***(Maximum 200 words)***
NASA's High-Speed Research Program sponsored the 1999 Aerodynamic Performance Technical Review on February 8-12, 1999 in Anaheim, California. The review was designed to bring together NASA and industry High-Speed Civil Transport (HSCT) Aerodynamic Performance technology development participants in the areas of Configuration Aerodynamics (transonic and supersonic cruise drag prediction and minimization), High Lift, and Flight Controls. The review objectives were to (1) report the progress and status of HSCT aerodynamic performance technology development; (2) disseminate this technology within the appropriate technical communities; and (3) promote synergy among the scientists and engineers working on HSCT aerodynamics. In particular, single and midpoint optimized HSCT configurations, HSCT high-lift system performance predictions, and HSCT simulation results were presented, along with executive summaries for all the Aerodynamic Performance technology areas. The HSR Aerodynamic Performance Technical Review was held simultaneously with the annual review of the following airframe technology areas: Materials and Structures, Environmental Impact, Flight Deck, and Technology Integration. Thus, a fourth objective of the Review was to promote synergy between the Aerodynamic Performance technology area and the other technology areas of the HSR Program.

14. SUBJECT TERMS
High-speed research; High-Speed Civil Transport

15. NUMBER OF PAGES
865

16. PRICE CODE
A99

17. SECURITY CLASSIFICATION OF REPORT	18. SECURITY CLASSIFICATION OF THIS PAGE	19. SECURITY CLASSIFICATION OF ABSTRACT	20. LIMITATION OF ABSTRACT
Unclassified	Unclassified	Unclassified	UL

NSN 7540-01-280-5500

Standard Form 298 (Rev. 2-89)
Prescribed by ANSI Std. Z39-18
298-102